

**Evolution Of The Subcontinental Lithospheric Mantle
Below A Major Tectono-Volcanic Structure:
Constraints From Mantle Xenoliths Along The
Cameroon Volcanic Line**

Inaugural dissertation
of the Faculty of Science,
University of Bern

presented by

Siggy Signe, Nformidah-Ndah

from Cameroon

Supervisors of the doctoral thesis:

Prof. Jörg Hermann

Institute of Geological Sciences, University of Bern

Dr. Peter Tollan

Department of Earth Sciences, ETH Zurich

Evolution Of The Subcontinental Lithospheric Mantle Below A Major Tectono-Volcanic Structure: Constraints From Mantle Xenoliths Along The Cameroon Volcanic Line

Inauguraldissertation
der Philosophisch-naturwissenschaftlichen Fakultät der
Universität Bern

vorgelegt von

Siggy Signe, Nformidah-Ndah

Von Kamerun

Leiter der Arbeit:

Prof. Jörg Hermann
Institut für Geologie, Universität Bern

Dr. Peter Tollan
Departement Erdwissenschaften, ETH Zürich

Von der Philosophisch-naturwissenschaftlichen Fakultät angenommen

Bern, 12 November 2021

Der Dekan:
Prof. Dr. Zoltan Balogh

This work is licensed under CC BY-NC-ND 4.0.

To view a copy of this license, visit <http://creativecommons.org/licenses/by-nc-nd/4.0/>



**Attribution-NonCommercial-
NoDerivatives 4.0 International
(CC BY-NC-ND 4.0)**

TABLE OF CONTENT

Abstract.....	v
List of figures	ix
List of tables	xii
Appendices	xiii

CHAPTER I

GENERAL INTRODUCTION.....	1
I.1. RATIONALE AND OBJECTIVES.....	3
I.2. GEOLOGIC SETTING.....	6
I.2.1. The Precambrian basement of Cameroon.....	6
I.2.2. The Cameroon Volcanic Line	7
I.2.2.1. The Kapsiki plateau	10
I.2.2.2. The Ngaoundere Plateau (Likok).....	12
I.2.2.3. The Oku Volcanic Field.....	13
I.3. ANALYTICAL TECHNIQUES/ METHODS	16
I.3.1. Sample preparation.....	16
I.3.2. Electron Probe Micro-Analyser.....	17
I.3.3. Laser Ablation Inductively Coupled Plasma Mass Spectrometry.....	17
I.3.4. Fourier Transform Infrared Spectroscopy	18
I.3.5. Image analysis	19
I.4. SUMMARY OF THESIS	19
REFERENCES	22

CHAPTER II

DEPLETION AND REFERTILISATION OF THE LITHOSPHERIC MANTLE BELOW THE KAPSIKI PLATEAU (NORTHERN CAMEROON VOLCANIC LINE) DEDUCED FROM TRACE ELEMENT AND H₂O SYSTEMATICS IN MANTLE XENOLITHS.....	33
II. 1. INTRODUCTION	36
II.2. RESULTS	38
II.2.1. Petrography	38
II.2.2. Mineral chemistry	40

II.2.2.1. Major element systematics.....	40
II.2.2.2. Trace element systematics	42
II.2.3. Infrared spectra and H ₂ O concentrations.....	46
II.2.4. Equilibrium temperatures and oxygen fugacity.....	46
II.3. DISCUSSION	49
II.3.1. Mantle xenoliths textures.....	49
II.3.2. Partial melting.....	49
II.3.3. Metasomatism.....	52
II.3.4. Fluid/melt composition.....	54
II.3.5. Implication of water budget.....	59
I.4. CONCLUSION	62
REFERENCES	63

CHAPTER III

NGAOUNDERE LIKOK AND THE OKU VOLCANIC FIELD.....	77
III.1. INTRODUCTION	79
III.2. RESULTS	81
III.2.1. Petrography/textures/microstructures.....	81
III.2.1.1. Basaltic cortex	85
III.2.1.2. Adamawa Volcanic massif xenoliths	86
III.2.1.3. Oku Volcanic Field xenoliths	87
III.2.1.4. Grain size distribution	90
III.2.2. Mineral chemistry	96
III.2.2.1. Major element systematics	96
III.2.2.2. Trace element systematics	112
III.2.2.3. Bulk rock composition.....	130
III.3. DISCUSSION	140
III.3.1. Equilibrium conditions and oxygen fugacity	140
III.3.1.1. Temperatures	140
III.3.1.2. Intermineral partition coefficients	147
III.3.1.3. Oxygen fugacity	148
III.3.2. Mantle depletion and melting model.....	149

III.3.3. Metasomatic processes	155
III.3.4.1. Origin of spongy textures and secondary clinopyroxene	156
III.3.4.2. Nature of metasomatism	158
III.3.4.3. Metasomatising agents	161
III.3.4.4. Significance of the positive Eu anomaly	167
III.3.4.5. Origin of olivine websterites	168
III.3.4. Orthopyroxene as a potential indicator of metasomatic processes	168
III.3.5. Interpretation of olivine trace elements (olivine as a petrological tracer)	170
III.4. CONCLUSION	171
REFERENCES	172

CHAPTER IV

WATER CONTENTS IN THE SUBCONTINENTAL LITHOSPHERIC MANTLE BELOW THE CAMEROON VOLCANIC LINE	189
IV.1. INTRODUCTION	191
IV.2. RESULTS	192
IV.2.1. Clinopyroxene	192
IV.2.2. Orthopyroxene	195
IV.2.3. Olivine	196
IV.3. DISCUSSION	197
IV.3.1. Significance of the infrared spectra and H ₂ O contents	197
IV.3.1.1. Olivine	197
IV.3.1.2. Orthopyroxene	198
IV.3.1.3. Clinopyroxene	199
IV.3.2. H ₂ O partitioning between clino- and orthopyroxene	200
IV.3.3. Initial H ₂ O content in the mantle source	204
IV.3.4. Control of H ₂ O contents by metasomatism	206
IV.3.5. Implications for the CVL	207
IV.4. CONCLUSION	208
REFERENCES	209

Chapter V

DISCUSSION AND CONCLUSION	217
V.1. INTRODUCTION	219
V.2. GEODYNAMIC CONTEXT AND MODELS.....	219
V.3. COMPOSITION AND ORIGIN OF MAGMATISM	223
V.4. THE SUBCONTINENTAL LITHOSPHERIC MANTLE BELOW THE CVL.	225
REFERENCES	231
Appendices.....	237
Declaration of consent	272
Curriculum vitae.....	Error! Bookmark not defined.

ABSTRACT

The Cameroon Volcanic Line represents an important but enigmatic geologic structure on the African continent. It is an oceanic and a continental alignment of volcanoes and plutons with no spatial age progression along a distance of ~1600 km, even though magmatism has been ongoing for the last 70 Ma. A single process whereby magma is generated from one region to another is therefore unlikely in this case and different mechanisms could be involved especially if melting occurred at different times under different conditions. Tracing the evolution of the sub-continental lithospheric mantle below the Cameroon Volcanic Line is therefore essential to understand surface manifestations through time, since it is possible that the SCLM was significantly modified during the Pan-African orogeny and the geodynamic processes that occurred during this time are poorly understood.

The CVL is built across two distinct lithostructural domains in Cameroon; the North-West Cameroon and the Adamawa Yade domains delimited by NNE-SSW faults. Xenoliths were collected from these domains at the Oku Volcanic Field and the Kapsiki Plateau for the North-West Cameroon Domain and the Adamawa Volcanic Massif for the Adamawa Yade Domain. These domains correspond to a juvenile Proterozoic area and a Paleoproterozoic area with Archean relics respectively. Major and trace element systematics including the evaluation of water contents in 33 mantle xenolith samples associated with alkaline basalts from the CVL were investigated to constrain mantle processes and equilibrium conditions.

The xenoliths sampled are mainly clinopyroxene bearing spinel harzburgites for the Kapsiki plateau and spinel lherzolites for the Oku Volcanic Field and Adamawa Volcanic Plateau. Subordinate olivine websterites are also found in the Oku Volcanic Field. Two-pyroxene thermometry based on major element concentrations, Ca in orthopyroxene and Al in olivine thermometers shows two temperature groups, ranging from 810 to 1030°C and 1020 to 1160°C. The high and low-temperature groups are restricted to xenoliths from the Oku Volcanic Field and Adamawa Volcanic Plateau, whereas the Kapsiki xenoliths fall in the low-temperature group.

A simple non-modal fractional partial melting model applied to trace element concentration of orthopyroxenes show that the CVL xenoliths have been affected by

variable degrees of partial melting ranging from 0-30%. The xenoliths from the Kapsiki are the most refractory with partial melting always above 20%. For the Oku Volcanic Field and Adamawa Volcanic Plateau, partial melting is below 15%.

Xenoliths from the CVL show evidence of modal metasomatism with the presence of secondary clinopyroxenes and amphibole. Cryptic metasomatism is shown by variable enrichments in LREEs and MREEs and incompatible trace elements. Discrimination diagrams of Ti/Eu vs. (La/Yb)_N in clinopyroxene show that xenoliths from the Kapsiki plateau were metasomatized by carbonatite-silicate melts/fluids; those from the Oku Volcanic Field show both metasomatism by silicate and carbonatite melts/fluids while the Adamawa Volcanic Plateau xenoliths are dominated by silicate metasomatism with minor indications of carbonatite metasomatism. A group of samples from the Oku Volcanic Field do not show any evidence for metasomatism but are rather similar to a MORB source mantle. Amphiboles from the Oku Volcanic Field display trace element patterns that are consistent with metasomatic activity that was linked to subduction, likely related to the Pan African orogeny. Other trace element ratios such as Ti/Sr and Zr/Hf in orthopyroxene efficiently distinguish between the different metasomatic agents, which indicates that orthopyroxene could be as useful as clinopyroxenes in tracing mantle metasomatism especially when clinopyroxene is absent. On the other hand, trace elements in olivine are more challenging due to very low concentration and a dominant control of temperature on trace element incorporation.

The water contents of olivine and pyroxenes were obtained by FTIR spectroscopy using unpolarised light on unoriented crystals. Olivine water contents are very low <2ppm and have been attributed to its depleted chemistry e.g., low Ti (0.6-34 ug/g) and low temperature of equilibration with Cr (31-108 ug/g), which hindered hydrogen incorporation. Orthopyroxene water contents fall within a narrow range and are similar in all locations along the CVL. Clinopyroxenes show two sets of water contents. The water contents for the Kapsiki plateau and the Oku Volcanic Field are low (15-320 ppm) whereas, for the Adamawa Volcanic Plateau, they are extremely high (560-910 ppm). These differences in water contents were interpreted to reflect the low and high-water activity of metasomatizing fluids for the North-West Cameroon Domain and Adamawa Yade Domain respectively. Calculated bulk rock water contents are very low (16±10

ppm), which indicates that metasomatism did not result in the weakening of the mantle below the CVL by hydrogen related defects.

While there are no traces of carbonatite magmatism along the CVL, there is widespread evidence for carbonatite-silicate melts that reacted with the mantle and that could be the source for mantle derived CO₂ outgassing in the Oku Volcanic Field. The calculated fO_2 of the mantle is overall reducing (0.09-2.28), suggesting that carbon mantle outgassing occurs in the form of CH₄.

Our new data provides evidence for local and regional heterogeneity of the SCLM below the CVL and the geochemical features observed are in favour of small-scale local convection proposed for by the edge convection model for the origin of the CVL magmatism.

LIST OF FIGURES

Chapter I

Figure 1.1: Sample location of studied xenoliths along the Cameroon Volcanic Line....	5
Figure 1.2: Generalised geologic map of a portion of West Gondwana b) Geologic map of Cameroon, showing major lithotectonic units	8
Figure 1.3: Cameroon Volcanic Line with major Cenozoic centres and the Central African Shear Zone. b) Geological map of Kapsiki	11
Figure 1.4: Geologic map of the Adamawa region	14
Figure 1.5: Geologic map of the Oku Volcanic Field	15

Chapter II

Figure 2.1: Thin section scan and micro photographs of Kapsiki xenolith.....	39
Figure 2.2.a: Average Mg# of olivine, ortho- and clinopyroxene. b) major element compositions of orthopyroxene and c, d) clinopyroxene showing two generations.	41
Figure 2.4: Orthopyroxene and clinopyroxene REEs normalised to primitive mantle values of Palme and O’Neill, 2014.	44
Figure 2.5.a: Orthopyroxene and b) Clinopyroxene TEs normalised to primitive mantle values of Palme and O’Neill, 2014.	45
Figure 2.6: Average unpolarised FTIR spectra for a) olivine, orthopyroxene, and b) clinopyroxenes from the Kapsiki peridotites.....	47
Figure 2.7.a: Mg# in olivine versus Cr# in spinel b) Cr# versus TiO ₂ in spinel.	51
Figure 2.8: Fractional partial melting model of orthopyroxene trace elements compared to Kapsiki orthopyroxene REE data.....	51
Figure 2.9: Trace element plots of clinopyroxene compared to literature data from intra plate, subduction and Abyssal settings.....	55
Figure 2.10a: Plot of Ti/Eu vs chondrite normalised La/Yb ratios in clinopyroxenes, compared to clinopyroxenes from the Cameroon Volcanic Line. b, c) Plot of Ti/Eu vs Zr/Hf and Ti/Sr vs Ti/Eu in clinopyroxenes compared samples from the French Massif Central. d.) Ca/Al vs Mg# in clinopyroxene	57
Figure 2.11a: Water contents of orthopyroxene and clinopyroxene as a function depth. (b) Variation of Al ₂ O ₃ (wt. %) in orthopyroxene as a function of depth	62

Chapter III

Figure 3.1: Sample location of studied xenoliths along the Cameroon Volcanic Line .	82
Figure 3.2: Photographs of hand samples of CVL xenoliths.	83
Figure 3.3: Photomicrographs of thin sections of CVL host basalts	86
Figure 3.4: Photomicrographs of xenoliths from the Adamawa Volcanic massif	87
Figure 3.5: Photomicrographs of thin sections of xenoliths from Enep	89
Figure 3.6: Photomicrographs of thin sections of Etome and Kuk	91
Figure 3.7: Photomicrographs of thin sections of Nyos and Oku xenoliths	92
Figure 3.9: Representative grain size distribution histograms of mantle xenolith minerals of the Cameroon Volcanic Line.	94
Figure 3.10: Major element compositions of olivine and orthopyroxene.	97
Figure 3.11: Core-rim major elements profiles for olivine in contact with host basalt .	98
Figure 3.12: Major element variation trends in clinopyroxene from the CVL xenoliths showing core, rim and spongy rim compositions	99
Figure 3.13: Major element plots of primary vs secondary clinopyroxenes in CVL xenoliths	100
Figure 3.15: Major element compositions of CVL amphibole	102
Figure 3.16: Trace element plots of olivine showing different elements vs Mg#.	113
Figure 3.17: Trace element plots of olivine showing different elements vs Al	114
Figure 3.18: Primitive mantle and chondrite normalized trace element diagrams for clinopyroxenes of group 1, 2 and 3 xenoliths.	119
Figures 3.18 cont'd: Primitive mantle and chondrite normalized trace element diagrams for clinopyroxenes of groups 4 and 5 xenoliths.	121
Figure 3.19: Primitive mantle normalized trace element patterns of heterogeneous clinopyroxenes (Group 6)	123
Figure 3.20: Primitive mantle normalized trace element patterns of secondary clinopyroxenes compared to the primary ones	124
Figure 3.21: Trace element concentrations and ratios of clinopyroxenes from the CVL xenoliths.	127
Figure 3.22: Primitive mantle and chondrite normalized trace element diagrams for orthopyroxenes of groups 1, 2 and 3 xenoliths.	128

Figure 3.22: Primitive mantle and chondrite normalized trace element diagrams for orthopyroxenes of group 4, 5 and 6 xenoliths. 129

Figure 3.23: Primitive mantle and chondrite normalized trace element diagrams for amphiboles..... 130

Figure 3.24: Variation of calculated whole rock major elements vs MgO..... 135

Figure 3.25: Primitive mantle normalized patterns of calculated whole rock compositions of the CVL xenoliths 138

Figure 3.26 a-e: Comparison of equilibrium temperatures calculated using different methods and f) Vanadium concentrations in ol versus oxygen fugacity..... 143

Figure 3.27: Inversion diagram for the calculation of equilibrium temperatures based on the temperature dependence of REE partitioning between orthopyroxene and clinopyroxene. 146

Figure 3.28: Orthopyroxene-clinopyroxene partition coefficients compared with partition coefficients of well equilibrated xenolith samples 148

Figure 3.29a: Plot of Cr# in spinel versus Fo in olivine for the studied xenoliths compared to Cameroon Volcanic Line olivines. b) Cr# in spinel versus TiO₂ in spinel 151

Figure 3.30: Fractional partial melting model of orthopyroxene trace elements compared to CVL orthopyroxene REE data. 153

Figure 3.31: Fractional partial melting model of clinopyroxene trace elements compared to CVL clinopyroxene REE data..... 154

Figure 3.32: Trace element plots of clinopyroxenes compared to literature data from intra plate, subduction and Abyssal settings..... 160

Figure 3.33 (a, b): Plots of Ti/Eu vs La/Yb in clinopyroxenes and orthopyroxenes in the studied xenoliths compared to the Kapsiki pyroxenes ((c, d, e, f). Plot of Ti/Eu vs Zr/Hf and Ti/Sr vs Ti/Eu in clinopyroxenes and orthopyroxenes. 163

Figure 3.34: Nb vs Zr (a) and Ti/Nb vs Zr/Nb (b) for amphiboles in CVL xenoliths. 166

Chapter IV

Figure 4.1: Representative average unpolarised infrared spectra of clinopyroxenes of the studied xenoliths..... 194

Figure 4.2: Representative average inferred spectra of orthopyroxene and olivine from the Cameroon Volcanic Line.	196
Figure 4.3: Variations of H ₂ O contents in orthopyroxene and clinopyroxene.....	201
Figure 4.4a: Partitioning (D _{cpx/opx}) of H ₂ O between coexisting orthopyroxene and clinopyroxene 4.4b) Expansion of 4.4a to show samples from the OVF. 4.4c) Relationship between temperature and partitioning of H ₂ O in the studied xenoliths..	202
Figure 4.5: H ₂ O contents vs clinopyroxene major element composition for the Oku Volcanic Field xenoliths.	203
Figure 4.6: H ₂ O contents vs orthopyroxene major element composition for the Oku Volcanic Field xenoliths.	204
Figure 4.7: H ₂ O contents vs clinopyroxene major element composition for the Ngaoundere Likok xenoliths.....	208

Chapter V

Figure 5.1: Potential geodynamical models for the formation of the CVL	220
Figure 5.2: (A) NW-SE cross-section illustrating the major surface tectonic features of Cameroon and its surroundings. (B) Lithospheric-scale cross-section along the same trace of Fig. 5.2 A	223
Figure 5.3: Conceptual cross-section illustrating the metacratonization of the northern edge of the Congo craton and the Adamawa-Yade domain	224

LIST OF TABLES

Table 2.1: Temperature T (°C) estimates for Kapsiki xenoliths	48
Table 2.2: FTIR characteristics and average hydrogen contents of orthopyroxene and clinopyroxene.....	48
Table 3.2: Modal proportions of xenolith minerals (in volume %) obtained using Image J software.	84
Table 3.3: Average major element composition of olivine.....	103
Table 3.4: Average major element composition of orthopyroxene	105
Table 3.5: Average major element composition of clinopyroxene	107
Table 3.6: Average major element composition of spinel	109
Table 3.7: Average major element composition of amphibole	111

Table 3.7: Average trace element composition of olivine	115
Table 3.8: Average trace element composition of clinopyroxene	116
Table 3.9: Average trace element composition of orthopyroxene.....	132
Table 3.10: Trace element composition of amphibole	134
Table 3.11: Whole rock major element (wt. %) compositions of CVL xenoliths calculated by mass balance	136
Table 3.12: Whole rock trace element (wt. %) compositions of CVL xenoliths calculated by mass balance	137
Table 3.12: Calculated equilibration temperatures, and oxygen fugacity conditions for the CVL xenoliths	141
Table 3.13: Partial melting values (in %) estimated from the methods of De Hoog et al., 2010 (Cr# in ol), Hellebrand et al., 2001 (Cr# in sp) and modeling of clinopyroxene and orthopyroxene REEs.....	152
Table 4.1: FTIR characteristics and H ₂ O contents of xenoliths from the Cameroon Volcanic Line	193

APPENDICES

Appendix 1: Thin/Thick section scans of Cameroon Volcanic Line xenoliths.....	239
Appendix 2.1a: Major element composition of olivines from Kapsiki	240
Appendix 2.1b: Major element composition of orthopyroxenes from Kapsiki.....	246
Appendix 2.1c: Major element composition of clinopyroxenes from Kapsiki	251
Appendix 2.1d: Major element composition of spinels from Kapsiki	254
Appendix 2.2a: Trace element composition of olivines from Kapsiki.....	257
Appendix 2.2b: Trace element composition of orthopyroxenes from Kapsiki	259
Appendix 2.2c: Trace element composition of clinopyroxenes from Kapsiki.....	261
Appendix 3.1a: Major element composition of clinopyroxenes from Ngaoundere Likok (N11 and N11a).....	263
Appendix 3.1b: Major element composition secondary clinopyroxenes from Enep (En2a)	265
Appendix 3.1c: Major element composition of clinopyroxene spongy rims from Wum (We1a).....	267

Appendix 3.1d: Major element composition of clinopyroxene spongy rims from Kuk (K1).....	268
Appendix 3.2a: Trace element composition of clinopyroxenes from Ngaoundere Likok (N11and N11a)	269
Appendix 3.2b: Trace element composition of secondary clinopyroxenes from Enep (En2a).....	271

CHAPTER I: GENERAL INTRODUCTION

I.1. RATIONALE AND OBJECTIVES

The evolution of the Earth spans over 4.5 Ga, and for the past 3.6 Ga, it has been marked by successive episodes of convergence and subsequent rifting of supercontinents (SC), with a primary influence from huge mantle plumes or super plumes. The Earth's interior remains largely inaccessible and hence most of it is still geochemically unsampled. The Earth's mantle virtually constitutes all the silicate part of the Earth, making up 84% of its total volume. The Earth's upper mantle is made up of a hotter and weaker convective asthenospheric part and a solid, brittle lithospheric part. The lithospheric mantle is then subdivided into the subcontinental lithospheric mantle (SCLM) and the oceanic lithospheric mantle (OLM). The SCLM shows variations in thickness ranging from a few tens of km in rift zones to over 250 km beneath cratonic areas. It is also heterogeneous, mainly consisting of ultramafic rocks of varying compositions.

In some regions of the world, parts of the mantle have been tectonically exposed as orogenic peridotites and ophiolites. In intraplate regions, fragments of the Earth's mantle have been brought up to the Earth's surface as xenoliths in rocks of primarily alkaline composition. These xenoliths are direct samples of the upper mantle, which represent an image of the subcontinental lithospheric mantle (SCLM) at the time of eruption, hence, an important key to unravelling geochemical information on mantle processes (Bodinier et al., 2003; Pearson et al., 2003; Beccaluva et al., 2001; Bonadiman et al., 2001; Downes, 2001).

The Cameroon Volcanic Line (CVL), found in the western part of Africa is distinctive from other intraplate rift-related volcanoes. It consists of a chain of Cenozoic volcanoes developed simultaneously on the continental African plate and the Atlantic Ocean floor (Fig. 1.1). The CVL represents a strange array of volcanoes that do not show any systematic space-time migration from one volcano to the other (Aka et al., 2004; Marzoli et al., 2000; Lee et al., 1994) as observed in typical hotspot settings (e.g., the Hawaiian emperor chain), and so this has generated some debate about its origin. The CVL represents a unique tectonic setting with a passive margin between the oceanic and continental crusts, whereby a single process that evolves from one region to another is unrealistic. Based on Ar isotopic data, Marzoli et al., 1999 concluded that the whole CVL may not be interpreted as a surface expression of simple hotspots magmatism but involve

complex processes. Since different triggers of melting are envisaged, there must also be different processes involved as melting occurred at different times under different conditions.

The CVL is also known for inhabiting the infamous Lake Nyos, which is known for its catastrophic eruption of CO₂ gas. CO₂ outgassing also occurred at Lake Monoun, 30 km from the Nyos volcano. The trigger for this eruption is unclear, but the two hypotheses brought forth were; a volcano-phreatic eruption (Barberi et al., 1989; Tazieff, 1989) or a limnic eruption (Giggenbach, 1990; Kling et al., 1989; Kusakabe et al., 1989; Sigurdsson, 1988). In order to mitigate such natural disasters, it is important to look for clues, which could indicate a potential CO₂ source, not only around the Lake Nyos area but also along the whole line of volcanoes.

Mantle xenoliths erupted in alkaline basalts are common in several localities along the CVL. They document the petrological and geochemical evolution of the SCLM in this area, providing a window into mantle processes. This therefore provides a unique opportunity to study and understand the lithospheric mantle below an alignment of volcanoes with a distinctive, unsystematic space-time evolution. This seemingly random distribution accentuates variations in chemical composition, which in turn reflects the complexity of processes in the SCLM, especially small-scale chemical heterogeneity.

This work focuses on the study of mantle xenoliths from the ~1000 km continental sector of the CVL. Mantle xenolith samples were collected precisely at the Kapsiki plateau, the Adamawa Volcanic Field (AVF) at Ngaoundere Likok and the Oku Volcanic Field (OVF) at Kuk, Wum, Nyos, Etome, Enep and Oku (Fig. 1.2). This work presents the first geochemical data for several localities along the CVL (e.g., Etome, Kuk and Wum) complemented with new, complete, and detailed geochemical data for other localities (e.g., Kapsiki, Enep, Oku and Ngaoundere Likok). The Kapsiki plateau volcanism is the oldest along the CVL (Oligocene: ~32-29 Ma; Dunlop, 1983), it bears the northern-most known occurrence of mantle xenoliths, making it an ideal end member to investigate mantle processes. The OVF and the Ngaoundere plateau belong to two tectono-structurally distinct domains. The OVF is found in a juvenile Neoproterozoic domain with no evidence of Archean heritage (Penaye et al., 1993). The AVF is in the Paleoproterozoic domain with important Archean contribution (Toteu et al., 2004), which has been extensively reworked during the Pan-African orogeny (Toteu et al., 2004) and

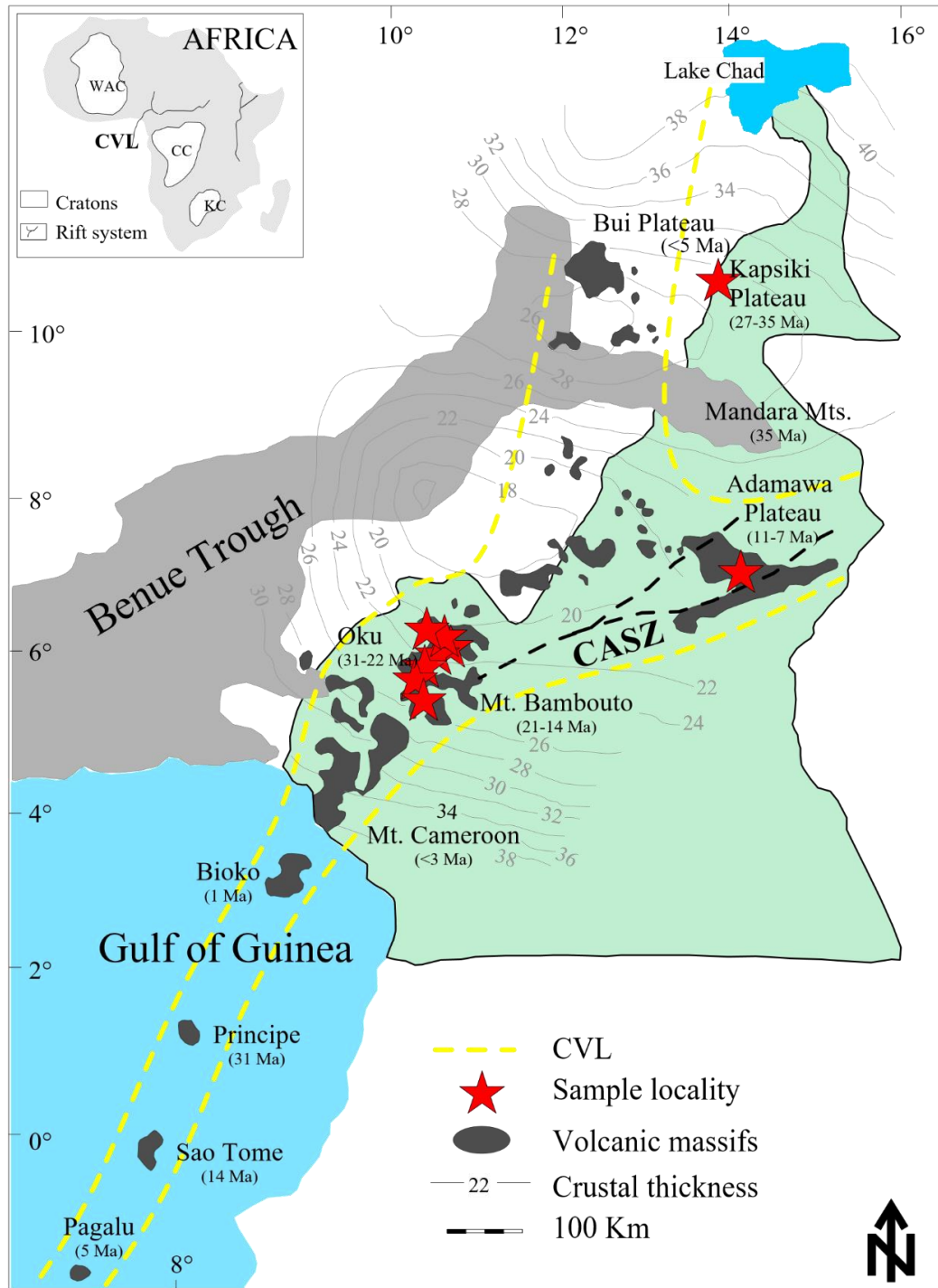


Figure 1.1: Sample location of the studied xenoliths along the Cameroon Volcanic Line (CVL) modified after Deruelle et al., 2007. Insert on the left shows the major cratons, the position of the CVL and the East African Rift system. The Central African Shear Zone is from Njiekak et al., 2008 and crustal thicknesses from Poudjom Djomani et al., 1995.

represents a transition between the northern margin of the Congo craton and the juvenile domain.

The main aim of this study is to characterize the lithospheric mantle below the CVL on a regional scale to better understand the implications for the evolution of the mantle from Archean to recent times.

For this, detailed major and trace element systematics including hydrogen contents on mantle xenolith minerals (olivine, orthopyroxene, clinopyroxene, spinel and amphibole) to attain the specific objectives relevant to this study, which are to:

1. Constrain the extent of partial melting.
2. Document and characterise the different metasomatic types using clinopyroxene and amphibole composition.
3. Determine if there is evidence for subduction-related metasomatism which was inherited during the Pan-African orogeny.
4. Find out if there are signs of CO₂ related metasomatism which could be related to CO₂ outgassing at volcanoes.
5. Evaluate the use of orthopyroxene and olivine as a tool for characterising metasomatic enrichments.
6. Evaluate the water contents of the SCLM below the region.
7. Assess the relationship between metasomatism and volatile enrichment of the mantle.
8. Evaluate information provided by the melting regime and mantle dynamics especially as it relates to the different tectono-structural units in Cameroon.

I.2. GEOLOGIC SETTING

I.2.1. THE PRECAMBRIAN BASEMENT OF CAMEROON

The Precambrian basement of Cameroon is composed of the Ntem complex, which represents the northern end of the Congo craton, and adjacent Proterozoic terrains formed during the convergence of Congo and West Africa cratons (Toteu et al., 2001).

Recent studies of the Precambrian domain in Centre Cameroon support the existence of two different blocks delineated by the NNE-SSW oriented Tchollire-Banyo Fault (TBF) with to the east and west, the Adamawa Yade Domain (AYD) and the North-West Cameroon Domain (NWCD) respectively.

While in the NWCD, the oldest Nd_{TDM} are of Paleoproterozoic age, the Adamawa Yade domain (AYD) is characterized by the existence of Archean relics interpreted as a probable inheritance from the Congo craton (Tchakounte et al, 2017; Ganwa et al., 2016). Geodynamic relations between the two domains are still disputed and are variably attributed to a collision following convergence between the West African and Congo-San Francisco cratons (Toteu et al., 2001), the collision between the Congo craton and the East Saharan ghost craton or to geodynamic processes that led to the detachment of the Adamawa block from the Congo craton and a subsequent convergence during the Neoproterozoic (Fuh et al., 2021; Tchakounte et al., 2017; Nkoumbou et al., 2014). The Adamawa Yade and North-West Cameroon domains are crosscut by a transcontinental NNE-SSW oriented shear zone known as the Adamawa Shear Zone (ASZ), following palinspatic reconstructions, and is prolonged into the Borborema Province of NE Brazil by the Pernambuco lineament (Van Schmus et al., 2008; Brito Neves et al., 2002).

1.2.2. THE CAMEROON VOLCANIC LINE

The CVL is a tectono-volcanic chain of volcanoes, which spans over 1600 km from the Gulf of Guinea up to the Lake Chad area (Mbowou et al., 2012; Déruelle et al., 1991) in the African continent, but shows no clear age progression (Déruelle et al., 2007, 2001, 1987; Fitton and Dunlop 1985; Geze 1953). Volcanoes occur in numerous N70°E shear zones of Pan-African age, which segments the continental crust and the upper mantle up to depths of 190 Km (Dorbath et al., 1986, 1984). The CVL forms a characteristic Y-shape with the area from the Gulf of Guinea to Lake Chad representing the trunk, while the Adamawa and Bui Plateau are the eastern and western branches respectively (Fig 1.1).

The CVL can conveniently be divided into an oceanic and a continental sector, where the oceanic sector comprises six main volcanoes on the islands of Bioko (Biao, Santa Isabel, San Carlos), Pagalu, Sao Tome and Principe (Déruelle et al., 1991). The continental sector hosts more than 60 anorogenic ring complexes of age 70-30 Ma

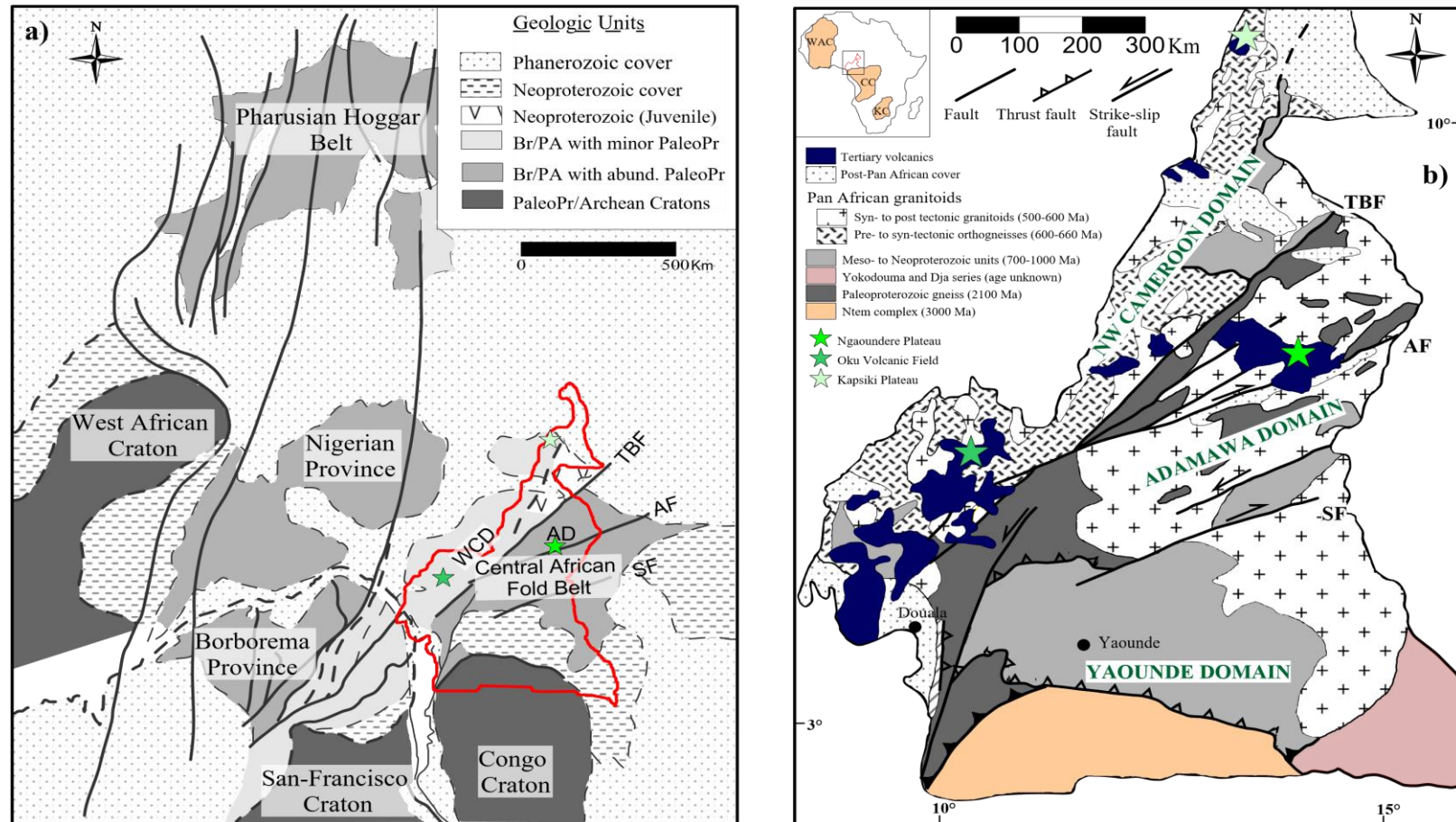


Figure 1.2: Generalised geologic map of a portion of West Gondwana about 500 Ma showing inferred geological provinces and potential correlations from Brazil to West-Central Africa (modified from Brito Neves et al., 2002). b) Geologic map of Cameroon, showing major lithotectonic units; note the relatively large amount of granitoid rocks in the eastern Cameroon basement (modified from Toteu et al., 2001). Legend: Br/PA, Brasiliano/Pan-African orogenic domains; PalaeoPr, Palaeoproterozoic crust; AD, Adamawa–Yadé domain; WCD, West Cameroon domain; AF, Adamawa fault; SF, Sanaga fault; TBF, Tcholliré–Banyo fault.

(Ngako et al., 2006) and 12 volcanic massifs of age 51.8 to <1 Ma (Wandji et al., 2009), which consists of horsts (Mt Etinde may form a unit with Mt. Cameroon, Mts Rumpi, Mt. Manengouba, Mts. Bambouto, Mt. Mbam and Mt Oku) alternating with grabens (Kumba, Tombel, Mbo, Ndop and Tikar plain) where relatively young monogenetic cones are dominant (Déruelle et al., 1991). This characteristic topography becomes less accentuated in the northern part of the line.

The continental sector lies between the West African and the Congo cratons which show different seismic and paleomagnetic characters (Poudjom Djomani et al., 1995; Plomerova et al., 1993). The crustal and lithospheric thickness of the CVL has been estimated at ~30-34 Km and 120-150 Km respectively except at the Ngaoundere plateau where uplift caused significant lithospheric thinning (Poudjom Djomani et al., 1997, 1995; Plomerova et al., 1993).

The CVL basement primarily consists of Pan-African granitic rocks (Marzoli et al., 2000; Lassere, 1978), which are crosscut by the N070°E oriented Central African Shear Zone (CASZ) (Poudjom Djomani et al., 1995; Moreau et al., 1987). The oceanic part of the CVL is entirely volcanic (Burke, 2001), with rocks ranging from nephelinite, basanite, and basalts to trachytes and phonolites (Déruelle et al., 1991; Fitton, 1987; Fitton and Dunlop, 1985). The continental part consists of both plutonic complexes and volcanic massifs (Deruelle et al., 2007; Kamdem et al., 2002; Ngounouno et al., 2001; Njonfang and Moreau, 2000) with predominant alkaline mafic to intermediate rocks (basalts, basanites, trachytes and phonolites). Basaltic rocks from both the continental and oceanic sectors show similarities in their isotopic and trace element signatures (Déruelle et al., 2007) which are similar to St. Helena basalts but trace element compositions of the Ngaoundere plateau basalts are higher.

The origin of the CVL is still in debate, however, the most widely accepted structural hypothesis is the reworking of Pan-African fractures (Moreau et al., 1987) which gave rise to a succession of 'en-echelon' mega tension gashes and could be responsible for the presence of hotlines in the asthenospheric mantle (Bonatti and Harrison, 1976). It has recently been interpreted by Montigny et al., 2004 as large lithospheric cracks tapping a hot deep asthenospheric source, which is also, supported by deep imaging seismic and gravity studies in the oceanic part of the line (Meyers et al., 1998). It is concluded that the CVL most likely results from reactivation of lithospheric

cracks (shear zones) tapping sub-lithospheric mantle with little to moderate reaction with the lithospheric mantle (Asaah et al., 2015; Déruelle et al., 2007; Meyers et al., 1998), rather than resulting from melting of a deep mantle plume (Lee et al., 1994).

Peridotite and pyroxenite xenoliths have been found in the continental and oceanic parts of the CVL (Caldeira and Munha, 2002) at Bioko and Pagalu (Matsukage and Oya, 2010); Mt. Cameroon (Wandji et al., 2009; Ngonouno and Déruelle 2007; Déruelle et al., 2001; Ngounouno et al., 2001; Déruelle et al., 1998); Barombi Mbo: (Pinter et al., 2015; Teitchou et al., 2007; Lee et al., 1996), Kuk (Nformidah, 2016), Wum (Nformidah, 2016), Etome (Nformidah, 2016) Enep: (Lee et al., 1996), Nyos (Temdjim, 2012; Temdjim et al., 2004), Nji (Princivalle et al., 2000), Adamawa Plateau (Temdjim et al., 2019; Nkouandou et al., 2015; Nguihdama et al., 2014; Nkouandou and Temdjim, 2011; Dautria and Girod, 1986; Girod et al., 1984), Kapsiki plateau (Nformidah et al., submitted; Tamen et al., 2015; Nguihdama, 2007). The CVL xenoliths occur as enclaves in Cenozoic alkaline basalt rocks and are mainly spinel lherzolites with subordinate harzburgites, wehrlites and pyroxenites. Garnet (Lee et al., 1996) and plagioclase (Temdjim et al., 2019) bearing xenoliths occur in the Ngaoundere region.

1.2.2.1. The Kapsiki plateau

The Kapsiki plateau is in the Far Northern part of Cameroon (Fig. 1.2; 1.3). This Far-Northern part is composed of three main geological units: quaternary deposits of Lake Chad and the surrounding areas, (Tsozue et al., 2017; Adjia et al., 2013), volcanic to sub-volcanic complexes associated with the Cameroon Volcanic Line (CVL) (Deruelle et al., 2007, 2001; Ngounouno et al., 2000) and igneous and metamorphic rocks related to the Cameroon Pan African Belt (Toteu et al., 2001).

The Kapsiki plateau culminates at mean altitudes of 800 m, it is dominated by volcanic complexes and covers an area of 150 km² (Fig. 1.3). Volcanic activity in the Kapsiki plateau is distinguished from other CVL volcanoes by a relative abundance of felsic and intermediate rocks relative to basanites. Felsic and intermediate volcanism was accompanied by abundant intrusive rocks not reported in other parts of the CVL. In terms of age, felsic, transitional, and mafic volcanic rocks are relatively old and are of similar ages, which can be bracketed between 27 and 35 Ma (Vincent and Armstrong, 1973; Dunlop, 1983). The alignment of volcanic plugs corresponds to major directions N30°E

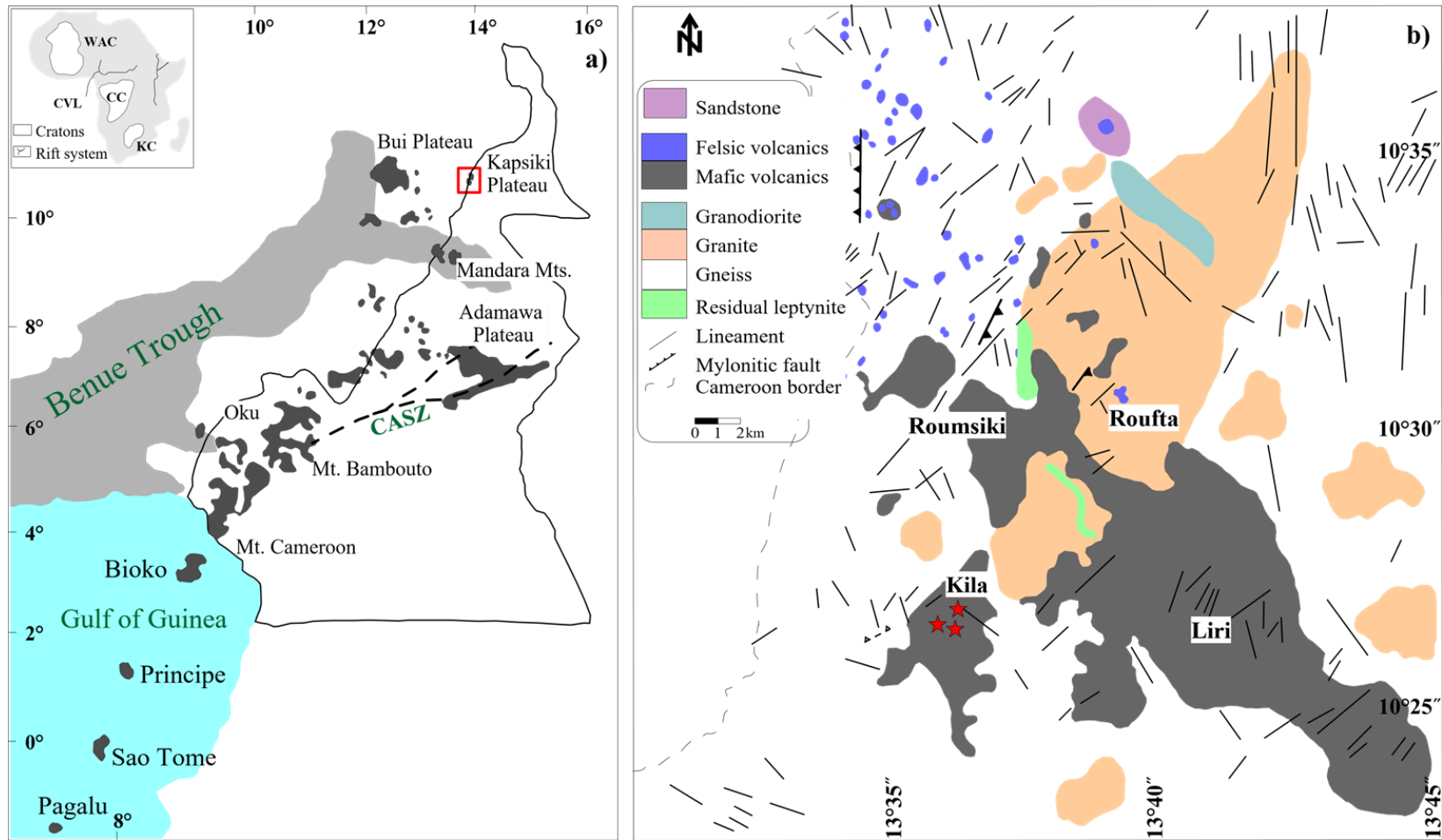


Figure 1.3: Cameroon Volcanic Line (CVL) with major Cenozoic centres and the Central African Shear Zone (CASZ). The left insert shows the position of the CVL in Africa and the major cratons. b) Geological map of Kapsiki (modified from Tamen et al., 2015) extrapolated from Fig.1a. The red stars indicate where the xenoliths were collected.

that is dominant and subsidiary N65°E and N165°E. The three directions correspond to the direction of the Cameroon Line, the Adamawa Shear Zone, and the Benue trough, which are the main regional trends well known in the Precambrian basement (Regnault et al., 1986). The orientation of these three main regional lineaments in conjunction with coeval ages of felsic, intermediate, and mafic volcanism (27 and 35 Ma) suggests that a single reactivation episode in the Tertiary led to the volcanic activity in the Kapsiki plateau. Moreover, volcanic ages for the Kapsiki plateau basalts contribute to rule out any polarity of ages along the CVL, in response to the displacement of the African plate towards the Northeast.

Mantle xenoliths were sampled in Cenozoic alkaline basaltic flow around longitude 13°36'E and latitude 10°26'N (Fig. 1. 3b) at about 5 km to the south-west of Kila village. They are hosted by a basaltic flow, which is a south-western branch of a SE-NW oriented flow that also extend from Rhumsiki to Liri.

From a geodynamic point of view, the Kapsiki plateau lies above a Pan-African basement, which belongs to the northern unit of the Pan-African domain of Cameroon. The lithology comprises sensu-stricto Pan-African granitoids and their host orthogneissic basement. The oldest Nd and Hf TDM ages recorded in the area are Paleoproterozoic (Bute et al, 2019), which differ from Pan-African rocks with Archean heritage found elsewhere in Pan-African terrains such in the Adamawa Yade domain (Ganwa et al., 2016). The Kapsiki plateau is located at the southern edge of the Saharan Metacraton (Goussi Ngalamo et al., 2018) and the geodynamic model proposed for the Pan-African basement of the Kapsikis is a lithospheric delamination that led to abundant widespread magmatism at about 580 Ma (Bute et al., 2019). Various studies in the field of geodynamics (Ferre et al., 2002) and geophysics (Pasyanos and Nyblade, 2007) point out a lithospheric thinning because in the framework of the delamination model, the decompressional melting of the asthenosphere leads to a diapirism since the mantle removed is to be replaced. The Moho below the Kapsikis is estimated between 24 and 33 km (Kemgang Ghomsi et al., 2020; Tokam et al., 2010; Poudjom Djomani et al., 1995).

I.2.2.2. The Ngaoundere Plateau (Likok)

The Ngaoundere plateau is part of the uplifted Adamawa Volcanic Massif (AVM), sandwiched between the Tchollire Banyo fault and Djerem Mbere strike-slip faults. These faults are part of the Central African Shear Zone (CASZ), reactivated in the

Cretaceous (Moreau et al., 1987) during the opening of the South Atlantic Ocean. The Ngaoundere plateau represents the eastern branch of the CVL (Poudjom Djomani et al., 1997) and it is crosscut by numerous rejuvenated Pan-African strike-slip faults (N00°E, N30°E, N50°E, N70°E, N90°E and N160°E) down to the mantle (Dorbath et al., 1984). The AVM constitutes part of the Adamawa Yade domain (AYD), which is bordered to the north and south by the North-West Cameroon and the Yaounde domains respectively (Goussi Ngalamo et al., 2017; Tchakounté et al., 2017). The AYD is comprised of relics of Archean and Paleoproterozoic age (Tchakounté et al., 2017; Ganwa et al., 2016) following decratonization processes at the northern end of the Congo craton after Eburnean (2.1 Ga) and Pan-African (600 Ma) orogenies (Tchakounte et al., 2017).

From a geophysical point of view, the Adamawa plateau was formed during the Cenozoic and then subsequently uplifted relative to its surroundings (Nnange et al., 2001; Okereke, 1988) due to the upward movement of the lithosphere-asthenosphere boundary (Ambeh et al., 1989; Brown and Fairhead, 1983). The depth of the Moho and the lithosphere-asthenospheric boundary below the plateau is shallow and corresponds to depths of 25 and 70 Km respectively, which shows crustal and lithospheric thinning below the region (Goussi Ngalamo et al., 2018; Poudjom Djomani et al., 1997; Poudjom Djomani et al., 1992).

The basement rocks are mainly comprised of Precambrian gneisses, migmatites and metasediments (Ngako et al., 1991) which are cut across by granitoids of Neoproterozoic age (U-Th-Pb: $615 - 575 \pm 27$ Ma) (Ganwa et al., 2008; Tchameni et al., 2006), and are partially covered by alkaline to peralkaline Cretaceous to Quaternary lava flows (Nkouandou et al., 2008; Temdjim et al., 2004). Volcanism along the line was induced by the reworking of Pan-African faults during the Mesozoic and the Cenozoic with basaltic flows and blocks bearing mantle xenoliths common in the area (Njombie Wagsong et al., 2018; Mbowou et al., 2017; Nguihdama et al., 2014; Nkouandou and Temdjim, 2011; Matsukage and Oya, 2010; Lee et al., 1996) and were sampled at Ngaoundere Likok (N07°16'10"/ E13°14'18"/ Alt: 1200m).

I.2.2.3. The Oku Volcanic Field

The Oku Volcanic Field (OVF) is one of the major volcanic centres along the CVL and is located halfway through the continental part of the line. It is a complex stratovolcanic edifice of approximately 90 km in diameter that culminates at altitudes of

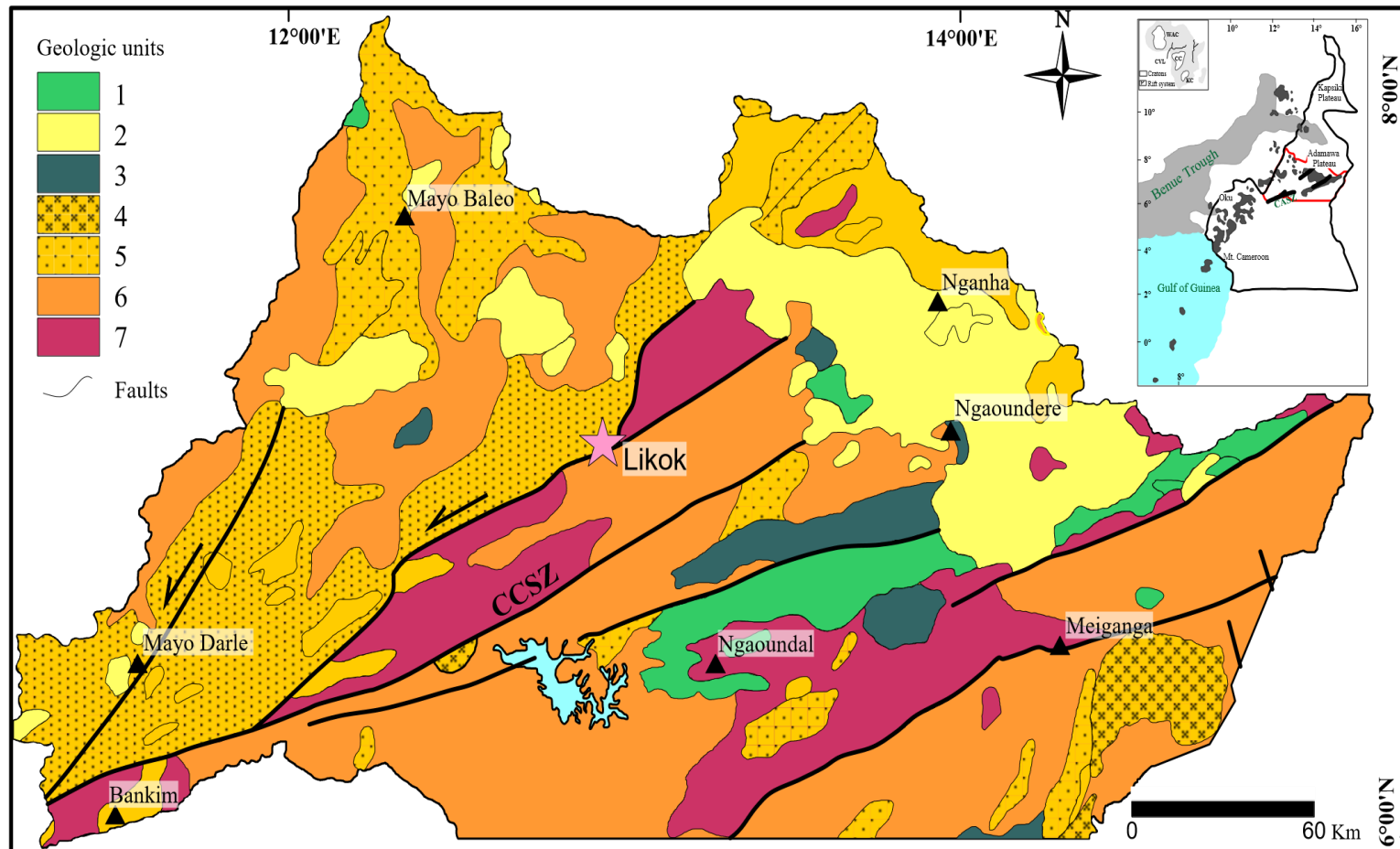


Figure 1.4: Geologic map of the Adamawa region (modified after Le Maréchal, 1976). CCSZ represents the Central Cameroon Shear Zone. 1: Early to late Cretaceous sedimentary formations; 2: Neogene-Paleogene volcanic formations from the Cameroon Volcanic Line; 3: Cambrian-Ordovician and early Paleozoic plutonic formations; 4: Neoproterozoic epimetamorphic formations; 5: Neoproterozoic plutonic and metamorphic formations; 6: Neoproterozoic to Cambrian plutonic and metamorphic formations; 7: Paleoproterozoic (Early Eburnean) plutonic and anatectic formations. (From Njeudjang et al., 2020).

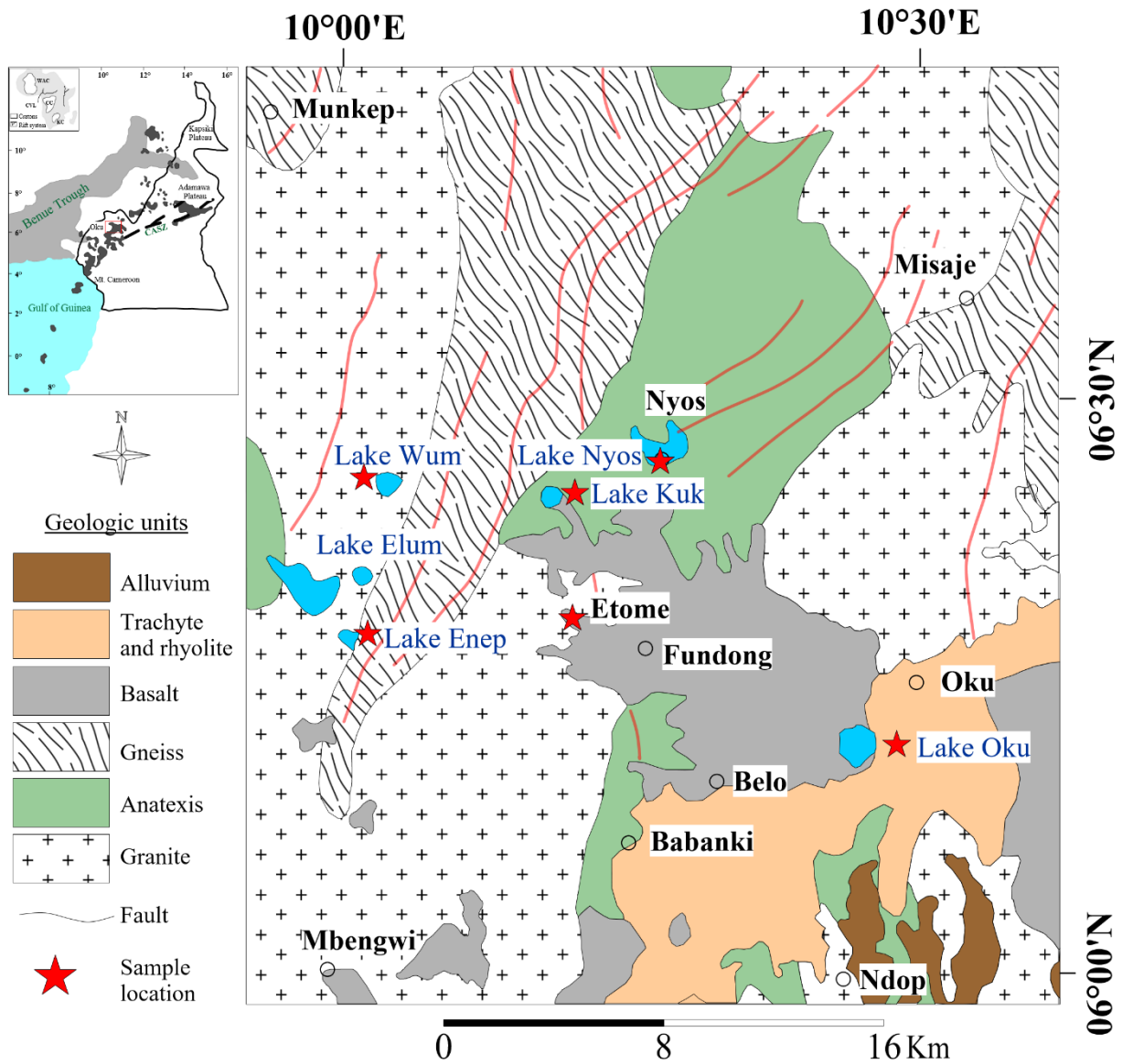


Figure 1.5: Geologic map of the Oku Volcanic Field (modified from Asaah et al., 2015). The inset on the left shows the position of the Oku volcanic group along the Cameroon Volcanic Line.

3011m (Njilah, 1991). It is composed of four main volcanoes (Oku, Babanki, Nyos and Nkambe). The Precambrian basement of the OVF belongs to the NWCD, which is in the north-western part of the Adamawa Yade domain and is essentially made of juvenile Neoproterozoic crust (Li et al., 2017; Toteu et al., 2004). Volcanism in the OVF occurred since the Oligocene (Marzoli et al., 2000; Marzoli et al., 1999; Fitton and Dunlop, 1985) and the products of eruption range from basanites to alkali basalts through hawaiites, mugearites to trachyte-rhyolite flows, high-level intrusions and intercalated pyroclastics (Kamgang et al., 2013; Njilah et al., 2007; Marzoli et al., 2000; Marzoli et al., 1999) which cut through highly faulted (N70°E) orthogneissic and granitic basement rocks of Precambrian age (Li et al., 2017).

I.3. ANALYTICAL TECHNIQUES/ METHODS

I.3.1. SAMPLE PREPARATION

Over 100 mantle xenolith samples were collected during the field campaign. From ~30 xenolith samples, epoxy grain mounts were fabricated. Clear transparent crystals, which are void of inclusions and alteration, were handpicked from loose xenolith material by handpicking under a binocular microscope. They were then mounted in epoxy resin, double-polished and thickness measured using an analogue micrometre. This approach was chosen for most of the analysis rather than in situ measurements on thin sections because this study was intended to be a survey of a large set of samples from several localities.

Representative mantle xenolith samples (20) were then selected based on their freshness (least possible alteration by surface processes or reaction with the host basalt) and from the results obtained during the preliminary studies. From the xenoliths were prepared 11 unoriented thin (30 µm) and 19 thick (300 µm) sections providing the largest exposure. Petrographic observations were performed using an Olympus BX41 microscope equipped with an Olympus SC30 digital camera, and the image acquisition software analysis get IT. All subsequent analyses were carried out at the Institute of Geological Sciences, University of Bern. The analysis of trace elements was carried out at the Swiss Federal Institute of Technology (ETH Zurich) except for the Kapsiki samples.

I.3.2. ELECTRON PROBE MICRO-ANALYSER (EPMA)

Major and minor element concentrations of olivine, orthopyroxene, clinopyroxene and spinel were determined using a JEOL JXA 8200 super probe. Data were collected at 15 kV accelerating voltage, 20 nA beam current with a beam diameter of 1-3 μm depending on the size of the grain analysed. Counting times of 20-60 s were applied depending on the element and mineral analyzed. Natural and synthetic minerals were used as standards. The following elements were analysed: Si, Ti, Al, Cr, Fe, Mn, Mg, Ni, Ca, Na, K. Where possible, core and rim compositions were measured for olivine and pyroxenes.

I.3.3. LASER ABLATION INDUCTIVELY COUPLED PLASMA MASS SPECTROMETRY (LA-ICP-MS)

Trace element concentrations were determined using an Australian Scientific Instrument (now Applied Spectra), Resonetics RESOLUTIONSE 193nm excimer laser system with a fast washout two-volume cell, coupled to an Agilent 7900 quadrupole ICP-MS. Ablation was conducted in a He atmosphere at a frequency of 5-10 Hz, energy density of 6 J/cm^2 and a beam diameter of 50-100 μm . The ablated material was extracted in a stream of He (0.4l/min), which was subsequently combined with Ar (0.88 l/min) and N_2 (3ml/min) before entering the ICP. The laser system is coupled to an Agilent 7900 quadrupole ICP-MS instrument and was operated at a frequency of 5-10 Hz, energy density of 6 J/cm^2 for a beam diameter of 50-100 μm . Ablation was done in a 0.4 l/min He stream and a combination of He, Ar and N_2 transported the ablated material to the ICP at a flow rate of 0.88 l/min. The glass NIST 612 was used as the primary standard, with glasses T1G, BHVO and GOR132 as secondary standards (Jochum et al., 2011, 2006, 2005).

The elements analyzed were ^7Li , ^{23}Na , ^{25}Mg , ^{27}Al , ^{29}Si , ^{31}P , ^{43}Ca , ^{45}Sc , ^{47}Ti , ^{51}V , ^{53}Cr , ^{55}Mn , ^{57}Fe , ^{59}Co , ^{61}Ni , ^{88}Sr , ^{89}Y , ^{90}Zr , ^{93}Nb , ^{178}Hf , ^{208}Pb , ^{232}Th , ^{238}U and the REEs. For olivine, the list was modified due to the substantially lower concentrations of most elements; only ^7Li , ^{11}B , ^{23}Na , ^{25}Mg , ^{27}Al , ^{29}Si , ^{31}P , ^{43}Ca , ^{45}Sc , ^{47}Ti , ^{51}V , ^{53}Cr , ^{55}Mn , ^{57}Fe , ^{59}Co , ^{61}Ni , ^{66}Zn , ^{89}Y and ^{90}Zr were measured. The data obtained were evaluated using IOLITE (Paton et al., 2011). The results were normalized using Ca values for

clinopyroxene. For olivine and orthopyroxene, Si values obtained from electron microprobe analysis were used.

I.3.4. FOURIER TRANSFORM INFRARED SPECTROSCOPY (FTIR)

The H₂O contents of the NAMs (olivine, orthopyroxene and clinopyroxene) of xenoliths from the CVL were measured at the Institute of Geological Sciences, University of Bern. Measurements were performed on double polished thick sections of 300 µm. Analysis on these thick sections were complemented by analysis on grain mounts for other samples. A total of 16 thick sections and 17 grain mounts were used. The grain mounts were prepared by crushing the xenolith samples and then selecting the NAMs by handpicking. The grains obtained were then embedded in epoxy and polished on both surfaces. The grain sizes, which range from 120-880 µm for orthopyroxenes and 80-600 µm for clinopyroxenes were measured using an analogue micrometre.

The H₂O contents of olivine and pyroxenes and information on the local bonding environment of hydrogen were determined by transmission FTIR spectroscopy using a Bruker Tensor II Fourier transform infrared spectrometer equipped with a nitrogen-cooled mercury cadmium telluride (MCT) detector coupled to a Hyperion 3000 microscope with an automated stage. This method has the advantage of being non-destructive with very low detection limits (<1 ppm). The number of scans was 128; the resolution was set at 4 cm⁻¹ with an aperture size of 20x20 µm to 50x50 µm depending on the grain size and availability of inclusion and lamellae-free zones. The spectra were collected using unpolarised light and on un-oriented crystals. The infrared spectra of olivine and pyroxene were obtained in the core and rims where possible, between 3800-3000 cm⁻¹.

The data obtained were processed using the OPUS software package; the spectra were corrected for atmospheric contamination using the software algorithm before the baseline was subtracted using the concave rubber band correction method using 64 baseline points and four iterations. Identical spectra of minerals from the same sample were averaged and the spectral ranges of structurally bond hydroxyl were integrated using the B method.

The H₂O contents were calculated using the modified Beer-Lambert Law: $C = A / (I \times t)$, where C is the H₂O concentration (in weight ppm), A is the integral area (cm⁻²) of absorption bands in the region of interest, I is the integral specific absorption coefficient of minerals (ppm⁻¹ cm⁻²), and t is the thickness of the section. The integrated area was multiplied by 3 to get the total absorbance (Kovacs et al., 2008) and integral specific coefficients of 5.32, 14.84 and 7.09 ppm⁻¹cm⁻² were used for olivine, orthopyroxene and clinopyroxene respectively (Bell et al. 2003, 1995). Clinopyroxene spectra showing OH bands attributed to the presence of amphibole were excluded during the quantification of the water contents from the Kapsiki xenoliths (Chapter2).

I.3.5. IMAGE ANALYSIS

The grain sizes and proportions of the different mineral phases are obtained using a Java-based image processing software, Image J. The scanned image of the thin section is converted from colour to greyscale and then to binary image by adjusting the threshold. The image pixels are then converted to real units (mm) and the sizes of the grains measured. Only the longest axis of each grain is considered. The modal proportions of the different mineral phases of the xenoliths were obtained by image thresholding to find the percentages of the minerals present.

I.4. SUMMARY OF THESIS

This thesis is composed of 5 chapters. Chapter II has been accepted with minor revisions in the Journal of African Earth Sciences. The chapters are summarised as follows:

Chapter I

This chapter defines the objectives and research questions to be addressed by this work. An overview of the geologic settings of the different sample localities is presented and the different analytical technics used to tackle the research questions are given.

Chapter II

In this chapter, detailed major and trace element analysis as well as H₂O contents of mantle xenoliths from the Kapsiki plateau are presented. The Kapsiki xenoliths derive from the north-eastern end of the line, providing an important end member to investigate depletion and metasomatic processes in the lithospheric mantle. Xenoliths are mainly depleted hazburgites, which have experienced multiple metasomatic episodes preceding partial melting.

Using trace element systematics of ortho- and clinopyroxene, we infer that the mantle below the region has been mainly metasomatized by carbonatite-silicate melts. This shows that orthopyroxene also has the potential to be used to infer metasomatic enrichments, which is very important especially for xenoliths that are void of clinopyroxene. The very low H₂O contents compared to typical sub-continental peridotites could be attributed to the depleted nature of the xenoliths or reflect lower water activities of carbonatitic melts relative to alkaline melts.

Chapter III

This chapter consists of detailed major and trace element analysis of mantle xenoliths from the Adamawa Volcanic Field and the Oku Volcanic Field, which represent two distinct tectono-structural units along the CVL. These two units are quite similar in terms of major mineral compositions.

Mineral trace element concentrations of clinopyroxenes show homogeneous compositions for individual samples of the OVF xenoliths while the AVF xenoliths are characterised by heterogeneous compositions. Orthopyroxene trace element signatures mimic that of clinopyroxene, and from different trace element ratios, we conclude that orthopyroxene is a good candidate which could be used in addition to clinopyroxene to constrain metasomatism. Olivine on the other hand is trickier to use because changes in temperature highly influence their trace element composition compared to mantle processes like partial melting and melt-rock reactions. Trace element systematics therefore show that the mantle below these regions has been subjected to varying degrees of partial melting and are characterised by metasomatism by melts of carbonatite, silicate, carbonatite-silicate, and MORB-type compositions.

Weak signatures for subduction-related metasomatism were constrained from amphibole composition, but there are no clear indications of CO₂-related metasomatism. A major finding of this chapter is that there is no systematic relation between the type of metasomatism with temperature of equilibration, crustal thickness, or geographic distribution.

Chapter IV

This chapter is dedicated to the quantification of H₂O contents in the mantle below the CVL and their significance. The H₂O contents of olivine are generally below detection limits. This is interpreted as resulting from the depleted chemistry of olivine which inhibited hydrogen incorporation. H₂O of orthopyroxenes is consistently low in all samples and ranges from 9-82 ppm. There is a striking difference in the H₂O contents of the two tectono-structural units (Chapter 3) with exceptionally low and very high hydrogen contents in clinopyroxene, which indicates a possible hydrogen gain in clinopyroxene compared to orthopyroxene. We conclude that orthopyroxene records the most reliable hydrogen contents for the CVL mantle.

The calculated bulk H₂O contents of NAMs of the CVL xenoliths are generally very low resulting in an average mantle with 16±10 ppm H₂O. This is significantly lower when compared to spinel facies mantle xenoliths worldwide, even though the CVL xenoliths show evidence for modal and cryptic metasomatism. The low H₂O contents could be related to low H₂O activity in the metasomatic fluids.

Chapter V

This chapter summarizes the main data presented in Chapters 2-4, puts the findings into a tectonic context, addresses the eight principle questions posed in section I.1, and gives conclusions and perspectives.

REFERENCES

- Adjia, H.Z., Villiéras, F., Kamga, R., Thomas, F., 2013. Mineralogy and Physico-Chemical Properties of Alluvial Clays from Far-North Region of Cameroon: A Tool for an Environmental Problem. *Int. J. Water Res. Environ. Eng.* 5, 54-66.
- Aka, F.T., Nagao, K., Kusakabe, M., Sumino, H., Tanyileke, G., Ateba, B., Hell, J.V., 2004. Symmetrical helium isotope distribution on the Cameroon Volcanic Line. *West Africa Chemical Geology* 203, 205-223.
- Ambeh WB, Fairhead JD, Francis DJ, Nnange JM, Djallo S. Seismicity of the Mount Cameroon region West Africa. *Journal African Earth Sciences.* 1989; 5 (9):1-7.
- Asaah A. N. E., Yokoyama T., Aka F. T., Usui T., Kuritani T., Wirmvem M. J., Iwamori H., Fozing E. M., Tamen J., Mofor G. Z., Ohba T., Tanyileke G., Hell J. V., 2015. Geochemistry of lavas from maar-bearing volcanoes in the Oku Volcanic Group of the Cameroon Volcanic Line. *Chem Geol* 406:55–69.
- Barberi, F., Chelini, W., Marinelli, G., Martini, M., 1989. The gas cloud of Lake Nyos (Cameroon, 1986): results of the Italian technical mission. *J. Volcanol. Geotherm.Res.* 39 (2–3), 125–134.
- Beccaluva, L., Bonadiman, C., Coltorti, M., Salvini, L., Siena, F., 2001. Depletion events, nature of metasomatizing agent and timing of enrichment processes in lithospheric mantle xenoliths from the Veneto Volcanic Province. *J. Petrol.* 42, 173–188.
- Bell, D.R., Ihinger, P.D., Rossman, G.R., 1995. Quantitative analysis of trace OH in garnet and pyroxenes. *Am. Mineral.* 80, 465–474.
- Bell, D.R., Rossman, G.R., Maldener, J., Endisch, D., Rauch, F., 2003. Hydroxide in olivine: a quantitative determination of the absolute amount and calibration of the IR spectrum. *J. Geophys. Res. Solid Earth* 108.
- Bodinier, J.-L. & Godard, M. (2003). Orogenic, ophiolitic, and abyssal peridotites. In: Turekian, K. K. & Holland, H. D. (eds) *Treatise on Geochemistry*. Elsevier, Amsterdam2, 103–170.
- Bonadiman, C., Coltorti, M., Milani, L., Salvini, L., Siena, F., Tassinari, R., 2001. Metasomatism in the lithospheric mantle and its relationships to magmatism in the Veneto Volcanic province. *Period. Mineral.* 70, 333–357.
- Bonatti, E., C.G.A. Harrison. Hotlines in the Earth's mantle. *Nature*, 263 (1976), pp. 402-404.
- Brito Neves, B. B., Van Schmus, W. R. & Fetter, A. H. 2002. North-western Africa– North-eastern Brazil. Major tectonic links and correlation problems. *Journal of African Earth Sciences*, 34, 275 – 278.

- Browne, S.E., Fairhead, J.D., 1983. A gravity study of the Central African Rift system: a model of continental disruption 1. The Ngaoundere and Abu Gabra rifts. *Tectonophysics* 94, 187-203.
- Burke, K., 2001. Origin of the Cameroon Line of volcano-capped swells. *The Journal of Geology* 109, 349-362.
- Bute, S.I., Yang, X.-Y., Cao, J., Liu, L., Deng, J.-H., Haruna, I.V., Girei, M.B., Abubakar, U., Akhtar, S., 2019. Origin and tectonic implications of ferroan alkali-calcic granitoids from the Hawal Massif, east-eastern Nigeria terrane: clues from geochemistry and zircon U-Pb Hf isotopes. *Int. Geol. Rev.* 62:129–152
- Caldeira, R., Munhá, J.M., 2002. Petrology of ultramafic nodules from Sao Tomé Island, Cameroon Volcanic line (oceanic sector). *J. Afr. Earth Sci.* 34 :231–246
- Dautria, J.-M., Girod, M., 1986. Les enclaves de lherzolites a spinelle et plagioclase du volcan de Dibi (Adamaoua, Cameroun) : des temoins d'un manteau superieur anormal. *Bull. Mineral.* 109, 275-288.
- Deruelle, B., Moreau, C., Nkoubou, C., Kambou, R., Lissom, J., Njonfang, E., Ghogomu, R.T., Nono, A., 1991. The Cameroon line: a review. In: Kampunzu, A.B., Lubala, R.T. (Eds.), *Magmatism in Extensional Structural Settings: The Phanerozoic African Plate*. Springer, Berlin, pp. 275-327.
- Deruelle, B., N'ni, J., Kambou, R., 1987. Mount Cameroon: an active volcano of the Cameroon Line. *Journal of African Earth Sciences* 6, 197-214.
- Déruelle, B., Ngounouno, I. and Demaiffe, D. 2007. The "Cameroon Hot Line" (CHL): A Unique Example of Active Alkaline Intraplate Structure in both Oceanic and Continental Lithospheres. *Compt. Rendus Geosci.* 339, 589-600.
- Déruelle, B., Ngounouno, I., Bardintzeff, M.J., 2001. Wherlites et pyroxénites en nodules dans les basaltes du Mt. Cameroun : évidence d'un métasomatisme mantellique. *J. Soc. Géosci. D'Afrique* 1, 90-91.
- Déruelle, B., Ngounouno, I., Nkoumbou, C., 1998. Mt Cameroon, Mt Etinde, and Bioko Is-land volcanoes of the Cameroon hot Line'. *Evolution of Ocean Island Volcanoes, Pen-rose Conference, Galapagos Islands*, p. 28.
- Dorbath, C., L. Dorbath, J. Fairhead, and G. Stuart, 1986. A teleseismic delay time study across the Central African shear zone in the Adamawa region of Cameroon, West Africa, *Geophys. J. R. Astr. Soc.*, 86(3), 751–766.
- Dorbath, L., Dorbath, C., Stuart, G.W., Fairhead, J.D., 1984. Structure de la croûte sous le plateau de l'Adamaoua (Cameroun). *Comptes Rendus l'Academie Sci. Paris* 298, 539-542.

- Downes, H., 2001. Formation and modification of the shallow subcontinental lithospheric mantle; a review of geochemical evidence from ultramafic xenolith suites and tectonically emplaced ultramafic massifs of western and central Europe. *J. Petrol.* 42, 233–250.
- Dunlop, H.M., 1983. Strontium isotope geochemistry and potassium \pm argon studies on volcanic rocks from the Cameroon line, West Africa. PhD thesis, Univ. Edinburgh, 347p.
- Ferré, E., Gleizes, G., and Caby, R., 2002. Obliquely convergent tectonics and granite emplacement in the Trans-Saharan belt of Eastern Nigeria: a synthesis. *Precambrian Res.* 114: 199–219.
- Fitton, J.G. & Dunlop H.M. (1985). The Cameroon Line, West Africa and its bearing on the origin of oceanic and continental alkali basalt. *Earth. Planet. Sci. Lett.* 72, 23-38.
- Fitton, J.D., Dunlop, H.M., 1985. The Cameroon line, West Africa and its bearing on the origin of oceanic and continental alkali basalts. *Earth and Planetary Science Letters* 72, 23-38.
- Fitton, J.G., 1987. The Cameroon Line, West Africa: a comparison between oceanic and continental alkaline volcanism. In: Fitton, J.G., Upton, B.G.J. (Eds.), *Alkaline Igneous Rocks*, 30. Geological Society London Special Publications, pp. 273-291.
- Fuh CG, Tchakounte N.J., Kundu O.M., Tchop J.L., Nkoumbou C (2021). Four Pan-African plutonic sets of the Colomines gold district (East-Cameroon): petrogenesis, K-Ar dating and geodynamic significance. *J. Afr. Earth Sci* 181:104220
- Ganwa A.A., Klötzli U.S., Diguim Kepnamou A., Hauzenberger C., 2016. Multiple Ediacaran tectono-metamorphic events in the Adamawa-Yadé Domain of the Central Africa Fold Belt: Insight from the zircon U–Pb LAM-ICP-MS geochronology of the metadiorite of Meiganga (Central Cameroon). *Geol. J.* 2018; 1–14.
- Ganwa, A.A., Frisch, W., Siebel, W., Ekodeck, G.E., Cosmas, S.K., Ngako, V., 2008. Archean inheritances in the pyroxene-amphibole bearing gneiss of the Méiganga area (Central North Cameroon): Geochemical and $^{207}\text{Pb}/^{206}\text{Pb}$ age imprints. *C. R. Géoscience*, 340, 211–222.
- Gèze, B., 1953. Les volcans du Cameroun occidental. *Bulletin volcanologique*, sér II 13, 63–92 (16 plates).
- Giggenbach, W., 1990. Water and gas chemistry of Lake Nyos and its bearing on the eruptive process. *J. Volcanol. Geotherm. Res.* 42 (4), 337–362.
- Girod M., Dautria J.-M., Balle, Soba D. (1984). Estimation de la profondeur du manteau du Moho sous le massif volcanique de l'Adamaoua (Cameroun) à partir de l'étude d'enclaves de lherzolite. *Comptes Rendus de l'Académie des Sciences Paris* 298, 699-704.

- Goussi Ngalamo, J.F., Bisso, D., Abdelsalam, M.G., Atekwana, E.A., Katumwehe, A.B., Ekodeck, G.E., 2017. Geophysical imaging of metacratonization in the northern edge of the Congo craton in Cameroon. *J. Afr. Earth Sci.* 129, 94–107.
- Goussi, Ngalamo, J. F., Sob, M., Bisso, D., Abdelsalam, M. G., Atekwana, E., & Ekodeck, G. E., 2018. Lithospheric structure beneath the Central Africa Orogenic Belt in Cameroon from the analysis of satellite gravity and passive seismic data. *Tectonophysics* 745, 326–337.
- Jochum, K. P., Stoll, B., Herwig, K., Willbold, M., Hofmann, A. W., Amini, M., Aarburg, S., Abouchami, W., Hellebrand, E., Mocek, B., Raczek, I., Stracke, A., Alard, O., Bouman, C., Becker, St., Dücking, M., Brätz, H., Klemm, R., de Bruin, D., Canil, D., Cornell, D., de Hoog, C.-J., Dalpé, C., Danyushevsky, L., Eisenhauer, A., Gao, Y., Snow, J.E., Groschopf, N., Günther, D., Latkoczy, C., Guillong, M., Hauri, E., Höfer, H.E., Lahaye, Y., Horz, K., Jacob, D. E., Kasemann, S. A., Kent, A. J. R., Ludwig, T., Zack, T., Mason, P. R. D., Meixner, A., Rosner, M., Misawa, K., Nash, B. P., Pfänder, J., Premo, W. R., Sun, W. D., Tiepolo, M., Vannucci, R., Vennemann, T., Wayne, D., Woodhead, J. D., 2006. MPI-DING reference glasses for in-situ microanalysis: new reference values for element concentrations and isotope ratios. *Geochem. Geophys. Geosyst.* 7 (2), Q02008.
- Jochum, K.P., Nohl, U., Herwig, K., Lammel, E., Stoll, B., Hofmann, A.W., 2005. GeoReM: A new geochemical database for reference materials and isotopic standards. *Geostand. Geoanalyt. Res.* 29, 333–338.
- Jochum, K.P., Weis, U., Stoll, B., Kuzmin, D., Yang, Q., Raczek, I., Jacob, D.E., Stracke, A., Birbaum, K., D.A., Frick, Günther D., Enzweiler, J., 2011. Determination of Reference Values for NIST SRM 610-617 Glasses Following ISO Guidelines. *Geostand. Geoanalyt. Res.* 35(4), 397–429.
- Kamdem, J.B., Kraml, M., Keller, J., Henjes-Kunst, F., 2002. CameroonLine magmatism: conventional K/Ar and single crystal laser⁴⁰Ar/³⁹Ar ages of rocks and minerals from the Hossere Nigo androgenic complex, Cameroon. *Journal of African Earth Sciences* 35, 99–105.
- Kamgang, P., Chazot, G., Njonfang, E., Ngongang, N.B.T., Tchoua, F.M., 2013. Mantle sources and magma evolution beneath the Cameroon Volcanic Line: geochemistry of mafic rocks from the Bamenda Mountains (NW Cameroon). *Gondwana Research* 24, 727-741.
- Kemgang, Ghomsi, F. E., Sévérin, N., Mandal, A., Nyam, F. E. A., Tenzer, R., Tokam Kamga, A. P., & Nouayou, R., 2020. Cameroon’s crustal configuration from global gravity and topographic models and seismic data. *J. Afr. Earth Sci.*, 103657.

- Kling, G. W., Tuttle, M.L., Evans, W.C., 1989. The evolution of thermal structure and water chemistry in Lake Nyos. *J. Volcanol. Geotherm. Res.* 39 (2–3), 151–165.
- Kovacs, I., Hermann, J., O'Neill, H. St. C., FitzGerald, J.D., Sambridge, M., Horvath, G., 2008. Quantitative absorbance spectroscopy with unpolarized light, Part II: Experimental evaluation and development of a protocol for quantitative analysis of mineral IR spectra. *Am. Mineral.* 93, 765-778.
- Kusakabe, M., Ohsumi, T., Aramaki, S., 1989. The Lake Nyos gas disaster: chemical and isotopic evidence in waters and dissolved gases from three Cameroonian crater lakes, Nyos, Monoun and Wum. *J. Volcanol. Geotherm. Res.* 39 (2–3),167–185.
- Lasserre, M., 1978. Mise au point sur les granitoïdes dits “ultime” du Cameroun : gisement, pétrographie et géochronologie. *Bull BRGM (2) IV*, 143-159.
- Lee, D. C., Halliday N., Davies G. R., Essene E. J., Fitton G. J., Temdjim, R., 1996. Melt enrichment of shallow depleted mantle: a detailed petrological, trace element and isotopic study of mantle-derived xenoliths and megacrysts from the Cameroon Line. *J. Petrol.* 37:415–441.
- Lee, D.C., Halliday, A.N., Fitton, J.F., Poli, G., 1994. Isotopic variation with distance and time in the volcanic Islands of the Cameroon line: evidence for a mantle plume origin. *Earth and Planetary Science Letters* 123, 119-138.
- Liu, C-Z, Yang, L-Y, Li X-H, Tchouankoue, J.P., 2017. Age and Sr-Nd-Hf isotopes of the sub-continental lithospheric mantle beneath the Cameroon Volcanic Line: constraints from the Nyos mantle xenoliths. *Chem Geol* 455, 84–97.
- Marzoli A, Renne PR, Piccirillo EM, Castorina F, Bellieni G, Melfi AJ, Nyobe JB & N’ni J (1999) silicic magmas from the continental Cameroon Volcanic Line (Oku, Bambouto and Ngaoundere):⁴⁰Ar-³⁹Ar dates, petrology, Sr-Nd-O isotopes and their petrogenetic significance. *Contrib. Mineral. Petrol.* 135, 133-150.
- Marzoli A., Piccirillo, E.M., Renne, P.R., Bellieni, G., Iacumin, M., Nyobe, J.B., Aka, F.T., 2000. The Cameroon Volcanic Line revisited: petrogenesis of continental basaltic magmas from lithospheric and asthenospheric mantle sources. *J. Petrol.* 41, 87-109.
- Matsukage, K.N., Oya, M., 2010. Petrological and chemical variability of peridotite xenoliths from the Cameroon Volcanic Line, West Africa: an evidence for plume emplacement. *J. Mineral. Petrol. Sci.* 105, 57–69.
- Mbowou, G. I. B., C. Lagmet, S. Nomade, I. Ngounouno, B. Deruelle, and D. Ohnenstetter, 2012. Petrology of the Late Cretaceous peralkaline rhyolites (pantellerite and commendite) from Lake Chad, Central Africa, *J. Geosci.*, 57, 127–141.

- Mbowou, G.I., Nguihdama, D., Yamgouot, F.N., Ntounde, M., Youpoungam, A.A., Ngounouno, I., 2017. Mineral chemistry of wehrlite xenoliths hosted in basalts from the SW of Hossere Dammougale (Adamawa Plateau, Cameroon): thermobarometric implications. *Open J. Geol.* 7, 1465–1477.
- Meyers, J., Rosendahl, B.R., Harrison, C.G., Ding, Z.D., 1998. Deep-imaging seismic and gravity results from the offshore Cameroon Volcanic Line, and speculation of African hotlines. *Tectonophysics* 284, 31-63.
- Montigny, R., I. Ngounouno, and B. Deruelle (2004), Âges KAr des roches magmatiques du fossé de Garoua (Cameroun): Leur place dans le cadre de la Ligne du Cameroun, *Comptes Rendus Geosci.*, 336(16), 1463–1471.
- Moreau C, Regnault JM, Déruelle B, Robineau B. A new tectonic model for the Cameroun line, Central Africa. *Tectonophysics*. 1987; 139: 317-334.
- Nformidah, N.S.S, 2016. Mineralogic and fluid inclusion study of mantle xenoliths from Kuk, Wum and Etome (North-West Cameroon): implications for CO₂ concentrations.
- Nformidah, N.S.S, Tollan, P.M.E., Hermann J., Tchouankoue, J.P., submitted. Depletion and refertilisation of the lithospheric mantle below the kapsiki plateau (northern Cameroon Volcanic Line) deduced from trace element and H₂O systematics in mantle xenoliths.
- Ngako, V., Jégouzo, P., Nzenti, J.P., 1991. Le Cisaillement Centre Camerounais. Role structural et géodynamique dans l'orogénèse panafricaine. *Comptes Rendus Académie Sciences Paris* 313, 457–463.
- Ngako, V., Njonfang, E., Aka, F.T., Affaton, P., Nnange, J.M., 2006. The North-South Paleozoic to Quaternary trend of alkaline magmatism from Niger-Nigeria to Cameroon: complex interaction between hotspots and Precambrian faults. *Journal of African Earth Sciences* 45 (3), 241-256.
- Ngounouno, I., Déruelle, B. and Demaiffe, D., 2000. Petrology of the Bimodal Cenozoic Volcanism of the Kapsiki Plateau (Northernmost Cameroon, Central Africa). *J. Vol. Geothermal Res.*, 102, 21-44.
- Ngounouno, I., Deruelle, B., Bardintzeff, J.M., 2001. Wehrlite and clinopyroxenite xenoliths from Mt Cameroon: implications for lithospheric processes. XI European Union of Geosciences meeting, Strasbourg, 8-12 April 2001. *J. Conf. Abstr.* 6, 474-475.
- Nguihdama D (2007). *Pétrologie des xénolites des lherzolites à spinelle de Liri (Sud du Plateau Kapsiki, Cameroun)*. Unpublished MSci. thesis, Université Yaoundé 1 Cameroun, pp 1-50.

- Nguihdama, D., Chazot, G., Kamgang, P., Mbouwou, G.I.B., Ngounouno, I., 2014. Spinel bearing lherzolite xenoliths from Hossere Garba (Likok, Adamawa-Cameroon): mineral compositions and geothermobarometric implications. *Int. J. Geosci.* 5, 1435–1444.
- Njeudjang, K., Essi, J.M.A., Kana, J.D., Teikeu, W.A., Nouck, P.N., Djongyang, N., Tchinda, R., 2020. Gravity investigation of the Cameroon volcanic line in Adamawa region: geothermal features and structural control. *J. Afr. Earth Sci.* 165, 103809.
- Njilah I. K., (1991). Geochemistry and Petrogenesis of Tertiary-Quaternary volcanic rocks from the Oku-Ndu Area, N.W. Cameroon. PhD thesis, Univ. of Leeds, 345p.
- Njilah, K., Temdjim, R., Nzolang, C., Tchuitchou, R., Ajonina, H., 2007. Geochemistry of Tertiary-Quaternary lavas of Mt. Oku, Northwest Cameroon, 040. *Revisita facultad de ingenieria Universidad de Antioquia*, Junio, pp. 59-75.
- Njombie Wagsong, P.M., Temdjim, R., Foley, S.F., 2018. Petrology of spinel lherzolite xenoliths from Youkou volcano, Adamawa Massif, Cameroon Volcanic Line: mineralogical and geochemical fingerprints of sub-rift mantle processes. *Contrib. Mineral. Petrol.* 173, 13.
- Njonfang, E., Moreau, C., 2000. The mafic mineralogy of the Pandé massif, Tikar plain, Cameroon: Implications for a peralkaline affinity and emplacement from highly evolved alkaline magma. *Mineralogical Magazine* 64, 525–537.
- Nkouandou, O. F., Bardintzeff, J.-M., Fagny, A.M., 2015. Sub-continental lithospheric mantle structure beneath the Adamawa plateau inferred from the petrology of ultramafic xenoliths from Ngaoundere (Adamawa Plateau, Cameroon, Central Africa). *J. Afr. Earth Sci.* 111, 26–40.
- Nkouandou, O. F., Ngounouno, I., D'éruelle, B., Ohnenstetter, D., Montigny, R., Demaiffe, D., 2008. Petrography of the Mio-Pliocene volcanism to the North and East of Ngaound'éré (Adamawa, Cameroon). *Compt. Rendus Geosci.* 340, 28–37.
- Nkouandou, O. F., Temdjim, R., 2011. Petrology of spinel lherzolite xenoliths and host basaltic lava from Ngao Voglar volcano, Adamawa Massif (Cameroon Volcanic Line, West Africa): equilibrium conditions and mantle characteristics. *J. Geosci.* 56, 375-387.
- Nkoumbou, C., Barbey, P., Yonta-Ngouné, C., Paquette, J.L., Villiéras, F., 2014. Pre-collisional geodynamic context of the southern margin of the Pan-African fold belt in Cameroon. *Journal of African Earth Sciences* 99, 245–260.
- Nnange, J.M., Poudjom-Djomani, Y.H., Fairhead, J.D., Ebinger, C., 2001. Determination of the isostatic compensation mechanism of the region of the Adamawa dome, west-central Africa using the admittance technique of gravity data. *Afr. J. Sci. Technol. Sci. Eng. Ser.* 1 (4), 29–35.

- Okereke C. S. Contrasting modes of rifting: The Benue trough and the Cameroon volcanic line, West Africa. *Tectonophysics*. 1988; 7:775-784.
- Pasyanos, M., Nyblade, A., 2007. A top to bottom lithospheric study of Africa and Arabia, *Tectonophysics* 444 (1–4), 27– 44.
- Paton, C., Hellestrom, J., Paul, B., Woodhead, J., Hergt, J., 2011. Iolite: freeware for the visualisation and processing of mass spectrometric data. *J. Anal. At. Spectrom.* 26, 2508–2518.
- Pearson, D. G., Canil, D. & Shirey, S. B. (2003). Mantle samples included in volcanic rocks: xenoliths and diamonds. In: Carlson, R. W. (ed.). *The Mantle and Core. Treatise of Geochemistry, Vol.2.* Amsterdam: Elsevier, pp. 172-260.
- Penaye, J., Toteu, S. F., Van Schumus, W. R. & Nzenti, J. P. (1993) U-Pb and Sm-Nd geochronologic data on the Yaoundé series, Cameroon: reinterpretation of the granulitic rocks as the suture of a collision in the "Centrafrican belt". *Comptes Rendus de l'Académie des Sciences, Sciences de la Terre et des Planètes*, 317, 789-794.
- Pintér, Zs, Patkó, L., Djoukam, J.F.T., Kovács, I., Tchouankoue, J.P., Falus, G., Konc, Z., Tommasi, A., Barou, F., Mihály, J., Németh, Cs, Jeffries, T., 2015. Characterization of the sub-continental lithospheric mantle beneath the Cameroon volcanic line inferred from alkaline basalt hosted peridotite xenoliths from Barombi Mbo and Nyos Lakes. *J. Afr. Earth Sci.* 111, 170–193.
- Plomerova, J., V. Babuška, C. Dorbath, L. Dorbath, and R. Lillie, 1993. Deep lithospheric structure across the Central African shear zone in Cameroon, *Geophys. J. Int.*, 115(2), 381–390.
- Poudjom Djomani, Y.H., Diament, M., Albouy, Y., 1992. Mechanical behaviour of the lithosphere beneath the Adamawa uplift (Cameroon, West Africa) based on gravity data. *Journal of African Earth Sciences* 15, 81-90.
- Poudjom Djomani, Y.H., Diament, M., Wilson, M., 1997. Lithospheric structure across the Adamawa plateau (Cameroon) from gravity studies. *Tectonophysics*, 273 (1997), pp. 317-327.
- Poudjom-Djomani, Y.H., Nnange, J.M., Diament, M., Ebinger, C.J, Fairhead, J.D., 1995. Effective elastic thickness and crustal thickness variations in West Central Africa inferred from gravity data. *J. Geophys. Res. Solid Earth* 100 (10-11): 22047-22070.
- Princivalle, F., Salviulo, G., Marzoli, A., Piccirillo, E.M., 2000. Clinopyroxene of spinel peridotite mantle xenoliths from Lake Nji (Cameroon Volcanic Line, W. Africa): crystal chemistry and petrological implications. *Contrib. Mineral. Petrol.* 139, 503-508.

- Regnault, J.M., 1986. "Cameroon Geological Synthesis," Department of Mines and Geology, Yaounde. 119p.
- Sigurdsson, H., 1988. Gas bursts from Cameroon crater lakes: a new natural hazard. *Disasters* 12 (2), 131–146.
- Tamen J., Nkoumbou C., Reusser E., Tchoua F., 2015. Petrology and geochemistry of mantle xenoliths from the Kapsiki Plateau (Cameroon Volcanic Line): Implications for lithospheric upwelling. *J. Afr. Earth Sci.* 101:119–134.
- Tazieff, H., 1989. Mechanisms of the Nyos carbon dioxide disaster and of so-called phreatic steam eruptions. *J. Volcanol. Geotherm. Res.* 39 (2–3), 109–116.
- Tchakounté J, Eglinger A, Toteu SF, Zeh A, Nkoumbou C, Mvondo Ondo J, Penaye J, Wit de M, Barbey P (2017) The Adamawa Yadé domain, a piece of Archean crust in the Neoproterozoic Central African orogenic belt (Bafia area, Cameroon). *Precambrian Res* 299: 210–229.
- Tchameni, R., Pouclet, A., Penaye, J., Ganwa, A.A. and Toteu, S.F. (2006). Petrography and Geochemistry of the Ngaoundéré Pan-African Granitoids in Central North Cameroon: Implications for Their Sources and Geological Setting. *Journal of African Earth Sciences*, 44, 511-529.
- Teitchou, M.I., Gregoire, M., Dantas, C., Tchoua, F.M., 2007. Le manteau superieur a l'aplomb de la plaine de Kumba (ligne du Cameroun), d'apres les enclaves de peridotites a spinelles dans les laves basaltiques. *Comptes Rendus Geosci.* 339, 101-109.
- Temdjim, R., 2012. Ultramafic xenoliths from Lake Nyos area, Cameroon volcanic line, West-central Africa: petrography, mineral chemistry, equilibration conditions and metasomatic features. *Chem. Erde* 72, 39-60.
- Temdjim, R., Boivin, P., Chazot, G., Robin, C., Rouleau, E., 2004. L'heterogeneite du manteau superieur a l'aplomb du volcan du Nyos (Cameroun) révélée par les enclaves ultrabasiqes. *Comptes Rendus Geosci.* 336, 1239-1244.
- Temdjim, R., Njombie Wagsong, P.M., Nzakou, T.J.A., Foley, S.F., 2019. Variation in mantle lithology and composition beneath the Ngao Bilta volcano, Adamawa Massif, Cameroon volcanic line, West-central Africa. *Geosci. Front.* 11, 665–677.
- Tokam, A.-P. K., Tabod, C. T., Nyblade, A. A., Julià, J., Wiens, D. A., Pasyanos, M. E., 2010. Structure of the crust beneath Cameroon, West Africa, from the joint inversion of Rayleigh wave group velocities and receiver functions. *Geophys. J. Int.* 183, 1061– 1076.
- Toteu, S. F., Van Schmus, W. R., Penaye, J., Michard, A., 2001. New U-Pb, and Sm-Nd data from North-Central Cameroon and its bearing on the pre-Pan-African history of Central Africa. *Pre. Res.* 108: 45-73.

- Toteu, S.F., Penaye, J., Djomani, Y.P., 2004. U–Pb and Sm–Nd evidence for Eburnean and PanAfrican high-grade metamorphism in cratonic rocks of southern Cameroon. *Can. J. Earth Sci.* 41, 73–85.
- Tsozué, D., Nzeugang, A.N., Azinwi, P.T., 2017. Genesis and Classification of Soils Developed on Gabbro in the High Reliefs of Maroua Region, North Cameroon. *Eurasian J. Soil Sci.*, 6, 168-177.
- Van Schmus, W.R., Oliviera, E.P., Silva Filho, A.F., Toteu, S.F., Penaye, J., Guimares, I.P., 2008. Proterozoic links between the Borborema Province, NE Brazil, and the Central African Fold Belt. In: Pankurst, R.J., RAJ, Trouw, Brito Neves, B.B., de Wit, M.J. (Eds.), *WestGondwana: Pre-Cenozoic Correlations Across the South Atlantic Region*, 294th ed. Geological Society of London, London, pp. 69–100 (Special Publications).
- Vincent, P.M., Armstrong, R.L., 1973. Volcanism of the Kapsiki Plateau (North Cameroon) and the underlying sedimentary formations. *Coll. African Geol.*, Florence, abst. unpubl.
- Wandji, P., Tsafack, J.P.F., Bardintzeff, J.M., Nkouathio, D.G., Dongmo, A.K., Bellon, H., Guillou, H., 2009. Xenoliths of dunites, wehrlites and clinopyroxenites in the basanites from Batoke volcanic cone (Mount Cameroon, Central Africa): petrogenetic implications. *Mineral. Petrol.* 98, 81.

CHAPTER II:

**DEPLETION AND REFERTILISATION OF THE
LITHOSPHERIC MANTLE BELOW THE KAPSIKI
PLATEAU (NORTHERN CAMEROON VOLCANIC LINE)
DEDUCED FROM TRACE ELEMENT AND H₂O
SYSTEMATICS IN MANTLE XENOLITHS**

ABSTRACT

Clinopyroxene bearing spinel harzburgites recovered from Cenozoic alkaline basalts from the Kapsiki plateau were investigated with the aim of understanding depletion and enrichment processes in the subcontinental lithospheric mantle below a major tectonic line. Concentrations of major and trace elements (including H) were determined in-situ in olivine, orthopyroxene, clinopyroxene and spinel by EPMA, LA-ICP-MS and FTIR. The xenoliths are refractory with high olivine (0.91-0.92) and orthopyroxene (0.92-0.93) Mg# coupled with relatively high modal proportions of clinopyroxene (5-8%) and a remarkably wide range in clinopyroxene Mg# (0.91-0.94), interpreted to reflect high degrees of partial melting followed by modal and chemical metasomatic refertilization. Fractional partial melting model of orthopyroxene trace elements in a depleted mantle indicates 20-30% of melting.

Clinopyroxenes show two groups based on their CaO contents (18.7-18.9 and 20.6-22.6 wt.%) suggesting a secondary origin and modal metasomatism. The low Ca clinopyroxenes were the latest to be formed, and the wide range of clinopyroxene Mg# shows a lack of equilibrium with the corresponding minerals. The high Ca clinopyroxenes record ancient metasomatic events that are also documented in orthopyroxene. Cryptic metasomatism is shown by strong progressive enrichments in LREEs and MREEs of orthopyroxene and clinopyroxene. Th vs La and Sr vs Nd of clinopyroxene are used to identify different generations of metasomatism. Ti/Eu vs (La/Yb)_N and Zr/Hf systematics indicate that the metasomatizing agent has a carbonatite and a silicate component.

The structural hydroxyl contents of the different mineral phases are very low (<1 ppm for olivine, 40-48 ppm for orthopyroxene and 164-277 ppm for clinopyroxene). The very low water contents compared to typical sub-continental peridotites could be attributed to the depleted nature of the xenoliths or reflect lower water activities of carbonatitic melts relative to alkaline melts. Estimated fO_2 values expressed as $\Delta\log FMQ$, (where FMQ corresponds to the fayalite magnetite-quartz oxygen buffer) range from -0.42 to -0.26 and are consistent with only minor OH stretching regions of 3520 cm^{-1} in orthopyroxene, that is related to a ferric iron defect.

The combination of textural investigations, major, and trace element and H₂O data suggest that a refractory subcontinental lithospheric mantle was affected by several episodes of intraplate metasomatism dominated by carbonatite-silicate melts above the North-Eastern end of the Cameroon Volcanic line.

Keywords: Kapsiki plateau, partial melting, harzburgites, carbonatite metasomatism, silicate metasomatism

II. 1. INTRODUCTION

The subcontinental lithospheric mantle documents a long and complex evolution history with multiple depletion and enrichment events (Griffin et al., 2008). Disentangling the sequences of events and distinguishing between modal and cryptic metasomatism is often challenging. With the development of in-situ trace element analyses with low detection limits, the systematic study of major and trace compositions of clinopyroxene has been instrumental to constrain different types of metasomatic agents (e.g., Uenver-Thiele et al., 2017; Coltorti et al., 1999). Classifications traditionally focused on clinopyroxene compositions, as it is the phase in peridotites with the highest concentration of incompatible elements (WittEickschen and O'Neill, 2005; Eggins et al., 1998). For example, discrimination diagrams using Ti/Eu coupled with La/Yb (Coltorti et al., 1999) or Zr/Hf (Uenver Thiele et al., 2017) in clinopyroxene have been used to distinguish between carbonatite melt, carbonated silicate melt, silicate melt or subduction-related fluids as metasomatic agents. Hydrogen is an additional incompatible element in olivine, orthopyroxene and clinopyroxene (Hirschmann et al., 2009) that can give important insights into equilibrium and refertilization processes, since H₂O is a major component in many of these reacting fluids/melts (Tollan et al. 2015; Doucet et al., 2014; Peslier et al., 2012). Combined investigations of H together with incompatible trace elements in ortho- and clinopyroxene in mantle peridotites are a powerful tool to investigate complex mantle metasomatism (Peslier et al., 2012).

The Cameroon Volcanic Line (CVL) provides a good opportunity to investigate sub-continental lithospheric mantle in a complex fault zone, as many alkaline basalts that carry mantle xenoliths have been found (Pinter et al., 2015; Tamen et al., 2015; Ngounouno et al., 2008; Caldeira and Munha 2002; Lee et al., 1996). The N30°E trending

CVL formed during the Cenozoic and is segmented by several N70°E shear zones of Pan-African age which cut across both the continental crust and the upper mantle to a depth of 160 km (Deruelle et al., 2007). The Pan African belt was formed by the convergence and collision of the San Francisco-Congo cratons, the West African craton, and a Pan African mobile domain (Tokam et al., 2010; Toteu et al., 2004). In such orogenic environments where more than one crustal block has been involved, geodynamic processes such as subduction, collision or lithospheric delamination can lead to the destruction of the base of the lithosphere and hence local significant modifications of the upper mantle (Liu et al., 2017).

The Kapsiki plateau volcanism of Oligocene age (32-29 Ma, Dunlop, 1983) is close to the oldest volcanic rocks (rhyolites, 64.4 ± 0.4 Ma) of the CVL evidenced in the southern part of Chad at about 300 km to the NNE, reported by Mbowou et al., 2012. The Kapsiki plateau bears the northernmost known occurrence of mantle xenoliths along the CVL (Tamen et al., 2015) providing an important endmember to investigate depletion and metasomatic processes in the lithospheric mantle. Extended volcanism during the Cenozoic (Deruelle et al., 2007), interactions between magmas of sub-lithospheric origin and the SCLM and the speculated juvenile state of the lithospheric mantle (Marzoli et al., 2015; 2000) represent processes that might have led to such metasomatism. An added advantage is that some of the Kapsiki xenoliths are highly depleted (this work), therefore, they can easily record minor metasomatic events and are instrumental in providing insights into the state of the mantle before interactions with percolating melts, which can quickly conceal earlier metasomatic events. The Kapsiki xenoliths, therefore, are a key to understand and decipher the SCLM below the rest of the line.

This work presents new data on mineral major and trace elements plus H contents of mantle xenoliths brought to the surface by Cenozoic alkaline magmas from the Kapsiki plateau in the Kila area and discusses their implication for the nature and evolution of the SCLM below an important lithospheric fault zone. A combination of data from different analytical techniques is used to decode the different mantle processes like partial melting, metasomatism and the different possible metasomatic agents, which modified the mantle and are still debated for the CVL (Pinter et al., 2015; Tamen et al., 2015). New clinopyroxene trace element discrimination diagrams for inferring small degrees of

metasomatism by carbonatite-silicate melts are developed and have the potential to be applied to cryptic metasomatism documented in orthopyroxene.

II.2. RESULTS

II.2.1. PETROGRAPHY

The Kapsiki xenoliths hosted in Cenozoic alkali basalts are sub-angular to rounded ranging from 6 to 10 cm across and they show a sharp contact with the host basalt. According to the classification of Mercier and Nicolas (1975), they are coarse-grained with protogranular to porphyroclastic textures (Fig. 2.1a, b). Olivine and orthopyroxene range in size from 0.2-8 mm where the neoblasts are euhedral and the porphyroclasts are subhedral with strain features presenting as cracks. Kink bands are common in large olivine and orthopyroxene porphyroclasts (Fig. 2.1b). Clinopyroxene is subhedral, much smaller than the coexisting minerals (ranging in size from 0.2-1 mm) and sits in interstitial position between olivine and orthopyroxene with most of them being closely associated to orthopyroxene (Fig. 2.1a). Some of the clinopyroxenes along the boundary with the host basalt show rims with a distinct spongy texture. These textures occur also in pristine parts of the xenoliths and clinopyroxene in direct contact with the host basalt does not show such features (Fig. 2c). Exsolution lamellae of clinopyroxene are common in the central part of orthopyroxene porphyroclasts (Fig. 2.1d). Vermicular dark-brown spinel occurs as holly-leaf shapes in interstitial position between olivine and pyroxenes (Fig. 2.1e).

Modal proportions obtained from visual estimates of olivine (~60-64 vol. %), orthopyroxene (~30-34 %) and clinopyroxene (~4-6 %) and projected on Steckeisen's (1976) classification diagram of ultramafic rocks fall close to the Iherzolite-harzburgite boundary. Sample Ka7 shows the highest proportion of clinopyroxene (~6%). Spinel occurs in minor proportions (~2 %) and no hydrous phases are present except for tiny amphibole lamellae in clinopyroxene.

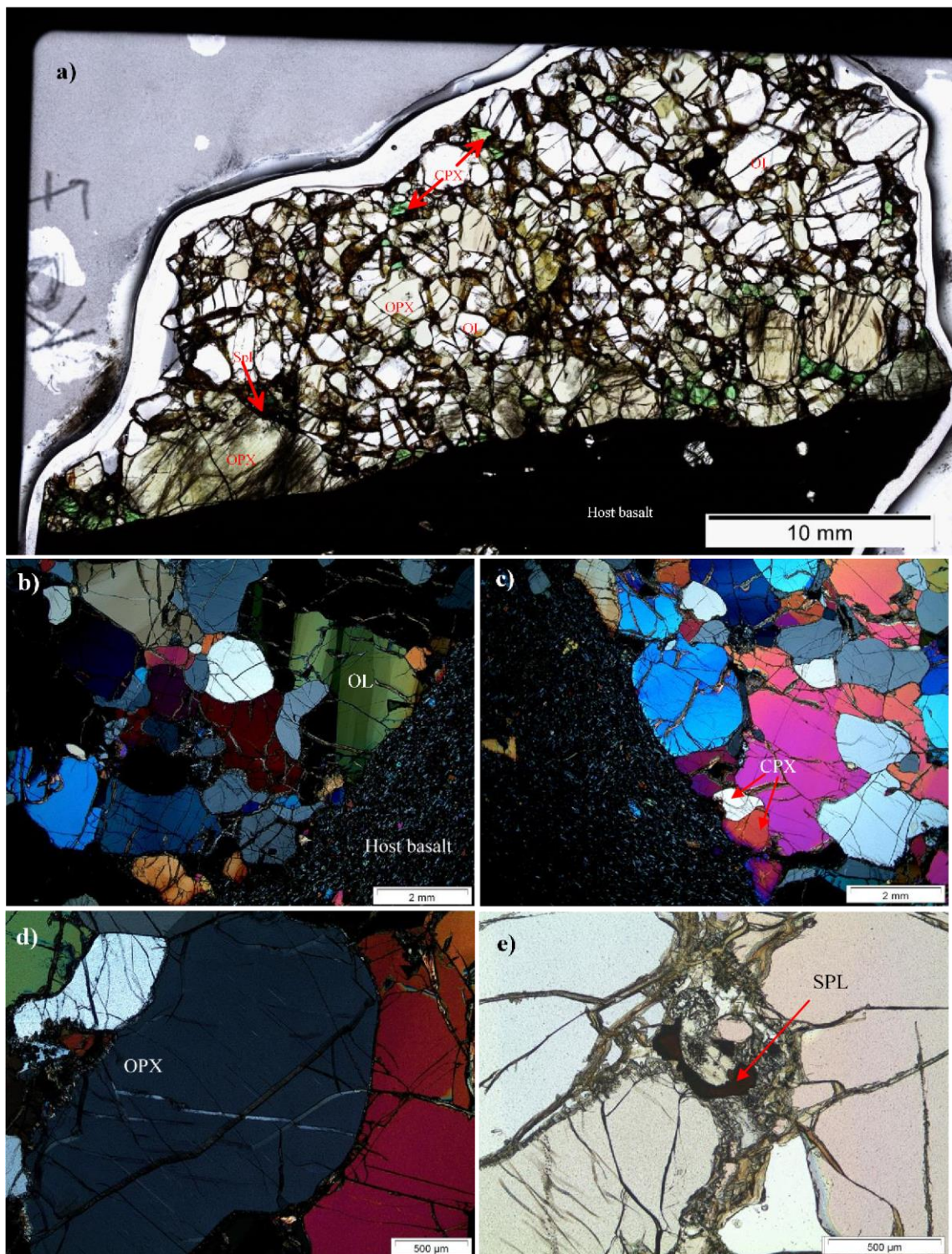


Figure 2.1 (a): Thin section scan of Kapsiki xenolith showing large olivine and orthopyroxene crystals, with smaller clinopyroxene in interstitial position (Ka7); (b) large olivine showing kink bands and a sharp contact at the host basalt-xenolith boundary (Ka1); (c) clinopyroxene which shows no interaction with the host basalt (Ka2); (d) exsolution lamella of clinopyroxene in orthopyroxene (Ka1); (e) dark brown spinel with the coexisting mineral showing melt veinlets (Ka1).

II.2.2. MINERAL CHEMISTRY

EPMA and LA-ICP-MS analysis of the different phases are reported in the Supplementary Data Appendix 2.1 and 2.2.

II.2.2.1. Major elements

Olivine grains are relatively homogeneous with no major core-rim or porphyroclast-neoblast chemical variations. Sample Ka1 is the most refractory with average Mg# ($\text{Mg}/(\text{Mg}+\text{Fe})$) of 0.917 ± 0.001 (Fig. 2.2a) (Supplementary material, Appendix 2.1), MnO contents of 0.13 ± 0.01 and NiO contents of 0.42 ± 0.03 . Olivine of sample Ka2 has Mg# of 0.914 ± 0.001 , MnO and NiO contents of 0.13 ± 0.01 and 0.43 ± 0.02 respectively. Sample Ka7 is identical to sample Ka2 with Mg# of 0.913 ± 0.001 , MnO and NiO of 0.14 ± 0.01 and 0.42 ± 0.03 respectively. There is a clear difference in Mg# between samples Ka1 and Ka2, Ka7, however, in terms of MnO and NiO, they all overlap within error.

Orthopyroxene grains have chemically identical porphyroclasts and neoblasts. Calculated Mg#s range from 0.92-0.93 (Supplementary material, Appendix 2.1, Fig. 2.2b) and are 0.5% (Ka1), 0.3% (Ka2) and 0.6% (Ka7) higher than the coexisting olivines. End member compositions are $\text{En}_{90.4}\text{-}\text{En}_{91.9}\text{Fs}_{7.3}\text{-}\text{Fs}_{8.2}\text{Wo}_{0.7}\text{-}\text{Wo}_{1.3}$, $\text{En}_{90.1}\text{-}\text{En}_{90.9}\text{Fs}_{8.3}\text{-}\text{Fs}_{8.8}\text{Wo}_{0.8}\text{-}\text{Wo}_{1.2}$, $\text{En}_{90.3}\text{-}\text{En}_{91.2}\text{Fs}_{8.0}\text{-}\text{Fs}_{8.7}\text{Wo}_{0.7}\text{-}\text{Wo}_{1.4}$ for Ka1, Ka2 and Ka7 respectively. The TiO_2 , CaO and Al_2O_3 contents are low (0.02-0.09, 0.36-0.75 and 1.32-2.31 wt% respectively) while Cr_2O_3 contents are relatively high (0.29-0.65 wt.%).

Unlike olivine and orthopyroxene, clinopyroxene shows considerable intergrain chemical variations in TiO_2 , Cr_2O_3 , CaO, Na_2O and Mg#, with compositions ranging from Cr-rich diopside to Cr-rich augite ($\text{En}_{47.7}\text{-}\text{En}_{48.8}\text{Fs}_{33.3}\text{-}\text{Fs}_{35.1}\text{Wo}_{42.4}\text{-}\text{Wo}_{48.8}$). Two groups can be distinguished based principally on their CaO contents and Mg# (Fig. 2.2c, d). The first group has low CaO contents (18.7-18.9 wt.%) (Supplementary material, Appendix 2.1) and the lowest Mg# (0.91-0.92) and occurs only in sample Ka1. The second group has high CaO contents (20.62-22.57 wt.%), Mg# which varies more, extending to higher values (0.91-0.94) and is found in all samples. Group 1 clinopyroxenes show higher Al_2O_3 contents (Fig. 2.2c) in the range of 3.7-3.8 (Supplementary material, Appendix 2.1), group 2 clinopyroxenes show a wider range of Al_2O_3 contents with values of 2.9-

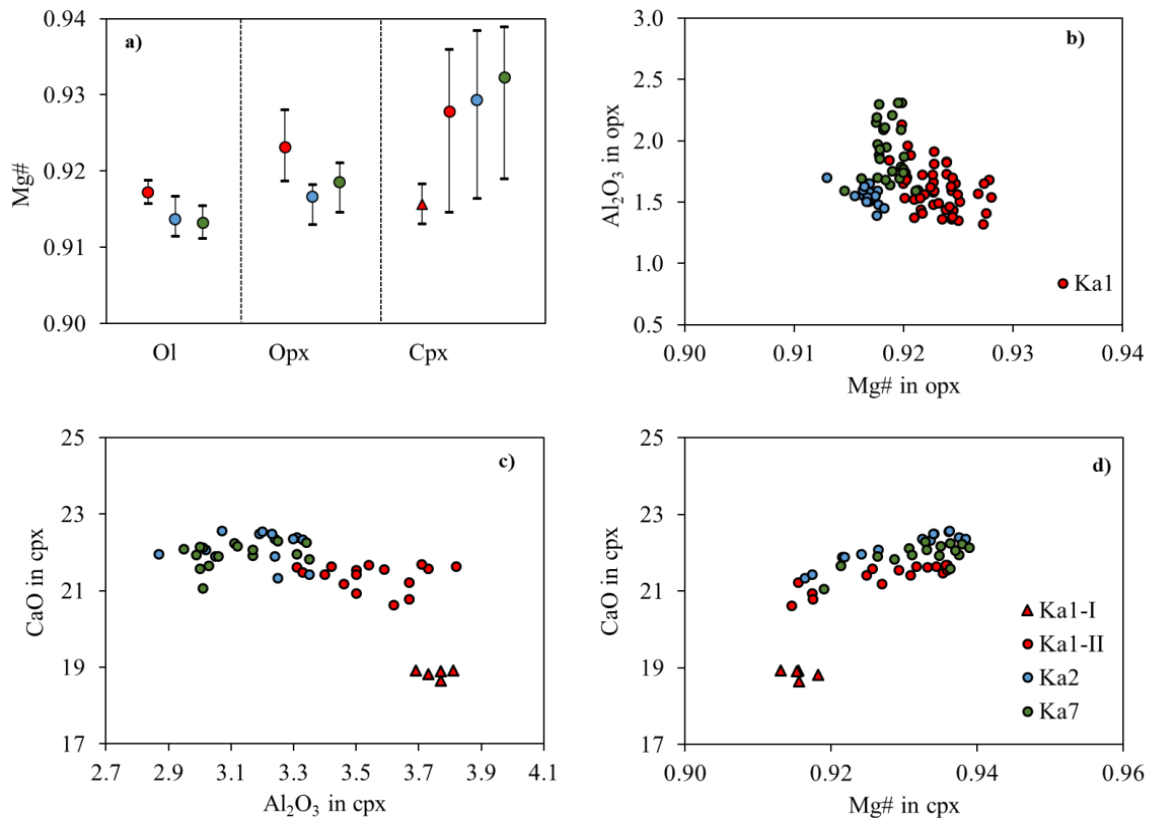


Figure 2.2.a: Average Mg# of olivine, ortho- and clinopyroxene. The bars represent minimum and maximum values. b) major element compositions of orthopyroxene and c, d) clinopyroxene showing two generations.

3.8 wt.% with sample Ka1 showing the highest values. TiO₂ contents in group 1 and 2 range from 0.13-0.26 and 0.11-0.24 wt.% (Supplementary material, Appendix 2.1) respectively and Na₂O ranges from 1.20-1.47 wt.% (group1) and 0.27-1.83 wt.% (group 2).

Spinels from Kapsiki samples are relatively heterogeneous with Cr₂O₃ contents of 39.0-44.4, 36.2-38.9 and 35.7-38.3 wt.%, Al₂O₃ contents of 23.9-29.8, 28.8-32.1 and 29.1-31.7 wt.%, TiO₂ contents of 0.11-0.48, 0.11-0.25 and 0.13-0.25 wt.% (Supplementary material, Appendix 2.1) in samples Ka1, Ka2 and Ka7 respectively. Mg#s are 0.62-0.68 for Ka1 and 0.64-0.68 for Ka2 and Ka7 while Cr# (Cr/Cr+Al) are 0.47-0.55 for Ka1, 0.43-0.48 for Ka2 and 0.43-0.47 for Ka7. Fe³⁺/ΣFe, with Fe³⁺ calculated based on charge balance, ranges from 0.07-0.16 for Ka1 and 0.08-0.19 for Ka2 and Ka7.

II.2.2.2. Trace elements

Measurements were done in the cores of olivine, orthopyroxene and clinopyroxene. Compared to the global distribution of mantle olivine compositions (De Hoog et al. 2010), Kapsiki olivines contain typical concentrations of Na (46-62 $\mu\text{g/g}$) and relatively low Al (60-92 $\mu\text{g/g}$), Ti (5-13 $\mu\text{g/g}$) and Cr (77-150 $\mu\text{g/g}$) (Supplementary material, Appendix 2.2). The concentrations of Na, Al, and Cr are correlated, (Fig. 2.3a, b), indicating coupled substitutions of the type CrAlMg-1Si-1 and CrNaMg-2 . Lithium correlates with Na in Ka2 and Ka7 at higher Li concentrations, while no correlation is visible in Ka1 that has lower Li contents (Fig. 2.3c). Generally, Ka2 and Ka7 olivines plot on a continuous trend whereas Ka1 is situated in a different field (Fig. 2.3a, b). Calcium (480-610 $\mu\text{g/g}$) is higher than typical spinel peridotite xenoliths (De Hoog et al., 2010). Although Y (920 ng/g) and Zr (9-13 ng/g) concentrations are very low, a clear distinction between Ka1 and Ka2, Ka7 exists (Fig. 2.3d).

REE concentrations normalized to the primitive mantle (PM) values of Palme and O'Neil, 2014 (Fig. 2.4b, d, f) show that clinopyroxene values are up to 10 times higher than PM values except for HREEs in sample Ka2 and Ka7, which are similar to or slightly lower than PM values. In sample Ka1, a few clinopyroxene grains show HREEs slightly above PM values. Clinopyroxenes from Ka2 and Ka7 (Fig. 2.4d, f) have minimal inter-grain variation in MREE and HREE concentrations ($(\text{Nd/Yb})_N = 1-3$, $\text{Yb}_N = 0.65-1.03$) but significant variation in LREE concentrations ($(\text{La/Yb})_N = 2-23$ and $(\text{La/Nd})_N = 1-9$). Clinopyroxenes from sample Ka1 differ in that they show greater inter-grain variation in MREEs and HREEs in addition to LREEs.

PM-normalized trace element plots show strong but variable relative depletions in Rb, Ba, Nb and weak negative Pb and Ti anomalies in samples Ka2 and Ka7 (Fig. 2.5b). Clinopyroxenes from Ka1 have similar features to those from samples Ka2 and Ka7, but they are more enriched in most elements and show significant intergrain variability. Three groups of TE patterns can be distinguished which are however unrelated to the textures in the sample. Group 1 clinopyroxene grains are more enriched than those from group 3, particularly in Rb, Ba, Nb and LREEs, while group 2 is intermediate between the two groups. The group 2 clinopyroxenes show the lowest Ca contents. For all three groups, concentrations of Th and U are similar to or lower than those of clinopyroxenes from Ka2 and Ka7.

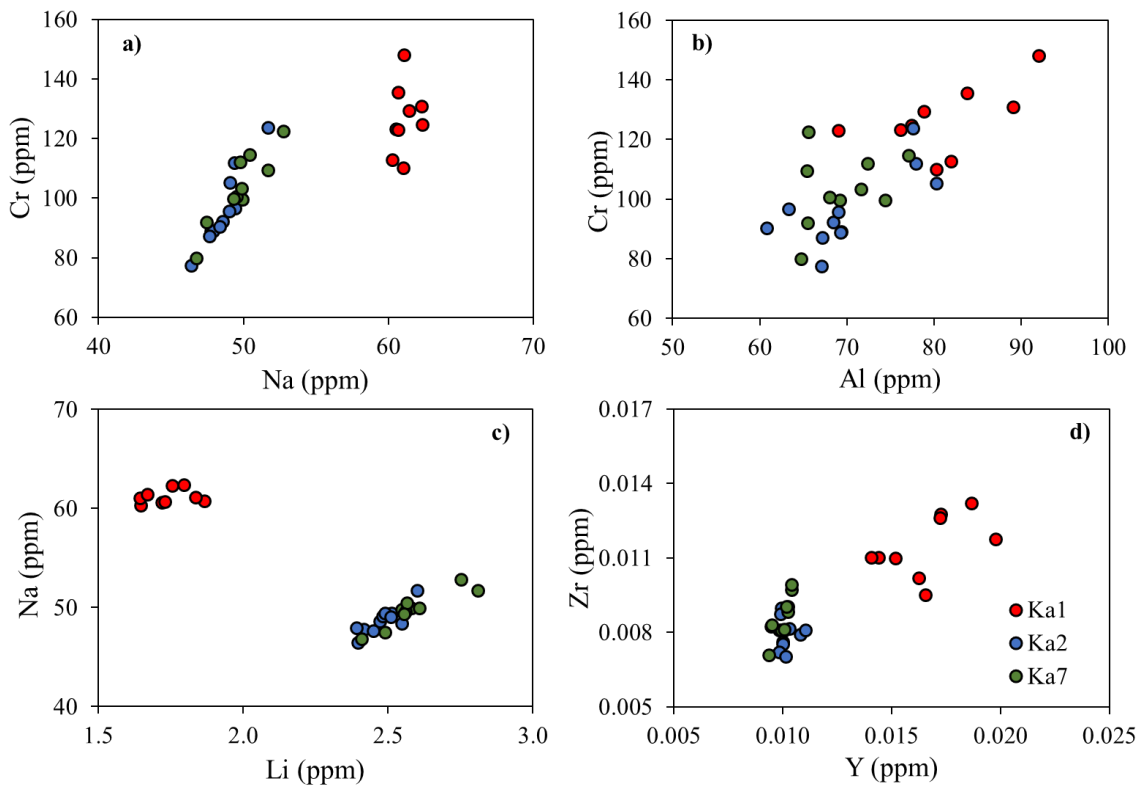


Figure 2.3: Trace element compositions of olivine showing two groups of compositions.

Orthopyroxene REEs (Fig. 2.4a, c, e) generally show a spoon shape with $(\text{Nd/Lu})_N < 1$ and $(\text{La/Nd})_N > 1$. Orthopyroxenes from Ka1 show stronger enrichments in both LREE and MREE, resulting in an overall flat REE pattern, compared to those of the other samples. Orthopyroxene from Ka7 shows two distinct patterns: a more LREE- and MREE enriched pattern, similar to Ka1, and a second, which is more similar to Ka2. Trace element patterns (Fig. 2.5a) show Th and U enrichments, a negative Nb anomaly, highly variable Sr concentrations (typically positive anomalies) and prominent positive Ti anomalies.

Overall, clinopyroxene and orthopyroxene REE plots show the same characteristic patterns (similar LREE to MREE enrichments in sample Ka1 and LREE enrichments in Ka2 and Ka7) and similar widespread compositions or shifts in the patterns except sample Ka7 orthopyroxene which shows a group of LREE- to MREE enrichments. Orthopyroxene and clinopyroxenes from all samples have almost identical Ti except for sample Ka1 clinopyroxenes, which shows variations. The HREEs of orthopyroxene of Ka1 are more depleted than the other samples, whereas those of

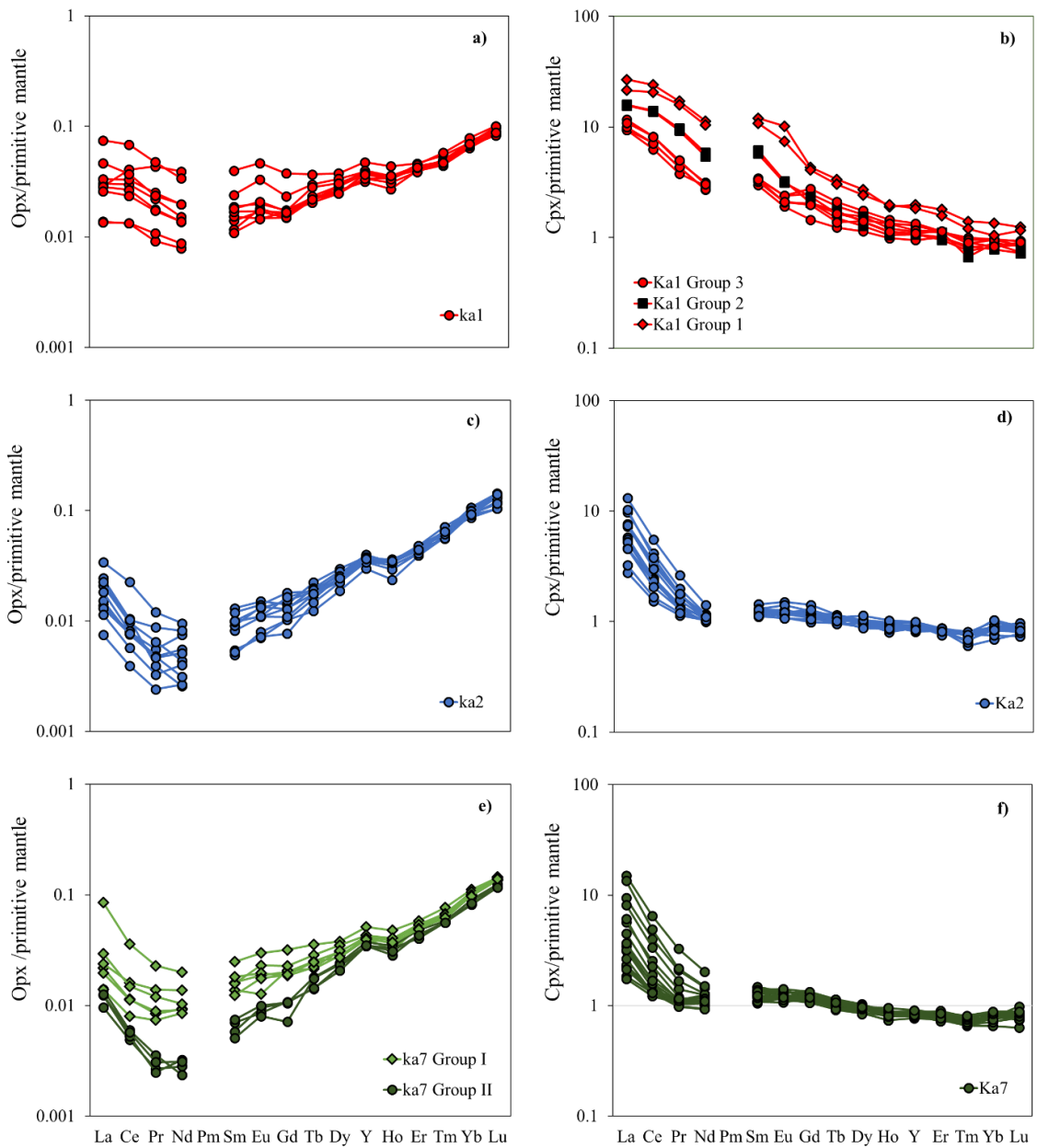


Figure 2.4: Orthopyroxene and clinopyroxene REEs normalised to primitive mantle values of Palme and O'Neill, 2014.

clinopyroxenes are more enriched. Clinopyroxenes from Ka1 show significant variation than orthopyroxene particularly Nb. In general, Ka1 clinopyroxenes are more enriched than the other samples while orthopyroxenes are not, and they show more overlap.

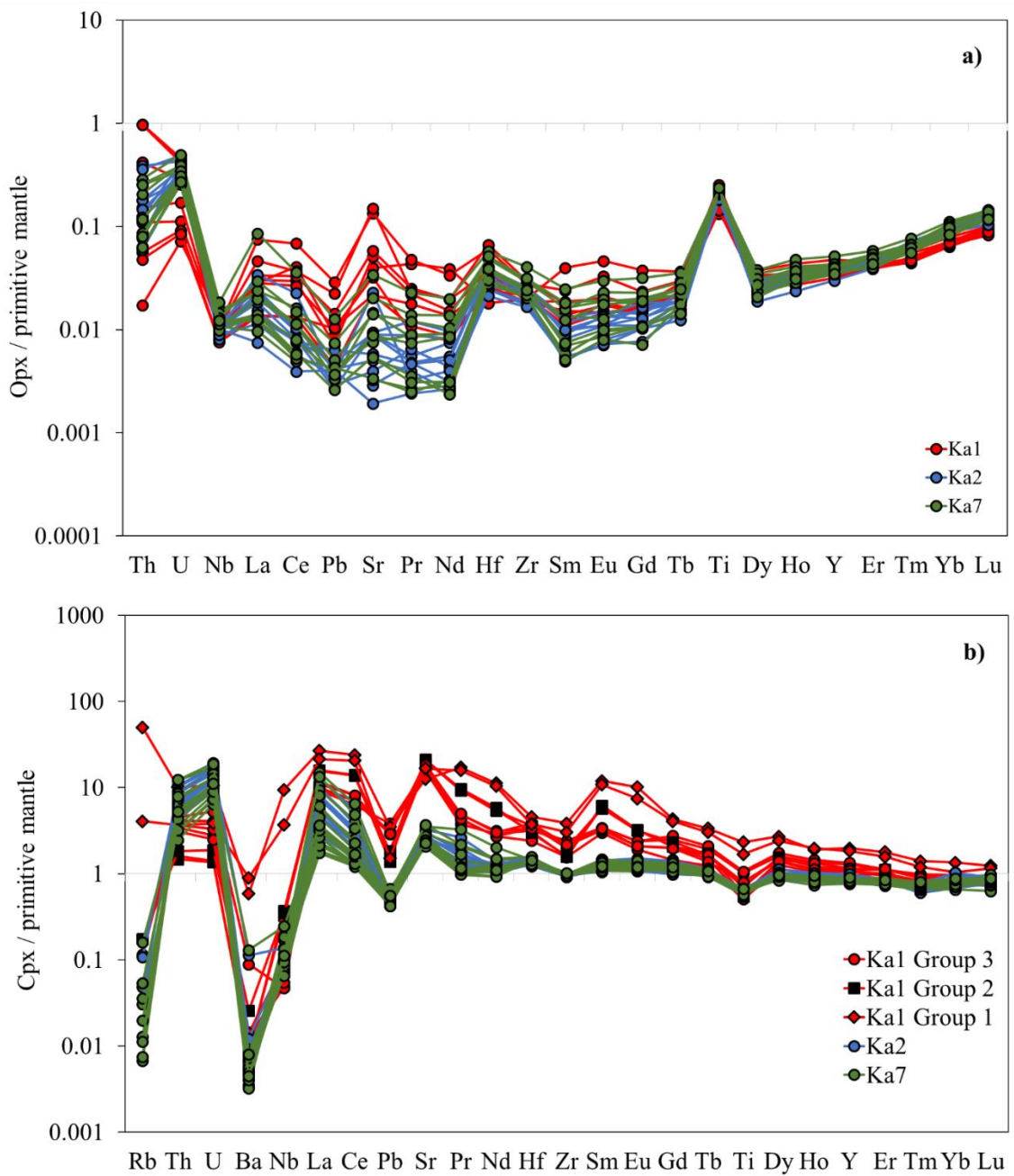


Figure 2.5a: Orthopyroxene and b) Clinopyroxene TEs normalised to primitive mantle values of Palme and O'Neill, 2014.

II.2.3. INFRARED SPECTRA AND H₂O CONCENTRATIONS

Average unpolarized infrared spectra of the orthopyroxene and clinopyroxene show a range of absorption bands in the OH stretching/vibration region between 3800-3000 cm⁻¹. Orthopyroxenes from all samples have two prominent OH absorption bands at 3597 and ~3415 cm⁻¹ (Fig. 2.6a). Additional weaker bands sometimes occur at ~3748 and ~3733 cm⁻¹. Sample Ka2 shows very weak bands at ~3524 cm⁻¹ and Ka7 shows an additional prominent band at ~3519 cm⁻¹ (Fig. 2.6a), which is not observed in the orthopyroxene from the other Kapsiki samples. Clinopyroxene from sample Ka1 exhibits a prominent band at 3638 cm⁻¹ with a shoulder at 3685 cm⁻¹. Samples Ka2 and Ka7 show four bands: a variably intense band at 3682 cm⁻¹, a more consistently intense band at 3638 cm⁻¹ and weaker bands at ~3527 and ~3448 cm⁻¹. Bands at 3682 cm⁻¹ can be attributed to the presence of amphibole lamellae (Della Ventura et al., 2007; Ingrin et al., 1989). Olivine spectra show no detectable OH bands (Fig. 2.6a).

Calculated average H₂O contents (Table 2) in Kapsiki xenoliths are 277 ppm and 285 ppm for clinopyroxenes of Ka2 (3 clinopyroxenes) and Ka7 (4 clinopyroxenes). The H₂O contents in Ka1 clinopyroxenes are much lower (164 ppm). Clinopyroxene spectra containing amphibole bands at ~3682 cm⁻¹ (Fig. 2.6b) were not considered during the calculations. Orthopyroxenes H₂O contents in all samples are in the same range from 40-48 ppm with sample Ka7 showing the highest H₂O which could be because of the extra band at ~3519. Olivine shows very low H₂O contents below the limit of detection (<1 ppm).

II.2.4. EQUILIBRIUM TEMPERATURES AND OXYGEN FUGACITY

Temperatures were calculated using several geothermometers (Table 2.1). Olivine thermometers of De Hoog et al., 2010 assuming pressures of 1.5 GPa yielded T_{Ca-ol}, T_{Al-ol} and T_{Cr-ol} of 1000-1010 °C, 920-960 °C and 950-970 °C respectively. The use of olivine is advantageous over pyroxenes because chemical diffusion in olivine tends to be faster at least for Ca and probably Cr (Tollan et al. 2015) and hence olivine may therefore be more responsive to late-stage thermal events that are not recorded by pyroxene (De Hoog et al., 2010).

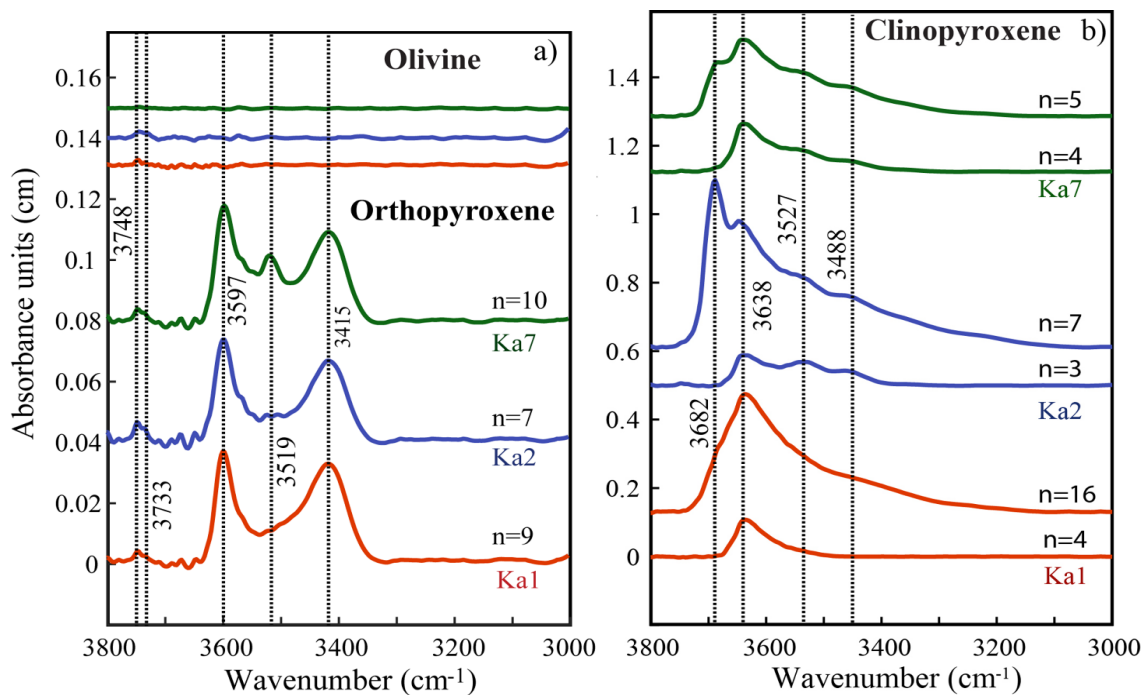


Figure 2.6: Average unpolarised FTIR spectra for a) olivine, orthopyroxene, and b) clinopyroxenes from the Kapsiki peridotites, the peak at 3682 cm^{-1} corresponds to amphibole bands Ka1 (red), Ka2 (blue), Ka7 (green). The water content values are in ppm and n is the number of grains analysed.

The Ca-in-orthopyroxene geothermometer of Brey and Köhler (1990) ($T_{\text{Ca-opx}}$) yielded temperatures of $890\text{--}900\text{ }^{\circ}\text{C}$. The olivine-spinel geothermometer (Jianping et al., 1995), which is an improved calibration of Fabries 1979, based on the partitioning of Mg^{2+} and Fe^{2+} between coexisting olivine and spinel gave temperatures of $930\text{--}980\text{ }^{\circ}\text{C}$. The olivine-spinel Al exchange thermometer of Coogan et al., 2014 yielded temperatures of $920\text{--}1060\text{ }^{\circ}\text{C}$.

Accurate application of two-pyroxene thermometry relies on the assumption that orthopyroxene and clinopyroxene are in chemical equilibrium. Both Ka2 and Ka7 contain clinopyroxene that has considerably higher and more variable Mg# than coexisting orthopyroxene (Fig. 2.2a), implying that equilibrium in these samples was not achieved. Ka1 contains two populations of clinopyroxene, one of which has lower and more homogeneous Mg# similar to that of coexisting olivine and orthopyroxene. Although perfect equilibrium cannot be demonstrated, pyroxene thermometry will give an indication of differences in equilibration temperatures. As the pyroxene solvus is

Table 2.1: Temperature T (°C) estimates for Kapsiki xenoliths

Samples	De Hoog et al., 2002			Coogan et al., 2014	Jianping et al., 1995	Brey and Kohler 1990
	T _{Al-ol}	T _{Cr-ol}	T _{Ca-ol}	T _{Al-ol-Sp}	T _{ol-sp}	BKN _{Br&Kö}
Ka1	950±10	973±10	1011±10	1061	980	1146 (low Ca) 881 (high Ca)
Ka2	924±12	954±10	1002±4	995	929	837
Ka7	927±9	953±7	1005±3	917	939	864

Table 2.2: FTIR characteristics and average hydrogen contents of orthopyroxene and clinopyroxene.

Sample	Orthopyroxene				Clinopyroxene			
	Absorbtion bands	Analyzed grains	Integral absorbance (cm ⁻¹)	H ₂ O (ppm)	Absorbtion bands	Analyzed grains	Integral absorbance (cm ⁻¹)	H ₂ O (ppm)
Ka1	3748, 3733, 3597, 3519, 3415	9	6.82 ± 0.78	46 ± 5	3682, 3638, 3527, 3488	5	11.42 ± 0.99	152 ± 16
Ka2	3748, 3733, 3597, 3415	7	6.00 ± 1.48	40 ± 8	3682, 3638, 3527, 3489	3	19.65 ± 5.12	277 ± 23
Ka7	3748, 3733, 3597, 3415	10	7.15 ± 1.46	48 ± 9	3682, 3638, 3527, 3489	4	20.24 ± 4.98	285 ± 48

asymmetric, the variations in clinopyroxene compositions are more sensitive to temperature changes and hence the two-pyroxene thermometer provides information on the conditions of clinopyroxene formation. Application of the two-pyroxene thermometer of Brey and Kohler, 1990 gives temperatures of 881 and 1146 °C for the high and low Ca clinopyroxene populations, respectively.

The redox state of the Kapsiki xenoliths were estimated from the olivine-orthopyroxene-spinel oxygen geobarometer of Ballhaus et al., 1991. Estimated fO_2 values of (expressed as $\Delta\log\text{FMQ}$, where FMQ corresponds to the fayalite-magnetite-quartz oxygen buffer) -0.39, -0.42 and -0.26 were obtained for Ka1, Ka2 and Ka7 respectively assuming pressures of 1.5 GPa and using temperatures calculated from the olivine-spinel geothermometer of Jianping et al., 1995.

II.3. DISCUSSION

II.3.1. INTERPRETATION OF TEXTURES IN THE XENOLITHS

The Kapsiki xenoliths show a sharp contact with the host basalt, which indicates rapid transport to the surface. However, a few clinopyroxene grains show spongy rims, which are randomly distributed within the sample, they show a sharp contact with the coexisting minerals and both the low and high CaO clinopyroxenes display the spongy rims. The coexisting minerals are devoid of any reaction textures. The origin of spongy textures in clinopyroxene remains under debate and have been attributed to, interactions of the xenolith with the host basalt (Shaw and Dingwell, 2008; Shaw et al., 2006), fluid/melt interaction before the transport of the xenolith to the surface (Bonadiman et al., 2008; 2005) or decompression induced melting (Su et al., 2011). The absence of relict melts along the spongy clinopyroxene argues against interactions with the host basalt. It is expected that interaction of the depleted mantle xenoliths with a basaltic melt would lead to clinopyroxene with a lower Mg# than olivine and orthopyroxene. However, the Mg# of clinopyroxene is always higher than coexisting olivine and orthopyroxene (Fig. 2.2a). Additionally, clinopyroxene show similar trace element enrichment patterns as orthopyroxene, providing evidence for cryptic metasomatism.

Therefore, we conclude that there is no evidence of secondary clinopyroxene due to interaction of the xenolith with the host basalt. Therefore, the observed textures and chemical trends are related to the evolution of the lithospheric mantle below the Kapsiki

Plateau prior to the beginning of volcanic activity at 27-35 Ma as dated by Vincent and Armstrong, 1973 and Dunlop, 1983.

II.3.2. PARTIAL MELTING

The removal of melt from the SCLM leads to both changes in mineralogy and chemistry with a transition from lherzolitic to harzburgitic assemblages. High olivine and orthopyroxene Mg# coupled with high spinel Cr# and the low pyroxene Al₂O₃ are common for the Kapsiki xenoliths. The compositional association of spinel Cr# and olivine Fo contents (Mg#) (Fig. 2.7a) defined by Arai, 1994 and used to qualify melt extraction shows that sample Ka1 is the most refractory with average Mg# (Mg/(Mg+Fe)) of 0.92, but Ka2 and Ka7 are moderately refractory with average Mg# of 0.91. Such Mg# values are higher than typical mantle olivines (0.86-0.90) (Pearson et al., 2014) indicating substantial degrees of partial melting beneath the Kapsiki plateau. The xenoliths thus represent the most refractory components in the continental CVL but are similar to xenoliths from the oceanic part of the line (Sao Tome; Caldeira and Munhá, 2002) (Fig. 2.7a).

To provide a quantitative estimate of the degree of partial melting, the methods of Hellebrand et al. (2001) and De Hoog et al. (2010) were applied, which are based on the Cr# of spinel and olivine respectively. The methods yielded 16-18% (spinel Cr#) and 12-16% (olivine Cr#) of partial melting, which is consistent with estimates of the degree of partial melting of olivine Mg# from Bernstein et al., 2007 of 15-30% for Mg# of 0.91-0.92. The high spinel Cr# could, however, also be due to modifications during interactions with fluids/melts (Gamal El Dien et al., 2019; Pearce et al., 2000). Extends of partial melting calculated for other CVL peridotites using the method of Hellebrand et al., 2001 yielded 1-14% (Liu et al., 2017) which are lower than for the Kapsiki xenoliths. Based on the model of Pearce et al., 2000, for spinel Cr# of 0.45-0.50 generated through partial melting, TiO₂ contents should be less than 0.1 wt.%. The Cr# versus TiO₂ contents in spinel (Fig. 2.7b) suggests that the Kapsiki xenoliths interacted with melts that led to an increase in TiO₂ contents.

A simple fractional partial melting model of orthopyroxene trace elements in a depleted mantle compared to measured orthopyroxene REE data (Fig. 2.8) was used to estimate the degree of partial melting. Orthopyroxene was used since clinopyroxene

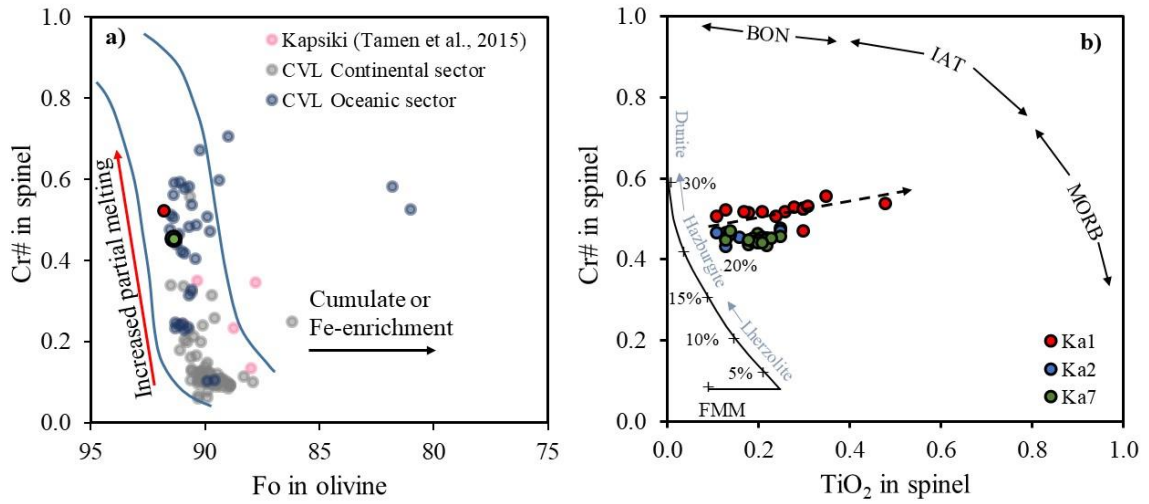


Figure 2.7a: Mg# in olivine versus Cr# in spinel showing the compositional variation of Kapsiki peridotites and peridotites from the Cameroon Line. b) Cr# in spinel versus TiO₂ in spinel.

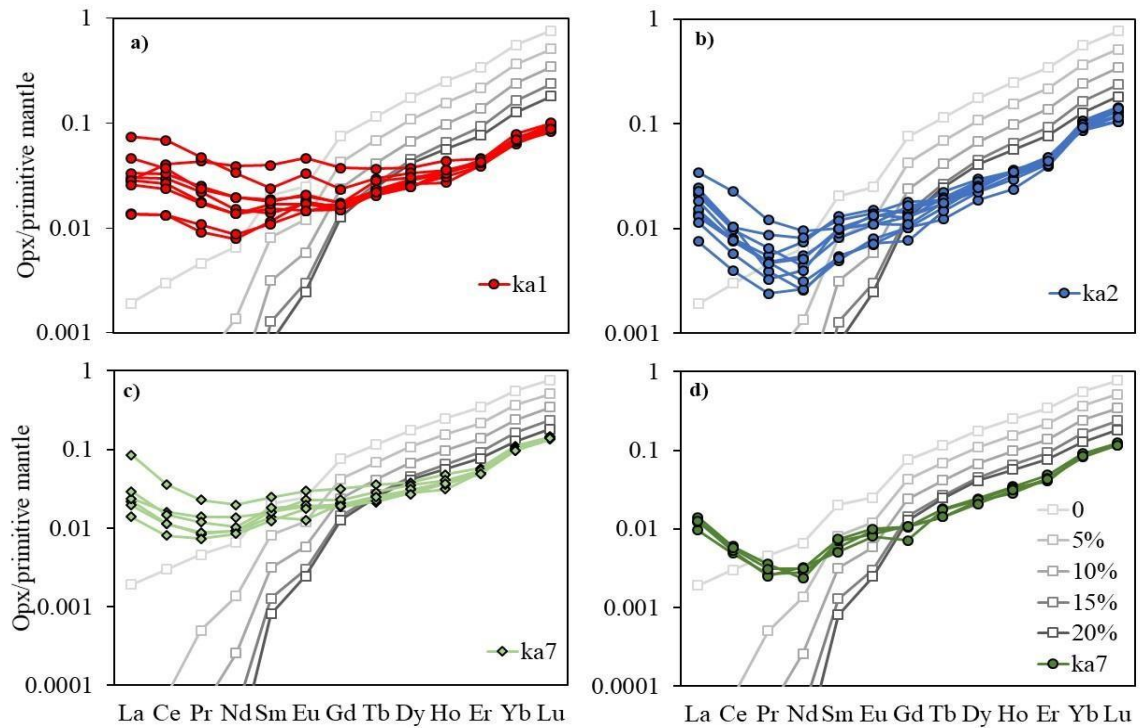


Figure 2.8: Fractional partial melting model of orthopyroxene trace elements compared to Kapsiki orthopyroxene REE data.

appears to be secondary (see below) and thus are not expected to record partial melting events. This model applies a nonmodal fractional equation (Johnson et al., 1990) to a starting composition (DMM source composition from Workmann and Hart, 2005, mineral mode and melting mode from Johnson et al., 1990 and partition coefficients ($D^{\text{cpx/melt}}$ for REE (Hart and Dunn 1993), $D^{\text{cpx/melt}}$ for Pr, Eu, Gd, Tb, Ho, Tm (Ionov et al., 2002) and $D^{\text{opx/melt}}$, $D^{\text{ol/melt}}$, $D^{\text{spl/melt}}$ (Ionov et al., 2002 and references therein). HREEs (Lu-Ho) are consistent with > 20% of partial melting. MREE through to LREE however, are progressively more enriched in the Kapsiki orthopyroxene compared to the modelled compositions, clearly indicating reaction with relatively LREE and MREE enriched fluids after the depletion event(s). In the spinel stability field, olivine Mg# of 91.5 is approximately the point of clinopyroxene consumption, which will be at about 25% of partial melting (Bernstein et al., 2007; Hellebrand et al., 2001).

In summary, the Mg# of olivine and orthopyroxene and the HREE patterns of orthopyroxene are the most reliable tools to calculate the degree of melt depletion, while Cr# of spinel is likely to have been modified during subsequent metasomatism. Both the Mg#s and the HREE contents of orthopyroxene are consistent with 20-30% of melt extraction before the metasomatic refertilization. This means that parts of an ancient Archean/Proterozoic SCLM of lherzolitic composition was depleted by the extraction of basaltic melts leaving a mantle with little or no clinopyroxene of harzburgitic composition and depleted chemistry. The presence of such a highly depleted lithospheric subcontinental mantle indicates that old cratonic fragments persist and thus the proposed lithospheric delamination that led to abundant widespread magmatism at about 580 Ma (Bute et al., 2019) did not completely remove the lithospheric mantle below the northern extension of the CVL.

II.3.3. METASOMATISM

The observed modal proportions of clinopyroxene (6-8%) are inconsistent with the proportions expected following the estimated 20-30% of partial melting experienced beneath Kapsiki, which indicates that the clinopyroxene must have been added subsequently. This is supported by the much smaller grain size of clinopyroxene (Fig. 2.1a, c). Features like highly variable pyroxene LREE enrichments and differing Mg# of clinopyroxenes between crystals in the same sample cannot be accounted for by partial melting and clearly indicate that the mantle must have undergone secondary processes.

Trace elements can be diagnostic of the type of metasomatic agent due to their differing behaviours depending on the nature and source of the fluid and the method through which the fluid interacts with the mantle. Such considerable variability of elements within the same sample (Fig. 2.4) reflects fluctuations during interactions which result in spatial changes in trace element concentrations due to chromatographic processes which are highly dependent on the relative mineral/melt partition coefficients of each of the elements (Ionov et al., 2002).

The Kapsiki xenoliths show evidence for both modal and cryptic metasomatism. Modal metasomatism is indicated by the presence of two groups of clinopyroxenes; a low and high Ca group (Fig. 2.2c, d), which are in interstitial positions (Fig. 2.1a) and are smaller in size than the coexisting minerals, which indicates that they crystallized at a later stage. The low Ca clinopyroxenes record a higher temperature (1150 °C) while the high Ca types show more of interactions with carbonatite-silicate and silicate melts and lower temperatures (840-880°C) (Table 1). Pyroxenes which recorded the higher temperatures were, therefore, the latest to be formed and probably formed shortly before eruption. This shows that metasomatism by melts enriched in Ca and incompatible trace elements (Scott et al., 2014a) could be a precursor of xenolith formation and eruption.

Cryptic metasomatism shown by geochemical fingerprints of fluids or melts are expressed as a gradation from low to high incompatible element enrichments in orthopyroxene and both groups of clinopyroxene (Fig. 2.4, 2.5). These samples were far enough from the metasomatic source for the chromatographic effect to be recorded only in the LREE (Uenver-Thiele et al., 2017; Ionov et al., 2002) for Ka2 and Ka7, sample Ka1 was closer to the metasomatic source because even the MREE were perturbed. In a rock with a lherzolite lithology, clinopyroxene melts preferentially to olivine and orthopyroxene during decompression of the mantle, which means that clinopyroxene can easily be exhausted at low degrees of partial melting (~25%) leaving an olivine-orthopyroxene residue (Walter 2003). As such, orthopyroxene would probably be more sensitive to metasomatism (Scott et al., 2016, 2014b). Orthopyroxenes from all samples show the same style of metasomatic enrichment as clinopyroxenes in REEs in all samples.

Selective enrichments in Th, U, Sr and LREE in samples Ka2 and Ka7 depict interactions with a metasomatic agent at low melt/rock ratios (Gregoire et al., 2009). Alternatively, additional MREE enrichments in Ka1 point to possible infiltration of a fluid or melt (Gregoire et al., 2005) at higher melt rock ratios. The general enrichment in all

elements especially Rb, Ba, Sr, Nb and MREEs of group 1 clinopyroxene (Fig. 2.4b, c, f) of sample Ka1 is also consistent with interactions with fluids or melts of different composition.

II.3.4. FLUID/MELT COMPOSITION

The nature and composition of metasomatizing fluids can be constrained from the mineralogic and chemical compositions of xenoliths, as such, trace element patterns and ratios are very important tools that can be used to discriminate different metasomatic fluids/melts. However, the occurrence of different trace element enrichment patterns in the Kapsiki xenoliths complicates their interpretation and brings in the possibility for multiple metasomatic agents. It is important when interpreting normalized mineral compositions to consider whether element anomalies are due to secondary processes (e.g., fluid metasomatism) or whether they are an artefact of relative compatibility. For example, the negative anomalies in Rb and Ba are typical features of clinopyroxene and are due to their greater incompatibility relative to neighboring elements.

Mantle metasomatism has generally been ascribed to infiltration by silicate melts (Zangana et al., 1999), carbonatite melts (Shu and Brey, 2015; Yaxley et al., 1998; Rudnick et al., 1993), aqueous or CO₂-rich fluids (Downes, 2001; O'Reilly and Griffin, 1988) and subduction-related fluids/melts (Pearce et al., 2005). Silicate melts are characterized by high concentrations of incompatible trace elements (Th, U, Ba, Nb, Sr, K, LREEs) (Zangana et al., 1999). Carbonatite melts are more enriched in moderately to highly incompatible trace elements (Rb, Th, U, Ba, Sr, K, Cs, LREEs), Eu and are depleted in HFSEs (Zr, Hf, Ti, Nb, Ta) compared to silicate melts (Liu et al., 2019; Dasgupta and Hirschmann, 2006; Lenoir et al., 2000). Additionally, high La/Yb, Ca/Al, Zr/Hf and low Ti/Eu ratios are characteristic for carbonatite melts (Rudnick et al., 1993). Fractionated incompatible trace elements accompanied by positive LILE Pb plus negative HFSE anomalies, point to a mantle that has been metasomatized by subduction-related fluids (Pearce et al., 2005). Fig. 2.9 shows a series of plots using diagnostic trace elements (primitive mantle normalized values) of the clinopyroxenes, compared with published data from peridotites where the tectonic setting (intraplate, subduction or abyssal peridotite) is known. We assume, therefore, that the trace element compositions from these studies are representative of the type of fluids/processes that characterize each tectonic environment. The Sr-Nd diagram effectively separates the abyssal and subduction-related peridotites

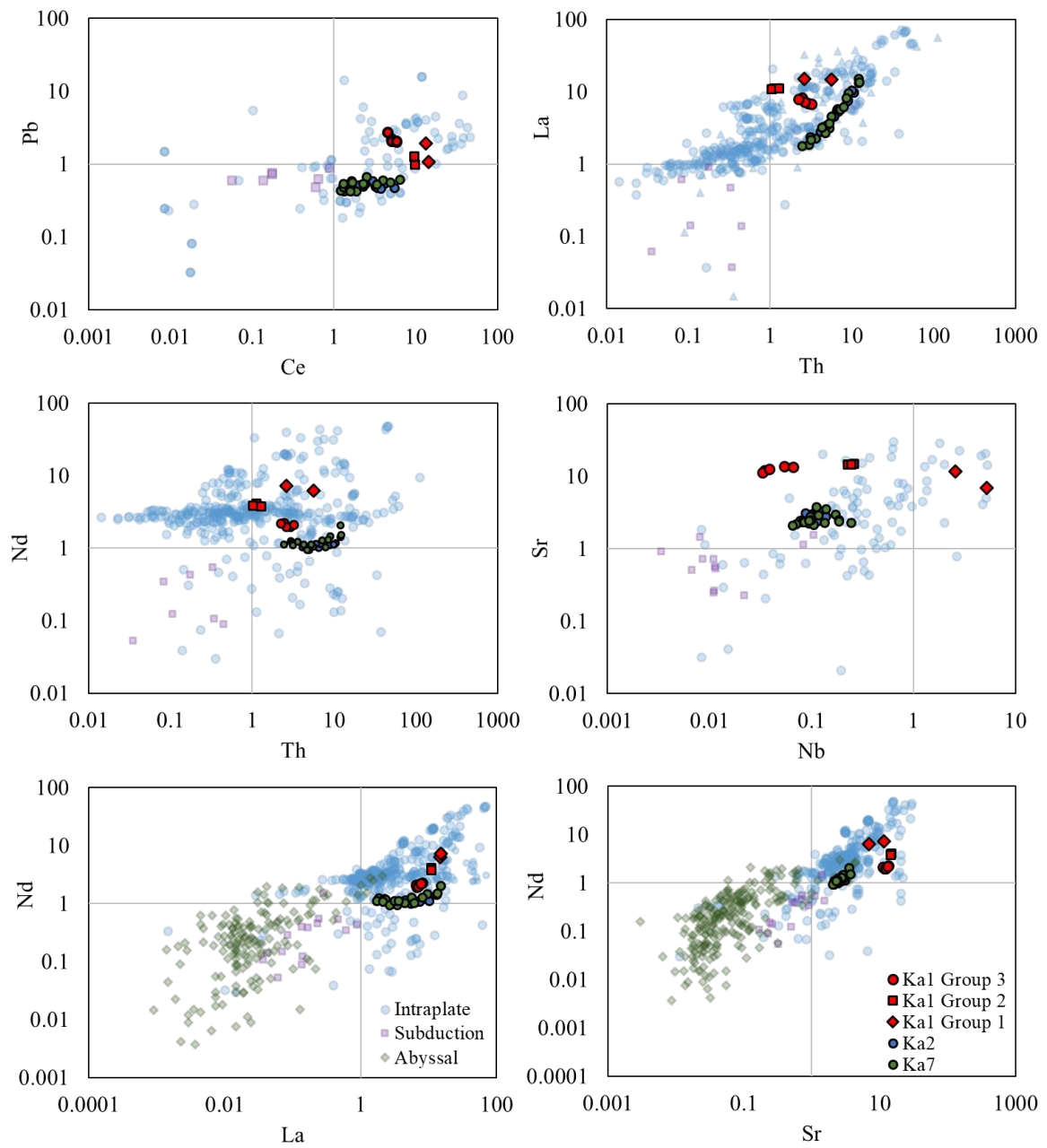


Figure 2.9: Trace element plots of clinopyroxene compared to literature data from intra plate (Unenver-Thiele et al., 2017; Scott et al., 2016; McCoy et al., 2015; Scott et al., 2014a), subduction (Tollan et al., 2017; Bernard and Ionov 2013) and Abyssal settings (Waren, 2016). Values are normalized to primitive mantle values of Palme and O’Neill 2014.

from the intraplate peridotites. These trace element plots show that the Kapsiki xenoliths are different from xenoliths from the abyssal and subduction settings, and they fall in the same domain as those from intraplate settings. Within the intraplate group, the Th-La diagram nicely separates the continuous trends of Ka2, Ka7 from Ka1, which shows three distinct groups of compositions (Fig. 2.9). Negative Nb anomalies are inconsistent with metasomatism by alkaline melt but combined with strong enrichments in U and Th indicate the involvement of a carbonatite fluid component.

The discrimination of silicate and carbonatite melts using Ti/Eu vs $(La/Yb)_N$ in cpx (Coltorti et al., 1999) systematics shows that one group of Ka1 clinopyroxene with high $(La/Yb)_N$ ratios falls in the carbonatite field (Fig. 2.10a). The second group of Ka1 clinopyroxenes alongside Ka2 and Ka7 clinopyroxenes with high $(La/Yb)_N$ and high Ti/Eu do not show well-defined compositions, which could be a result of metasomatism by a mixed melt of varying proportions or a gradual overprinting of one fluid type by the other (Su et al., 2010). A few Ka2 and Ka7 grains show low $(La/Yb)_N$ and high Ti/Eu ratios are indicative of dominant interactions with basaltic melts (Xu et al., 2003), the lowest $(La/Yb)_N$ values are representative of an approximate end member which has been modified by silicate melts with a minimum influence from carbonatites. CVL clinopyroxenes from Befang (Tedonkenfack et al., 2021) and Nyos (Liu et al., 2017; Teitchou et al., 2011), show low $(La/Yb)_N$ ratios and high Ti/Eu ratios and have been ascribed to metasomatism by depleted MORB mantle. Those from Nyos show evidence for both silicate and carbonatite metasomatism but they differ from most of the Kapsiki clinopyroxenes which do not show metasomatism by well-defined end member fluids but show evidence for metasomatism by fluids of varying composition. In the discrimination diagram of Zr/Hf vs Ti/Eu , Kapsiki samples were compared to those from the French Massif Central (FMC) (Uenver-Thiele et al., 2017) (Fig. 2.10b) where trace element compositions and oxidation state measurements were used to constrain metasomatic processes. The Kapsiki xenoliths are similar to the FMC xenoliths, as both show evidence for metasomatism by carbonatite-silicate melts and silicate melts. This also correlates quite well with results from the Ti/Eu and $(La/Yb)_N$ plots. The Kapsiki xenoliths also show oxidation state values at the lower end of those obtained for FMC xenoliths which range from $FMQ - 0.47$ to $FMQ + 1.66$. The non-cratonic SCLM is heterogeneous in terms of oxidation state which implies an overprint by different types and intensities of metasomatism (Uenver-Thiele et al., 2017; Foley, 2010). Ti/Sr ratios of Ka1 samples range from 1-11, Ka2 and Ka7 ratios are much higher in the range of 9-18.

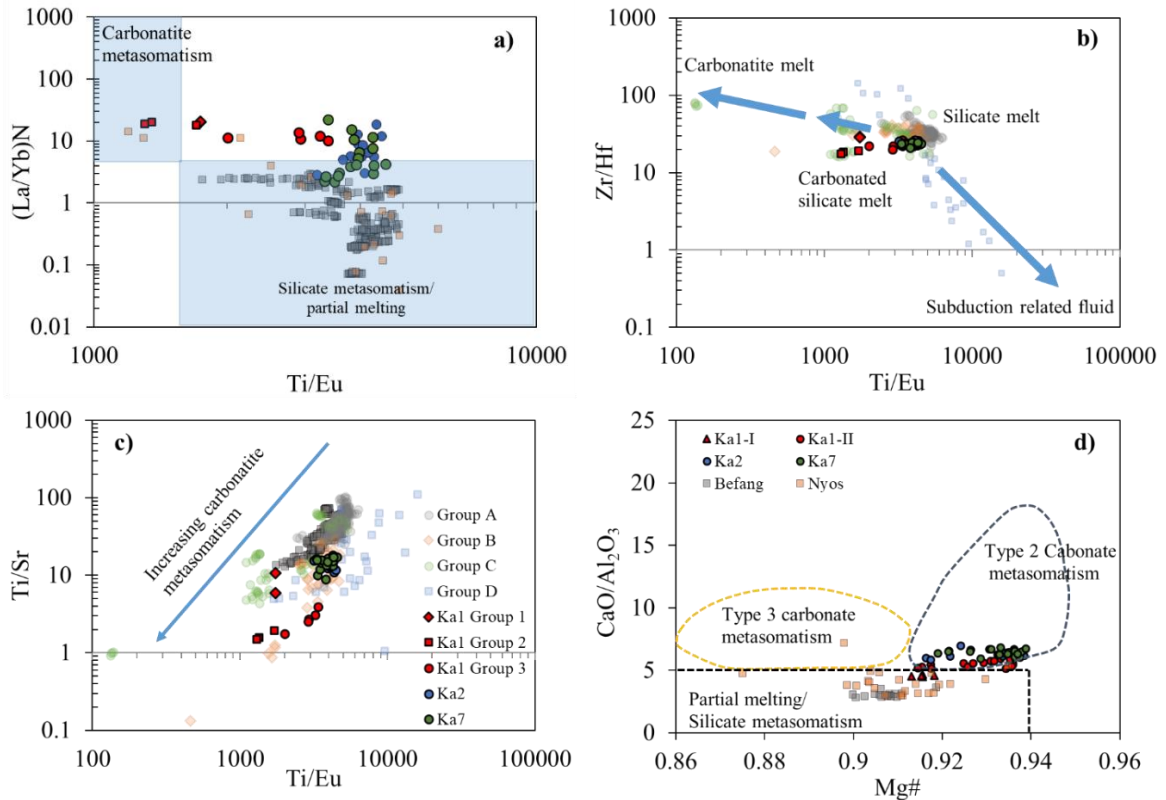


Figure 2.10a: Plot of Ti/Eu vs chondrite normalised (McDonough and Sun, 1995) La/Yb ratios in clinopyroxenes, compared to clinopyroxenes for Befang (Tendonkack et al., 2021) and Nyos (Liu et al., 2017, Teitchou et al., 2011). Fields for carbonatite and silicate metasomatism are from Coltorti et al., 1999. b. c) Plot of Ti/Eu vs Zr/Hf and Ti/Sr vs Ti/Eu in clinopyroxenes compared samples from the French Massif Central (Uenver-Thiele et al., 2017), Groups A-D represent the degree of LREE to MREE enrichments in clinopyroxene. d.) Ca/Al vs Mg# in clinopyroxene. Fields are from Zong et al., 2018.

Clinopyroxene metasomatized by carbonatite melts worldwide show low Ti/Sr ratios (Scott et al., 2014a: Ti/Sr=1-5, Norman 1998=2-4; Fig. 2.10c). They are similar to clinopyroxenes from the FMC (Uenver Thiele et al., 2017) and the CVL (Tendonkack et al., 2021, Liu et al., 2017; Teitchou et al., 2011), but generally show more carbonatitic affinity than CVL clinopyroxenes (Fig. 2.10c). Ca/Al major element ratio (Rudnick et al., 1993) in clinopyroxenes is also an important geochemical metasomatic tracer. Results from experimental studies show that low Ca/Al values <5 record interactions with silicate melts (Wang et al., 2010; Yaxley and Green, 1998) while Ca/Al ratios >5 were attributed to carbonatite interactions (Gervasoni et al., 2017; Brey et al., 2008; Klemme et al., 1995; Dalton and Wood, 1993). Ca/Al values of 4-8 are also consistent with metasomatism induced by small amounts of volatile-rich melts (Xu et al., 2003). The plots of Ca/Al versus Mg# (Fig. 2.10d) shows that most of the Kapsiki xenoliths straddle the silicate-

carbonatite boundary and most of them fall in the type 2 carbonatite field defined by Zong et al., 2018 and are similar to other peridotites in Cenozoic volcanic rocks worldwide. The CVL xenoliths fall in the silicate metasomatism domain while a few xenoliths from Nyos straddle the boundary between silicate metasomatism and type 3 carbonatite metasomatism (Fig. 2.10d).

Type 2 carbonatite metasomatism is characterized by high Mg# (>91) and Ca/Al ratios of 5-8 while type 3 shows lower Mg# (0.86-0.91) and a narrow range of Ca/Al ratios (5-11) (Zong et al., 2018). Kapsiki xenoliths represent depleted residues (high Mg#) after the extraction of basaltic melts but have close to or modal compositions of lherzolites. This shows evidence for metasomatism by melts enriched in Ca and incompatible trace elements (Scott et al., 2014a) which led to the formation of the secondary clinopyroxenes. A puzzling feature is the observation of very high Mg# in the metasomatic clinopyroxene (0.92-0.94) compared to the residual olivine and orthopyroxene (0.91-0.92). Primary carbonatite melts in equilibrium with peridotites have an Mg# of 0.85-0.90 (Hamouda and Keshav, 2015) that is significantly higher than the Mg# of 0.70 for primary silicate melts. We speculate that the reaction of such a carbonate melt component in a mixed silicate-carbonate melt with a depleted peridotite will result in clinopyroxene with an elevated Mg#.

All the discrimination diagrams (Fig. 2.9, 2.10) for mantle metasomatism are based on clinopyroxene compositions. This is reasonable as clinopyroxene is newly formed during the metasomatic process and displays the highest concentrations of incompatible trace elements among the mantle phases. The drawback of this approach is that only clinopyroxene bearing samples can be classified. Our study of the Kapsiki xenoliths shows that orthopyroxene experienced cryptic metasomatism and the incompatible trace element patterns display some similar features to the clinopyroxene patterns (Fig. 2.5). Therefore, it is proposed that Sr-Nd and Th-La discrimination diagrams for the classification of metasomatic agents might be possible also using orthopyroxene compositions. Also, olivine shows some promising trends. However, many of these trace elements are strongly modified by sub-solidus cooling (Tollan et al. 2017; De Hoog et al. 2010) and comprehensive database for such classifications are still missing.

In summary, major and trace element systematics of the Kapsiki clinopyroxenes provides clear evidence for metasomatism by varying proportions of carbonate and

silicate melts. This metasomatism may have been a single event with a hybridized melt, or separate events produced by variable overprinting of the end member compositions (Beard et al. 2007). It is not possible to distinguish between these two options based on the available data.

II.3.5. IMPLICATION OF WATER BUDGET

NAMs in the Earth's mantle contain variable amounts of hydrogen structurally bonded as hydroxyl (Bell and Rossman, 1992) in their crystal lattice, thus can be a significant hydrogen reservoir (Ingrin and Skogby, 2000). Hydrogen contents and the hydrogen activity of fluids in the mantle show substantial variability and can largely influence the physical and chemical properties of the mantle (Van der Lee et al., 2008), hence, play an important role in understanding mantle dynamics (Bonadiman et al., 2009). Metasomatic agents that interact with the mantle can have highly variable H₂O contents and activities (aH₂O). For example, subduction zone fluids are likely to be highly enriched in H₂O with high aH₂O, whereas carbonatitic fluids should have much higher CO₂ contents and thus lower aH₂O. Hydrogen in NAMs may therefore be a powerful tool that can be used to differentiate between some of these different metasomatic components. Despite this, most studies trying to link metasomatism with hydrogen in minerals struggle to find straightforward links. One reason for this may be that H diffuses significantly faster than other trace elements, and thus may re-equilibrate post-metasomatism, eradicating any original correlations with co-enriched/depleted elements (e.g., Denis et al. 2018). Another reason is that the hydrogen contents of NAMs may not necessarily have a direct correlation with the hydrogen contents of fluids, since H incorporation in NAMs is strongly dependent on the availability of defects which is directly linked to parameters such as pressure, aH₂O, mineral chemistry and fO₂ (Tollan et al. 2017; Ardia et al. 2012; Berry et al. 2005).

Olivines from the Kapsiki xenoliths show no OH stretching bands and the H₂O contents are therefore estimated to be <1 ppm. The very low olivine H₂O content is a common feature of peridotite xenoliths and has been interpreted to be due to rapid diffusion of H in olivine during transport to the surface by H₂O-undersaturated magmas (Tian et al., 2017; Xia et al., 2010; Demouchy et al., 2006; Peslier and Luhr, 2006). Alternatively, low water contents caused by depleted chemistry (particularly low Ti and Cr contents and high Na/Cr) and low aH₂O could have inhibited H incorporation (Tollan

et al., 2018, 2017). The Kapsiki olivines are different from other olivines along the CVL (Pinter et al., 2015) which show characteristic OH stretching bands at 3573 and 3525 cm^{-1} (Ti substitution), 3229 cm^{-1} (Mg substitution) and consequently higher H_2O contents (0.6-6.6 ppm). Tollan et al., 2018 showed that when interacting with a pure H_2O fluid ($a_{\text{H}_2\text{O}} = 1$) at 1.5 GPa, the 5-10 $\mu\text{g/g}$ Ti measured in the Kapsiki olivines studied here should generate easily detectable bands at 3572 and 3525 cm^{-1} (3-6 ppm H_2O). This is therefore consistent with the expected much lower $a_{\text{H}_2\text{O}}$ of the metasomatic agents beneath Kapsiki.

Orthopyroxene FTIR spectra show five OH stretching bands. The most prominent are at ~ 3600 , 3520 and 3415 cm^{-1} and the position of the bands are similar to reported orthopyroxene spectra (Pinter et al., 2015) along the Cameroon Volcanic Line and other localities (Patko et al., 2019; Demouchy et al., 2015; Li et al., 2015; Bonadiman et al., 2009). The most striking feature in these spectra and the major difference with those from the CVL is the stretching region at ~ 3520 , which is absent in Ka1 and Ka2 and present in Ka7 (Fig. 2.6a). Also, the bands at 3415 cm^{-1} are more intense in the Kapsiki samples. In orthopyroxene, two main peaks (3600 and 3420 cm^{-1}) are insensitive to oxygen fugacity, however, the peak at ~ 3525 cm^{-1} has been shown to increase with increasing $f\text{O}_2$ (Tollan and Hermann, 2019). This is consistent with observations in the Kapsiki sample with Ka7 showing the highest $f\text{O}_2$ and the most prominent bands at 3519 cm^{-1} . Based on experimental studies, the specific substitution mechanism related to the presence of the OH stretching regions at 3600 and 3420 cm^{-1} has been linked to the presence of hydrated Si vacancies and tetrahedral Al based (Prechtel and Stalder, 2012). The orthopyroxene spectra can also give information on the associated tectonic setting, for example, the spectra from off-craton intraplate (this study; Bonadiman et al., 2009; Li et al., 2008; Grant et al., 2007b), cratonic (Peslier et al., 2012), arc (Tollan and Hermann 2019; Peslier et al., 2002) and abyssal (Schmadicke et al., 2011; Gose et al., 2009; Skogby et al., 1990) orthopyroxene are distinctly different. Calculated average orthopyroxene hydrogen contents range from 40-50 ppm are lower than in most peridotites from off-cratonic settings (Pinter et al., 2015; Grant et al., 2007b; Peslier and Luhr, 2006; Demouchy et al., 2006) which could be influenced by the depleted chemistry (low Al_2O_3) (Tollan and Hermann, 2019).

Clinopyroxenes (Fig. 2.6b) show two distinct spectra in all samples; the first type with prominent OH stretching bands at ~ 3638 cm^{-1} and two less prominent at ~ 3525 and

$\sim 3488 \text{ cm}^{-1}$. The second spectra type shows an additional band at $\sim 3682 \text{ cm}^{-1}$ which can be attributed to the presence of amphibole lamellae in clinopyroxene (Della Ventura et al., 2007). As in the case of orthopyroxene, substitution mechanisms in clinopyroxenes are also not yet well constrained but are thought to be principally controlled by coupled substitution of H with tetrahedral Al (O’Leary et al. 2010; Stadler and Ludwig, 2007).

The H₂O concentrations of both orthopyroxene (40-48 ug/g) and clinopyroxene (164-288 ug/g) are on the low end of the global distribution of H₂O concentrations (Demouchy and Bolfan-Casanova 2016) (Fig. 2.11). This is somewhat surprising given the strong evidence for modal metasomatism and enrichment of highly incompatible elements. We suggest that the principle explanation for this is that the contribution of carbonatite melt resulted in a much lower aH₂O compared to a typical metasomatizing agent and considering the strong relationship between aH₂O and H₂O solubility (Tollan et al. 2017). The H₂O concentration ratios between clinopyroxene and orthopyroxene ($R_{\text{cpx/opx}}$) range from 3-7 and are much higher than the value proposed to reflect equilibrium partitioning ($R_{\text{cpx/opx}} = 2.1$) by Demouchy and Bolfan-Casanova, 2016. This could indicate that the mantle below the region did not attain a state of equilibration before eruption, that the orthopyroxenes preferentially lost H₂O compared to clinopyroxenes during ascent or that substantially different substitution mechanisms are operating in the Kapsiki crystals. The major element composition of Kapsiki pyroxenes is unremarkable compared to the global mantle array, discounting the latter option. Furthermore, core-rim H₂O measurements in orthopyroxene grains show no systematic variation, indicating that H-loss during ascent is also an unlikely explanation. A possible explanation is that orthopyroxene is a residual phase, whose H₂O contents were modified through H diffusion (decoration) during metasomatism.

Clinopyroxene on the other hand was modally added through crystallisation, and the H₂O defects and concentrations thus reflect crystallization processes, rather than H diffusion/vacancy decoration. These different mechanisms of incorporating H have been shown to result in quite substantial differences in stable defects and H₂O solubility (Tollan et al. 2018). This study therefore highlights the vital importance of establishing the origin of each mineral phase and mechanisms of H incorporation when interpreting the H₂O concentrations.

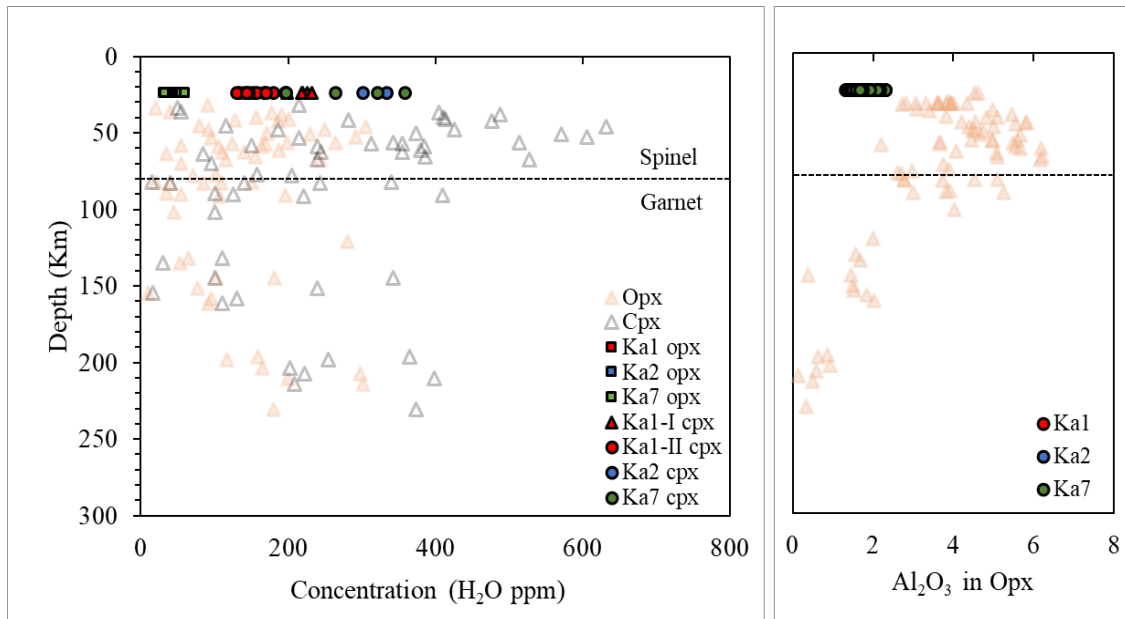


Figure 2.11a: Water contents (ppm) of orthopyroxene and clinopyroxene as a function depth. (b) Variation of Al₂O₃ (wt. %) in orthopyroxene as a function of depth. Comparisons are done with data from Demouchy and Bolfan-Cassanova 2016.

I.4. CONCLUSION

The Kapsiki plateau in the Far-Northern part of Cameroon bears the northernmost occurrence of mantle xenoliths. Peridotite xenoliths in basaltic rocks are ideal candidates to investigate depletion and enrichment events in the lithospheric mantle below an important tectonic line at the initiation of major volcanic activity.

Ancient melt depletion events in the peridotites are best documented with the high Mg# of 0.91-0.92 in olivine and orthopyroxene, high Cr# of 0.40-0.55 in spinel and steep HREE patterns in orthopyroxene. All indicators provide consistent evidence for 20-30 % melt depletion corresponding to conditions where clinopyroxene is lost from the residues.

The harzburgites then experienced multiple episodes of metasomatic events that resulted in different enrichment trends in the studied samples and bulk addition of clinopyroxene. At least two episodes of clinopyroxene addition/modification are documented. An earlier metasomatism produced clinopyroxene with equilibration temperatures of 840-880°C whereas a later event crystallized low Ca clinopyroxene with equilibration temperatures of 1150°C that must have occurred shortly before transport of

the samples to the surface by the volcanic activity. The metasomatic events produced TiO₂ enrichment in spinel, characteristic incompatible trace element enrichments in clinopyroxene and orthopyroxene. Moreover, the H₂O content of clinopyroxene and orthopyroxene can also be used to infer metasomatic agents. The resulting picture is that samples Ka2 and Ka7 were metasomatized by carbonate-silicate melts, whereas Ka1 has multiple sources with one population characteristic of carbonate melts. In both melts the H₂O activity was likely lower than in silicate melts, resulting in a less pronounced H₂O enrichment. Clinopyroxene has a significantly higher Mg# of 0.92-0.94 than olivine and orthopyroxene, which is also interpreted as a characteristic signature of metasomatism by carbonate melts.

A series of discrimination diagrams were developed based on clinopyroxene trace element compositions to distinguish between different types of clinopyroxene in mantle peridotites. The Sr vs. Nd diagram effectively separates abyssal and subduction-related peridotites from intraplate peridotites, whereas the Th vs La diagram provides insight into different types of metasomatism in an intraplate setting. Our study shows that orthopyroxene that experienced cryptic metasomatism displays comparable features. This opens the possibility to also use orthopyroxene as indicator for mantle metasomatic processes once a comprehensive database is available.

REFERENCES

- Adjia, H.Z., Villiéras, F., Kamga, R., Thomas, F., 2013. Mineralogy and Physico-Chemical Properties of Alluvial Clays from Far-North Region of Cameroon: A Tool for an Environmental Problem. *Int. J. Water Res. Environ. Eng.* 5, 54-66.
- Arai, S., 1994. Characterization of spinel peridotites by olivine-spinel compositional relationships: Review and interpretation. *Chem. Geol.* 113(3-4), 191–204.
- Ardia, P., Hirschmann, M.M., Withers, A.C., Tenner, T.J., 2012. H₂O storage capacity of olivine at 5–8 GPa and consequences for dehydration partial melting of the upper mantle., 345-348.
- Ballhaus, C.G., Berry, R.F., Green, D.H., 1991. High-pressure calibration of the olivine-orthopyroxene-spinel oxygen barometer, implications for the oxidation state of the upper mantle. *Contrib. Mineral. Petrol.* 107, 7–40.

- Beard, A.D., Downes, H., Mason, P.R.D., Vetrin, V.R., 2007. Depletion and enrichment processes in the lithospheric mantle beneath the Kola Peninsula (Russia): Evidence from spinel lherzolite and wehrlite xenoliths. *Lithos* 94 (1-4), 1–24.
- Bell, D.R., Ihinger, P.D., Rossman, G.R., 1995. Quantitative analysis of trace OH in garnet and pyroxenes. *Am. Mineral.* 80, 465–474.
- Bell, D.R., Rossman, G.R., 1992. Water in Earth's mantle: the role of nominally anhydrous minerals. *Science* 255 (5050), 1391-1397.
- Bell, D.R., Rossman, G.R., Maldener, J., Endisch, D., Rauch, F., 2003. Hydroxide in olivine: a quantitative determination of the absolute amount and calibration of the IR spectrum. *J. Geophys. Res., Solid Earth* 108, 2105.
- Bénard, A., and Ionov, D. A. 2013. Melt–and fluid–rock interaction in supra-subduction lithospheric mantle: Evidence from andesite-hosted veined peridotite xenoliths, *J. Petrol.*, 54, 2339– 2378.
- Bernstein, S., Kelemen, P. B., Hanghøj, K., 2007. Consistent olivine Mg# in cratonic mantle reflects Archean mantle melting to the exhaustion of orthopyroxene. *Geology* 35(5), 459.
- Berry, A. J., Hermann, J., O'Neill, Hugh S. C., Foran, G. J., 2005. Fingerprinting the water site in mantle olivine. *Geology*, 33(11), 869.
- Bonadiman, C., Coltorti, M., Beccaluva, L., Siena, F., 2005. Kimberlite-like Metasomatism and ‘Garnet Signature’ in Spinel-peridotite Xenoliths from Sal, Cape Verde Archipelago: Relics of a Subcontinental Mantle Domain within the Atlantic Oceanic Lithosphere? *J. Petrol.*, 46, 2465-2493.
- Bonadiman, C., Coltorti, M., Beccaluva, L., Siena, F., 2008. Mantle metasomatism vs. host magma interaction: the ongoing controversy. *Geophysical Research Abstracts* 10, EGU2008-A-09723.
- Bonadiman, C., Hao, Y., Coltorti, M., Dallai, L., Faccini, B., Huang, Y., Xia, Q., 2009. Water contents of pyroxenes in intraplate lithospheric mantle. *Eur. J. Mineral.* 21(3), pp. 637-647.
- Brey G.P., Bulatov V.K., Girnis A.V., Lahaye Y., 2008. Experimental melting of carbonated peridotite at 6–10 GPa. *J. Petrol.* 49: 797–821.
- Brey, G.P., Köhler, T.P., 1990. Geothermobarometry in natural four-phase lherzolites: Part II. New thermobarometers and practical assessment of existing thermobarometers. *J. Petrol.* 31, 1353–1378.
- Bute, S.I., Yang, X.-Y., Cao, J., Liu, L., Deng, J.-H., Haruna, I.V., Girei, M.B., Abubakar, U., Akhtar, S., 2019. Origin and tectonic implications of ferroan alkali-calcic granitoids from the Hawal Massif, east-eastern Nigeria terrane: clues from geochemistry and zircon U-Pb Hf isotopes. *Int. Geol. Rev.* 62:129–152.

- Caldeira, R., Munhá, J.M., 2002. Petrology of ultramafic nodules from Sao Tomé Island, Cameroon Volcanic line (oceanic sector). *J. Afr. Earth Sci.* 34:231–246
- Coltorti, M., Bonadiman, C., Hinton, R.W., Siena, F., Upton, B.G.J., 1999. Carbonatite metasomatism of the oceanic upper mantle: evidence from clinopyroxenes and glasses in ultramafic xenoliths of Grande Comore, Indian Ocean. *J. Petrol.* 40, 133–165.
- Coogan, L.A., Saunders, A.D., Wilson, R.N., 2014. Aluminum-in-olivine thermometry of primitive basalts: Evidence of an anomalously hot mantle source for large igneous provinces. *Chem. Geol.* 368, 1–10.
- Dalton, J.A., Wood, B.J., 1993. The composition of primary carbonate melts and their evolution through wall rock reaction in the mantle. *Earth Planet. Sci. Lett.* 119, 511–525.
- Dasgupta, R., Hirschmann, M.M., 2006. Melting in the Earth's deep upper mantle caused by carbon dioxide. *Nature* 440 (7084), 659–662.
- De Hoog J.C.M., Gall L., Cornell D.H., 2010. Trace element geochemistry of mantle olivine and application to mantle petrogenesis and geothermobarometry. *Chem. Geol.* 270:196– 215.
- Della Ventura, G., Oberti, R. Hawthorne, F.C., Bellatreccia F., 2007. FTIR spectroscopy of Ti-rich pargasites from Lherz and the detection of O₂ at the anionic O₃ site in amphiboles. *Am. Mineral.* 92 (10), pp. 1645-1651.
- Demouchy, S., Bolfan-Casanova, N., 2016. Distribution and transport of hydrogen in the lithospheric mantle: a review. *Lithos* 240, 402–425.
- Demouchy, S., Ishikawa, A., Tommasi, A., Alard, O., Keshav, S., 2015. Characterization of hydration in the mantle lithosphere: peridotite xenoliths from the Ontong Java Plateau as an example. *Lithos* 212–215, 189–201.
- Demouchy, S., Jacobsen, S.D., Gaillard, F., Stern, C.R., 2006. Rapid magma ascent recorded by water diffusion profiles in mantle olivine. *Geology* 34(6), 429.
- Denis, C.M.M., Demouchy, S., Alard, O., 2018. Heterogeneous hydrogen distribution in orthopyroxene from veined mantle peridotite (San Carlos, Arizona): Impact of melt-rock interactions. *Lithos*, (), S0024493718300112.
- Déruelle, B., Ngounouno, I. and Demaiffe, D. 2007. The "Cameroon Hot Line" (CHL): A Unique Example of Active Alkaline Intraplate Structure in both Oceanic and Continental Lithospheres. *Compt. Rendus Geosci.* 339, 589-600.
- Déruelle, B., Ngounouno, I., Bardintzeff, M.J., 2001. Wherlites et pyroxénites en nodules dans les basaltes du Mt. Cameroun : évidence d'un métasomatisme mantellique. *J. Soc. Géosci. D'Afrique*. 1, 90-91.
- Doucet, L.S., Peslier, A.H., Ionov, D.A., Brandon, A.D., Golovin, A.V., Goncharov, A.G., Ashchepkov, I.V., 2014. High water contents in the Siberian cratonic mantle linked to

- metasomatism: an FTIR study of Udachnaya peridotite xenoliths. *Geochim. Cosmochim. Acta* 137, 159–187.
- Downes, H., 2001. Formation and modification of the shallow subcontinental lithospheric mantle; a review of geochemical evidence from ultramafic xenolith suites and tectonically emplaced ultramafic massifs of western and central Europe. *J. Petrol.* 42, 233–250.
- Dunlop, H.M., 1983. Strontium isotope geochemistry and potassium \pm argon studies on volcanic rocks from the Cameroon line, West Africa. PhD thesis, Univ. Edinburgh, 347p.
- Eggins, S.M., Rudnick, R.L., McDonough, W.F., 1998. The composition of peridotites and their minerals: a laser-ablation ICP–MS study *Earth Planet. Sci. Lett.* 154 (1) (1998), pp. 53–71.
- Fabriès, J., 1979. Spinel-Olivine geothermometry in peridotites from ultramafic complexes. *Contrib. Mineral. Petrol.* 69: 329–336
- Ferré, E., Gleizes, G., and Caby, R., 2002. Obliquely convergent tectonics and granite emplacement in the Trans-Saharan belt of Eastern Nigeria: a synthesis. *Precambrian Res.* 114: 199–219.
- Fitton, J.G., 1983. Active versus passive continental rifting: evidence from the West African rift system. *Tectonophysics* 93, 473–481.
- Foley, S.F., 2010. A reappraisal of redox melting in the Earth's mantle as a function of tectonic setting and time. *J. Petrol.* 52, 1363–1391.
- Gamal El Dien, H., Arai, S., Doucet, L., Li, Z., Kil, Y., Fougereuse, D., Reddy, S. M., Saxey, D. Y., Hamdy M., 2019. Cr–spinel records metasomatism not petrogenesis of mantle rocks. *Nature Comm.* 5103.
- Ganwa A.A., Klötzli U.S., Diguim Kepnamou A., Hauzenberger C., 2016. Multiple Ediacaran tectono-metamorphic events in the Adamawa-Yadé Domain of the Central Africa Fold Belt: Insight from the zircon U–Pb LAM-ICP-MS geochronology of the metadiorite of Meiganga (Central Cameroon). *Geol. J.* 2018; 1–14.
- Gervasoni F., Klemme S., Rohrbach A., Grützner T., Berndt J. 2017. Experimental constraints on mantle metasomatism caused by silicate and carbonate melts. *Lithos* 282-283: 173–186.
- Gose, J., Schmädicke, E., & Beran, A., 2009. Water in enstatite from Mid-Atlantic Ridge peridotite: Evidence for the water content of sub-oceanic mantle? *Geology* 37(6), 543–546.
- Goussi, Ngalamo, J.F., Sob, M., Bisso, D., Abdelsalam, M. G., Atekwana, E., & Ekodeck, G. E., 2018. Lithospheric structure beneath the Central Africa Orogenic Belt in Cameroon from

- the analysis of satellite gravity and passive seismic data. *Tectonophysics* 745, 326-337.
- Grant, K.J., Kohn, S.C., and Brooker, R.A., 2007b. The partitioning of water between olivine, orthopyroxene and melt synthesised in the system albite-forsterite-H₂O, *Earth Planet. Sci. Lett.*, 260, 227–241.
- Grégoire, M., Langlade, J.A., Delpech, G., Dantas, C., Ceuleneer, G., 2009. Nature and evolution of the lithospheric mantle beneath the passive margin of East Oman: Evidence from mantle xenoliths sampled by Cenozoic alkaline lavas. *Lithos* 112/3, 203–216.
- Grégoire, M., Tinguely, C., Bell, D.R., Le Roex, A.P., 2005. Spinel lherzolite xenoliths from the Premier kimberlite (Kaalvaal craton, South Africa): nature and evolution of the shallow upper mantle beneath the Bushveld complex. *Lithos* 84, 185–205.
- Griffin, W. L., O'Reilly, S. Y., Afonso, J. C., Begg, G. C., 2008. The Composition and Evolution of Lithospheric Mantle: A Re-evaluation and its Tectonic Implications. *J. Petrol.* 50(7), 1185–1204.
- Hammouda, T., Keshav, S., 2015. Melting in the mantle in the presence of carbon: Review of experiments and discussion on the origin of carbonatites. *Chem. Geol.* 418, 171–188.
- Hart, S. R. & Dunn, T., 1993. Experimental cpx/melt partitioning of 24 trace elements. *Contrib. Mineral. Petrol.* 113, 1–8.
- Hellebrand, E., Snow, J.E., Dick, H.J.B., Hofmann, A., 2001. Coupled major and trace elements as indicators of the extent of melting in mid-ocean-ridge peridotites. *Nature* 410, 677–681.
- Hirschmann, M.M., Tenner, T., Aubaud, C., Withers, A.C., 2009. Dehydration melting of nominally anhydrous mantle: The primacy of partitioning. *Phys. Earth Planet. Inter.* 176(1-2), 54–68.
- Ingrin, J. and H. Skogby, 2000. Hydrogen in nominally anhydrous upper-mantle minerals: concentration levels and implications. *Eur. J. Mineral* 12, 543-570, 2000.
- Ingrin, J., Latrous, K., Doukhan, J. C., Doukhan, N., 1989. Water in diopside: an electron microscopy and infrared spectroscopy study. *Eur. J. Mineral.* 327–342.
- Ionov, D.A., Bodinier, J.L., Mukasa, S.B., Zanetti, A., 2002. Mechanisms and sources of mantle metasomatism: major and trace element compositions of peridotite xenoliths from Spitsbergen in the context of Numerical Modelling. *J. Petrol.* 43, 2219–2259.
- Jianping, L., Kornprobst, J., Vielzeuf, D., Fabries, J., 1995. An improved experimental calibration of the olivine-spinel geothermometer. *Chin. J. of Geochem.* 14, 68–77.
- Jochum, K. P., Stoll, B., Herwig, K., Willbold, M., Hofmann, A. W., Amini, M., Aarburg, S., Abouchami, W., Hellebrand, E., Mocek, B., Raczek, I., Stracke, A., Alard, O., Bouman, C., Becker, St., Dücking, M., Brätz, H., Klemd, R., de Bruin, D., Canil, D., Cornell, D.,

- de Hoog, C.-J., Dalpé, C., Danyushevsky, L., Eisenhauer, A., Gao, Y., Snow, J.E., Groschopf, N., Günther, D., Latkoczy, C., Guillong, M., Hauri, E., Höfer, H.E., Lahaye, Y., Horz, K., Jacob, D. E., Kasemann, S. A., Kent, A. J. R., Ludwig, T., Zack, T., Mason, P. R. D., Meixner, A., Rosner, M., Misawa, K., Nash, B. P., Pfänder, J., Premo, W. R., Sun, W. D., Tiepolo, M., Vannucci, R., Vennemann, T., Wayne, D., Woodhead, J. D., 2006. MPI-DING reference glasses for in-situ microanalysis: new reference values for element concentrations and isotope ratios. *Geochem. Geophys. Geosyst.* 7 (2), Q02008.
- Jochum, K.P., Nohl, U., Herwig, K., Lammel, E., Stoll, B., Hofmann, A.W., 2005. GeoReM: A new geochemical database for reference materials and isotopic standards. *Geostand. Geoanalyt. Res.* 29, 333–338.
- Jochum, K.P., Weis, U., Stoll, B., Kuzmin, D., Yang, Q., Raczek, I., Jacob, D.E., Stracke, A., Birbaum, K., D.A., Frick, Günther D., Enzweiler, J., 2011. Determination of Reference Values for NIST SRM 610-617 Glasses Following ISO Guidelines. *Geostand. Geoanalyt. Res.* 35(4), 397–429.
- Johnson, K. T. M., Dick, H. J. B. & Shimizu, N., 1990. Melting in the oceanic upper mantle: an ion microprobe study of diopsides in abyssal peridotites. *J. Geophys. Res.* 95, 2661–2678.
- Kemgang, Ghomsi, F. E., Sévérin, N., Mandal, A., Nyam, F. E. A., Tenzer, R., Tokam Kamga, A. P., & Nouayou, R., 2020. Cameroon's crustal configuration from global gravity and topographic models and seismic data. *J. Afr. Earth Sci.*, 103657.
- Klemme, S., van der Laan, S. R., Foley, S. F., Gunther, D., 1995. Experimentally determined trace and minor element partitioning between clinopyroxene and carbonatite melt under upper mantle conditions. *Earth Planet. Sci. Lett.* 133, 439–448.
- Kovacs, I., Hermann, J., O'Neill, H. St. C., FitzGerald, J.D., Sambridge, M., Horvath, G., 2008. Quantitative absorbance spectroscopy with unpolarized light, Part II: Experimental evaluation and development of a protocol for quantitative analysis of mineral IR spectra. *Am. Mineral.* 93, 765-778.
- Lee, D. C., Halliday N., Davies G. R., Essene E. J., Fitton G. J., Temdjim, R., 1996. Melt enrichment of shallow depleted mantle: a detailed petrological, trace element and isotopic study of mantle-derived xenoliths and megacrysts from the Cameroon Line. *J. Petrol.* 37 :415–441.
- Lenoir, X., Garrido, C. J., Bodinier, J. L. & Dautria, J. M., 2000. Contrasting lithospheric mantle domains beneath the Massif Central (France) revealed by geochemistry of peridotite xenoliths. *Earth Planet. Sci. Lett.* 181, 359-375.

- Li, P., Xia, Q.K., Deloule, E., Chen, H., Gu, X.Y., Feng M., 2015. Temporal variation of H₂O content in the lithospheric mantle beneath the eastern North China craton: Implications for the destruction of cratons. *Gondwana Res.* 28 (1), 276-287.
- Li, Z. X., C. A. Lee, A. H. Peslier, A. Lenard, and S. J. Mackwell, 2008. Water contents in mantle xenoliths from the Colorado Plateau and vicinity: Implications for the mantle rheology and hydration-induced thinning of continental lithosphere, *J. Geophys. Res.*, 113, B09210.
- Liu, C-Z, Yang, L-Y, Li X-H, Tchouankoue, J.P. (2017). Age and Sr-Nd-Hf isotopes of the sub-continental lithospheric mantle beneath the Cameroon Volcanic Line: constraints from the Nyos mantle xenoliths. *Chem Geol* 455, 84–97. Liu S. A, Wang Z. Z., Li S. G., Huang J., Yang W., 2016. Zinc isotope evidence for a largescale carbonated mantle beneath eastern China. *Earth Planet Sci Lett*, 444: 169–178.
- Liu, J., Graham Pearson, D., Shu, Q., Sigurdsson, H., Thomassot, E., Alard, O., 2020. Dating post-Archean lithospheric mantle: insights from Re-Os and Lu-Hf isotopic systematics of the Cameroon Volcanic Line peridotites. *Geochim. Cosmochim. Acta*.
- Marzoli A., Piccirillo, E.M., Renne, P.R., Bellieni, G., Iacumin, M., Nyobe, J.B., Aka, F.T., 2000. The Cameroon Volcanic Line revisited: petrogenesis of continental basaltic magmas from lithospheric and asthenospheric mantle sources. *J. Petrol.* 41, 87-109.
- Marzoli, A., Aka, F. T., Merle, R., Callegaro, S., & N'ni, J., 2015. Deep to shallow crustal differentiation of within-plate alkaline magmatism at Mt. Bambouto volcano, Cameroon Line. *Lithos* 220-223, 272–288.
- Mbowou, G.I.B., C. Lagmet, S. Nomade, I. Ngounouno, B. Deruelle, and D. Ohnenstetter, 2012. Petrology of the Late Cretaceous peralkaline rhyolites (pantellerite and commendite) from Lake Chad, Central Africa, *J. Geosci.*, 57, 127–141.
- McCoy-West, A.J., Bennett, V.C., O'Neill, H.S.C., Hermann, J., Puchtel, I. S., 2015. The Interplay between Melting, Refertilization and Carbonatite Metasomatism in Off Cratonic Lithospheric Mantle under Zealandia: an Integrated Major, Trace and Platinum Group Element Study. *J. Petrol.* 56(3), 563–604.
- McDonough, W.F., Sun, S.-s., 1995. The composition of the Earth. *Chem. Geol.* 120, 223–253.
- Mercier, J.-C.C., Carter, N.L., 1975. Pyroxene geotherms. *J. Geophys. Res.* 80, 3349–3362.
- Moundi, A., Ménard, J.-J., Reusser, E., Tchoua, M. F., and Dietrich, V. J., 1996. Découverte de basaltes transitionnels dans le secteur continental de la Ligne du Cameroun (massif du Mbam, Ouest-Cameroun) : *Compt. Rendus Académ. Sci. de Paris*, v. 322, p. 831– 837.
- Moundi, A., Wandji, P., Bardintzeff, J. -M., Ménard, J. -J., Okomo Atouba, L. C., Reusser, E., Bellon, H., and Tchoua, M. F., 2007. Les basaltes éocènes à affinité transitionnelle du

- plateau Bamoun, témoins d'un réservoir mantellique enrichi sous la ligne volcanique du Cameroun : *Compt. Rendus Geosci.* v. 339, 396–406.
- Ngounouno I., Nguihdama D., Kamgang P., Deruelle D., 2008. Petrology of spinel lherzolite xenoliths in alkali basalts from Liri, South of the Kapsiki Plateau (Northernmost Cameroon Hot Line). *J. Cameroon Academy Sci.* 8, 1, 31-42.
- Ngounouno, I., Déruelle, B. and Demaiffe, D., 2000. Petrology of the Bimodal Cenozoic Volcanism of the Kapsiki Plateau (Northernmost Cameroon, Central Africa). *J. Vol. Geothermal Res.*, 102, 21-44.
- Norman, M. D., 1998. Melting and metasomatism in the continental lithosphere: laser ablation ICPMS analysis of minerals in spinel lherzolites from eastern Australia *Contrib. Mineral. Petrol.*, 130 (1998), pp. 240-255.
- O'Leary, J.A., Gaetani, G.A., Hauri, E.H., 2010. The effect of tetrahedral Al³⁺ on the partitioning of water between clinopyroxene and silicate melt. *Earth Planet. Sci. Lett.* 297, 111–120.
- O'Reilly, S.Y., Griffin, W.L., 1988. Mantle metasomatism beneath western Victoria, Australia: I. Metasomatic processes in Cr-diopside lherzolites. *Geochim. Cosmochim. Acta* 52 (1988), pp. 433-447.
- Palme, H., O'Neill, H. S. C., 2014. Cosmochemical Estimates of Mantle Composition. *Treatise on Geochemistry*, 1–39.
- Pasyanos, M., Nyblade, A., 2007. A top to bottom lithospheric study of Africa and Arabia, *Tectonophysics* 444 (1–4), 27– 44.
- Patkó, L., Liptai, N., Kovács, I.J., Aradi, L.E., Xia, Q.-K., Ingrin, J., Mihály, J., O'Reilly, S., Griffin, W.L., Wesztergom, V., Szabó, C., 2019. Extremely low structural hydroxyl contents in upper mantle xenoliths from the Nógrád-Gömör Volcanic Field (northern Pannonian Basin): geodynamic implications and the role of post-eruptive reequilibration. *Chem. Geol.*, 507, 23-41.
- Paton, C., Hellestrom, J., Paul, B., Woodhead, J., Hergt, J., 2011. Iolite: freeware for the visualisation and processing of mass spectrometric data. *J. Anal. At. Spectrom.* 26, 2508–2518.
- Pearce, J. A., Barker, P. F., Edwards, S. J., Parkinson, I. J., Leat, P. T., 2000. Geochemistry and tectonic significance of peridotites from the South Sandwich arc-basin system, South Atlantic. *Contrib. Mineral. Petrol.* 139(1), 36–53.
- Pearce, J. A., Stern, R. J., Bloomer, S. H., Fryer, P., 2005. Geochemical mapping of the Mariana arc-basin system: Implications for the nature and distribution of subduction components. *Geochemistry, Geophys. Geosystems.* 6, Q07006.
- Pearson, D. G., Canil, D., Shirey, S. B., 2014. Mantle Samples Included in Volcanic Rocks. *Treatise on Geochemistry*, 169–253.

- Peslier, A.H., Luhr, J. F., Post, J. 2002. Low water contents in pyroxenes from spinel-peridotites of the oxidized, sub-arc mantle wedge. *Earth Planet. Sci. Lett.* 201(1), 69–86.
- Peslier, A.H., Luhr, J.F., 2006. Hydrogen loss from olivines in mantle xenoliths from Simcoe (USA) and Mexico: Mafic alkalic magma ascent rates and water budget of the subcontinental lithosphere. *Earth Planet. Sci. Lett.* 242 (3–4), pp. 302-319.
- Peslier, A.H., Woodland, A.B., Bell, D.R., Lazarov, M., Lapen, T.J., 2012. Metasomatic control of water contents in the Kaapvaal cratonic mantle. *Geochim. Cosmochim. Acta* 97, 213–246.
- Pintér, Zs, Patkó, L., Djoukam, J.F.T., Kovács, I., Tchouankoue, J.P., Falus, G., Konc, Z., Tommasi, A., Barou, F., Mihály, J., Németh, Cs, Jeffries, T., 2015. Characterization of the sub-continental lithospheric mantle beneath the Cameroon volcanic line inferred from alkaline basalt hosted peridotite xenoliths from Barombi Mbo and Nyos Lakes. *J. Afr. Earth Sci.* 111, 170–193.
- Poudjom Djomani, Y.H., Diament, M., Wilson, M., 1997. Lithospheric structure across the Adamawa plateau (Cameroon) from gravity studies. *Tectonophysics*, 273 (1997), pp. 317-327.
- Poudjom-Djomani, Y.H., Nnange, J.M., Diament, M., Ebinger, C.J, Fairhead, J.D., 1995. Effective elastic thickness and crustal thickness variations in West Central Africa inferred from gravity data. *J. Geophys. Res. Solid Earth* 100 (10-11): 22047-22070.
- Prechtel, F., Stalder, R., 2012. OH-defects in Al- and Cr- doped synthetic enstatites and defect geobarometry on natural orthopyroxenes from Earth's mantle. *Eur. J. Mineral.* 24, 471–481.
- Regnault, J.M., 1986. "Cameroon Geological Synthesis," Department of Mines and Geology, Yaounde. 119p
- Rudnick, R.L., McDonough, W.F., Chappell, B.W., 1993. Carbonatite metasomatism in the northern Tanzanian mantle: petrographic and geochemical characteristics. *Earth Planet. Sci. Lett.* 114, 463–475.
- Schmädicke, E., Gose, J., and Will, T.M., 2011. Heterogeneous mantle underneath the North Atlantic: Evidence from water in orthopyroxene, mineral composition and equilibrium conditions of spinel peridotite from different locations at the Mid-Atlantic Ridge. *Lithos* 125, 308–320.
- Scott, J. M., Liu, J., Pearson, D. G., Waight, T. E., 2016. Mantle depletion and metasomatism recorded in orthopyroxene in highly depleted peridotites. *Chem. Geol.*, 441, 280–291.
- Scott, J. M., Waight, T. E., van der Meer, Q. H. A., Palin, J. M., Cooper, A. F., Münker, C., 2014a. Metasomatized ancient lithospheric mantle beneath the young Zealandia

- microcontinent and its role in HIMU-like intraplate magmatism. *Geochem. Geophys. Geosyst.* 15(9), 3477–3501.
- Scott, J.M., Hodgkinson A., Palin J.M., Waight T.E., Van der Meer Q.H.A., Cooper A.F., 2014b. Ancient melt depletion overprinted by young carbonatitic metasomatism in the New Zealand lithospheric mantle. *Contrib. Mineral. Petrol.* 167: 963.
- Shaw, C.S.J., Dingwell, D.B., 2008. Experimental peridotite–melt reaction at one atmosphere: a textural and chemical study. *Contributions to Mineralogy and Petrology* 155, 199-214.
- Shaw, C.S.J., Heidelbach, F., Dingwell, D.B., 2006. The origin of reaction textures in mantle peridotite xenoliths from Sal Island, Cape Verde: the case for “metasomatism” by the host lava. *Contributions to Mineralogy and Petrology* 151, 681-697.
- Shu, Q., Brey, G.P., 2015. Ancient mantle metasomatism recorded in subcalcic garnet xenocrysts: temporal links between mantle metasomatism diamond growth and crustal tectono magmatism *Earth Planet. Sci. Lett.*, 418, 27-39.
- Skogby, H., Bell, D.R., Rossman, G.R., 1990. Hydroxide in pyroxene; variations in the natural environment. *Am. Mineral.* 75 (7-8): 764–774.
- Stalder, R., Ludwig, T., 2007. OH incorporation in synthetic diopside. *Eur. J. Mineral.*, 19 (3) (2007), 373-380.
- Streckeisen, A. 1976. To each plutonic rock its proper name. *Earth Sci. Rev.*, 12 (1), 1976, pp. 1-33.
- Su, B.-X., Zhang, H.-F., Sakyi, P. A., Ying, J.-F., Tang, Y.-J., Yang, Y.-H., Zhao, X.-M., 2010. Compositionally stratified lithosphere and carbonatite metasomatism recorded in mantle xenoliths from the Western Qinling (Central China). *Lithos* 116(1-2), 111–128.
- Su, B.X., Zhang, H.F., Sakyi, P.A., Zhang, Y.H., Ying, J.F., Tang, Y.J., Qin, K.Z., Xiao, Y., Zhao, X.M., Mao, Q., Ma, Y.G., 2011. The origin of spongy texture in minerals of mantle xenoliths from the Western Qinling, central China. *Contrib. Mineral. Petrol.*, 161, 465-482.
- Tamen J., Nkoumbou C., Reusser E., Tchoua F., 2015. Petrology and geochemistry of mantle xenoliths from the Kapsiki Plateau (Cameroon Volcanic Line): Implications for lithospheric upwelling. *J. Afr. Earth Sci.* 101:119–134.
- Tedonkenfack, S.S.T., Puziewicz, J., Aulbach, S., Ntaflos, T., Kaczmarek, M.-A., Matusiak-Małek, M., Kukuła, A., Ziobro, M., 2021. Lithospheric mantle refertilization by DMM-Derived melts beneath the Cameroon Volcanic Line – a case study of the Befang xenolith suite (Oku Volcanic Group, Cameroon). *Contrib. Mineral. Petrol.*, 176:37.
- Teitchou, M.I., Grégoire, M., Temdjim, R., Ghogomu, R.T., Ngwa, C., Aka, F.T., 2011. Mineralogical and geochemical fingerprints of mantle metasomatism beneath Nyos volcano (Cameroon volcanic line). In: Beccaluva, L., Bianchini, G., Wilson, M. (Eds.),

- Volcanism and Evolution of the African Lithosphere: Geological Society of America Special Paper 478, pp. 193–210
- Tian, Z.Z., Liu, J., Xia, Q.K., Ingrin, J., Hao, Y.T., Depecker C., 2017. Water concentration profiles in natural mantle orthopyroxenes: a geochronometer for long annealing of xenoliths within magma. *Geology* 45 (1), pp. 87-90.
- Tokam, A.-P. K., Tabod, C. T., Nyblade, A. A., Julià, J., Wiens, D. A., Pasyanos, M. E., 2010. Structure of the crust beneath Cameroon, West Africa, from the joint inversion of Rayleigh wave group velocities and receiver functions. *Geophys. J. Int.* 183, 1061– 1076.
- Tollan, P.M.E., Hermann, J., 2019. Arc magmas oxidized by water dissociation and hydrogen incorporation in orthopyroxene. *Nature Geosci.* 12(8), 667–671.
- Tollan, P.M.E., O’Neill, H.St.C., Hermann, J., Benedictus, A., Arculus, R.J., 2015. Frozen melt-rock reaction in a peridotite xenolith from sub-arc mantle recorded by diffusion of trace elements and water in olivine. *Earth Planet. Sci. Lett.* 422, 169-181
- Tollan, P.M.E., O’Neill, H.S.C., Hermann, J., 2018. The role of trace elements in controlling H incorporation in San Carlos olivine. *Contrib. Mineral. Petrol.*, 173(11).
- Tollan, P.M.E., Smith, R., O’Neill, H.S.C., Hermann, J., 2017. The responses of the four main substitution mechanisms of H in olivine to H₂O activity at 1050 °C and 3 GPa. *Progress in Earth and Planetary Science*, 4(1).
- Toteu, S. F., Van Schmus, W. R., Penaye, J., Michard, A., 2001. New U-Pb, and Sm-Nd data from North-Central Cameroon and its bearing on the pre-Pan-African history of Central Africa. *Pre. Res.* 108: 45-73.
- Toteu, S.F., Penaye, J., Djomani, Y.P., 2004. U–Pb and Sm-Nd evidence for Eburnean and PanAfrican high-grade metamorphism in cratonic rocks of southern Cameroon. *Can. J. Earth Sci.* 41, 73–85.
- Tsozué, D., Nzeugang, A.N., Azinwi, P.T., 2017. Genesis and Classification of Soils Developed on Gabbro in the High Reliefs of Maroua Region, North Cameroon. *Eurasian J. Soil Sci.*, 6, 168-177.
- Uenver-Thiele, L., Woodland, A. B., Seitz, H.-M., Downes, H., Altherr, R., 2017. Metasomatic Processes Revealed by Trace Element and Redox Signatures of the Lithospheric Mantle Beneath the Massif Central, France. *J. Petrol.* 58(3), 395–422.
- Van der Lee, S., Regenauer-Lieb, K., Yuen, D.A., 2008. The role of water in connecting past and future episodes of subduction. *Earth Planet. Sci. Lett.* 273, 15–27.
- Vincent, P.M., Armstrong, R.L., 1973. Volcanism of the Kapsiki Plateau (North Cameroon) and the underlying sedimentary formations. *Coll. African Geol.*, Florence, abst. unpubl.
- Walter M. J., 2003. Melt extraction and compositional variability in mantle lithosphere. In: Holland H., D., Turekian KK (eds) *Treatise on geochemistry*. Elsevier, 363–394.

- Wang, C., Jin, Z.M., Gao, S., Zhang, J.F., Zheng, S., 2010. Eclogite-melt/peridotite reaction: experimental constraints on the destruction mechanism of the North China Craton. *Sci. China Earth Sci.* 40, 541–555.
- Warren, J.M., 2016. Global variations in abyssal peridotite compositions. *Lithos* 248-251, 193–219.
- Witt-Eickchen, G., O'Neill, H.S.C., 2005. The effect of temperature on the equilibrium distribution of trace elements between clinopyroxene, orthopyroxene, olivine and spinel in upper mantle peridotite. *Chem. Geol.* 221(1-2), 65–101
- Workman, R.K., Hart, S.R., 2005. Major and trace element composition of the depleted MORB mantle (DMM). *Earth Planet. Sci. Lett.* 231, 53–72.
- Xia, Q. K., Hao, Y. T., Li, P., Deloule, E., Coltorti, M., Dallai, L., Yang, X. Z., Feng, M., 2010. Low water content of the Cenozoic lithospheric mantle beneath the eastern part of the North China Craton. *J. Geophys. Res. Solid Earth*, 115, B07207.
- Xu, Y.-G., Menzies, M.A., Thirlwall, M.F., Huang, X.-L., Liu, Y., Chen, X.-M., 2003. "Reactive" harzburgites from Huinan, NE China: products of the lithosphere-asthenosphere interaction during lithospheric thinning? *Geochim. Cosmochim. Acta* 67(3), 487–505.
- Yaxley G. M., Green D. H., 1998. Reactions between eclogite and peridotite: Mantle refertilisation by subduction of oceanic crust. *Schweiz Mineral Petrogr. Mitt.* 78: 243–255.
- Yaxley, G. M., Green, D. H., Kamenetsky, V., 1998. Carbonatite Metasomatism in the Southeastern Australian Lithosphere. *J. Petrol.* 39 (11-12), 1917–1930.
- Zangana, N., Downes, H., Thirlwall, M., Marriner, G., Bea, F., 1999. Geochemical variation in peridotite xenoliths and their constituent clinopyroxenes from Ray Pic (French Massif Central): implications for the composition of the shallow lithospheric mantle. *Chem. Geol.* 153(1-4), 11–35.
- Zong, K., Liu, Y., 2018. Carbonate metasomatism in the lithospheric mantle: implications for cratonic destruction in North China. *Sci. China Earth Sci.* 61, 711–729.

CHAPTER III:
NGAOUNDERE LIKOK AND OKU
VOLCANIC FIELD

III.1. INTRODUCTION

The Cameroon Volcanic Line (CVL), according to scientific discussions is an interesting area to investigate the long and complex evolution history of the SCLM below an alignment of volcanoes with a distinctive unsystematic space-time evolution. The CVL is built on the Pan-African basement of Cameroon, which consists of three domains with distinct lithological, structural and metamorphic characters (Nzenti et al., 1994; Toteu et al., 2004). These from north to south are: the North West Cameroon domain (NWCD), the Adamawa Yade domain (AYD) and the South Cameroon domain (SCD). These domains make up part of the larger Central African fold belt (CAFB) which is situated between the Congo craton, the Saharan metacraton and the Western Nigerian Shield (Caxito et al., 2020; Ngako et al., 2008; Van Schmus et al., 2008).

Nd isotopic data shows that the NWCD is a juvenile domain consisting of Neoproterozoic magmas (Penaye et al., 1993) without any isotopic or geochronological evidence of Archean heritage (Toteu et al., 2001). The AYD constitutes the transition between the northern margin of the Congo craton and the NWCD, which has been intensely reworked during the Pan African orogeny (Toteu et al., 2004). TDM ages and zircon dating shows that this domain is Paleoproterozoic with an important Archean contribution (Toteu et al., 2004). The SCD consists of a metamorphic series, which has been thrust southwards onto the Congo craton. Sm-Nd isotopic data shows that the rocks of this series are derived from protoliths, which form from diverse sources of Neoproterozoic and Paleoproterozoic ages with no major contribution from the Congo craton (Toteu et al., 2001; Ngnotué et al., 2000; Penaye et al., 1993).

Abundant mantle xenoliths have been found in several localities in the AYD and the NWCD, however, none has been reported for the SCD. These xenoliths represent fragments of the upper mantle brought to the surface by rocks of alkaline nature. Because the origin CVL remains enigmatic, it is therefore imperative to carry out detailed studies to understand the evolution of the SCLM below these regions. The SCLM below these domains has not been well constrained, the characterization of these distinct regions is, therefore, an important step. In this study, we focus on xenoliths from volcanoes in the Oku Volcanic Field (OVF) found in the NWCD and the Adamawa Volcanic Field (AVF) found in the AYD. These volcanoes are part of the 1600Km long chain of Tertiary to recent volcanoes of the CVL.

Mantle xenoliths worldwide show evidence for modifications by mantle processes, which include partial melting and melt rock reactions (Beccaluva et al., 2001; Churikova et al., 2001; Downes et al., 2001). The melts/fluids involved during such processes range in composition from $\text{CO}_2 \pm \text{H}_2\text{O}$ (Cvetkovic et al., 2010; Ionov et al., 1994; Kempton, 1987), silicate (Raffone et al., 2009; Zhang et al., 2000; Zangana et al., 1999) and carbonatite (Scott et al., 2014; Gregoire et al., 2000; Coltorti et al., 1999; Yaxley et al., 1998; Rudnick et al., 1993; Green and Wallace, 1988) rich fluids. Therefore understanding the nature and evolution of the mantle in the two different lithostructural domains is paramount as the identification of mantle processes, which modify the SCLM is fundamental in unravelling the geochemical history of the region.

The main aim of this study is therefore to characterize the lithospheric mantle below the juvenile North West Cameroon Domain and the reworked Adamawa Yade Domain in order to reconstruct the geologic history of the mantle on a regional scale.

In order to attain this, I, therefore;

1. Categorize the samples based on their petrography and measure their chemical composition.
2. Model the extent of melt extraction prior to metasomatic enrichments.
3. Appraise variations in temperature distributions from equilibrium conditions and the implications for sampling depths of xenolith samples.
4. Distinguish between the effects of host basalt-xenolith interactions and metasomatic enrichments.
5. Individuate the metasomatic type(s) and discriminate the corresponding metasomatic agents using clinopyroxene and amphibole compositions (silicate vs carbonatite metasomatism and intraplate vs subduction signatures).
6. Evaluate the use of olivine and orthopyroxene trace element compositions as metasomatic indicators.

Numerous mantle xenoliths were collected in several localities along the CVL from the AVF (at Ngaoundere Likok) which is found in the AYD and the OVF (at Kuk, Nyos, Wum, Etome, Enep and Oku) in the NWCD. Detailed petrographic studies

accompanied by major and trace element analysis were done using EPMA and LA-ICP-MS techniques (See methods in chapter I) on 16 selected mantle xenolith samples (3 from the AVF and 13 from OVF).

This chapter presents the first geochemical data for several localities along the CVL (e.g. Etome, Kuk and Wum) complemented with new, complete and detailed geochemical data for other localities (e.g. Enep, Oku and Ngaoundere Likok).

III.2. RESULTS

III.2.1. PETROGRAPHY/TEXTURES/MICROSTRUCTURES

Macroscopic observations

The studied xenoliths were collected along the CVL region around volcanic lakes in the OVF, at Etome (E1a, E8), Enep (En1a, En2a), Kuk (K1, K1a, K5), Nyos (Ny1a, Ny3), Oku (Ok1a, Ok1), Wum east (We1a), Wum west (Ww1a) and in the Adamawa Volcanic massif (AVM) in the Ngaoundere Plateau around Likok (N11a, N11, N18) (Fig. 3.1). Information on the location and age of the volcanoes is presented in Table 3.1. Xenoliths from the CVL outcrop as angular and subrounded blocks to ovoid boulders ranging from 2cm to about 25cm in diameter (eg. Fig. 3.2), with some of them incrustated in fine-grained, black and massive volcanic projecta (intra alkaline volcanic bombs). Xenoliths from Ngaoundere Likok show relatively coarse grains (>0.5 cm). The boundary between the host basalt and xenolith shows evidence of modification with a scorched appearance. (Fig. 3.2b).

The host basalt rocks of the OVF samples show different physical appearances depending on the locality. Those from Kuk, Etome and Nyos appear as a very thin layer of <0.5cm which envelopes the xenolith (Fig. 3. 2c). They are strongly altered and eroded. The host basalt rocks from Wum west and Nyos show less alteration and are vesicular while those from Wum east and Oku are compact and fresh.

The xenoliths from Kuk, Enep and Etome range in size from 5-25 cm. The largest samples are characterized by a massive friable nature and intense weathering. Abundant reddish-brown products of alteration (iddingsite) are common on the surface and rim area of the xenoliths while the cores are less altered (Fig. 3.2c). Samples from Enep show a characteristic layering (Fig. 3.2d). Wum west and Nyos samples are fresh and abundant

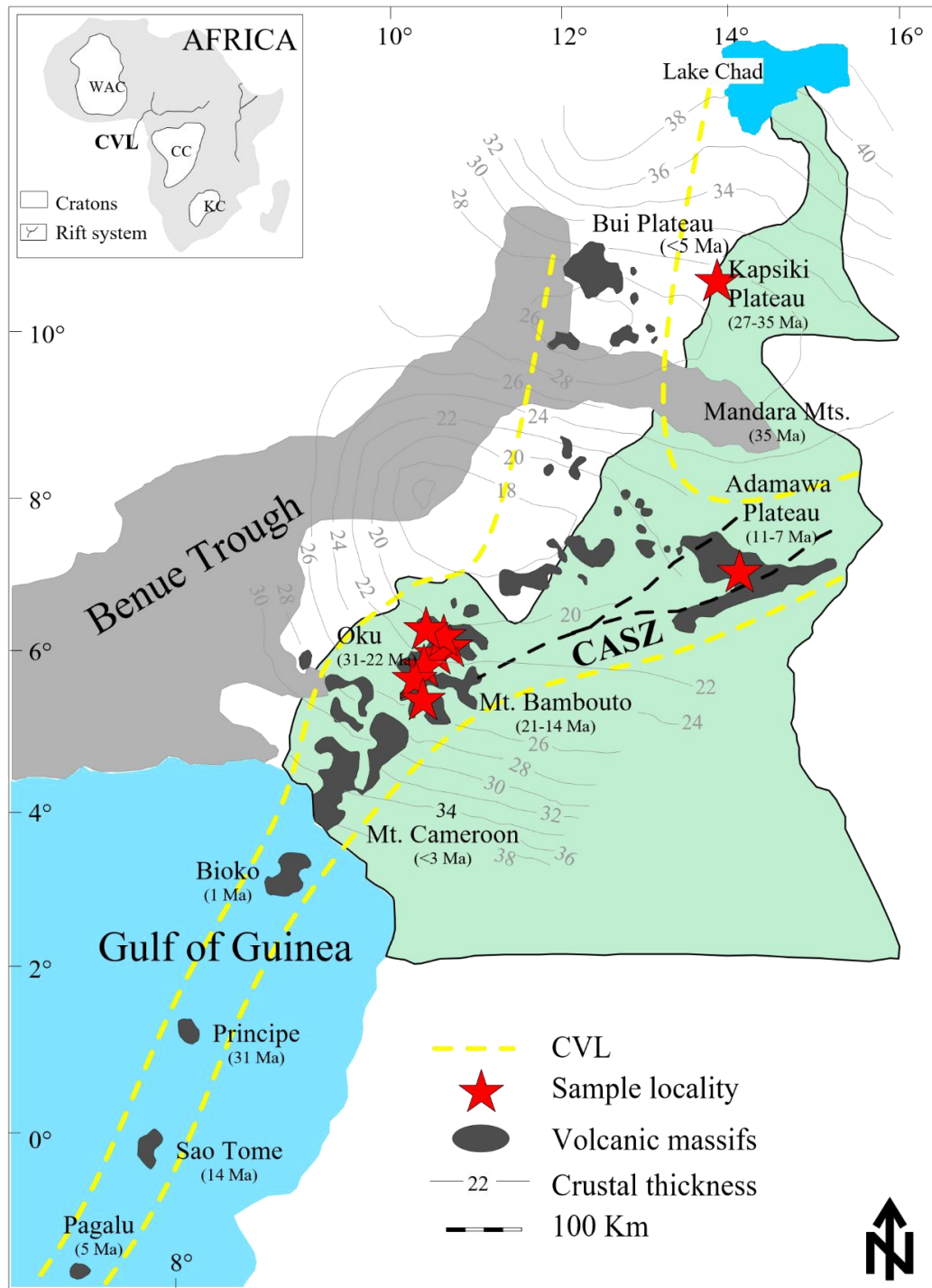


Figure 3.1: Sample location of the studied xenoliths along the Cameroon Volcanic Line (CVL) modified after Deruelle et al., 2007. Insert on the left shows the major cratons, the position of the CVL and the East African Rift system. The Central African Shear Zone is from Njiekak et al., 2008 and crustal thicknesses from Poudjom Djomani et al., 1995.

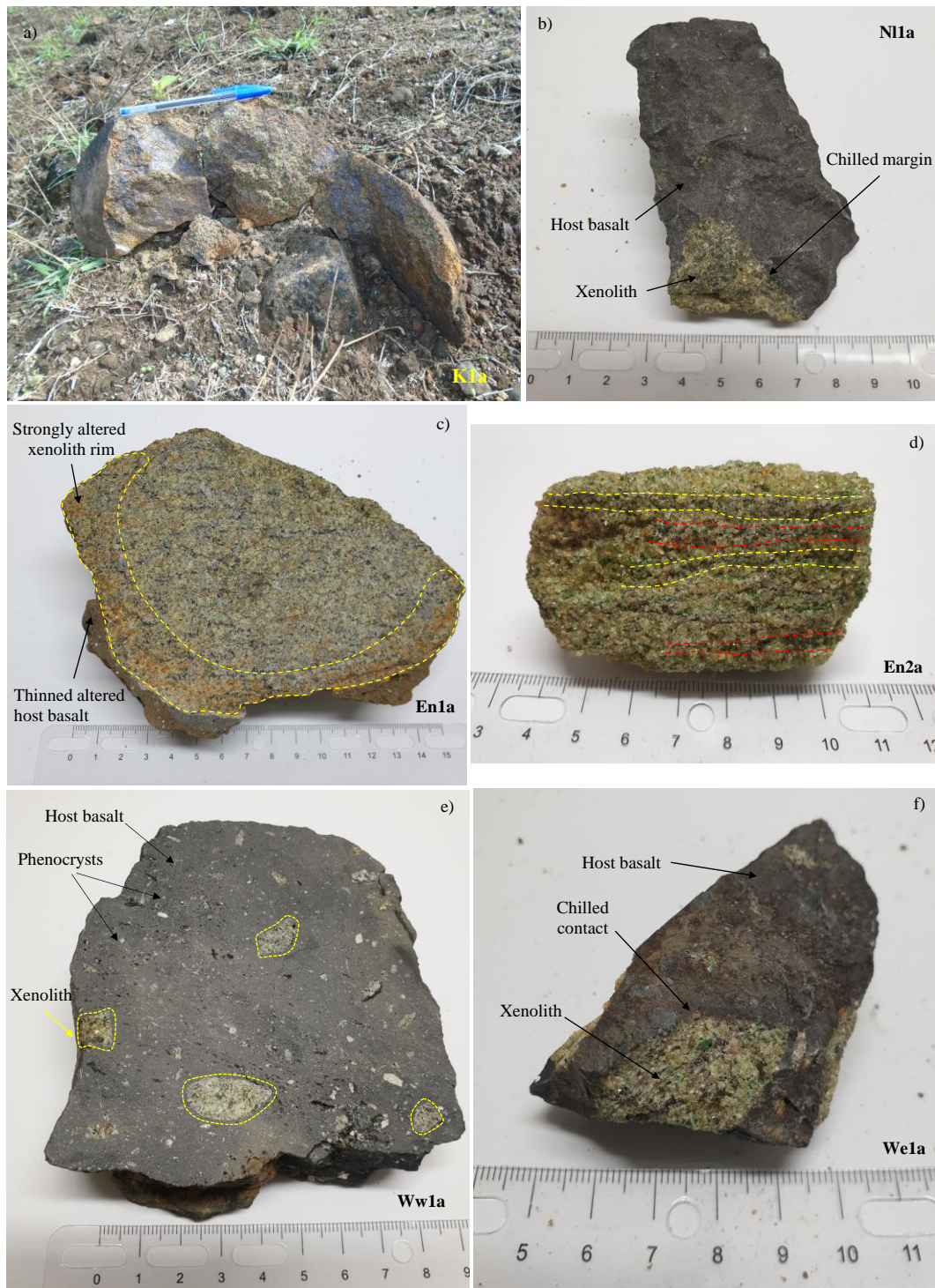


Figure 3.2: Photographs of hand samples of CVL xenoliths. (a) Large altered Kuk (K1a) xenolith. (b) Fresh sample from Ngaoundere Likok (N11a) showing a charred rim with the microlitic porphyric host basalt. (c) Sample from Enep (En1a) showing a thinned host basalt and strong weathering at the rim area. (d) Sample from Enep (En2a) showing a foliated texture. (e) Sample from Wum (Ww1a) characterised by abundant xenoliths of small sizes distributed within the vacuolar microlitic porphyric textured host basalt. (f) Sample from Wum (We1a) showing a chilled contact with the host basalt.

Table 3.1: Location, petrography and age information of xenolith bearing rocks from the CVL. The ages for the Adamawa Volcanic Field are from Gouhier et al., 1974; Marzoli et al., 1999; Fagny et al., 2012 and for the Oku Volcanic Field, from Fitton and Dunlop 1985; Marzoli et al., 1999, 2000; Asaah et al., 2015.

	Locality	Sample	Geographic coordinates/ altitude	Volcanism age	Host basalt texture
AVF	Likok	N11 N11a N18	N07°16'10"/ E13°14'18"/ Alt: 1200m	11-7 Ma	Microlitic porphyric
	Etome	E1a E8	N06°18'00"/ E10°12'58"/ Alt: 1414m		Vacuolar microlitic porphyric
	Enep	En1a En2a	N06°17'27"/ E10°01'59"/ Alt: 621m		Vacuolar microlitic porphyric
OVF	Kuk	K1 K1a K5	N06°22'48"/ E10°13'27"/ Alt:1492m	31-22 Ma	Vacuolar microlitic porphyric
	Nyos	Ny1a Ny3	N06°27'29"/ E10°15'42"/ Alt: 31m		Vacuolar microlitic porphyric
	Oku	Ok1 Ok1a	N06°13'06"/ E10°26'32"/ Alt:2446m		Microlitic porphyric
	Wum	Ww1a We1a	N06°24'29"/ E10°03'08"/ Alt: 1085m N06°24'06"/ E10°03'43"/ Alt: 1095m		

Table 3.2: Modal proportions of xenolith minerals (in volume %) obtained using Image J software.

	Locality	Sample	Modal composition				
			O1	Opx	Cpx	Spl	Amp
AVF	Likok	N11	55	35	6	4	
		N11a	25	40	30	5	
		N18	55	35	10		
OVF	Etome	E1a	57	23	18	2	
		E8	54	28	16	2	
	Enep	En1a	25	40	25	10	
		En2a	50	30	16	4	
	Kuk	K1	45	40	10	5	
		K1a	60	20	17	3	
		K5	40	30	25	5	
	Nyos	Ny1a	50	30	20		
		Ny3	55	25	15	5	
	Oku	Ok1	40	46	10	4	
		Ok1a	30	57	10	3	
	Wum	Ww1a	50	20	18	3	9
We1a		47	20	18	5	10	

and occur in small sizes of 1-3 and 4-10 cm in diameter respectively, disseminated within the host basalt alongside numerous xenocrysts especially in the Wum west sample (Fig. 3.2e). Wum east and Oku xenoliths are fresh and range in size from 2-10 cm and 1-2 cm respectively. The host basalt-xenolith boundary for the Wum east sample appears scorched (Fig. 3.2f) while for the Oku sample, it is sharp.

Using the image analysis software Image J, the modal proportions of the different mineral phases of the xenoliths were obtained by image thresholding (see methods, chapter 1). The main constituting mineral phases observed are light green olivine (25-60%), dark brown orthopyroxene (20-57%), emerald-green clinopyroxene (6-30%) and light brown to reddish-brown spinel (2-10%). Samples from Wum contain a hydroxyl bearing phase, amphibole (~10%). A summary of the modal composition is given in Table 3.2. Based on their modal composition and according to the classification of Streckeisen, 1976, these xenoliths can be classified as lherzolites (Nl8, Ny1a), spinel bearing lherzolites (Nl1, E1a, E8, En2a, K1, K1a, K5, Ny3, and Ok1), spinel bearing olivine websterites (Nl1a, En1a, Ok1a) and amphibole bearing spinel lherzolites (Ww1a, We1a).

Microscopic Observations

III.2.1.1. Basaltic cortex

The host basalt rocks of the CVL xenoliths show vacuolar microlitic porphyric (En1a, E1a, K1a, Ny1a) (Fig. 3.3a) and microlitic porphyric (Nl1a, Ok1a, Ww1a, We1a) (Fig. 3.3b) textures (Table 3.1). They comprise abundant micrograins (0.2-0.7mm) of olivine and pyroxene in a fine-grained matrix of plagioclase microlites and a groundmass of opaque oxides. Phenocrysts/xenocrysts (0.7-2.5 mm) of olivine and pyroxenes are common within the host basalt and sometimes show reaction rims. Visual estimates of the modal proportions of the phenocrysts vary in the different samples between 10-20%. Most samples show a reaction rim at the host basalt-xenolith interface (especially at places where they are in contact with clinopyroxene, (En1a, E1a, and Ok1a). Samples Nl1a and We1a show in addition, textural evidence for infiltration of the host basalt (Fig. 3.3c) while samples K1a, Ny1a and Ww1a show a sharp contact with the host basalt (Fig.3.3d).

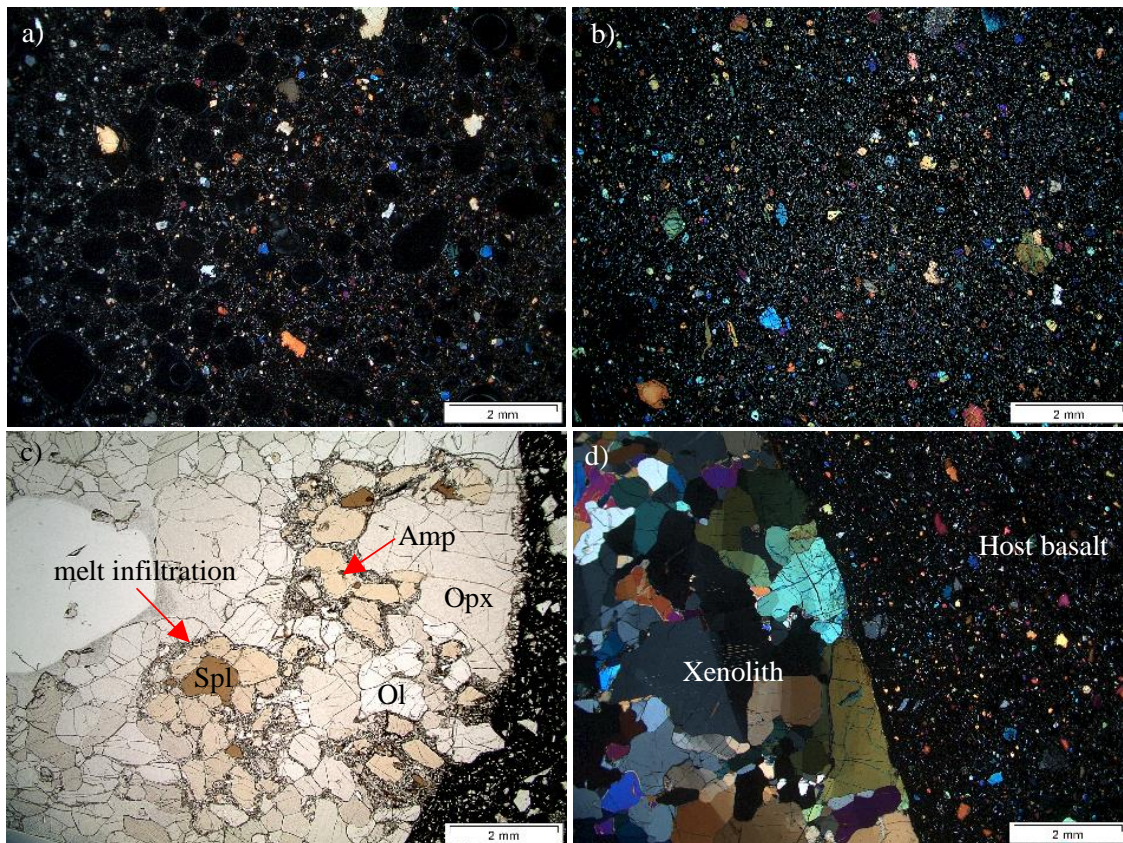


Figure 3.3: Photomicrographs of thin sections of CVL host basalts showing (a) Vacuolar microlitic porphyric texture in sample E1a and (b) Microlitic porphyric texture in sample Ok1a. (c) Reacted host basalt xenolith interface and evidence for melt infiltration in sample We1a. (d) Sample Ww1a showing a sharp unreacted host basalt-xenolith interface. Figures a, b and d were taken under cross polarized light while c under plan polarized light.

III.2.1.2. Adamawa Volcanic massif xenoliths

The AVM xenoliths show protogranular textures (Fig. 3.4a, b), according to the classification of Mercier and Nicolas, 1975. Several networks of cracks crosscutting olivine crystals are filled with reddish-brown products of alteration (iddingsite) (Fig. 3.4a) while those observed in pyroxenes are filled with fine grains of opaque oxides. The abundance of cracks makes it challenging to evaluate their grain sizes. Olivine and orthopyroxene crystals are generally larger than clinopyroxene crystals. Spongy rims are common in the clinopyroxenes (Fig. 3.4c,d). Some orthopyroxene grains display exsolution lamellae of clinopyroxene and also tiny secondary clinopyroxene grains are present at their rims (Fig. 3.4a). Some olivine and orthopyroxene crystals show deformation structures (kink bands and undulose extinction) (Fig. 3.4b, c). Light brown amoeboid spinels with black outer rims disintegrated from the xenolith are found in the

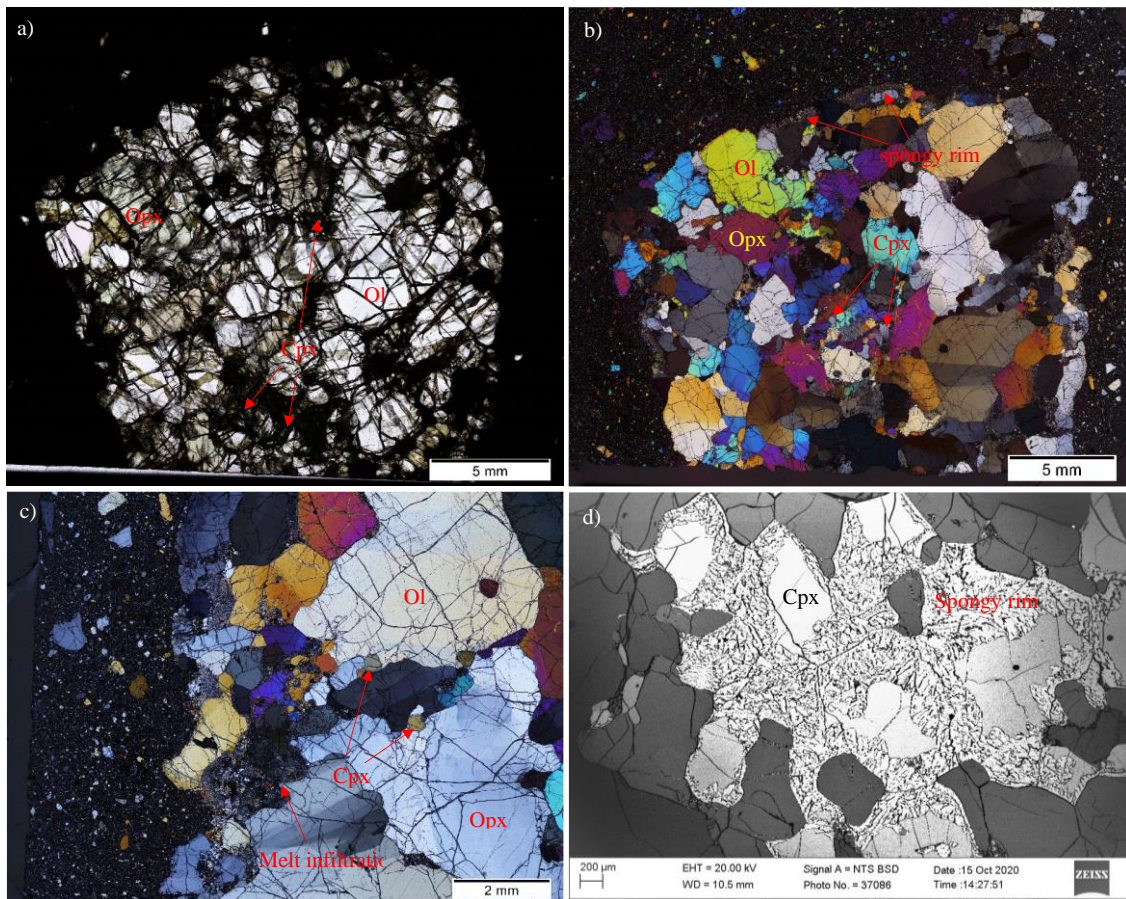


Figure 3.4: Photomicrographs of mantle xenoliths from the Adamawa Volcanic massif (AVM) under cross polarized light showing (a) Protogranular textures, characterised by a network of cracks in large olivines and the presence of tiny clinopyroxenes growing at the rims of large orthopyroxene grains. (b) Protogranular textures (c) Kink bands in olivine and orthopyroxene and evidence for fluid infiltration. (d) Backscattered image of clinopyroxenes with spongy rims.

host basalt. The basalt-xenolith boundary is characterized by a spongy appearance indicating reactions with the host basalt (Fig. 3.4c, d).

III.2.1.3. Oku Volcanic Field xenoliths

Xenoliths from Enep show protogranular to porphyroclastic textures. Sample En1a is characterized by very large orthopyroxene grains (0.4-4.6 mm) and smaller olivine crystals (0.3-2.3 mm) (Fig. 3.5a, c, d). Clinopyroxenes are also as large in size as the coexisting minerals (0.4-4 mm) but most of the grains show centripetal replacement by a spongy rim leaving behind a core of about 0.4-1.8 mm (Fig. 3.5a, b, d). The cores of most of the clinopyroxenes have tiny blebs of melt inclusions that are parallel to orthopyroxene lamellae, while orthopyroxenes have exsolution lamellae of

clinopyroxene (Fig. 3.5c). Light brown holly leaf spinel with black rims is common (Fig. 3.5d). Sample En2a is distinguished by its foliated/sheared nature, showing a preferential orientation of crystals (Fig. 3.5e), with very large olivine grains (0.3-3.9 mm), smaller orthopyroxene (0.2-2.5 mm) and clinopyroxene grains (0.1-1.2 mm). Clinopyroxenes are generally less abundant (16%) than the coexisting minerals and are found in interstitial position between olivines and orthopyroxenes. A second generation of clinopyroxene (very tiny grains <0.2 mm) can be found growing in disturbed sublayers containing a mixture of large grains of reddish-brown spinel and fine-grained opaque minerals (Fig. 3.5f, g, h). All grains are generally elongated; olivine and orthopyroxene show polygonisation and curvilinear grain boundaries at almost 120° (Fig. 3.5e). The contact between the host basalt and xenolith show a spongy texture where clinopyroxene is present.

Etome xenoliths are protogranular with olivine crystals (0.4-2.6 mm) being the most abundant phase (54-57%) (Fig. 3.6a). These are larger than ortho- (0.2-2.11 mm) and clinopyroxenes (0.2-1.6 mm). Olivine and pyroxene grains have curvilinear to straight grain boundaries, polygonal shapes, and present triple grain boundaries close to 120°. Spinel is light brown and has an amoeboid shape (Fig. 3.6b). These xenoliths show no evidence of melt infiltration or deformation textures and they show a sharp contact with the host basalt (Fig. 3.6a).

Kuk xenoliths show porphyroclastic textures with large olivine (0.3-5 mm) and orthopyroxene (0.4-4.6 mm) grains (Fig. 3.6c). A second population of smaller grains (<0.4 mm) can also be observed. Kink bands are common in olivine (Fig. 3.6d) and pyroxenes. Clinopyroxene grains are smaller in size (0.2-1.6 mm), occur in interstitial position and are characterized by spongy rims (Fig. 3.6c, e, f). Exsolutions of clinopyroxenes are also common in orthopyroxene. Dark brown spinels with black rims are present (Fig. 3.6g) and the contact with the host basalt is sharp (Fig. 3.6d, h).

Xenoliths from Nyos show transitional textures from protogranular to porphyroclastic. Olivine and orthopyroxene grains show two populations based on their sizes, the larger grains (up to 5 mm) are subhedral with some showing kink bands while the smaller grains are generally less than 1mm (Fig. 3.7a). Clinopyroxenes (0.2-1.7 mm) are smaller, with some of them showing spongy rims (Fig. 3.7b) and exsolution lamellae (Fig. 3.7c). Tiny melt inclusions are also common in the centre of the clinopyroxenes. A few tiny fluid inclusion trails have been observed in these xenoliths (Fig. 3.7d). Pale

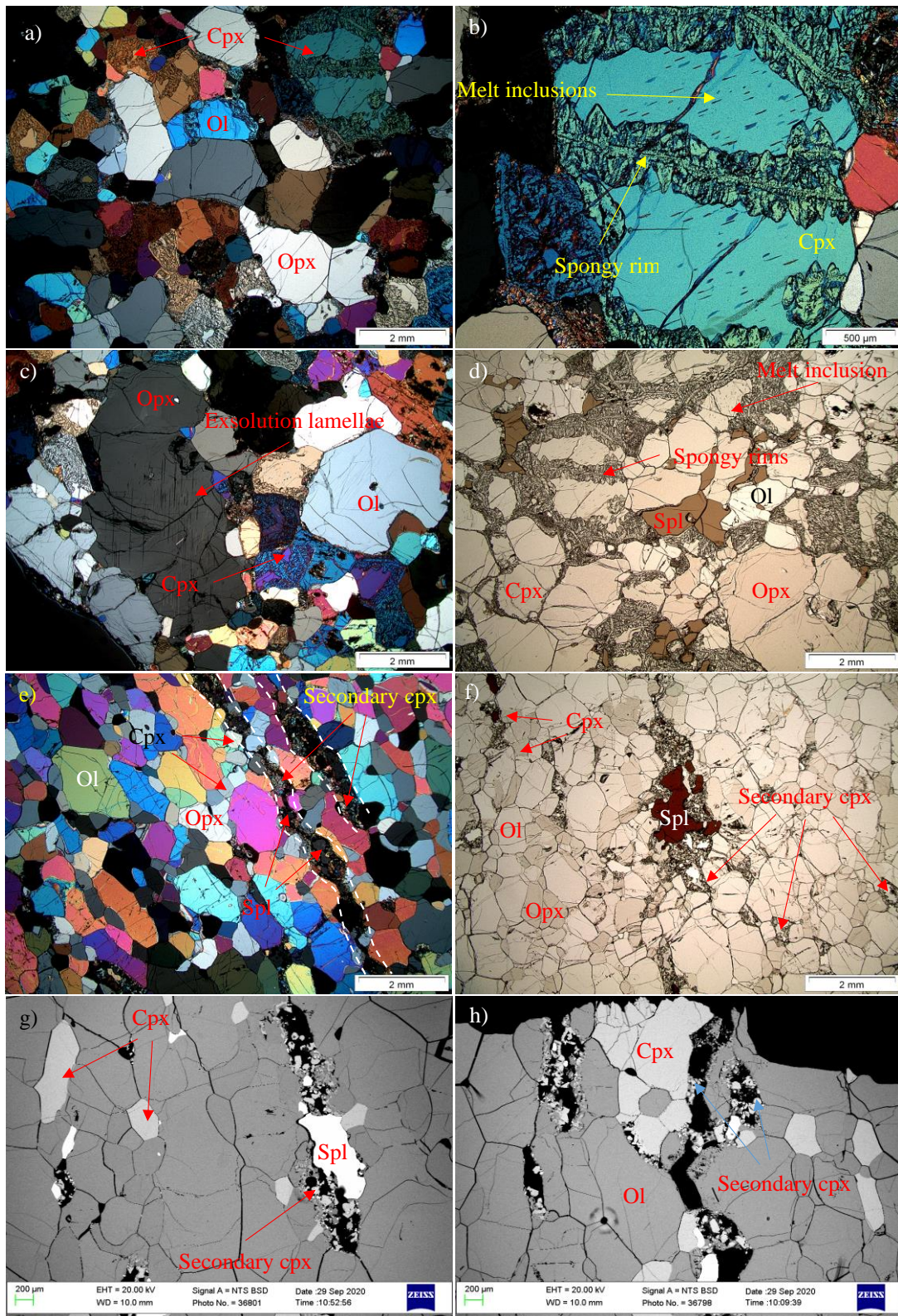


Figure 3.5: Photomicrographs of thin sections of xenoliths from Enep showing (a) Small olivine grains relative to pyroxenes. (b) Centripetal replacement of clinopyroxene by a spongy rim and cores with melt inclusions. (c) Orthopyroxene with exsolution lamellae of clinopyroxene. (d) Holly leaf spinel with black rims. (e, f, g, h) Foliated texture with secondary clinopyroxene and spinel in disturbed layers. Figures a, b, c and e were taken under cross polarised light, d and f under plane polarised light and g and h are backscattered images.

brown holly leaf spinel is also common.

Samples from the Oku show protogranular textures (Fig. 3.7e). Olivine (0.5-4.8 mm) and orthopyroxene (0.5-2.5 mm) are subhedral, elongated and characterized by a network of cracks (Fig. 3.7f). Kink bands are common in olivines (Fig. 3.7e). Clinopyroxenes (0.5-1.5 mm) are generally subhedral and smaller in size than the coexisting minerals. Dark brown symplectites of spinel are abundant. The minerals at the host basalt-xenolith interface show reaction rims.

Wum (We1a and Ww1a) samples are characterized by protogranular and transitional (protogranular to porphyroclastic) textures respectively. We1a has euhedral to subhedral olivine (0.3-3.2 mm) and orthopyroxene (0.3-3.5 mm) grains with polygonal grain boundaries showing triple point junctions. Ww1a shows large subhedral olivine (0.6-4.7 mm), orthopyroxene (0.5-2.8 mm) grains, and smaller grains, which are identical in size to the clinopyroxenes. Clinopyroxene (0.1-0.7 mm) shows spongy rims (Fig. 3.8a, b, c) and exsolution lamellae of orthopyroxene are common (Fig. 3.8a). The hydrous phase amphibole is common in Wum xenoliths and normally appears alongside spinel (Fig. 3.8a, b). Reaction rims are also common around amphiboles. We1a shows interactions in the host basalt-xenolith interface especially in areas where pyroxenes are present. There is also textural evidence for melt infiltration (Fig. 3.8d), while sample Ww1a shows a sharp xenolith-host basalt interface (3.8e, f).

III.2.1.4. Grain size distribution

Representative grain size histograms for CVL are shown in Fig. 3.9. The CVL xenoliths generally show a normal grain size distribution for most samples with no pronounced bimodal distribution. The sizes of olivine and pyroxenes are generally slightly larger than the coexisting clinopyroxene. Samples from Etome (E1, E8) and En2a show olivine grain sizes that are slightly larger than the coexisting orthopyroxene and clinopyroxene, which are sensibly of the same size. The orthopyroxenes of sample En1a are larger than the coexisting olivine and clinopyroxene of similar sizes. Samples from Kuk (K1, K1a, K5) and sample N18 show moderate bimodal distribution for olivine and orthopyroxene.

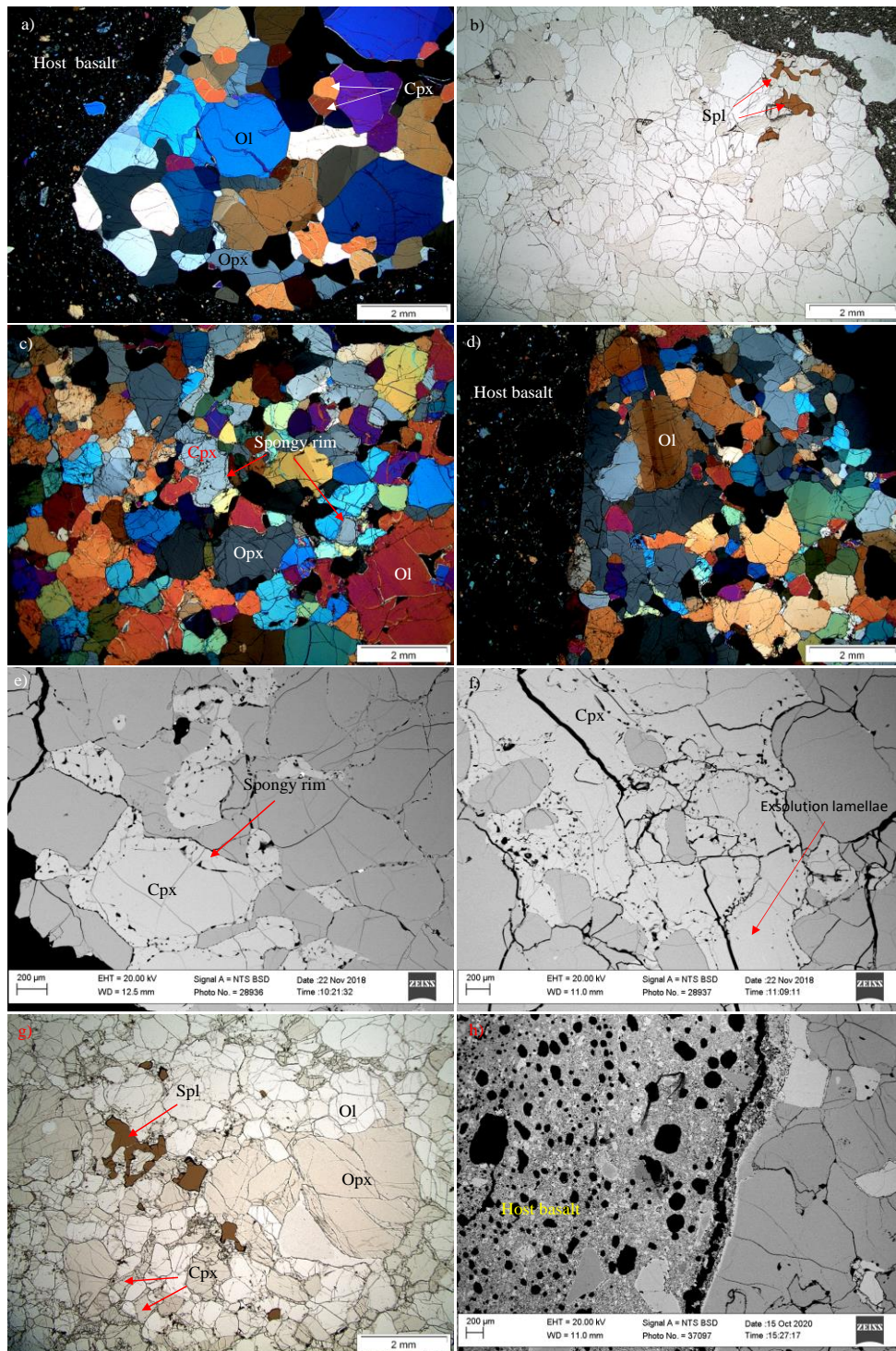


Figure 3.6: Photomicrographs of thin sections showing (a) Protogranular textures in sample E1a. (b) Light brown amoeboid-shaped spinel. (c) Porphyroclastic textures in sample K1. (d) Kink bands in olivine (e, f) spongy rims in clinopyroxene. (g) Dark brown spinel with black rims. (h) A sharp xenolith- host basalt interface. Figures a, c, d were taken under cross polarised light, b, b under plain polarised light and e, f, h are backscattered images.

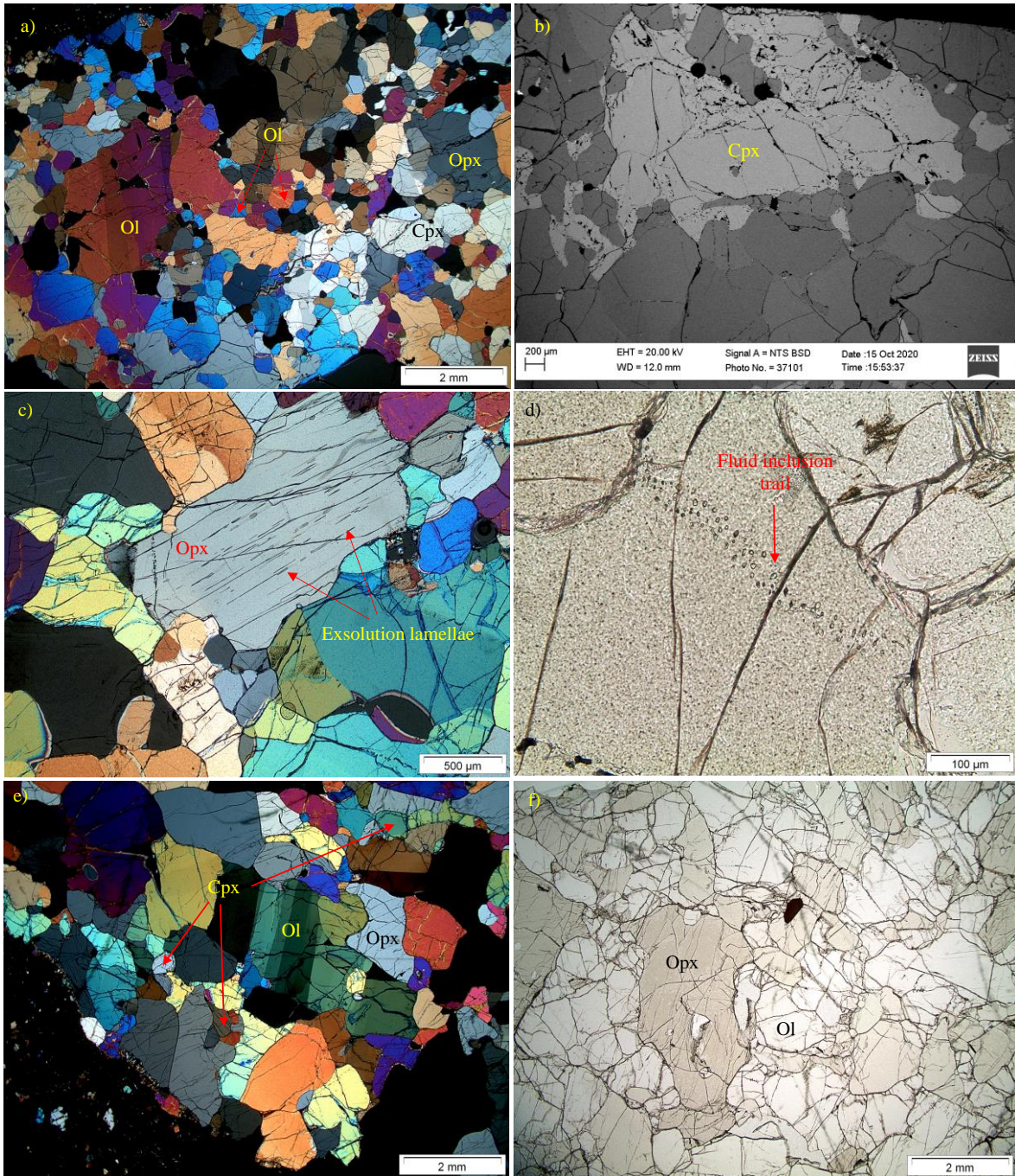


Figure 3.7: Photomicrographs of thin sections of (a) Nyos xenoliths showing transtional textures with kink bands common in olivine. (b, c) Clinopyroxene with spongy rims and exsolution lamellae. (d) Tiny fluid inclusion trails. (e) Protogranular textures in Oku sample. (f) Network of cracks in olivine and orthopyroxene. Figures a, c, e were taken under cross polarised light, b is a backscattered image and d and f under plain polarised light.

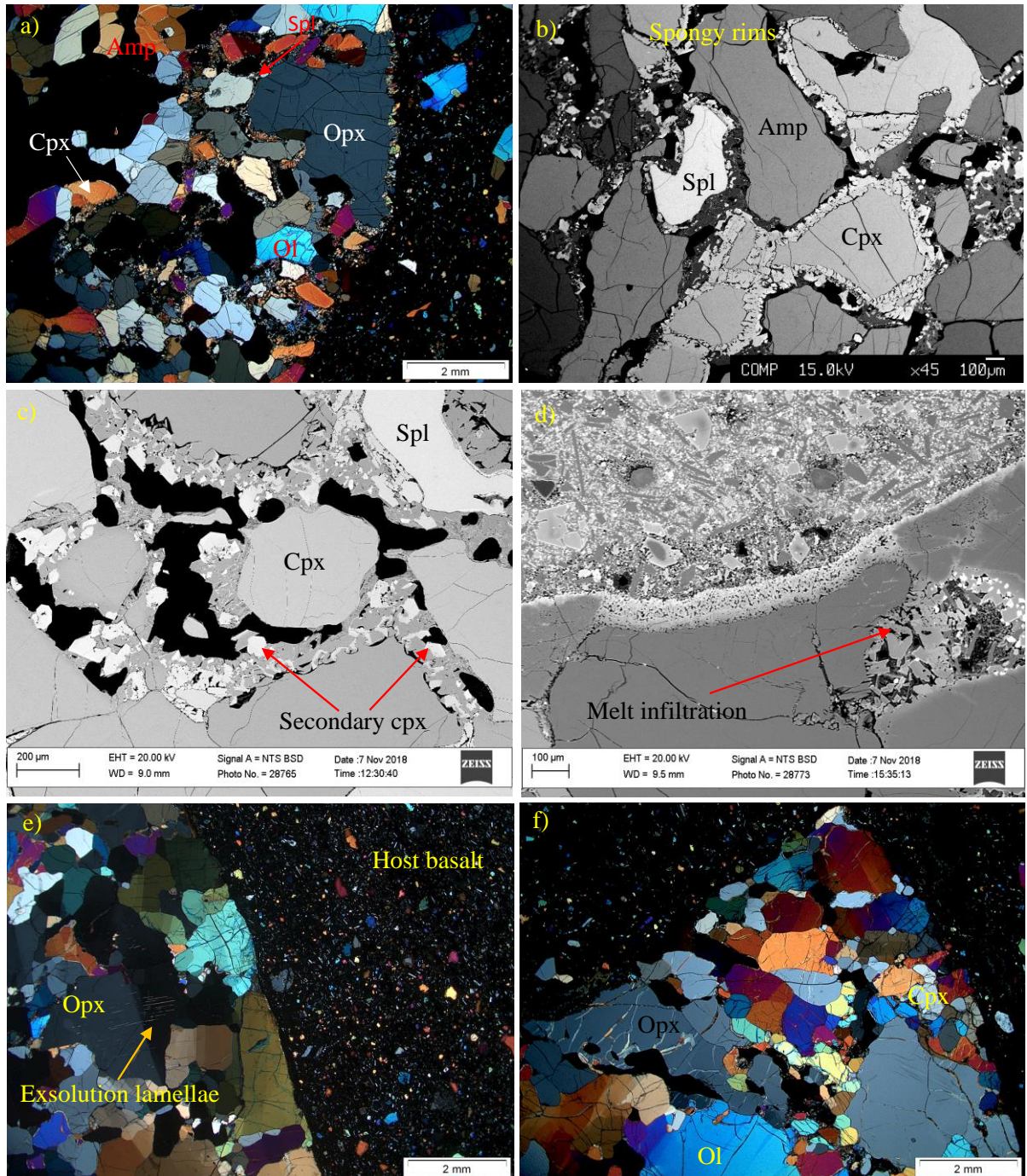


Figure 3.8: Photomicrographs of thin sections of Wum samples showing (a, b, c) Clinopyroxenes with spongy rims and a close association of amphibole and spinel. (d) Textural evidence for melt infiltration and (e, f) A sharp contact between the xenolith and the host basalt. Figures a, e, f are taken under cross polarized light while b, c, d are backscattered images.

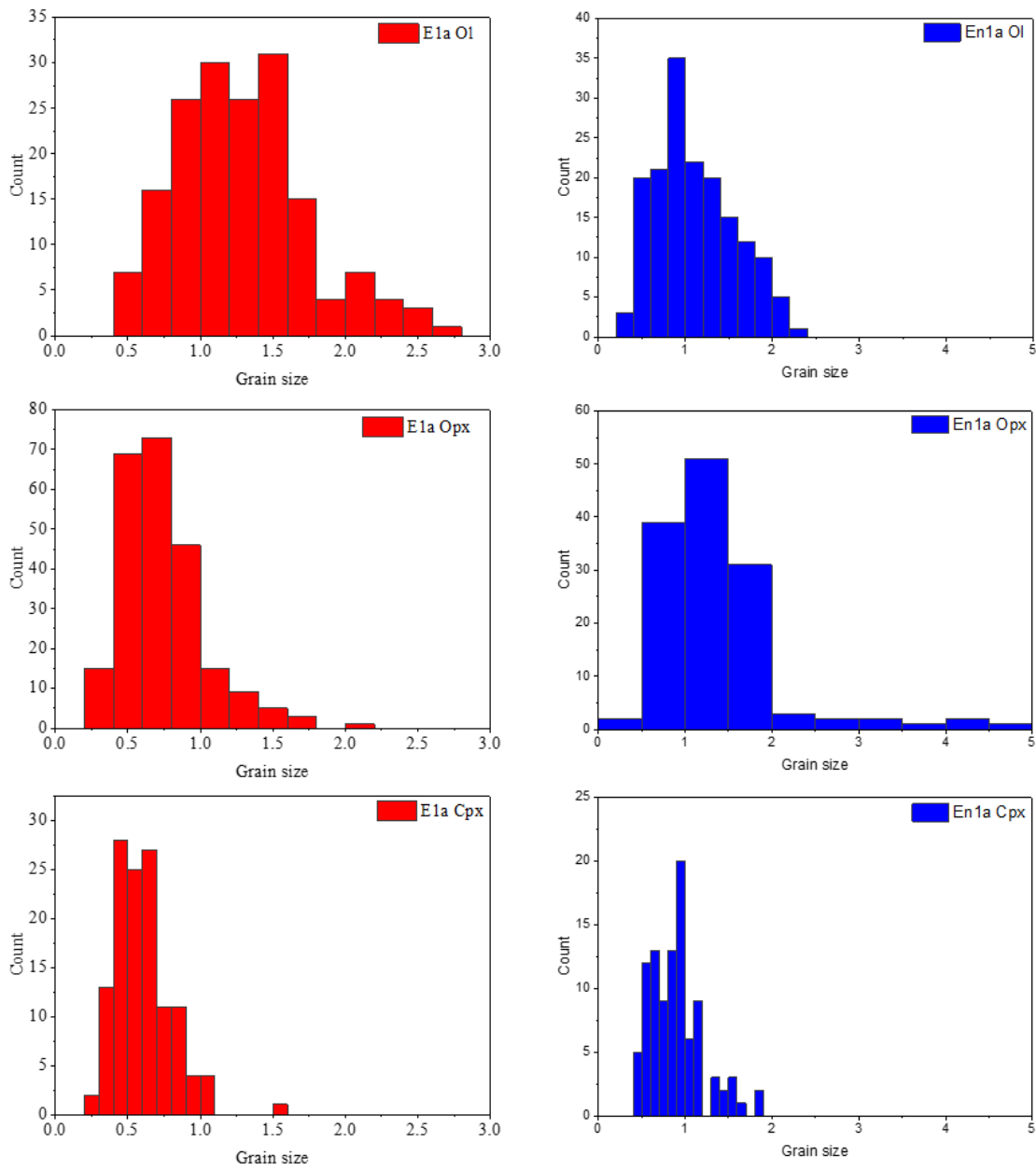


Figure 3.9: Representative grain size distribution histograms of mantle xenolith minerals of the Cameroon Volcanic Line.

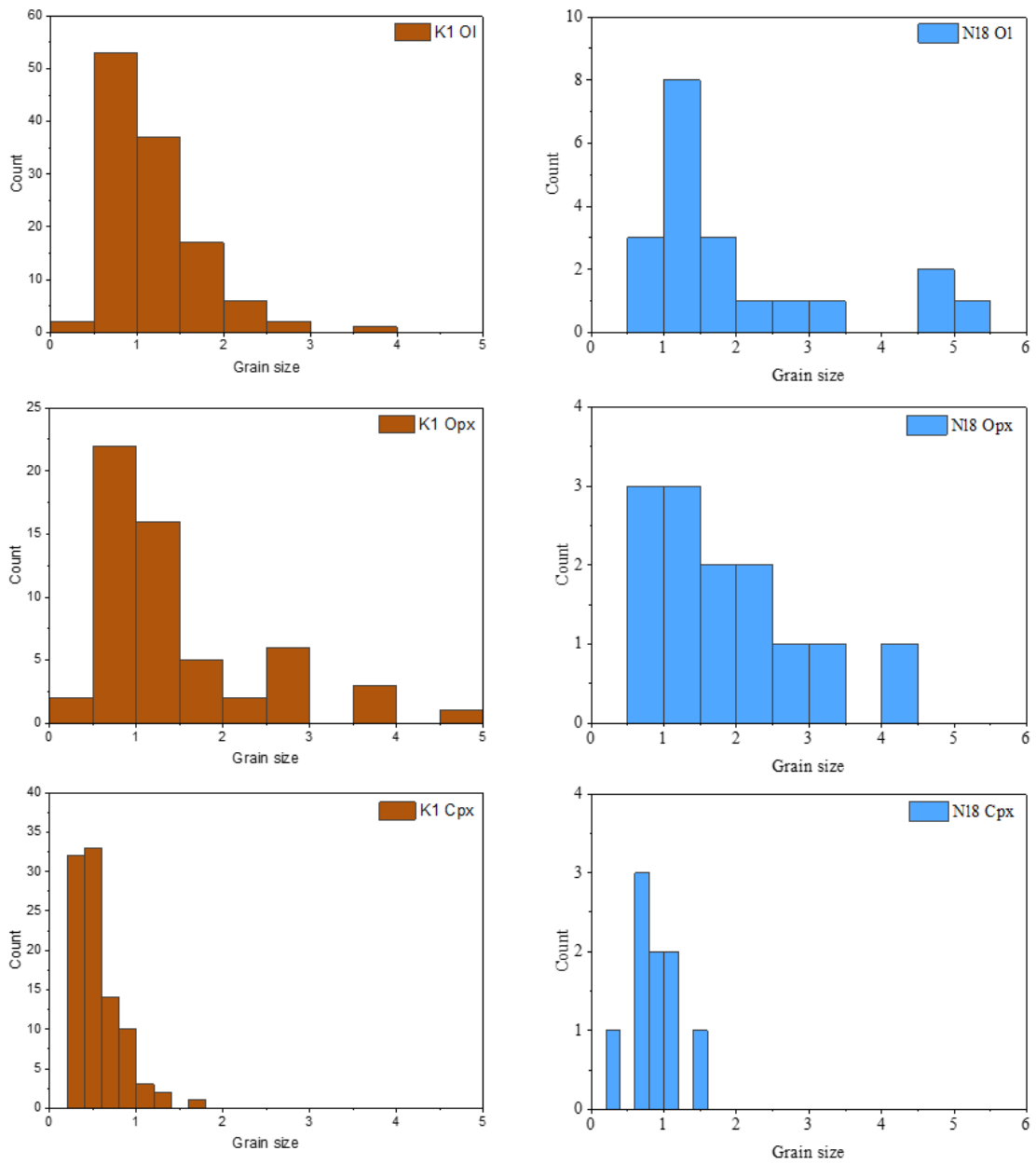


Figure 3.9 cont'd: Representative grain size distribution histograms of mantle xenolith minerals of the Cameroon Volcanic Line.

III.2.2. MINERAL CHEMISTRY

Homogeneous samples are reported as averages in Tables 3.3-3.6 for olivine, orthopyroxene, clinopyroxene, spinel and amphibole. The full data set for heterogeneous samples (N11, N11a), secondary clinopyroxene (En2a) and spongy rims (We1a, K1) are reported in appendix 3.1.

III.2.2.1. MAJOR ELEMENTS

III.2.2.1.1. Olivine

Olivines are homogeneous in all samples with no considerable core-rim or intergrain variations. MnO and NiO values range from 0.11-0.18 wt % and 0.34-0.48 wt % respectively (Table 3.3). Two olivine groups can be distinguished based on the Mg# ($Mg/(Mg+Fe)$) (Fig. 3.10a); samples from Etome (E1a, E8), Enep (En2a) and Nyos (Ny1, Ny3) have higher Mg#s (0.908-0.917) than those from Ngaoundere Likok (N11, N11a, N18), Kuk (K1, K1a, K5), Oku (Ok1, Ok1a), Enep (En1a) and Wum (We1a, Ww1a) which represent the lower Mg# group (0.896- 0.906). Samples from Enep fall in both the high and low Mg# group, which is an evidence for small-scale heterogeneity in the area. CaO contents are less than 0.2 wt% (0.04-0.13 wt %) in all samples while Al₂O₃ and Cr₂O₃ contents are lower than 0.11 wt %.

Major element profiles obtained from olivine in direct contact with the host basalt show that concentrations of Fe, Ca and Mn systematically increase towards the rims, while the Mg# decreases (Fig. 3.11).

III.2.2.1.2. Orthopyroxene

Orthopyroxenes are unzoned with enstatitic composition (En_{87.2-90.1}Fs_{8.0-10.5}Wo_{0.07-3.0}), Mg# of 0.896-0.921 and generally very low TiO₂ contents (<0.16 wt %). Cr₂O₃ (0.22-0.57 wt %) (Fig. 3.10b) and CaO (0.34-0.98 wt %) contents are lower than in the Oku samples which show higher contents (Cr₂O₃: 0.84-0.96 wt %; CaO: 1.35-1.55 wt %). Al₂O₃ contents are higher (3.32-5.29 wt %) compared to sample En2a which shows lower contents (2.20-2.74 wt %) (Fig. 3.10c). Mg# of orthopyroxenes are higher than that of olivine, however, there is a good correlation between the Mg#s of the two mineral phases (Fig. 3.10d).

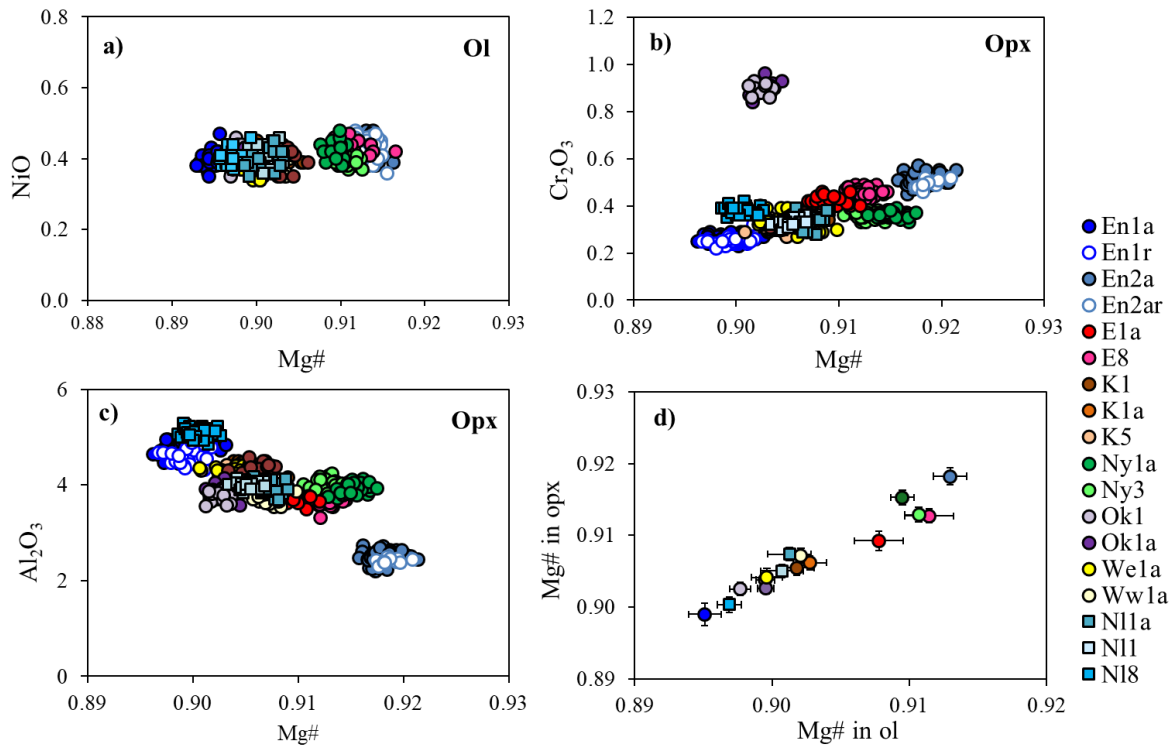


Figure 3.10: Major element compositions of olivine and orthopyroxene. (a) NiO vs Mg# showing two distinct groups. (b) Mg# vs Cr₂O₃ in orthopyroxene. (c) Mg# vs Al₂O₃ in orthopyroxene. (d) Relationship between the average Mg# in olivine and orthopyroxene showing a positive correlation.

III.2.2.1.3. Clinopyroxene

Clinopyroxenes from the CVL xenoliths show a wide range of compositions (En_{44.6-52.4}Fs_{3.76.5}Wo_{41.5-49.9}). They straddle the diopside-augite boundary in the clinopyroxene classification diagram of Morimoto et al., 1988 (not shown), but they show no major core-rim differences. The Al₂O₃ concentrations range from 2.94-7.93 wt % and they are generally negatively correlated with Mg#. Plots of Al₂O₃ vs Mg# (Fig. 3.12a) show four different clinopyroxene clusters. Samples En1, We1a, N18, K1a, K5, K1 (cluster 1) show low Mg# (0.888-0.914) but the highest Al₂O₃ contents (6.25-7.93 wt %), samples Ny1a, Ny3 and Ww1a (cluster 2) show higher Mg# (0.912-0.925) and lower Al₂O₃ (5.40-6.49 wt %) than cluster 1. Samples Ok1 and Ok1a (cluster 3) have identical Mg# (0.891-0.916) to cluster 1 samples but lower Al₂O₃ (4.32-4.93 wt %), samples E1a, En2a and E8 (cluster 4) have the higher Mg# (0.917-0.932) than cluster 3 samples and identical Al₂O₃ (4.15-4.80 wt %).

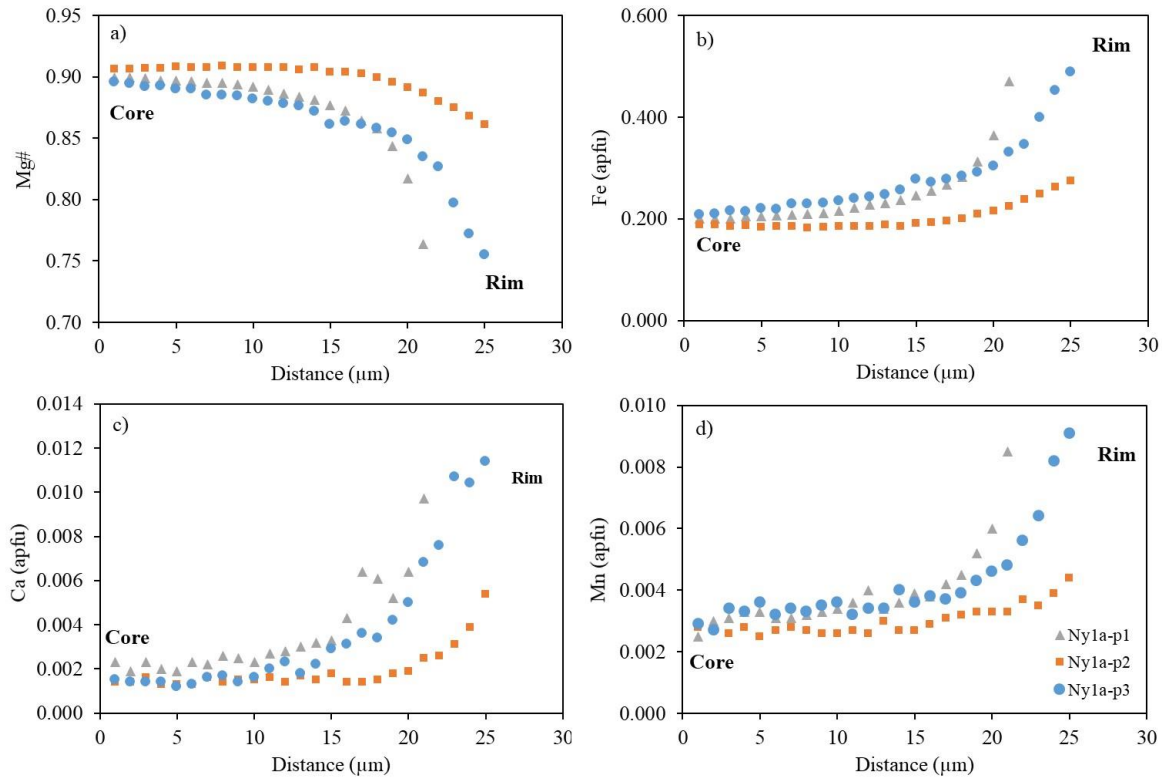


Figure 3.11: Core-rim major elements profiles for olivine in contact with the host basalt showing a systematic increase in composition for Ca, Fe and Mn and a decrease in Mg#.

Secondary clinopyroxenes in sample En2a which are distinguishable by their smaller sizes occur along disturbed layers and show a wide range of compositions (Mg#: 0.907-0.933, Al_2O_3 : 4.41-9.63, Cr_2O_3 : 1.35-4.10, TiO_2 : 0-0.28, Na_2O : 0.47-1.83, CaO: 20.41-24.05) and are more enriched in Al_2O_3 and Cr_2O_3 (Fig. 3.13a, b, c; Appendix 3.2a), but lower in Na_2O contents relatively to the primary ones. Samples N11 and N11a also show two clinopyroxene populations distinguished by their Al_2O_3 contents, (Fig. 3.13a, b; Appendix 3.2a). No major core-rim differences were observed. Na_2O contents vary between 0.43-2.57 wt % and show a positive correlation with Al_2O_3 (Fig. 3.12b) except samples En2a and N11a (N11a-2 subgroup) which fall out of the trend.

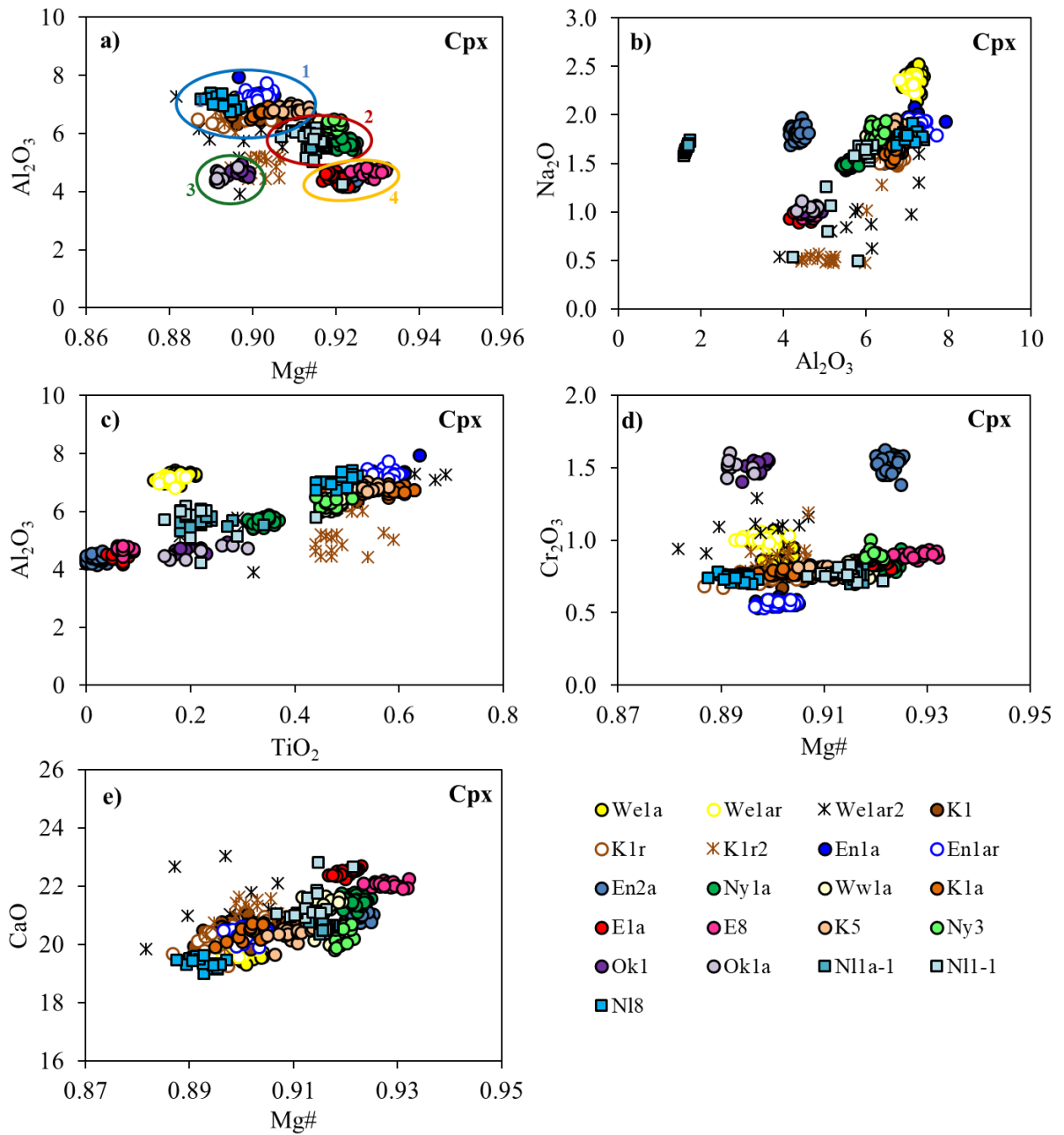


Figure 3.12: Major element variation trends in clinopyroxene from the CVL xenoliths showing core, rim and spongy rim compositions (eg. We1a: core; We1ar: rim; We1ar2: spongy rim).

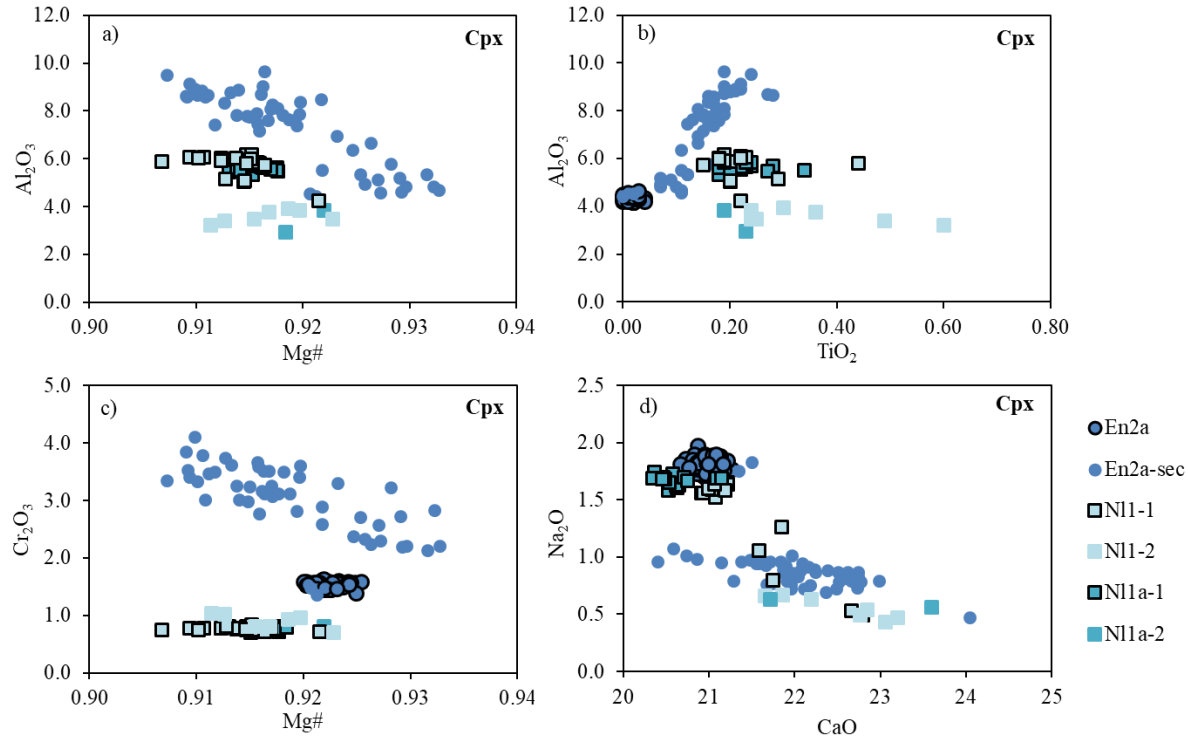


Figure 3.13: Major element plots of primary vs secondary clinopyroxenes in CVL xenoliths

Sample We1a shows the highest Na_2O contents (2.34-2.57 wt %) while the low Al_2O_3 clinopyroxene of samples N11 and N11a together with the Oku and Etome samples show the lowest contents (0.43-1.74 wt%). TiO_2 contents vary between 0.00-0.64 wt % and show a positive correlation with Al_2O_3 (Fig. 3.12c) except for the We1a sample which has low TiO_2 (0.13-0.31 wt %) contents despite the very high Al_2O_3 contents (6.89-7.40 wt %) and subgroups 1 of samples N11 and N11a (Appendix 3.2b).

All samples show a slight positive correlation of Cr_2O_3 with Mg# (Fig. 3.12d) except for sample En1a, which shows lower contents and samples Ok1, Ok1a and En2a which are significantly higher. Secondary clinopyroxenes of sample En2a show the highest concentrations and a negative correlation with Mg# (Fig. 3.13c). A wide range of CaO contents is observed (19.01-24.04 wt %), which shows a positive correlation with Mg# (Fig. 3.12e). The highest contents are observed in samples E1 and E8 while the lowest in samples Ok1, Ok1a and N18. Plots of Na_2O vs CaO show that the secondary clinopyroxenes have lower Na_2O contents and higher CaO when compared to the primary ones (Fig. 3.13d).

Generally, the spongy rims of the clinopyroxenes (Fig. 3.12) of samples K1 and We1a show higher TiO₂ and Cr₂O₃ and lower Na₂O contents than the core compositions. CaO contents are higher in the spongy rim for sample We1a while Al₂O₃ and Mg# show a wide range from lower to higher contents. For K1 samples, the CaO contents and Mg# are similar in both the core and spongy rims while the Al₂O₃ contents show variable contents.

III.2.2.1.4. Spinel

Spinel shows a huge compositional range in the different samples. The Cr# (Cr/(Cr+Al)) in spinel varies in the different samples with the highest (0.37-0.42) in samples En2a, Ok1a and Ok1 while the lowest values (0.11-0.20) are in samples E8, N3, K1a, K1 and We1a (Fig. 3.14a). Mantle spinel normally contains less than 0.2 wt % of TiO₂. From the plot of TiO₂ vs Mg# (Fig. 3.14b), three groups with distinct composition are identified; one with low TiO₂ and low Mg# (En1a, En2a), another group with higher and more variable TiO₂ and corresponding higher Mg# (E1a, E8, K1, K1a, K5, Ny3, Ww1a, We1a, N11) and the third with high TiO₂ and low Mg# (Ok1, Ok1a, N11a). TiO₂ shows a positive correlation with Mg# (Mg/(Mg+Fe²⁺)) except for samples N11a, Ok1 and Ok1a which fall out of the trend (Fig. 3.14b).

Also, based on Mg# and Cr#, three different spinel groups can be chemically distinguished (Fig. 3.14a); group 1 is characterized by Al₂O₃ = 32-37 wt %, Cr₂O₃ = 31-35 wt %, Cr# = 0.37-0.42 and Mg# = 0.66-0.70 (Ok1, Ok1a, En2a); group 2 has Al₂O₃ = 51-52 wt %, Cr₂O₃ = 18-19 wt %, Cr# = 0.19-0.20 and Mg# = 0.74-0.75 and group 3 is typified by Al₂O₃ = 55-57 wt %, Cr₂O₃ = 10-13 wt %, Cr# = 0.11-0.14 and Mg# = 0.74-0.80 (Table 3.6). The MnO and NiO contents differ from one group to another, they vary between 0.28-0.41 wt %; 0.17-0.38 wt % (group 1), 0.19-0.23 wt %; 0.13-0.27 wt % (group 2) and 0.13-0.27 wt %; 0.27-0.46 wt % (group 3) respectively.

III.2.2.1.5. Amphibole

Pargasitic amphibole (according to the classification of Leake et al., 1997) is present in all Wum samples. They are magnesian, showing different composition with Mg# of 0.87-0.88 and 0.89-0.90 for We1a and Ww1a respectively and Al₂O₃ contents, which range from 14.74-15.93 wt %. TiO₂ and Na₂O (Fig. 3.15a) contents range from 1.00-2.00 and 3.37-4.21

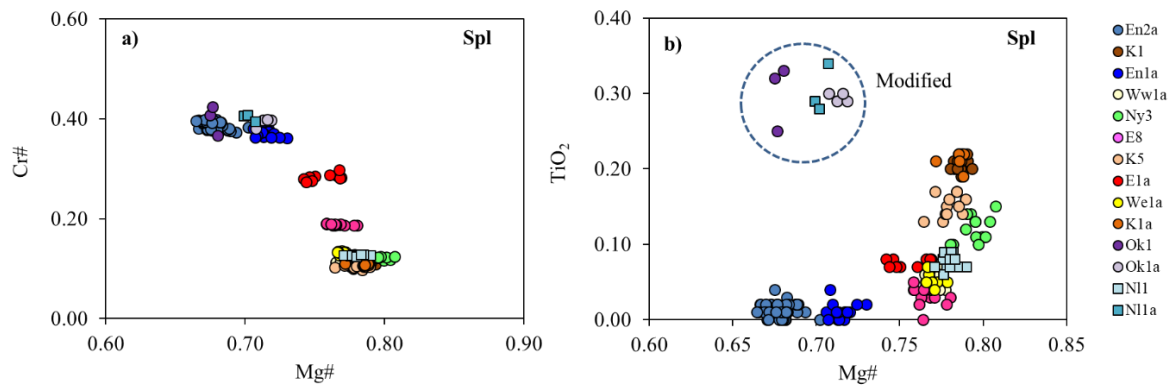


Figure 3.14: Major element variation plots of CVL spinel. (b) TiO₂ vs Mg#

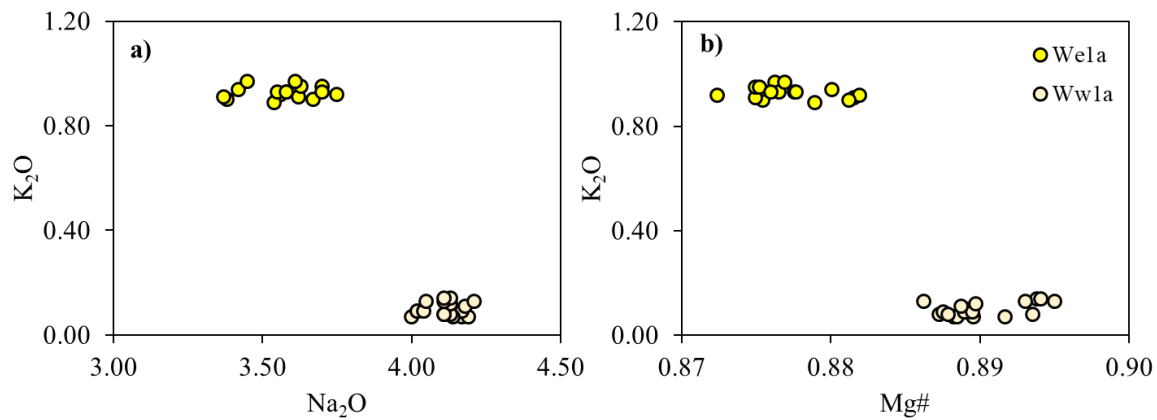


Figure 3.15: Major element compositions of CVL amphibole

wt % with Ww1a samples showing the highest values. Although K₂O contents are low, We1a (0.89-0.97 wt %) shows even lower contents than Ww1a (0.07-0.14 wt %) (Fig. 3.15a, b). Wum amphiboles are calcic ($Ca > Na + K > 1.08$; $Ca/Na > 1$) with high FeO_t contents (3.53-4.28 wt %) and low Cr₂O₃ contents (1.05-1.38 wt %).

Table 3.3: Average major element composition of olivine

OL	Ngaoundere Likok						Enep						Etome			
	NI1 (45)	Std	NI1a (18)	Std	NI8 (23)	Std	En1a (42)	Std	En2a (46)	Std	En2ar (29)	Std	E1a (8)	Std	E8 (20)	Std
SiO₂	40.8	0.34	40.9	0.18	40.7	0.20	40.8	0.19	41.3	0.19	41.2	0.20	41.2	0.17	41.2	0.17
TiO₂	0.00	0.01	-	0.01	-	0.01	0.01	0.01	0.01	0.01	-	0.01	0.00	0.01	-	0.01
Al₂O₃	0.01	0.01	0.02	0.03	0.03	0.03	0.02	0.02	0.01	0.02	0.01	0.02	0.02	0.01	0.02	0.01
Cr₂O₃	0.01	0.01	0.01	0.01	0.01	0.01	0.01	0.01	0.01	0.01	0.01	0.01	0.01	0.01	0.01	0.01
FeO	9.71	0.13	9.63	0.09	10.1	0.09	10.3	0.12	8.52	0.12	8.45	0.11	8.64	0.20	8.64	0.20
MnO	0.14	0.01	0.15	0.01	0.15	0.01	0.16	0.01	0.13	0.01	0.13	0.01	0.14	0.01	0.14	0.01
NiO	0.40	0.03	0.40	0.03	0.40	0.02	0.40	0.02	0.42	0.03	0.43	0.03	0.43	0.03	0.43	0.03
MgO	49.4	0.44	49.3	0.54	49.2	0.26	49.1	0.20	50.1	0.43	50.0	0.56	49.9	0.22	50	0.22
CaO	0.06	0.01	0.06	0.02	0.08	0.01	0.07	0.01	0.04	0.01	0.04	0.01	0.05	0.01	0.05	0.01
Na₂O	0.01	0.01	0.02	0.02	0.01	0.01	0.02	0.01	0.01	0.01	0.01	0.01	0.01	0.01	0.01	0.01
Total	101		101		101		101		101		100		100		100	
Si	0.994	0.007	0.997	0.005	0.992	0.005	0.994	0.004	1.001	0.005	1.003	0.006	1.001	0.003	1.001	0.003
Ti	0.000	0.000	-	0.000	-	0.000	0.000	0.000	0.000	0.000	-	0.000	0.000	0.000	-	0.000
Al	0.000	0.000	0.001	0.001	0.001	0.001	0.001	0.001	0.000	0.000	0.000	0.001	0.000	0.000	0.000	0.000
Cr	0.000	0.000	0.000	0.000	0.000	0.000	0.000	0.000	0.000	0.000	0.000	0.000	0.000	0.000	0.000	0.000
Fe²⁺	0.198	0.003	0.196	0.003	0.206	0.002	0.209	0.003	0.173	0.002	0.172	0.002	0.176	0.004	0.176	0.004
Mn	0.003	0.000	0.003	0.000	0.003	0.000	0.003	0.000	0.003	0.000	0.003	0.000	0.003	0.000	0.003	0.000
Ni	0.008	0.001	0.008	0.000	0.008	0.000	0.008	0.000	0.008	0.000	0.008	0.001	0.008	0.001	0.008	0.001
Mg	1.795	0.008	1.792	0.008	1.788	0.005	1.782	0.004	1.813	0.006	1.812	0.008	1.809	0.004	1.809	0.004
Ca	0.001	0.000	0.002	0.001	0.002	0.000	0.002	0.000	0.001	0.000	0.001	0.000	0.001	0.000	0.001	0.000
Na	0.001	0.000	0.001	0.001	0.001	0.001	0.001	0.001	0.001	0.001	0.000	0.001	0.000	0.000	0.000	0.000
Total	3.000		3.000		3.000		3.000		3.000		3.000		3.000		3.000	
Mg#	0.901		0.901		0.897		0.895		0.913		0.913		0.911		0.911	

Table 3.3 cont'd

OL	Kuk						Nyos				Oku				Wum			
	K1 (51)	Std	K1a (29)	Std	K5 (20)	Std	Ny1a (17)	Std	Ny3 (19)	Std	Ok1 (16)	Std	Ok1a (21)	Std	We1a (52)	Std	Ww1a (47)	Std
SiO₂	40.9	0.42	40.8	0.16	40.7	0.23	41.3	0.15	40.7	0.19	40.8	0.14	40.6	0.36	41.1	0.20	40.8	0.32
TiO₂	0.01	0.01	0.01	0.01	0.01	0.01	-	-	0.01	0.01	0.01	0.01	0.01	0.01	-	0.01	-	0.01
Al₂O₃	0.04	0.02	0.04	0.02	0.03	0.02	0.01	0.02	0.02	0.02	0.05	0.03	0.05	0.02	0.02	0.01	0.01	0.01
Cr₂O₃	0.01	0.01	0.02	0.01	0.01	0.01	0.01	0.01	0.01	0.01	0.04	0.01	0.04	0.01	0.01	0.01	0.01	0.01
FeO	9.61	0.13	9.56	0.12	9.86	0.06	8.91	0.07	8.74	0.08	9.78	0.07	9.87	0.07	9.83	0.12	9.56	0.08
MnO	0.15	0.01	0.15	0.01	0.15	0.01	0.14	0.01	0.14	0.01	0.14	0.01	0.15	0.01	0.15	0.01	0.14	0.01
NiO	0.39	0.02	0.40	0.03	0.40	0.02	0.43	0.03	0.40	0.01	0.40	0.02	0.41	0.03	0.39	0.02	0.40	0.02
MgO	49.5	0.32	49.8	0.20	49.5	0.22	50.2	0.30	50.0	0.25	49.2	0.21	48.6	0.35	49.4	0.24	49.4	0.28
CaO	0.11	0.01	0.10	0.01	0.10	0.01	0.05	0.01	0.06	0.01	0.13	0.01	0.13	0.01	0.08	0.02	0.04	0.01
Na₂O	0.01	0.01	0.01	0.01	0.02	0.01	0.02	0.01	0.01	0.01	0.00	0.01	0.02	0.02	0.02	0.01	-	0.01
Total	101		101		101		101		100		100		100		101		100	
Si	0.994	0.008	0.991	0.003	0.990	0.003	0.997	0.004	0.992	0.004	0.995	0.004	0.998	0.008	0.997	0.005	0.996	0.005
Ti	0.000	0.000	0.000	0.000	0.000	0.000	-	-	0.000	0.000	0.000	0.000	0.000	0.000	-	0.000	-	0.000
Al	0.001	0.000	0.001	0.001	0.001	0.001	0.000	0.001	0.001	0.001	0.001	0.001	0.001	0.001	0.001	0.000	0.000	0.000
Cr	0.000	0.000	0.000	0.000	0.000	0.000	0.000	0.000	0.000	0.000	0.001	0.000	0.001	0.000	0.000	0.000	0.000	0.000
Fe²⁺	0.195	0.003	0.194	0.002	0.200	0.001	0.180	0.002	0.178	0.002	0.200	0.001	0.203	0.001	0.200	0.002	0.195	0.002
Mn	0.003	0.000	0.003	0.000	0.003	0.000	0.003	0.000	0.003	0.000	0.003	0.000	0.003	0.000	0.003	0.000	0.003	0.000
Ni	0.008	0.000	0.008	0.000	0.008	0.000	0.008	0.000	0.008	0.000	0.008	0.000	0.008	0.001	0.008	0.000	0.008	0.000
Mg	1.795	0.008	1.800	0.005	1.794	0.004	1.808	0.005	1.816	0.005	1.789	0.004	1.781	0.007	1.789	0.005	1.797	0.005
Ca	0.003	0.000	0.003	0.000	0.002	0.000	0.001	0.000	0.002	0.000	0.003	0.000	0.003	0.000	0.002	0.000	0.001	0.000
Na	0.001	0.000	0.000	0.001	0.001	0.001	0.001	0.001	0.001	0.001	0.000	0.000	0.001	0.001	0.001	0.000	-	0.000
Total	3.000																	
Mg#	0.902		0.903		0.899		0.909		0.911		0.900		0.898		0.900		0.902	

Table 3.4: Average major element composition of orthopyroxene

OPX	Ngaoundere Likok						Enep						Etome					
	NII (20)	Std	NIIa (20)	Std	NI8 (35)	Std	En1a (54)	Std	En1ar (35)	Std	En2a (66)	Std	En2ar (11)	Std	E1a (27)	Std	E8 (39)	Std
SiO ₂	55.3	0.13	55.7	0.18	54.9	0.20	55.0	0.24	55.1	0.23	56.6	0.32	56.9	0.18	55.2	0.38	55.7	0.24
TiO ₂	0.05	0.01	0.06	0.02	0.13	0.01	0.12	0.01	0.12	0.01	0.01	0.01	0.00	0.00	0.02	0.01	0.02	0.01
Al ₂ O ₃	4.00	0.08	3.96	0.14	5.09	0.10	4.72	0.13	4.62	0.14	2.52	0.11	2.41	0.06	3.73	0.09	3.68	0.09
Cr ₂ O ₃	0.33	0.01	0.35	0.03	0.38	0.02	0.26	0.01	0.25	0.02	0.51	0.02	0.50	0.02	0.42	0.02	0.46	0.02
Fe ₂ O ₃	0.10	0.28	0.63	0.45	0.56	0.45	0.21	0.30	0.28	0.31	0.29	0.49	0.20	0.25	0.36	0.56	1.02	0.53
FeO	5.98	0.24	5.51	0.39	5.90	0.39	6.30	0.28	6.19	0.28	5.18	0.46	5.23	0.25	5.56	0.53	4.86	0.46
MnO	0.14	0.01	0.15	0.01	0.15	0.01	0.16	0.01	0.15	0.01	0.15	0.01	0.14	0.01	0.14	0.01	0.14	0.01
NiO	0.10	0.02	0.11	0.02	0.11	0.02	0.10	0.02	0.10	0.02	0.10	0.02	0.11	0.02	0.11	0.02	0.11	0.02
MgO	32.5	0.39	33.4	0.16	32.5	0.22	32.4	0.27	32.5	0.26	34.3	0.21	34.4	0.24	33.0	0.32	33.9	0.19
CaO	0.68	0.02	0.67	0.02	0.87	0.02	0.63	0.03	0.68	0.05	0.56	0.02	0.54	0.02	0.67	0.02	0.65	0.01
Na ₂ O	0.10	0.01	0.10	0.02	0.14	0.03	0.11	0.02	0.13	0.02	0.08	0.02	0.07	0.02	0.05	0.01	0.05	0.02
K ₂ O	-	-	0.01	0.01	-	-	0.01	0.01	0.01	0.01	-	-	0.01	0.01	-	-	-	-
Total	99		101		101		100		100		100		100		99		101	
Si	1.925	0.009	1.910	0.008	1.887	0.006	1.902	0.009	1.903	0.009	1.943	0.008	1.948	0.008	1.918	0.010	1.908	0.008
Ti	0.001	0.000	0.001	0.000	0.003	0.000	0.003	0.000	0.003	0.000	0.000	0.000	0.000	0.000	0.000	0.000	0.001	0.000
Al	0.164	0.004	0.160	0.005	0.206	0.004	0.192	0.005	0.188	0.005	0.102	0.004	0.097	0.002	0.153	0.004	0.148	0.004
Cr	0.009	0.000	0.009	0.001	0.010	0.000	0.007	0.000	0.007	0.000	0.014	0.001	0.013	0.000	0.012	0.000	0.012	0.000
Fe ³⁺	0.003	0.007	0.016	0.012	0.014	0.012	0.005	0.008	0.007	0.008	0.007	0.013	0.005	0.006	0.009	0.015	0.026	0.014
Fe ²⁺	0.174	0.008	0.158	0.011	0.169	0.011	0.182	0.008	0.179	0.009	0.149	0.013	0.150	0.008	0.161	0.015	0.139	0.013
Mn	0.004	0.000	0.004	0.000	0.004	0.000	0.005	0.000	0.005	0.000	0.004	0.000	0.004	0.000	0.004	0.000	0.004	0.000
Ni	0.003	0.000	0.003	0.001	0.003	0.001	0.003	0.001	0.003	0.000	0.003	0.000	0.003	0.001	0.003	0.001	0.003	0.001
Mg	1.685	0.011	1.707	0.005	1.661	0.007	1.669	0.007	1.671	0.007	1.752	0.008	1.754	0.007	1.710	0.013	1.731	0.007
Ca	0.025	0.001	0.025	0.001	0.032	0.001	0.023	0.001	0.025	0.002	0.021	0.001	0.020	0.001	0.025	0.001	0.024	0.000
Na	0.007	0.001	0.006	0.001	0.009	0.002	0.008	0.002	0.009	0.002	0.006	0.001	0.005	0.001	0.004	0.001	0.003	0.001
K	-	-	0.000	0.000	-	-	0.000	0.000	0.000	0.000	-	-	0.000	0.000	-	-	-	-
Total	4.000		4.000		4.000		4.000		4.000		4.000		4.000		4.000		4.000	
Mg#	0.905		0.907		0.900		0.899		0.900		0.918		0.919		0.909		0.913	
Cr#	0.052		0.055		0.048		0.036		0.035		0.120		0.121		0.071		0.077	
Wo	0.013	0.000	0.013	0.000	0.017	0.000	0.012	0.001	0.013	0.001	0.011	0.000	0.010	0.000	0.013	0.000	0.012	0.000
En	0.891	0.001	0.894	0.001	0.883	0.001	0.886	0.002	0.886	0.002	0.906	0.001	0.907	0.001	0.895	0.001	0.899	0.001
Fs	0.096	0.001	0.094	0.001	0.100	0.001	0.102	0.002	0.101	0.001	0.083	0.001	0.082	0.001	0.092	0.001	0.088	0.001

Table 3.4 cont'd

OPX	Kuk						Nyos				Oku				Wum			
	K1 (39)	Std	K1a (28)	Std	K5 (35)	Std	Ny1 (34)	Std	N3 (37)	Std	Ok1 (16)	Std	Ok1a (18)	Std	We1a (34)	Std	Ww1a (21)	Std
SiO ₂	54.7	0.28	55.5	0.30	55.0	0.71	56.0	0.21	55.1	0.28	55.2	0.25	54.9	0.18	55.6	0.49	55.4	0.61
TiO ₂	0.11	0.01	0.13	0.01	0.12	0.01	0.07	0.01	0.10	0.01	0.09	0.01	0.10	0.02	0.04	0.01	0.09	0.01
Al ₂ O ₃	4.33	0.09	4.35	0.08	4.23	0.08	3.92	0.11	4.03	0.10	3.72	0.11	3.81	0.14	4.28	0.08	3.75	0.11
Cr ₂ O ₃	0.33	0.02	0.35	0.01	0.32	0.02	0.36	0.01	0.36	0.01	0.90	0.02	0.90	0.03	0.34	0.02	0.30	0.01
Fe ₂ O ₃	0.90	0.64	0.68	0.48	1.03	0.69	0.25	0.33	1.09	0.59	0.29	0.44	0.86	0.45	0.59	0.58	0.67	0.67
FeO	5.30	0.57	5.53	0.44	5.34	0.66	5.34	0.26	4.73	0.52	5.94	0.39	5.44	0.42	5.73	0.52	5.49	0.56
MnO	0.15	0.01	0.15	0.01	0.15	0.01	0.15	0.01	0.14	0.01	0.15	0.01	0.15	0.01	0.15	0.01	0.15	0.01
NiO	0.11	0.02	0.11	0.02	0.10	0.02	0.10	0.02	0.10	0.02	0.12	0.02	0.11	0.01	0.10	0.02	0.09	0.02
MgO	32.8	0.22	33.3	0.20	33.1	0.21	33.7	0.22	33.6	0.20	32.3	0.24	32.3	0.20	33.1	0.18	33.4	0.13
CaO	0.67	0.10	0.63	0.09	0.61	0.07	0.57	0.02	0.57	0.03	1.44	0.05	1.48	0.04	0.58	0.06	0.42	0.08
Na ₂ O	0.13	0.02	0.11	0.02	0.11	0.02	0.08	0.01	0.10	0.02	0.07	0.01	0.13	0.02	0.15	0.02	0.07	0.01
K ₂ O	-	-	-	-	-	-	0.01	0.01	-	-	-	-	0.01	0.00	-	-	-	-
Total	100		101		100		101		100		100		100		101		100	
Si	1.897	0.008	1.900	0.007	1.897	0.010	1.917	0.007	1.900	0.009	1.912	0.009	1.901	0.006	1.906	0.008	1.913	0.013
Ti	0.003	0.000	0.003	0.000	0.003	0.000	0.002	0.000	0.003	0.000	0.002	0.000	0.003	0.000	0.001	0.000	0.002	0.000
Al	0.177	0.003	0.176	0.003	0.172	0.003	0.158	0.004	0.164	0.004	0.152	0.004	0.156	0.006	0.173	0.003	0.153	0.005
Cr	0.009	0.000	0.009	0.000	0.009	0.000	0.010	0.000	0.010	0.000	0.024	0.001	0.025	0.001	0.009	0.001	0.008	0.000
Fe ³⁺	0.023	0.017	0.017	0.012	0.027	0.018	0.006	0.008	0.028	0.015	0.007	0.012	0.022	0.012	0.015	0.015	0.018	0.018
Fe ²⁺	0.154	0.017	0.158	0.013	0.154	0.018	0.153	0.007	0.136	0.015	0.172	0.012	0.157	0.012	0.164	0.015	0.159	0.016
Mn	0.004	0.000	0.004	0.000	0.004	0.000	0.004	0.000	0.004	0.000	0.004	0.000	0.004	0.000	0.004	0.000	0.004	0.000
Ni	0.003	0.001	0.003	0.000	0.003	0.001	0.003	0.001	0.003	0.001	0.003	0.000	0.003	0.000	0.003	0.001	0.002	0.000
Mg	1.696	0.010	1.698	0.008	1.701	0.010	1.720	0.007	1.724	0.006	1.664	0.009	1.666	0.008	1.693	0.008	1.721	0.009
Ca	0.025	0.004	0.023	0.003	0.023	0.002	0.021	0.001	0.021	0.001	0.054	0.002	0.055	0.002	0.021	0.002	0.015	0.003
Na	0.009	0.001	0.008	0.001	0.007	0.001	0.006	0.001	0.007	0.001	0.005	0.001	0.008	0.001	0.010	0.001	0.005	0.001
K	-	-	-	-	-	-	0.001	0.000	-	-	-	-	0.000	0.000	-	-	-	-
Total	4.000																	
Mg#	0.905		0.906		0.904		0.915		0.913		0.903		0.903		0.904		0.907	
Cr#	0.048		0.051		0.048		0.059		0.056		0.139		0.136		0.050		0.051	
Wo	0.013	0.002	0.012	0.002	0.012	0.001	0.011	0.000	0.011	0.001	0.028	0.001	0.029	0.001	0.011	0.001	0.008	0.001
En	0.892	0.002	0.893	0.002	0.891	0.002	0.903	0.001	0.901	0.001	0.875	0.001	0.875	0.001	0.892	0.002	0.898	0.001
Fs	0.095	0.001	0.095	0.001	0.097	0.001	0.086	0.001	0.088	0.001	0.097	0.001	0.097	0.001	0.097	0.001	0.094	0.001

Table 3.5: Average major element composition of clinopyroxene

CPX	Ene _p				Eto _m e						Kuk							
	En1a		En2a		E1a (21)		E8 (20)		K1 (25)		K1a (25)		K5 (19)					
	Core (34)	Std	Rim (22)	Std	Core (55)	Std	Core	Std	Core	std	Core (25)	std	Rim (19)	std	core	Std	core	Std
SiO₂	52.2	0.31	52.1	0.28	53.8	0.30	52.2	0.35	53.2	0.21	51.3	0.36	51.3	0.30	51.5	0.50	52.3	0.21
TiO₂	0.57	0.02	0.57	0.02	0.02	0.01	0.06	0.01	0.07	0.01	0.50	0.02	0.50	0.02	0.59	0.02	0.55	0.02
Al₂O₃	7.26	0.15	7.29	0.14	4.35	0.10	4.47	0.13	4.69	0.10	6.63	0.19	6.63	0.20	6.76	0.11	6.80	0.10
Cr₂O₃	0.57	0.02	0.56	0.02	1.53	0.05	0.85	0.02	0.90	0.02	0.74	0.02	0.73	0.03	0.78	0.02	0.78	0.03
Fe₂O₃	1.28	0.66	1.34	0.63	0.74	0.50	1.22	0.67	0.33	0.31	1.70	0.76	1.70	0.59	2.10	0.85	0.78	0.45
FeO	1.68	0.59	1.65	0.54	1.62	0.45	1.32	0.62	1.93	0.29	1.38	0.58	1.50	0.49	0.95	0.80	1.92	0.40
MnO	0.10	0.01	0.10	0.01	0.09	0.01	0.09	0.01	0.09	0.01	0.09	0.01	0.09	0.01	0.09	0.01	0.10	0.01
NiO	0.05	0.02	0.04	0.02	0.04	0.02	0.04	0.02	0.04	0.02	0.06	0.02	0.06	0.02	0.06	0.02	0.04	0.02
MgO	14.6	0.19	14.7	0.23	15.3	0.18	15.6	0.10	16.2	0.20	14.8	0.27	15.0	0.37	15.2	0.20	14.8	0.21
CaO	20.4	0.11	20.4	0.20	21.0	0.12	22.5	0.11	22.0	0.09	20.6	0.29	20.3	0.47	20.5	0.25	20.3	0.21
Na₂O	1.91	0.05	1.89	0.05	1.82	0.05	0.95	0.02	0.97	0.03	1.64	0.10	1.59	0.10	1.68	0.09	1.86	0.05
K₂O	0.01	0.01	0.01	0.01	0.01	0.01	-	-	-	0.01	-	-	-	-	0.01	-	-	0.01
Total	101		101		100		99		100		99		99		100		100	
Si	1.873	0.008	1.870	0.006	1.939	0.007	1.907	0.007	1.916	0.005	1.868	0.010	1.866	0.008	1.859	0.013	1.884	0.006
Ti	0.015	0.001	0.016	0.000	0.001	0.000	0.002	0.000	0.002	0.000	0.014	0.001	0.014	0.000	0.016	0.001	0.015	0.000
Al	0.307	0.006	0.308	0.006	0.185	0.004	0.192	0.005	0.199	0.004	0.284	0.008	0.284	0.009	0.287	0.004	0.289	0.004
Cr	0.016	0.001	0.016	0.000	0.044	0.001	0.025	0.000	0.026	0.000	0.021	0.001	0.021	0.001	0.022	0.000	0.022	0.001
Fe³⁺	0.035	0.018	0.036	0.017	0.020	0.013	0.033	0.018	0.009	0.008	0.047	0.021	0.047	0.016	0.057	0.023	0.021	0.012
Fe²⁺	0.050	0.018	0.050	0.016	0.049	0.014	0.040	0.019	0.058	0.009	0.042	0.018	0.046	0.015	0.029	0.024	0.058	0.012
Mn	0.003	0.000	0.003	0.000	0.003	0.000	0.003	0.000	0.003	0.000	0.003	0.000	0.003	0.000	0.003	0.000	0.003	0.000
Ni	0.001	0.001	0.001	0.000	0.001	0.001	0.001	0.000	0.001	0.001	0.002	0.001	0.002	0.000	0.002	0.001	0.001	0.001
Mg	0.780	0.009	0.785	0.011	0.821	0.008	0.851	0.006	0.868	0.008	0.801	0.015	0.812	0.020	0.815	0.010	0.793	0.010
Ca	0.786	0.005	0.784	0.007	0.810	0.005	0.879	0.006	0.851	0.005	0.803	0.011	0.793	0.018	0.793	0.011	0.784	0.009
Na	0.133	0.004	0.131	0.003	0.127	0.003	0.067	0.002	0.068	0.002	0.116	0.007	0.112	0.007	0.117	0.006	0.130	0.004
K	0.000	0.000	0.000	0.000	0.000	0.000	-	-	-	0.000	-	-	-	-	0.000	-	-	0.000
Total	4.000		4.000		4.000		4.000		4.000		4.000		4.000		4.000		4.000	
Mg#	0.902		0.901		0.922		0.920		0.928		0.901		0.898		0.905		0.910	
Cr#	0.050		0.049		0.191		0.113		0.114		0.070		0.069		0.072		0.072	
Wo	0.475	0.004	0.473	0.005	0.476	0.003	0.487	0.002	0.476	0.003	0.474	0.009	0.466	0.013	0.467	0.006	0.473	0.006
En	0.472	0.004	0.473	0.005	0.482	0.003	0.471	0.001	0.485	0.004	0.472	0.006	0.478	0.009	0.481	0.004	0.478	0.005
Fs	0.053	0.001	0.054	0.001	0.042	0.001	0.042	0.001	0.039	0.001	0.054	0.004	0.056	0.004	0.052	0.003	0.049	0.002

Table 3.5 cont'd

CPX	Nyos				Oku				Wum							
	Ny1a (34)		Ny3 (14)		Ok1 (11)		Ok1a (9)		Core (46)		We1a (46)		SR (11)		Ww1a (30)	
	core	Std	Rim (23)	std	SR (11)	Std	Core	Std								
SiO ₂	52.6	0.39	52.5	0.18	52.3	0.20	52.5	0.10	53.2	0.26	53.1	0.37	51.6	0.72	52.8	0.24
TiO ₂	0.34	0.01	0.47	0.02	0.20	0.03	0.21	0.06	0.17	0.02	0.16	0.01	0.49	0.27	0.47	0.01
Al ₂ O ₃	5.64	0.13	6.28	0.14	4.68	0.12	4.55	0.20	7.20	0.11	7.09	0.10	6.01	1.05	6.18	0.12
Cr ₂ O ₃	0.83	0.04	0.90	0.04	1.50	0.05	1.51	0.05	0.96	0.06	1.00	0.03	1.08	0.11	0.78	0.04
Fe ₂ O ₃	1.15	0.68	0.46	0.37	0.82	0.38	0.22	0.45	0.59	0.48	0.78	0.55	0.70	0.54	0.30	0.39
FeO	1.27	0.60	1.91	0.33	2.75	0.33	3.30	0.38	2.26	0.44	2.17	0.49	2.55	0.66	2.10	0.32
MnO	0.08	0.01	0.08	0.01	0.10	0.01	0.12	0.02	0.10	0.01	0.09	0.01	0.09	0.01	0.09	0.01
NiO	0.05	0.02	0.04	0.02	0.06	0.02	0.06	0.02	0.04	0.02	0.06	0.02	0.06	0.02	0.04	0.02
MgO	15.3	0.21	14.9	0.14	17.0	0.20	16.3	0.49	14.2	0.13	14.2	0.16	15.4	0.55	14.5	0.15
CaO	21.5	0.16	20.3	0.29	19.3	0.12	19.2	0.15	19.6	0.13	19.6	0.09	21.4	1.00	21.2	0.51
Na ₂ O	1.50	0.04	1.84	0.07	1.00	0.01	1.04	0.03	2.33	0.15	2.34	0.05	0.96	0.31	1.71	0.04
K ₂ O	0.01	0.01	-	-	0.01	0.01	0.02	0.01	-	-	-	-	0.01	0.01	-	-
Total	100		100		100		99		101		101		100		100	
Si	1.896	0.010	1.900	0.008	1.897	0.005	1.922	0.019	1.906	0.008	1.903	0.008	1.867	0.023	1.905	0.012
Ti	0.009	0.000	0.013	0.000	0.006	0.001	0.006	0.002	0.005	0.000	0.004	0.000	0.013	0.007	0.013	0.000
Al	0.239	0.006	0.268	0.005	0.200	0.005	0.196	0.007	0.304	0.005	0.299	0.004	0.256	0.045	0.263	0.005
Cr	0.024	0.001	0.026	0.001	0.043	0.001	0.044	0.002	0.027	0.002	0.028	0.001	0.031	0.003	0.022	0.001
Fe ³⁺	0.031	0.018	0.012	0.010	0.022	0.010	0.006	0.012	0.016	0.013	0.021	0.015	0.019	0.015	0.008	0.010
Fe ²⁺	0.038	0.018	0.058	0.010	0.083	0.010	0.101	0.012	0.068	0.013	0.065	0.015	0.077	0.020	0.063	0.010
Mn	0.003	0.000	0.003	0.000	0.003	0.000	0.004	0.001	0.003	0.000	0.003	0.000	0.003	0.000	0.003	0.000
Ni	0.001	0.001	0.001	0.001	0.002	0.000	0.002	0.000	0.001	0.001	0.002	0.000	0.002	0.001	0.001	0.000
Mg	0.822	0.009	0.803	0.006	0.921	0.009	0.891	0.019	0.756	0.007	0.758	0.008	0.834	0.030	0.782	0.006
Ca	0.831	0.008	0.787	0.007	0.752	0.005	0.754	0.008	0.753	0.005	0.754	0.004	0.830	0.040	0.821	0.016
Na	0.105	0.003	0.129	0.005	0.071	0.001	0.074	0.002	0.162	0.010	0.163	0.003	0.067	0.022	0.120	0.003
K	0.001	0.000	-	-	0.000	0.000	0.001	0.000	-	-	-	-	0.000	0.000	-	-
Total	4.000															
Mg#	0.922		0.919		0.897		0.893		0.901		0.898		0.897		0.916	
Cr#	0.090		0.088		0.177		0.182		0.082		0.087		0.108		0.078	
Wo	0.482	0.004	0.473	0.004	0.422	0.004	0.429	0.007	0.472	0.003	0.471	0.003	0.471	0.013	0.490	0.006
En	0.477	0.004	0.483	0.003	0.517	0.003	0.508	0.007	0.474	0.003	0.474	0.003	0.473	0.012	0.466	0.006
Fs	0.042	0.001	0.044	0.001	0.061	0.001	0.063	0.001	0.054	0.001	0.056	0.001	0.056	0.005	0.044	0.001

Table 3.6: Average major element composition of spinel

SPL	Ngaoundere Likok				Enep				Etome			
	N11 (15)	std	N11a (3)	std	En1 (15)	std	En2 (47)	std	E1 (10)	std	E8 (14)	std
SiO₂	0.01	0.01	0.01	0.01	-	-	0.01	0.02	0.01	0.01	-	-
TiO₂	0.08	0.01	0.30	0.03	0.01	0.01	0.01	0.01	0.07	0.01	0.03	0.01
Al₂O₃	57.0	0.20	33.4	0.45	36.6	0.67	36.0	0.57	43.9	0.60	51.8	0.47
Cr₂O₃	12.3	0.08	33.6	0.57	32.1	0.46	33.6	0.66	25.9	0.51	17.9	0.27
Fe₂O₃	0.30	0.21	4.20	0.25	2.44	0.23	0.55	0.29	0.82	0.47	0.80	0.51
FeO	10.0	0.21	12.2	0.15	11.8	0.28	13.2	0.28	10.5	0.45	10.5	0.35
MnO	0.21	0.01	0.46	0.02	0.45	0.03	0.35	0.03	0.34	0.02	0.25	0.03
NiO	0.38	0.02	0.25	0.04	0.21	0.03	0.22	0.03	0.27	0.03	0.34	0.03
MgO	20.0	0.16	16.2	0.18	16.6	0.20	15.6	0.24	18.3	0.34	19.3	0.12
CaO	0.01	0.00	-	-	-	-	-	-	0.01	0.01	-	-
Na₂O	0.02	0.01	0.01	0.01	0.01	0.01	0.01	0.01	0.01	0.01	0.01	0.01
Total	100		101		100		100		100		101	
Si	0.000	0.000	0.000	0.000	-	-	0.000	0.000	0.000	0.000	-	-
Ti	0.001	0.000	0.007	0.001	0.000	0.000	0.000	0.000	0.001	0.000	0.001	0.000
Al	1.740	0.004	1.132	0.010	1.226	0.016	1.222	0.017	1.420	0.018	1.610	0.006
Cr	0.252	0.002	0.764	0.016	0.723	0.013	0.766	0.017	0.561	0.012	0.374	0.004
Fe³⁺	0.006	0.004	0.091	0.005	0.052	0.005	0.012	0.006	0.017	0.010	0.016	0.010
Fe²⁺	0.217	0.005	0.294	0.004	0.280	0.007	0.317	0.008	0.241	0.011	0.231	0.007
Mn	0.005	0.000	0.011	0.000	0.011	0.001	0.009	0.001	0.008	0.001	0.006	0.001
Ni	0.008	0.000	0.006	0.001	0.005	0.001	0.005	0.001	0.006	0.001	0.007	0.001
Mg	0.770	0.005	0.694	0.004	0.702	0.006	0.668	0.008	0.746	0.012	0.756	0.006
Ca	0.000	0.000	-	-	-	-	-	-	0.000	0.000	-	-
Na	0.001	0.000	0.001	0.001	0.001	0.001	0.001	0.001	0.001	0.001	0.000	0.001
Total	3.000		3.000		3.000		3.000		3.000		3.000	
Mg#	0.781	0.005	0.703	0.004	0.715	0.007	0.678	0.008	0.756	0.011	0.766	0.007
Cr#	0.127	0.001	0.403	0.007	0.371	0.007	0.385	0.008	0.283	0.007	0.188	0.001

Table 3.6 cont'd

SPL	Kuk						Nyos		Oku				Wum			
	K1 (18)	std	K1a (5)	std	K5 (12)	std	Ny3 (14)	std	Ok1 (3)	std	Ok1a (4)	std	We1a (8)	std	Ww1a (15)	std
SiO ₂	0.06	0.02	0.06	0.02	0.04	0.01	0.02	0.02	0.08	0.02	0.03	0.01	0.04	0.01	0.02	0.01
TiO ₂	0.21	0.01	0.21	0.01	0.15	0.02	0.12	0.02	0.30	0.04	0.30	0.01	0.06	0.01	0.05	0.01
Al ₂ O ₃	56.7	0.39	57.1	0.19	58.0	0.24	56.7	0.46	34.0	1.99	33.5	0.72	55.6	0.37	58.0	0.18
Cr ₂ O ₃	10.6	0.13	10.3	0.13	9.95	0.24	11.7	0.22	33.6	2.16	32.3	0.44	12.6	0.26	11.1	0.08
Fe ₂ O ₃	1.88	0.32	1.87	0.55	1.44	0.35	0.84	0.45	2.66	0.39	4.68	0.30	1.24	0.21	0.14	0.15
FeO	9.75	0.16	9.90	0.27	10.1	0.30	9.39	0.43	13.3	0.12	11.8	0.25	10.4	0.18	10.4	0.13
MnO	0.18	0.02	0.17	0.02	0.19	0.01	0.19	0.01	0.29	0.03	0.27	0.03	0.21	0.01	0.19	0.01
NiO	0.39	0.02	0.42	0.03	0.42	0.02	0.38	0.03	0.28	0.03	0.26	0.02	0.37	0.02	0.39	0.03
MgO	20.2	0.12	20.1	0.28	20.1	0.24	20.2	0.23	15.6	0.18	16.4	0.06	19.5	0.14	19.7	0.23
CaO	0.01	0.01	-	-	0.01	0.01	0.02	0.04	0.01	0.01	0.01	0.02	0.01	0.01	0.01	0.01
Na ₂ O	0.01	0.01	0.01	0.01	0.01	0.01	0.02	0.03	0.01	0.02	0.01	0.01	0.02	0.01	0.01	0.01
Total	100															
Si	0.002	0.000	0.002	0.001	0.001	0.000	0.000	0.000	0.003	0.001	0.001	0.000	0.001	0.000	0.001	0.000
Ti	0.004	0.000	0.004	0.000	0.003	0.000	0.002	0.000	0.006	0.001	0.006	0.000	0.001	0.000	0.001	0.000
Al	1.735	0.008	1.742	0.007	1.762	0.007	1.738	0.009	1.157	0.060	1.144	0.020	1.712	0.007	1.770	0.008
Cr	0.217	0.003	0.211	0.004	0.203	0.005	0.241	0.005	0.768	0.054	0.740	0.013	0.260	0.006	0.227	0.001
Fe ³⁺	0.037	0.006	0.036	0.011	0.028	0.007	0.016	0.009	0.058	0.009	0.102	0.007	0.024	0.004	0.003	0.003
Fe ²⁺	0.212	0.003	0.214	0.007	0.218	0.007	0.204	0.009	0.321	0.003	0.284	0.005	0.227	0.004	0.225	0.003
Mn	0.004	0.000	0.004	0.000	0.004	0.000	0.004	0.000	0.007	0.001	0.007	0.001	0.005	0.000	0.004	0.000
Ni	0.008	0.000	0.009	0.001	0.009	0.000	0.008	0.001	0.007	0.001	0.006	0.000	0.008	0.000	0.008	0.001
Mg	0.781	0.003	0.777	0.006	0.772	0.007	0.784	0.008	0.673	0.003	0.709	0.005	0.760	0.004	0.760	0.008
Ca	0.000	-	-	0.000	0.000	0.000	0.000	0.001	0.000	0.000	0.000	0.000	0.000	0.000	0.000	0.000
Na	0.000	0.001	0.001	0.001	0.000	0.000	0.001	0.002	0.001	0.001	0.000	0.000	0.001	0.000	0.000	0.000
Total	3.000															
Mg#	0.787	0.003	0.784	0.007	0.780	0.007	0.793	0.009	0.677	0.003	0.714	0.005	0.770	0.004	0.771	0.004
Cr#	0.111	0.002	0.108	0.002	0.103	0.003	0.122	0.002	0.399	0.029	0.393	0.008	0.132	0.003	0.114	0.001

Table 3.7: Average major element composition of amphibole

AMP	Wum			
	We1a (17)	Std	Ww1a (20)	Std
SiO ₂	43.2	0.19	43.1	0.21
TiO ₂	1.06	0.04	1.86	0.13
Al ₂ O ₃	15.7	0.20	15.4	0.31
Cr ₂ O ₃	1.32	0.04	1.12	0.05
Fe ₂ O ₃	0.92	0.02	0.81	0.03
FeO	3.31	0.07	2.93	0.08
MnO	0.07	0.01	0.07	0.01
NiO	0.12	0.01	0.12	0.01
MgO	16.6	0.11	16.6	0.23
CaO	10.5	0.06	10.8	0.06
Na ₂ O	3.57	0.11	4.11	0.06
K ₂ O	0.93	0.02	0.10	0.02
H ₂ O	2.10	0.01	2.11	0.01
Total	99		99	
Si	6.150	0.019	6.140	0.017
Ti	0.114	0.004	0.199	0.014
Al	2.645	0.026	2.582	0.048
Cr	0.148	0.004	0.126	0.005
Fe ³⁺	0.099	0.002	0.087	0.003
Fe ²⁺	0.395	0.010	0.349	0.010
Mn	0.009	0.001	0.009	0.001
Ni	0.014	0.002	0.014	0.001
Mg	3.528	0.016	3.529	0.046
Ca	1.610	0.010	1.653	0.008
Na	0.987	0.033	1.136	0.019
K	0.169	0.004	0.018	0.005
H	2.000	0.000	2.000	0.000
Total	17.868	0.022	17.841	0.024
Mg#	0.877		0.890	

III.2.2.2. TRACE ELEMENTS

III.2.2.2.1. Olivine

Average trace element concentrations of olivine are reported in Table 3.7. They show a wide range of concentrations (0.6-34 ppm and 3-66 ppb respectively) and are broadly negatively correlated with Mg# (Fig. 3.16a, b). Mn is mainly hosted by olivine. Its concentration range from 844-1060 ppm and correlates negatively with Mg# (Fig. 3.16c). The concentrations of Al, Ca and V in olivine range from 43-247 ppm, 200-845 ppm, 1.4-6.1 ppm respectively, with samples from Oku showing the highest contents. They all show a negative correlation with Mg# (Fig. 3.16d, e, and f). Plotted against Al concentrations, Cr, V, Sc, Ca, Y and Ti show a positive correlation (Fig. 3.17). The samples from Oku show the highest concentrations except for Y and Ti where samples K1 and K1a show higher concentrations (Fig. 3.17e, f). Generally, the Oku samples show the highest concentrations for Cr, Ca and Al, while the Wum samples show the lowest contents.

CVL olivines show Li contents which range from 1.5-3.9 ppm. Samples from Enep (En1a, En2a), Kuk (K1, K1a, K5), Wum (We1a, Ww1a), Nyos (Ny3), Ngaoundere Likok (N11, N11a, N18) and some Oku (Ok1, Ok1a) samples are more enriched than the primitive mantle especially the N1 samples which show the highest concentrations (2.24-3.89 ppm) (Fig. 3.17g). Na contents range from 20-140 ppm. Etome samples show the lowest contents while Ww1a have the highest contents. Li vs Na plots show two distinct trends (not shown); the first shows a positive correlation while the second shows identical Li contents for varying Na contents. Na contents show a positive correlation with Al (Fig. 3.17h) while Li does not show a considerable variation with increasing Al contents (Fig. 3.17g). Ngaoundere Likok samples however show slight variations in Li contents.

III.2.2.2.2. Clinopyroxene

Average trace element abundances of homogeneous clinopyroxene are listed in Table 3.8 and the full trace element abundances of heterogeneous clinopyroxenes and secondary clinopyroxenes are shown in Appendix 3.2. Primitive mantle and chondrite normalized patterns are illustrated in Fig. 3.18. Clinopyroxenes from the CVL xenoliths show considerable inter (e.g. samples N11, N11a) and intra sample compositional variability,

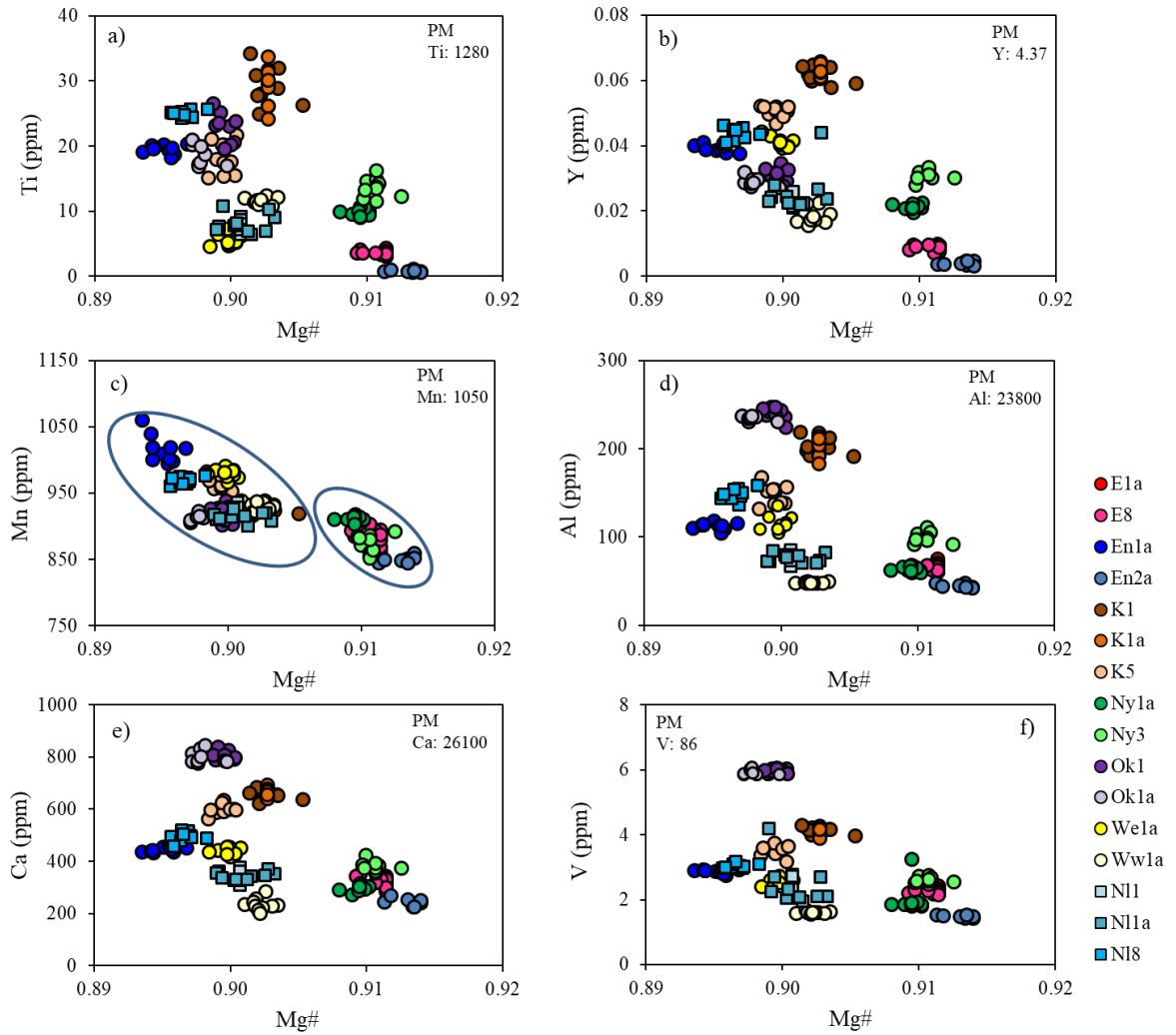


Figure 3.16: Trace element plots of olivine showing different elements vs Mg#.

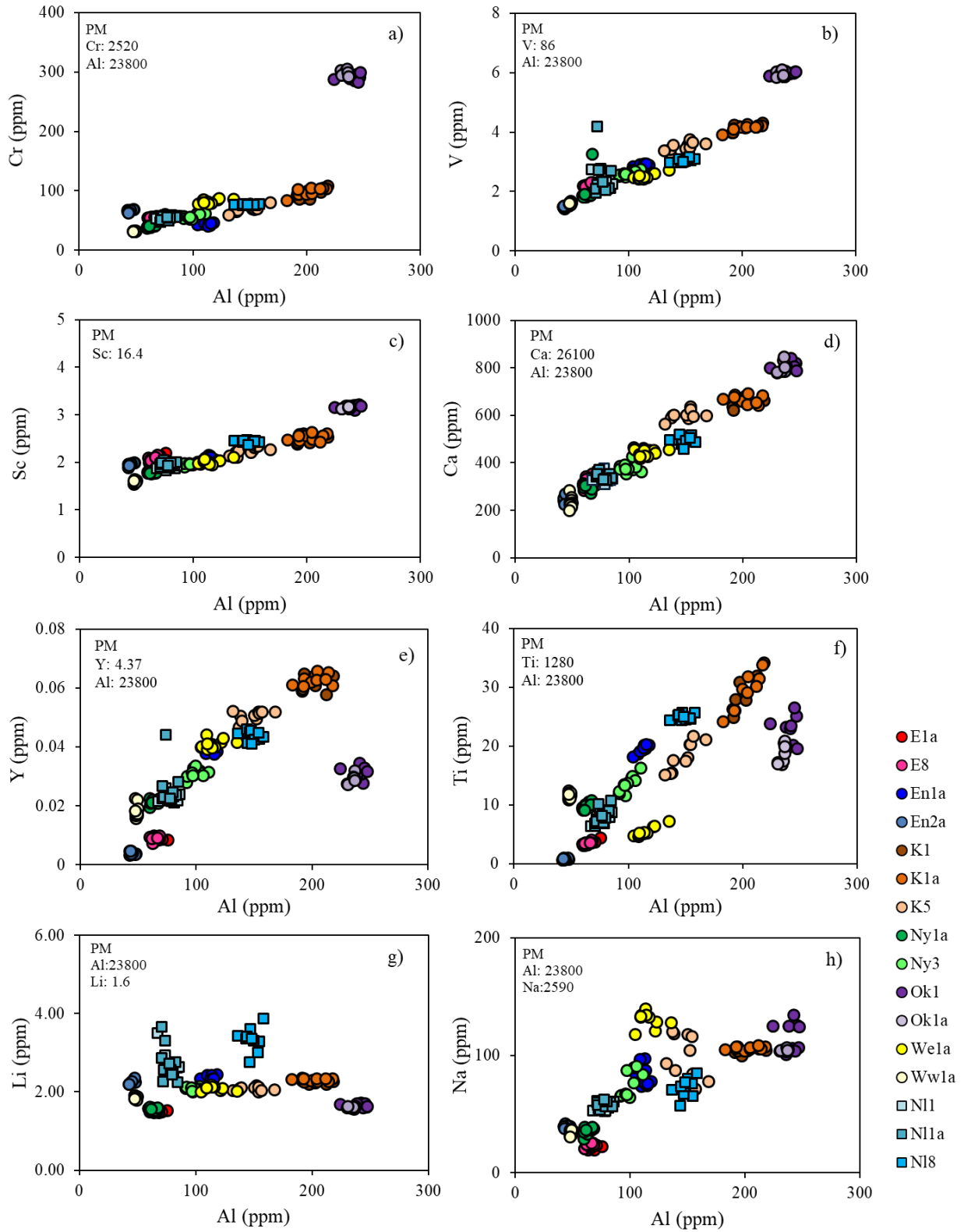


Figure 3.17: Trace element plots of olivine showing different elements vs Al

Table 3.7: Average trace element composition of olivine

OL	Ngaoundere Likok						Enep				Etome			
	N11 (9)	std	N11a (10)	std	N18 (10)	std	En1a (10)	std	En2a (8)	std	E1a (10)	std	E8 (10)	std
Li	2.74	0.32	2.74	0.45	3.34	0.30	2.36	0.05	2.70	0.11	1.51	0.03	1.54	0.04
Na	56.5	3.18	58.3	2.96	72.5	7.93	81.8	9.13	39.1	1.30	22.7	1.52	23.0	2.00
Mg	357467	8068	324413	8012	329358	37881	328654	9457	325119	3753	327223	10068	330319	13876
Al	78.2	5.47	76.3	4.98	148	6.34	112	3.95	44.6	2.07	66.4	4.70	64.5	2.74
Ca	337	20.1	345	14.5	495	17.6	446	10.7	242	15.6	319	16.1	322	19.9
Sc	1.89	0.03	1.97	0.04	2.43	0.04	2.07	0.05	1.95	0.03	2.08	0.07	2.08	0.04
Ti	7.99	1.01	8.08	1.46	24.9	0.51	19.5	0.69	0.77	0.15	3.51	0.41	3.48	0.21
V	2.27	0.29	2.44	0.67	3.03	0.07	2.87	0.06	1.49	0.04	2.26	0.08	2.23	0.05
Cr	56.3	2.24	52.9	3.89	76.2	1.12	43.7	1.82	66.2	2.20	55.4	1.94	55.1	1.02
Mn	930	3.68	914	7.41	969	5.65	1016	20.7	849	4.84	866	12.7	889	9.93
Fe	71290	779	74474	805	80893	726	84863	2580	64536	513	70922	786	74924	2907
Co	132	1.74	139	2.10	133	2.97	138	1.68	133	1.57	138	1.91	134	1.51
Ni	2665	20.6	2721	21.9	2703	88.1	2786	43.2	2860	26.9	2933	13.2	2911	28.4
Cu	3.343	0.386	3.447	0.725	4.302	0.629	4.159	0.077	2.957	0.095	3.561	0.071	3.474	0.104
Y	0.023	0.002	0.026	0.007	0.044	0.002	0.039	0.001	0.004	0.001	0.009	0.001	0.009	0.001
Zr	0.030	0.010	0.034	0.010	0.061	0.002	0.015	0.002	0.040	0.010	0.004	0.001	0.004	0.001

OL	Kuk						Nyos				Oku		Wum					
	K1 (8)	std	K1a (9)	std	K5 (10)	std	Ny1a (10)	std	Ny3 (10)	std	Ok1 (10)	std	Ok1a (8)	std	We1a (10)	std	Ww1a (10)	std
Li	2.26	0.05	2.31	0.03	2.08	0.05	1.56	0.03	2.08	0.05	1.65	0.05	1.61	0.02	2.09	0.06	1.84	0.04
Na	104	2.08	106	1.41	98.9	18.5	35.8	3.08	75.5	11.1	116	12.1	105	1.09	130	6.54	34.5	2.14
Mg	339778	5157	402667	5639	304599	7196	347615	16032	324816	16171	321162	9078	319878	9372	355554	11692	331821	5795
Al	201	9.91	202	11.4	148	11.2	63.4	3.08	99.8	6.08	240	6.90	235	2.79	116	9.02	48.5	0.81
Ca	657	20.1	667	18.6	599	19.6	298	12.2	379	19.5	806	17.4	802	25.4	439	14.0	234	23.4
Sc	2.50	0.09	2.53	0.07	2.24	0.08	1.80	0.04	1.97	0.04	3.17	0.03	3.15	0.03	2.02	0.05	1.60	0.03
Ti	29.1	3.08	29.1	3.12	18.2	2.46	9.77	0.55	13.6	1.46	22.5	2.42	18.5	1.63	5.46	0.86	11.5	0.50
V	4.14	0.11	4.14	0.10	3.50	0.17	1.99	0.44	2.61	0.09	5.98	0.06	5.93	0.09	2.51	0.10	1.61	0.03
Cr	93.6	8.00	98.2	7.19	69.1	6.08	40.5	3.26	56.6	3.70	291	5.49	297	5.30	82.2	3.60	31.6	0.32
Mn	924	5.45	929	4.63	969	11.6	911	4.39	873	14.1	922	11.5	913	5.31	979	6.69	930	6.05
Fe	72869	816	74464	452	81801	3019	66332	1106	71439	567	78659	635	75832	517	74180	769	76298	256
Co	137	1.40	137	1.49	133	2.61	132	1.00	133	1.96	138	2.21	139	1.57	143	2.51	132	1.95
Ni	2724	22.4	2758	10.7	2744	68.7	2833	32.5	2714	16.1	2791	29.0	2779	21.5	2740	32.7	2654	29.8
Cu	3.09	0.09	3.13	0.10	3.43	0.17	3.45	0.09	3.89	0.10	4.16	0.18	4.19	0.10	4.52	0.13	2.74	0.10
Y	0.061	0.003	0.063	0.002	0.051	0.002	0.021	0.001	0.031	0.002	0.031	0.002	0.029	0.002	0.041	0.002	0.018	0.002
Zr	0.023	0.003	0.022	0.002	0.018	0.002	0.006	0.001	0.013	0.008	0.047	0.003	0.044	0.001	0.018	0.002	0.005	0.001

Table 3.8: Average trace element composition of clinopyroxene

CPX	Ngaoundere Likok		Etome				Enep								Kuk			
	N18 (6)	std	E1a (10)	Std	E8 (10)	Std	En1a				En2a				K1 (8)	std	K1a (9)	std
							Core (9)	std	SR (4)	std	Cpx1 (8)	std	Sec-Cpx (20)	std				
Rb	0.04	-	bdl	bdl	bdl	bdl	bdl	bdl	0.06	0.05	0.04	-	0.16	0.37	0.01	0.01	0.01	0.01
Th	0.62	0.02	0.16	0.01	0.17	0.01	0.11	0.02	0.06	0.02	2.95	0.19	0.37	0.20	0.47	0.13	0.62	0.15
U	0.18	0.01	0.05	0.00	0.05	0.00	0.06	0.01	0.03	0.01	0.67	0.03	0.04	0.04	0.24	0.08	0.29	0.10
Ba	0.53	0.94	0.08	0.01	0.09	0.01	0.03	0.02	1.67	0.86	0.11	0.12	0.74	2.01	0.54	0.64	0.76	0.90
Nb	0.69	0.03	0.81	0.02	0.80	0.02	0.01	0.00	0.04	0.03	0.45	0.14	5.23	3.97	0.09	0.02	0.08	0.01
Ta	0.10	0.01	0.07	0.01	0.07	0.01	0.00	0.00	0.00	0.00	0.14	0.03	1.46	0.66	0.01	0.00	0.01	0.00
La	7.28	0.18	4.75	0.11	5.32	0.23	0.68	0.04	0.71	0.01	7.73	0.24	4.23	0.71	1.05	0.10	1.13	0.10
Ce	19.9	0.77	9.69	0.44	11.8	0.72	3.04	0.09	3.07	0.08	12.5	0.46	10.4	1.48	2.78	0.07	2.74	0.06
Pb	0.18	0.01	0.05	0.00	0.05	0.01	0.37	0.01	0.16	0.06	0.55	0.04	0.18	0.21	0.47	0.26	0.50	0.22
Sr	141	3.51	41.4	3.28	51.7	6.88	63.0	1.11	28.1	5.54	25.2	0.40	9.54	1.21	56.7	2.98	58.7	2.09
Pr	2.94	0.10	0.96	0.07	1.27	0.12	0.64	0.02	0.69	0.03	1.20	0.08	1.33	0.17	0.51	0.02	0.53	0.01
Nd	15.2	0.58	3.11	0.30	4.50	0.534	4.16	0.12	4.57	0.16	3.94	0.25	5.47	0.63	3.33	0.08	3.36	0.05
Hf	2.49	0.07	0.05	0.01	0.06	0.00	0.99	0.03	1.03	0.08	6.69	2.11	12.0	3.20	0.93	0.03	0.92	0.03
Zr	91.1	3.79	2.99	0.42	4.33	0.719	30.4	0.90	30.5	2.51	217	17.0	234	37.7	26.7	0.80	26.3	0.51
Sm	4.32	0.08	0.42	0.05	0.64	0.09	1.73	0.05	1.98	0.05	0.70	0.05	1.25	0.14	1.47	0.04	1.52	0.03
Eu	1.44	0.05	0.14	0.01	0.21	0.02	0.71	0.02	0.79	0.04	0.20	0.01	0.36	0.04	0.62	0.01	0.66	0.01
Gd	4.11	0.13	0.41	0.03	0.55	0.05	2.54	0.08	2.86	0.11	0.53	0.04	1.08	0.10	2.31	0.04	2.46	0.05
Tb	0.59	0.02	0.09	0.00	0.10	0.00	0.46	0.01	0.52	0.01	0.09	0.01	0.19	0.02	0.44	0.01	0.46	0.01
Ti	2937	92.8	425	11.5	425	13.8	3533	123	4402	1097	112	22.3	1192	213	3593	102	3725	72.3
Dy	3.44	0.08	0.75	0.03	0.80	0.05	3.21	0.10	3.70	0.16	0.65	0.05	1.28	0.13	3.21	0.05	3.32	0.06
Ho	0.66	0.01	0.19	0.00	0.20	0.01	0.70	0.02	0.80	0.03	0.14	0.01	0.28	0.03	0.70	0.01	0.72	0.02
Y	16.8	0.26	5.20	0.10	5.23	0.19	18.3	0.48	21.0	0.69	3.87	0.21	7.63	0.77	18.3	0.31	19.0	0.30
Er	1.80	0.04	0.64	0.02	0.66	0.03	2.07	0.07	2.34	0.10	0.47	0.03	0.90	0.10	2.09	0.05	2.16	0.05
Tm	0.25	0.01	0.10	0.00	0.10	0.01	0.28	0.01	0.32	0.01	0.08	0.01	0.14	0.02	0.29	0.01	0.30	0.01
Yb	1.65	0.04	0.75	0.02	0.75	0.04	1.96	0.06	2.2	0.06	0.60	0.04	1.05	0.12	1.94	0.05	2.07	0.06
Lu	0.23	0.01	0.11	0.00	0.11	0.00	0.27	0.01	0.30	0.02	0.09	0.01	0.15	0.02	0.28	0.01	0.29	0.01
Sc	57.7	1.59	66.5	2.10	63.6	2.33	62.7	1.26	73.5	4.03	93.3	2.79	194	12.0	69.7	1.63	71.1	1.64
V	209	4.71	244	2.61	228	6.41	253	5.85	286	15.5	229	3.60	488	111	267	3.45	274	3.31
Cr	4570	170	5711	130	5577	162	3491	87.9	3968	236	9152	366	21234	2138	5093	78.7	5265	891

Table 3.8 cont'd:

CPX	Kuk		Nyos				Oku				Wum					
	K5 (10)	std	Ny1a (5)	std	Ny3 (13)	std	Ok1 (6)	std	Ok1a (5)	std	Wela		Ww1a (15)	std		
											Core (19)	std	SR (2)	std		
Rb	0.02	-	bdl	bdl	bdl	bdl	0.04	0.03	bdl	bdl	bdl	bdl	0.50	0.06	0.03	-
Th	0.21	0.02	0.14	0.03	0.22	0.05	0.08	0.00	0.08	0.01	16	1.55	2.76	1.22	0.01	0.00
U	0.08	0.01	0.05	0.00	0.16	0.02	0.02	0.00	0.02	0.00	2.56	0.31	0.30	0.18	0.00	0.00
Ba	0.42	0.80	0.03	0.01	0.12	0.03	0.51	0.05	0.52	0.02	4.36	14.7	15.9	2.34	0.20	0.38
Nb	0.08	0.01	0.04	0.00	0.06	0.01	0.56	0.04	0.57	0.03	0.13	0.12	0.59	0.01	0.06	0.08
Ta	0.01	0.00	0.01	0.00	0.00	0.00	0.06	0.00	0.06	0.01	0.00	0.00	0.03	0.03	0.01	0.00
La	1.48	0.13	0.41	0.02	1.24	0.07	1.87	0.06	1.93	0.07	57.0	2.75	29.6	0.00	0.49	0.01
Ce	3.16	0.19	1.52	0.02	2.74	0.13	5.70	0.24	5.90	0.21	76.7	3.15	61.0	3.71	2.15	0.06
Pb	0.24	0.04	0.23	0.02	0.65	0.03	0.02	0.00	0.02	0.00	0.75	0.06	0.11	0.03	0.08	0.00
Sr	67.1	3.11	36.8	0.37	68.5	1.97	86.4	2.53	89.5	1.43	122	2.34	94.4	16.6	52.9	1.18
Pr	0.53	0.02	0.31	0.01	0.46	0.02	0.91	0.04	0.97	0.03	6.21	0.54	5.97	0.27	0.45	0.02
Nd	3.36	0.12	2.14	0.02	2.91	0.11	4.93	0.24	5.13	0.13	18.2	2.19	21.1	0.18	3.08	0.12
Hf	0.82	0.04	0.65	0.02	0.73	0.03	0.44	0.04	0.48	0.06	0.81	0.04	0.87	0.24	0.88	0.03
Zr	25.5	1.05	17.8	0.33	22.4	0.99	16.0	1.10	16.7	0.89	28.5	3.37	32.0	4.88	26.2	0.52
Sm	1.46	0.03	1.09	0.03	1.30	0.06	1.41	0.09	1.50	0.05	2.89	0.37	3.80	0.09	1.43	0.04
Eu	0.62	0.03	0.48	0.01	0.55	0.03	0.50	0.02	0.53	0.03	1.05	0.10	1.31	0.04	0.62	0.01
Gd	2.26	0.08	1.90	0.02	1.98	0.07	1.38	0.07	1.47	0.10	2.63	0.25	3.31	0.05	2.31	0.06
Tb	0.42	0.01	0.37	0.01	0.37	0.02	0.20	0.01	0.22	0.01	0.44	0.03	0.54	0.03	0.44	0.01
Ti	3343	112	2033	23.8	2791	125	1201	179	1273	233	1149	206	2512	882	3169	93.32
Dy	3.05	0.14	2.74	0.05	2.69	0.11	1.19	0.08	1.29	0.09	2.98	0.13	3.43	0.02	3.13	0.07
Ho	0.67	0.02	0.63	0.01	0.59	0.03	0.23	0.01	0.24	0.02	0.62	0.03	0.69	0.02	0.70	0.01
Y	17.3	0.63	15.9	0.26	15.4	0.57	5.74	0.31	6.04	0.34	16.3	0.53	18.1	0.19	18.1	0.26
Er	2.01	0.07	1.87	0.06	1.76	0.07	0.60	0.05	0.66	0.04	1.83	0.06	2.00	0.04	2.11	0.03
Tm	0.28	0.01	0.26	0.01	0.24	0.01	0.08	0.00	0.08	0.00	0.26	0.01	0.27	0.00	0.29	0.01
Yb	1.89	0.07	1.79	0.07	1.69	0.07	0.50	0.03	0.55	0.02	1.76	0.06	1.84	0.03	1.98	0.04
Lu	0.27	0.01	0.24	0.01	0.24	0.01	0.07	0.00	0.07	0.00	0.25	0.01	0.26	0.00	0.28	0.00
Sc	68.0	2.71	71.5	0.90	72.2	3.00	43.9	2.11	45.9	0.94	65.8	1.72	71.8	1.08	76.7	1.54
V	261	7.86	246	1.33	261	7.87	213	9.23	225	3.02	248	7.15	261	0.36	265	2.75
Cr	4903	194	5214	197	5409	206	9119	373	9184	294	6060	520	7219	500	5496	310

however, most samples show consistent patterns (e.g. samples Ny1, Ny3, En1a, En2a, Ok1, Ok1a, We1a, Ww1a, NI8).

a) Homogeneous clinopyroxene

Clinopyroxenes are subdivided into 5 groups based on their chondrite normalized REE patterns.

- ✚ Group 1 clinopyroxenes (En1a, Ny1a, Ww1a) are characterized by flat HREEs to MREEs and depleted LREEs patterns (Fig. 3.18a). Primitive mantle normalized trace element patterns (Fig. 3.18b) show negative Ba anomalies and slight negative Ti anomalies, which are above PM values. Th and U show slight enrichments except in Ww1a where they are below PM values. Primitive mantle normalized values of Th/U, Nd/Yb and Zr/Hf range from 0.42-0.80, 0.39-0.79 and 0.75-0.93 respectively while Ti_N and Pb_N contents are from 1.60-2.93 and 0.43-2.12 respectively.
- ✚ Group 2 clinopyroxenes (Ok1, Ok1a, NI8) show decreasing normalized concentrations from MREEs to HREEs and flat to downwards-dipping (towards La) LREE (Fig. 3.18c). This group shows strongly negative Rb, Ba, Pb and minor Ti anomalies (Fig. 3.18d). The Ti and Pb values are above PM values, while for the Ok samples, the negative Pb anomaly is more pronounced and falls below PM values. $(Th/U)_N$, $(Nd/Yb)_N$ and $(Zr/Hf)_N$ range from 0.88-1.39, 3.16-3.73 and 0.91-1.11 respectively while Ti_N and Pb_N contents are from 0.77-2.39 and 0.10-1.04 respectively. The NI8 clinopyroxenes are generally more enriched than those from Oku.
- ✚ Group 3 clinopyroxenes (K1, K1a, K5, Ny3) show LREE patterns which are similar to group 1, except that they show slight and variable enrichments in La and Ce and considerable intergrain variability in trace elements (except for sample Ny3) (Fig. 3.18e). Samples K1, K1a and K5 show negative Rb, Ba and slight negative Ti anomalies. K1 and K1a show negative to positive anomalies in Pb, Ny3 shows a slight positive anomaly but a negative anomaly is seen in sample K5 that equally shows a slight positive Sr anomaly (Fig. 3.18f). This group however shows higher concentrations of Th and U than group 1, while group 1 shows more pronounced Ba

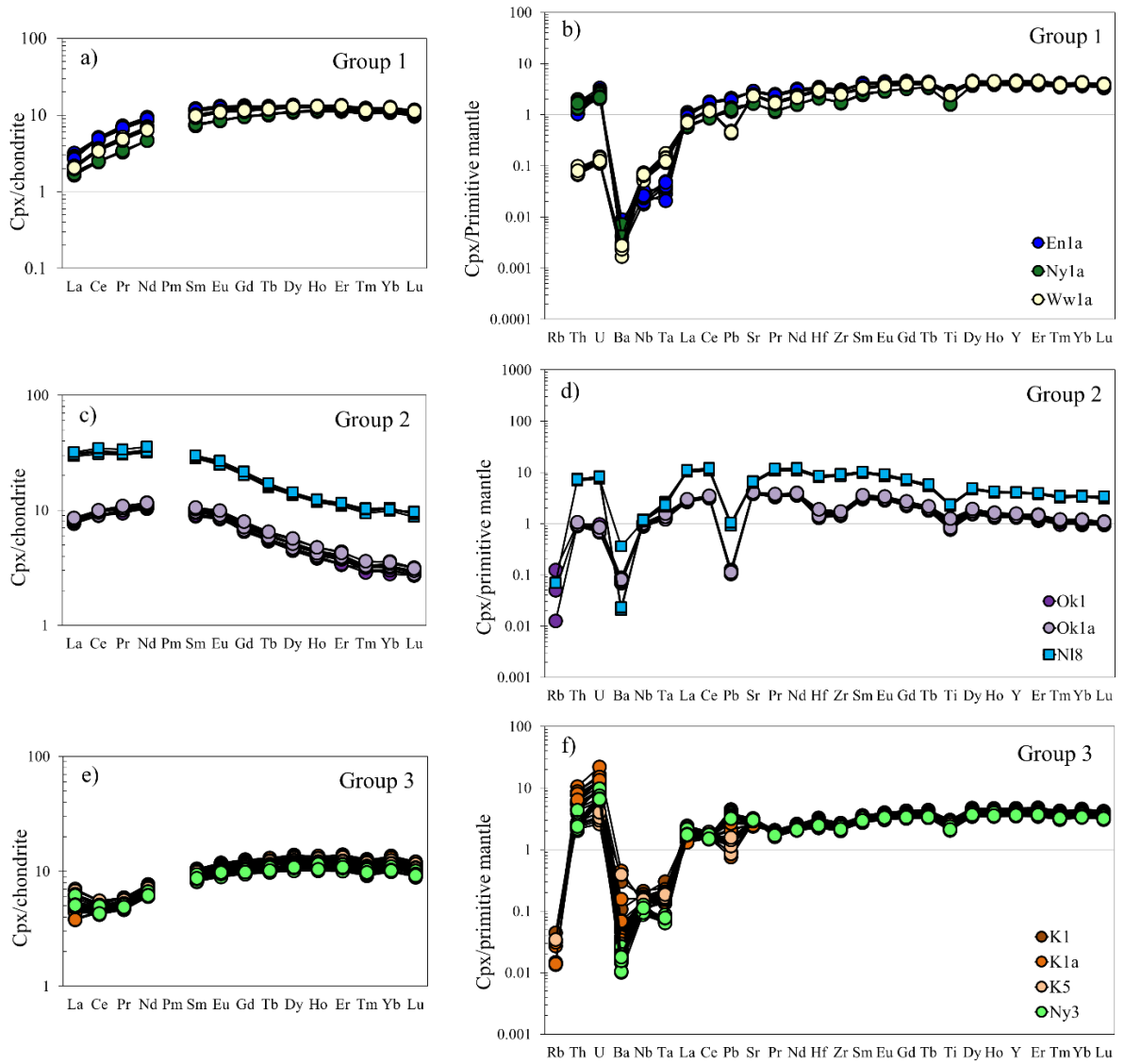


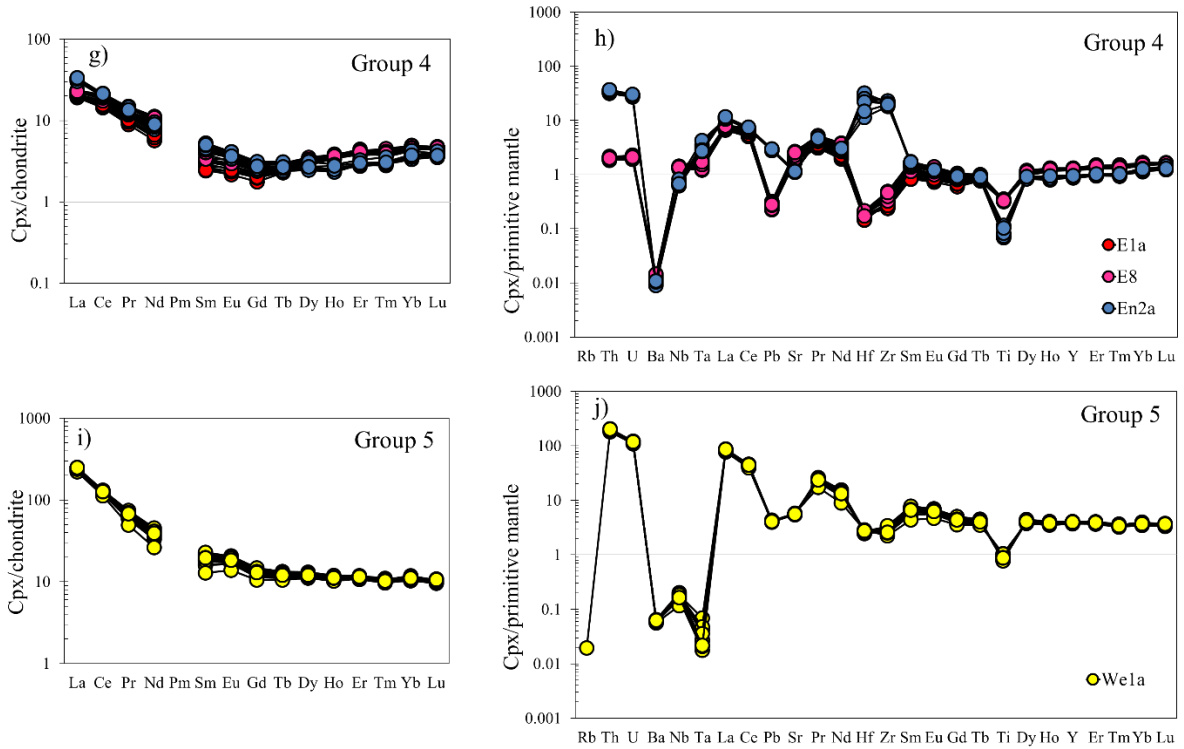
Figure 3.18: Primitive mantle and chondrite normalized trace element diagrams for clinopyroxenes of group 1, 2 and 3 xenoliths.

negative anomalies and Nb, Ta concentrations. $(\text{Th}/\text{U})_N$, $(\text{Nd}/\text{Yb})_N$ and $(\text{Zr}/\text{Hf})_N$ range from 0.32-0.83, 0.55-0.66 and 0.77-0.96 respectively while Ti_N and Pb_N contents are from 2.05-3.00 ppm and 0.76-4.49 ppm respectively.

- ✚ Group 4 clinopyroxenes (E1, E8, En2a) show a slight decrease in normalized concentrations from HREEs to MREEs and relative enrichments in MREEs to LREEs (MREEs are lower relative to HREEs) (Fig. 3.18g). These clinopyroxenes show negative Ba, Pb and Ti anomalies (Fig. 3.18h), which are all below PM values except for sample En2a, which does not show any Pb anomaly. Their $(\text{Th}/\text{U})_N$, $(\text{Nd}/\text{Yb})_N$ and $(\text{Zr}/\text{Hf})_N$ range from 0.88-1.23, 1.31-2.53 and 0.67-0.78 respectively, while Ti_N and Pb_N contents are from 0.07-1.04 and 0.22-3.45 respectively. The trace element patterns of sample En2a shows differences from the other patterns. It shows higher concentrations of Th and U, positive Zr and Hf anomalies and the absence of a Pb anomaly.
- ✚ Group 5 clinopyroxenes (We1a) exhibit flat HREE patterns, slightly enriched MREEs and very strong LREE enrichments (Fig. 3.18i). They show strongly negative Rb, Ba, Ta, and weaker Ti anomalies and slight negative Pb and Sr (above PM) anomalies (Fig. 3.18j). Their $(\text{Th}/\text{U})_N$, $(\text{Nd}/\text{Yb})_N$ and $(\text{Zr}/\text{Hf})_N$ ratios range from 1.66-1.71, 2.56-4.15 and 0.78-1.36 respectively while Ti_N and Pb_N contents are from 0.77-1.04 and 3.97-4.31 respectively.

b) Heterogeneous clinopyroxene

- ✚ Group 6 clinopyroxenes (N11, N11a) have flat HREE to MREE and show enriched LREEs (Fig. 3.19). Some of the clinopyroxenes show a positive Eu anomaly (Fig. 3.19g), and they represent the most enriched in LREEs and incompatible elements. One clinopyroxene from sample N11a shows characteristics of the group 1 clinopyroxenes. N11 and N11a samples show considerable variability e.g. Ba_N ranges from 0.01-12.83, $(\text{Th}/\text{U})_N$, $(\text{Nd}/\text{Yb})_N$ and $(\text{Zr}/\text{Hf})_N$ from 0.61-1.66, 0.90-1.87 and 1.07-2.63 respectively while Ti_N and Pb_N contents are from 0.78-2.46 ppm and 0.10-2.36 ppm respectively. Group 6 clinopyroxenes can further be divided into 3 groups.



Figures 3.18 cont'd: Primitive mantle and chondrite normalized trace element diagrams for clinopyroxenes of groups 4 and 5 xenoliths.

Group 6-1 trace element patterns are homogeneous and show negative Rb, Ba, Ti and positive Th, U and Zr anomalies; group 6-2 is characterized by slight negative Rb, more pronounced Ba, Pb, Ti anomalies and positive Zr anomalies; group 6-3 shows negative Pb, Ti and positive Sr, Zr and Eu anomalies.

b) Heterogeneous clinopyroxene

- Group 6 clinopyroxenes (N11, N11a) have flat HREE to MREE and show enriched LREEs (Fig. 3.19). Some of the clinopyroxenes show a positive Eu anomaly (Fig. 3.19g), and they represent the most enriched in LREEs and incompatible elements. One clinopyroxene from sample N11a shows characteristics of the group 1 clinopyroxenes. N11 and N11a samples show considerable variability e.g. Ba_N ranges from 0.01-12.83, $(Th/U)_N$, $(Nd/Yb)_N$ and $(Zr/Hf)_N$ from 0.61-1.66, 0.90-1.87 and 1.07-2.63 respectively while Ti_N and Pb_N contents are from 0.78-2.46 ppm and 0.10-

2.36 ppm respectively. Group 6 clinopyroxenes can further be divided into 3 groups. Group 6-1 trace element patterns are homogeneous and show negative Rb, Ba, Ti and positive Th, U and Zr anomalies; group 6-2 is characterized by slight negative Rb, more pronounced Ba, Pb, Ti anomalies and positive Zr anomalies; group 6-3 shows negative Pb, Ti and positive Sr, Zr and Eu anomalies.

- ✚ Secondary clinopyroxenes from sample En2a show flat HREEs to MREEs, but they are enriched in LREEs (Fig. 3.20a). Their trace element patterns are identical to patterns of primary clinopyroxenes but differ in terms of enrichments and depletions, plus a wide range in composition is observed especially for LILEs (Rb, Ba, Th, U) and HFSEs (Nb, Ta, Zr). They are generally less enriched in Th, U, Pb, Sr, and more enriched in Nb, Th, Hf, Ti than the primary clinopyroxene (Fig. 3.20b).

Plots of trace element concentrations (Fig. 3.21a, b) and ratios (Fig. 3.21c, d, e, f) have been used to distinguish and understand the different clinopyroxene groups (eg. Nformidah et al., submitted). Group 1 clinopyroxenes show two subgroups that have identical Sr (53 ± 9 ppm) but different Ti (~ 2000 and > 3000 ppm) compositions. They show the lowest La (0.54 ± 0.1 ppm) compared to the other groups and have average Pb (0.20 ± 0.1 ppm) contents. Group 2 clinopyroxenes show two subgroups; a low Ti (< 2000 ppm), low Sr (88 ± 3 ppm) and a high Ti (> 2000 ppm), high Sr (141 ± 4 ppm) subgroup. The La vs Pb plot for this group shows a low La-Pb (1.90 ± 0.07 and 0.02 ± 0.001 ppm) subgroup and a subgroup with average values (7.28 ± 0.18 and 0.18 ± 0.01 ppm).

Group 3 clinopyroxenes have high Ti (2599-3822 ppm) and Pb (0.14-0.83 ppm) but low Sr (64 ± 6 ppm) and La (1.24 ± 0.2 ppm) contents. Group 4 clinopyroxenes show two distinct subgroups; very low Ti (93-448 ppm), but higher Sr (24-59 ppm) relative to the second, which has very low Sr (8-14 ppm), but higher Ti (736-1630 ppm) concentrations. Their Pb contents are in a narrow range (5 ± 1) while Pb varies between 0.02-0.81 ppm. Group 5 clinopyroxenes have average Ti contents (978-1320 ppm) and high Sr contents (122 ± 2 ppm), they show the highest La (57 ± 2 ppm) contents and Pb compositions of 0.75 ± 0.065 ppm. Group 6 clinopyroxenes show variability in both Ti (991-3105 ppm) and Sr (22-336 ppm) which is also observed in their La (1.47-9.72 ppm) and Pb (0.02-0.44 ppm) contents.

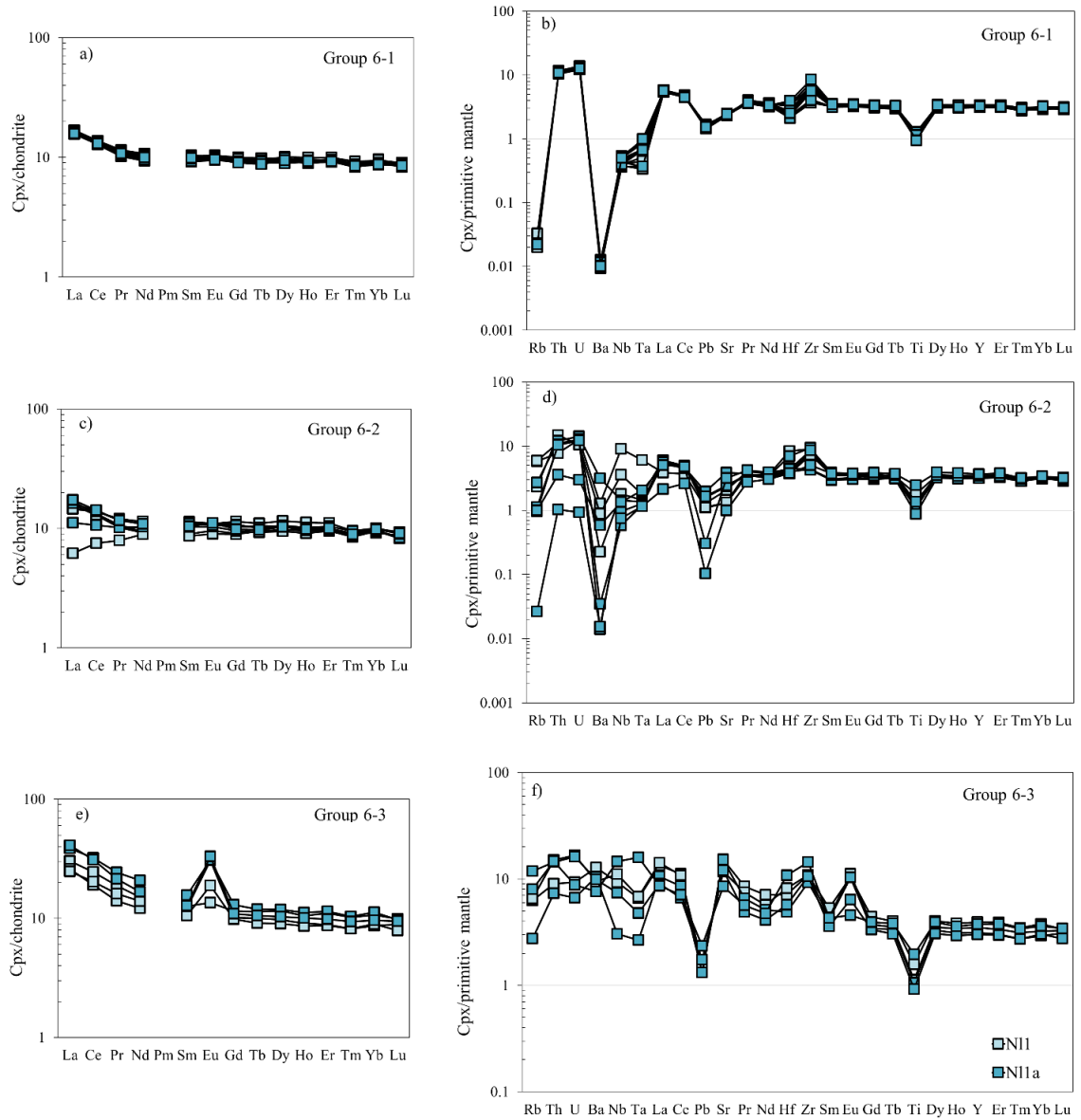


Figure 3.19: Primitive mantle normalized trace element patterns of heterogeneous clinopyroxenes (Group 6)

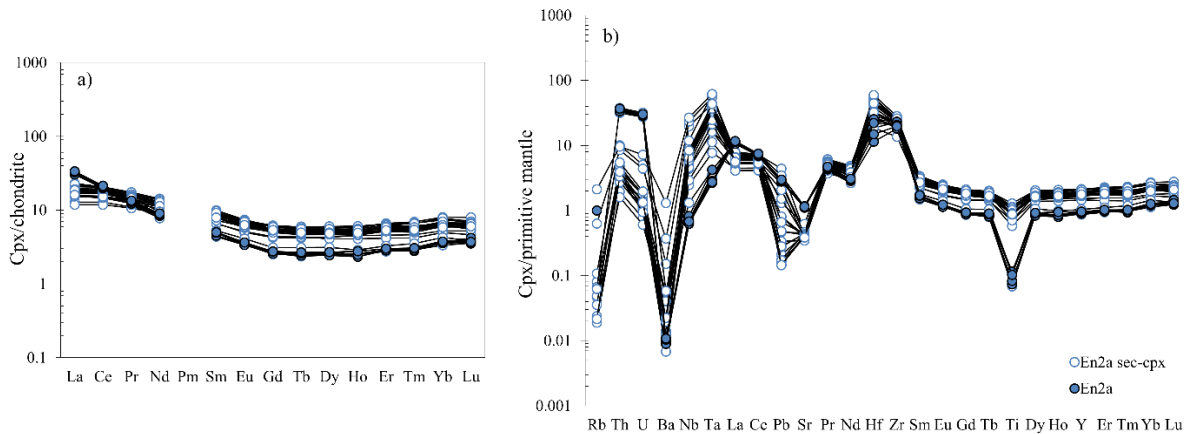


Figure 3.20: Primitive mantle normalized trace element patterns of secondary clinopyroxenes compared to the primary ones

Calculated Pb anomaly defined as $Pb_N / \sqrt{(Ce_N * Pr_N)}$ shows a range of values from 0.03-0.56. Values from groups 1, 3 and 5 range from 0.12-2.59. Group 2 samples have the lowest values (0.03-0.09) while groups 4 and 6 show a large spread and the highest values (0.04-0.56).

Trace element ratios (Fig. 3.21c, d, e, f) can also be used to characterise the different clinopyroxene groups. Fractionation of Th-U, Nb-Ta and Zr-Hf is sometimes observed, sometimes absent. These elements show considerable differences between samples, with Ta, Nb and Zr occasionally being more enriched than U, Ta and Hf.

In the Zr/Hf vs Hf plot (Fig. 3.21c), the two subgroups of group 4 clinopyroxenes represent extremes. The first one has the lowest Hf (0.04-7.63 ppm) contents and the highest Zr/Hf ratios while the second shows the lowest Zr/Hf (16-26) ratios and the highest Hf (5.60-17.88 ppm) contents. Groups 1, 2, 3 and 5 overlap and have identical Hf (0.39-2.58 ppm) and Zr/Hf: 25.78-46.43 contents while group 6 is slightly more enriched than the latter (Zr/Hf: 32.06-89.80; Hf: 0.64-3.26 ppm).

The Nb/Ta vs Ta plot (Fig. 3.21d) nicely distinguishes the group 5 clinopyroxenes which are more enriched (Nb/Ta: 37-120; Ta: 0.001-0.01 ppm) than the other groups while group 1 falls on the more depleted end (Nb/Ta: 6.20-61.44; Ta: 0.001-0.008 ppm); groups 2, 3, 5 and a subgroup of group 4 clinopyroxenes are between the two (Nb/Ta: 2.67-27.89;

Ta:0.003-0.69 ppm). The second subgroup is the most depleted (Nb/Ta: 2.36-6.23; Ta: 0.33-2.64 ppm).

In the Nd/Yb vs Th/U plot (Fig. 3.21f), groups 1 and 3 overlap and have the lowest values (Nd/Yb: 1.10-2.22 ppm; Th/U: 1.19-3.09); group 6 shows average ratios (Nd/Yb: 2.27-6.16; Th/U: 2.52-5.25, group 2 and 5 show the highest Nb/Yb ratios (8.87-11.66) but differ in their Th/U ratios (3.25-5.15 and 6.17-7.57 respectively). Group 5 shows ratios (Nd/Yb: 3.67-7.10; Th/U: 3.27-4.58) which are intermediate between groups 2 and 6, but the second subgroup show the highest Th/U ratios (4.96-13.01).

Of all the plots discussed above, the most discriminant is the La/Ce vs Nd/Yb discrimination plot (Fig. 3.21e). Groups 1 and 3 have identical Nd/Yb ratios but group 3 has higher La/Ce ratios (0.32-0.49). Groups 2 and 5 have the highest Nd/Yb ratios. Group 5 also has the highest La/Ce ratios (0.32-0.76). Groups 4 and 6 overlap and show intermediate ratios (0.32-0.64) between the other groups and the second subgroup of group 4 clinopyroxenes is distinguished.

III.2.2.2.3. Orthopyroxene

Trace element concentrations of orthopyroxenes are shown in Table 3.9. Primitive mantle normalized trace element patterns are presented in Fig. 3.22. They generally show negligible variability between grains but considerable variations between the different samples. However, positive Ti, Hf and Zr anomalies are common for all samples except for samples E1, E8 and We1a (Fig. 3.22 b, j) where they are absent. A negative Ba anomaly is also common in all samples except for a few where they are below detection limits (Fig. 3.22). As in the case of clinopyroxenes, they are divided into six different groups based on their chondrite normalized REE patterns.

- ✚ Group 1 (En1a, Ny1, Ww1a) shows depletions from HREEs to LREEs with slight enrichments in La (Fig. 3.22a). They are characterized by negative Th, Sr anomalies and positive U and Pb, anomalies (Fig. 3.22b).
- ✚ Group 2 (Ok1, Ok1a, Nl8) shows a decrease in normalized concentrations from HREEs to LREEs with a flattening of the MREEs (Fig. 3.22c). They show negative Th and Pb and positive Nb anomalies (Fig. 3.22d).

- ✚ Group 3 (K1, K1a, K5, Ny3) shows a decrease in normalized concentrations from HREEs to LREEs and flat LREE patterns with slight La enrichments (Fig. 3.22e). Positive anomalies are observed in U, Nb Ta and Pb, (Fig. 3.22f).
- ✚ Group 4 (E1, E8, En2a) patterns show a decrease in concentration from HREEs to MREEs, but then show slight enrichments from MREEs to LREEs (Fig. 3.22g). They are characterized by negative Ba, Sr anomalies and positive U, Nb, Ta anomalies (Fig. 3.22h). Samples E1a and E8 in addition show a slight positive Ti anomaly. Sample En2a shows more depleted HREEs and very high Hf, Zr, Th and U contents.
- ✚ Group 5 (We1a) is characterized by a decrease in HREEs, flat MREEs and enrichments in LREEs (Fig. 3.22i). Negative Rb, Ba, Pb and Sr anomalies are observed. Enrichments in Th, U, La and Ce are apparent (Fig. 3.22j).
- ✚ Group 6 (N11, N11a) shows a decrease in concentration from HREEs to LREEs except for one N11a orthopyroxene with shows an increase in LREEs (Fig. 3.22k). This group is characterized by enrichments in U. A slight negative Sr anomaly is observed (Fig. 3.22l).

Calculated Pb anomalies for orthopyroxenes are generally higher than for clinopyroxenes and range from 0.10-3.0. The highest values are observed in group 3 samples while the lowest occur in groups 2 and 5.

III.2.2.2.4. Amphibole

Trace element concentrations of amphiboles are shown in Table 3.10. Samples We1a and Ww1a are the only amphibole bearing samples. Sample Ww1a shows flat HREE to MREEs patterns with steep enrichments in the LREEs. It shows positive Pb and Ti anomalies (Fig. 3.23a). We1a shows flat HREE patterns, enrichments from MREEs to LREEs and negative Ta anomaly (Fig. 3.23b). The We1a amphibole is generally more enriched than the Ww1a sample.

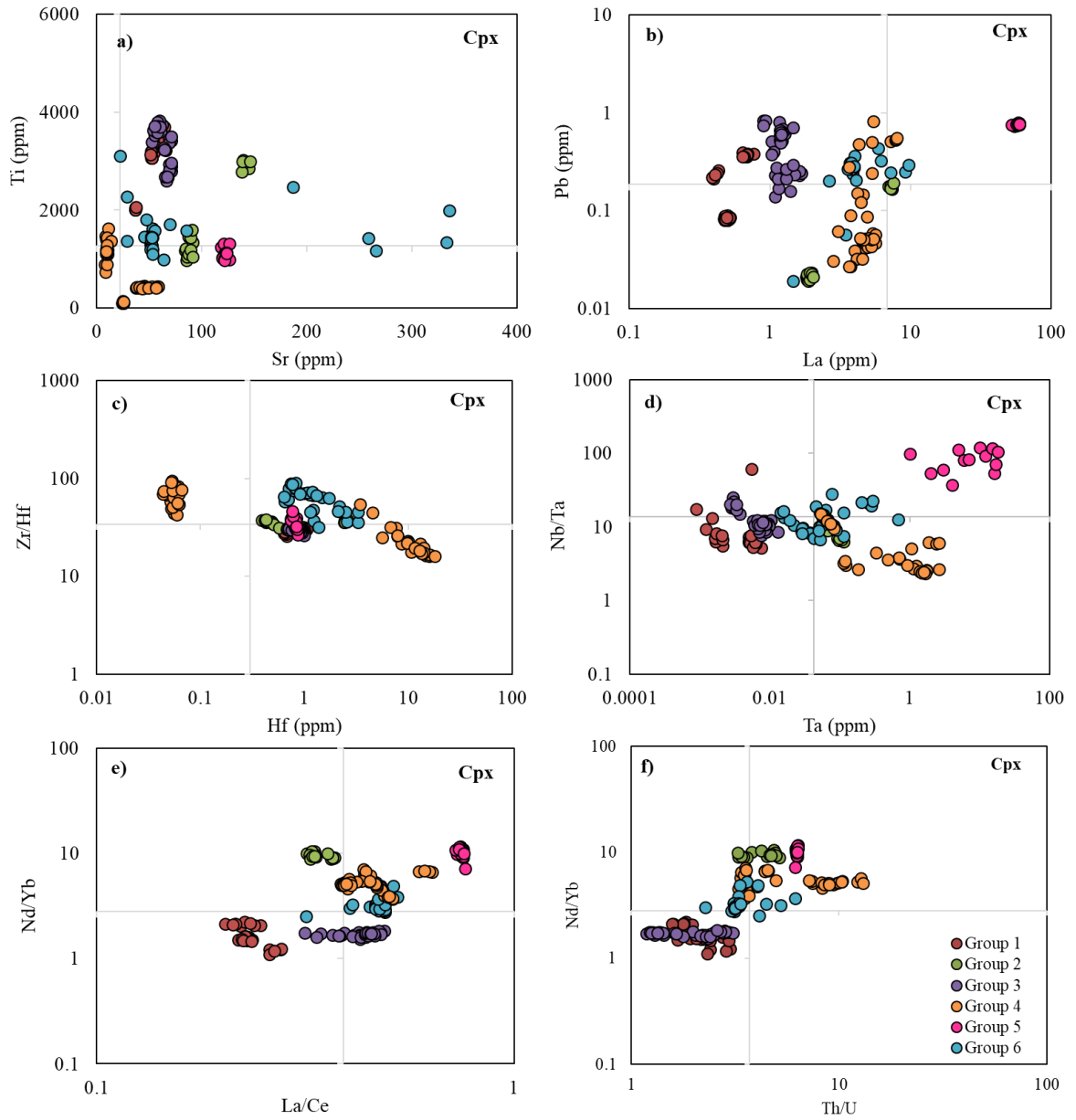


Figure 3.21: Trace element concentrations and ratios of clinopyroxenes from the CVL xenoliths.

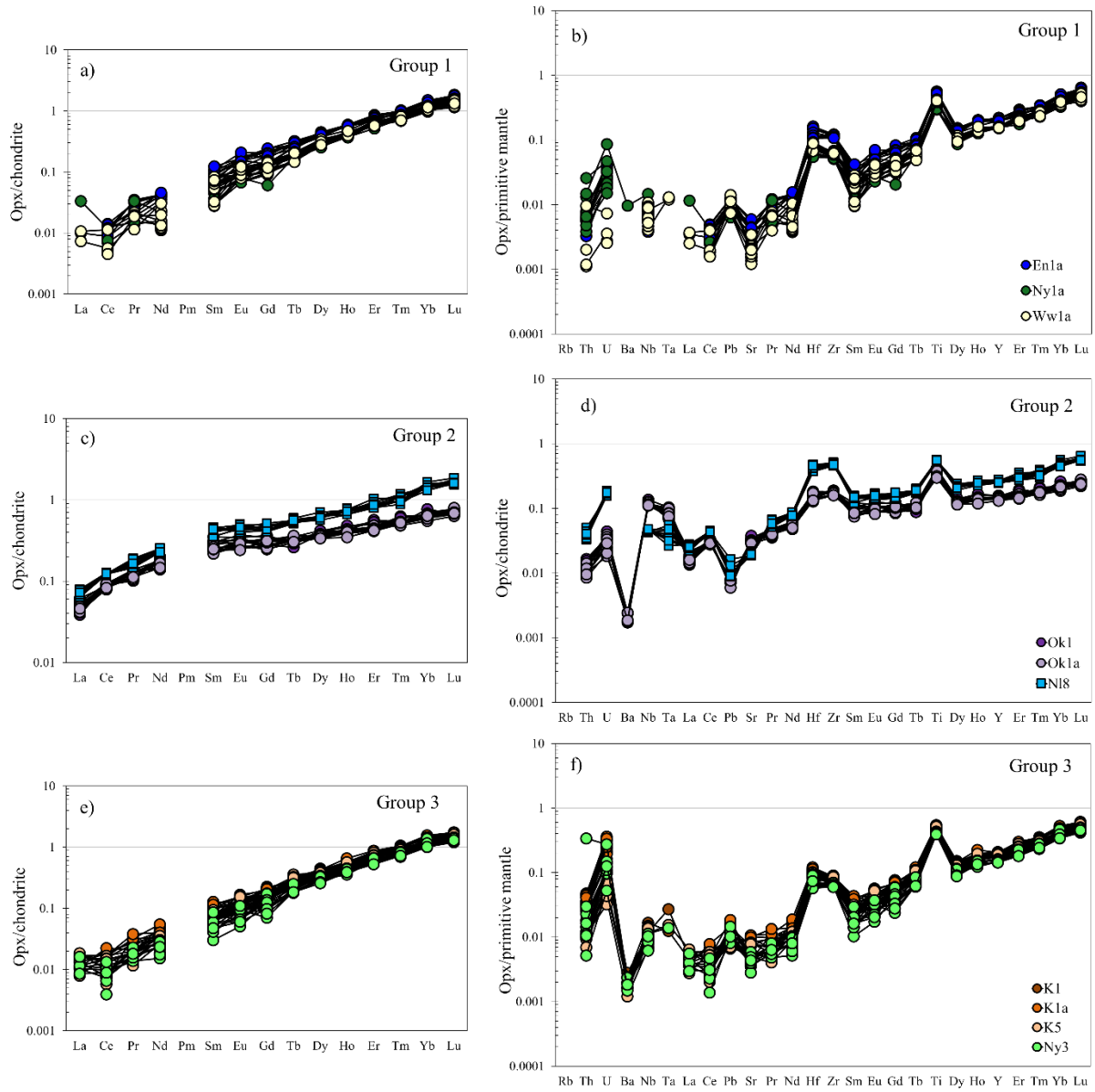


Figure 3.22: Primitive mantle and chondrite normalized trace element diagrams for orthopyroxenes of groups 1, 2 and 3 xenoliths.

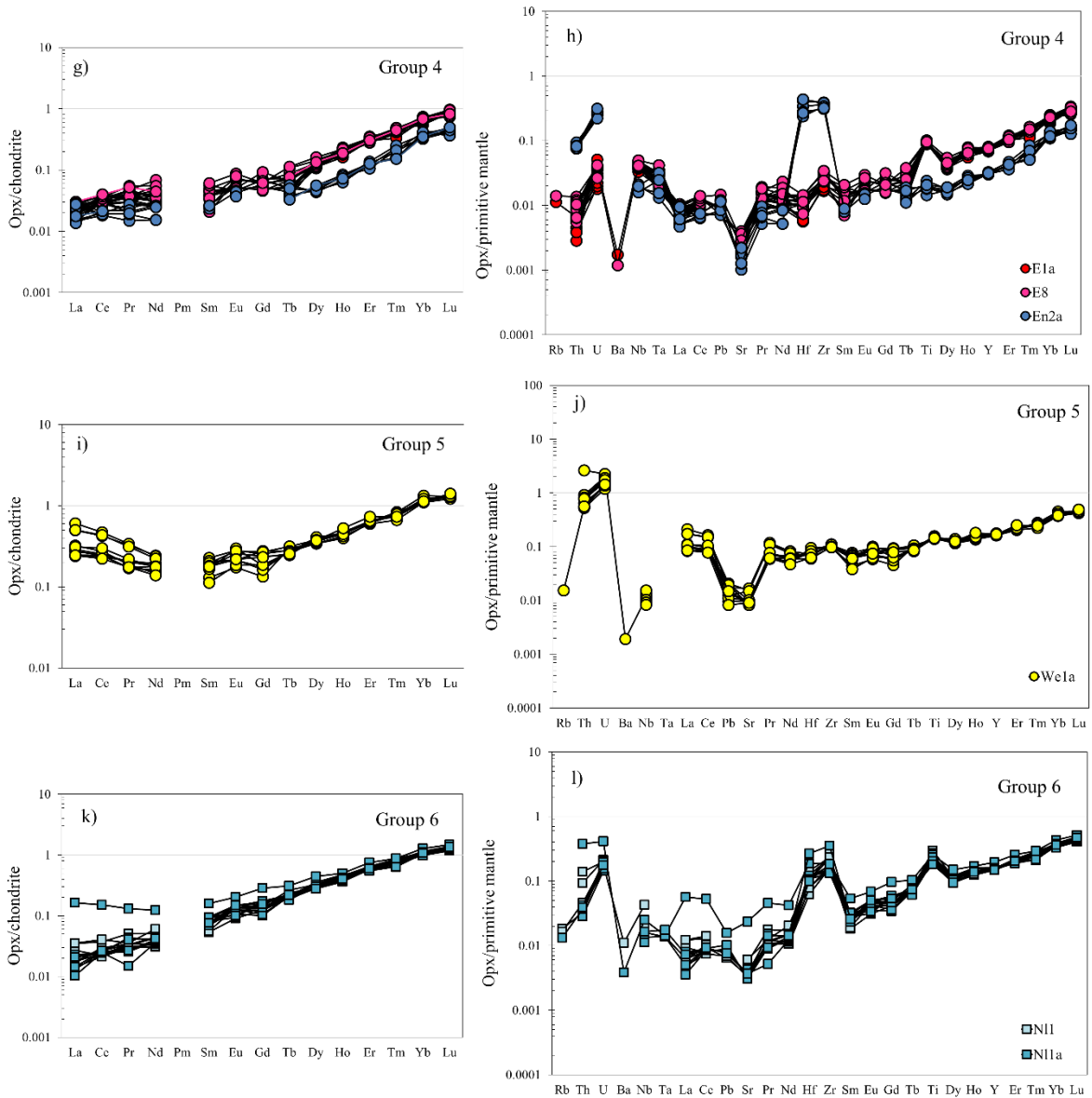


Figure 3.22: Primitive mantle and chondrite normalized trace element diagrams for orthopyroxenes of group 4, 5 and 6 xenoliths.

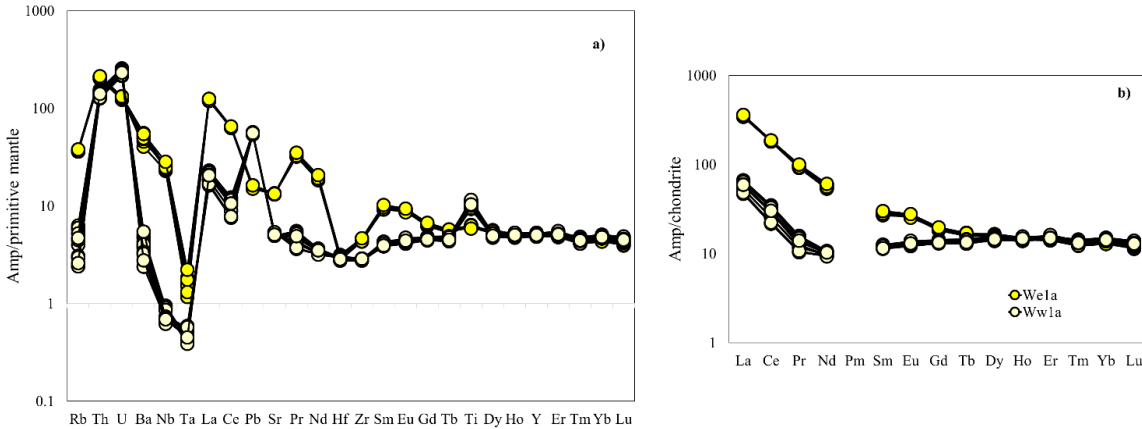


Figure 3.23: Primitive mantle and chondrite normalized trace element diagrams for amphiboles

III.2.2.3. BULK ROCK COMPOSITION

Whole-rock major element compositions of the CVL xenoliths were estimated from mineral compositions obtained by EPMA analysis, using the mass balance method. The results are reported in Tables 3.11 and 3.12. The CVL xenoliths show heterogeneous compositions. Enriched and depleted components (with reference to PM values of McDonough and Sun 1995) are common. Al_2O_3 and TiO_2 contents vary between 4.59-7.34 wt% and 0.10-0.27 wt% respectively for enriched samples (En1a, K1, K5, Ny3, We1a, Ww1a, N11a) and 2.29-3.96 wt% and 0.02-0.09 wt% for the depleted ones (E1a, E8, En2a, K1a, Ny1a, Ok1, Ok1a, N11, N18). An exception is sample K1a, which shows higher TiO_2 contents. FeO contents vary between 6.44-8.08 wt %, NiO (0.03-0.28 wt %), CaO (1.59-6.74 wt %) and Na_2O (0.10-0.81 wt %) and show a wide composition range. MgO contents show a general negative correlation with Al_2O_3 , CaO, Na_2O and TiO_2 (Fig. 3.24a-d) and correlate positively with NiO (Fig. 3.24e). This variability generally follows trends observed for upper mantle peridotites (Boyd, 1989; Frey and Prinz, 1978). The bulk Mg# ranges from 0.88-0.90 and shows a good correlation with olivine Mg# (Fig. 3.24f).

Whole rock trace element concentrations were calculated by mass balance. Mantle xenoliths from the CVL show multi-trace element patterns. The whole rock REE patterns are similar to clinopyroxene REE patterns except for one amphibole-bearing sample (Ww1a) (Fig. 3.25a, b). Group 1 samples (Fig. 3.25a, b) show LREE depletion except for the

amphibole-bearing sample Ww1a which shows enrichments. Negative Nb, Ta, and negative to positive Ti anomalies are evident. Sample Ww1a shows enrichments in U, Th and positive Pb and Ti anomalies. It is also generally more enriched than the other group 1 samples. Group 2 samples (Fig. 3.25c, d) show enrichments from HREEs to MREEs with a flattening of the LREEs. Sample N18 shows the most enrichment. Group 3 (Fig. 3.25e, f) have flat HREE to MREE patterns and depletions in LREEs with minor La enrichments. Trace element patterns show positive Th, U, Ti and negative Nb, Ta anomalies. Group 4 (Fig. 3.25g, h) shows steep enrichment from MREEs and LREEs with HREEs being more enriched than MREEs. Sample En2a is different from the other samples in that the MREEs do not show any depletion. Trace element patterns show negative Pb, Hf, Zr anomalies and a slight positive Ti anomaly. Sample En2a patterns have positive Ta, Hf, Zr and negative Sr anomalies. Group 5 sample (Fig. 3.25i, j) is amphibole bearing with strong LREE enrichment, positive Th, U and negative Ta anomalies. Group 6 (Fig. 3.25k, l) REE patterns are relatively flat with slight LREE enrichments and a positive Eu anomaly. Trace elements show slight Th, U enrichments and positive Zr anomalies.

Table 3.9: Average trace element composition of orthopyroxene

OPX	Ngaoundere Likok						Etome				Enep			
	Ni1 (9)	std	Ni1a (6)	std	Ni8 (10)	std	E1a (10)	std	E8 (10)	std	En1a (11)	std	En2a (7)	std
Rb	0.01	-	0.01	-	bdl	bdl	0.01	-	0.01	-	bdl	bdl	bdl	bdl
Th	0.00	0.00	0.01	0.01	0.00	0.00	0.00	0.00	0.00	0.00	0.00	0.00	0.01	0.00
U	0.00	0.00	0.00	0.00	0.00	0.00	0.00	0.00	0.00	0.00	0.00	0.00	0.01	0.00
Ba	0.08	-	0.03	-	bdl	bdl	0.01	-	0.01	-	bdl	bdl	bdl	bdl
Nb	0.01	0.01	0.01	0.00	0.03	0.00	0.02	0.00	0.03	0.00	0.00	0.00	0.01	0.00
Ta	0.00	0.00	0.00	0.00	0.00	0.00	0.00	0.00	0.00	0.00	bdl	bdl	0.00	0.00
La	0.01	0.00	0.01	0.01	0.02	0.00	0.01	0.00	0.01	0.00	0.00	-	0.00	0.00
Ce	0.02	0.00	0.03	0.03	0.08	0.00	0.02	0.00	0.02	0.00	0.01	0.00	0.01	0.00
Pb	0.00	0.00	0.00	0.00	0.00	0.00	bdl	bdl	0.00	0.00	0.00	0.00	0.00	0.00
Sr	0.09	0.02	0.15	0.18	0.44	0.02	0.06	0.01	0.07	0.01	0.10	0.02	0.04	0.01
Pr	0.00	0.00	0.00	0.00	0.02	0.00	0.00	0.00	0.00	0.00	0.00	0.00	0.00	0.00
Nd	0.02	0.00	0.02	0.02	0.11	0.01	0.01	0.00	0.02	0.01	0.02	0.00	0.01	0.00
Hf	0.03	0.01	0.04	0.02	0.13	0.01	0.00	0.00	0.00	0.00	0.04	0.01	0.10	0.03
Zr	2.02	0.42	2.02	0.83	4.99	0.17	0.20	0.02	0.29	0.04	1.18	0.05	3.65	0.32
Sm	0.01	0.00	0.01	0.00	0.06	0.01	0.00	0.00	0.01	0.00	0.01	0.00	0.00	0.00
Eu	0.01	0.00	0.01	0.00	0.03	0.00	0.00	0.00	0.00	0.00	0.01	0.00	0.00	0.00
Gd	0.03	0.00	0.03	0.01	0.09	0.01	0.01	0.00	0.01	0.00	0.04	0.01	bdl	bdl
Tb	0.01	0.00	0.01	0.00	0.02	0.00	0.00	0.00	0.00	0.00	0.01	0.00	0.00	0.00
Ti	294	41.6	285	34.9	687	15.5	115	1.47	120	5.16	673	26.9	24.5	3.72
Dy	0.07	0.01	0.08	0.01	0.15	0.01	0.03	0.00	0.03	0.00	0.10	0.01	0.01	0.00
Ho	0.02	0.00	0.02	0.00	0.04	0.00	0.01	0.00	0.01	0.00	0.03	0.00	0.00	0.00
Y	0.63	0.01	0.67	0.07	1.07	0.05	0.30	0.01	0.31	0.01	0.86	0.04	0.13	0.00
Er	0.10	0.00	0.10	0.01	0.14	0.01	0.05	0.00	0.05	0.00	0.12	0.01	0.02	0.00
Tm	0.02	0.00	0.02	0.00	0.03	0.00	0.01	0.00	0.01	0.00	0.02	0.00	0.00	0.00
Yb	0.17	0.01	0.18	0.02	0.24	0.02	0.10	0.01	0.11	0.01	0.22	0.01	0.06	0.01
Lu	0.03	0.00	0.03	0.00	0.04	0.00	0.02	0.00	0.02	0.00	0.04	0.00	0.01	0.00
Sc	12.1	0.14	12.1	0.31	14.7	0.52	16.4	0.24	16.3	0.69	13.2	0.62	12.3	0.22
V	63.5	1.62	65.5	4.16	79.3	1.68	91.6	1.37	91.0	3.75	87.0	3.60	53.0	1.30
Cr	2073	41.3	1928	128	2178	72.5	2557	56.4	2579	130	1627	66.3	2840	62.1

Table 3.9 cont'd:

OPX	Kuk						Nyos				Oku				Wum			
	K1 (8)	std	K1a (9)	std	K5 (10)	std	Ny1a (10)	std	Ny3 (11)	std	Ok1 (8)	std	Ok1a (7)	std	We1a (10)	std	Ww1a (10)	std
Rb	bdl	bdl	bdl	bdl	bdl	bdl	bdl	bdl	bdl	bdl	bdl	bdl	bdl	bdl	0.01	-	bdl	bdl
Th	0.00	0.00	0.00	0.00	0.00	0.00	0.00	0.00	0.00	0.01	0.00	0.00	0.00	0.00	0.07	0.05	0.00	0.00
U	0.00	0.00	0.01	0.00	0.00	0.00	0.00	0.00	0.00	0.00	0.00	0.00	0.00	0.00	0.04	0.01	0.00	0.00
Ba	0.01	0.00	0.01	0.00	0.01	0.00	0.07	-	0.01	0.00	0.01	0.00	0.02	0.00	0.01	-	bdl	bdl
Nb	0.01	0.00	0.01	0.00	0.01	0.00	0.01	0.00	0.01	0.00	0.07	0.00	0.07	0.00	0.01	0.00	0.00	0.00
Ta	0.00	0.00	bdl	bdl	0.00	-	bdl	bdl	0.00	-	0.00	0.00	0.00	0.00	bdl	bdl	0.00	0.00
La	0.00	0.00	0.00	0.00	0.00	0.00	0.01	-	0.00	0.00	0.01	0.00	0.01	0.00	0.08	0.03	0.00	0.00
Ce	0.01	0.00	0.01	0.00	0.01	0.00	0.00	0.00	0.01	0.00	0.06	0.00	0.05	0.00	0.19	0.06	0.00	0.00
Pb	0.00	0.00	0.00	0.00	0.00	0.00	0.00	0.00	0.00	0.00	0.00	-	0.00	0.00	0.00	0.00	0.00	0.00
Sr	0.17	0.05	0.15	0.05	0.11	0.03	0.04	0.01	0.10	0.02	0.71	0.07	0.67	0.03	0.25	0.07	0.05	0.01
Pr	0.00	0.00	0.00	0.00	0.00	0.00	0.00	0.00	0.00	0.00	0.01	0.00	0.01	0.00	0.02	0.01	0.00	0.00
Nd	0.02	0.00	0.02	0.00	0.01	0.00	0.01	0.00	0.01	0.00	0.08	0.01	0.08	0.01	0.09	0.02	0.01	0.00
Hf	0.03	0.00	0.03	0.00	0.03	0.00	0.02	0.00	0.02	0.00	0.05	0.00	0.05	0.01	0.02	0.00	0.02	0.00
Zr	0.85	0.04	0.87	0.02	0.85	0.05	0.55	0.02	0.66	0.04	1.87	0.06	1.77	0.08	1.07	0.06	0.65	0.03
Sm	0.01	0.00	0.01	0.00	0.01	0.00	0.01	0.00	0.01	0.00	0.04	0.01	0.04	0.00	0.03	0.01	0.01	0.00
Eu	0.01	0.00	0.01	0.00	0.01	0.00	0.00	0.00	0.00	0.00	0.02	0.00	0.02	0.00	0.01	0.00	0.01	0.00
Gd	0.03	0.01	0.04	0.01	0.03	0.00	0.02	0.01	0.02	0.01	0.06	0.01	0.06	0.01	0.04	0.01	0.03	0.00
Tb	0.01	0.00	0.01	0.00	0.01	0.00	0.01	0.00	0.01	0.00	0.01	0.00	0.01	0.00	0.01	0.00	0.01	0.00
Ti	648	15.9	672	9.90	621	30.3	385	9.31	515	20.7	489	25.5	462	57.4	183	6.38	517	14.6
Dy	0.09	0.01	0.10	0.00	0.09	0.01	0.07	0.01	0.07	0.01	0.10	0.00	0.09	0.00	0.09	0.01	0.08	0.01
Ho	0.03	0.00	0.03	0.00	0.03	0.00	0.02	0.00	0.02	0.00	0.02	0.00	0.02	0.00	0.02	0.00	0.02	0.00
Y	0.80	0.01	0.83	0.01	0.76	0.03	0.65	0.01	0.63	0.03	0.62	0.02	0.59	0.03	0.70	0.02	0.65	0.01
Er	0.12	0.01	0.13	0.01	0.11	0.01	0.10	0.01	0.10	0.01	0.08	0.01	0.07	0.00	0.10	0.01	0.10	0.00
Tm	0.02	0.00	0.02	0.00	0.02	0.00	0.02	0.00	0.02	0.00	0.01	0.00	0.01	0.00	0.02	0.00	0.02	0.00
Yb	0.21	0.01	0.23	0.01	0.20	0.01	0.17	0.01	0.18	0.02	0.11	0.01	0.10	0.01	0.19	0.01	0.19	0.01
Lu	0.04	0.00	0.04	0.00	0.04	0.00	0.03	0.00	0.03	0.00	0.02	0.00	0.02	0.00	0.03	0.00	0.03	0.00
Sc	12.7	0.252	13.0	0.163	12.8	0.688	12.9	0.152	12.7	0.519	16.7	0.575	16.0	0.211	10.8	0.208	12.2	0.160
V	82.4	1.49	84.0	1.16	83.8	3.47	75.3	1.02	79.5	2.95	101.1	3.31	96.4	1.73	62.6	1.21	74.8	1.55
Cr	2103	48.6	2067	32.0	2009	68.5	2057	45.6	2152	83.3	5195	227	4968	65.4	2381	45.1	1999	59.5

Table 3.10: Trace element composition of amphibole

AMP	Wum			
	We1a	std	Ww1a	std
Rb	22.2	0.34	2.54	0.88
Th	17.5	0.37	12.0	0.84
U	2.94	0.09	5.42	0.32
Ba	347	27.5	26.8	6.04
Nb	15.0	0.81	0.46	0.07
Ta	0.07	0.01	0.02	0.00
La	83.0	1.39	13.6	1.59
Ce	112	1.02	17.6	2.97
Pb	2.96	0.06	10.3	0.16
Sr	292	2.57	113	4.35
Pr	8.84	0.20	1.22	0.18
Nd	26.3	0.82	4.57	0.20
Hf	0.88	0.03	0.88	0.02
Zr	46.2	1.04	29.2	0.46
Sm	4.23	0.13	1.76	0.05
Eu	1.49	0.04	0.73	0.03
Gd	3.79	0.07	2.71	0.10
Tb	0.60	0.01	0.50	0.02
Ti	7809	184	13227	967
Dy	3.90	0.10	3.59	0.12
Ho	0.81	0.02	0.81	0.03
Y	21.5	0.26	20.9	0.68
Er	2.33	0.06	2.41	0.09
Tm	0.32	0.01	0.33	0.01
Yb	2.18	0.05	2.30	0.06
Lu	0.30	0.01	0.33	0.01

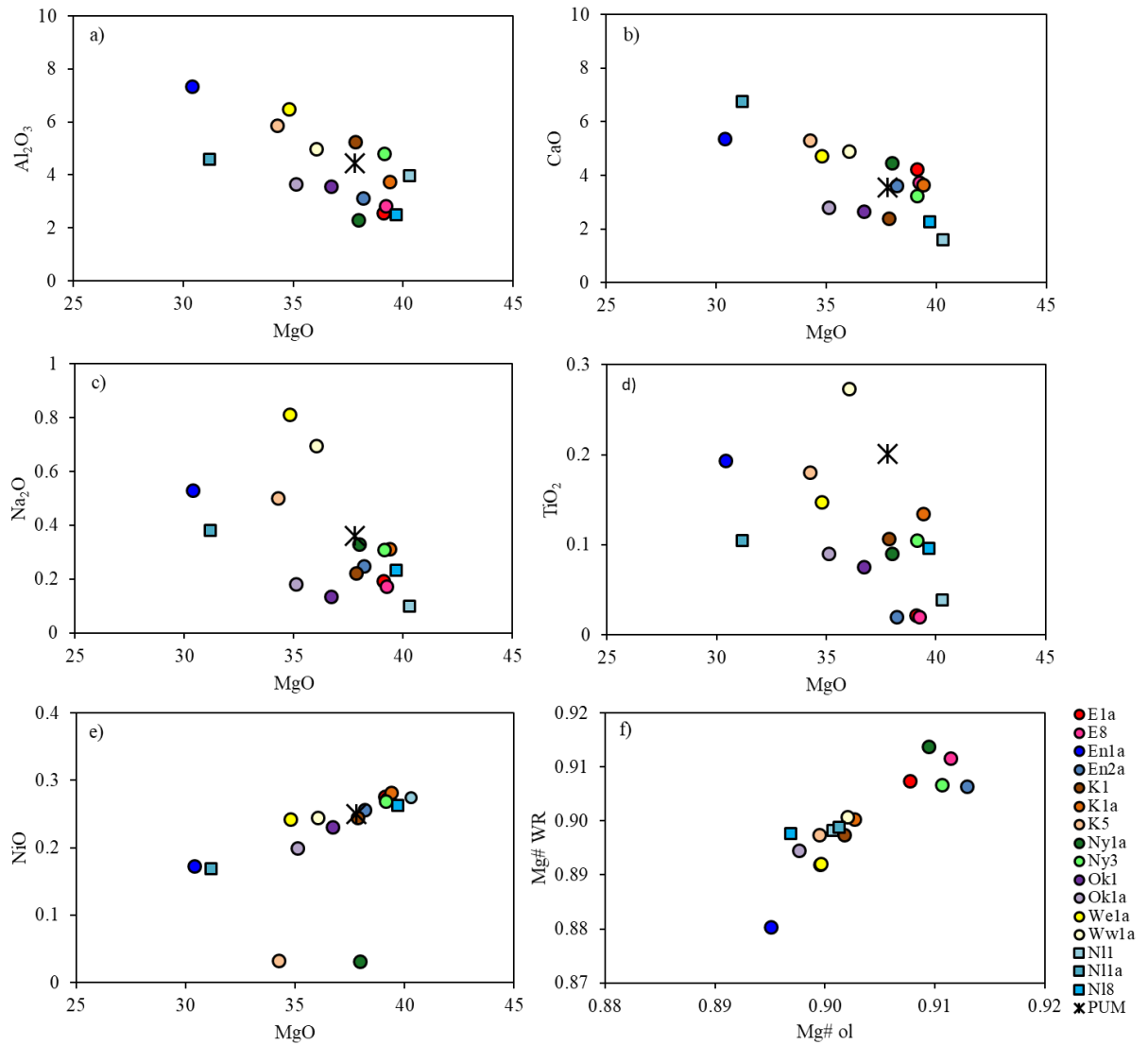


Figure 3.24: Variation of calculated whole rock major elements vs MgO (wt %)

Table 3.11: Whole rock major element (wt. %) compositions of CVL xenoliths calculated by mass balance

Whole Rock	Etome		Enep		Kuk			Nynos		Oku		Wum		Ngaoundere Likok		
	E1a	E8	En1a	En2a	K1	K1a	K5	Ny1a	Ny3	Ok1	Ok1a	We1a	Ww1a	N11	N11a	N18
SiO₂	45.52	46.13	45.08	45.74	45.38	44.04	45.66	47.60	44.06	46.81	48.74	44.02	44.81	44.89	48.19	46.52
TiO₂	0.02	0.02	0.19	0.02	0.11	0.13	0.18	0.09	0.10	0.08	0.09	0.15	0.27	0.04	0.10	0.10
Al₂O₃	2.55	2.81	7.34	3.12	5.25	3.73	5.86	2.29	4.80	3.55	3.65	6.47	4.98	3.96	4.59	2.49
Cr₂O₃	0.78	0.63	3.45	1.86	0.74	0.52	0.79	0.28	0.82	1.92	1.65	1.00	0.64	0.66	2.05	0.21
FeO	7.17	6.87	7.30	6.80	7.68	7.79	7.08	6.56	7.13	7.75	7.40	7.35	7.09	8.04	6.44	8.08
MnO	0.14	0.13	0.17	0.14	0.14	0.14	0.14	0.13	0.13	0.15	0.15	0.14	0.13	0.14	0.15	0.15
NiO	0.28	0.27	0.17	0.26	0.24	0.28	0.03	0.03	0.27	0.23	0.20	0.24	0.24	0.27	0.17	0.26
MgO	39.12	39.24	30.41	38.20	37.86	39.41	34.28	37.99	39.15	36.74	35.13	34.81	36.06	40.29	31.18	39.68
CaO	4.23	3.72	5.36	3.61	2.37	3.65	5.29	4.46	3.22	2.64	2.80	4.71	4.89	1.59	6.74	2.27
Na₂O	0.19	0.17	0.53	0.25	0.22	0.31	0.50	0.33	0.31	0.13	0.18	0.81	0.69	0.10	0.38	0.23
K₂O	-	-	0.01	-	-	-	-	0.01	-	-	0.01	0.09	0.01	-	0.01	-
H₂O	-	-	-	-	-	-	-	-	-	-	-	0.21	0.19	-	-	-
Total	100	100	100	100	100	100	100	100	100	100	100	100	100	100	100	100
Si	0.397	0.401	0.404	0.399	0.398	0.382	0.404	0.415	0.384	0.412	0.429	0.345	0.354	0.391	0.428	0.404
Ti	0.000	0.000	0.001	0.000	0.001	0.001	0.001	0.001	0.001	0.001	0.001	0.002	0.004	0.000	0.001	0.001
Al	0.029	0.031	0.076	0.034	0.053	0.041	0.060	0.027	0.049	0.038	0.039	0.084	0.072	0.041	0.048	0.030
Cr	0.007	0.006	0.023	0.016	0.005	0.005	0.007	0.004	0.007	0.014	0.012	0.008	0.006	0.005	0.015	0.002
Fe²	0.047	0.046	0.050	0.045	0.051	0.051	0.047	0.043	0.047	0.053	0.051	0.111	0.098	0.054	0.043	0.054
Mn	0.001	0.001	0.001	0.001	0.001	0.001	0.001	0.001	0.001	0.001	0.001	0.001	0.001	0.001	0.001	0.001
Ni	0.002	0.002	0.001	0.002	0.001	0.002	0.001	0.001	0.002	0.001	0.001	0.001	0.001	0.002	0.001	0.002
Mg	0.466	0.469	0.377	0.457	0.458	0.469	0.412	0.452	0.467	0.449	0.434	0.325	0.344	0.486	0.384	0.477
Ca	0.048	0.042	0.056	0.040	0.026	0.042	0.057	0.049	0.036	0.028	0.029	0.058	0.060	0.018	0.071	0.025
Na	0.004	0.003	0.010	0.005	0.004	0.006	0.010	0.007	0.006	0.003	0.003	0.025	0.025	0.002	0.007	0.005
K	0.000	0.000	0.000	0.000	0.000	0.000	0.000	0.000	0.000	0.000	0.000	0.003	0.000	0.000	0.000	0.000
H	0.000	0.000	0.000	0.000	0.000	0.000	0.000	0.000	0.000	0.000	0.000	0.038	0.036	0.000	0.000	0.000
Total	1.000	1.000	1.000	1.000	1.000	1.000	1.000	1.000	1.000	1.000	1.000	1.000	1.000	1.000	1.000	1.000
Mg#	0.907	0.912	0.880	0.906	0.897	0.900	0.897	0.914	0.907	0.892	0.894	0.892	0.901	0.898	0.899	0.898

Table 3.12: Whole rock trace element (wt. %) compositions of CVL xenoliths calculated by mass balance

WR	Etome		Enep		Kuk			Nyos		Oku		Wum		Ngaoundere Likok		
	E1a	E8	En1a	En2a	K1	K1a	K5	Ny1a	Ny3	Ok1	Ok1a	We1a	Ww1a	NI1	NI1a	NI8
Th	0.01	0.01	0.00	0.07	0.05	0.04	0.01	0.01	0.01	0.01	0.01	2.64	1.33	0.16	0.03	0.06
U	0.00	0.00	0.00	0.01	0.02	0.02	0.00	0.00	0.01	0.00	0.00	0.44	0.60	0.05	0.01	0.02
Nb	0.10	0.10	0.00	0.38	0.01	0.01	0.01	0.00	0.01	0.08	0.08	1.51	0.06	0.48	0.07	0.07
Ta	0.01	0.01	0.00	0.10	0.00	0.00	0.00	0.00	0.00	0.01	0.01	0.01	0.00	0.02	0.00	0.01
La	0.28	0.35	0.03	0.34	0.11	0.07	0.06	0.02	0.08	0.19	0.20	11.6	1.54	0.83	0.14	0.73
Ce	0.57	0.78	0.12	0.71	0.28	0.17	0.13	0.08	0.19	0.58	0.60	15.6	2.08	1.76	0.30	1.99
Pb	0.00	0.00	0.02	0.02	0.05	0.03	0.01	0.01	0.04	0.00	0.00	0.34	1.15	0.04	0.01	0.02
Sr	2.32	3.26	2.53	0.88	5.69	3.48	2.70	1.84	4.59	8.67	8.98	36.1	15.6	16.8	2.86	14.1
Pr	0.06	0.08	0.03	0.08	0.05	0.03	0.02	0.02	0.03	0.09	0.10	1.24	0.16	0.21	0.04	0.29
Nd	0.18	0.29	0.17	0.32	0.34	0.20	0.14	0.11	0.20	0.50	0.52	3.65	0.68	0.93	0.16	1.52
Hf	0.00	0.01	0.05	0.81	0.10	0.07	0.04	0.03	0.06	0.05	0.06	0.14	0.16	0.25	0.06	0.25
Zr	0.23	0.36	1.42	17.0	2.92	1.95	1.28	0.93	1.72	1.79	1.92	6.50	5.11	13.3	3.34	9.29
Sm	0.02	0.04	0.07	0.07	0.15	0.09	0.06	0.06	0.09	0.14	0.15	0.59	0.28	0.27	0.05	0.43
Eu	0.01	0.01	0.03	0.02	0.06	0.04	0.03	0.02	0.04	0.05	0.05	0.21	0.12	0.14	0.02	0.14
Gd	0.02	0.04	0.10	0.06	0.23	0.15	0.09	0.10	0.13	0.14	0.15	0.53	0.43	0.34	0.07	0.41
Tb	0.01	0.01	0.02	0.01	0.04	0.03	0.02	0.02	0.03	0.02	0.02	0.09	0.08	0.06	0.01	0.06
Ti	124	126	324	162	707	824	463	117	464	263	326	962	2161	452	196	313
Dy	0.04	0.05	0.13	0.07	0.33	0.21	0.13	0.14	0.19	0.12	0.13	0.56	0.58	0.42	0.08	0.35
Ho	0.01	0.01	0.03	0.02	0.07	0.05	0.03	0.03	0.04	0.02	0.02	0.12	0.13	0.09	0.02	0.07
Er	0.04	0.04	0.09	0.05	0.22	0.14	0.09	0.10	0.13	0.06	0.07	0.34	0.40	0.27	0.06	0.19
Tm	0.01	0.01	0.01	0.01	0.03	0.02	0.01	0.01	0.02	0.01	0.01	0.05	0.06	0.04	0.01	0.03
Yb	0.05	0.05	0.09	0.06	0.20	0.14	0.09	0.10	0.13	0.05	0.06	0.33	0.38	0.26	0.06	0.17
Lu	0.01	0.01	0.01	0.01	0.03	0.02	0.01	0.01	0.02	0.01	0.01	0.05	0.06	0.04	0.01	0.02

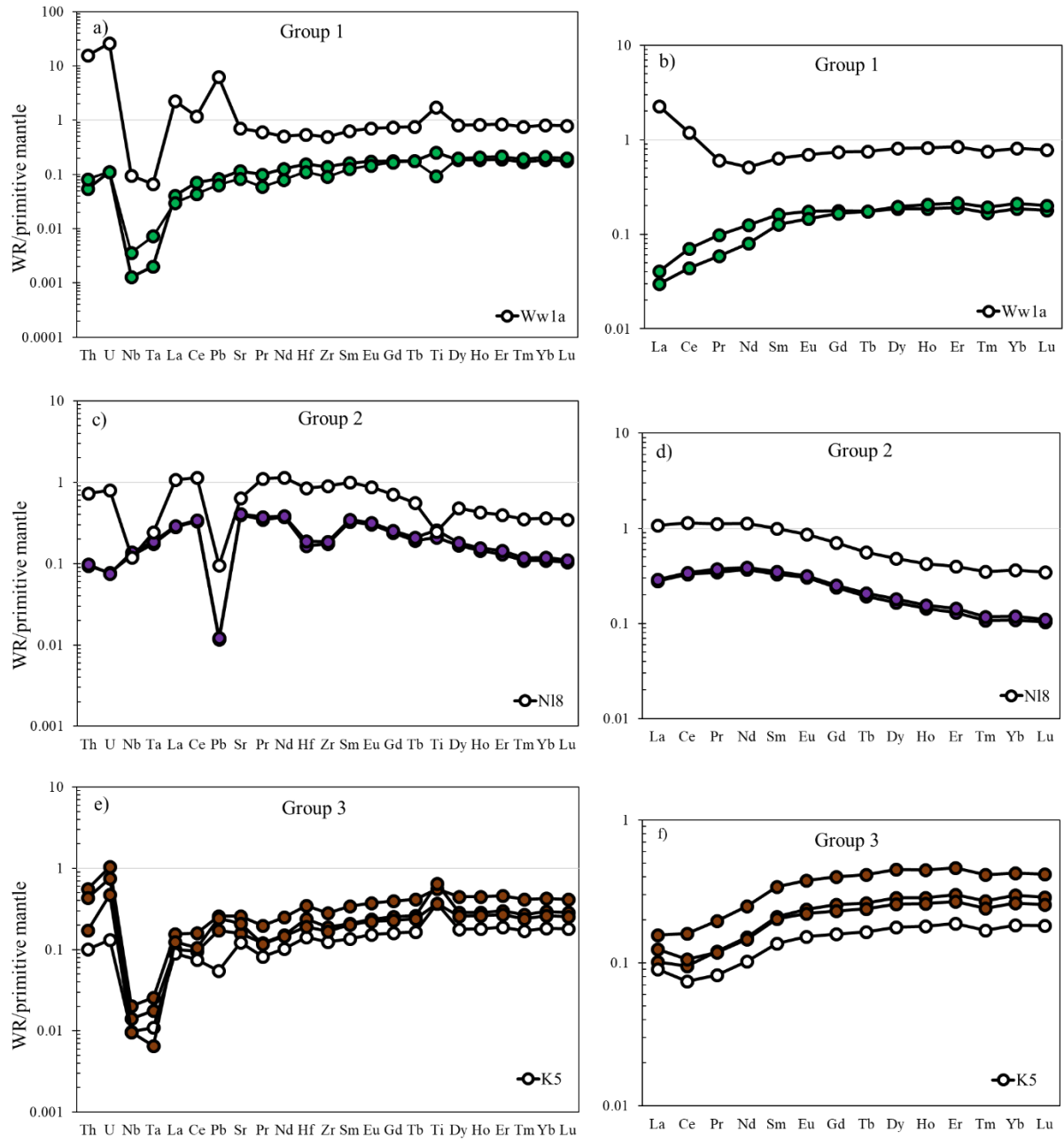


Figure 3.25: Primitive mantle normalized patterns of calculated whole rock compositions of the CVL xenoliths

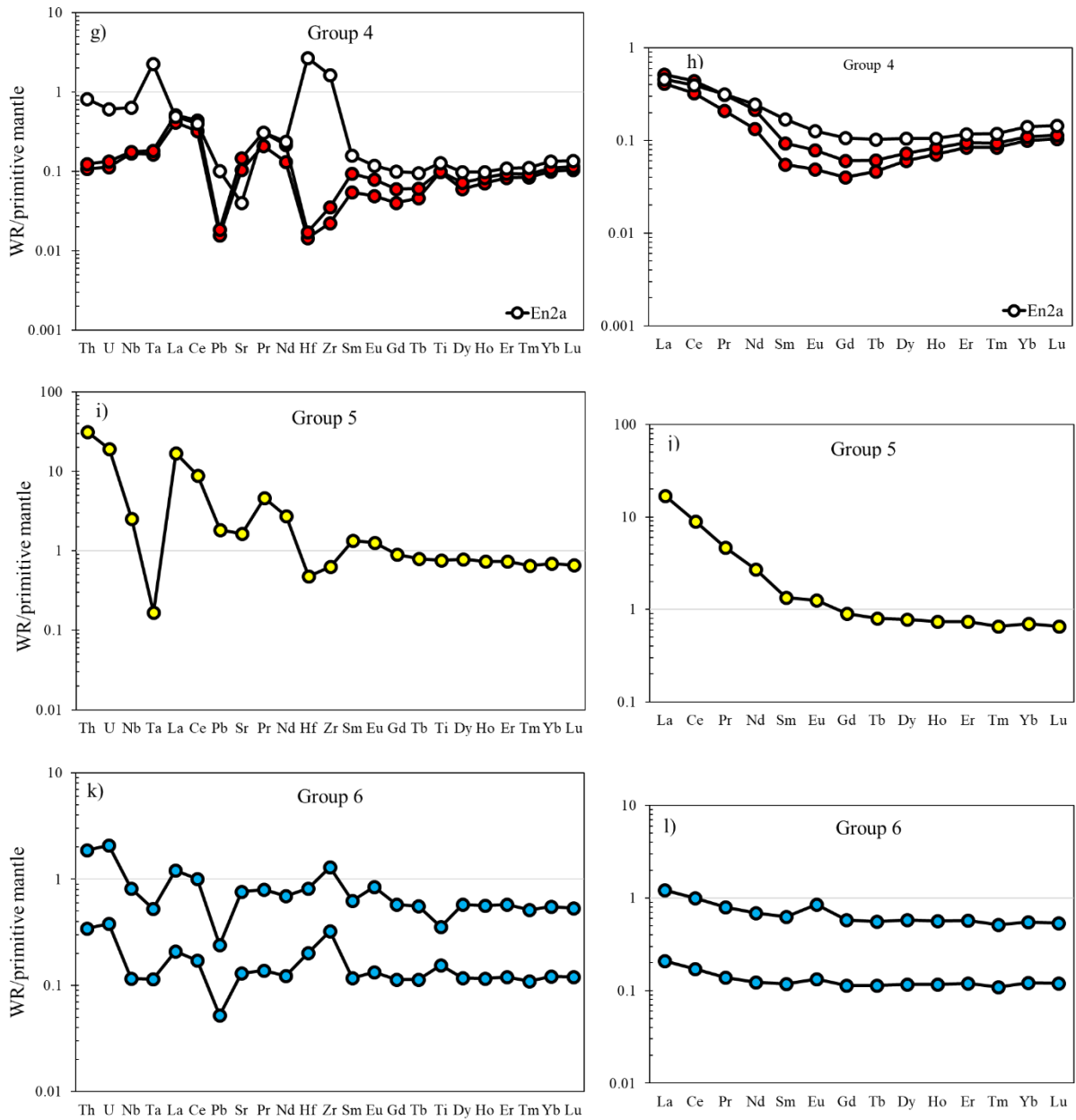


Figure 3.25 cont'd: Primitive mantle normalized patterns of calculated whole rock compositions of the CVL xenoliths.

III.3. DISCUSSION

III.3.1. EQUILIBRIUM CONDITIONS AND OXYGEN FUGACITY

III.3.1.1. Temperatures

The estimation of equilibration temperatures recorded by mineral chemical equilibria in mantle xenolith minerals provide valuable information on the physical state of the upper mantle at the time of entrainment in the host basalt and hence brings in more insights into the thermal evolution of the mantle in different tectonic settings. The chemical composition of the xenoliths can be used in accessing temperature conditions provided applicable coexisting mineral pairs like olivine-spinel and/or clinopyroxene-orthopyroxene are present. However, the reliability of the different geothermometers is highly dependent on the assumption of chemical equilibrium of the components involved in the corresponding exchange reactions. The CVL xenoliths do not show any major intergrain geochemical variability. Even though a few samples show petrographic evidence for perturbation by secondary processes (spongy rims in clinopyroxene in samples En2a, and presence of secondary clinopyroxene in samples En2a, N11a N11), only the core compositions of relatively homogeneous minerals were used in the calculations since they better preserve the initial compositions and influences due to exchange between the coexisting minerals and the host basalts are minimised. Secondary clinopyroxenes, which could be distinguished by their texture (Fig. 3.5 e, f) and mineral composition, were excluded from the calculations. This therefore allowed to assume equilibrium.

Equilibrium temperatures were calculated using the methods of Liang et al., 2013; Brey and Kohler 1990 (Ca in opx); the two-pyroxene thermometers of Wells 1977 and Brey and Kohler 1990; olivine-spinel thermometry of Jianping et al., 1995 and Coogan et al., 2014 and the Al in olivine thermometer of De Hoog et al., 2010. The results are listed in Table 3.12. Since different elements apply to different thermometers and these elements have different diffusional behaviour, the use of several thermometers is essential especially if changes occur within a relatively short geologic time frame. Mantle processes, however, occur over a wide time frame from as short as a couple of years to millennia and therefore the diffusion rates of different elements is important as it enables to capture different events occurring over a wide period of time.

Table 3.12: Calculated equilibration temperatures, and oxygen fugacity conditions for the CVL xenoliths

		TREE	±1s	TBKN1990	TW1977	TJ1995	TC2014	TCa in opx	Std	TAl in ol	Std	$\Delta \log f_{O_2}$ FMQ
Group 1	En1a	946	16	930	910	1100	1060	945	9	936	4	-1.01
	Ny1	872	43	870	880			922	7	878	7	
	Ww1a	860	31	850	850	880	900	860	33	846	2	-5.17
Group 2	Nl8	1032	30	1050	990			1018	7	986	5	
	Ok1	1187	20	1150	1100	990	1180	1157	10	1104	4	-0.68
	Ok1a	1075	18	1140	1080	1120	1200	1164	9	1102	1	0.09
Group 3	K1	922	23	930	920	940	1070	958	32	1029	8	-1.02
	K1a	950	12	960	940	920	1010	942	27	1032	9	-0.86
	K5	913	16	950	920	980	1120	939	21	982	11	-1.34
	Ny3	886	13	950	920	950	1110	925	11	932	8	-2.16
Group 4	E1a	976	65	810	860	1000	1010	959	6	894	7	-2.43
	E8	940	20	920	930	930	1000	951	4	892	4	-2.28
	En2a	894	47	870	870	890	990	918	8	872	5	-3.08
Group 5	We1a	930	33	960	910	940	1010	925	22	962	9	-1.58
Group 6	Nl1	–	–	890	950	960	930	964	6	909	7	-4.05
	Nl1a	937	25	925	980	1060	1060	956	7	904	8	0.01

TREE: REE thermometry of Liang et al., 2013

TBKN1990: Opx–cpx thermometer of Brey and Kohler, 1990

TW1977: Two-pyroxene thermometer of Wells, 1977

TJ1995: Ol–spl thermometry of Jianping et al., 1995

TC2014: Ol–spl thermometry of Coogan et al., 2014

TCa in Opx: calcium in opx thermometer of Brey and Kohler, 1990

TAl in Ol: Aluminium in ol thermometer of De Hoog 2010

The equilibria between the major components of spinel peridotites are not pressure sensitive (Kohler and Brey 1990), making the estimation of pressure conditions challenging. Since there is no direct method of determining equilibrium pressures for spinel facies mantle xenoliths, and no garnet or plagioclase was present, they were constrained mineralogically to the spinel stability field (8-18 kbars; O'Neil, 1981) and the pressure value of 15 kbars was used in temperature estimations. The two-pyroxene thermometer of Brey and Kohler 1990 based on the exchange of Fe and Mg (enstatite component) between orthopyroxene and clinopyroxene is insensitive to the presence of minor Fe³⁺ (all Fe was considered as Fe²⁺). Temperatures obtained using this geothermometer vary between 850-930°C for group 1 clinopyroxenes. Group 2 clinopyroxenes show the highest temperatures ranging from 1050-1150°C and group 3 ranges from 930-960°C. Group 4 samples show temperatures ranging from 890-950°C, group 5 from 810-920°C and group 6 is at ~ 960°C. The two-pyroxene geothermometer of Wells, 1977 based on the exchange of Fe and Mg in pyroxenes do not show any correlation with calculated Fe³⁺ from microprobe data (McGuire, 1988) (ie the thermometer is sensitive to Fe³⁺/Fe²⁺ ratio of clinopyroxene). Temperatures calculated using this thermometer are in agreement with the TBKN 1990 (Fig. 3.26a). They range from 850-910°C for group 1 clinopyroxenes, 990-1080°C for group 2, 920-950°C for group 3, 960-980°C for group 4, 860-930°C for group 5 and ~910°C for group 6.

Temperatures were calculated with the olivine-spinel thermometry of Jianping et al., 1995 which is an improved calibration of the method of Fabries, 1979 and the thermometer of Coogan et al., 2014. These thermometers are based on the equilibrium exchange of Mg²⁺ and Fe²⁺ between coexisting spinel and olivine and on the temperature dependence of Al exchange between olivine and Cr-spinel respectively. The two thermometers yielded similar values, however, temperatures from Coogan et al., 2014 are generally higher than those from the Jianping et al., 1995 method except for the group 4 samples (TJ1995: 960-1060°C; TC2014: 930-1060°C) where the opposite is observed or the temperatures overlap. Group 1 clinopyroxenes show considerable temperature variations (880-1100°C) and group 2 clinopyroxenes show higher temperatures (TJ1995: 990-1120°C; TC2014: 1180-1200°C). Group 3 and 5 show a narrow temperature range (TJ1995: 920-980°C; TC2014: 1010-1120°C and TJ1995: 890-1000°C; TC2014: 990-1010°C) respectively. Group 6 shows similar temperatures to groups 3 and 5 (TJ1995: ~940°C; TC2014: 1010°C).

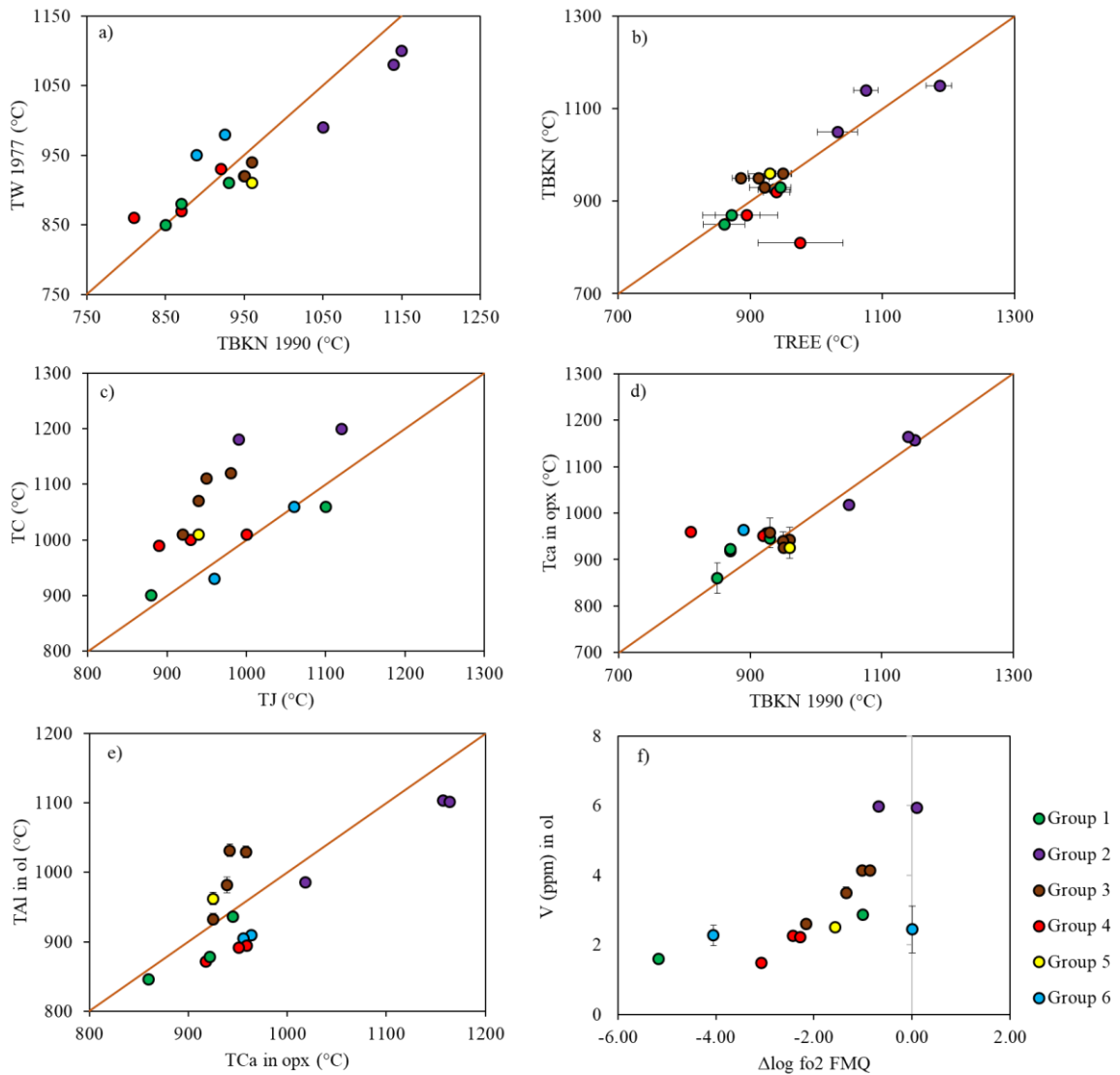


Figure 3.26: Comparison of equilibrium temperatures calculated using different methods. (a) Two-pyroxene thermometer of Wells, 1977 versus Opx–cpx thermometer of Brey and Kohler, 1990. (b) Opx–cpx thermometer of Brey and Kohler, 1990 versus REE thermometry of Liang et al., 2013. (c) Ol–spl thermometry of Coogan et al., 2014 versus Ol–spl thermometry of Jianping et al., 1995. (d) Calcium in opx thermometer of Brey and Kohler, 1990 versus Opx–cpx thermometer of Brey and Kohler, 1990. (e) Aluminium in ol thermometer of De Hoog 2010 versus Calcium in opx thermometer of Brey and Kohler, 1990 and f) Vanadium concentrations in ol versus oxygen fugacity.

The Al in olivine geothermometer of De Hoog et al., 2010 gives temperatures that are in the same range as the other thermometers. Groups 2 (986-1104°C) and 5 (872-894°C) show the highest and lowest temperatures respectively. Groups 3 and 4 show temperatures of 846-936°C; 932-1032°C and 904-909°C respectively. Group 6 (~962°C) shows identical temperatures to group 3.

The Ca in orthopyroxene thermometer of Brey and Kohler 1990, based on the solubility of Ca in orthopyroxene yielded consistent temperatures. Group 2 orthopyroxenes show the highest temperatures (1020-1160°C). Groups 1, 3 and 5 temperatures range from 920-950°C, while groups 4 and 6 range from 950-960°C.

Generally, all temperatures calculated with different thermometers show a good correlation especially those which, are based on the same mineral pairs (Fig. 3.26b-d). The two-pyroxene thermometer agrees well with the olivine-spinel thermometers although slightly higher temperatures were obtained from the olivine-spinel thermometers for most samples.

The diffusion rate of major and trace elements in pyroxenes is relatively slow compared to olivine (Muller et al., 2013; Dohmen et al., 2010a). A consensus on the rates at which different elements diffuse in olivine has not been met (eg. Cherniack 2010, Splander and O'Neil 2010). This is probably due to the diverse diffusion mechanisms in olivine, however, the most consistent elements from which diffusion have been obtained through numerous experimental studies include Fe, Mg, Ca, Ni and Mn (Dohmen and Chakraborty 2007; Holzapfel et al. 2007; Coogan et al. 2005; Petry et al. 2004). Generally, Fe-Mg diffusion between olivine and spinel (O'Neill and Wall, 1987; Dohmen & Chakraborty, 2007) is an order of magnitude faster than Ca and Mg-Fe exchange in pyroxenes (Brey and Kohler, 1990; Muller et al., 2013). Al diffusion in olivine is slow and so thermometers which are based on the exchange of Al between olivine and spinel give more reliable peak temperatures (De Hoog et al., 2010; Coogan et al., 2014). REE exchange between pyroxenes is the slowest (Liang et al., 2013). The fast diffusing elements are therefore reset during a fast reheating while the slow diffusing elements retain the ambient mantle conditions. The different thermometers show consistent results, which means that the thermal regime was stable for a long period of time for both the slow and fast diffusing elements to reach

equilibrium. The thermometer of Liang et al., 2013 based on the temperature dependence of REE exchange between coexisting ortho- and clinopyroxenes was then used to evaluate temperatures obtained from the other thermometers and the equilibrium conditions. Equation 1 ($\ln D_i^{\text{opx/cpx}} = A_i + B_i/T$) is applied to calibrate $D_i^{\text{opx/cpx}}$ as a function of temperature, where A_i and B_i are coefficients from partitioning experiments between pyroxene and melts and i is the element ionic radius. The plot of $\ln(D_i^{\text{opx/cpx}} - A_i)$ vs B_i defines a line that passes via the origin and the slope in this plot obtained through a least square inversion of the REE partitioning data defines equilibrium temperatures. REE and Y of group 2 samples (Nl8 and Ok1) fall on the regression line that passes through the origin (Fig. 3.27a) which indicates that the coexisting pyroxenes are well equilibrated. Sample Ok1a shows only very minor deviation of LREEs. This group shows the highest REE temperatures which range from 1030-1190 °C and are consistent with temperatures calculated from the two pyroxenes thermometers (1140-1150°C) (Fig. 3.26b). Samples from groups 1, 3, 5 and 6 show evidence for perturbation by secondary processes as their LREEs fall off the regression line (Fig. 3.27b). The temperatures obtained fall in a narrow overlapping; they range from 860-946°C, 886-950°C, 894-976°C and ~930°C for clinopyroxene groups 1, 3, 4 and 5 respectively. Sample Nl1 (group 6) shows REEs which significantly deviate from the regression line (Fig. 3.27c) indicating that all elements were affected by secondary processes (a temperature effect). The group 4 clinopyroxene group shows only slight deviations of the HREEs from the regression line (Fig. 3.27d) except for sample E8 with very minor LREE disturbance. This shows the involvement of processes, which affects the HREEs. In general, all the samples show temperatures, which are consistent with the two pyroxene thermometers except for sample Nl1 which completely falls off the regression line and E1a which shows evidence for secondary processes which affected the HREEs.

The Oku samples are distinct from the others by their relatively high temperatures (Table 3.12). However, the temperatures are similar, which indicates that they experienced a prolonged reheating before they were brought to the surface. Since their compositions do not drastically differ from the other samples, we cannot assume a completely different genetic process. They show temperatures that are similar to temperatures from other regions of the CVL (e.g Tedonkenfack et al., 2021; Njombie et al., 2018; Liu et al., 2017; Pinter et al., 2015; Nkouandou and Temdjim, 2011).

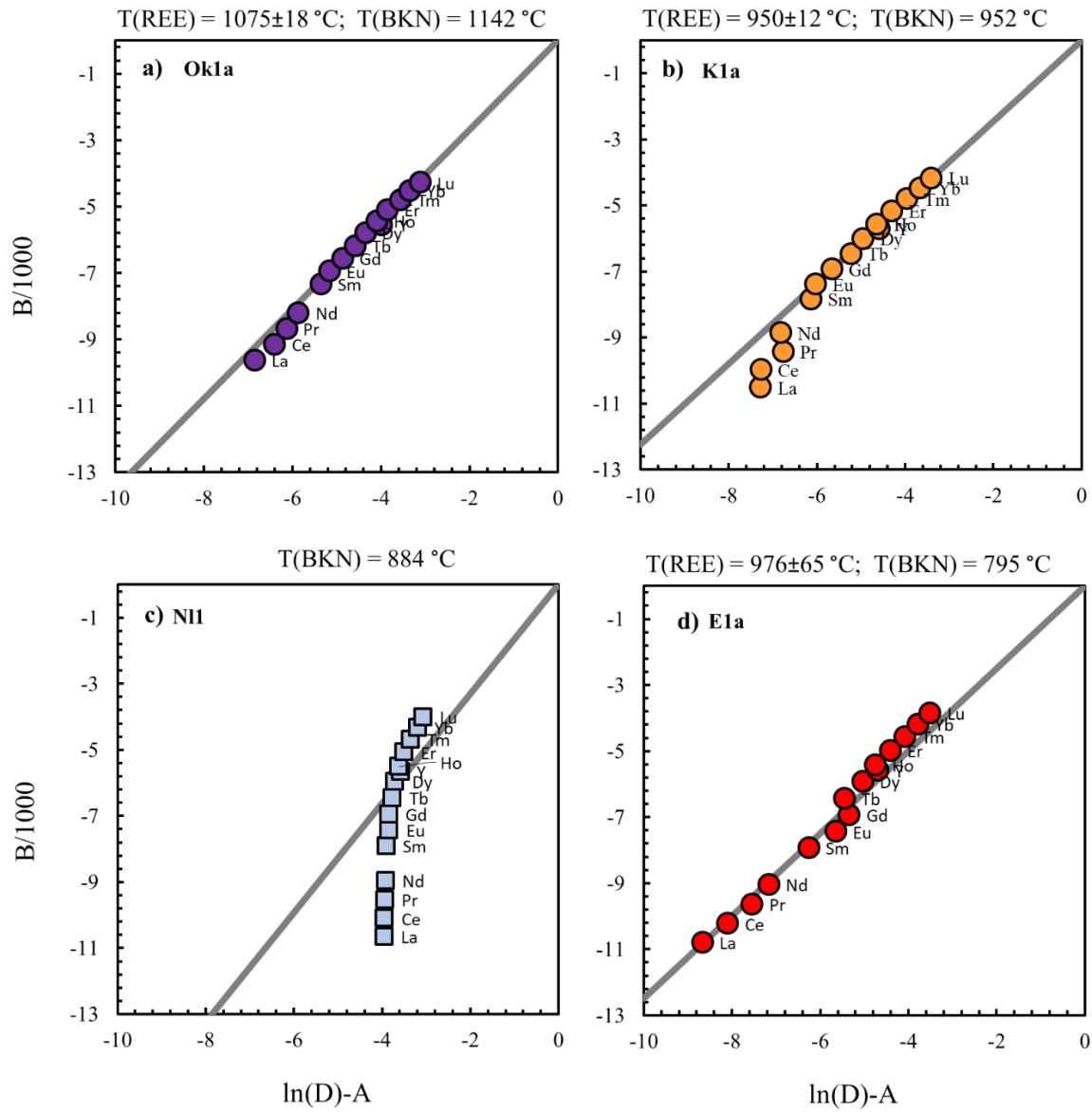


Figure 3.27: Inversion diagram for the calculation of equilibrium temperatures (Liang et al., 2013) based on the temperature dependence of REE partitioning between orthopyroxene and clinopyroxene.

Considering the low equilibrium temperature for the other samples, we assume that they are not residues of the partial melting event that generated the magma that transported them to the surface (i.e. they are not petrogenetically related). This implies that the processes, which affected the xenoliths are older than the melt. This is supported by the deformation texture (kink bands) of the xenoliths and exsolution lamellae of clinopyroxenes in orthopyroxenes. This exsolution texture occurs when the host orthopyroxene loses its stability due to cooling at low temperatures before the xenolith is ripped off by the melt and thus, they do not represent the melt source. The xenoliths, therefore, provide information on the lithospheric mantle of the CVL but not on the source rocks of the melt. Based on their textures and geothermometry, they likely derive from a similar P-T region with the possible exception of the Oku samples which show evidence for a deeper provenance.

III.3.1.2. Intermineral partition coefficients

Mineral pair partition coefficients of orthopyroxenes and clinopyroxenes have been obtained for CVL xenoliths. The prerequisite to obtain relevant partition is chemical equilibrium, therefore evaluating from the REE in 2-pyroxene thermometer of Liang et al., 2013, only well-equilibrated samples were used for this purpose. Group 2 samples (Ok1, Ok1a and N18) fit this condition, as they do not show any deviation from the regression line that passes through the origin (Fig. 3.27). Also, major and trace elements show very minor inter or intra grain variability which supports equilibrium. Trace element equilibrium is therefore assumed for these samples and two pyroxene partition coefficients (KD) are calculated. They are shown in Fig. 3.28. The opx/cpx partition coefficients for the CVL are >1 and generally fall in the same range as those calculated for other regions (Witt-Eickeschen and O'Neill, 2005). Clinopyroxene shows more enrichment, REE show a gentle downward trend from HREEs to MREEs. HFSE (Hf, Zr, Nb, Ta, Ti) show positive anomalies relative to the REEs. The HREEs are less incompatible in orthopyroxene than the LREEs. Additionally, Pb is also less compatible in orthopyroxene than Ce and Sr.

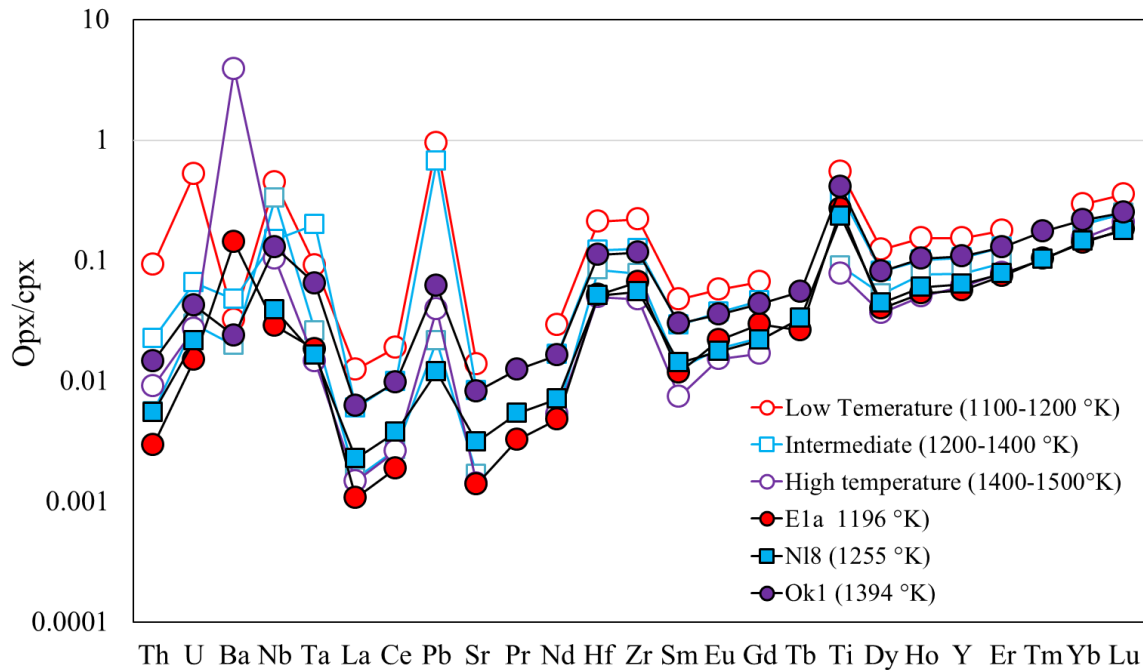


Figure 3.28: Orthopyroxene-clinopyroxene partition coefficients for samples NI8, E1a and Ok1 compared with partition coefficients of well equilibrated xenolith samples from Witt-Eickeschen and O'Neill, 2005.

III.3.1.3. Oxygen fugacity

Oxygen fugacity in the mantle is a measure of the amount of oxygen available to react with elements like carbon and iron and it controls several parameters, which are very useful in the interpretation of mantle processes. Iron is the most abundant and important redox-sensitive element in the mantle which, exists in both oxidized (Fe^{3+}) and reduced (Fe^{2+}) states, and hence, together with temperatures control the oxygen fugacity of the upper mantle. Oxygen fugacity was estimated using the method of Ballhaus et al., 1991 which is based on the reaction:



where Fe_2SiO_4 , $\text{Fe}_2\text{Si}_2\text{O}_6$ and Fe_3O_4 are the fayalite in olivine, ferrosillite in orthopyroxene and magnetite in spinel components. Spinel $\text{Fe}^{3+}/\Sigma\text{Fe}$ ratios were determined from EPMA measurements by assuming ideal stoichiometry of the spinel phase. Temperatures calculated

with the method of Jianping et al., 1995 were used and pressures were assumed to be at 15 kbars.

The fO_2 values of the CVL peridotites show reducing conditions ranging from 0.09 to $-2.28 \Delta_{\text{units}}$ relative to the FMQ (Fayalite-Magnetite-Quartz) buffer (Table 3.12) and they do not show any correlation with the Cr number of spinel. Note that a few samples show very unrealistic values (-3.08 to -5.17). This very low fO_2 in samples N11, En2a and Ww1a are unrealistic and they can be attributed to the limitations of this method at very low Fe^{3+} concentrations. The wide range of fO_2 values is also concordant with mantle heterogeneity under overall reduced conditions, especially when compared to MORB and arc mantle. A positive correlation of fO_2 with the V contents in olivine (Fig. 3.26f) is observed. Vanadium is a multivalent element (V^{2+} , V^{3+} , V^{4+} , V^{5+}) but occurs as V^{3+} and V^{4+} in terrestrial fO_2 values (Borisov et al., 1987): Its multivalent nature shows that its geochemical character is dependent on fO_2 and so can be used as a proxy for oxidation state in mantle peridotites. Vanadium changes from compatible to incompatible with increasing fO_2 .

III.3.2. MANTLE DEPLETION AND MELTING MODEL

The main indicators of partial melting are spinel Cr#, Al_2O_3 in clinopyroxene and Mg# in olivine. The olivine forsterite contents and spinel Cr# increase during partial melting whereas Al_2O_3 contents in pyroxenes decrease (Arai, 1994; Hellebrand et al., 2001). The studied xenoliths show a wide range of compositions on the olivine-spinel mantle array (OSMA) of Arai 1994 and appear to have experienced between 0-20% of partial melting (Fig. 3.29a). Most samples (groups 4 and 5) fall at the low end and correspond to melting of ~5% (except E8, which is at ~8%). Samples Ww1a (group 1) and N11 (group 6) also belong to this group. Sample E1a (group 4) shows higher Cr# and corresponds to ~12% of melting. The rest of the samples have Cr# of 0.37-0.40 and show up to ~18% of partial melting.

The Cr# vs TiO_2 plot (Fig. 3.29b) for spinel efficiently distinguishes between partial melting and melt-rock interactions (Pearce et al., 2000), and the results are consistent with the OSMA plot (Fig. 3.29a), however, some samples show TiO_2 contents which are much higher than expected for spinel with Cr# of 0.37-0.40. According to the model of Pearce et al., 2000, TiO_2 contents should be <0.1 wt % for spinel Cr# generated through partial

melting. This shows that the samples from group 2 (Ok1 and Ok1a) and group 6 (N11) have experienced modifications in their compositions through interaction with Ti-rich melts (Gamal El Dien et al., 2019; Pearce et al., 2000). Inversely, samples En1a (group1) and En2a (group 4) also show high Cr# (0.37-0.39) but their TiO₂ (0.01 wt %) contents are low, indicating that they were not affected by secondary processes.

The quantification of partial melting was also estimated using the methods of Hellebrand et al., 2001 and De Hoog et al., 2010 which are based on the Cr# of spinel and olivine respectively. The results obtained are listed in Table 3.13. Most of the samples show consistency between the two methods except for samples En1a and N11a, which show 14%,15% for the Hellebrand et al., 2001 method and 0%, 7% for the De Hoog et al., 2010 method respectively. The very moderate degrees of partial melting from the Hellebrand method could be a result of chemical changes in spinel during interactions with infiltrated melts. Textural evidence is shown by the centripetal replacement of clinopyroxene by spongy rims in sample En1a and reaction rims in sample N11a (Fig. 3.5a, b).

The partial melting process is expected to deplete the SCLM in incompatible major elements like Al as well as incompatible trace elements (REEs) while elements like Mg preferentially remain in the residue. However, there is a lack of correlation between the REEs and the Al₂O₃ contents of the samples.

To further evaluate the effects of partial melting, a simple non-modal fractional partial melting model based on clinopyroxene and orthopyroxene REEs (Figs. 3.30, 3.31) was applied to the xenoliths. The measured data for these silicate phases were compared to the modelled trace element budgets and the extent of partial melting extrapolated from HREE compositions as they are commonly unaffected by metasomatism.

The method is based on the application of a nonmodal fractional equation (Johnson et al., 1990) to a starting composition which comprises chemical parameters (DMM source composition from Workmann and Hart 2005, mineral and melting modes from Johnson et al., 1990, and element/mineral melt partition coefficients ($D^{\text{cpx/melt}}$ for REE (Hart and Dunn, 1993), $D^{\text{cpx/melt}}$ for Pr, Eu, Gd, Tb, Ho, Tm (Ionov et al., 2002) and $D^{\text{opx/melt}}$, $D^{\text{ol/melt}}$, $D^{\text{spl/melt}}$ (Ionov et al., 2002 and references therein). Results obtained from orthopyroxene REEs are consistent with the degree of partial melting obtained from the De Hoog et al., 2010 method

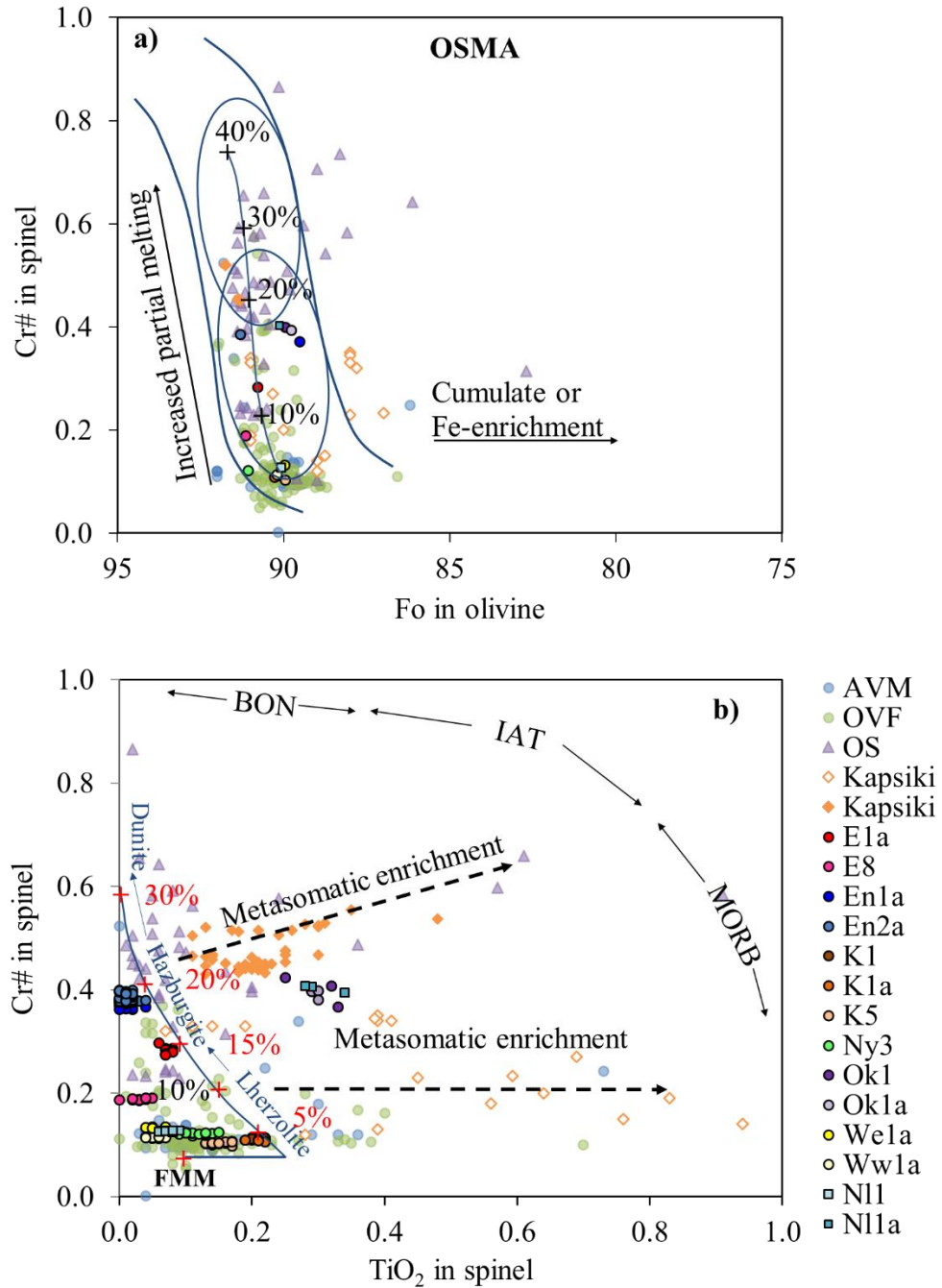


Figure 3.29a: Plot of Cr# in spinel versus Fo in olivine for the studied xenoliths compared to Cameroon Volcanic Line olivines. The olivine-spinel mantle array (OSMA) and melting trend are from Arai 1994; b) Cr# in spinel versus TiO₂ in spinel. AVF: Adamawa Volcanic Field (Temdjim, 2019; Njombie et al., 2018; Nkouandou et al., 2015; Lee et al., 1996); OVF: Oku Volcanic Field (Tedonkenfack et al., 2021; Liu et al., 2020; Liu et al., 2017; Pinter et al., 2015; Temdjim, 2012; Lee et al., 1996); OS: Oceanic sector (Caldiera et al., 2002; Lee et al., 1996). Closed symbols for Kapsiki are from this study (chapter 2) while the open symbols are from Tamen et al., 2015.

in all samples. Clinopyroxene yielded lower partial melting degrees (Fig. 3.30, 3.31) than the orthopyroxene except for samples from groups 1 (En1a), 2 (Ok1, Ok1a, N18) and 3 (K1, K1a, K5), which show consistency in the two phases.

Major and trace element compositions together with modal proportions of mantle xenoliths from the CVL show that the SCLM below the region has experienced melt extraction to various extents through partial melting.

Table 3.13: Partial melting values (in %) estimated from the methods of De Hoog et al., 2010 (Cr# in ol), Hellebrand et al., 2001 (Cr# in sp) and modeling of clinopyroxene and orthopyroxene REEs.

Samples		Cr# Ol	Cr# Spl	Opx REEs	Cpx REEs
Group 1	En1a	0	14	0-5	0
	Ny1a	6	-	5	0
	Ww1a	6	2	5	0
Group 2	Ok1	12	15	10	10
	Ok1a	13	15	10	10
	N18	3	-	0	0
Group 3	K1	2	2	0-5	0
	K1a	3	2	0-5	0
	K5	2	1	0-5	0
	Ny3	5	3	5	0
Group 4	E1	9	11	10	5-10
	E8	9	7	10	5-10
	En2a	14	14	15	10
Group 5	We1a	7	4	5	0
Group 6	N11	7	3	5	0
	N11a	7	15	5	0

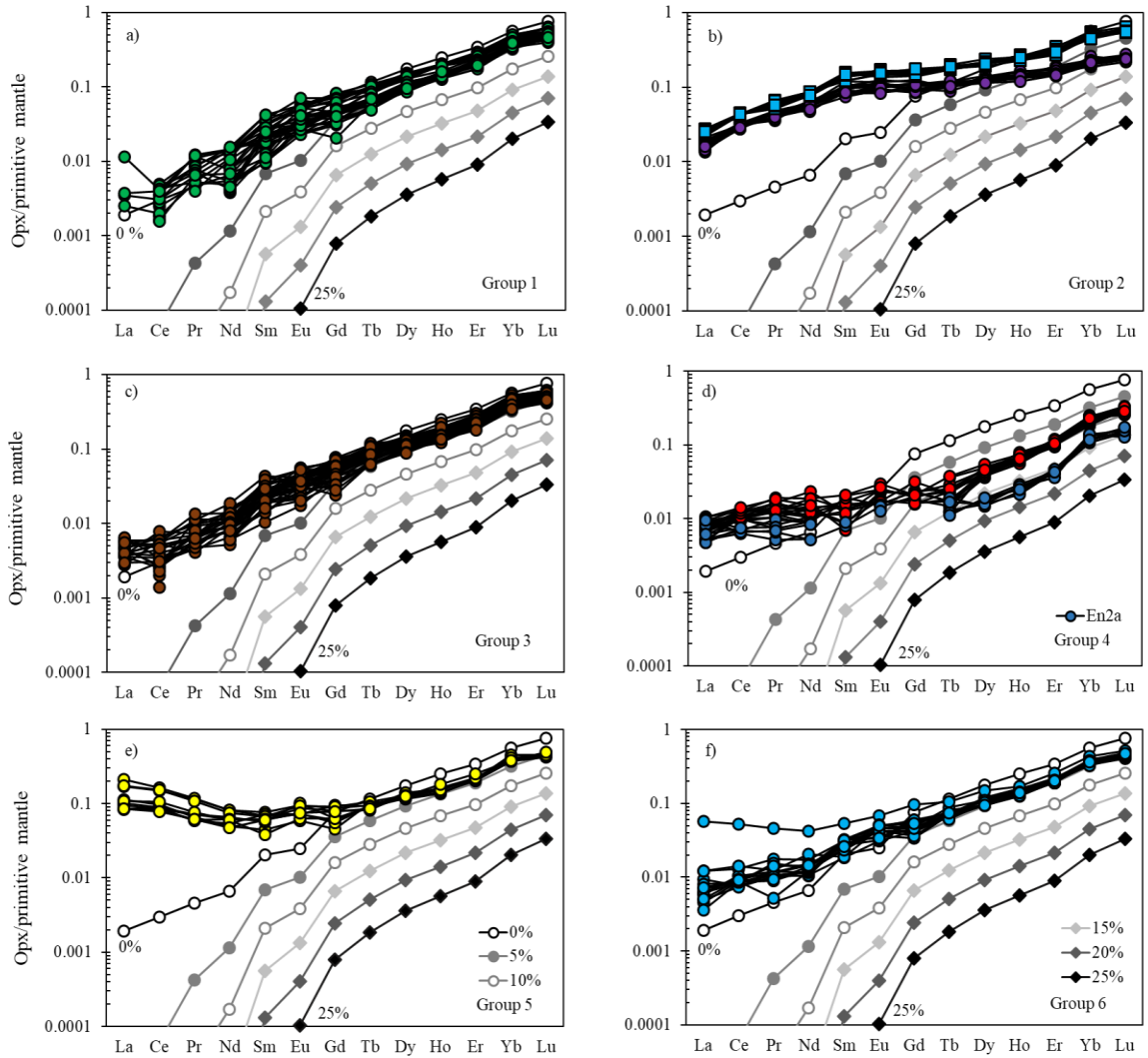


Figure 3.30: Fractional partial melting model of orthopyroxene trace elements compared to CVL orthopyroxene REE data (from this study).

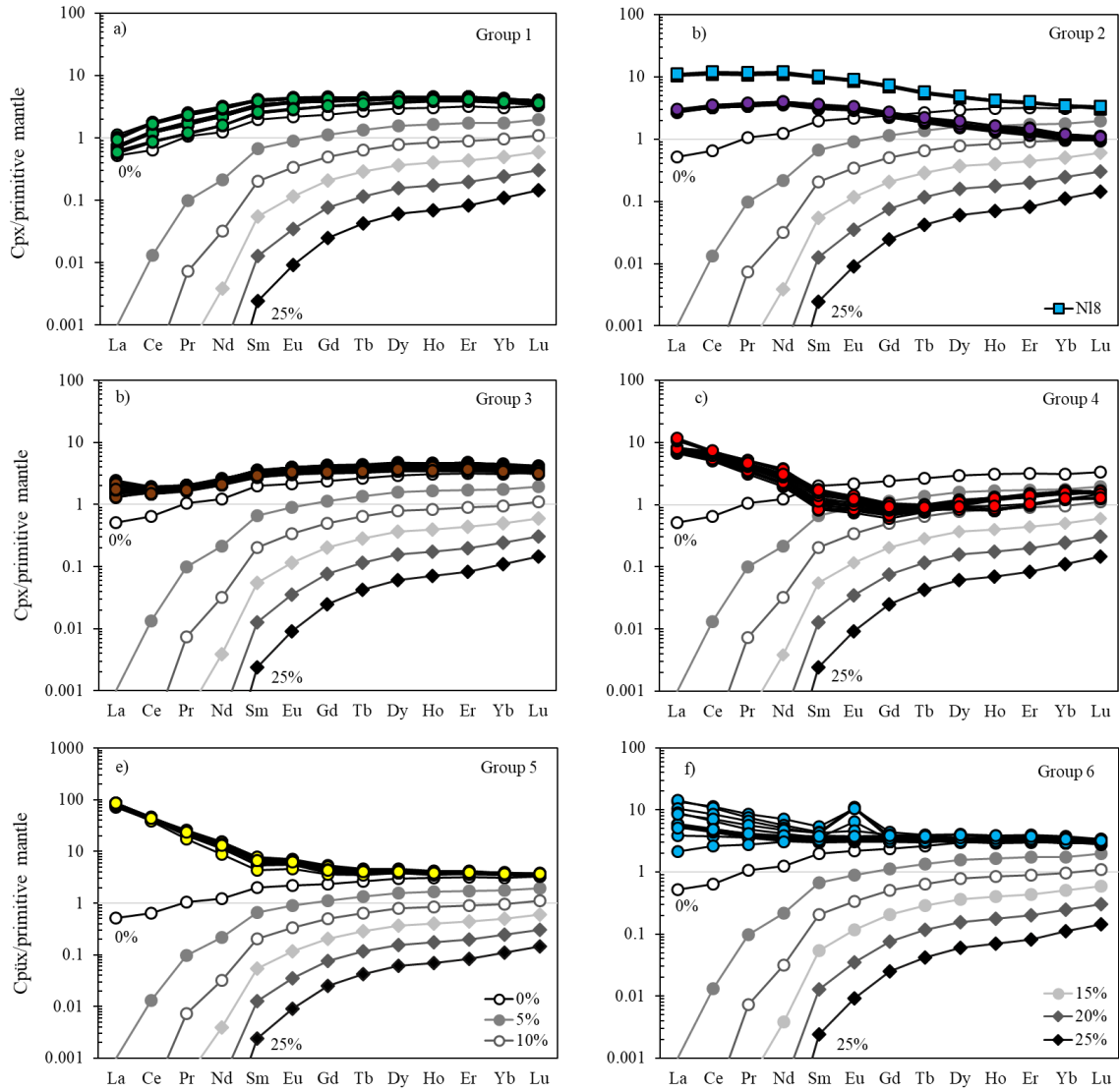


Figure 3.31: Fractional partial melting model of clinopyroxene trace elements compared to CVL clinopyroxene REE data (from this study).

III.3.3. METASOMATIC PROCESSES BASED ON CLINOPYROXENE AND AMPHIBOLE TRACE ELEMENTS

Mantle metasomatism has been defined as the physical and chemical changes which occur in the mantle during percolation of fluids and melts resulting in textural modifications, recrystallization, formation of new mineral phases and chemical transformation leading to the enrichment of mantle peridotites in incompatible trace elements (REEs, HFSEs and LILEs). Three main types of metasomatism have been identified (O'Reilly and Griffin, 2012) and include modal (introduction of new types of minerals); cryptic (chemical modification of existing phases without the addition of new phases) and stealth metasomatism (addition of minerals that already exist in the peridotite e.g clinopyroxene and garnet). Melt and fluid sources have been widely debated and suggested to originate from within the lithospheric mantle, convecting asthenospheric mantle, deep mantle plumes or subducted oceanic lithosphere (Beccaluva et al., 2001; Churikova et al., 2001, Downes et al., 2001).

Clinopyroxenes (e.g. Witt-Eickschen and O'Neil 2005; Zangana et al., 1999) and amphiboles are the main repository for volatiles and incompatible trace elements in the mantle and as such have efficiently been used to trace mantle processes. The CVL xenoliths show both textural and geochemical evidence of mantle metasomatism. Evidence of modal metasomatism (Ionov and Hofmann, 1995; Yaxley et al., 1991; Bodinier et al., 1988) is shown by the presence of the secondary hydrous phase amphibole in interstitial position in samples We1a and Ww1a, which indicates that they formed at a later stage than the coexisting minerals (Lee et al., 1996). Texturally, they show a close spatial association with spinel (Fig. 3.3c, 3.8a, b, c), which suggests that an Al-poor fluid/melt reacted preferentially to produce amphibole at locations where there was the supply of Al (Njombie et al., 2018) or conversely, this might also be caused by the preferential infiltration of melt along spinel grain boundaries because of surface energy constraints (Schafer and Foley, 2002). Stealth metasomatism is evidenced by the presence of secondary clinopyroxene in sample En2a. The modal proportion of clinopyroxene in a primitive mantle is ~19%, however, partial melting of 25% equates to the consumption of clinopyroxene leaving a residue of olivine, orthopyroxene and spinel (Walter, 2003). The high modal proportions of clinopyroxenes in almost all samples (15-30%) (table 3.2) is indicative of secondary enrichment processes

considering that the SCLM below the region has undergone partial melting to a certain extent.

Cryptic metasomatism is the most pervasive type and it is common in all studied samples. This is shown especially by LREE enrichment patterns (eg samples E1a, E8, En2a, We1a) (Fig. 3.18) and accompanying enrichment in other incompatible trace elements like Th, U, Zr and Hf. Furthermore, Al_2O_3 is moderately incompatible during partial melting (Herzberg, 2004; Walter, 2003) and therefore its concentration can also shed more light on metasomatic processes. The studied xenoliths generally show very high Al_2O_3 (up to averages of 5 wt% in orthopyroxene and 7 wt% in clinopyroxene) (Tables 3.4 and 3.5) compositions, which is inconsistent with mantle melting and indicates refertilization.

Be that as it may, the idea of the interaction of fluids/melts with a depleted mantle is not always a straightforward process but can also involve multiple stages of depletion and enrichment episodes. A simple example is seen in the REE patterns where some of the LREE enriched samples have lower concentrations of HREEs than those which show depleted LREE patterns (Fig. 3.18). We, therefore, discuss the processes which may lead to such interactions, with a special interest on the nature of metasomatism, the composition of the metasomatising fluid/melt and their provenance.

Host basalt-xenolith interactions and infiltration can create effects that are identical to mantle metasomatism (Miller et al., 2012; Wang et al., 2012; Scambelluri et al., 2009; Shaw et al., 2006). It is therefore imperative to first identify and evaluate the extent of such reactions in order to correctly interpret mantle processes.

III.3.4.1. Origin of spongy textures and secondary clinopyroxene

The occurrence of spongy/sieve textures in clinopyroxene is not uncommon but its origin is controversial and has been associated to different processes. It is therefore very important to understand how these microstructures were formed so as to correctly interpret upper mantle processes which occurred before and during the transportation of the xenoliths by the host basalt to the surface. Spongy textures in mantle xenoliths have been attributed to:

- Metasomatism by fluid/melt infiltration post entrainment by host basalt to the surface (Bonadiman et al., 2008; 2005; Carpenter et al., 2002).
- Incongruent dissolution of clinopyroxene by a Si and alkali-rich melt formed from the interaction of primary orthopyroxene and the host magma during transport. In this case, the reacted minerals are concentrated towards the xenolith-host basalt interface (Shaw and Dingwell, 2008; Shaw et al., 2006).
- Partial melting caused by pressure release during the ascent processes (Pan et al., 2018; Su et al., 2011; Ionov et al., 1994).

The spongy rims of clinopyroxenes from the CVL show higher CaO contents relatively to the unreacted cores. Generally, the trace element patterns of the spongy rims are similar to the unreacted clinopyroxene cores, even though they show higher concentrations (Fig. 3.20). Additionally, the proportions of Al^{IV} and Al^{VI} can be used to obtain the relative pressure conditions of the different clinopyroxene generations (Wass, 1979). It should however be noted that while they efficiently distinguish the pressure conditions of different clinopyroxene generations, they cannot provide an accurate estimation of the actual pressures. The higher Al^{VI} and Al^{VI}/Al^{IV} ratio for the unreacted cores, together with the lower Na₂O contents of the spongy rims is concordant with a lower pressure environment, further supporting a decompression process (e.g Ma et al., 2015). Primary orthopyroxene is void of any reaction textures and their boundary with the coexisting minerals is sharp.

For some samples, however, e.g. We1a and N18, there is evidence for interactions with the host basalt rock. The host basalt-xenolith interface is not sharp and the pyroxenes in direct contact with the host basalt show a reaction corona. In sample N18, tiny clinopyroxenes are growing at the rims of primary orthopyroxene (Fig. 3.4a). There is also a preferential concentration of the hydrous mineral amphibole, in close association with spinel towards the host basalt xenolith interface. Based on textual evidence, we can assume that the amphibole formed at an early stage followed by subsequent decompression induced melting of clinopyroxene and melt infiltration during transport to the surface. Reaction rims are common around the spinel and clinopyroxenes close to the host basalt, which is also a

strong indicator of infiltration of the host basalt. However, changes in chemical composition are limited to the rim area of the minerals (generally less than 20 μm) (Fig. 3.11).

III.3.4.2. Nature of metasomatism

The metasomatic nature can be constrained from trace element patterns of clinopyroxenes. The different clinopyroxene groups give insights into the chemical composition of the fluids/melts involved during metasomatism and or they represent the variable effects of the percolating fluids which interact with the peridotite wall rock (Uenver-Thiele et al., 2017; Ionov et al., 2002; Navon and Stolper 1987). A range of metasomatic signatures can therefore be produced from a single metasomatic agent depending on the distance from the source through reactive flow. The CVL xenoliths, represent a gradation from unmetasomatised to strongly metasomatised xenoliths.

Groups 1 and 3 clinopyroxenes have depleted LREE signatures which are coherent with melt extraction (Fig. 3.18a, e). Slight La and Ce enrichment are observed in group 3 clinopyroxenes (Fig. 3.18e). Group 1 is identical to patterns observed in unmetasomatised orogenic peridotites and characteristic of depleted MORB mantle (Bodinier and Godard, 2003). This group, therefore, represents the initial composition of the SCLM before the onset of metasomatic processes which start to reveal in group 3 and consequently become more pronounced in the other groups. Plots of La/Ce vs Nd/Yb and Th/U vs Nd/Yb (Figs. 3.21e and f) are below PM values or are just slightly above as in the case of La/Ce in group 3. These samples are considered to be located far enough from the metasomatic source to not witness any metasomatic enrichments (Uenver-Thiele et al 2017; Ionov et al., 2002).

Spoon-shaped patterns (group 4) indicate that the sample has undergone partial melting (Navon and Stolper, 1987) and subsequent enrichments by small melt infiltration which could be carbonatitic, mafic silicate or both (Marchev et al., 2017). In such samples, varying degrees of chromatographic effects are common (Fig. 3.18g, h). Group 3 clinopyroxene patterns show enrichments in La and Ce which can be attributed to the enrichment by small volume melts enriched in these elements relative to the other LREEs. Samples that show convex patterns (groups 5 and 6) reflect direct crystallization of melts in an open system which is supported by extremely high LREE concentrations in

clinopyroxenes (eg sample We1a). This kind of pattern can also be attributed to a state of equilibrium with LREE depleted silicate or non-silicate melts (Fan et al., 2000). Convex upwards patterns (group 2) depict equilibrium with LREE enriched melts (Xu and Bodinier 2004; Bodinier et al., 1988; Navon and Stolper 1987) and stipulate secondary melt infiltration processes post partial melting or as in the case of group 1, could indicate equilibrium with a melt that is enriched in HREE but has lower Nb and LREEs (Ionov et al., 2002).

Samples We1a (group 5) and Ww1a (group 1) both have substantial amounts of amphibole (9-10 wt %). These amphiboles show different trace element patterns, compared to each other and to their corresponding clinopyroxenes. Both samples show identical HREEs and MREEs but the clinopyroxene LREEs of the We1a sample show strong enrichments (Fig. 3.18i) while Ww1a is very depleted (Fig. 3.18a). This means that conversely as previously thought, the presence of amphibole is not directly related to the metasomatic intensity in the coexisting phases (Uenver-Thiele et al., 2017). Clinopyroxene trace element patterns of the two samples can be explained by the reactive flow model, but the process of amphibole crystallization is not identical as further confirmed by the difference in Nb concentration in both samples (higher for We1a samples) (Table 3.10). Both samples show identical degrees of partial melting, therefore, the presence of amphibole in the group 1 clinopyroxene samples does not tie with the reactive flow model since amphibole is expected to crystallize close to the metasomatic source or areas where equilibrium with the initial melt is obtained (Uenver-Thiele et al., 2017; Ionov et al., 2002). No other samples contain amphibole, and the lack of amphibole especially in group 1 clinopyroxene samples suggests that the metasomatic type is not linked to the presence of amphibole (Uenver-Thiele et al., 2017) and may represent two different processes.

A series of plots (Fig. 3.32) have been developed using trace element concentrations in clinopyroxene to distinguish between different tectonic settings (Nformidah et al., submitted). Different tectonic environments have fluids/melts that characterize them. Plots of La_N versus Nd_N and Sr_N versus Nd_N (Figs. 3.32c, e) clearly distinguish between clinopyroxenes from intraplate settings and those from Abyssal peridotites. The CVL clinopyroxenes do not however show any clear association with the clinopyroxenes from subduction zone peridotites.

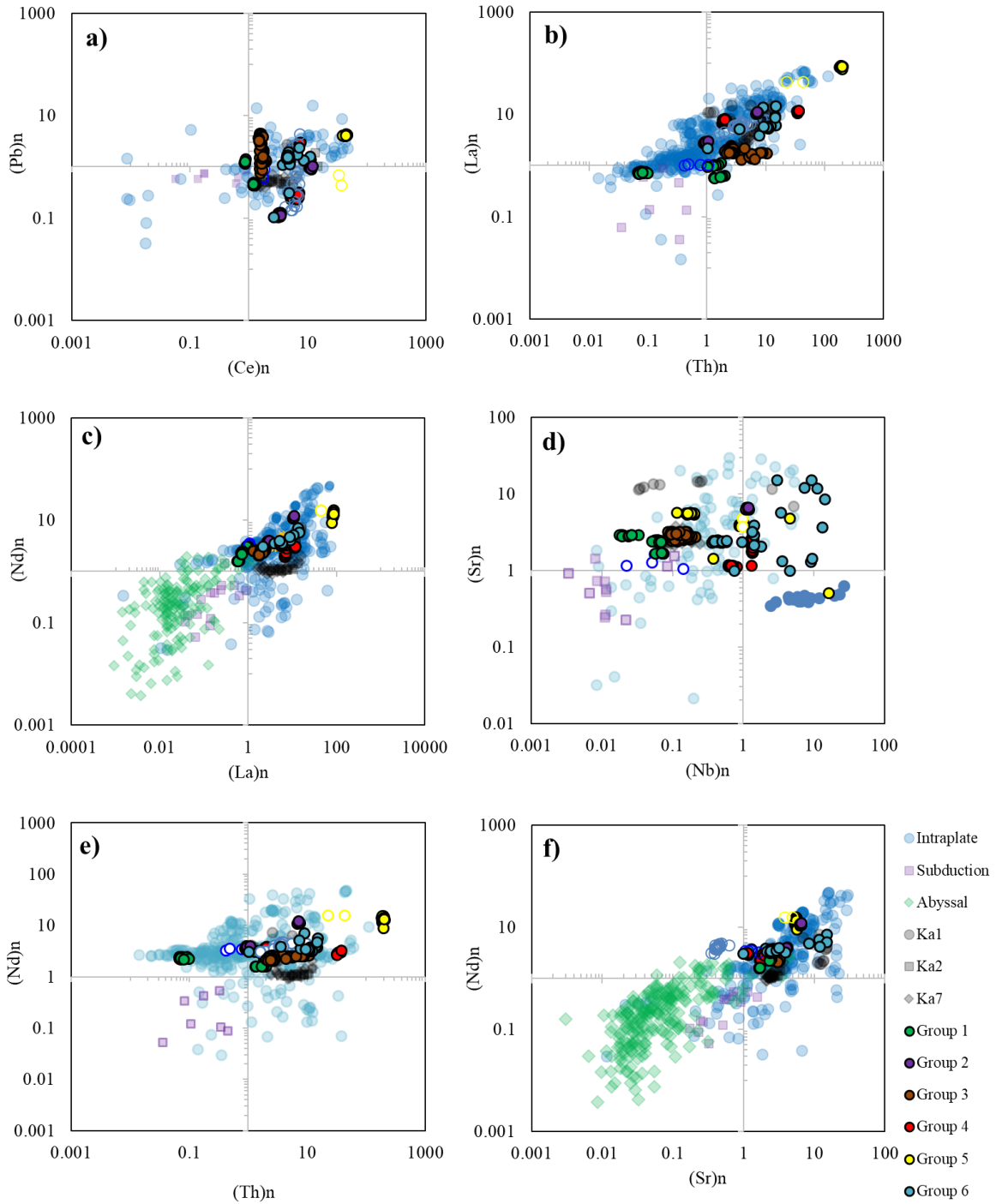


Figure 3.32: Trace element plots of clinopyroxenes compared to literature data from intra plate (Unenver-Thiele et al., 2017; Scott et al., 2016; McCoy et al., 2015; Scott et al., 2014a), subduction (Bernard and Ionov 2013; Tollan et al., 2017) and Abyssal settings (Waren, 2016). Values are normalized to primitive mantle values of Palme and O’Neill 2014.

III.3.4.3. Metasomatising agents

Mantle metasomatism has been ascribed to fluids of different compositions, which include (alkaline) basaltic melts (e.g. Gregoire et al., 2010, 2009; Coltorti et al., 2007; Ionov et al., 1999; Witt-Eickschen et al., 1998; Zanetti et al., 1996; Bodinier et al., 1990), alkaline or Fe–Ti-rich fluids or melts (e.g. Kalfoun et al., 2002; Gregoire et al., 2000a; Ionov, 1998), carbonatitic melts (Tschegg et al. 2012; Downes, 2001; Gorrying and Kay 2000; Grégoire et al. 2000; Coltorti et al. 1999; Yaxley et al. 1998; Yaxley and Green 1996; Klemme et al. 1995;; Schiano et al. 1994; Hauri et al., 1993; Ionov et al., 1993; Rudnick et al. 1993; Dautria et al., 1992; Green and Wallace, 1988) and subduction-related fluids or melts (e.g. Coltorti et al., 2007; Gregoire et al., 2001; Zanetti et al., 1999).

Multiple metasomatic processes and metasomatic overprinting however often makes it difficult to directly decipher these fluids/melts. Trace element ratios have been effectively used to differentiate between the different melt/fluid types. We, therefore, discuss the characteristics of the different metasomatic fluids/melts as they have unique signatures.

III.3.4.3.1. Alkaline vs carbonatite metasomatism

Alkaline silicate melts are commonly generated in the interior of tectonic plates. They are common in islands in oceanic basins and intracontinental tectonic settings. They form from the melting of metasomatic amphibole rich veins in the lithosphere (Pilet et al., 2008). These metasomatic veins crystallize from small low degree melts, which originate in the seismic low-velocity zone (Pilet et al., 2008). The interaction of these melts with peridotites in the mantle gives rise to melts of a large compositional spectrum ranging from basanites to alkali basalts.

Alkaline silicate melts are characterized by strong enrichments in LREEs (Zangana et al., 1999) and low abundances of Nb, Zr, Hf and Ti (Vannucci et al., 1998). Additional enrichment in Sr, Ba, K, Th and U reflect enrichment by this melt type (Zangana et al., 1999). Together with $(La/Yb)_N$, Ti/Eu ratios can be used as indicators of silicate versus carbonatite metasomatism (Klemme et al., 1995; Rudnick et al., 1993). Ti/Eu ratios are generally not affected by partial melting, therefore lherzolites and hazburgites are expected to retain the primitive mantle values (7740), however, interactions with carbonatites significantly lower Ti/Eu ratios. High Ti/Eu (>1500) ratios and low $(La/Yb)_N$ (<3–4) have been attributed to

metasomatism by silicate melts (Coltorti et al., 1999). The different clinopyroxene groups show well-defined patterns. Groups 1 and 3 fall in the silicate metasomatism field alongside group 2, they have Ti/Eu values, which are higher than values of clinopyroxene (except for sample Ny1a) in a primitive mantle assemblage rather reflecting variable degrees of partial melting (Uenver-Thiele et al., 2017). The high Ti/Eu ratios are a result of enrichment in Ti as compared to Eu. Group 6 shows a wide range of compositions, which go from the silicate to the carbonatite field boundary, a few grains which fall out of this domain, are those, which show positive Eu anomalies in their REE patterns. Group 4 also shows a wide range of composition where samples E1a and E8 do not fall in any of the fields and has been interpreted to represent the composition of two pure end-member fluids/melts in varying proportions or carbonated silicate melts. Sample En2a shows pure carbonatite compositions while the secondary cpx (En2a-sec) plots in two distinct fields showing both the silicate and carbonatite end members. The group 5 clinopyroxenes also show carbonatite compositions with few grains in the field of mixed melts. Textural evidence for the presence of silicate melt inclusions supports the presence of hydrous silicate melts in sample En1a (group 1) while the spongy textures around the clinopyroxene can be attributed to partial melting caused by pressure release during ascent processes (Pan et al., 2018; Su et al., 2011; Ionov et al., 1994).

Discrimination plots of Zr/Hf versus Ti/Eu (Fig. 3.33c) show a good correlation with the ratios used in discriminating the different tectonic settings as the CVL clinopyroxenes plot away from the subduction field. They mostly fall within the fields of carbonatite-silicate melts for groups 2, some 4 and 5 like the samples from Kapsikis while the groups 1, 3, some of groups 4 and 6 are clustered in the silicate metasomatism domain. Compared with xenoliths from the French Massif Central (FMC), they show similarities in terms of metasomatism by carbonated silicate and silicate melts but differ in that the FMC xenoliths show additional evidence for metasomatism by subduction-related fluids.

Carbonatite melts have low viscosity (Dawson et al., 1990), high trace element contents (Nelson et al., 1988) and can easily transport LILEs and REEs and fractionate them from HFSE, which makes them effective metasomatic agents (Green and Wallace, 1988; Yaxley et al., 1998; Rudnick et al., 1993). Carbonatite melts are more enriched in moderately

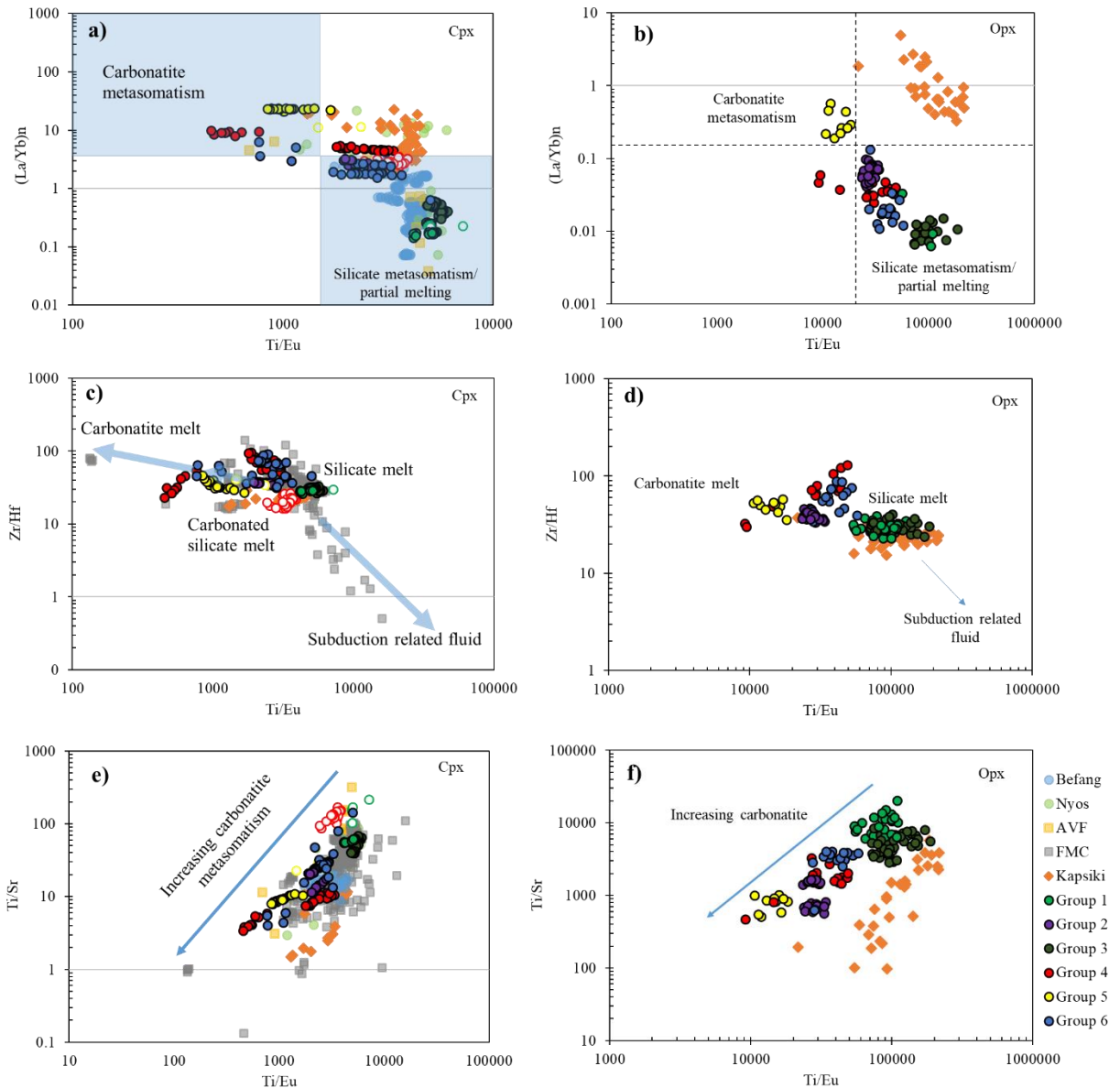


Figure 3.33 (a, b): Plots of Ti/Eu vs chondrite normalised (McDonough and Sun, 1995) La/Yb in clinopyroxenes and orthopyroxenes in the studied xenoliths compared to the Kapsiki pyroxenes (Nformidah et al., submitted), fields for carbonatite and silicate metasomatism are from Coltorti et al., 1999. The distribution of the different fields in clinopyroxene was used to infer an equivalent classification field for carbonatite and silicate metasomatism in orthopyroxene. (c, d, e, f). Plot of Ti/Eu vs Zr/Hf and Ti/Sr vs Ti/Eu in clinopyroxenes and orthopyroxenes. For clinopyroxenes, comparisons are made with xenoliths from the French Massif Central (FMC) (Uenver-Thiele et al., 2017) and other localities along the Cameroon Volcanic Line (Tendonkenfack et al., 2021; Liu et al., 2020; Liu et al., 2017; Nkouandou and Temdjim 2011).

to highly incompatible trace elements (Rb, Th, U, Ba, Sr, K, Cs, LREEs), Eu and are depleted in HFSEs (Zr, Hf, Ti, Nb, Ta) when compared to silicate melts (Liu et al., 2019; Dasgupta and Hirschmann, 2006; Lenoir et al., 2000). They are also characterized by high La/Yb, Ca/Al, Zr/Hf and low Ti/Eu ratios (Rudnick et al., 1993). Carbonatite melts generally originate from either the upwelling asthenosphere or recycling sedimentary carbonates (Grassi and Schmidt, 2011; Hoernle et al., 2002). Those related to subduction are characterized by the enrichment of water-soluble elements and depletion of HFSEs while those generated from the asthenosphere show no negative Nb or Ta anomalies. Additionally, high $(La/Yb)_N$ (>3-4) together with low Ti/Eu (<1500) ratios have been interpreted to result from interactions with a carbonatite melt (Coltorti et al., 1999; Rudnick et al., 1993) and this has therefore been used to discriminate carbonatite type from silicate type metasomatism. A sample from group 4 (En2a) and group 5 show high $(La/Yb)_N$ (>3-4) and low Ti/Eu (<1500) ratios which fall in the field defined for carbonatite metasomatism. Group 5 sample shows very steep LREE patterns accompanied by positive Th, U and negative Ta, Zr and Ti anomalies (Fig. 3.18j), which all correspond to indices of carbonatite metasomatism. The presence of amphibole with high Nb contents further supports this. Even though sample En2a falls in the field of carbonatite metasomatism, it shows geochemical characteristics (very high Zr and Hf) which cannot be explained for by this type of metasomatism. This is an uncommon feature for clinopyroxene in spinel peridotites, but it has been reported elsewhere (Kovács et al., 2004; Kilian et al., 2002) and accounted to for by low degree melt of unknown composition or a HFSE-rich (slab components) fluid generated from an upwelling depleted asthenosphere. The unusual enrichment in Zr and Hf in sample En2a has been attributed to a SiO₂-Na₂O-Al₂O₃ rich magma termed adakite (Coltorti et al., 2007) produced by melting a hydrous crust (Rapp et al., 1999). Sample En2a shows petrographic evidence for a convecting asthenospheric mantle origin.

Additionally, clinopyroxenes metasomatised by melts of carbonatite composition have been shown to have low Ti/Sr ratios which range from 1-5 (Scott et al., 2014; Norman, 1998). Clinopyroxenes from the CVL show a wide range of values between 1-200. Groups 1 and 3 show the highest values while groups 4, 5 and some of group 6 show the lowest values. This shows a good correlation with plots of $(La/Yb)_N$ versus Ti/Eu (Fig. 3.33a) where these samples fall in the carbonatite metasomatism domain.

III.3.4.3.2. Subduction-related metasomatism

The composition of amphibole is useful in constraining the conditions linked to its formation in the SCLM (Liptai et al., 2017; Coltorti et al., 2007). It has been suggested that volatile bearing minerals are formed as a result of reactions with either K₂O-rich, H₂O- or F- bearing subduction-related silicate (Szabo and Taylor, 1994) but can however have diverse provenance (Pilet et al., 2011). Trace element systematics have been efficiently used to differentiate between amphiboles formed in an intraplate environment from those formed in supra subduction environments (Coltorti et al., 2007). Ratios of Nb to HFSE (Ti, Zr, Hf) have been used since Nb is easily retained in subducting slabs and therefore occurs in low concentrations in subduction-related melts (Schmidt et al., 2004; Foley et al., 2000). Higher concentrations of Nb can be found in intraplate magmas, which come from the old subducted slab (Rudnick et al., 2000; Fitton, 1993; McDonough, 1991). Two samples from this study are amphibole bearing (Sample Ww1a in group 1 and We1a in group 5) and they fall within two distinct groups; the We1a samples fall in the overlap of the intraplate and subduction environment while the Ww1a corresponds to the supra subduction environment (Fig. 3.34). The We1a sample shows strong enrichment in amphibole MREEs to LREEs, while the Ww1a is enriched in only the LREE to a lesser extent relative to the former. This suggests that the Ww1a samples represent ancient metasomatic activities that were linked to subduction during the Pan-African orogeny, while the We1a metasomatism might be linked to more recent Cenozoic volcanic activities, which lead to the formation of the CVL. Texture evidence of alteration (melting) at the rims of amphibole and clinopyroxene indicates that they were initially formed in the supra subduction environment just like the Ww1a samples but later experienced enrichments by intraplate melts (Liptai et al., 2017).

This is seen in the wide range and generally lower Al₂O₃ and Na₂O contents (Fig. 3.12) of the spongy clinopyroxene rims relative to the core composition. The parallelism in clinopyroxene and amphibole REE patterns in sample We1a suggests that the former also underwent metasomatism by the same fluids (Liptai et al., 2017). The melt responsible for the crystallisation of amphibole in sample We1a is the same that enriched LREEs as shown by REE patterns, while in sample Ww1a, the amphibole forming fluid did not seem to affect the clinopyroxene. Samples from Kuk and Nyos (Ny3) also show slight positive Pb

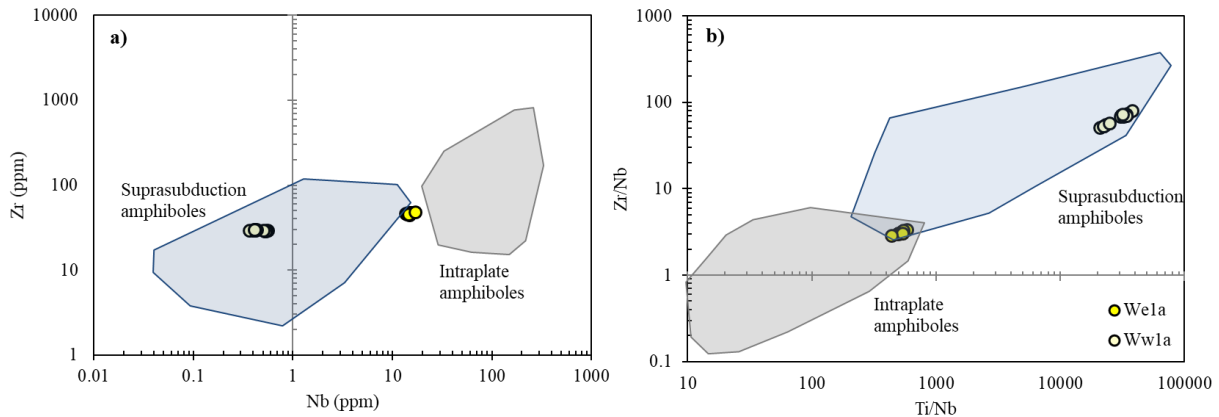


Figure 3.34: Nb vs Zr (a) and Ti/Nb vs Zr/Nb (b) for amphiboles in the CVL xenoliths. Fields for suprasubduction and intraplate origins are from Coltorti et al. (2007).

anomalies in their clinopyroxene trace element patterns, which represents relics of an ancient subduction event.

Though amphibole is absent in most of the studied xenoliths, they have however been reported in spinel lherzolites, websterites, wehrlites and pyroxenites for several localities along the CVL (eg. Mt. Cameroon: Deruelle et al., 1998; Mt Bambouto: Marzoli et al., 2000; Mt. Oku: Lee et al., 1996; Nyos: Temdjim et al., 2004; Wum: This study; Njombie Wagsong et al., 2018; Pinter et al., 2015; ; Nguihdama et al., 2014; Temdjim, 2012; Nkouandou and Temdjim, 2011; Teitchou et al., 2011; Matsukage and Oya, 2010; Caldeira and Munha, 2002; Princivalle et al., 2000).

III.3.4.3.3. MORB type silicate melt signatures

Samples from groups 1 and 3 xenoliths show characteristics of a MORB source mantle. They consist of lherzolites that are fertile in terms of major elements e.g Al_2O_3 (5.40-7.93) and Mg# (0.89-0.92) but show depleted incompatible trace elements.

The depleted MORB mantle trace element pattern is characterized by positive U anomalies, negative Ba, Pb and Ti anomalies while the LREEs are generally depleted relative to MREEs and HREEs. Clinopyroxenes from groups 1 and 3 show identical patterns, but in

addition, they show variable enrichments in U and Th and negative Rb anomalies. Some clinopyroxenes from group 3 show positive Pb anomalies, which can be attributed to an earlier subduction event. Group 1 samples do not show any Pb anomalies or enrichments but faithfully mimick the trace element pattern of the DMM. They are however much more depleted in Ba. Sample Ww1a can therefore be considered to have been metasomatized by a pure MORB-like silicate melt. This kind of metasomatism has been observed along the CVL in the OVF (Tendonkenfack et al., 2021). The other samples have experienced in addition, metasomatism by fluids/melts, which are enriched in Th, U and LREEs to various extents. The variations in LREEs and Th, U in the clinopyroxenes can be explained by the reactive flow model of Ionov et al 2002, and this also shows that the metasomatic intensity is directly proportional to the distance from the metasomatic source.

III.3.4.4. Significance of the positive Eu anomaly

Eu anomalies occur in xenoliths from Ngaoundere Likok (N11 and N11a) and were calculated as:

$$Eu_N/Eu^* = Eu_N / (\sqrt{Sm_N * Gd_N})$$

The calculated values show a wide range from 0.97-2.77. Eu is a heterovalent element (Eu^{2+} , Eu^{3+}) with high abundance in pyroxenes. Eu partitioning in clinopyroxene is primarily controlled by fO_2 while no effect is observed in orthopyroxene. Eu^{2+} and Eu^{3+} have slightly different partition coefficients. The partition coefficient of Eu^{3+} is similar to other REEs, while that of Eu^{2+} is different, making the bulk partition coefficient different compared to the neighboring REEs thereby creating an anomaly. Modelling of trace elements of orthopyroxene for partial melting in these samples show that they are residues of low degrees of partial melting (5%). Although clinopyroxenes show a strong positive Eu anomaly, orthopyroxenes are void of this feature.

High concentrations of Eu in clinopyroxene has been attributed either to partial melting under oxidising conditions, which favour Eu conservation in clinopyroxenes (Karner et al., 2010). Secondly, this feature has also been ascribed to the former occurrence of plagioclase, that is, a ghost plagioclase signature that has been preserved in the samples (Marchesi et al., 2013). Plagioclase breakdown during transition from plagioclase to spinel

facies releases Eu, which in excess can easily be incorporated into clinopyroxene. This facies transition can be obtained by temperature decrease at constant pressures (Irving and Green, 1970). The positive Eu anomalies in a plagioclase free host peridotites support refertilisation by a melt, which preserved signatures from an original plagioclase-rich source. The plagioclase likely formed from the crystallization of melts that were trapped in the xenolith during partial melting.

III.3.4.5. Origin of the olivine websterites

Websterites are not a primary mantle lithology and they represent a secondary lithology. The processes which generate websterites are expected to lead to compositional differences. However, the CVL websterites do not show any particular difference from the primary lithology (Iherzolites). The websterites probably formed from melt rock interactions and the similarity in composition could be due to a long residence period of the xenoliths in the mantle, which allowed time to exchange with the surrounding peridotite and re-equilibrate.

III.3.4. ORTHOPYROXENE AS A POTENTIAL AS INDICATOR FOR METASOMATIC PROCESSES

Clinopyroxene compositions have been extensively used to decode mantle processes. This however becomes complicated in mantle xenoliths where clinopyroxene has been partially or completely removed from the system during partial melting (Scott et al., 2016; Walter, 2003). Since orthopyroxenes can stay in mantle residues until after 40% of partial melting, they, become the next dominant repository for trace elements after amphibole and clinopyroxene and therefore play an important role in partitioning trace elements especially in highly depleted peridotites (Scott et al., 2016). Orthopyroxenes can therefore be used effectively to constrain metasomatic processes.

The metasomatic effects on orthopyroxene were evaluated using partial melting models. Comparing the primitive mantle normalized rare element patterns of these samples to theoretically modelled trends (Fig. 3.30, 3.31), shows that most of these samples did not only undergo melt extraction processes but also show evidence for cryptic metasomatism.

Such orthopyroxene enrichments have been previously reported in mantle xenoliths (e.g. Nformidah et al., submitted; Scott et al., 2016).

Compared with the melting trends, orthopyroxenes in groups 1 and 3 xenoliths show slight traces of La enrichment just like their clinopyroxene counterparts (Fig. 3.30a, c; 3.31a, c). Group 2 (except sample N18 which is enriched in MREEs and LREEs) are enriched in all elements except Yb and Lu (Fig. 3.30b). Group 4 (Fig. 3.30d) shows enrichments in MREEs and LREEs while group 6 (Fig. 3.30f) are just slightly enriched in LREEs. The group 5 samples (Fig. 3.30e) are the most enriched just like the coexisting clinopyroxenes, showing a very sharp increase in LREEs. LREEs behave incompatibly during partial melting and so their deviation from these melting trends suggests mantle metasomatism by different fluid/melt components and in different degrees.

Trace element ratios commonly used to distinguish between the effects of partial melting, silicate and carbonatite metasomatic in clinopyroxene can be used for the same purpose in orthopyroxene (Fig. 3.33b, d). High Ti/Eu (>7000) and low $(La/Yb)_N$ (~ 0.01) are represented by group 1 and 3 samples which show very little or no metasomatic effects (La, Ce enrichments), but record partial melting. The group 5 sample shows low Ti/Eu (<2000) but the highest $(La/Yb)_N$ (>0.1) which correspond to the carbonatite metasomatism group. Sample En2a (group 4) also segregates from the rest of the samples, but in opposition to group 5, it has lower $(La/Yb)_N$ (<0.1), and thus, falls within the range of carbonatite metasomatism. The rest of the samples show Ti/Eu values between the two previous and their $(La/Yb)_N$ values range from 0.01 to 0.1. They correspond to the silicate metasomatism group. The samples from group 4 (E1a, E8) do not give the same information as their clinopyroxene which fall in the silicate-carbonate domain. This could indicate that silicate metasomatism is an earlier metasomatism, which was recorded in both pyroxenes while the latter carbonate metasomatism was less widespread and had less effects. Orthopyroxenes from the Kapsiki plateau, which correspond to the northernmost occurrence of mantle xenoliths along the CVL (Nformidah et al., submitted), show clear silicate-carbonatite metasomatism and fall in a separate group from the rest of the samples. They are characterized by high Ti/Eu (>5000) and $(La/Yb)_N$ (~ 1) except one grain which diverts towards the carbonatite field. The results obtained are consistent with their clinopyroxene

data. Plots of Ti/Sr vs Ti/Eu also nicely segregates the different mantle processes in these samples (Fig. 3.33f).

III.3.5. INTERPRETATION OF OLIVINE TRACE ELEMENTS (OLIVINE AS A PETROLOGICAL TRACER)

Olivine is the most common mineral in the upper mantle and represents an important source of geochemical and petrological information on mantle dynamics (e.g De Hoog et al., 2010). Trace element concentration in olivine is highly dependent on fertility/melting, temperature and pressure. The elements controlled by temperature include Ca, Al, Cr, Sc and V (De Hoog et al., 2010; O'Reilly et al., 1997). Al contents increase with increasing temperatures and so can be used as a proxy for temperature. Group II (Cr, V, Sc, Ca, Na) and III (Ti, Y,) elements show an increase with increasing Al contents (Fig. 3.17).

The Mg# in olivine is the main indicator of the fertility of the mantle. The CVL xenoliths show two distinct groups of Mg#, which represent moderately depleted to fertile components, indicating a heterogeneous mantle below the line. The more fertile xenoliths are more enriched in incompatible trace elements (Fig. 3.16) and show lower Mg#. However, this does not seem to be a straightforward depletion process, as the samples also show different depletion trends and evidence of enrichments. The extent of melt depletion was calculated using the methods of Hellebrand et al. (2001) and De Hoog et al. (2010) based on the spinel Cr# and olivine respectively. This shows that the xenoliths were close to equilibrium and transport to the surface was fast, probably from a tectonically stable zone of the mantle.

Temperature has the greatest control on trace element composition of olivine compared to other mantle processes. Heating and cooling processes strongly disrupts any variation trends in trace element composition of olivine that were inherited from processes like partial melting and melt-rock reactions. This therefore makes it very challenging to use trace element compositions of olivine to constrain metasomatic processes.

III.4. CONCLUSION

In this study, detailed petrography and mineral chemistry of spinel facies mantle xenoliths from the CVL has been carried out.

- Textural evidence and modal composition show that the xenoliths are principally lherzolites and olivine websterites hosted in Cenozoic alkaline basalts.
- The SCLM below the region is quite fertile and shows overall agreement for small degrees of partial melt depletion with degrees of partial melting between 5-10%.
- Two samples show evidence for infiltration of the host basalt, but the effects are minimal as both clinopyroxene and orthopyroxene show similar geochemical characters.
- Trace element concentrations of clinopyroxene and amphibole show evidence for metasomatic enrichments by fluids/melts of different compositions, which include MORB-type silicate melt, alkaline and carbonatite melts. There is also evidence for overprinting of one alkaline by silicate fluids/melts or vice versa or conversely, a mixture of these metasomatic fluids in different proportions.
- There is limited evidence for a subduction type metasomatism, which could have been overprinted by MORB-type alkaline metasomatism.
- The evaluation of the use of olivine and orthopyroxene trace element compositions to constrain metasomatic enrichments shows that orthopyroxene is quite suitable for this and several elements can be used; Nb, Ta, Th, U, Sr and REE for the different melt types. The use of olivine is more challenging since temperature effects seem to be more dominant than the compositional effects of mantle processes.

REFERENCES

- Arai, S., 1994. Characterization of spinel peridotites by olivine-spinel compositional relationships: Review and interpretation. *Chem. Geol.* 113(3-4), 191–204.
- Asaah A. N. E., Yokoyama T., Aka F. T., Usui T., Kuritani T., Wirmvem M. J., Iwamori H., Fozing E. M., Tamen J., Mofor G. Z., Ohba T., Tanyileke G., Hell J. V., 2015. Geochemistry of lavas from maar-bearing volcanoes in the Oku Volcanic Group of the Cameroon Volcanic Line. *Chem Geol* 406:55–69.
- Ballhaus, C.G., Berry, R.F., Green, D.H., 1991. High-pressure calibration of the olivine-orthopyroxene-spinel oxygen barometer, implications for the oxidation state of the upper mantle. *Contrib. Mineral. Petrol.* 107, 7–40.
- Beccaluva L, Bonadiman C, Coltorti M, Salvini L, Siena F. Depletion events, nature of metasomatizing agent and timing of enrichment processes in lithospheric mantle xenoliths from the Veneto Volcanic Province, *Journal of Petrology*, 2001, vol. 42 (pg. 173-187)
- Bedini, R., Bodinier, J.-L., Dautria, J.-M. & Morten, L. (1997). Evolution of LILE-enriched small melt fractions in the litho-spheric mantle: a case study from the East African Rift. *Earth and Planetary Science Letters* 153, 67–83.
- Bénard, A., and D. A. Ionov (2013). Melt and fluid–rock interaction in supra-subduction lithospheric mantle: Evidence from andesite-hosted veined peridotite xenoliths, *J. Petrol.*, 54, 2339–2378.
- Bodinier, J.-L. & Godard, M. (2003). Orogenic, ophiolitic, and abyssal peridotites. In: Turekian, K. K. & Holland, H. D. (eds) *Treatise on Geochemistry*. Elsevier, Amsterdam 2, 103–170.
- Bodinier, J.L., Dupuy, C., Dostal, J., 1988. Geochemistry and petrogenesis of Eastern Pyrenean peridotites. *Geochim. Cosmo-chim. Acta* 52, 2893–2907.
- Bodinier, J.L., Vasseur, G., Vernieres, J., Dupuy, C., Fabries, J., 1990. Mechanisms of mantle metasomatism: geochemical evidence from the Lherz orogenic peridotite. *J. Petrol.* 31, 597–628.
- Bonadiman, C., Coltorti, M., Beccaluva, L., Siena, F., 2005. Kimberlite-like Metasomatism and ‘Garnet Signature’ in Spinel-peridotite Xenoliths from Sal, Cape Verde Archipelago: Relics of a Subcontinental Mantle Domain within the Atlantic Oceanic Lithosphere? *Journal of Petrology* 46, 2465-2493.
- Bonadiman, C., Coltorti, M., Beccaluva, L., Siena, F., 2008. Mantle metasomatism vs. host magma interaction: the ongoing controversy. *Geophysical Research Abstracts* 10, EGU 2008-A-09723.

- Borisov, A. A., Kadik, A. A., Zharkova, Y. V. & Kalinichenko, N. V., 1987. Effects of oxygen fugacity on the ratio between valency forms of vanadium in magmas. *Geochemistry International* 24,15-20.
- Boyd, F.R., 1989. Compositional distinction between oceanic and cratonic lithosphere. *Earth Planet. Sci. Lett.* 96, 15–26
- Brey, G.P., Köhler, T.P., 1990. Geothermobarometry in natural four-phase lherzolites: Part II. New thermobarometers and practical assessment of existing thermobarometers. *J. Petrol.* 31, 1353–1378.
- Caldeira, R., Munhá, J.M., 2002. Petrology of ultramafic nodules from Sao Tomé Island, Cameroon Volcanic line (oceanic sector). *J. Afr. Earth Sci.* 34:231–246
- Carpenter, R.L., Edgar, A.D., Thibault, Y., 2002. Origin of spongy textures in clinopyroxene and spinel from mantle xenoliths, Hessian Depression, Germany. *Mineralogy and Petrology* 74, 149–162.
- Caxito, F.A., Santos, L.C.M.D.L., Ganade, C.E., Bendaoud, A., Fettous, E.H., Bouyo, M.H., 2020. Toward an integrated model of geological evolution for NE Brazil-NW Africa: The Borborema Province and its connections to the Trans-Saharan (Benino-Nigerian and Tuareg shields) and Central African orogens. *Brazilian Journal of Geology* 50 (2).
- Cherniak D J. REE diffusion in olivine, *American Mineralogist*, 2010, vol. 95 (pg. 362-368)
- Churikova, T., Dorendorf, F. & Wörner, G., 2001. Sources and fluids in the mantle wedge below Kamchatka, evidence from across-arc geochemical variation. *Journal of Petrology* 42, 1567–1593.
- Coltorti, M., Bonadiman, C., Faccini, B., Gregoire, M., O'Reilly, S. Y. & Powell, W., 2007. Amphiboles from suprasubduction and intraplate lithospheric mantle. *Lithos* 99, 68–84.
- Coltorti, M., Bonadiman, C., Hinton, R.W., Siena, F., Upton, B.G.J., 1999. Carbonatite metasomatism of the oceanic upper mantle: evidence from clinopyroxenes and glasses in ultramafic xenoliths of Grande Comore, Indian Ocean. *J. Petrol.* 40, 133–165.
- Coogan, L. A., Hain, A., Stahl, S. & Chakraborty, S., 2005. Experimental determination of the diffusion coefficient for calcium in olivine between 900_C and 1500_C. *Geochimica et Cosmochimica Acta* 69, 3683–3694.
- Coogan, L.A., Saunders, A.D., Wilson, R.N., 2014. Aluminum-in-olivine thermometry of primitive basalts: Evidence of an anomalously hot mantle source for large igneous provinces. *Chem. Geol.* 368, 1–10.
- Cvetkovi_c, V., Downes, H., Prelevic, D., Hock, V. and Lazarov, M., 2010. Mafic alkaline metasomatism in the lithosphere underneath East Serbia: evidence from the study of

- xenoliths and host alkali basalts. In: Coltorti, M., Downes, H., Gregoire, M. & O'Reilly, S. Y. (eds) *Petrological Evolution of the European Lithospheric Mantle*. Geological Society, London, Special Publications 337, 213–239.
- Dasgupta, R., Hirschmann, M.M., 2006. Melting in the Earth's deep upper mantle caused by carbon dioxide. *Nature* 440 (7084), 659–662.
- Dautria J-M, Dupuy C, Takherist D, Dostal J (1992) Carbonate metasomatism in the lithospheric mantle: peridotitic xenoliths from a melilitic district of the Sahara basin. *Contrib Mineral Petrol* 111:37–52
- Dawson, J.B., H. Pinkerton, G.E. Norton and D.M. Pyle, Physicochemical properties of alkali carbonatite lavas: Data from the 1988 eruption of Oldoinyo Lengai, Tanzania, *Geology* 18, 260-263, 1990.
- De Hoog J.C.M., Gall L., Cornell D.H., 2010. Trace element geochemistry of mantle olivine and application to mantle petrogenesis and geothermobarometry. *Chem. Geol.* 270:196–215.
- Déruelle, B., Ngounouno, I., Nkoumbou, C., 1998. Mt Cameroon, Mt Etinde, and Bioko Is-land volcanoes of the 'Cameroon hot Line'. *Evolution of Ocean Island Volcanoes*, Pen-rose Conference, Galapagos Islands, p. 28
- Dohmen R, Kasemann S. A., Coogan L, Chakraborty S. Diffusion of Li in olivine. Part I: Experimental observations and a multi-species diffusion model, *Geochimica et Cosmochimica Acta*, 2010, vol. 74 (pg. 274-292)
- Dohmen, R. & Chakraborty, S. (2007a). Fe-Mg diffusion in olivine I: experimental determination between 700 and 1,200_C as a function of composition, crystal orientation and oxygen fugacity. *Physics and Chemistry of Minerals* 34, 389–407.
- Dohmen, R. & Chakraborty, S. (2007b). Fe–Mg diffusion in olivine II: point defect chemistry, change of diffusion mechanisms and a model for calculation of diffusion coefficients in natural olivine. *Physics and Chemistry of Minerals* 34, 409–430.
- Downes H, Thirlwall MF, Trayhorn SC (2001) Miocene subduction-related magmatism in southern Sardinia: Sr-Nd and oxy-gen isotopic evidence for mantle source enrichment. *J Volcanol Geotherm Res* 106:1–21
- Downes, H., 2001. Formation and modification of the shallow subcontinental lithospheric mantle; a review of geochemical evidence from ultramafic xenolith suites and tectonically emplaced ultramafic massifs of western and central Europe. *J. Petrol.* 42, 233–250.
- Fabriès, J., 1979. Spinel-Olivine geothermometry in peridotites from ultramafic complexes. *Contrib. Mineral. Petrol.* 69: 329–336.

- Fagny, M.F., Nkouandou, O.F., Temdjim, R., Bardintzeff, J.M., Guillou, H., Stumbea, D., Boutale, A., 2016. New ⁴⁰Ar ages of Tchabal Mbabo alkaline volcano massif, Cameroon volcanic line and Adamawa plateau (Central Africa). *Int. J. Adv. Geosci.* 4 (2), 62-71.
- Fan, W.M., Zhang, H.F., Baker, J., Jarvis, K.E., Mason, P.R.D., Menzies, M.A., 2000. On and off the north China craton: where is the Archaean keel? *J. Petrol.* 41, 933–950.
- Fitton J.G. and Dunlop H.M. (1985) The Cameroon Line, West Africa and its bearing on the origin of oceanic and continental alkali basalt. *Earth. Planet. Sci. Lett.* 72, 23-38.
- Foley, S. F., Barth, M. G. & Jenner, G. A. (2000). Rutile/melt partition coefficients for trace elements and an assessment of the influence of rutile on the trace element characteristics of subduction zone magmas. *Geochimica et Cosmochimica Acta* 64, 933–938.
- Fréménias O., Coussaert N., Berger J., Mercier J-C. C., Demaiffe D. Metasomatism and melting history of a Variscan lithospheric mantle domain: evidence from the Puy Beaunit xenoliths (French Massif Central), *Contributions to Mineralogy and Petrology*, 2004, vol. 148 (pg. 13-28).
- Frey, F. A. & Prinz, M. (1978). Ultramafic inclusions from San Carlos, Arizona: petrologic and geochemical data bearing on their petrogenesis. *Earth and Planetary Science Letters* 38, 129–176.
- Gamal El Dien, H., Arai, S., Doucet, L., Li, Z., Kil, Y., Fougereuse, D., Reddy, S. M., Saxey, D. Y., Hamdy M., 2019. Cr–spinel records metasomatism not petrogenesis of mantle rocks. *Nature Comm.* 5103.
- Gorring M L, Kay S M. Carbonatite metasomatized peridotite xenoliths from southern Patagonia: implications for lithospheric processes and Neogene plateau magmatism, *Contributions to Mineralogy and Petrology*, 2000, vol. 140 (pg. 55-72)
- Gouhier J, Nougier J & Nougier D (1974). Contribution à l'étude volcanologique du Cameroun : Ligne du Cameroun-Adamaoua. *Annales Fac. Sci., Cameroun* 17, 3-49.
- Grassi, D., Schmidt, M., 2011. Melting of carbonated pelites at 8–13 GPa: Generating Krich carbonatites for mantle metasomatism. *Contrib. Mineral. Petrol.* 162 (1), 169–191.
- Green, D. H. & Wallace, M. E. (1988). Mantle metasomatism by ephemeral carbonatite melts. *Nature* 336, 459–462
- Gregoire, M., Chevet, J. & Maaloe, S. (2010). Composite xenoliths from Spitzbergen: evidence of the circulation of MORB-related melts within the upper mantle. In: Coltorti, M., Downes, H., Gregoire, M. & O'Reilly, S. Y. (eds) *Petrological Evolution of the European Lithospheric Mantle*. Geological Society, London, Special Publications 337, 71-86.

- Grégoire, M., Langlade, J.A., Delpech, G., Dantas, C., Ceuleneer, G., 2009. Nature and evolution of the lithospheric mantle beneath the passive margin of East Oman: Evidence from mantle xenoliths sampled by Cenozoic alkaline lavas. *Lithos* 112/3, 203–216.
- Gregoire, M., McInnes, B. I. A. & O'Reilly, S. Y. (2001). Hydrous metasomatism of oceanic sub-arc mantle, Lihir, Papua New Guinea Part 2. Trace element characteristics of slab-derived fluids. *Lithos* 59, 91-108.
- Gregoire, M., Moine, B. N., O'Reilly, S. Y., Cottin, J. Y. & Giret, A. (2000). Trace element residence and partitioning in mantle xenoliths metasomatized by highly alkaline, silicate- and carbonate-rich melts Kerguelen Islands, Indian Ocean. *Journal of Petrology* 41, 477–509.
- Hart, S. R. & Dunn, T., 1993. Experimental cpx/melt partitioning of 24 trace elements. *Contrib. Mineral. Petrol.* 113, 1–8.
- Hauri, E. H., Shimizu, N., Dieu, J. J. & Hart, S. R. (1993). Evidence for hot-spot-related carbonatite metasomatism in the oceanic upper mantle. *Nature* 365, 221–227
- Hellebrand, E., Snow, J.E., Dick, H.J.B., Hofmann, A., 2001. Coupled major and trace elements as indicators of the extent of melting in mid-ocean-ridge peridotites. *Nature* 410, 677–681.
- Herzberg, C. (2004). Geodynamic information in peridotite petrology. *Journal of Petrology* 45, 2507–2530
- Hoernle, K., Tilton, G., Bas, M.J.L., Duggen, S., Garbe-Schönberg, D., 2002. Geochemistry of oceanic carbonatites compared with continental carbonatites: mantle recycling of oceanic crustal carbonate. *Contrib. Mineral. Petrol.* 142 (5), 520–542.
- Holzapfel, C., Chakraborty, S., Rubie, D. C. & Frost, D. J. Effect of pressure on Fe-Mg, Ni and Mn diffusion in $(\text{Fe}_x\text{Mg}_{1-x})_2\text{SiO}_4$ olivine. *Phys. Earth Planet. Inter.* **162**, 186–198 (2007)
- Ionov, D. A. & Hofmann, A.W. (1995). Nb–Ta-rich mantle amphiboles and micas: implications for subduction-related metasomatic trace element fractionations. *Earth and Planetary Science Letters* **131**, 341–356.
- Ionov DA, Dupuy C, O'Reilly SY, Koplova MG, Genshaft Y, (1993) Carbonated peridotite xenoliths from Spitsbergen: implications for trace element signature of mantle carbonate metasomatism. *Earth Planet Sci Lett* 119: 283-297
- Ionov DA, Griffin WL, O'Reilly SY (1999) Off-craton garnet and spinel peridotite xenoliths from Dsun-Bussular, SE Mongolia. In: *Proceedings of the 7th international Kimberlite conference, Red Roof Design, Cape Town*, pp 383–390.
- Ionov, D. A., Dupuy, C., O'Reilly, S. Y., Kopylova, M. G. & Genshaft, Y. S. (1993). Carbonated peridotite xenoliths from Spitsbergen: implications for trace element signature of mantle carbonate metasomatism. *Earth and Planetary Science Letters* **119**, 283–297.

- Ionov, D. A., Gregoire, M. & Prikhod'ko, V. S. (1999). Feldspar–Ti-oxide metasomatism in off-cratonic continental and oceanic upper mantle. *Earth and Planetary Science Letters* **165**, 37–44.
- Ionov, D. (1998). Trace element composition of mantle-derived carbonates and coexisting phases in peridotite xenoliths from alkali basalts. *Journal of Petrology* **39**, 1931–1941.
- Ionov, D.A., Bodinier, J.L., Mukasa, S.B., Zanetti, A., 2002. Mechanisms and sources of mantle metasomatism: major and trace element compositions of peridotite xenoliths from Spitsbergen in the context of Numerical Modelling. *J. Petrol.* **43**, 2219–2259.
- Ionov, D.A., Bodinier, J.L., Mukasa, S.B., Zanetti, A., 2002. Mechanisms and sources of mantle metasomatism: major and trace element compositions of peridotite xenoliths from Spitsbergen in the context of Numerical Modelling. *J. Petrol.* **43**, 2219–2259.
- Ionov, D.A., Hofmann, N.W., Shimizu, N., 1994. Metasomatism-induced melting in mantle xenoliths from Mongolia. *Journal of Petrology* **35**, 753–785.
- Irving, A., Green, D.H., 1970. Experimental duplication of mineral assemblages in basic inclusions of the Delegate breccia pipes. *Physics of the Earth and Planetary Interiors* **3**, 385–389.
- Jianping, L., Kornprobst, J., Vielzeuf, D., Fabries, J., 1995. An improved experimental 906 calibration of the olivine-spinel geothermometer. *Chin. J. of Geochem.* **14**, 68–77.
- Johnson, K. T. M., Dick, H. J. B. & Shimizu, N., 1990. Melting in the oceanic upper mantle: an ion microprobe study of diopsides in abyssal peridotites. *J. Geophys. Res.* **95**, 2661–2678.
- Kalfoun, F., Ionov, D., & Merlet, C. (2002). HFSE residence and Nb/Ta ratios in metasomatised, rutile-bearing mantle peridotites. *Earth and Planetary Science Letters*, **199**(1-2), 49–65.
- Karner, J.M., Papike, J.J., Sutton, P.V., Burger, P.V., Shearer, C.K., Le, L., Newville, M., Choi, Y., 2010. Partitioning of Eu between augite and a highly spiked Martian basalt composition as a function of oxygen fugacity (IW-1 to QFM): determination of Eu²⁺/Eu³⁺ ratios by XANES. *American Mineralogist* **95**, 410–413.
- Kempton, P. D. (1987). Mineralogic and geochemical evidence for differing styles of metasomatism in spinel lherzolite xenoliths: enriched mantle source regions of basalts? In: Menzies, M. A. & Hawkesworth, C. J. (eds) *Mantle Metasomatism*. London: Academic Press, pp. 45–89.
- Kilian, R., Stern, C.R., 2002. Constraints on the interaction between slab melts and the mantle wedge from adakitic glass in peridotite xenoliths. *Eur. J. Mineral.* **14** (1), 25–36
- Klemme, S., van der Laan, S. R., Foley, S. F., Gunther, D., 1995. Experimentally determined trace and minor element partitioning between clinopyroxene and carbonatite melt under upper mantle conditions. *Earth Planet. Sci. Lett.* **133**, 439–448.

- Kohler, T., Brey, G.P., 1990. Calcium exchange between olivine and clinopyroxene calibrated as a geothermobarometer for natural peridotites from 2 to 60 kb with applications. *Geochim. Cosmochim. Acta* 54, 2375–2388.
- Kovacs, I., Zajacz, Z. & Szabo, C. (2004). Type-II xenoliths and related metasomatism from the Nograd–Gomor Volcanic Field, Carpathian–Pannonian region (northern Hungary–southern Slovakia). *Tectonophysics* 393, 139–161.
- Le Roux, V., Bodinier, J.-L., Tommasi, A., Alard, O., Dautria, J.-M., Vauchez, A. & Riches, A. (2007). The Lherz spinel lherzolite: refertilized rather than pristine mantle. *Earth and Planetary Science Letters* 259, 599–612.
- Leake, B.E., Woolley, A.R., Arps, C.E.S., Birch, W.D., Gilbert, M.C., Grice, J.D., Hawthorne, F.C., Kato, A., Kisch, H.J., Krivovichev, V.G., Linthout, K., Laird, J., Mandarino, J.A., Maresch, W.V., Nickel, E.H., Rock, N.M.S., Schumacher, J.C., Smith, D.C., Stephenson, N.C.N., Ungaretti, L., Whittaker, E.J.W., Youzhi, G., 1997. Nomenclature of amphiboles: report of the subcommittee on amphiboles of the international mineralogical association, commission on new minerals and mineral names. *American Mineralogist* 82, 1019–1037
- Lee, C.-T. A., Harbert, A., & Leeman, W. P. (2007). Extension of lattice strain theory to mineral/mineral rare-earth element partitioning: An approach for assessing disequilibrium and developing internally consistent partition coefficients between olivine, orthopyroxene, clinopyroxene and basaltic melt. *Geochimica et Cosmochimica Acta*, 71(2), 481–496.
- Lee, D. C., Halliday N., Davies G. R., Essene E. J., Fitton G. J., Temdjim, R., 1996. Melt enrichment of shallow depleted mantle: a detailed petrological, trace element and isotopic study of mantle-derived xenoliths and megacrysts from the Cameroon Line. *J. Petrol.* 37:415–441.
- Liang, Y., Sun, C., Yao, L., 2013. A REE-two-pyroxene thermometer for mafic and ultra-mafic rocks. *Geochimica et Cosmochimica Acta* 102, 246–260
- Liptai, N., Patkó, L., Kovács, I.J., Hidas, K., Pintér, Z., Jeffries, T., Zajacz, Z., O'Reilly, S.Y., Griffin, W.L., Pearson, N.J. and Szabó, C., 2017. Multiple metasomatism beneath the Nograd–Gömör Volcanic Field (Northern Pannonian Basin) revealed by upper mantle peridotite xenoliths. *Journal of Petrology*, 58(6), pp.1107-1144.
- Liu C-Z, Yang L-Y, Li X-H, Tchoukoue JP (2017) Age and Sr-Nd-Hf isotopes of the sub-continental lithospheric mantle beneath the Cameroon Volcanic Line: constraints from the Nyos mantle xenoliths. *Chem Geol* 455:84–97.
- Liu J, Pearson GJ, Shu Q, Sigurdsson H, Thomassot E, Alard O (2020) Dating post-Archean lithospheric mantle: insights from Re-Os and Lu-Hf isotopic systematics of the Cameroon Volcanic Line peridotites. *Geochim Cosmochim Acta* 278:177–198

- Liu, C.Z., Yang, L.Y., Li, X.H., Tchouankoue, J.P., 2017. Age and Sr-Nd-Hf isotopes of the subcontinental lithospheric mantle beneath the Cameroon Volcanic Line: constraints from the Nyos mantle xenoliths. *Chem. Geol.* 455, 84–97.
- Ma, G.S.K., Wang, K.L., Malpas, J., Iizuka, Y., Xenophontos, C., Turkmani, A.A., Chan, G.H.N., Usuki, T., Chan, Q.H.S., 2015. In: Khan, A., Deschamps, F. (Eds.), *Melt Pockets and Spongy Clinopyroxenes in Mantle Xenoliths from the Plio-Quaternary Al Ghab Volcanic Field, NW Syria: Implications for the Metasomatic Evolution of the Lithosphere*. Springer Geophysics, pp. 205–258 *The Earth's Heterogeneous Mantle: A Geophysical, Geodynamical and Geochemical Perspective*.
- Marchesi, C., Garrido, C. J., Bosch, D., Bodinier, J. L., Gervilla, F., & Hidas, K. (2013). Mantle refertilization by melts of crustal-derived garnet pyroxenite: evidence from the Ronda peridotite massif, southern Spain. *Earth and Planetary Science Letters*, 362, 66-75.
- Marchev, P., Arai, S., Vaselli, O., Costa, F., Zanetti, A., Downes, H., 2017. Metasomatic reaction phenomena from entrainment to surface cooling: evidence from mantle peridotite xenoliths from Bulgaria. *J. Petrol.* 58 (3), 599–640.
- Marzoli A, Renne PR, Piccirillo EM, Castorina F, Bellieni G, Melfi A. J, Nyobe JB & N'ni J (1999) silicic magmas from the continental Cameroon Volcanic Line (Oku, Bambouto and Ngaoundere): ^{40}Ar - ^{39}Ar dates, petrology, Sr-Nd-O isotopes and their petrogenetic significance. *Contrib. Mineral. Petrol.* 135, 133-150.
- Marzoli, A., E. M. Piccirillo, P. R. Renne, G. Bellieni, M. Iacumin, J. B. Nyobe, and A. T. Tongwa (2000), The Cameroon Volcanic Line revisited: Petrogenesis of continental basaltic magmas from lithospheric and asthenospheric mantle sources, *J. Petrol.*, 41(1), 87– 109.
- Matsukage, K.N., Oya, M., 2010. Petrological and chemical variability of peridotite xenoliths from the Cameroon Volcanic Line, West Africa: an evidence for plume emplacement. *J. Mineral. Petrol. Sci.* 105, 57–69.
- McCoy-West, A.J., Bennett, V.C., O'Neill, H.S.C., Hermann, J., Puchtel, I. S., 2015. The Interplay between Melting, Refertilization and Carbonatite Metasomatism in Off Cratonic Lithospheric Mantle under Zealandia: an Integrated Major, Trace and Platinum Group Element Study. *J. Petrol.* 56(3), 563–604.
- McDonough, W. F. & Sun, S.-S. (1995). The composition of the Earth. *Chemical Geology* 120, 223–253.
- McDonough, W.F., 1991. Partial melting of subducted oceanic crust and isolation of its residual eclogitic lithology. *Philos. Trans. R. Soc. London, Ser. A*, 335: 407-4 IS.

- McGuire, A. V., 1988. Petrology of mantle xenoliths from Harrat al Kishb: the mantle beneath western Saudi Arabia. *J. Petrology* 29, 73-92
- Mercier, J.-C.C., Carter, N.L., 1975. Pyroxene geotherms. *J. Geophys. Res.* 80, 3349–3362.
- Miller, C., Zanetti, A., Thoni, M., Konzett, J. & Klotzli, U. (2012). Mafic and silica-rich glasses in mantle xenoliths from Wauen-Namus, Libya: Textural and geochemical evidence for peridotite–melt reactions. *Lithos* 128, 11–26.
- Morimoto, N. (1988): Nomenclature of pyroxenes. *Mineral. Mag.*, 52: 535-550.
- Müller, T., Dohmen, R., Becker, H. W., Ter Heege, J. H. & Chakraborty, S., 2013. Fe–Mg interdiffusion rates in clinopyroxene: experimental data and implications for Fe–Mg exchange geothermometers. *Contrib. Mineral. Petrol.* **166**, 1563–16576.
- Navon, O., Stolper, E., 1987. Geochemical consequence of melt percolation—the upper mantle as a chromatographic column. *J. Petrol.* 95, 285–307.
- Nelson, D. R., A. R. Chivas, B. W. Chappell, and M. T. McCulloch, Geochemical and isotopic systematics in carbonatites and implications for the evolution of ocean-island sources, *Geochim. Cosmochim. Acta*, 52, 1-17, 1988.
- Nformidah, N.S.S, Tollan, P.M.E., Hermann J., Tchouankoue, J.P., submitted. Depletion and refertilisation of the lithospheric mantle below the kapsiki plateau (northern Cameroon Volcanic Line) deduced from trace element and H₂O systematics in mantle xenoliths.
- Ngako, V., Affaton, P., Njonfang, E., 2008. Pan-African tectonics in northwestern Cameroon: implication for the history of western Gondwana. *Gondwana Research* 14, 509–522.
- Ngnotué, T., Nzenti, J. P., Barbey, P. and Tchoua, F. M., “The Ntui-Betamba High Grade Gneiss: A Northward Extension of the Pan-African Yaoundé Gneisses in Cameroon,” *Journal of African Earth Sciences*, Vol. 31, No. 2, 2000, pp. 369-381
- Nguidama, D., Chazot, G., Kamgang, P., Mbouwou, G.I.B., Ngounouno, I., 2014. Spinel-bearing lherzolite xenoliths from Hossere Garba (Likok, Adamawa-Cameroon): mineral compositions and geothermobarometric implications. *Int. J. Geosci.* 5, 1435–1444.
- Njiekak, G., Deorr, W., Tchoankoue, J.P., Zulauf, G., 2008. U-Pb zircon and micro fabric data of (meta) granitoids of western Cameroon: constrains on the timing of pluton emplacement and deformation in the Pan-African belt of central Africa. *Lithos* 102, 460e477.
- Njombie Wagsong, P.M., Temdjim, R., Foley, S.F., 2018. Petrology of spinel lherzolite xenoliths from Youkou volcano, Adamawa Massif, Cameroon Volcanic Line: mineralogical and geochemical fingerprints of sub-rift mantle processes. *Contrib. Mineral. Petrol.* 173, 13.
- Nkouandou, O. F., J.-M. Bardintzeff, and A. M. Fagny (2015), Sub-continental lithospheric mantle structure beneath the Adamawa plateau inferred from the petrology of ultramafic xenoliths

- from Ngaoundéré (Adamawa plateau, Cameroon, Central Africa), *J. Afr. Earth Sci.*, 111, 26–40.
- Nkouandou, O.F., Temdjim, R., 2011. Petrology of spinel lherzolite xenoliths and hostbasaltic lava from Ngao Voglar volcano, Adawama Massif (Cameroon VolcanicLine, West Africa): equilibrium conditions and mantle characteristics. *J. Geosci.*56, 375-387.
- Norman, M. D., 1998. Melting and metasomatism in the continental lithosphere: laser ablation ICPMS analysis of minerals in spinel lherzolites from eastern Australia *Contrib. Mineral. Petrol.*, 130 (1998), pp. 240-255.
- Nzenti, J.P., Barbey, P., Bertrand, J.-M., Macaudie`re, J., 1994. La Chaine panafricaine au Cameroun : cherchons suture et mode`le ! 15^e Re´-union des sciences de la terre Socie té Gé`ologique de France, Nancy, France 99.
- O'Neill, H. S. C. & Wall, V. J. (1987). The olivine–orthopyroxene–spinel oxygen geobarometer, the nickel precipitation curve, and the oxygen fugacity of the Earth's upper mantle. *Journal of Petrology* 28, 1169–1191.
- O'Neill, H. St. C., 1981. The transition between spinel lherzolite and garnet lherzolite and its use as a geobarometer. *Contrib. Mineral. Petrol.* 77, 185–194
- O'Reilly, S.Y., Griffin, W.L., 2012. Mantle metasomatism. In: Harlov, D.E., Austrheim, H. (Eds.), *Metasomatism and the chemical transformation of rock. Lecture Notes in Earth System Sciences.* Springer-Verlag, Berlin Heidelberg, pp. 467–528.
- O'Reilly et al., 1997. S.Y. O'Reilly, D. Chen, W.L. Griffin, C.G. Ryan. Minor elements in olivine from spinel lherzolite xenoliths: implications for thermobarometry. *Mineralogical Magazine*, 61 (1997), pp. 257-269
- Palme, H., O'Neill, H. S. C., 2014. Cosmochemical Estimates of Mantle Composition. *Treatise on Geochemistry*, 1–39.
- Pan, S., Zheng, J., Yin, Z., Griffin, W.L., Xia, M., Lin, A., Zhang, H., 2018. Spongy texture in mantle clinopyroxene records decompression-induced melting. *Lithos* 320-321, 144–154.
- Pearce, J. A., Barker, P. F., Edwards, S. J., Parkinson, I. J., Leat, P. T., 2000. Geochemistry and tectonic significance of peridotites from the South Sandwich arc-basin system, South Atlantic. *Contrib. Mineral. Petrol.* 139(1), 36–53.
- Pearce, J. A., Stern, R. J., Bloomer, S. H., Fryer, P., 2005. Geochemical mapping of the Mariana arc-basin system: Implications for the nature and distribution of subduction components. *Geochemistry, Geophys. Geosystems.* 6, Q07006.

- Pearson, D. G., Canil, D. & Shirey, S. B. (2003). Mantle samples included in volcanic rocks: xenoliths and diamonds. In: Carlson, R. W. (ed.). *The Mantle and Core. Treatise of Geochemistry, Vol.2.* Amsterdam: Elsevier, pp. 172-260.
- Penaye, J., Toteu, S. F., Van Schumus, W. R. & Nzenti, J. P. (1993) U-Pb and Sm-Nd geochronologic data on the Yaoundé series, Cameroon: reinterpretation of the granulitic rocks as the suture of a collision in the "Centrafrican belt". *Comptes Rendus de l'Académie des Sciences, Sciences de la Terre et des Planètes*, 317, 789-794.
- Petry, C., Chakraborty, S. & Palme, H. Experimental determination of Ni diffusion coefficients in olivine and their dependence on temperature, composition, oxygen fugacity, and crystallographic orientation. *Geochim. Cosmochim. Acta* **68**, 4179–4188 (2004).
- Pilet, S., Baker, M.B., Stolper, E.M., 2008. Metasomatized lithosphere and the origin of alkaline lavas. *Science* 320, 916–919.
- Pilet, S., Baker, M. B., Müntener, O., Stolper, E. M., 2011. Monte Carlo simulations of metasomatic enrichment in the lithosphere and implications for the source of alkaline basalts. *Journal of Petrology* 52, 1415-1442.
- Pintér, Zs, Patkó, L., Djoukam, J.F.T., Kovács, I., Tchouankoue, J.P., Falus, G., Konc, Z., Tommasi, A., Barou, F., Mihály, J., Németh, Cs, Jeffries, T., 2015. Characterization of the sub-continental lithospheric mantle beneath the Cameroon volcanic line inferred from alkaline basalt hosted peridotite xenoliths from Barombi Mbo and Nyos Lakes. *J. Afr. Earth Sci.* 111, 170–193.
- Pirnia, T., Saccani, E., & Arai, S. (2018). Spinel and plagioclase peridotites of the Nain ophiolite (Central Iran): Evidence for the incipient stage of oceanic basin formation. *Lithos*, 310-311, 1–19.
- Poudjom-Djomani, Y.H., Nnange, J.M., Diament, M., Ebinger, C.J, Fairhead, J.D., 1995. Effective elastic thickness and crustal thickness variations in West Central Africa inferred from gravity data. *J. Geophys. Res. Solid Earth* 100 (10-11): 22047-22070.
- Princivalle, F., Salviulo, G., Marzoli, Piccirillo, E.M., 2000. Clinopyroxene of spinel peridotite mantle from Lake Nji (Cameroon volcanic line, West Africa): crystal chemistry and petrological implication. *Contrib. Mineral. Petrol.* 139, 503–508.
- Raffone, N., Chazot, G., Pin, C., Vannucci, R. & Zanetti, A. (2009). Metasomatism in the lithospheric mantle beneath Middle Atlas (Morocco) and the origin of Fe- and Mg-rich wehrlites. *Journal of Petrology* 50, 197–249.

- Rapp, R. P., Shimizu, N., Norman, M. D. & Applegate, G. S. (1999). Reaction between slab-derived melts and peridotite in the mantle wedge: experimental constraints at 3·8 GPa. *Chemical Geology* 160, 335-356.
- Rudnick, R. L., Barth, M., Horn, I. & McDonough, W. F. (2000). Rutile-bearing refractory eclogites: missing link between continents and depleted mantle. *Science* 287, 278–281.
- Rudnick, R.L., McDonough, W.F., Chappell, B.W., 1993. Carbonatite metasomatism in the northern Tanzanian mantle: petrographic and geochemical characteristics. *Earth Planet. Sci. Lett.* 114, 463–475.
- Scambelluri, M., Vannucci, R., De Stefano, A., Preite-Martinez, M., Rivalenti, G. (2009). CO₂ fluid and silicate glass as monitors of alkali basalt/peridotite interaction in the mantle wedge beneath Gobernador Gregores, Southern Patagonia. *Lithos* 107, 121–133.
- Schafer, F.N., Foley, S.F., 2002. The effect of crystal orientation on the wetting behaviour of silicate melts on the surfaces of peridotite minerals. *Contrib. Mineral. Petrol.* 143, 254–262
- Schiano P, Clocchiatti R, Shimizu N, Weis D, Mattielli N (1994). Cogenetic silica-rich and carbonate-rich melts trapped in mantle minerals in Kerguelen ultramafic xenoliths: implications for metasomatism in the oceanic upper mantle. *Earth Planet Sci Lett* 123: 167-178
- Schmidt, M. W., Vielzeuf, D. & Auzanneau, E. Melting and dissolution of subducting crust at high pressures: the key role of white mica. *Earth Planet. Sci. Lett.* **228**, 65–84 (2004)
- Scott, J. M., Liu, J., Pearson, D. G., Waight, T. E., 2016. Mantle depletion and metasomatism recorded in orthopyroxene in highly depleted peridotites. *Chem. Geol.*, 441, 280–291.
- Scott, J. M., Liu, J., Pearson, D. G., Waight, T. E., 2016. Mantle depletion and metasomatism recorded in orthopyroxene in highly depleted peridotites. *Chem. Geol.*, 441, 280–291.
- Scott, J. M., Waight, T. E., van der Meer, Q. H. A., Palin, J. M., Cooper, A. F., Münker, C., 2014a. Metasomatized ancient lithospheric mantle beneath the young Zealandia 1047 microcontinent and its role in HIMU-like intraplate magmatism. *Geochem. Geophys. 1048 Geosyst.* 15(9), 3477–3501.
- Scott, J.M., Hodgkinson A., Palin J.M., Waight T.E., Van der Meer Q.H.A., Cooper A.F., 2014. Ancient melt depletion overprinted by young carbonatitic metasomatism in the New Zealand lithospheric mantle. *Contrib. Mineral. Petrol.* 167: 963.
- Shaw, C.S.J., Dingwell, D.B., 2008. Experimental peridotite–melt reaction at one atmosphere: a textural and chemical study. *Contributions to Mineralogy and Petrology* 155, 199-214.

- Shaw, C.S.J., Heidelbach, F., Dingwell, D.B., 2006. The origin of reaction textures in mantle peridotite xenoliths from Sal Island, Cape Verde: the case for ‘‘metasomatism’’ by the host lava. *Contributions to Mineralogy and Petrology* 151, 681-697.
- Spandler, C. & O’Neill, H. Diffusion and partition coefficients of minor and trace elements in San Carlos olivine at 1,300°C with some geochemical implications. *Contrib. Mineral. Petrol.* **159**, 791–818 (2010)
- Streckeisen, A. 1976. To each plutonic rock its proper name. *Earth Sci. Rev.*, 12 (1), 1976, pp. 1-33.
- Su, B.X., Zhang, H.F., Sakyi, P.A., Zhang, Y.H., Ying, J.F., Tang, Y.J., Qin, K.Z., Xiao, Y., Zhao, X.M., Mao, Q., Ma, Y.G., 2011. The origin of spongy texture in minerals of mantle xenoliths from the Western Qinling, central China. *Contributions to Mineralogy and Petrology* 161, 465-482.
- Sun, C., Liang, Y., 2012. Distribution of REE between clinopyroxene and basaltic melt along a mantle adiabat: effects of major element composition, water, and temperature. *Contributions to Mineralogy and Petrology* 163, 807–823
- Szabo, C. & Taylor, L. A. (1994). Mantle petrology and geochemistry beneath the Nograd–Gomor Volcanic Field, Carpathian–Pannonian region. *International Geology Review* 36, 328–358
- Tamen, J., Nkoumbou, C., Reusser, E., Tchoua, F., 2015. Petrology and geochemistry of mantle xenoliths from the Kapsiki Plateau (Cameroon Volcanic Line): implications for lithospheric upwelling. *J. Afr. Earth Sci.* 101, 119–134.
- Tang, M., McDonough, W.F., Ash, R.D., 2017. Europium and strontium anomalies in the MORB source mantle. *Geochimica et Cosmochimica Acta* 197, 132–141.
- Tedonkenfack, S.S., Puziewicz, J., Aulbach, S., Ntaflos, T., Kaczmarek, M.A., Matusiak-Malek, M., Kukuła, A. and Ziobro, M., 2021. Lithospheric mantle refertilization by DMM-derived melts beneath the Cameroon Volcanic Line—a case study of the Befang xenolith suite (Oku Volcanic Group, Cameroon). *Contributions to Mineralogy and Petrology*, 176(5), pp.1-18.
- Teitchou, M., Gregoire, M., Temdjim, R., Ghogomu, R.T., Ngwa, C., Aka, F.T., 2011. Mineralogical and geochemical fingerprints of mantle metasomatism beneath Nyosvolcano (Cameroon Volcanic Line). *Geol. Soc. Am. Spec. Pap.* 47, 193–210.
- Temdjim, R., Njombie Wagsong, P.M., Nzakou, T.J.A., Foley, S.F., 2019. Variation in mantle lithology and composition beneath the Ngao Bilta volcano, Adamawa Massif, Cameroon volcanic line, West-central Africa. *Geosci. Front.* 11, 665–677.
- Temdjim, R., 2012. Ultramafic xenoliths from Lake Nyos area, Cameroon volcanic line, West-central Africa: petrography, mineral chemistry, equilibration conditions and metasomatic features. *Chem. Erde* 72, 39–60

- Temdjim, R., Boivin, P., Chazot, G., Robin, C., Rouleau, E., 2004. L'heterogeneite du manteau superieur a l'aplomb du volcan du Nyos (Cameroun) révelée par les enclaves ultrabasiques. *Comptes Rendus Geosci.* 336, 1239-1244.
- Tollan, P.M.E., Smith, R., O'Neill, H.S.C., Hermann, J., 2017. The responses of the four main 1092 substitution mechanisms of H in olivine to H₂O activity at 1050 °C and 3 GPa. *Progress 1093 in Earth and Planetary Science*, 4(1).
- Toteu, S. F., Van Schmus, W. R., Penaye, J., Michard, A., 2001. New U-Pb, and Sm-Nd data from North-Central Cameroon and its bearing on the pre-Pan-African history of Central Africa. *Pre. Res.* 108: 45-73.
- Toteu, S.F., Penaye, J., Djomani, Y.P., 2004. U–Pb and Sm-Nd evidence for Eburnean and PanAfrican high-grade metamorphism in cratonic rocks of southern Cameroon. *Can. J. Earth Sci.* 41, 73–85.
- Tschegg, C., Ntaflos, T., Akinin, V.V. and Hauzenberger, C., 2012. Carbonate-rich melt infiltration in peridotite xenoliths from the Eurasian–North American modern plate boundary (Chersky Range, Yakutia). *Contributions to Mineralogy and Petrology*, 164(3), pp.441-455.
- Uenver-Thiele, L., Woodland, A. B., Seitz, H.-M., Downes, H., Altherr, R., 2017. Metasomatic Processes Revealed by Trace Element and Redox Signatures of the Lithospheric Mantle Beneath the Massif Central, France. *J. Petrol.* 58(3), 395–422.
- Van der Wal, D. & Bodinier, J.-L. (1996). Origin of the recrystallisation front in the Ronda peridotite by km-scale pervasive porous melt flow. *Contributions to Mineralogy and Petrology* 122, 387–405.
- Van Schmus, W.R., Oliviera, E.P., Silva Filho, A.F., Toteu, S.F., Penaye, J., Guimares, I.P., 2008. Proterozoic links between the Borborema Province, NE Brazil, and the Central African Fold Belt. In: Pankurst, R.J., RAJ, Trouw, Brito Neves, B.B., de Wit, M.J. (Eds.), *West Gondwana: Pre-Cenozoic Correlations Across the South Atlantic Region*, 294th ed. Geological Society of London, London, pp. 69–100 (Special Publications).
- Vannucci, R., Bottazzi, P., Wulff-Pedersen, E. & Neumann, E.-R. (1998). Partitioning of REE, Y, Sr, Zr and Ti between clinopyroxene and silicate melts in the mantle under La Palma (Canary Islands): implications for the nature of the metasomatic agents. *Earth and Planetary Science Letters* 158, 39–51.
- Vaselli, O., Downes, H., Thirlwall, M. F., Vannucci, R. & Coradossi, N. (1996). Spinel-peridotite xenoliths from Kapfenstein (Graz Basin, Eastern Austria): a geochemical and petrological study. *Mineralogy and Petrology* 57, 23–50.

- Walter M. J., 2003. Melt extraction and compositional variability in mantle lithosphere. In: Holland H., D., Turekian KK (eds) *Treatise on geochemistry*. Elsevier, 363–394.
- Wang, Y., Han, B., Griffin, W. L., Zhang L., & Shu, G. (2012). Post-entrainment mineral-magma interaction in mantle xenoliths from Inner Mongolia, Western North China Craton. *Journal of Earth Science*, 23(1), 54-76.
- Warren, J.M., 2016. Global variations in abyssal peridotite compositions. *Lithos* 248-251, 193–1116 219.
- Wass, S., 1979. Multiple origins of clinopyroxenes in alkali basaltic rocks. *Lithos* 12, 115–132.
- Wells, P.R.A., 1977. Pyroxene thermometry simple and complex systems. *Contrib. Mineral. Petrol.* 62, 129–139.
- Witt-Eickchen, G., Kramm, U., 1998. Evidence for the multiple stage evolution of the subcontinental lithospheric mantle beneath the Eifel (Germany) from pyroxenite and composite pyroxenite/peridotite xenoliths. *Contrib. Mineral. Petrol.* 131,258–272.
- Witt-Eickchen, G., O'Neill, H.S.C., 2005. The effect of temperature on the equilibrium distribution of trace elements between clinopyroxene, orthopyroxene, olivine and spinel in upper mantle peridotite. *Chem. Geol.* 221 (1), 65–101
- Workman, R.K., Hart, S.R., 2005. Major and trace element composition of the depleted MORB mantle (DMM). *Earth and Planetary Science Letters* 231, 53–72.
- Xu, Y.G., Bodinier, J.-L., 2004. Contrasting enrichments in high and low temperature xenoliths from Nushan, Eastern China: results of a single metasomatic event during lithospheric accretion? *J. Petrol.* 45, 321–341.
- Yaxley G. M., Green D. H., 1996. Experimental reconstruction of sodic dolomitic carbonatite melts from metasomatised lithosphere. *Contributions to Mineralogy and Petrology*, vol. 124 (pg. 359-364).
- Yaxley G. M., Green D. H., 1998. Reactions between eclogite and peridotite: Mantle refertilisation by subduction of oceanic crust. *Schweiz Mineral Petrogr. Mitt.* 78: 243–255.
- Yaxley, G. M., Green, D. H., Kamenetsky, V., 1998. Carbonatite Metasomatism in the Southeastern Australian Lithosphere. *J. Petrol.* 39 (11-12), 1917–1930.
- Yaxley, G.M., Crawford, A.J., Green, D.H., 1991. Evidence for carbonatite metasomatism in spinel peridotite xenoliths from western Victoria, Australia. *Earth Planet. Sci. Lett.* 107, 305–317.
- Yaxley, G.M., Green, D.H., 1998. Reactions between eclogite and peridotite: mantle refertilisation by subduction of oceanic crust. *Schweiz. Mineral. Petrogr. Mitt.* 78,243–255.

- Zanetti, A., Mazzucchelli, M., Rivalenti, G. & Vannucci, R. (1999). The Finero phlogopite-peridotite massif: an example of subduction-related metasomatism. *Contributions to Mineralogy and Petrology* 134, 107–122
- Zanetti, A., Vannucci, R., Bottazzi, P., Oberti, R., Ottolini, L., 1996. Infiltration metasomatism at Lherz and monitored by systematic ion-microprobe investigations close to a hornblende vein. *Chemical Geology* 134, 113–133
- Zangana, N., Downes, H., Thirlwall, M., Marriner, G., Bea, F., 1999. Geochemical variation in peridotite xenoliths and their constituent clinopyroxenes from Ray Pic (French Massif Central): implications for the composition of the shallow lithospheric mantle. *Chem. Geol.* 153(1-4), 11–35.
- Zhang, M., Suddaby, P., O'Reilly, S.Y., Norman, M., Qiu, J., 2000. Nature of the lithospheric mantle beneath the eastern part of the Central Asian fold belt: mantle xenolith evidence. *Tectonophysics* 328, 131–156.

CHAPTER IV:
WATER CONTENTS IN THE SUBCONTINENTAL
LITHOSPHERIC MANTLE BELOW THE
CAMEROON VOLCANIC LINE

IV.1. INTRODUCTION

The term ‘water’ when associated with the deep Earth refers to H incorporated in minerals or melts/fluids. Nominally anhydrous minerals (NAMs) eg. olivine and pyroxenes do not have hydrogen in their stoichiometric chemical formulas, however, H can be incorporated as point defects (vacancies), by replacing cations in the mineral structure (Demouchy and Bolfan Cassanova 2016). In hydrous mineral phases like mica, phlogopite, chlorite and amphibole, ‘water’ is incorporated as hydroxyl OH (Bizimis and Peslier, 2015; Green, 2015), while in fluids and melts, H can be hosted as H₂O, hydroxyl OH, H₂ (hydrogen gas), CH₄ (methane), or H₂S (hydrogen sulphide) (Peslier et al., 2017).

Hydrogen incorporated in NAMs (olivine and pyroxenes) in the upper mantle has a significant effect on the physico-chemical properties such as melting temperatures (Green et al., 2010), electrical resistivity/conductivity (Selway et al., 2014), lithospheric rheology (Liptai et al., 2021), seismic wave propagation, heat transfer, diffusion rates of coexisting ions and deformation behaviour (Demouchy et al., 2012), which in turn controls the stability of continents (cratons and lithospheric delamination) (Xia et al., 2013; Peslier et al., 2012; Peslier et al., 2010).

In this chapter, we report the first FTIR data (except for the Nyos locality which has been reported by Pinter et al., 2015) of NAMs from several localities along the CVL, in the Oku Volcanic Field (OVF) and the Adamawa Volcanic Field (AVF) in conjunction with the Kapsiki xenoliths presented in chapter 2. These two volcanic fields are found in the West Cameroon and Adamawa Yade domains respectively, which represent distinct blocks formed during the Pan African Orogeny. NNE-SSW Tchollire-Banyo Fault (TBF) (See chapter 1) delimits these domains (Toteu et al., 2001). The Adamawa Yade domain is located at the northern edge of the Congo craton and the presence of Archean relics, which were possibly inherited from the Congo craton (Tchakounte et al, 2017; Ganwa et al., 2016) characterize it. The OVF in the West Cameroon domain is juvenile and has been dated to be Proterozoic (Tchakounte et al, 2017; Ganwa et al., 2016). The geodynamic relationships between these two domains remain unclear and there is no striking difference in the mineral chemistry and equilibration conditions of mantle xenoliths from the different fields. In the previous chapter, (Chapter 3), it has been shown that large parts of the mantle below the

CVL are affected by silicate and or carbonatite metasomatism. In this chapter, it will be evaluated if such metasomatism is related to an increase in H₂O contents of the lithospheric mantle. Special emphasis will be placed on whether olivine, orthopyroxene or clinopyroxene is suited to record the H₂O contents below the CVL. The samples obtained for this study were mainly spinel bearing mantle xenoliths. A total of 30 samples were investigated, four from the AVF at Ngaoundere Likok and 26 from 7 different localities in the OVF.

IV.2. RESULTS

Calculated average H₂O contents of olivine, orthopyroxene and clinopyroxenes are shown in table 4.1 and representative infrared spectra in Figs. 4.1, and 4.2. Since these are unpolarised measurements, the more unoriented grains are measured, the more accurate the estimations. It should however be noted that even though some of the measured averages are few, the pyroxene measurements are still accurate (Patko et al., 2019; Liu et al., 2015; Xia et al., 2013a), because the method of Kovacs et al., 2008 for unpolarised infrared measurements on unoriented anisotropic minerals (e.g. olivine and pyroxenes) make it possible to accurately determine the structural hydroxyl of a few grains.

IV.2.1. CLINOPYROXENE

Clinopyroxenes from the CVL show heterogeneous spectra and a shift in the peak position is generally common within and between samples. The IR absorption bands of clinopyroxenes are mainly located at 3680-3690 cm⁻¹, between 3625-3640 cm⁻¹, 3610-3615 cm⁻¹, 3515-3540 cm⁻¹ and 3445-3465 cm⁻¹. They can be grouped into 5 different types based on the band position and number of OH peaks (Fig. 4.1).

- The type 1 spectra are characterized by OH bands at ~3630, ~3530 and ~3455 cm⁻¹ with the largest peak at ~3630 cm⁻¹. It is the most common type in clinopyroxenes of the CVL xenoliths and represents 42% of the studied xenoliths. This spectra type has previously been reported in clinopyroxenes from the CVL (Pinter et al., 2015) and is common in natural samples worldwide. Calculated average H₂O contents cover a wide range from 15-149 ppm.

Table 4.1: FTIR characteristics and H₂O contents of xenoliths from the Cameroon Volcanic Line

Sample	Olivine			Orthopyroxene			Clinopyroxene			D _{cpx/opx}		
	Number of grains	Absorbtion bands	H ₂ O (ppm) Core	Number of grains	Absorbtion bands	H ₂ O (ppm) Core Rim	Number of grains	Absorbtion bands	H ₂ O (ppm) Core Rim			
NI1*	–	–	–	4	3695, 3600, 3415	10±3	–	9	3680 ^o , 3640	604±200	–	59
NI1a*	–	–	–	4	3600, 3415	12±2	–	8	3680 ^o , 3640	588±170	–	48
NI5	–	–	–	5	3590, 3520, 3415	22±5	–	4	3680 ^o , 3630	637±109	–	29
NI8*	–	–	–	3	3600, 3415	24±12	–	2	3680 ^o , 3635	909±226	–	37
En1a*	–	–	–	12	3590, 3523	30±7	–	14	3615, 3530	120±39	–	4.9
En2a*	–	–	–	13	3570, 3520	12±2	–	8	3630	120±48	–	10
E1a*	–	–	–	10	3570, 3520	8.9±3	6.7±2	10	3640, 3525	22±4	–	2.6
E2	–	–	–	5	3580, 3520, 3410	37±4	28±9	6	3635, 3530, 3455	114±26	–	3.1
E8*	–	–	–	7	3575, 3520	10±3	–	4	3640, 3520, 3455	15±5	–	1.5
E15	–	–	–	4	3575, 3520	12±4	–	7	3615, 3530, 3455 ^a	81±46	60±45	6.7
K1*	–	–	–	8	3590, 3520	54±10	34±6	11	3630, 3530, 3460	210±19	152±22	3.9
K1a*	–	–	–	11	3597, 3520, 3415	27±7	24±3	15	3630, 3525, 3455	121±35	–	4.5
K4	–	–	–	4	3590, 3520	53±42	–	4	3615, 3525, 3455	218±35	–	4.1
K5*	–	–	–	11	3600, 3415	34±6	–	4	3635	200±44	–	6.9
K6	3	3572, 3540 ^a , 3525	2.8	6	3590, 3520, 3415	82±12	77±3	3	3615, 3530, 3455	271±29	–	3.3
K7	3	3572, 3525	0.48	5	3588, 3520, 3415	43±18	39±13	3	3635, 3525, 3455	109±44	–	2.5
Ny1a*	–	–	–	9	3590, 3520	11±3	–	3	3635	56±14	–	5.3
Ny3	–	–	–	20	3585, 3520	20±8	–	7	3635	78±39	–	4.0
Ny6	–	–	–	5	3588, 3520, 3415	44±8	–	3	3613, 3535, 3455	291±53	–	6.5
Ok1*	–	–	–	10	3567, 3520, 3217, 3120	26±7	–	2	3515	50±20	–	1.9
Ok1a*	–	–	–	15	3566, 3520	19±9	13±7	8	3515	27±17	–	1.3
We1a (Dry)*	–	–	–	8	3590, 3520, 3415	30±5	–	19	3630, 3525, 3445	118±39	–	3.9
We1a (Wet)*	–	–	–	–	–	–	–	4	3690 ^o , 3630, 3525, 3445	232±138	–	7.6
We4	–	–	–	3	3592, 3522, 3415	35±3	30±3	5	3615, 3525, 3455	155±83	–	4.4
We6	–	–	–	4	3597, 3520, 3415	23±12	–	2	3630, 3445	84±9	–	3.6
We8	–	–	–	2	3598, 3520, 3415	31±6	–	7	3630, 3455	324±22	–	10
Ww1a*	–	–	–	14	3594, 3521, 3410	16±3	–	12	3633, 3525 ^a , 3448 ^a	90±26	–	5.7
Ww2	–	–	–	3	3595, 3520, 3403	10±8	–	4	3630, 3530, 3453	122±22	65±10	12
Ww3	–	–	–	6	3596, 3521, 3410	25±9	–	6	3630, 3530, 3463	149±58	–	5.9
Ww4	–	–	–	2	3595, 3522, 3420	18±1	–	6	3629, 3527, 3448	44±20	–	2.3
Ww7	–	–	–	5	3598, 3520, 3415	20±4	–	3	3632, 3538 ^a , 3455 ^a	86±22	–	4.3

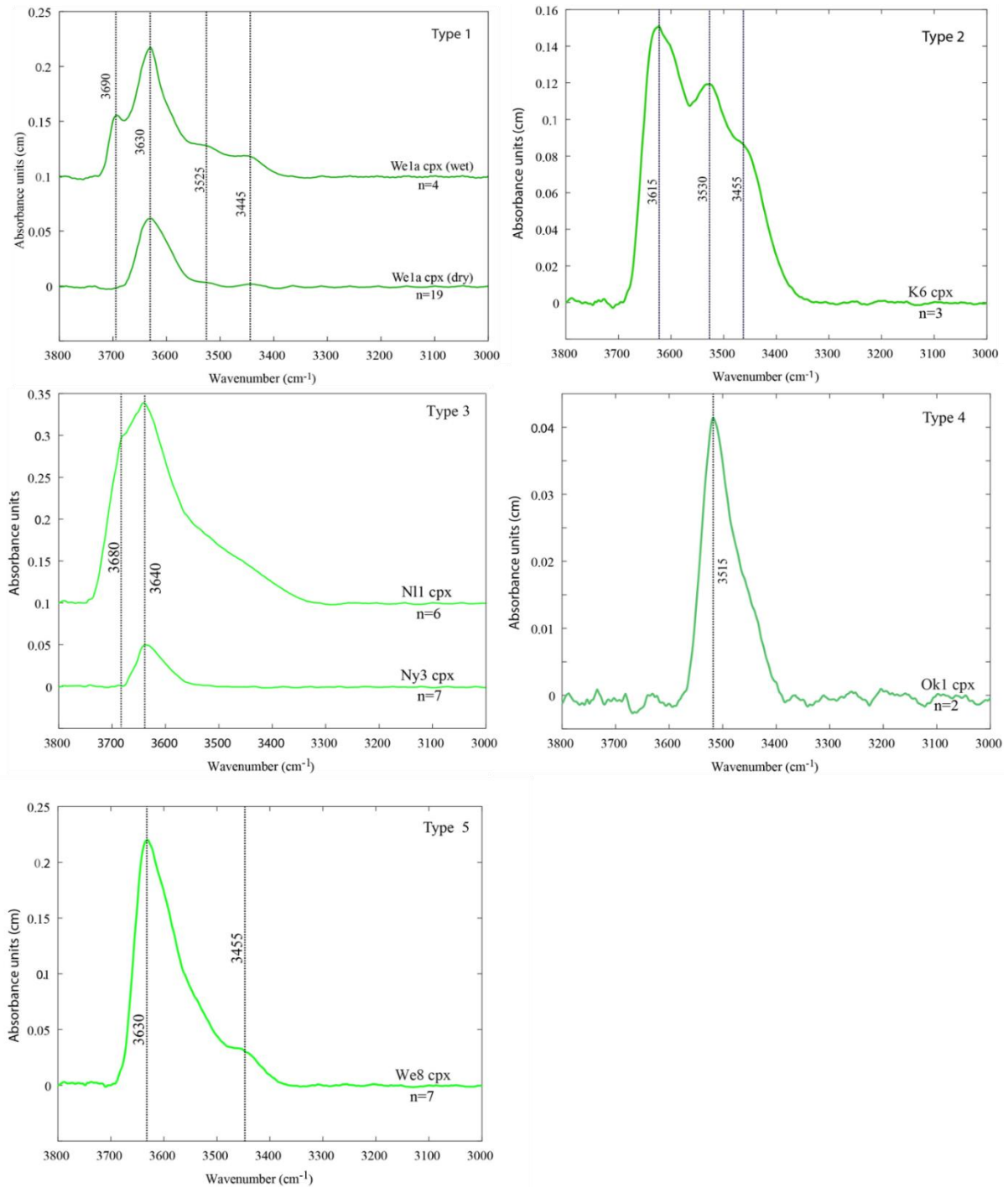


Figure 4.1: Representative average unpolarised infrared spectra of clinopyroxenes of the studied xenoliths.

- The type 2 spectra show bands at 3615, 3530 and 3455 cm^{-1} . They are less common and occur in 19% of the studied samples. They show higher average H_2O contents than the type 1 spectra, ranging from 81- 291 ppm.
- The type 3 spectra show a unique band at $\sim 3635 \text{ cm}^{-1}$ and represent 26% of the xenoliths. This is the dominant spectra type in the Ngaoundere Likok samples and they also show minor bands at $\sim 3680 \text{ cm}^{-1}$. The H_2O contents in these samples are also very high, ranging from 588-909 ppm. The other samples, which show this spectrum, type from the OVF contain comparatively very low H_2O contents of 39-142 ppm.
- The type 4 spectra constitute a main band at $\sim 3515 \text{ cm}^{-1}$ and have very low H_2O contents from 27-50 ppm. They are present in 6% of the samples.
- The type 5 spectra show a main band at ~ 3630 and a minor band at $\sim 3455 \text{ cm}^{-1}$. It is seen in 6% of samples. Their H_2O contents range from 84-324 ppm.

Generally, measured H_2O contents at the rims of the clinopyroxenes are slightly lower than at the cores but never approach zero (Table 4.1).

IV.2.2. ORTHOPYROXENE

As observed in clinopyroxenes, orthopyroxenes show several spectra types. The main absorption bands occur at 3580-3600 cm^{-1} , 3585-3565 cm^{-1} , 3565-3575 cm^{-1} , 3520-3525 cm^{-1} and 3400-3415 cm^{-1} . In total three different types have been distinguished (Fig. 4.2a-c).

- Type A spectra constitutes 97% of the orthopyroxenes and shows OH absorption bands at 3600, 3525 and 3415 cm^{-1} .
- Type B spectra constitutes 13% of the orthopyroxenes and show OH absorption bands at 3600 and 3415 cm^{-1} . This spectra type is only observed in samples from Ngaoundere Likok. One sample shows a minor band at 3695 cm^{-1} .
- Type C spectra makes up 20% of orthopyroxenes, it consists of OH bands at 3575 and 3525 cm^{-1} .

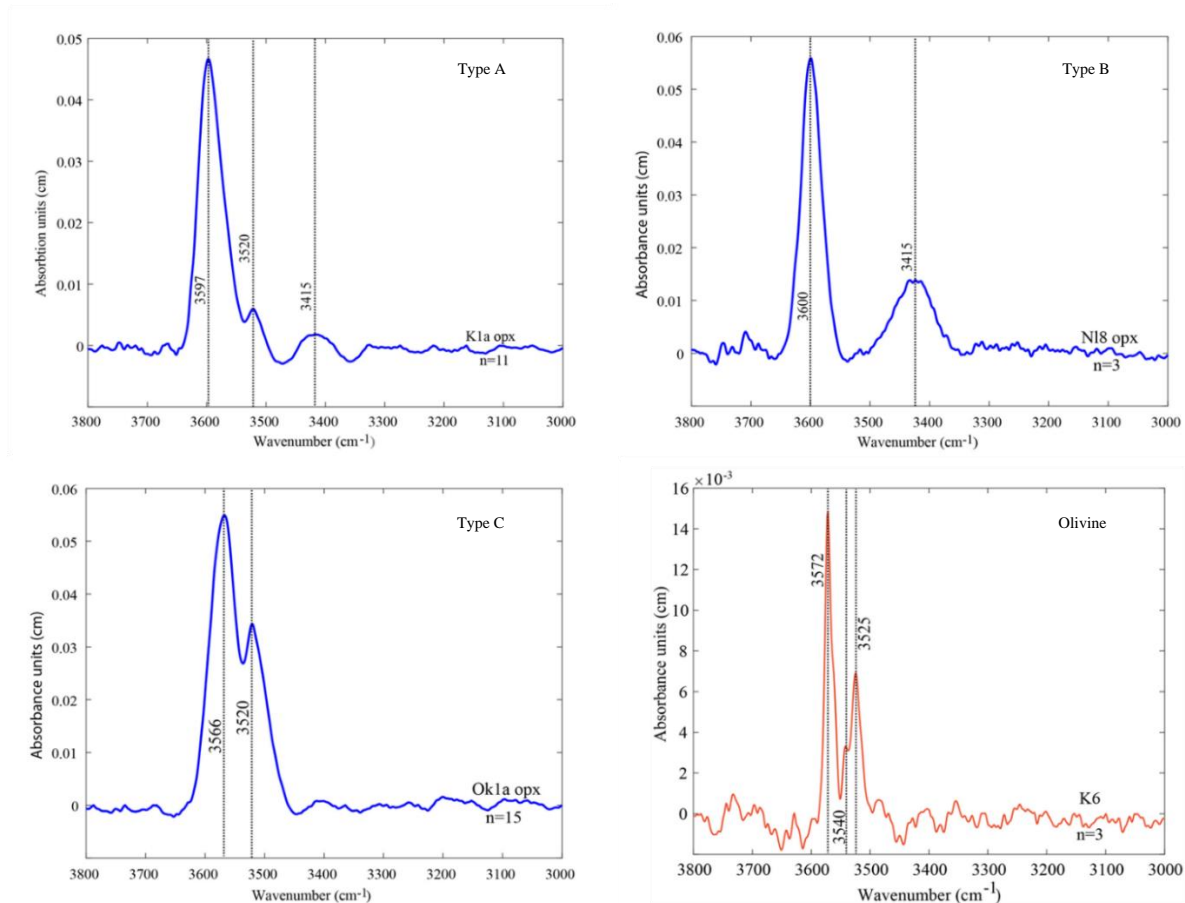


Figure 4.2: Representative average inferred spectra of orthopyroxene and olivine from the Cameroon Volcanic Line.

The H₂O contents of orthopyroxenes show a narrow range while clinopyroxenes show a huge variability. The H₂O contents of orthopyroxenes are more consistent regardless of the locality or spectra type and they range from 9-82 ppm. The H₂O contents are also lower at the rims relative to the cores in some orthopyroxene grains.

IV.2.3. OLIVINE

Olivines generally do not show any visible OH absorption bands except for some Kuk samples which show weak bands at 3572 cm⁻¹, 3525 cm⁻¹ and a minor band is sometimes observed at 3540 cm⁻¹ (Fig. 2d). These bands have been reported in other studies and are typical of mantle olivine (Li et al., 2008; Grant et al., 2007; Peslier and Luhr, 2006). They display very low H₂O contents, which are below 3 ppm (Table 4.1).

IV.3. DISCUSSION

IV.3.1. SIGNIFICANCE OF THE INFRARED SPECTRA AND H₂O CONTENTS

The site defects which hosts hydrogen in different NAMs can be inferred from the OH vibrating regions of the infrared spectra and they correspond to different modes of hydroxyl incorporation (Beran and Putnis, 1983).

IV.3.1.1. Olivine

Generally, the olivines from this study are below the limit of detection (they show no absorption bands in the OH stretching region). Results from experimental studies show that the solubility of hydrogen decreases with a decrease in pressure (Mackwell & Kohlstedt, 1990), especially in olivine. Hydrogen, therefore, most likely diffuses out of the xenolith minerals as the xenolith ascends due to decompression (Demouchy et al., 2006; Peslier and Luhr, 2006). This has also been supported by the observation of diffusion profiles in olivine (Peslier and Bizmis 2015; Denis et al., 2013; Peslier et al., 2008; Demouchy et al., 2006; Peslier and Luhr, 2006; Demouchy et al., 2003).

The expected H₂O contents for the CVL olivines calculated using the partition coefficient between orthopyroxene and olivine (Demouchy and Bolfan Casanova, 2016) shows that the H₂O contents are lower than 2 ppm. This indicates that the H₂O contents of olivines were initially very low.

Experimental studies have shown that there is a close link between the concentration of elements and the substitution mechanism of hydrogen in olivine (Tollan et al., 2018, 2017; Berry et al., 2005). The CVL olivines show low Ti (0.6-34 ug/g) and Cr (31-108 ug/g, except Oku samples with 280-300 ug/g). Decreasing the Al and Cr contents in olivine decreases solubility (Rauch and Keppler, 2002) and increases the rate of hydrogen diffusion (Schlechler, 2011). This indicates that the depleted chemistry coupled with low aH₂O could have inhibited H incorporation (Tollan et al., 2018; Tollan et al., 2017). This shows that mantle conditions below the CVL do not favor hydrogen incorporation. The observed correlation of Cr and Ti with Al and the olivine temperatures (Fig. 3.17a, f; Table 3.12) provide evidence that hydrogen incorporation into olivine is hindered at low temperatures.

Two samples from the Kuk area however show weak OH bands at 3572, 3525 cm^{-1} and a minor shoulder at 3540 cm^{-1} (Fig. 4.2d; Table 4.1). The bands at 3572 and 3525 cm^{-1} have been assigned to Ti clinohumite point defects, whereby two hydrogens are incorporated in the vacant tetrahedral site to compensate for Ti^{4+} in the octahedral site (Kovacs et al., 2010; Berry et al., 2005).

Calculated H_2O contents for olivines in these samples are below 3 ppm. Olivines from Kuk have the highest Ti contents (up to 34 $\mu\text{g/g}$). The observed correlation between the H_2O contents and the small Ti clinohumite defects suggests that H solubility could simply be higher in these olivines compared to those with lower Ti contents. The observed correlation of small Ti clinohumite point defects in olivine suggests that this is the most stable configuration that is less affected by diffusion modification than other types of defects. The very low H_2O contents of olivines in this study is overall in agreement with very low reported H_2O contents for other CVL localities which include the Barombi-Mbo (2.8- 6.6 ppm) and Nyos localities (0.6-3.4 ppm) (Pinter et al., 2015). They fall in the range of values reported for other non-cratonic settings, even though they are mostly at the low end (eg Demouchy and Bolfan-Casanova., 2016; Peslier 2010; Peslier et al., 2007). Olivine with no H_2O contents have also been reported for xenoliths in other localities (eg. Denis et al., 2018; Xia et al., 2010; Yang et al., 2008).

IV.3.1.2. Orthopyroxene

OH bands are common in the FTIR spectra of mantle orthopyroxene, and some appear to be related to oxygen fugacity. Those at 3544, 3520, 3390, 3325 and 3060 cm^{-1} are redox-sensitive and show an increase in intensity with increasing oxygen fugacity (Tollan and Hermann, 2019). Other common bands appear at 3600 and 3420 cm^{-1} but they do not show any relationship with oxygen fugacity. In orthopyroxenes from this study, OH bands are common at ~ 3595 , ~ 3575 , ~ 3520 and ~ 3415 cm^{-1} and they agree well with natural samples from different tectonic settings worldwide except the band at 3575 cm^{-1} , which is uncommon (eg. Demouchy et al., 2015; Denis et al., 2015; Xia et al., 2010; Bonadiman et al., 2009; Peslier et al., 2002). Previously studied orthopyroxenes from Nyos and Barombi

Mbo also show bands at the same position except for the 3575 cm^{-1} which is absent and additional bands at $\sim 3307\text{ cm}^{-1}$ (Pinter et al., 2015).

The redox-sensitive bands (at $\sim 3520\text{ cm}^{-1}$) are generally absent from the Ngaoundere Likok samples (Fig. 4.2b) but more common in the samples from OVF (Fig. 4.2a). Bands at 3520 cm^{-1} are more pronounced than bands at $\sim 3415\text{ cm}^{-1}$ but weaker than the bands at $\sim 3595\text{ cm}^{-1}$. Sample Ok1a displays a prominent band at 3520 cm^{-1} (Fig. 4.2c) and this sample also shows the highest oxygen fugacity around QFM. In other samples, the band is less prominent reflecting the general reducing conditions of the lithospheric mantle below the region. Based on experimental studies, the bands at 3600 and 3420 cm^{-1} have been attributed to the presence of Si vacancies and tetrahedral Al (Prechtel and Staldler 2012). OH bands at 3695 cm^{-1} , which sometimes occur in samples from Ngaoundere Likok (Fig. 4.2), are associated with hydrous lamellae (eg amphibole) in pyroxene (Kovacs et al., 2012; Della Ventura et al., 2007).

Calculated H₂O contents for orthopyroxenes from all studied xenoliths are very low and consistent. They range between 9-82 ppm with 83% of samples having concentrations below 40 ppm. These values are lower than in most peridotites from non-cratonic mantle xenoliths (Grant et al., 2007b; Demouchy et al., 2006; Peslier and Luhr, 2006). Previously reported values for Nyos are in the same range but those from Barombi-Mbo are much higher (Pinter et al., 2015). Hydrogen diffusion is uncommon in orthopyroxenes but has been recently reported (eg Tollan and Hermann, 2019; Denis et al., 2018; Tian et al., 2017). Calculated H₂O contents for the rims of most orthopyroxenes show approximately the same values as the cores. A few samples show lower water contents at the rims, however, the values do not differ significantly from the core composition and never approach zero, which indicates diffusion loss of H in orthopyroxene is insignificant.

IV.3.1.3. Clinopyroxene

Clinopyroxenes in this study are characterized by OH bands, which show shifts in the band positions amongst different samples. The main bands are at 3630 , 3615 , 3525 , 3515 and 3455 cm^{-1} . Due to limited research and the complexity of clinopyroxene, the different substitution mechanisms related to the different OH bands remain unclear. Nevertheless, a

first-order band assignment is possible through comparison with experimental studies. The high wavenumber bands at 3600 cm^{-1} are primarily controlled by coupled substitution of H with tetrahedral Al (O’Leary et al., 2010; Stalder and Ludwig 2007). The minor shoulder-like bands at 3680 cm^{-1} that are common in samples from Ngaoundere Likok have been attributed to the presence of amphibole lamellae (Della Ventura et al., 2007; Ingrin et al., 1989).

Calculated H₂O contents show two distinct groups for the CVL xenoliths. The first group constitutes xenoliths from the OVF with H₂O contents ranging from 16-324 ppm (average of 124 ppm), which fall in the lower end of global values. The second group is mainly constituted by xenoliths from Ngaoundere Likok where H₂O contents range from 588-909 ppm (average of 685 ppm). They show higher H₂O contents than the global values. Even though the infrared spectra of clinopyroxenes from Ngaoundere Likok samples show weak bands at 3680 cm^{-1} which are related to hydrous minerals (amphibole) (Table 4.1), the H₂O contents are still reliable since the hydrous mineral may form at the expense of the hydroxyl contents of the host clinopyroxene (Kang et al., 2017; Schmadicke and Gose 2017). However, even if the hydroxyl was external, their contribution to the H₂O contents will only be minimal as they occur as weak bands.

IV.3.2. H₂O PARTITIONING BETWEEN CLINO- AND ORTHOPYROXENE

H₂O partition coefficients between clinopyroxenes and orthopyroxenes are highly variable (Figs, 4.3, 4.4), ranging from 1.1-60 (Table 4.1) in the studied xenoliths. Studies on natural xenolith samples have shown that the normal range for $D^{\text{cpx/opx}}$ values is between 1.5-3.5 (Peslier et al., 2017; Xia et al, 2017). A few samples from the study area fall within this range, but 65% show higher values. When plotted with H₂O contents, the samples from the OVF show weak negative MgO, SiO₂ and Mg# correlation, and weak positive trends for TiO₂, Al₂O₃ and Na₂O in clinopyroxenes (Fig. 4.5). Weak positive correlations are also observed in TiO₂, Al₂O₃, FeO and Na₂O for orthopyroxenes while SiO₂ shows a weak negative correlation (Fig. 4.6).

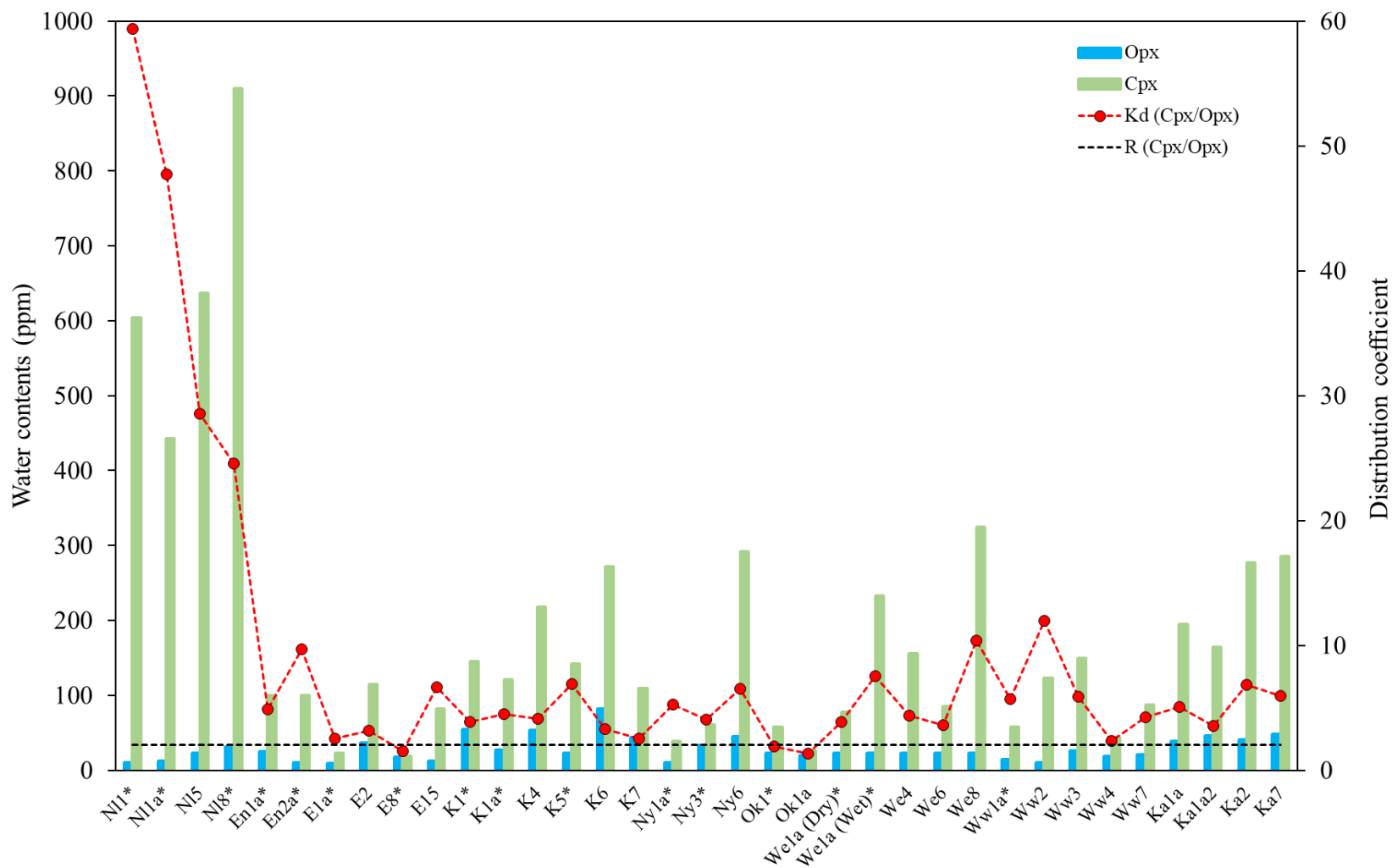


Figure 4.3: Variations of H₂O contents in orthopyroxene and clinopyroxene. R (cpx/opx) is the water concentration ratio between clinopyroxene and orthopyroxene, which equals 2.1 (Demouchy and Casanova, 2016). Kd (cpx/opx) is the partition values between clinopyroxene and orthopyroxene in the CVL xenoliths. They are compared to the H₂O contents of pyroxenes in Kapsiki xenoliths. The stars represent thick section analysis while the rest are on grain mounts.

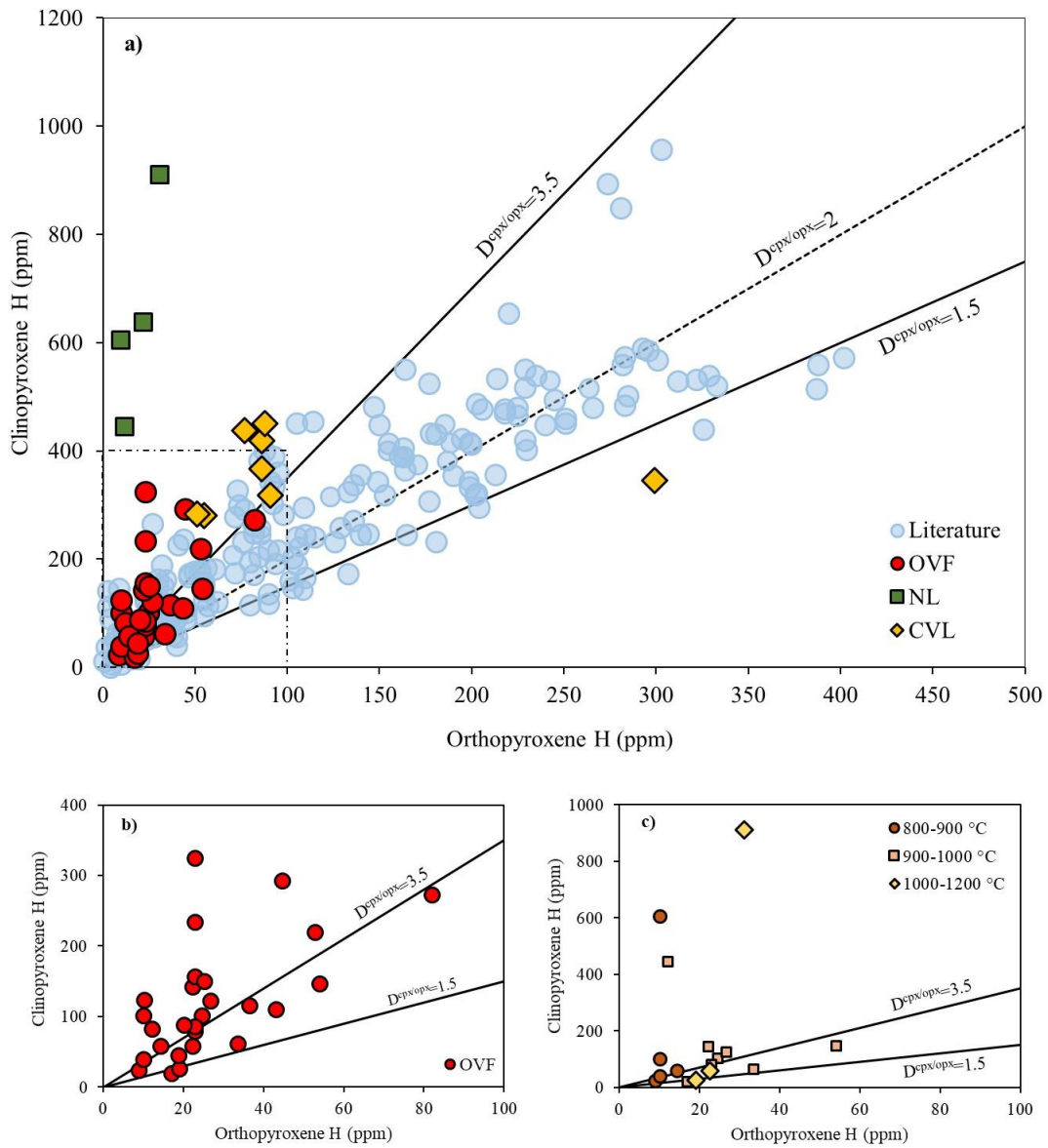


Figure 4.4a: Partitioning ($D_{\text{cpX/opX}}$) of H_2O between coexisting orthopyroxene and clinopyroxene in this study (Oku Volcanic Field (OVF), Ngaoundere Likok (NL)) compared to available data for other Cameroon Volcanic Line (CVL) (Pinter et al., 2015), xenoliths and different tectonic settings from the literature (Patko et al., 2019; Hao et al., 2014; Hao et al., 2012; Yu et al., 2011; Bonadiman et al., 2009; Yang et al., 2008; Peslier et al., 2002). The lines which represent the normal range between 1.5-3.5 are from Xia et al., 2017. 4.4b) Expansion of 4.4a to show samples from the OVF. 4.4c) Relationship between temperature and partitioning of H_2O in the studied xenoliths.

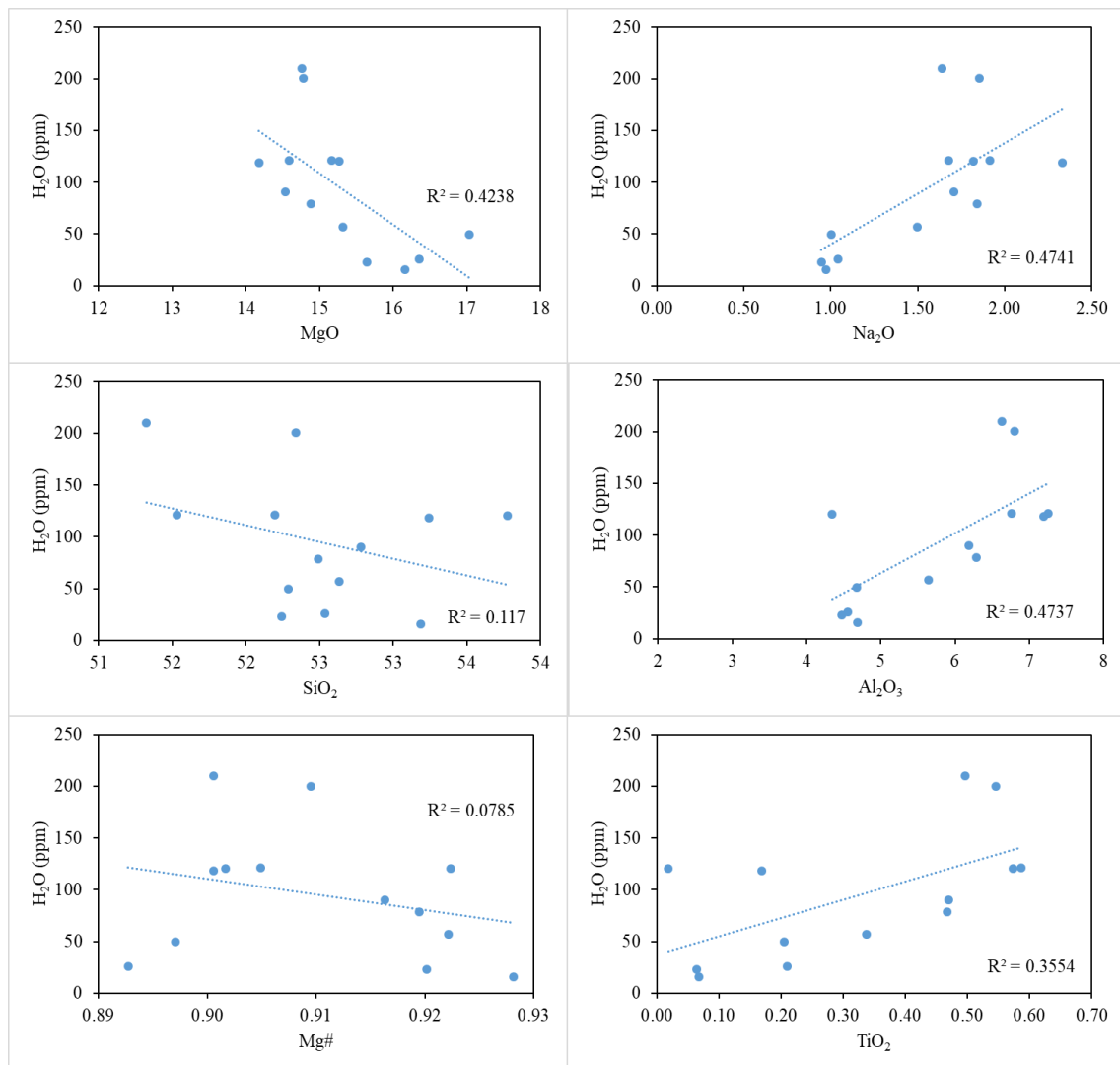


Figure 4.5: H₂O contents vs clinopyroxene major element composition for the Oku Volcanic Field xenoliths.

When the whole data set is considered (Fig. 4.3) it is evident that clinopyroxene displays much larger variations in H₂O contents than orthopyroxene. This is particularly prominent for the Ngaoundere Likok samples. The group 6 clinopyroxene patterns with variable REE contents and different amounts of LREE enrichment are also found in the Ngaoundere Likok samples (Fig. 3.19). This indicates that the metasomatic introduction or modification of clinopyroxene in these samples went together with enrichment in H₂O that is not mirrored with a simultaneous increase in H₂O in orthopyroxene. We therefore consider that in these samples the high value for H₂O partitioning between cpx and opx is related to a selective gain of H₂O in clinopyroxene either by the formation of new metasomatic or by equilibration of existing clinopyroxene. Generally, the grain size of

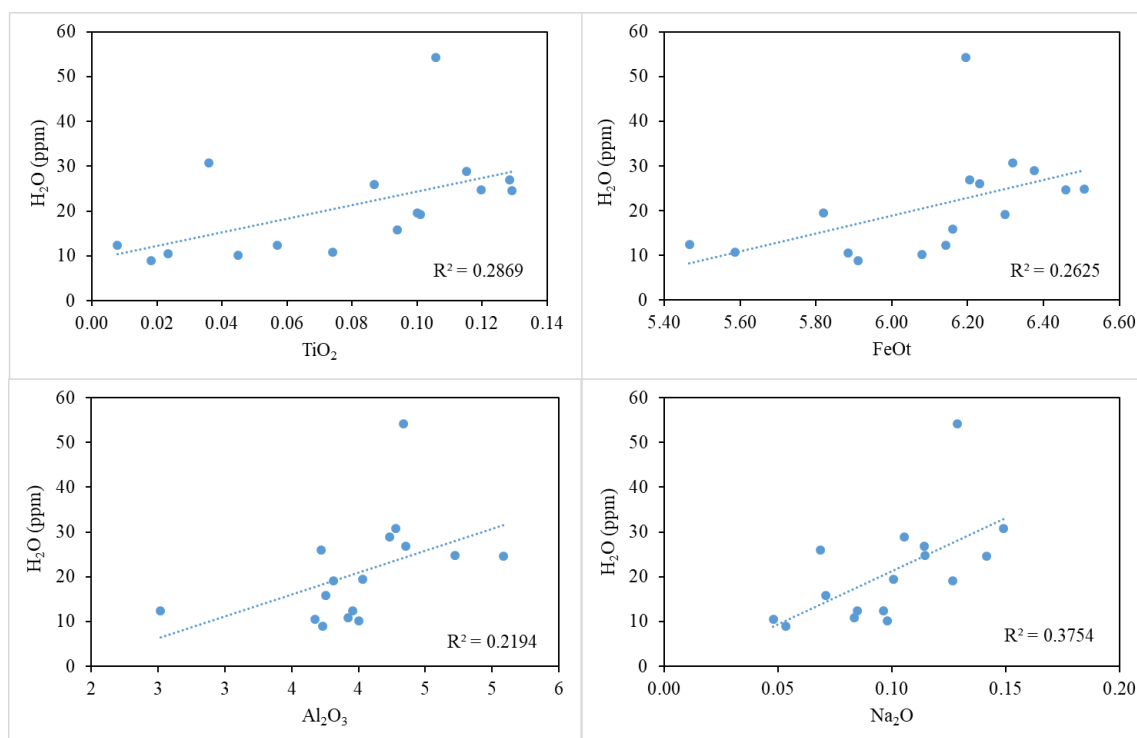


Figure 4.6: H₂O contents vs orthopyroxene major element composition for the Oku Volcanic Field xenoliths.

clinopyroxene is significantly smaller than for orthopyroxene (Fig. 3.9), making clinopyroxene more prone to equilibration.

IV.3.3. INITIAL H₂O CONTENT IN THE MANTLE SOURCE

Most olivines in this study are void of OH absorption bands. Hydrogen loss is commonly shown as diffusion profiles in NAMs (Peslier et al., 2008; Peslier and Luhr 2006; Demouchy et al., 2003), and can be influenced by temperature, pressure, chemical composition and oxygen fugacity (Demouchy et al., 2016; Stalder and Skogby, 2007; Demouchy and Mackwell, 2006; Demouchy and Mackwell, 2003; Stalder and Skogby, 2003). However, we cannot effectively evaluate hydrogen loss in the olivines of this study because most of their H₂O contents are below detection limits.

Some studies have shown that pyroxenes preserve their initial H₂O contents to a certain extent while olivine does not (Xia et al., 2017; Denis et al., 2015; Xia et al., 2010; Gose et al., 2009; Peslier et al., 2002). Hydrogen diffusivity in olivine is fast (Demouchy and Mackwell, 2003; Kohstedt and Mackwell, 1998; Mackwell and Kohstedt, 1990) and hydrogen in olivine is controlled by mantle processes such as melt percolation, magma

ascent and metasomatism (Satsukawa et al., 2017; Demouchy et al., 2015; Denis et al., 2015 ; Denis et al., 2013; Demouchy et al., 2006; Peslier and Luhr, 2006). Olivine has therefore been considered unreliable to provide an accurate estimate of H₂O contents in the mantle (Demouchy and Bolfan-Casanova, 2016; Denis et al., 2013). Pyroxenes have in the past been considered to better preserve the original H₂O contents (Xia et al., 2019; Demouchy and Bolfan-Casanova, 2016; Peslier, 2010; Xia et al., 2010) because H₂O partitioning values between cpx and opx in the majority of cases show values which reflect equilibrium (Warren and Hauri, 2014; Yu et al., 2011; Xia et al., 2010; Yang et al., 2008).

Recent studies have interrogated the use of orthopyroxene as a valid proxy for mantle H₂O concentrations (Denis et al., 2018; Tian et al., 2017) because of reported dehydration profiles. The lack of profiles in most orthopyroxenes reported worldwide (Demouchy et al., 2015; Denis et al., 2015; Warren and Hauri, 2014; Yu et al., 2011; Xia et al., 2010; Yang et al., 2008; Peslier et al., 2002) has been attributed to fast hydrogen diffusion and easy re-equilibration in this mineral (Xu et al., 2019; Denis et al., 2018; Tian et al., 2017). However, in recent studies, hydrogen diffusion in orthopyroxene has been reported to be much slower relative to clinopyroxene, which could make it a better indicator of the H₂O concentrations (Wang et al., 2021). This however does not guarantee that orthopyroxene H₂O contents represent the initial H₂O contents. The orthopyroxenes from the CVL in contrast to clinopyroxenes however show a consistent distribution of H₂O contents in all the localities which show that they equilibrated at mantle conditions of the region.

A few pyroxene grains show slightly lower H₂O contents in their rims relatively to their cores, which indicates a limited loss by diffusion. However, rim compositions never go to zero. Therefore, it appears that hydrogen loss during the ascent of the xenoliths in the pyroxenes is negligible. As the H₂O partitioning between clino- and orthopyroxene deviates from the published equilibrium value, it is important to evaluate whether clinopyroxene has gained or orthopyroxene has lost H₂O. The H₂O contents of the Ngaoundere Likok clinopyroxenes are significantly higher (588-909 ppm) than those from the OVF (16-324 ppm) while orthopyroxene H₂O contents are less variable regardless of the locality (9-82 ppm). There is evidence for newly formed metasomatic clinopyroxene that is not in equilibrium with orthopyroxene in many samples. Moreover, the grain size of clinopyroxene is generally 2-5 times smaller than orthopyroxene,

making it more prone to diffusional equilibration., We therefore consider the relatively uniform H₂O contents of orthopyroxenes in all the studied samples to be the best proxy for the mantle H₂O content below the CVL. In a second step, we can now estimate initial mantle H₂O contents. We consider for a typical lithospheric mantle 60% olivine, 30% orthopyroxene and 10% clinopyroxene and we apply a cpx/opx H₂O partitioning of 2 (Demouchy and Bolfan-Casanova, 2015; Denis et al., 2015; Xia et al., 2010) and opx/ol partitioning of 5 (Demouchy and Bolfan Casanova, 2016). For the average of 27±16 ppm H₂O in orthopyroxene, we obtain a mantle H₂O content of 16±10 ppm H₂O. This is significantly lower than the estimated MORB mantle H₂O of 50-200 ppm H₂O (Hirschmann, 2006).

IV.3.4. CONTROL OF H₂O CONTENTS BY METASOMATISM

Hydrogen is a highly incompatible element with partition coefficients ($D^{\text{cpx/melt}}$) between La and Ce (Hauri et al., 2006; Dixon et al., 2002) or even lower (Novella et al., 2014; O’Leary et al., 2010) making it very highly sensitive to depletion and enrichment events in the mantle. Hydrogen contents of NAMs can thus be easily modified by partial melting processes or mantle metasomatism (Denis et al., 2015; Peslier et al., 2015; Doucet et al., 2014; Peslier et al., 2012).

Yb in clinopyroxene, Al₂O₃ in clinopyroxene and Mg# in olivine are the proxies commonly used for melt depletion. A negative correlation is expected between H₂O and these proxies if the H₂O content is primarily controlled by partial melting (e.g. Hao et al., 2014). In this study, the H₂O contents of clinopyroxenes and orthopyroxenes show no well-defined correlation with the index of partial melting which implies that partial melting does not control the variable H₂O contents in the different samples.

The influence of metasomatism on the H₂O contents of the CVL xenoliths can be investigated using trace element concentrations of clinopyroxene since they show pervasive and different styles of metasomatism. LREEs do not show any clear correlation with clinopyroxene H₂O contents, they however show a weak correlation with MREEs. Fluids of different composition have metasomatised the clinopyroxene groups in this study. The different metasomatic fluids that react in the upper mantle are characterized by varying hydrogen contents and hydrogen activity (Van der Lee et al., 2008).

Clinopyroxenes metasomatised by silicate and carbonated silicate melts show very low H₂O contents, which range from 15-50 ppm. These are the group 2 and 4 clinopyroxenes according to the classification in chapter 3. An exception is sample En2a which is more enriched in some incompatible trace elements and also shows higher H₂O contents (120 ppm). Groups 1 and 3 clinopyroxenes show patterns, which are similar to the depleted MORB mantle (DMM). These samples also show very low H₂O contents (56-120 ppm), except for group 3 which show slight enrichments in La and has the highest H₂O contents recorded for samples from the OVF (121-218 ppm). The sample from group 5, which has been metasomatised by carbonatite melts shows higher H₂O contents than for samples, which were affected by silicate metasomatism (118 ppm for dry clinopyroxenes and up to 232 ppm for wet ones). The higher H₂O contents relative to samples that were metasomatised by silicate melts is due to hydrous metasomatism as seen by the modal addition of amphibole in this sample.

Samples from Ngaoundere Likok exceptionally show very high H₂O contents (588-909 ppm) even though they are dominated by silicate metasomatism. When plotted separately against the H₂O contents, the Ngaoundere Likok xenoliths show positive correlations with TiO₂, Al₂O₃, and a negative correlation with CaO (Fig. 4.7). They are also correlated with REEs and show a particularly strong positive correlation with La/Yb (Fig. 4.7), which is commonly used as a proxy for metasomatism. The xenoliths from the OVF on the other hand show only weak positive correlations with TiO₂ and Al₂O₃ but no correlation with La/Yb. This indicates that the higher H₂O contents of Ngaoundere Likok xenoliths could be related to metasomatism by fluids with higher water activity while for the OVF, the metasomatic fluids generally had low water activity.

IV.3.5. IMPLICATIONS FOR THE CVL

The H₂O contents of olivine and orthopyroxenes of the different geologic units (NWCD and AYD) of the CVL are similar. This indicates that the different geologic units do not influence the H₂O contents. However, clinopyroxenes from the two units are very different. This has been interpreted to reflect the low and high water activities of different matasomatising fluids of the different units.

Water plays an important role in the mantle. Olivine is the most abundant component of the mantle, and small amounts of hydrogen incorporated in its structure greatly contribute to the water budget (Bell and Rossman, 1992). High water contents

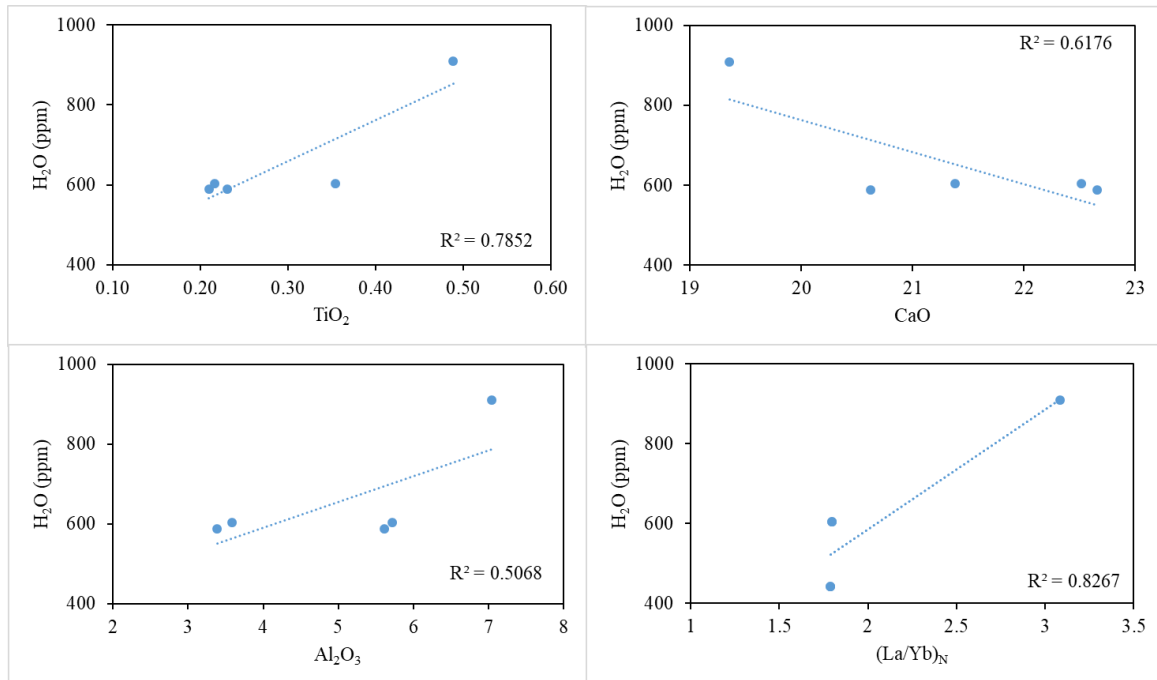


Figure 4.7: H₂O contents vs clinopyroxene major element composition for the Ngaoundere Likok xenoliths.

will highly influence physical properties like decreasing the melting point (Maksimv, 2003), viscosity (Karato and Jung, 2003; Mei and Kohlstedt, 2000a; Mei and Kohlstedt, 2000b), enhance grain boundary migration (Jung and Karato, 2001a), increase electrical conductivity (Fei and Katsura, 2020; Novella et al., 2017), increase ionic diffusion of major elements in mantle minerals (Demouchy et al., 2007) and weaken the strength of single crystals and polycrystalline olivine (Demouchy et al., 2012; Hirth and Kohlstedt, 2003).

The low H₂O contents of the CVL xenoliths, therefore, imply that the lithospheric mantle has more stable continental roots (Karato, 2010; Pollack, 1986) and increased lithospheric strength.

IV.4. CONCLUSION

- Orthopyroxenes display low H₂O contents and show a narrow range. Clinopyroxenes show a very large range and consists of very low and exceptionally high contents, which suggests that they could have gained H₂O.

The majority of olivines are dry and might have lost their hydrogen contents during the ascent of the xenoliths. This indicates that orthopyroxenes record the most reliable water contents for the mantle below the CVL.

- Partitioning coefficients of H₂O between pyroxenes are highly variable with some samples showing significantly higher values than those expected for equilibrium partitioning.
- The H₂O contents of NAMs of the CVL xenoliths are generally very low resulting in an average mantle with 16±10 ppm H₂O indicating an increased lithospheric strength. This is significantly lower when compared to spinel facies mantle xenoliths worldwide, even though the CVL xenoliths show evidence for modal and cryptic metasomatism. The low H₂O contents could be related to low H₂O activity in the metasomatic fluids.

REFERENCES

- Bell, D.R., Rossman, G.R., 1992. Water in Earth's mantle: the role of nominally anhydrous minerals. *Science* 255, 1391–1397
- Beran, A., Putnis, A., 1983. A model of the OH positions in olivine, derived from infrared spectroscopic investigations. *Physics and Chemistry of Minerals* 9, 57–60.
- Berry A. J., Hermann J., O'Neill H. S. C. and Foran G. J. (2005). Fingerprinting the water site in mantle olivine. *Geology* 33, 869–872.
- Bizimis, M., Peslier, A.H., 2015. Water in Hawaiian garnet pyroxenites: implications for water heterogeneity in the mantle. *Chemical Geology* 397, 61–75.
- Bonadiman, C., Hao, Y., Coltorti, M., Dallai, L., Faccini, B., Huang, Y., Xia, Q., 2009. Water contents of pyroxenes in the intraplate lithospheric mantle. *European Journal of Mineralogy* 21, 637–647.
- Della Ventura, G., Oberti, R., Hawthorne, F.C., Bellatreccia, F., 2007. FTIR spectroscopy of Ti-rich pargasites from Lherz and the detection of O²⁻ at the anionic O³ site in amphiboles. *Am. Mineral.* 92 (10), 1645–1651.
- Demouchy S., Mackwell S. J., Kohlstedt D. L., (2007). Influence of hydrogen on Fe–Mg interdiffusion in (Mg, Fe) O and implications for Earth's lower mantle, *Contributions to Mineralogy and Petrology*, 2007, vol. 154 (pg. 279-289).
- Demouchy S. and Mackwell S. (2006). Mechanisms of hydrogen incorporation and diffusion in iron-bearing olivine. *Phys. Chem. Miner.* 33, 347–355.

- Demouchy S., Jacobsen S. D., Gaillard F. and Stem C. R. (2006). Rapid magma ascent recorded by water diffusion profiles in mantle olivine. *Geology* 34, 429–432.
- Demouchy S., Tommasi A., Barou F., Mainprice D. and Cordier P. (2012) Deformation of olivine in torsion under hydrous conditions. *Phys. Earth Planet. Inter.*202–203, 56–70.
- Demouchy, S., & Bolfan-Casanova, N. (2016). Distribution and transport of hydrogen in the lithospheric mantle: A review. *Lithos*, 240–243, 402–425.
- Demouchy, S., & Mackwell, S. (2003). Water diffusion in synthetic iron-free forsterite. *Physics and Chemistry of Minerals*, 30(8), 486-494.
- Demouchy, S., Bolfan-Casanova, N., 2016. Distribution and transport of hydrogen in the lithospheric mantle: a review. *Lithos* 240, 402–425.
- Demouchy, S., Gaillard, F., Stern, C.R. and Mackwell, S. (2003). Water diffusion as a natural process in olivine crystals from garnet peridotite xenoliths in basalts. *Geophysical Research Abstracts* 5, 03216
- Demouchy, S., Ishikawa, A., Tommasi, A., Alard, O., Keshav, S., 2015. Characterization of hydration in the mantle lithosphere: peridotite xenoliths from the Ontong Java Plateau as an example. *Lithos* 212–215, 189–201.
- Denis C. M. M., Alard O. and Demouchy S. (2015). Water content and hydrogen behavior during metasomatism in the upper-most mantle beneath Ray Pic volcano (Massif Central, France). *Lithos* 236–237, 256–274.
- Denis C. M. M., Demouchy S. and Alard O. (2018). Heterogeneous hydrogen distribution in orthopyroxene from veined mantle peridotite (San Carlos, Arizona): Impact of melt-rock interactions. *Lithos* 302–303, 298–311.
- Denis, C.M.M., Demouchy, S., Shaw, C.S.J., 2013. Evidence of dehydration in peridotites from Eifel Volcanic Field and estimates of the rate of magma ascent. *Journal of Volcanology and Geothermal Research* 258, 85–99.
- Dixon, J.E., Leist, L., Langmuir, C., Schilling, J.-G., 2002. Recycled dehydrated lithosphere observed in plume-influenced mid-ocean-ridge basalt. *Nature* 420, 385–389.
- Doucet L. S., Peslier A. H., Ionov D. A., Brandon A. D., Golovin A. V., Goncharov A. G. and Ashchepkov I. V. (2014) High water contents in the Siberian cratonic mantle linked to metasomatism: An FTIR study of Udachnaya peridotite xenoliths. *Geochim. Cosmochim. Acta* 137, 159–187.
- Fei, H., Druzhbin, D., Katsura, T., 2020. The effect of water on ionic conductivity in olivine. *J. Geophys. Res.: Solid Earth* 125, e2019JB019313.
- Ganwa A.A., Klötzli U.S., Diguim Kepnamou A., Hauzenberger C., 2016. Multiple Ediacaran tectono-metamorphic events in the Adamawa-Yadé Domain of the Central Africa Fold

- Belt: Insight from the zircon U–Pb LAM-ICP-MS geochronology of the metadiorite of Meiganga (Central Cameroon). *Geol. J.* 2018; 1–14.
- Gose, J., Schmadicke, E., Beran, A., 2009. Water in enstatite from Mid-Atlantic Ridge peridotite: evidence for the water content of suboceanic mantle? *Geology* 37 (6), 543–546.
- Grant K., Ingrin J., Lorand J. P. and Dumas P. (2007) Water partitioning between mantle minerals from peridotite xenoliths. *Contrib. Mineral. Petrol.* 154, 15–34.
- Grant, K.J., Kohn, S.C., Brooker, R.A., 2007b. The partitioning of water between olivine, orthopyroxene and melt synthesised in the system albite–forsterite–H₂O. *Earth and Planetary Science Letters* 260, 227–241.
- Green, D.H., 2015. Experimental petrology of peridotites, including effects of water and carbon on melting in the Earth's upper mantle. *Phy. Chem. Miner.* 42, 95-122.
- Green, D.H., Hibberson, W.O., Kovács, I., Rosenthal, A., 2010. Water and its influence on the lithosphere-asthenosphere boundary. *Nature* 467, 448–451.
- Griffin, Y., W.L., Wesztergom, V., Szabó, C., 2019. Extremely low structural hydroxyl contents in upper mantle xenoliths from the N'ogr'ad-Gömör Volcanic Field (northern Pannonian Basin): Geodynamic implications and the role of post-eruptive re-equilibration. *Chem. Geol.* 507, 23–41.
- Hao, Y., Xia, Q., Li, Q., Chen, H., Feng, M., 2014. Partial melting control of water contents in the Cenozoic lithospheric mantle of the Cathaysia block of South China. *Chem. Geol.* 380, 7–19.
- Hao, Y., Xia, Q.K., Liu, S.C., Feng, M., Zhang, Y.P., 2012. Recognizing juvenile and relict lithospheric mantle beneath the North China Craton: combined analysis of H₂O, major and trace elements and Sr-Nd isotope compositions of clinopyroxenes. *Lithos* 149, 136-145.
- Hauri E. H., Gaetani G. A. and Green T. H. (2006). Partitioning of water during melting of the Earth's upper mantle at H₂O undersaturated conditions. *Earth Planet. Sci. Lett.* 248, 715–734.
- Hirschmann, M.M., 2006. Water, melting, and the deep Earth H₂O cycle. *Annual Review of Earth and Planetary Sciences* 34, 629–653.
- Hirth, G., Kohlstedt, D.L., 2003. Rheology of the upper mantle and the mantle wedge: a view from the experimentalists. In: Eiler, J.E. (Ed.), *Inside the Subduction Factory*. American Geophysical Union, Washington DC, pp. 83–105.
- Ingrin, J., Latrous, K., Doukhan, J.C., Doukhan, N., 1989. Water in diopside: an electron microscopy and infrared spectroscopy study. *Eur. J. Mineral.* 327–342.

- Kang, P., Lamb, W.M., Drury, M., 2017. Using mineral equilibria to estimate H₂O activities in peridotites from the Western Gneiss Region of Norway. *Am. Mineral.* 102(5),1021–1036.
- Karato, S., 2010. Rheology of the deep upper mantle and its implications for the preservation of the continental roots: a review. *Tectonophysics* 481, 82–98.
- Karato, S., Jung, H., 2003. Effects of pressure on high-temperature dislocation creep in olivine polycrystals. *Philosophical Magazine. A* 83, 401–414.
- Kohlstedt, D.L., Mackwell, S.J., 1998. Diffusion of hydrogen and intrinsic point defects in olivine. *Zeitschrift für Physikalische Chemie* 207, 147–162.
- Kovács I., Hermann J., O’Neill H. S. C., Gerald J. F., Sambridge M. and Horvath G. (2008) Quantitative absorbance spectroscopy with unpolarized light: Part II. Experimental evaluation and development of a protocol for quantitative analysis of mineral IR spectra. *Amer. Miner.*93, 765–778.
- Kovacs I., O’Neill H. S. C., Hermann J. and Hauri E. H. (2010). Site-specific infrared O-H absorption coefficients for water substitution into olivine. *Am. Mineral.* 95, 292–299.
- Kovacs, I., Falus, Gy, Stuart, G., Hidas, K., Szabo, Cs, Flower, M.F.J., Hegedus, E., Posgay, K., Zilahi-Sebess, L., 2012. Seismic anisotropy and deformation patterns in upper mantle xenoliths from the central Carpathian Pannonian region: asthenospheric flow as a driving force for Cenozoic extension and extrusion? *Tectonophysics* 514-517, 168-179.
- Kovács, I., Green, D.H., Rosenthal, A., Hermann, J., O’Neill, H.S.C., Hibberson, W.O., Udvardi, B., 2012. An experimental study of water in nominally anhydrous minerals in the upper mantle near the water-saturated solidus. *Journal of Petrology* 53, 2067–2093.
- Li Z. X. A., Lee C. T. A., Peslier A. H., Lenardic A. and Mackwell S. J. (2008) Water contents in mantle xenoliths from the Colorado Plateau and vicinity: Implications for the mantle rheology and hydration-induced thinning of continental lithosphere. *J. Geophys. Res. Solid Earth*, 113.
- Liptai, N., Lange, T.P., Patkó, L., Pintér, Zs, Berkesi, M., Aradi, L.E., Szabó, Cs., Kovács, I. J., 2021. Effect of ‘water’ on the rheology of the lithospheric mantle in young extensional basin systems as shown by xenoliths from the Carpathian-Pannonian region. *Global Planet. Chang.* 196, 103364.
- Liu, J., Xia, Q. K., Deloule, E., Ingrin, J., Chen, H., Feng, M., 2015. Water content and oxygen isotopic composition of alkali basalts from the Taihang Mountains, China: recycled oceanic components in the mantle source. *J. Petrol.* 56(4), 681–702.
- Mackwell S. J. and Kohlstedt D. L. (1990) Diffusion of hydrogen in olivine: Implications for water in the Mantle. *J. Geophys. Res.* 95, 5079–5088.

- Maksimov, A.P., 2003. Effect of water on the melting curves of minerals: the olivine-melt equilibrium. *Geochemistry International* 41, 947–958.
- Mei, S., Kohlstedt, D.L., 2000a. Influence of water on plastic deformation of olivine aggregates (1): diffusion creep regimes. *Journal of Geophysical Research* 105, 21457–21469.
- Mei, S., Kohlstedt, D.L., 2000b. Influence of water on plastic deformation of olivine aggregates (2): dislocation creep regimes. *Journal of Geophysical Research* 105, 21471–21481.
- Novella D., Frost D. J., Hauri E. H., Bureau H., Raepsaet C. and Roberge M. (2014) The distribution of H₂O between silicate melt and nominally anhydrous peridotite and the onset of hydrous melting in the deep upper mantle. *Earth Planet. Sci. Lett.* 400, 1–13.
- Novella, D., Jacobsen, B., Weber, P.K., Tyburczy, J.A., Ryerson, F.J., DuFrane, W.L., 2017. Hydrogen self-diffusion in single-crystal olivine and electrical conductivity of the Earth's mantle. *Scientific report* 7 (1), 5344.
- O'Leary J. A., Gaetani G. A. and Hauri E. H. (2010) The effect of tetrahedral Al³⁺ on the partitioning of water between clinopyroxene and silicate melt. *Earth Planet. Sci. Lett.* 297, 111–120.
- Patkó, L., Liptai, N., Kovács, I.J., Aradi, L.E., Xia, Q.-K., Ingrin, J., Mihály, J., O'Reilly, S.
- Peslier A. H. and Luhr J. F. (2006) Hydrogen loss from olivines in mantle xenoliths from Simcoe (USA) and Mexico: Mafic alkali magma ascent rates and water budget of the sub-continental lithosphere. *Earth Planet. Sci. Lett.* 242, 302–319.
- Peslier A. H., Luhr J. and Post J. (2002). Low water contents in pyroxenes from spinel-peridotites of the oxidized, sub-arc mantle wedge. *Earth Planet. Sci. Lett.* 201, 69–86.
- Peslier A. H., Schönbacher M., Busemann H. and Karato S. I. (2017). Water in the Earth's interior: Distribution and origin. *Space Sci. Rev.*, 1–68.
- Peslier A. H., Woodland A. B. and Wolff J. A. (2008). Fast kimberlite ascent rates estimated from hydrogen diffusion profiles in xenolithic mantle olivines from southern Africa. *Geochim. Cosmochim. Acta* 72, 2711–2722.
- Peslier A. H., Woodland A. B., Bell D. R. and Lazarov M. (2010). Olivine water contents in the continental lithosphere and the longevity of cratons. *Nature* 467, 78–81.
- Peslier A. H., Woodland A. B., Bell D. R., Lazarov M. and Lapen T. J. (2012). Metasomatic control of water contents in the Kaapvaal cratonic mantle. *Geochim. Cosmochim. Acta* 97, 213–246.
- Peslier, A.H., 2010. A review of water contents of nominally anhydrous natural minerals in the mantles of Earth, Mars and the Moon. *Journal of Volcanology and Geothermal Research* 197, 239–258.

- Peslier, A.H., Bizimis, M., 2015. Water in Hawaiian peridotite minerals: A case for a dry metasomatized oceanic mantle lithosphere. *Geochemistry, Geophysics, Geosystems* 16, 1211–1232.
- Peslier, A.H., Bizimis, M., Matney, M., 2015. Water disequilibrium in olivines from Hawaiian peridotites: recent metasomatism, H diffusion and magma ascent rates. *Geochimica et Cosmochimica Acta* 154, 98–117.
- Peslier, A.H., Snow, J.E., Hellebrand, E., Von Der Handt, A., 2007. Low water contents in minerals from Gakkel ridge abyssal peridotites, Arctic Ocean, paper presented at 17th V. M. Goldschmidt Conference, Geochemical Society, Cologne, Germany.
- Pintér, Zs, Patkó, L., Djoukam, J.F.T., Kovács, I., Tchouankoue, J.P., Falus, Gy, Konc, Z., Tommasi, A., Barou, F., Mihály, J., Németh, Cs, Jeffries, T., 2015. Characterization of the sub-continental lithospheric mantle beneath the Cameroon volcanic line inferred from alkaline basalt hosted peridotite xenoliths from Barombi Mbo and Nyos Lakes. *J. Afr. Earth Sci.* 111, 170–193.
- Pollack, H.K., 1986. Cratonization and the thermal evolution of the mantle. *Earth and Planetary Science Letters* 80, 175–182.
- Prechtel F. and Stalder R. (2012) OH-defects in Al- and Cr- doped synthetic enstatites and defect geobarometry on natural orthopyroxenes from the Earth's mantle. *Eur. J. Mineral* 24,471–481.
- Rauch M. and Keppler H. (2002) Water solubility in orthopyroxene. *Contrib. Mineral Petrol.* 143, 525–536.
- Satsukawa T., Godard M., Demouchy S., Michibayashi K. and Ildefonse B. (2017) Chemical interactions in the subduction factory: New insights from an in situ trace element and hydrogen study of the Ichinomegata and Oki-Dogo mantle xenoliths (Japan). *Geochim. Cosmochim. Acta* 208, 234–267.
- Schlechter E. (2011) Electrical conductivity and hydrogen diffusion in synthetic orthopyroxene single-crystals Ph. D. thesis. Niedersächsische Staats-und Universitätsbibliothek Göttingen.
- Schmädicke, E., Gose, J., 2017. Water transport by subduction: clues from garnet of Erzgebirge UH Peclogite. *Am. Mineral.* 102(5), 975–986.
- Selway, K., Yi, J., Karato, S.I., 2014. Water content of the Tanzanian lithosphere from magnetotelluric data: implications for cratonic growth and stability. *Earth Planet. Sci. Lett.* 388, 175–186.
- Stalder, R. and Skogby, H. (2003) Hydrogen diffusion in natural and synthetic orthopyroxene. *Physics and Chemistry of Minerals*, 30, 12–19.

- Stalder, R., Ludwig, T., 2007. OH incorporation in synthetic diopside. *Eur. J. Mineral.* 19, 373-380.
- Tchakounté J, Eglinger A, Toteu SF, Zeh A, Nkoumbou C, Mvondo Ondo J, Penaye J, Wit de M, Barbey P (2017) The Adamawa Yadé domain, a piece of Archean crust in the Neoproterozoic Central African orogenic belt (Bafia area, Cameroon). *Precambrian Res* 299: 210–229.
- Tian Z. Z., Liu J., Xia Q. K., Ingrin J., Hao Y. T. and Christophe D. (2017) Water concentration profiles in natural mantle orthopyroxenes: A geochronometer for long annealing of xenoliths within magma. *Geology* 45, 87–90.
- Tollan P. and Hermann J. (2019) Arc magmas oxidized by water dissociation and hydrogen incorporation in orthopyroxene. *Nat. Geosci.* 12, 667–671.
- Tollan, P. M. E., Smith, R., O'Neill, H. S. C., & Hermann, J. (2017). The responses of the four main substitution mechanisms of H in olivine to H₂O activity at 1050 °C and 3 GPa. *Progress in Earth and Planetary Science*, 4(1), 14.
- Tollan, P.M.E., O'Neill, H.S.C., Hermann, J. 2018. The role of trace elements in controlling H incorporation in San Carlos olivine. *Contrib. to Mineral. Petrol.* 173, 1–23.
- Toteu, S. F., Van Schmus, W. R., Penaye, J., Michard, A., 2001. New U-Pb, and Sm-Nd data from North-Central Cameroon and its bearing on the pre-Pan-African history of Central Africa. *Pre. Res.* 108: 45-73.
- Van der Lee, S., Regenauer-Lieb, K., Yuen, D.A., 2008. The role of water in connecting past and future episodes of subduction. *Earth Planet. Sci. Lett.* 273, 15–27.
- Wang Y.-F., Qin J.-Y., Soustelle V., Zhang J.-F. and Xu H.-J. (2021). Pyroxene does not always preserve its source hydrogen concentration: Clues from some peridotite xenoliths. *Geochim. Cosmochim. Acta* 292, 382–408.
- Warren J. M. and Hauri E. H. (2014). Pyroxenes as tracers of mantle water variations. *J. Geophys. Res. Solid Earth* 119, 1851–1881.
- Xia Q.-K., Liu J., Kovacs I., Hao Y.-T., Li P., Yang X.-Z., Chen H. and Sheng Y.-M. (2019). Water in the upper mantle and deep crust of eastern China: concentration, distribution and implications. *Natl. Sci. Rev.* 6, 125–144.
- Xia, Q.-K., Hao, Y., Li, P., Deloule, E., Coltorti, M., Dallai, L., Yang, X., Feng, M., 2010. Low water content of the Cenozoic lithospheric mantle beneath the eastern part of the North China Craton. *Journal of Geophysical Research* 115, B07207.
- Xia, Q.-K., Hao, Y.-T., Liu, S.-C., Gu, X.-Y., Feng, M., 2013. Water contents of the Cenozoic lithospheric mantle beneath the western part of the North China Craton: peridotite xenolith constraints. *Gondwana Research* 23, 108–118.

- Xia, Q.K., Liu, J., Kovács, I., Hao, Y.T., Li, P., Yang, X.Z., Chen, H., Sheng, Y.M., 2017. Water in the Upper Mantle and Deep Crust of Eastern China: Concentration, distribution and implications. *National Science Review*
- Xu Y., Tang W., Hui H., Rudnick R. L., Shang S. and Zhang Z. (2019) Reconciling the discrepancy between the dehydration rates in mantle olivine and pyroxene during xenolith emplacement. *Geochim. Cosmochim. Acta* 267, 179–195.
- Yang, X.-Z., Xia, Q.-K., Deloule, E., Dallai, L., Fan, Q.-C., Feng, M., 2008. Water in minerals of the continental lithospheric mantle and overlying lower crust: a comparative study of peridotite and granulite xenoliths from the North China Craton. *Chemical Geology* 256, 33–45.
- Yu, Y., Xu, X.-S., Griffin, W.L., O'Reilly, S.Y., Xia, Q.-K., 2011. H₂O contents and their modification in the Cenozoic subcontinental lithospheric mantle beneath the Cathaysia block, SE China. *Lithos* 126, 182–197.

Chapter V:

DISCUSSION AND CONCLUSION

V.1. INTRODUCTION

In this chapter, a brief tectonic history and geodynamic context is given for the key features of the Cameroon Volcanic Line (CVL). This serves as a basis for main models that have been proposed to explain the origin of volcanism along the line. A summary of the information that can be gained from the composition of the lavas along the CVL is discussed, which shed light on the degree of melting and composition of the asthenospheric mantle below the CVL. The results from our detailed study of the mantle xenoliths hosted in these lavas are then discussed in this wider context to answer the eight key questions presented in the first chapter and to shed new light on the metasomatic processes in the lithospheric mantle below a major tectonic line.

V.2. GEODYNAMIC CONTEXT AND MODELS

The origin of the CVL remains unclear. Numerous studies based on geological (Burke, 2001; Fitton, 1980), geochemical (Njonfang et al., 2011; Lee et al., 1994; Deruelle et al., 1991; Fitton and Dunlop, 1985), structural (King and Anderson, 1995; Moreau et al., 1987), geophysical (Milelli et al., 2012; Reusch et al., 2010; Fairhead, 1988) and geochronological (Aka et al., 2004; Dunlop and Fitton, 1979) studies have been proposed. No single model can explain the origin of the CVL but they are complementary and address different aspects as it relates to its origin and evolution. These models include: (a) single or multiple mantle plumes (Ngako et al., 2006), (b) pre-existing lithospheric structures (Ebinger and Sleep, 1998), and models based on convection driven by various forces (King and Ritsema, 2000; Meyers et al., 1998; King and Anderson, 1998, 1995). A summary of these suggested models from Adam et al., 2015 is shown in Fig. 5.1.

The age range for the different volcanoes has been summarized in Chapter 1. On a larger scale, the tectono magmatic history of the CVL is closely linked to the adjacent Jos plateau and the Benue Trough and can be grouped into four main events:

1. Preceding the development of the Jos Plateau was the initiation of magmatic activity in the Benue Trough (147 Ma; Coulon et al., 1996) which was concomitant with the emplacement of anorogenic ring complexes.

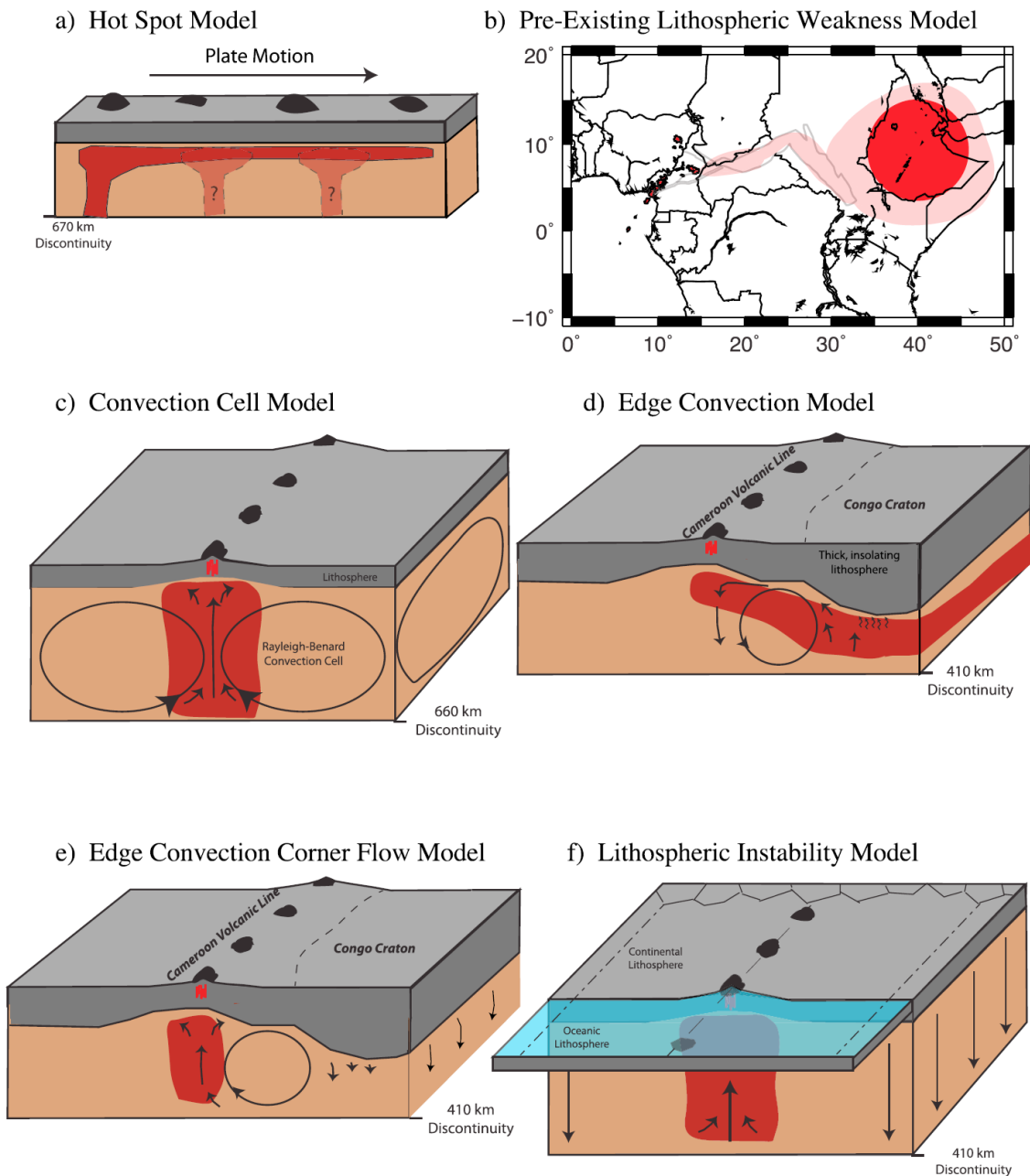


Figure 5.1: Potential geodynamical models for the formation of the CVL. (a) Hot spot or multiple hot spot model. (b) Pre-existing weakness model, with possible transport of material from the Afar hot spot (from Reusch et al., 2010; after Ebinger and Sleep, 1998). (c) Rayleigh-Baynard convection cell model (after Meyers et al., 1998). (d) Edge convection model with the lateral flow of warm material from beneath the Congo Craton (King and Anderson, 1995). (e) Corner-flow eddy model (King and Ritsema, 2000; King and Anderson, 1998). (f) Lithospheric instability along the continental margin (Milelli et al., 2012).

2. Preceding the development of the Jos Plateau was the initiation of magmatic activity in the Benue Trough (147 Ma; Coulon et al., 1996) which was concomitant with the emplacement of anorogenic ring complexes.
3. At about 100 Ma, was the transition to the second stage of magmatic activity in the Benue trough (106-95 Ma), which coincides with the opening of the Equatorial Atlantic Ocean (Wilson, 1992; Wilson and Giroud, 1992).
4. At 66-30 Ma (Lasserre, 1966) was the latest magmatic activity in the Benue Trough and the initiation of intrusive activity in the continental part of the CVL.
5. From 45 Ma to present, volcanic activity occurred along the CVL (Aka et al., 2004; Marzoli et al., 2000; Fitton and Dunlop, 1985).

The CVL represents a strange array of volcanoes with no clear age progression as in the case of hotspot volcanoes. Therefore, a hot spot origin for the CVL (Fig. 5.1a) can be excluded.

A second model proposed that the CVL is related to a lithospheric weakness that is inherited from the assembly of cratons in Precambrian times (Fig. 5.1b). The western part of Cameroon lies to the North-Western border of the Congo craton, in the amalgamation corridor formed during the Precambrian orogeny (Ngako et al., 2008; Njiekak et al., 2008). Trans-lithospheric fractures associated with these Precambrian orogenic activities in the region led some authors to suggest that the origin of the Cameroon Volcanic Line was from a reworking of Precambrian fractures (Moreau et al., 1987).

Recent dating works on basalt dykes from the southern continental part of the CVL (Tchouankoue et al., 2014) and the granitic wall of Nyos Lake (Aka et al., 2018) provided ages spanning between the Paleozoic and the Mesozoic. The presence of these dykes, therefore, stresses the importance of trans-lithospheric fractures that affected the Oku Volcanic Field and the Cameroon Volcanic Line corridor in general as well as reworking, which throughout the Phanerozoic led to the intrusion of magmatic rocks. Although the geodynamic model for the region during the Precambrian is still debated, various authors suggested models such as subduction and or collision (Djouka et al., 2008; Toteu et al., 2004) and metacratonization of the northern border of the Congo craton (Kwekam et al., 2010). The predominance of Precambrian geodynamic influence in the Oku Volcanic Field is strengthened by ages of 2.6 Ga and 1.87 Ga (Re-Os method) obtained for Nyos xenoliths (Liu et al., 2017). Geodynamic models that involve

subduction environments and mantle recycling can justify some metasomatic features shown by the studied peridotites as well as similar rocks from Nyos maar (e.g. Pinter et al., 2015).

The third type of model is based on different patterns of mantle upwelling. Geophysical data shows that the mantle below the CVL is characterized by slow seismic wave speed. The lithosphere-asthenosphere boundary below the Congo craton has been estimated at a depth of 250 Km, whereas for the CVL, the lithosphere is <100 km thick (Fishwick, 2010). The Adamawa region (which is at the northern edge of the Congo craton) shows evidence for a thinned lithosphere (~70 km) (Plomerova et al., 1993) while the crustal thickness for the Congo craton (43-48 km) is also higher than for the rest of the CVL (35-39 km) (Tokam et al., 2010) (Fig. 5.2 from Goussi Ngalamo et al., 2018). Based on these data, a symmetric convection model (Fig. 5.1c) is not feasible. The different lithospheric thickness on either side of the CVL is consistent with edge convection models (Fig. 5.1d, e). The Adamawa domain, which constitutes the Eastern branch of the CVL probably originated from a combination of geodynamic processes related to the Central African Shear Zone (CASZ) and the northern edge of the Congo Craton. Volcanism in the area was either triggered by the reactivation of shear zones or lithospheric delamination, which resulted in a thinned lithosphere (Gallacher and Bastow, 2012; Plomerova et al., 1993) (Fig. 5.3; Goussi Ngalamo et al., 2017). This thinned lithosphere is parallel to the edge of the Congo Craton, which constitutes a thicker crust (Goussi Galamo et al., 2017). This geometry creates a lithospheric discontinuity which was inherited during the amalgamation of the Congo Craton in conjunction with a general upwelling of the Adamawa plateau, related to the African deep upwelling documented in Large Low Shear Velocity Provinces (LLSVP) (Bower et al., 2013). This geometry results in a regional flow pattern with an edge flow convection with downwelling adjacent to the craton and upwelling 200-700 km away (Reusch et al., 2011).

The fourth type of model (Fig. 5. 1f) is based on a lithospheric instability perpendicular to the continental margin (Milleli et al., 2012). This model is controlled by differential cooling of the thick continental lithosphere relative to the thinner oceanic lithosphere (Adams et al., 2015).

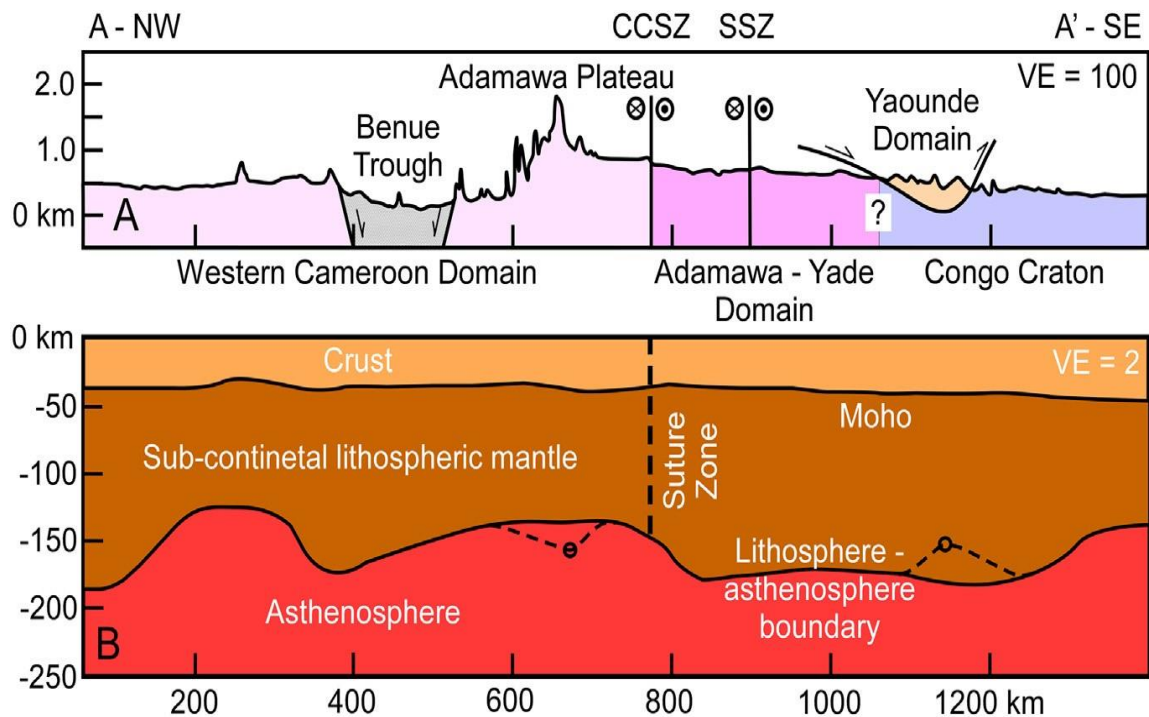


Figure 5.2: (A) NW-SE cross-section illustrating the major surface tectonic features of Cameroon and its surroundings. (B) Lithospheric-scale cross-section along the same trace of Fig. 5.2 A showing the Moho and lithosphere-asthenosphere boundary (LAB) depth variation. The depth values of the Moho and LAB are from the maps in Figs. 4A and 5A (in Goussi Ngalamo et al., 2018). The dashed lines with small circles represent data points that are smoothed out because the anomalies are beyond the resolution of the analysis. CCSZ = Central Cameroon shear zone system. SSZ= Sanaga shear zone

V.3. COMPOSITION AND ORIGIN OF MAGMATISM

Volcanic activity along the CVL range in age from Eocene to Recent times (Holocene) (Njome and de Wit, 2014). The western Cameroon highlands which encompasses Mts Oku and Mts Bamboutous (Fig 1.1) shows earlier magmatic activity from Oligocene to Miocene, while volcanic activity in the Adamawa plateau is younger and was initiated from Miocene to Quaternary (Marzoli et al., 2000). Lavas show a wide composition range, from mafic (nephelinites, basanites, alkali basalts) to felsic (phonolites, trachytes, rhyolites) end members (Marzoli et al., 2000). Even though most volcanoes along the CVL are composed only of mafic lavas, the lavas of the OVF and AVF are bimodal with a Daly gap (between SiO_2 58 and 64 wt%) (Asaah et al., 2015).

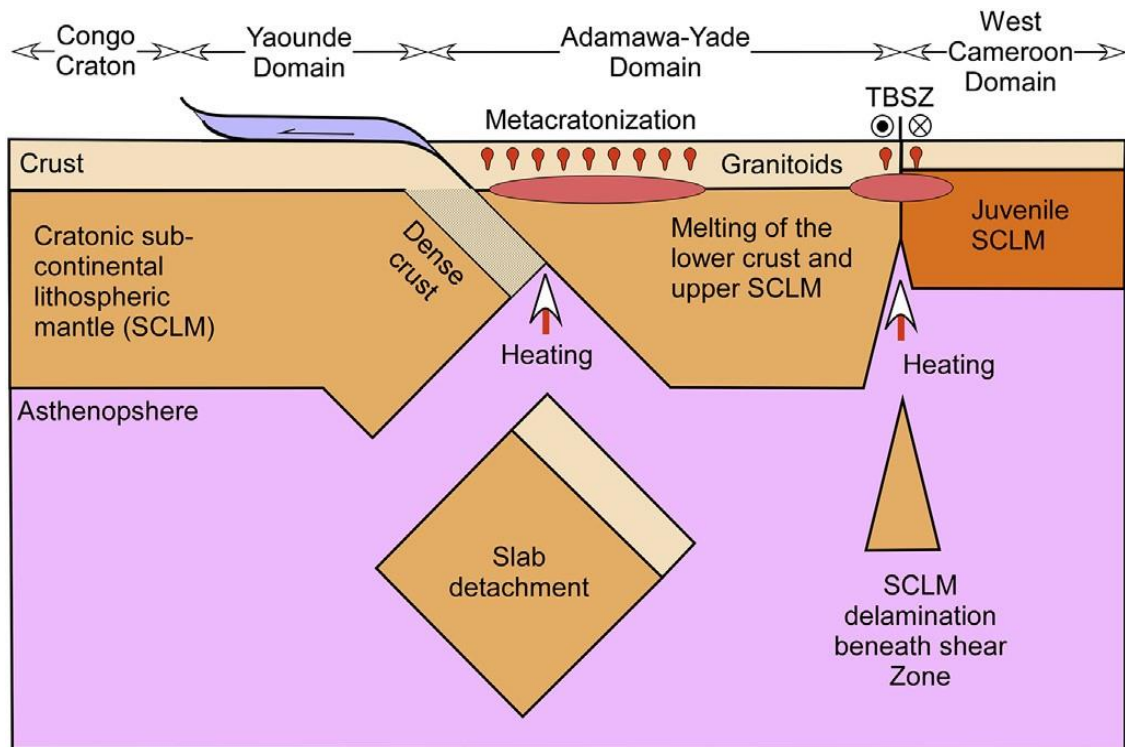


Figure 5.3: Conceptual cross-section illustrating the metacratonization of the northern edge of the Congo craton and the Adamawa-Yade domain through melting of the lower crust and upper sub-continental lithospheric mantle (SCLM) through ascending asthenosphere, possibly due to slab detachment (From Goussi Ngalamo et al., 2017).

Trace element and isotopic (Sr-Nd) systematics show a similarity in composition in basalts from both the continental and oceanic sectors of the line, which indicates a similar asthenospheric source (Marzoli et al., 2000; Fitton & Dunlop, 1985). However, a lithospheric source has been proposed for transitional plateau basalts which are as old as ca. 50Ma (e.g. Ngongang Tchikankou et al., 2021; Lemdjou et al., 2020). The basalts from the western highlands show variations in trace element composition (from high to low) which could originate from the mixing of variable amounts of melts from an asthenospheric component (anhydrous lherzolite source) (Nkouandou and Temdjim, 2011; Lee et al., 1996) and melts that originate from an amphibole bearing peridotite source (Asaah et al., 2015). A disparity has been observed in younger (15-4 Ma) basanites and alkali basalts, which show unusually high trace element concentrations and were reported to be generated from an incompatible element enriched, amphibole-bearing lithospheric source (Marzoli et al., 2000).

The origin of the CVL basalt magmatism remains enigmatic owing to geochemical evidence, which indicates the possibility of overprinting of asthenospheric

signatures by continental lithospheric signatures. Even though previous studies based on isotopes and trace element systematics have shown that the CVL basalts originate from a metasomatised asthenospheric mantle, (Marzoli et al., 2000; Ballentine et al., 1997; Lee et al., 1994; Halliday et al., 1990), recent studies based on major and trace element systematics (Asaah et al., 2015) show that the parent magmas which generate the CVL basalts come from the melting of a garnet-bearing mantle source except for the case of the Ngaoundere plateau where melting in the spinel stability field has been reported, which is consistent with a thinned lithospheric mantle (Poudjom Djomani et al., 1997, 1995; Plomerova *et al.*, 1993). Asaah et al., 2015 suggested that melting occurred dominantly in the garnet stability field with melting modes of <3% for Ngaoundere plateau and <5% for the OVF in the presence of 6-10% garnet and below 5% garnet. This suggests that the heterogeneity in the CVL upper mantle (lithosphere-asthenosphere boundary) is strongly related to the depths of origin and the degree of partial melting.

The composition of lavas relates to the conditions of the asthenospheric mantle. The overall low degree of mantle melting documented in the lavas along the CVL agree with the edge convection models and are more difficult to reconcile with a hot-spot model. This study focused on mantle xenoliths within the lavas to gain complementary information in the lithospheric mantle below the CVL.

V.4. THE SUBCONTINENTAL LITHOSPHERIC MANTLE BELOW THE CVL

The CVL xenoliths show that the SCLM below the CVL has undergone a complex evolution. Distinguishing between the lithospheric mantle in the old and the juvenile lithospheric mantle domains is challenging. To address the nature of magmatism along the CVL, the generation and modification of the subcontinental lithospheric mantle as documented in mantle xenoliths provides additional important evidence. In this section, the main results to answers the key questions posed in Chapter I are presented and the implications of the findings for the different geodynamic models are discussed.

V.4.1. Constrain the extent of partial melting in the subcontinental mantle

The heterogeneity of the mantle below the CVL cannot be explained by a single process but involves complex processes working in association. The xenoliths from the CVL (olivine websterites and lherzolites) generally show low to moderate degrees of partial melting (predating the formation of the CVL lavas) in the range of 0-15%. The

Kapsiki plateau, which is found in the juvenile North-West Cameroon domain and represents the northern-most known occurrence of mantle xenoliths along the line, is characterized by the most depleted mantle. The harzburgites from the Kapsiki plateau appear to be more depleted and are shown to record higher degrees of partial melting (20-30%). The Kapsiki xenoliths show high Mg# between 91-92 and are characterized by very low Al₂O₃ (3-4 wt%). However, enrichment in incompatible trace elements shows that these xenoliths are not simple residues of partial melting but have been affected by metasomatic processes. Xenoliths from the OVF show degrees of partial melting in the range of 0-15%, while the Ngaoundere Likok samples show less than 5%.

Peridotites from the cratonic mantle have characteristics that are indicative of very high degrees of melt extraction which include high Mg# in the range of 91.5-93.5 (Walter, 1998), and extreme depletions in CaO and Al₂O₃ (Walter, 1999). Typical fertile peridotites show lower Mg# (88-89). Experimental studies on peridotites from the cratonic mantle showed 30-50% of partial melting between 1400°C to 1750°C (Lee and Chin, 2014). The xenoliths from the Kapsiki show degrees of partial melting which are rather close to that of the cratonic mantle, which shows that the SCLM below the Kapsiki plateau represents an older part of the line. On the other hand, all the other samples display a relatively small degree of partial melting, indicating that the subcontinental mantle below the OVF and the Ngaoundere Likok don't represent remnants of a thinned cratonic mantle.

V.4.2. Document and characterise the different metasomatic types using clinopyroxene and amphibole composition.

Some samples show evidence for modal metasomatism with the presence of amphibole and secondary clinopyroxene while cryptic metasomatism is shown by enrichments in incompatible trace elements of pyroxenes. Based on the REE patterns of the clinopyroxenes, the CVL xenoliths can be subdivided into 8 distinct groups, which show LREE depleted to enriched patterns and sometimes MREE enrichment. From the geochemical signatures of clinopyroxenes, several metasomatic agents were identified. The different signatures are indicative of multiple metasomatic interactions both at the local as well as at the regional scale.

Based on ratios of Ti/Eu vs (La/Yb)_N, samples from Kapsiki show clear evidence for metasomatism by silicate-carbonatite melts. The samples from the Ngaoundere Likok

region are mainly metasomatised by melts of silicate composition, they however show slight traces of the involvement of a carbonatite melt component. The xenoliths from the OVF are shown to have been mainly metasomatised by silicate melts. They also show evidence for weak silicate-carbonatite metasomatism and carbonatite metasomatism. Sample En2a, which shows evidence for metasomatism by carbonatite, melts, however, show contradicting geochemical signatures, which cannot be accounted for by this melt, type (enrichments in Zr and Hf) and are therefore attributed to metasomatism by melts of ‘adakitic’ composition. In addition and opposition to the Kapsiki and the Ngaoundere Likok area, the OVF shows limited evidence for metasomatism by MORB type silicate melts. Overall, the predominance of silicate-carbonate metasomatism indicates that trace-element rich melts from small degrees of partial melting in the asthenosphere interacted with the lithospheric mantle.

V.4.3. Determine if there is evidence for subduction-related metasomatism, which was inherited during the Pan-African orogeny.

The CVL xenoliths show weak geochemical indications for subduction-related metasomatism (eg the positive Pb anomaly in some clinopyroxene and the amphibole composition). It has been suggested that volatile bearing minerals like amphibole are reaction products of K₂O-, H₂O or F-rich (hydrous melts) bearing subduction-related melt and peridotite (Szabo and Taylor 1994) or may have an asthenospheric origin. (e.g. Berkesi et al. 2019).

Two samples from this study show evidence of modal metasomatism by the presence of pargasitic amphibole. The composition of HFSEs (Nb, Ti, Zr, Hf) in amphiboles can be used to differentiate between amphiboles formed in a subduction environment from that formed in an intraplate environment (Coltorti et al., 2007). Nb is easily retained in the subducting slab and therefore expected to occur in low concentrations in subduction-related melts. The presence of amphibole with low Nb contents suggests that parts of the mantle were affected by ancient subduction-related metasomatic events most likely during the Pan-African orogeny. The fact, that only two samples showed evidence for limited subduction-related metasomatism provides evidence that this is not a widespread process below the CVL. Moreover, the calculated oxygen fugacity of the xenoliths ranges from values close to QFM to QFM -2.28

indicating that there has not been a regional scale oxidation of the subcontinental lithospheric mantle.

V.4.4. Find out if there are signs of CO₂ related metasomatism, which could be related to CO₂ outgassing at volcanoes.

Carbonatites seem to play an important role in metasomatic processes below the CVL. However, no carbonatites were observed. This suggests that melts of such composition only passed through and reacted with the mantle. This melt type is likely common in low degree mantle melts. The initial melt formation that led to the formation of the CVL volcanoes most likely started with highly enriched melts that reacted with the mantle that they passed through while subsequent melts only acted as a transport media and did not react with the SCLM. A mantle source for CO₂ outgassing cannot be discarded since there is evidence for metasomatism by melts with a carbonatite component. Because of the overall reducing conditions of the mantle below the line, the carbon mantle outgassing, therefore, occurs in the form of CH₄.

V.4.5. Evaluate the use of orthopyroxene and olivine as a tool for characterising metasomatic enrichments.

It is important to note that orthopyroxene is a promising tool that can be used to complement trace element concentrations in clinopyroxenes in constraining metasomatic enrichments. This is particularly useful in cases where clinopyroxene is added during interactions with mafic melts and shows signs of modification such as spongy textures or it has been completely exhausted during partial melting, orthopyroxene becomes the next important mineral that can be used to constrain metasomatic enrichments. Plots of Ti/Eu vs (La/Yb)_N and Ti/Sr vs Ti/Eu have been shown to efficiently distinguish the different metasomatic agents as in the case of clinopyroxenes. Therefore, it is suggested that orthopyroxene trace elements will be very useful in future studies to investigate mantle metasomatism in xenoliths where clinopyroxene is absent.

The use of trace element concentrations in olivine in identifying the different metasomatic agents is very challenging due to its very low concentrations. Olivine does not faithfully record metasomatism because variations in temperature and fertility both affect the trace element systematics.

V.4.6. Evaluate the H₂O contents of the SCLM below the region.

Mantle xenoliths from the CVL show extremely low structural H₂O contents. Olivine has no H₂O. Orthopyroxene H₂O contents are very low and fall within a narrow range for all studied localities. The H₂O contents of clinopyroxenes show two distinct groups which correspond to the different tectono-structural units. Xenoliths from the Kapsiki plateau and the OVF in the West Cameroon domain (WCD) show lower water contents. Those from the Adamawa domain show very high H₂O contents.

Partitioning of H₂O between cpx/opx is widely variable and significantly higher than the average range, which shows that the clinopyroxene H₂O contents are much higher than the coexisting orthopyroxene. The narrow range and similar H₂O contents of orthopyroxenes from the CVL irrespective of the different domains show that orthopyroxene H₂O contents could be the most reliable in such refertilised mantle. Olivine's H₂O contents was lost during the transport of the xenoliths to the surface, while clinopyroxene might have gained H₂O.

V.4.7. Assess the relationship between metasomatism and volatile enrichment of the mantle.

There is no clear correlation between the H₂O contents in the different mineral phases and the geochemical indices of partial melting. Correlations are however observed with metasomatic indices, especially for the Ngaoundere Likok xenoliths. The generally low H₂O contents for the CVL xenoliths despite pervasive metasomatism can therefore be attributed to the low H₂O activity during metasomatism. In addition, the low H₂O contents could be due to low water activity during extension, before the eruption of the CVL volcanoes in the Cenozoic.

Water plays an important role in the upper mantle as it has an effect on the rheological properties of the SCLM (e.g Liptai et al., 2021). Upper mantle minerals deformed under hydrous conditions are significantly weaker than in dry conditions. The generally low H₂O contents especially in olivine and orthopyroxene indicates that refertilization might not lead to significant hydrolytic weakening of the upper mantle below the CVL. Therefore, it is unlikely that the observed thinning of the lithospheric mantle below the CVL is related to delamination.

V.4.8. Evaluate information provided by the melting regime and mantle dynamics especially as it relates to the different tectono-structural units in Cameroon.

Xenoliths from the OVF and the AVF, which represent the NWCD and the Adamawa domain, are geochemically similar. The xenoliths from the AVF however show lower degrees of partial melting. Textural and geochemical evidence show that even though the studied xenoliths all come from the spinel stability field, they represent three distinct regions of the mantle, which include SCLM affected by subduction, a normal SCLM and the convecting mantle. The xenolith from the convecting part of the mantle shows depleted geochemical characteristics with 15% of partial melting. The main difference observed between these two units is the absence of MORB type silicate melt signatures in the AVP.

Temperature estimates from the xenoliths suggest that metasomatism occurred at different times for the different xenolith localities even though no clear trends are observed with spatial distribution or crustal thickness. Some samples displaying hot equilibration temperatures of 1050°C to 1140°C were metasomatised shortly before entrapment in host basalt and this could be a precursor for the eruption. Other samples cool back to temperatures of 810°C to 860°C, compatible with an elevated geotherm, characteristic for alkaline magmatism.

Recent studies using 1D shear wave velocity models (Tokam et al., 2010) show that the crustal thickness below the CVL is similar and range from 35-39 km. Results from this study (e.g metasomatic type, equilibrium temperature or oxygen fugacity) do not show a clear correlation with the crustal thickness or age of the volcanoes. There is also a large heterogeneity at the local scale and similarities between the OVF and the Ngaoundere Likok xenoliths, however, they are different from the Kapsiki xenoliths in terms of chemistry. This favours the interpretation of local and repeated metasomatism by small degree partial melts, which have a carbonatite and an alkali basalt component. These features are expected in small scale and local convection as proposed in the edge convection model and the choice model for the formation of the CVL.

REFERENCES

- Adams, A. N., D. A. Wiens, A. A. Nyblade, G. G. Euler, P. J. Shore, and R. Tibi, 2015. Lithospheric instability and the source of the Cameroon Volcanic Line: Evidence from Rayleigh wave phase velocity tomography, *J. Geophys. Res. Solid Earth*, 120, 1708–1727.
- Aka, F.T., Hasegawa, T., Nche, L.A., Asaah, A.N.E., Mimba, M.E., Teitchou, I., Ngwa, C., Miyabuchi, Y., Kobayashi, T., Kankeu, B., Yokoyama, T., Tanyileke, G., Ohba, T., Hell, J.V., Kusakabe, M., 2018. Upper Triassic mafic dykes of Lake Nyos, Cameroon (West Africa) I: K-Ar age evidence within the context of the Cameroon Line magmatism, and the tectonic significance. *J. Afr. Earth Sci.* 141, 49–59.
- Aka, F.T., Nagao, K., Kusakabe, M., Sumino, H., Tanyileke, G., Ateba, B., Hell, J.V., 2004. Symmetrical helium isotope distribution on the Cameroon Volcanic Line. *West Africa. Chemical Geology* 203, 205-223.
- Asaah, A.N.E., Yokoyama, T., Aka, F.T., Usui, T., Kuritani, T., Wirmvem, M.J., Iwamori, H., Fozing, E.M., Tamen, J., Mofor, G.Z., Ohba, T., Tanyileke, G. and Hell, J.V. (2015) Geochemistry of lavas from maar-bearing volcanoes in the Oku Volcanic Group of the Cameroon Volcanic Line. *Chem. Geol.* 406, 55-69.
- Ballentine, C.J., Lee, D.C. and Halliday, A.N. (1997) Hafnium isotopic studies of the Cameroon line and new HIMU paradoxes. *Chem. Geol.* 139, 111-124.
- Berkési, M., Czuppon, G., Szabó, C., Kovács, I., Ferrero, S., Boiron, M.C., Peiffert, C., 2019. Pargasite in fluid inclusions of mantle xenoliths from northeast Australia (Mt. Quincan): Evidence of interaction with asthenospheric fluid. *Chem. Geol.* 508, 182–196.
- Bower DJ, Gurnis M, Seton M. 2013. Lower mantle structure from paleogeographically constrained dynamic Earth models. *Geochem. Geophys. Geosyst.* 14:44–63.
- Burke, K., 2001. Origin of the Cameroon Line of volcano-capped swells. *The Journal of Geology* 109, 349-362.
- Coltorti, M., Bonadiman, C., Faccini, B., Gregoire, M., O'Reilly, S. Y. & Powell, W., 2007. Amphiboles from supra subduction and intraplate lithospheric mantle. *Lithos* 99, 68–84.
- Coulon, C., Vidal, P., Dupuy, C., Baudin, P., Popoff, M., Maluski, H., and Hermitte, D. (1996). The Mesozoic to early Cenozoic magmatism of the Benue Trough (Nigeria); geochemical evidence for the involvement of the St Helena plume. *Journal of Petrology*, 37(6), 1341-1358.
- Deruelle, B., Moreau, C., Nkoubou, C., Kambou, R., Lissom, J., Njonfang, E., Ghogomu, R.T., Nono, A., 1991. The Cameroon line: a review. In: Kampunzu, A.B., Lubala, R.T. (Eds.),

- Magmatism in Extensional Structural Settings: The Phanerozoic African Plate. Springer, Berlin, pp. 275-327.
- Djouka-Fonkwé M. L., Schulz B., Schüssler U., Tchouankoué J. P., Nzolang C., 2008. Geochemistry of the Bafoussam Pan-African I- and S-type granitoids in western Cameroon. *Journal of African Earth Sciences*, 50, pp. 148-167.
- Dunlop, H. M., and J. G. Fitton (1979), K-Ar and Sr-isotopic study of the volcanic rocks of the island of Principe, West Africa—Evidence for mantle heterogeneity beneath the Gulf of Guinea. *Contrib. Mineral. Petrol.*, 71(2), 125–131.
- Ebinger, C., and N. Sleep (1998), Cenozoic magmatism throughout East Africa resulting from impact of a single plume. *Nature*, 395, 788–791.
- Fairhead, J.D. (1988) Mesozoic plate tectonic reconstructions of the central South Atlantic Ocean: The role of the West and Central African rift system. *Tectonophysics* 155, 181-191.
- Fishwick, S. (2010), Surface wave tomography: Imaging of the lithosphere-asthenosphere boundary beneath central and southern Africa. *Lithos*, 120(1–2), 63–73.
- Fitton, J.D., 1980. The Benue Trough and the Cameroon line migrating rift systems in West Africa. *Earth and Planetary Science Letters* 51, 132-138.
- Fitton, J.G., Dunlop, H.M., 1985. The Cameroon line, West Africa, and its bearing on the origin of oceanic and continental alkali basalt. *Earth Planet. Sci. Lett.* 72, 23–38.
- Gallacher, R. J., and I. D. Bastow, 2012. The development of magmatism along the Cameroon Volcanic Line: Evidence from teleseismic receiver functions, *Tectonics*, 31, TC3018.
- Goussi Ngalamo, J. F., Sobh, M., Bisso, D., Abdelsalam, M. G., Atekwana, E., & Ekodeck, G. E. (2018). Lithospheric structure beneath the Central Africa orogenic belt in Cameroon from the analysis of satellite gravity and passive seismic data. *Tectonophysics*, 745, 326–337.
- Goussi Ngalamo, J.F., Bisso, D., Abdelsalam, M.G., Atekwana, E.A., Katumwehe, A.B., Ekodeck, G.E., 2017. Geophysical imaging of metacratonization in the northern edge of the Congo craton in Cameroon. *J. Afr. Earth Sci.* 129, 94–107.
- Halliday, A.N., Davidson, J.P., Holden, P., DeWolf, C., Lee, D.-C. and Fitton, J.G. (1990) Trace-element fractionation in plumes and the origin of HIMU mantle beneath the Cameroon line. *Nature* 347, 523-528.
- King, S.D. and Anderson, D.L. (1998) Edge-driven convection. *Earth Planet. Sci. Lett.* 160, 289-296.
- King, S.D. and Ritsema, J. (2000) African Hot Spot Volcanism: Small-Scale Convection in the Upper Mantle Beneath Cratons. *Science* 290, 1137-1140.

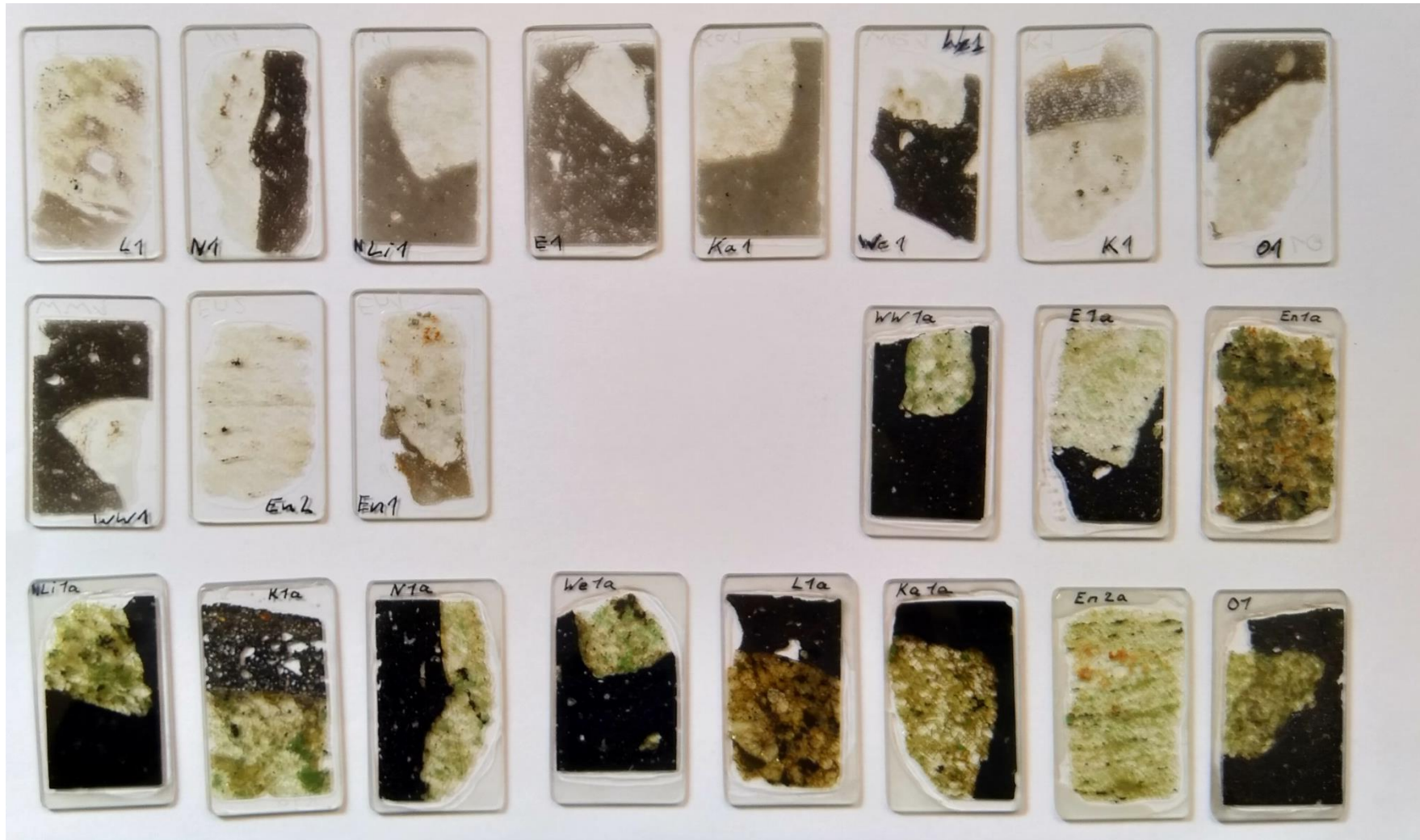
- King, S.D., Anderson, D.L., 1995. An alternative mechanism of flood basalt formation. *Earth and Planetary Science Letters* 136, 269-279.
- Kwékam M., Liégeois J. P., Njonfang E., Affaton P., Hartmann G., Tchoua F., 2010. Nature, origin, and significance of the Fomopéa Pan-African High-K calcalkaline plutonic complex in the Central African fold belt (Cameroon). *Journal of African Earth Science*, 54, pp. 79-95.
- Lasserre, M., 1966. Confirmation de l'existence d'une série de granites tertiaires au Cameroun. *Bull BRGM* 3, 141-148.
- Lee, D. C., Halliday N., Davies G. R., Essene E. J., Fitton G. J., Temdjim, R., 1996. Melt enrichment of shallow depleted mantle: a detailed petrological, trace element and isotopic study of mantle-derived xenoliths and megacrysts from the Cameroon Line. *J. Petrol.* 37:415–441.
- Lee, C.-T. A., & Chin, E. J. (2014). Calculating melting temperatures and pressures of peridotite protoliths: Implications for the origin of cratonic mantle. *Earth and Planetary Science Letters*, 403, 273–286.
- Lee, D.C., Halliday, A.N., Fitton, J.F., Poli, G., 1994. Isotopic variation with distance and time in the volcanic Islands of the Cameroon line: evidence for a mantle plume origin. *Earth and Planetary Science Letters* 123, 119-138.
- Lemdjou YB, Zhang D, Tchouankoue JP, Hu J, Tchoumeignie Ngongang NB, Tamehe LS, Yuan Y (2020) Elemental and Sr-Nd-Pb isotopic compositions, and K-Ar ages of transitional and alkaline plateau basalts from the eastern edge of the West Cameroon Highlands (Cameroon Volcanic Line). *Lithos*.
- Liptai, N., Lange, T.P., Patkó, L., Pintér, Z., Berkesi, M., Aradi, L.E., Szabó, C., Kovács, I. J., 2021. Effect of water on the rheology of the lithospheric mantle in young extensional basin systems as shown by xenoliths from the Carpathian-Pannonian region. *Glob. Planet. Chang.* 196, 103364.
- Liu C-Z, Yang L-Y, Li X-H, Tchouankoue JP, 2017. Age and Sr-Nd-Hf isotopes of the sub-continental lithospheric mantle beneath the Cameroon Volcanic Line: constraints from the Nyos mantle xenoliths. *Chem Geol* 455:84–97.
- Liu C-Z, Yang L-Y, Li X-H, Tchouankoue JP (2017) Age and Sr-Nd-Hf isotopes of the sub-continental lithospheric mantle beneath the Cameroon Volcanic Line: constraints from the Nyos mantle xenoliths. *Chem Geol* 455:84–97.
- Marzoli, A., Peccirillo, E.M., Renne, P.R., Bellieni, G., Iacumin, M., Nyobe, J.B., Tongwa, A.T., 2000. The Cameroon Volcanic Line revisited: petrogenesis of continental basaltic magmas from lithospheric and asthenospheric mantle sources. *Journal of Petrology* 41, 87-109.

- Meyers, J., Rosendahl, B.R., Harrison, C.G., Ding, Z.D., 1998. Deep-imaging seismic and gravity results from the offshore Cameroon Volcanic Line, and speculation of African hotlines. *Tectonophysics* 284, 31-63.
- Milelli, L., L. Fourel, and C. Jaupart, 2012. A lithospheric instability origin for the Cameroon Volcanic Line, *Earth Planet. Sci. Lett.*, 335-336, 80–87.
- Moreau C., Regnault J.M., Deruelle B., Robineau B., 1987. A new tectonic model for the Cameroon line, central Africa. - *Tectonophysics* 141: pp. 317-334.
- Moreau, C., Regnault, J.M., Deruelle, B., Robineau, B., 1987. A new tectonic model for the Cameroon Line, Central Africa. *Tectonophysics* 139, 317-334.
- Ngako V., Affaton P., & Njonfang E., 2008. Pan-African tectonic in northwestern Cameroon: Implication for history of Western Gondwana. *Gondwana Research*, 14, pp. 509-522.
- Ngako, V., Njonfang, E., Aka, F.T., Affaton, P., Nnange, J.M., 2006. The North-South PalaPaleozoic to Quaternary trend of alkaline magmatism from Niger-Nigeria to Cameroon: complex interaction between hotspots and Precambrian faults. *Journal of African Earth Sciences* 45 (3), 241-256.
- Tchikankou, N. L. N., Kamgang, P., Chazot, G., Agranier, A., Bellon, H., Nonnotte, P., & Kwekam, M. (2020). Mantle source evolution beneath the Cameroon volcanic line: geochemical and geochronological evidences from Fotouni volcanic series, Western Cameroon. *Arabian Journal of Geosciences*, 13(24), 1-20.
- Njiekak G., Dörr W., Tchouankoué J. P., Zulauf G., 2008. U-Pb zircon and micro fabric data of (meta) granitoids of western Cameroon: Constraints on the timing of pluton emplacement and deformation in the Pan-African belt of central Africa. *Lithos*, 102, pp. 460-477.
- Njome, M. S. & de Wit, M. J. (2014). The Cameroon Line: analysis of an intraplate magmatic province transecting both oceanic and continental lithospheres: constraints, controversies and models. *Earth-Science Reviews* 139, 168–194
- Njonfang, E., Nono, A., Kamgang, P., Ngako, V., Tchoua, F.M., 2011. Cameroon line magmatism (Central Africa): a reappraisal. In: Beccaluva, L., Bianchini, G., Wilson, M. (Eds.), *Volcanism and Evolution of the African Lithosphere*. GSA, Special Paper, 478, pp. 173-191.
- Nkouandou, O.F., Temdjim, R., 2011. Petrology of spinel lherzolite xenoliths and host basaltic lava from Ngao Voglar volcano, Adawama Massif (Cameroon Volcanic Line, West Africa): equilibrium conditions and mantle characteristics. *J. Geosci.* 56, 375-387.
- Pintér, Zs, Patkó, L., Djoukam, J.F.T., Kovács, I., Tchouankoué, J.P., Falus, G., Konc, Z., Tommasi, A., Barou, F., Mihály, J., Németh, Cs, Jeffries, T., 2015. Characterization of the sub-continental lithospheric mantle beneath the Cameroon volcanic line inferred

- from alkaline basalt hosted peridotite xenoliths from Barombi Mbo and Nyos Lakes. *J. Afr. Earth Sci.* 111, 170–193.
- Plomerová, J., V. Babuska, C. Dorbath, L. Dorbath, and R. J. Lillie, 1993. Deep lithospheric structure across the Central African Shear Zone in Cameroon, *Geophys. J. Int.*, 115, 381–390.
- Poudjom Djomani, Y., J. Nnange, M. Diament, C. Ebinger, and J. Fairhead (1995), Effective elastic thickness and crustal thickness variations in west-central Africa inferred from gravity data. *J. Geophys. Res.*, 100(B11), 22047–22070.
- Poudjom Djomani, Y.H., Diament, M., Wilson, M., 1997. Lithospheric structure across the Adamawa Plateau (Cameroon) from gravity studies. *Tectonophysics* 273, 317-327.
- Reusch, A., A. Nyblade, R. Tibi, D. Wiens, P. Shore, A. Bekoa, C. Tabod, and J. Ngange, 2011. Mantle transition zone thickness beneath Cameroon: Evidence for an upper mantle origin for the Cameroon Volcanic Line, *Geophys. J. Int.*, 187, 1146–1150.
- Reusch, A.M., Nyblade, A.A., Wiens, D.A., Shore, P.J., Ateba, B., Tabod, C.T., Nnange, J.M., 2010. Upper mantle structure beneath Cameroon from body wave tomography and the origin of the Cameroon Volcanic Line. *Geochemistry, Geophysics, Geosystems* 11(10).
- Szabo, C. & Taylor, L. A. (1994). Mantle petrology and geochemistry beneath the Nograd–Gomor Volcanic Field, Carpathian–Pannonian region. *International Geology Review* 36, 328–358.
- Tchouankoue J.P., Simeni Wambo N.A., Kagou Dongmo A., Li X-H., 2014. $^{40}\text{Ar}/^{39}\text{Ar}$ dating of basaltic dyke swarm in Western Cameroon: Evidences of Late Paleozoic and Mesozoic Magmatism in the corridor of the Cameroon Line. *Journal of African Earth Sciences*, vol. 93, pp.14-22.
- Tokam, A., C. Tabod, A. Nyblade, J. Julià, D. Wiens, and M. Pasyanos (2010), Structure of the crust beneath Cameroon, West Africa, from the joint inversion of Rayleigh wave group velocities and receiver functions, *Geophys. J. Int.*, 183(2), 1061–1076.
- Toteu S. F., Penaye J., Poudjoun D. Y. H., 2004. Geodynamic evolution of the Pan-African belt in Central Africa with special reference to Cameroon. *Can. J. Earth Sci.*, 41, pp. 73-85.
- Walter, M.J. (1998) Melting of garnet peridotite and the origin of komatiite and depleted lithosphere. *J. Petrol.* 39, 29-60.
- Walter, M.J., 1999. Melting residues of fertile peridotite and the origin of cratonic lithosphere. In: Fei, Y., Bertka, C.M., Mysen, B.O. (Eds.), *Mantle Petrology: Field Observations and High-Pressure Experimentation: A Tribute to Francis R. (Joe) Boyd*. In: *Geochem. Soc. Spec. Pub.*, pp. 225–239.

- Wilson, M., 1992. Magmatism and continental rifting during the opening of the South Atlantic Ocean: a consequence of Lower Cretaceous super-plume activity? in: magmatism and the causes of continental Break-up. Geological Society Special Publications 68, 241-255.
- Wilson, M., and Guiraud, R. (1992). Magmatism and rifting in Western and Central Africa, from Late Jurassic to Recent times. Tectonophysics, 213(1-2), 203-225.

APPENDICES



Appendix 1: Thin/Thick section scans of Cameroon Volcanic Line xenoliths (This study)

Appendix 2.1a: Major element composition of olivines from Kapsiki

Olivine	Kapsiki 1																				
Grain	o11	o12	o13	o14	o15	o16	o17	o18	o19	o110	o111	o112	o113	o114	o115	o116	o117	o118	o119	o120	o121
SiO ₂	41.00	40.82	41.15	40.93	41.18	40.83	41.28	41.08	41.01	41.16	40.87	40.89	40.72	40.91	41.37	40.81	41.32	41.19	41.15	40.94	40.98
TiO ₂	0.02	-	-	-	0.02	-	-	-	-	-	-	-	-	-	0.02	-	-	-	-	-	-
Al ₂ O ₃	0.04	0.02	-	-	-	-	0.03	-	0.05	0.02	-	-	0.02	0.03	0.04	0.04	0.06	0.04	0.02	-	0.05
Cr ₂ O ₃	0.02	0.03	0.03	0.02	0.03	0.02	0.02	0.02	-	0.02	0.02	-	-	-	0.04	0.02	0.04	0.03	0.04	0.04	0.02
FeO	8.11	8.08	8.06	8.05	8.15	7.99	8.07	8.13	8.19	8.14	8.14	8.11	7.98	8.18	8.08	8.09	8.11	8.16	8.00	8.18	8.19
MnO	0.11	0.14	0.12	0.13	0.13	0.14	0.14	0.13	0.12	0.14	0.12	0.12	0.13	0.10	0.13	0.12	0.13	0.14	0.10	0.12	0.12
NiO	0.44	0.40	0.44	0.39	0.39	0.44	0.42	0.41	0.40	0.44	0.39	0.41	0.41	0.43	0.43	0.45	0.45	0.45	0.44	0.45	0.43
MgO	50.73	50.73	50.91	51.09	50.64	50.54	50.63	50.73	50.53	50.52	50.71	50.61	50.55	50.85	50.70	50.37	50.80	50.22	50.72	50.80	50.74
CaO	0.07	0.07	0.07	0.07	0.09	0.09	0.07	0.08	0.09	0.09	0.08	0.08	0.06	0.08	0.09	0.08	0.08	0.08	0.07	0.08	0.09
Na ₂ O	-	-	-	-	0.02	0.03	0.02	-	-	-	-	0.02	0.04	0.06	-	-	-	-	0.03	-	0.03
Total	101	100	101	101	101	100	101	101	100	101	100	100	100	101	101	100	101	100	101	101	101
Si	0.994	0.992	0.994	0.991	0.997	0.994	0.998	0.995	0.995	0.998	0.993	0.994	0.993	0.991	0.998	0.995	0.997	1.000	0.996	0.992	0.993
Ti	0.000	-	-	-	0.000	-	-	-	-	-	-	-	-	-	0.000	-	-	-	-	-	-
Al	0.001	0.000	-	-	-	-	0.001	-	0.001	0.001	-	-	0.001	0.001	0.001	0.001	0.002	0.001	0.001	-	0.002
Cr	0.000	0.001	0.001	0.000	0.001	0.000	0.000	0.000	-	0.000	0.000	-	-	-	0.001	0.001	0.001	0.001	0.001	0.001	0.000
Fe ²⁺	0.164	0.164	0.163	0.163	0.165	0.163	0.163	0.165	0.166	0.165	0.165	0.165	0.163	0.166	0.163	0.165	0.164	0.166	0.162	0.166	0.166
Mn	0.002	0.003	0.003	0.003	0.003	0.003	0.003	0.003	0.002	0.003	0.002	0.002	0.003	0.002	0.003	0.003	0.003	0.003	0.002	0.002	0.003
Ni	0.009	0.008	0.009	0.008	0.008	0.009	0.008	0.008	0.008	0.009	0.008	0.008	0.008	0.008	0.008	0.009	0.009	0.009	0.009	0.009	0.008
Mg	1.832	1.838	1.834	1.843	1.827	1.834	1.825	1.832	1.828	1.825	1.836	1.834	1.837	1.836	1.824	1.830	1.827	1.818	1.831	1.835	1.832
Ca	0.002	0.002	0.002	0.002	0.002	0.002	0.002	0.002	0.002	0.002	0.002	0.002	0.002	0.002	0.002	0.002	0.002	0.002	0.002	0.002	0.002
Na	-	-	-	-	0.001	0.002	0.001	-	-	-	-	0.001	0.002	0.003	-	-	-	-	0.001	-	0.001
Total	3.006	3.008	3.005	3.009	3.003	3.006	3.002	3.005	3.004	3.002	3.007	3.007	3.008	3.010	3.001	3.005	3.002	2.999	3.004	3.008	3.007
Mg#	0.918	0.918	0.918	0.919	0.917	0.919	0.918	0.917	0.917	0.917	0.917	0.918	0.919	0.917	0.918	0.917	0.918	0.916	0.919	0.917	0.917

Appendix 2.1a cont'd

Olivine	Kapsiki 1																					
Grain	o122	o123	o124	o125	o128	o129	o130	o132	o133	o134	o136	o137	o138	o139	o141	o143	o144	o145	o147	o148	o149	o150
SiO ₂	41.17	41.12	41.28	40.98	40.89	40.75	40.95	41.22	40.95	40.96	41.38	41.16	40.46	40.81	40.77	40.68	40.74	40.41	40.66	41.12	40.90	40.81
TiO ₂	-	-	-	-	-	-	-	-	0.02	-	-	-	0.02	-	-	-	-	-	-	-	-	-
Al ₂ O ₃	-	-	0.02	0.05	0.03	0.04	-	0.03	-	-	0.03	-	-	0.03	-	0.05	-	0.02	0.04	-	-	0.05
Cr ₂ O ₃	-	0.02	-	-	-	0.03	0.02	-	0.02	0.02	-	0.02	0.02	-	0.03	0.03	0.02	0.02	-	-	0.02	0.03
FeO	8.27	8.14	8.17	8.21	8.23	8.12	8.15	8.23	8.21	8.24	8.26	8.26	8.12	8.18	8.20	8.20	8.25	8.09	8.20	8.30	8.30	8.15
MnO	0.12	0.13	0.13	0.12	0.14	0.15	0.11	0.13	0.12	0.14	0.12	0.11	0.13	0.10	0.13	0.11	0.13	0.11	0.13	0.13	0.13	0.13
NiO	0.41	0.38	0.41	0.38	0.43	0.46	0.39	0.43	0.42	0.44	0.47	0.38	0.42	0.38	0.40	0.43	0.42	0.39	0.41	0.43	0.42	0.43
MgO	50.78	50.96	50.67	50.41	50.93	51.00	50.59	50.45	50.49	50.87	50.87	50.66	50.62	50.80	50.91	51.05	50.96	50.72	50.99	51.07	50.59	50.78
CaO	0.08	0.09	0.07	0.08	0.07	0.06	0.07	0.08	0.07	0.08	0.08	0.08	0.09	0.09	0.07	0.07	0.06	0.07	0.08	0.08	0.08	0.06
Na ₂ O	-	0.04	-	-	-	-	-	0.03	-	0.05	-	0.04	-	0.03	-	0.02	-	0.02	-	-	-	0.03
Total	101	101	101	100	101	101	100	101	100	101	101	101	100	100	101	101	101	100	101	101	100	100
Si	0.995	0.993	0.998	0.996	0.990	0.988	0.995	0.998	0.995	0.991	0.996	0.996	0.988	0.991	0.989	0.986	0.988	0.987	0.987	0.992	0.993	0.991
Ti	-	-	-	-	-	-	-	-	0.000	-	-	-	0.000	-	-	-	-	-	-	-	-	-
Al	-	-	0.000	0.001	0.001	0.001	-	0.001	-	-	0.001	-	-	0.001	-	0.002	-	0.001	0.001	-	-	0.001
Cr	-	0.000	-	-	-	0.001	0.000	-	0.000	0.001	-	0.001	0.000	-	0.001	0.001	0.001	0.000	-	-	0.000	0.001
Fe ²⁺	0.167	0.164	0.165	0.167	0.167	0.165	0.166	0.167	0.167	0.167	0.166	0.167	0.166	0.166	0.166	0.166	0.167	0.165	0.167	0.167	0.169	0.165
Mn	0.002	0.003	0.003	0.003	0.003	0.003	0.002	0.003	0.003	0.003	0.003	0.002	0.003	0.002	0.003	0.002	0.003	0.002	0.003	0.003	0.003	0.003
Ni	0.008	0.007	0.008	0.008	0.008	0.009	0.008	0.008	0.008	0.009	0.009	0.007	0.008	0.008	0.008	0.008	0.008	0.008	0.008	0.008	0.008	0.008
Mg	1.830	1.835	1.826	1.826	1.839	1.843	1.832	1.821	1.829	1.835	1.826	1.827	1.843	1.838	1.842	1.845	1.843	1.847	1.845	1.836	1.831	1.837
Ca	0.002	0.002	0.002	0.002	0.002	0.002	0.002	0.002	0.002	0.002	0.002	0.002	0.003	0.002	0.002	0.002	0.002	0.002	0.002	0.002	0.002	0.002
Na	-	0.002	-	-	-	-	-	0.001	-	0.003	-	0.002	-	0.001	-	0.001	-	0.001	-	-	-	0.002
Total	3.005	3.008	3.002	3.003	3.010	3.011	3.005	3.002	3.005	3.010	3.004	3.005	3.011	3.010	3.010	3.013	3.012	3.013	3.012	3.009	3.007	3.009
Mg#	0.916	0.918	0.917	0.916	0.917	0.918	0.917	0.916	0.916	0.917	0.917	0.916	0.917	0.917	0.917	0.917	0.917	0.918	0.917	0.916	0.916	0.917

Appendix 2.1a cont'd

Olivine	Kapsiki 2																	
Grain	ol1	ol2	ol3	ol4	ol5	ol6	ol8	ol9	ol10	ol11	ol12	ol13	ol14	ol15	ol16	ol17	ol18	ol19
SiO ₂	40.91	41.11	40.84	40.98	40.90	41.15	41.03	40.78	41.19	41.11	40.61	41.10	41.34	41.27	41.06	40.99	41.06	40.68
TiO ₂	0.02	-	-	-	-	-	-	-	-	-	-	-	-	-	-	-	-	-
Al ₂ O ₃	-	0.03	-	-	0.03	-	0.02	-	-	-	0.05	-	0.06	-	-	0.02	-	-
Cr ₂ O ₃	0.02	-	-	-	0.03	0.03	-	0.02	-	-	-	0.02	0.04	-	-	0.03	0.02	0.02
FeO	8.32	8.43	8.22	8.48	8.40	8.52	8.46	8.15	8.14	8.28	8.05	8.13	8.05	8.19	8.29	8.45	8.60	8.46
MnO	0.11	0.13	0.13	0.13	0.13	0.14	0.13	0.14	0.14	0.13	0.14	0.13	0.15	0.12	0.13	0.13	0.13	0.13
NiO	0.41	0.41	0.42	0.42	0.42	0.43	0.41	0.43	0.45	0.43	0.41	0.39	0.41	0.41	0.44	0.46	0.42	0.47
MgO	49.30	49.62	50.26	49.63	49.60	50.25	49.53	49.80	49.77	49.60	49.68	49.51	49.55	49.83	49.53	49.55	50.22	50.75
CaO	0.07	0.06	0.08	0.07	0.06	0.08	0.06	0.08	0.07	0.07	0.08	0.07	0.07	0.08	0.07	0.07	0.06	0.07
Na ₂ O	-	-	-	-	-	-	0.03	-	-	-	-	0.02	-	-	-	0.02	-	0.02
Total	99	100	100	100	100	101	100	99	100	100	99	99	100	100	100	100	101	101
Si	1.005	1.004	0.996	1.002	1.001	0.998	1.004	1.000	1.005	1.005	0.999	1.006	1.009	1.005	1.005	1.003	0.997	0.988
Ti	0.000	-	-	-	-	-	-	-	-	-	-	-	-	-	-	-	-	-
Al	-	0.001	-	-	0.001	-	0.001	-	-	-	0.002	-	0.002	-	-	0.001	-	-
Cr	0.001	-	-	-	0.001	0.001	-	0.000	-	-	-	0.001	0.001	-	-	0.001	0.000	0.000
Fe ²⁺	0.171	0.172	0.168	0.173	0.172	0.173	0.173	0.167	0.166	0.169	0.166	0.167	0.164	0.167	0.170	0.173	0.175	0.172
Mn	0.002	0.003	0.003	0.003	0.003	0.003	0.003	0.003	0.003	0.003	0.003	0.003	0.003	0.002	0.003	0.003	0.003	0.003
Ni	0.008	0.008	0.008	0.008	0.008	0.008	0.008	0.009	0.009	0.009	0.008	0.008	0.008	0.008	0.009	0.009	0.008	0.009
Mg	1.806	1.806	1.827	1.809	1.810	1.817	1.806	1.819	1.810	1.807	1.821	1.807	1.802	1.810	1.807	1.806	1.818	1.837
Ca	0.002	0.002	0.002	0.002	0.002	0.002	0.002	0.002	0.002	0.002	0.002	0.002	0.002	0.002	0.002	0.002	0.002	0.002
Na	-	-	-	-	-	-	0.001	-	-	-	-	0.001	-	-	-	0.001	-	0.001
Total	2.995	2.996	3.004	2.998	2.998	3.002	2.997	3.001	2.996	2.995	3.000	2.994	2.990	2.995	2.995	2.998	3.003	3.012
Mg#	0.914	0.913	0.916	0.913	0.913	0.913	0.913	0.916	0.916	0.914	0.917	0.916	0.916	0.916	0.914	0.913	0.912	0.914

Appendix 2.1a cont'd

Olivine Grain	Kapsiki 2																		
	ol20	ol21	ol22	ol23	ol24	ol25	ol26	ol27	ol28	ol29	ol30	ol31	ol32	ol33	ol34	ol35	ol36	ol37	ol38
SiO ₂	40.99	41.00	40.68	40.32	40.73	41.11	40.87	40.82	40.94	40.74	40.88	40.79	40.72	41.00	40.87	40.88	41.10	40.93	40.68
TiO ₂	0.02	-	0.02	-	-	-	-	-	-	-	-	-	-	-	-	-	-	-	-
Al ₂ O ₃	-	-	0.02	-	0.05	0.03	0.04	-	-	0.04	0.05	0.02	-	-	0.02	-	-	-	-
Cr ₂ O ₃	0.03	0.03	-	0.02	0.02	0.03	0.02	-	0.02	-	-	-	0.02	0.02	-	-	-	-	-
FeO	8.52	8.64	8.65	8.56	8.44	8.59	8.75	8.55	8.57	8.60	8.53	8.58	8.57	8.75	8.57	8.66	8.70	8.55	8.65
MnO	0.14	0.15	0.14	0.15	0.15	0.10	0.12	0.12	0.12	0.12	0.14	0.13	0.12	0.11	0.13	0.14	0.14	0.13	0.12
NiO	0.40	0.45	0.39	0.42	0.45	0.41	0.41	0.46	0.43	0.45	0.39	0.44	0.44	0.46	0.41	0.43	0.41	0.42	0.41
MgO	50.64	51.02	50.59	50.40	50.34	50.72	50.96	50.44	50.45	50.38	51.03	51.19	51.04	50.50	50.48	50.62	50.50	50.80	50.29
CaO	0.07	0.08	0.08	0.07	0.06	0.08	0.07	0.07	0.08	0.09	0.08	0.08	0.07	0.06	0.06	0.08	0.06	0.06	0.08
Na ₂ O	-	0.02	-	0.03	-	-	-	-	-	0.02	-	-	-	0.02	-	0.03	-	-	-
Total	101	101	101	100	100	101	101	100	101	100	101	101	101	101	101	101	101	101	100
Si	0.993	0.988	0.989	0.986	0.992	0.993	0.987	0.992	0.994	0.991	0.988	0.985	0.986	0.993	0.993	0.991	0.995	0.991	0.992
Ti	0.000	-	0.000	-	-	-	-	-	-	-	-	-	-	-	-	-	-	-	-
Al	-	-	0.000	-	0.001	0.001	0.001	-	-	0.001	0.001	0.001	-	-	0.000	-	-	-	-
Cr	0.001	0.001	-	0.001	0.000	0.001	0.000	-	0.000	-	-	-	0.000	0.000	-	-	-	-	-
Fe ²⁺	0.173	0.174	0.176	0.175	0.172	0.174	0.177	0.174	0.174	0.175	0.172	0.173	0.174	0.177	0.174	0.176	0.176	0.173	0.176
Mn	0.003	0.003	0.003	0.003	0.003	0.002	0.003	0.003	0.003	0.003	0.003	0.003	0.003	0.002	0.003	0.003	0.003	0.003	0.003
Ni	0.008	0.009	0.008	0.008	0.009	0.008	0.008	0.009	0.008	0.009	0.008	0.009	0.009	0.009	0.008	0.008	0.008	0.008	0.008
Mg	1.828	1.833	1.833	1.837	1.828	1.826	1.834	1.828	1.825	1.827	1.838	1.842	1.842	1.823	1.828	1.829	1.822	1.833	1.827
Ca	0.002	0.002	0.002	0.002	0.002	0.002	0.002	0.002	0.002	0.002	0.002	0.002	0.002	0.002	0.002	0.002	0.002	0.002	0.002
Na	-	0.001	-	0.002	-	-	-	-	-	0.001	-	-	-	0.001	-	0.002	-	-	-
Total	3.007	3.012	3.011	3.014	3.007	3.006	3.013	3.007	3.006	3.009	3.012	3.015	3.014	3.008	3.007	3.010	3.006	3.009	3.009
Mg#	0.914	0.913	0.912	0.913	0.914	0.913	0.912	0.913	0.913	0.913	0.914	0.914	0.914	0.911	0.913	0.912	0.912	0.914	0.912

Appendix 2.1a cont'd

Olivine	Kapsiki7											
Grain	ol1	ol2	ol3	ol4	ol5	ol6	ol7	ol8	ol9	ol10	ol11	ol12
SiO ₂	40.37	40.78	40.68	40.42	40.75	40.74	41.14	41.12	41.08	40.53	40.67	40.85
TiO ₂	-	-	-	-	-	-	-	-	-	-	-	-
Al ₂ O ₃	-	-	0.03	0.03	-	-	-	-	-	0.02	-	-
Cr ₂ O ₃	0.02	0.02	-	-	-	0.02	0.03	0.03	-	-	-	0.03
FeO	8.48	8.58	8.72	8.56	8.61	8.52	8.34	8.38	8.27	8.45	8.37	8.50
MnO	0.14	0.13	0.14	0.10	0.13	0.13	0.13	0.14	0.15	0.14	0.15	0.16
NiO	0.40	0.44	0.43	0.41	0.42	0.45	0.42	0.44	0.40	0.43	0.41	0.41
MgO	49.65	49.70	50.17	49.64	49.74	49.73	50.67	50.02	49.66	50.07	49.64	49.45
CaO	0.08	0.07	0.07	0.09	0.07	0.08	0.07	0.06	0.07	0.08	0.07	0.08
Na ₂ O	-	-	-	0.02	0.02	0.02	0.02	-	-	-	-	0.02
Total	99	100	100	99	100	100	101	100	100	100	99	100
Si	0.994	0.998	0.992	0.994	0.998	0.998	0.995	1.000	1.004	0.992	0.999	1.002
Ti	-	-	-	-	-	-	-	-	-	-	-	-
Al	-	-	0.001	0.001	-	-	-	-	-	0.000	-	-
Cr	0.001	0.000	-	-	-	0.000	0.001	0.001	-	-	-	0.001
Fe ²⁺	0.175	0.176	0.178	0.176	0.176	0.175	0.169	0.171	0.169	0.173	0.172	0.174
Mn	0.003	0.003	0.003	0.002	0.003	0.003	0.003	0.003	0.003	0.003	0.003	0.003
Ni	0.008	0.009	0.009	0.008	0.008	0.009	0.008	0.009	0.008	0.009	0.008	0.008
Mg	1.823	1.814	1.824	1.821	1.815	1.815	1.827	1.814	1.810	1.828	1.817	1.808
Ca	0.002	0.002	0.002	0.002	0.002	0.002	0.002	0.002	0.002	0.002	0.002	0.002
Na	-	-	-	0.001	0.001	0.001	0.001	-	-	-	-	0.001
Total	3.006	3.002	3.008	3.006	3.003	3.003	3.005	2.999	2.996	3.007	3.001	2.999
Mg#	0.913	0.912	0.911	0.912	0.911	0.912	0.915	0.914	0.915	0.914	0.914	0.912

Appendix 2.1a cont'd

Olivine	Kapsiki7												
Grain	ol14	ol15	ol16	ol17	ol18	ol19	ol20	ol21	ol22	ol23	ol24	ol25	ol26
SiO ₂	40.88	41.06	40.60	40.60	40.98	40.95	41.12	40.81	40.71	40.73	40.69	40.94	40.60
TiO ₂	-	-	-	-	-	-	-	-	-	-	-	-	-
Al ₂ O ₃	0.02	0.02	0.03	-	-	-	-	0.02	-	-	-	-	-
Cr ₂ O ₃	-	0.02	0.02	-	-	0.02	0.02	0.02	0.03	-	-	-	0.03
FeO	8.39	8.48	8.28	8.30	8.29	8.40	8.63	8.56	8.67	8.41	8.55	8.45	8.68
MnO	0.14	0.15	0.13	0.12	0.14	0.15	0.13	0.13	0.13	0.13	0.13	0.12	0.13
NiO	0.37	0.42	0.44	0.38	0.44	0.46	0.39	0.37	0.43	0.38	0.45	0.45	0.43
MgO	49.92	50.03	49.62	49.87	49.52	49.67	50.39	50.54	50.46	50.51	50.55	50.40	50.79
CaO	0.08	0.08	0.07	0.06	0.07	0.08	0.06	0.07	0.07	0.07	0.08	0.07	0.07
Na ₂ O	-	-	-	-	0.02	-	-	0.02	0.03	-	-	-	-
Total	100	100	99	99	99	100	101	101	101	100	100	100	101
Si	0.999	0.999	0.998	0.996	1.004	1.001	0.996	0.991	0.990	0.992	0.990	0.995	0.986
Ti	-	-	-	-	-	-	-	-	-	-	-	-	-
Al	0.000	0.001	0.001	-	-	-	-	0.000	-	-	-	-	-
Cr	-	0.000	0.000	-	-	0.000	0.000	0.000	0.001	-	-	-	0.001
Fe ²⁺	0.171	0.173	0.170	0.170	0.170	0.172	0.175	0.174	0.176	0.171	0.174	0.172	0.176
Mn	0.003	0.003	0.003	0.003	0.003	0.003	0.003	0.003	0.003	0.003	0.003	0.003	0.003
Ni	0.007	0.008	0.009	0.008	0.009	0.009	0.008	0.007	0.008	0.007	0.009	0.009	0.009
Mg	1.818	1.814	1.818	1.824	1.808	1.811	1.820	1.830	1.829	1.833	1.833	1.825	1.838
Ca	0.002	0.002	0.002	0.002	0.002	0.002	0.002	0.002	0.002	0.002	0.002	0.002	0.002
Na	-	-	-	-	0.001	-	-	0.001	0.001	-	-	-	-
Total	3.001	3.001	3.001	3.004	2.996	2.999	3.003	3.009	3.010	3.009	3.010	3.005	3.014
Mg#	0.914	0.913	0.914	0.915	0.914	0.913	0.912	0.913	0.912	0.915	0.913	0.914	0.912

Appendix 2.1b: Major element composition of orthopyroxenes from Kapsiki

OPX	Kapsiki 1																								
	opx1	opx2	opx3	opx4	opx5	opx6	opx7	opx8	opx9	opx10	opx11	opx12	opx13	opx14	opx15	opx16	opx17	opx18	opx19	opx20	opx21	opx22	opx23	opx24	opx24
SiO ₂	56.99	56.43	56.96	57.29	56.85	56.97	56.97	57.21	56.65	56.77	57.01	56.49	56.84	56.86	56.74	56.89	56.48	56.69	56.95	57.18	57.19	57.03	57.13	56.75	56.87
TiO ₂	0.04	0.05	0.03	0.05	0.04	0.05	0.03	0.02	0.09	0.04	0.05	0.06	0.07	0.05	0.05	0.07	0.05	0.05	0.03	0.07	0.04	0.04	0.03	0.03	0.04
Al ₂ O ₃	1.70	1.84	1.48	1.58	1.66	1.58	1.37	1.36	1.74	1.88	1.59	1.96	1.65	1.68	1.52	1.81	2.13	1.60	1.56	1.49	1.53	1.72	1.53	1.44	1.41
Cr ₂ O ₃	0.46	0.56	0.42	0.34	0.40	0.47	0.39	0.33	0.51	0.54	0.40	0.60	0.56	0.47	0.44	0.53	0.59	0.48	0.41	0.36	0.41	0.47	0.41	0.40	0.39
FeO	5.35	5.39	5.27	5.25	5.24	5.33	5.36	5.23	5.37	5.38	5.19	5.31	5.36	5.32	5.26	5.22	5.30	5.31	5.24	5.26	5.35	5.24	5.27	5.21	5.25
Fe ₂ O ₃	-	-	-	-	-	-	-	-	-	-	-	-	-	-	-	-	-	-	-	-	-	-	-	-	-
MnO	0.13	0.14	0.15	0.14	0.14	0.14	0.16	0.16	0.15	0.15	0.13	0.14	0.14	0.15	0.17	0.16	0.14	0.14	0.14	0.14	0.13	0.13	0.14	0.13	0.15
NiO	0.09	0.07	0.13	0.10	0.12	0.08	0.13	0.14	0.10	0.08	0.08	0.08	0.09	0.10	0.09	0.08	0.09	0.09	0.08	0.15	0.10	0.10	0.08	0.10	0.09
MgO	34.66	34.17	35.32	35.18	35.10	34.94	35.05	35.43	34.73	35.04	34.81	34.45	34.59	34.46	34.40	35.01	34.14	34.87	34.73	35.48	34.58	34.60	34.72	34.37	34.71
CaO	0.43	0.70	0.45	0.65	0.39	0.53	0.42	0.51	0.46	0.47	0.63	0.61	0.40	0.60	0.47	0.70	0.57	0.38	0.49	0.47	0.42	0.42	0.66	0.39	
Na ₂ O	0.06	0.07	0.07	0.10	0.07	0.08	0.08	0.06	0.08	0.06	0.09	0.06	0.09	0.07	0.07	0.05	0.08	0.07	0.05	0.04	0.08	0.07	0.04	0.09	0.11
Total	100	99	100	101	100	100	100	100	100	100	100	100	100	100	99	100	100	100	100	101	100	100	100	99	99
Si	1.960	1.954	1.954	1.957	1.954	1.956	1.961	1.959	1.951	1.946	1.962	1.949	1.956	1.963	1.964	1.951	1.949	1.954	1.962	1.956	1.967	1.962	1.966	1.967	1.966
Ti	0.001	0.001	0.001	0.001	0.001	0.001	0.001	0.001	0.002	0.001	0.001	0.002	0.002	0.001	0.001	0.001	0.002	0.001	0.001	0.001	0.002	0.001	0.001	0.001	0.001
Al	0.069	0.075	0.060	0.063	0.067	0.064	0.056	0.055	0.071	0.076	0.065	0.080	0.067	0.068	0.062	0.073	0.087	0.065	0.063	0.060	0.062	0.070	0.062	0.059	0.057
Cr	0.013	0.015	0.011	0.009	0.011	0.013	0.011	0.009	0.014	0.015	0.011	0.017	0.015	0.013	0.012	0.014	0.016	0.013	0.011	0.010	0.011	0.013	0.011	0.011	0.011
Fe ³⁺	-	-	-	-	-	-	-	-	-	-	-	-	-	-	-	-	-	-	-	-	-	-	-	-	-
Fe ²⁺	0.154	0.156	0.151	0.150	0.151	0.153	0.154	0.150	0.155	0.154	0.149	0.153	0.154	0.154	0.152	0.150	0.153	0.153	0.151	0.151	0.154	0.151	0.152	0.151	0.152
Mn	0.004	0.004	0.004	0.004	0.004	0.004	0.005	0.005	0.004	0.004	0.004	0.004	0.004	0.004	0.005	0.005	0.004	0.004	0.004	0.004	0.004	0.004	0.004	0.004	0.005
Ni	0.003	0.002	0.004	0.003	0.003	0.002	0.004	0.004	0.003	0.002	0.002	0.002	0.003	0.003	0.003	0.002	0.002	0.002	0.002	0.004	0.003	0.003	0.002	0.003	0.002
Mg	1.777	1.763	1.806	1.791	1.798	1.788	1.798	1.809	1.783	1.790	1.785	1.771	1.774	1.773	1.774	1.789	1.756	1.791	1.783	1.809	1.772	1.774	1.781	1.775	1.788
Ca	0.016	0.026	0.016	0.024	0.014	0.019	0.016	0.015	0.019	0.017	0.017	0.023	0.022	0.015	0.022	0.017	0.026	0.021	0.020	0.014	0.018	0.017	0.015	0.025	0.015
Na	0.004	0.005	0.004	0.007	0.004	0.005	0.005	0.004	0.005	0.004	0.006	0.004	0.006	0.005	0.005	0.003	0.006	0.005	0.003	0.002	0.005	0.005	0.003	0.006	0.008
Total	4.000	4.002	4.012	4.009	4.008	4.007	4.008	4.011	4.007	4.010	4.003	4.004	4.004	3.998	4.000	4.006	4.001	4.009	4.002	4.010	3.998	3.999	3.998	4.001	4.004
Mg#	0.920	0.919	0.923	0.923	0.923	0.921	0.921	0.924	0.920	0.921	0.923	0.920	0.920	0.920	0.921	0.923	0.920	0.921	0.922	0.923	0.920	0.922	0.921	0.922	0.922
Wo	0.008	0.013	0.008	0.012	0.007	0.010	0.008	0.008	0.010	0.009	0.009	0.012	0.011	0.008	0.011	0.009	0.013	0.011	0.010	0.007	0.009	0.009	0.008	0.013	0.007
En	0.911	0.904	0.913	0.910	0.914	0.910	0.912	0.914	0.909	0.911	0.913	0.907	0.908	0.911	0.908	0.913	0.906	0.909	0.911	0.915	0.910	0.912	0.912	0.908	0.913
Fs	0.081	0.082	0.079	0.078	0.079	0.080	0.081	0.078	0.081	0.081	0.078	0.081	0.081	0.081	0.080	0.079	0.081	0.080	0.079	0.078	0.081	0.079	0.080	0.079	0.080

Appendix 2.1b cont'd

OPX	Kapsiki 1																							
Grain	opx25	opx26	opx27	opx28	opx29	opx30	opx31	opx32	opx33	opx34	opx35	opx36	opx37	opx38	opx39	opx40	opx41	opx42	opx43	opx44	opx45	opx46	opx47	opx48
SiO ₂	57.45	57.38	56.84	56.75	56.25	56.94	56.97	56.59	56.53	56.83	57.14	56.94	56.82	56.80	57.36	56.66	56.69	57.10	57.12	57.16	57.63	57.26	57.28	57.54
TiO ₂	0.02	0.03	0.05	0.06	0.04	0.03	0.03	0.03	0.06	0.06	0.02	0.05	0.02	0.03	0.04	0.04	0.05	0.04	0.05	0.06	0.04	0.04	0.06	0.02
Al ₂ O ₃	1.43	1.36	1.91	1.72	1.83	1.65	1.44	1.46	1.62	1.59	1.35	1.50	1.38	1.63	1.56	1.73	1.70	1.82	1.54	1.68	1.41	1.57	1.65	1.32
Cr ₂ O ₃	0.36	0.29	0.49	0.46	0.38	0.41	0.43	0.35	0.45	0.43	0.37	0.43	0.39	0.49	0.38	0.48	0.48	0.46	0.39	0.51	0.33	0.45	0.40	0.32
FeO	5.15	5.16	5.20	5.28	5.21	5.15	5.19	5.20	5.29	5.13	5.13	5.08	5.16	5.14	5.13	5.17	5.09	5.14	4.80	4.74	4.87	4.92	4.85	4.82
Fe ₂ O ₃	-	-	-	-	-	-	-	-	-	-	-	-	-	-	-	-	-	-	-	-	-	-	-	-
MnO	0.13	0.13	0.13	0.16	0.13	0.13	0.13	0.15	0.14	0.14	0.13	0.14	0.13	0.13	0.15	0.12	0.13	0.13	0.13	0.15	0.12	0.14	0.15	0.16
NiO	0.10	0.11	0.11	0.07	0.12	0.07	0.10	0.15	0.09	0.07	0.12	0.10	0.08	0.10	0.13	0.10	0.11	0.10	0.09	0.10	0.13	0.09	0.09	0.10
MgO	35.41	35.40	34.86	35.36	35.50	35.50	35.34	35.55	35.29	35.20	35.50	35.25	35.41	35.24	35.48	35.24	34.96	35.03	34.72	34.18	34.96	34.96	34.72	34.49
CaO	0.37	0.39	0.45	0.56	0.43	0.39	0.43	0.37	0.51	0.51	0.39	0.40	0.47	0.51	0.43	0.50	0.59	0.54	0.42	0.59	0.44	0.46	0.44	0.36
Na ₂ O	0.03	0.10	0.07	0.05	0.11	0.06	0.08	0.04	0.05	0.05	0.06	0.11	0.07	0.08	0.03	0.05	0.07	0.07	0.04	0.06	0.07	0.10	0.03	0.08
Total	100	100	100	100	100	100	100	100	100	100	100	100	100	100	101	100	100	100	99	99	100	100	100	99
Si	1.963	1.963	1.951	1.944	1.937	1.950	1.956	1.949	1.945	1.953	1.959	1.956	1.955	1.950	1.957	1.947	1.952	1.954	1.970	1.973	1.975	1.964	1.969	1.985
Ti	0.000	0.001	0.001	0.001	0.001	0.001	0.001	0.001	0.002	0.001	0.000	0.001	0.001	0.001	0.001	0.001	0.001	0.001	0.001	0.002	0.001	0.001	0.002	0.001
Al	0.058	0.055	0.077	0.069	0.074	0.066	0.058	0.059	0.066	0.064	0.055	0.061	0.056	0.066	0.063	0.070	0.069	0.073	0.063	0.068	0.057	0.064	0.067	0.054
Cr	0.010	0.008	0.013	0.013	0.011	0.011	0.012	0.009	0.012	0.012	0.010	0.012	0.011	0.013	0.010	0.013	0.013	0.013	0.011	0.014	0.009	0.012	0.011	0.009
Fe ³⁺	-	-	-	-	-	-	-	-	-	-	-	-	-	-	-	-	-	-	-	-	-	-	-	-
Fe ²⁺	0.147	0.148	0.149	0.151	0.150	0.148	0.149	0.150	0.152	0.148	0.147	0.146	0.148	0.148	0.146	0.149	0.147	0.147	0.139	0.137	0.140	0.141	0.139	0.139
Mn	0.004	0.004	0.004	0.005	0.004	0.004	0.004	0.004	0.004	0.004	0.004	0.004	0.004	0.004	0.004	0.003	0.004	0.004	0.004	0.005	0.004	0.004	0.005	0.005
Ni	0.003	0.003	0.003	0.002	0.003	0.002	0.003	0.004	0.002	0.002	0.003	0.003	0.002	0.003	0.004	0.003	0.003	0.003	0.003	0.003	0.004	0.003	0.003	0.003
Mg	1.804	1.805	1.784	1.806	1.822	1.812	1.808	1.824	1.810	1.803	1.814	1.805	1.815	1.803	1.804	1.805	1.794	1.786	1.785	1.759	1.785	1.787	1.779	1.773
Ca	0.014	0.014	0.017	0.021	0.016	0.014	0.016	0.014	0.019	0.019	0.014	0.015	0.018	0.019	0.016	0.019	0.022	0.020	0.016	0.022	0.016	0.017	0.016	0.013
Na	0.002	0.007	0.004	0.004	0.007	0.004	0.005	0.003	0.004	0.004	0.004	0.007	0.004	0.006	0.002	0.004	0.005	0.004	0.002	0.004	0.005	0.007	0.002	0.005
Total	4.004	4.008	4.005	4.015	4.024	4.013	4.011	4.018	4.016	4.009	4.011	4.010	4.014	4.012	4.007	4.013	4.008	4.005	3.993	3.986	3.994	4.000	3.992	3.986
Mg#	0.925	0.924	0.923	0.923	0.924	0.925	0.924	0.924	0.922	0.924	0.925	0.925	0.924	0.924	0.925	0.924	0.924	0.924	0.928	0.928	0.928	0.927	0.927	0.927
Wo	0.007	0.007	0.009	0.010	0.008	0.007	0.008	0.007	0.010	0.010	0.007	0.008	0.009	0.010	0.008	0.009	0.011	0.010	0.008	0.011	0.008	0.009	0.008	0.007
En	0.916	0.916	0.913	0.911	0.915	0.916	0.915	0.916	0.912	0.914	0.917	0.916	0.915	0.914	0.916	0.914	0.912	0.913	0.919	0.915	0.918	0.917	0.917	0.919
Fs	0.077	0.077	0.078	0.079	0.077	0.077	0.077	0.077	0.079	0.077	0.076	0.076	0.077	0.077	0.077	0.077	0.076	0.077	0.073	0.074	0.074	0.074	0.074	0.074

Appendix 2.1b cont'd

OPX Grain	Kapsiki 2															
	opx2	opx3	opx5	opx6	opx7	opx8	opx9	opx10	opx11	opx13	opx14	opx15	opx16	opx17	opx18	opx19
SiO ₂	57.18	56.93	57.50	56.78	57.17	56.88	57.18	56.43	56.82	57.39	56.80	57.03	57.28	57.08	57.12	56.74
TiO ₂	0.06	0.06	0.04	0.04	0.05	0.05	0.06	0.08	0.02	0.05	0.06	0.06	0.06	0.05	0.04	0.05
Al ₂ O ₃	1.55	1.70	1.59	1.55	1.65	1.58	1.39	1.65	1.55	1.50	1.48	1.54	1.60	1.45	1.63	1.50
Cr ₂ O ₃	0.44	0.49	0.42	0.45	0.44	0.39	0.36	0.48	0.38	0.38	0.44	0.45	0.40	0.37	0.46	0.41
FeO	5.57	5.73	5.48	5.53	5.54	5.56	5.52	5.54	5.50	5.56	5.54	5.59	5.55	5.47	5.53	5.55
Fe ₂ O ₃	-	-	-	-	-	-	-	-	-	-	-	-	-	-	-	-
MnO	0.14	0.14	0.15	0.14	0.15	0.14	0.15	0.13	0.13	0.14	0.15	0.14	0.17	0.14	0.15	0.14
NiO	0.08	0.08	0.09	0.09	0.08	0.11	0.14	0.08	0.13	0.08	0.10	0.06	0.11	0.10	0.06	0.05
MgO	33.91	33.75	34.26	33.98	34.19	34.43	34.47	34.29	34.31	34.39	34.66	34.52	34.07	34.46	34.01	34.23
CaO	0.40	0.60	0.42	0.61	0.51	0.46	0.47	0.54	0.46	0.44	0.50	0.44	0.44	0.45	0.55	0.47
Na ₂ O	0.03	0.06	0.04	0.06	0.01	0.06	0.05	0.03	0.07	0.05	0.03	0.01	0.04	0.05	0.03	0.02
Total	99	100	100	99	100	100	100	99	99	100	100	100	100	100	100	99
Si	1.977	1.969	1.975	1.969	1.969	1.964	1.971	1.957	1.966	1.973	1.960	1.964	1.974	1.969	1.972	1.967
Ti	0.002	0.002	0.001	0.001	0.001	0.001	0.001	0.002	0.001	0.001	0.002	0.001	0.002	0.001	0.001	0.001
Al	0.063	0.069	0.064	0.063	0.067	0.064	0.056	0.068	0.063	0.061	0.060	0.063	0.065	0.059	0.066	0.062
Cr	0.012	0.013	0.012	0.013	0.012	0.011	0.010	0.013	0.010	0.010	0.012	0.012	0.011	0.010	0.013	0.011
Fe ³⁺	-	-	-	-	-	-	-	-	-	-	-	-	-	-	-	-
Fe ²⁺	0.161	0.166	0.157	0.160	0.160	0.161	0.159	0.161	0.159	0.160	0.160	0.161	0.160	0.158	0.160	0.161
Mn	0.004	0.004	0.004	0.004	0.004	0.004	0.004	0.004	0.004	0.004	0.005	0.004	0.005	0.004	0.004	0.004
Ni	0.002	0.002	0.002	0.003	0.002	0.003	0.004	0.002	0.004	0.002	0.003	0.002	0.003	0.003	0.002	0.001
Mg	1.747	1.739	1.754	1.756	1.755	1.771	1.770	1.773	1.769	1.762	1.782	1.772	1.750	1.772	1.750	1.769
Ca	0.015	0.022	0.016	0.023	0.019	0.017	0.017	0.020	0.017	0.016	0.018	0.016	0.016	0.017	0.020	0.017
Na	0.002	0.004	0.002	0.004	0.001	0.004	0.003	0.002	0.005	0.003	0.002	0.001	0.002	0.003	0.002	0.001
Total	3.985	3.990	3.987	3.995	3.991	4.000	3.997	4.002	3.999	3.992	4.004	3.997	3.988	3.997	3.989	3.996
Mg#	0.916	0.913	0.918	0.916	0.917	0.917	0.918	0.917	0.917	0.917	0.918	0.917	0.916	0.918	0.916	0.917
Wo	0.008	0.011	0.008	0.012	0.010	0.009	0.009	0.010	0.009	0.008	0.009	0.008	0.008	0.009	0.011	0.009
En	0.906	0.901	0.908	0.904	0.906	0.907	0.907	0.906	0.908	0.907	0.907	0.907	0.906	0.909	0.905	0.907
Fs	0.086	0.088	0.084	0.085	0.085	0.084	0.084	0.084	0.084	0.084	0.084	0.085	0.085	0.083	0.085	0.085

Appendix 2.1b cont'd

OPX Grain	Kapsiki 7											
	opx1	opx2	opx3	opx4	opx6	opx7	opx8	opx9	opx10	opx11	opx12	opx13
SiO ₂	57.46	57.50	57.17	56.78	57.22	56.94	57.25	57.56	57.15	57.27	57.39	56.67
TiO ₂	0.04	0.04	0.03	0.04	0.07	0.05	0.03	0.04	0.04	0.06	0.05	0.06
Al ₂ O ₃	1.70	1.79	1.69	2.09	1.88	2.15	1.85	1.64	1.87	1.77	1.74	2.30
Cr ₂ O ₃	0.33	0.39	0.35	0.51	0.43	0.55	0.38	0.33	0.41	0.31	0.41	0.58
FeO	5.56	5.43	5.44	5.47	5.49	5.50	5.51	5.48	5.43	5.41	5.44	5.49
Fe ₂ O ₃	-	-	-	-	-	-	-	-	-	-	-	-
MnO	0.15	0.15	0.13	0.13	0.14	0.14	0.13	0.16	0.15	0.15	0.14	0.16
NiO	0.11	0.10	0.10	0.12	0.12	0.05	0.09	0.10	0.10	0.13	0.06	0.08
MgO	34.76	34.95	34.95	34.44	34.37	34.32	34.54	34.79	35.07	34.90	35.10	34.37
CaO	0.43	0.42	0.42	0.67	0.56	0.75	0.46	0.47	0.47	0.44	0.42	0.69
Na ₂ O	0.05	0.10	0.06	0.05	0.06	0.07	0.05	0.08	0.04	0.08	0.04	0.06
Total	101	101	100	100	100	101	100	101	101	101	101	100
Si	1.964	1.960	1.959	1.949	1.961	1.950	1.962	1.965	1.952	1.959	1.957	1.943
Ti	0.001	0.001	0.001	0.001	0.002	0.001	0.001	0.001	0.001	0.002	0.001	0.002
Al	0.069	0.072	0.068	0.085	0.076	0.087	0.075	0.066	0.075	0.071	0.070	0.093
Cr	0.009	0.011	0.010	0.014	0.012	0.015	0.010	0.009	0.011	0.009	0.011	0.016
Fe ³⁺	-	-	-	-	-	-	-	-	-	-	-	-
Fe ²⁺	0.159	0.155	0.156	0.157	0.157	0.158	0.158	0.157	0.155	0.155	0.155	0.157
Mn	0.004	0.004	0.004	0.004	0.004	0.004	0.004	0.005	0.004	0.004	0.004	0.005
Ni	0.003	0.003	0.003	0.003	0.003	0.001	0.003	0.003	0.003	0.004	0.002	0.002
Mg	1.771	1.775	1.785	1.762	1.756	1.752	1.764	1.770	1.785	1.779	1.784	1.756
Ca	0.016	0.015	0.016	0.025	0.020	0.027	0.017	0.017	0.017	0.016	0.016	0.025
Na	0.004	0.006	0.004	0.003	0.004	0.005	0.003	0.005	0.002	0.005	0.003	0.004
Total	3.998	4.002	4.004	4.002	3.995	4.000	3.996	3.999	4.006	4.003	4.002	4.004
Mg#	0.918	0.920	0.920	0.918	0.918	0.918	0.918	0.919	0.920	0.920	0.920	0.918
Wo	0.008	0.008	0.008	0.013	0.011	0.014	0.009	0.009	0.009	0.008	0.008	0.013
En	0.908	0.910	0.911	0.905	0.906	0.903	0.908	0.908	0.910	0.910	0.911	0.904
Fs	0.084	0.082	0.081	0.082	0.083	0.083	0.083	0.083	0.081	0.081	0.081	0.083

Appendix 2.1b cont'd

OPX Grain	Kapsiki 7											
	opx1	opx2	opx3	opx4	opx6	opx7	opx8	opx9	opx10	opx11	opx12	opx13
SiO ₂	57.46	57.50	57.17	56.78	57.22	56.94	57.25	57.56	57.15	57.27	57.39	56.67
TiO ₂	0.04	0.04	0.03	0.04	0.07	0.05	0.03	0.04	0.04	0.06	0.05	0.06
Al ₂ O ₃	1.70	1.79	1.69	2.09	1.88	2.15	1.85	1.64	1.87	1.77	1.74	2.30
Cr ₂ O ₃	0.33	0.39	0.35	0.51	0.43	0.55	0.38	0.33	0.41	0.31	0.41	0.58
FeO	5.56	5.43	5.44	5.47	5.49	5.50	5.51	5.48	5.43	5.41	5.44	5.49
Fe ₂ O ₃	-	-	-	-	-	-	-	-	-	-	-	-
MnO	0.15	0.15	0.13	0.13	0.14	0.14	0.13	0.16	0.15	0.15	0.14	0.16
NiO	0.11	0.10	0.10	0.12	0.12	0.05	0.09	0.10	0.10	0.13	0.06	0.08
MgO	34.76	34.95	34.95	34.44	34.37	34.32	34.54	34.79	35.07	34.90	35.10	34.37
CaO	0.43	0.42	0.42	0.67	0.56	0.75	0.46	0.47	0.47	0.44	0.42	0.69
Na ₂ O	0.05	0.10	0.06	0.05	0.06	0.07	0.05	0.08	0.04	0.08	0.04	0.06
Total	101	101	100	100	100	101	100	101	101	101	101	100
Si	1.964	1.960	1.959	1.949	1.961	1.950	1.962	1.965	1.952	1.959	1.957	1.943
Ti	0.001	0.001	0.001	0.001	0.002	0.001	0.001	0.001	0.001	0.002	0.001	0.002
Al	0.069	0.072	0.068	0.085	0.076	0.087	0.075	0.066	0.075	0.071	0.070	0.093
Cr	0.009	0.011	0.010	0.014	0.012	0.015	0.010	0.009	0.011	0.009	0.011	0.016
Fe ³⁺	-	-	-	-	-	-	-	-	-	-	-	-
Fe ²⁺	0.159	0.155	0.156	0.157	0.157	0.158	0.158	0.157	0.155	0.155	0.155	0.157
Mn	0.004	0.004	0.004	0.004	0.004	0.004	0.004	0.005	0.004	0.004	0.004	0.005
Ni	0.003	0.003	0.003	0.003	0.003	0.001	0.003	0.003	0.003	0.004	0.002	0.002
Mg	1.771	1.775	1.785	1.762	1.756	1.752	1.764	1.770	1.785	1.779	1.784	1.756
Ca	0.016	0.015	0.016	0.025	0.020	0.027	0.017	0.017	0.017	0.016	0.016	0.025
Na	0.004	0.006	0.004	0.003	0.004	0.005	0.003	0.005	0.002	0.005	0.003	0.004
Total	3.998	4.002	4.004	4.002	3.995	4.000	3.996	3.999	4.006	4.003	4.002	4.004
Mg#	0.918	0.920	0.920	0.918	0.918	0.918	0.918	0.919	0.920	0.920	0.920	0.918
Wo	0.008	0.008	0.008	0.013	0.011	0.014	0.009	0.009	0.009	0.008	0.008	0.013
En	0.908	0.910	0.911	0.905	0.906	0.903	0.908	0.908	0.910	0.910	0.911	0.904
Fs	0.084	0.082	0.081	0.082	0.083	0.083	0.083	0.083	0.081	0.081	0.081	0.083

Appendix 2.1c: Major element composition of clinopyroxenes from Kapsiki

CPX	Kapsiki 1																				
	Group 1					Group 2															
	Grain	cpx1	cpx2	cpx3	cpx4	cpx5	cpx6	cpx7	cpx8	cpx9	cpx10	cpx11	cpx12	cpx13	cpx14	cpx15	cpx16	cpx17	cpx18	cpx19	cpx20
SiO ₂	53.37	53.35	53.49	53.76	53.63	53.52	53.11	53.36	53.68	53.53	53.21	53.22	53.17	53.02	53.59	52.86	52.86	53.26	53.36	52.97	53.93
TiO ₂	0.26	0.22	0.13	0.15	0.16	0.24	0.16	0.20	0.21	0.21	0.21	0.16	0.18	0.17	0.23	0.11	0.19	0.23	0.21	0.22	0.18
Al ₂ O ₃	3.81	3.77	3.69	3.77	3.73	3.31	3.50	3.54	3.50	3.40	3.33	3.50	3.42	3.73	3.59	3.67	3.62	3.71	3.46	3.67	3.82
Cr ₂ O ₃	1.64	1.62	1.70	1.83	1.64	1.68	1.66	1.62	1.74	1.66	1.72	1.69	1.62	1.62	1.73	1.68	1.63	1.57	1.55	1.59	1.66
Fe ₂ O ₃	-	-	-	-	-	-	-	-	-	-	-	-	-	-	-	-	-	-	-	-	-
FeO	2.81	2.73	2.68	2.73	2.62	1.99	2.62	1.89	2.09	2.06	1.89	2.26	2.03	2.26	1.93	2.66	2.74	1.97	2.34	2.69	1.97
MnO	0.09	0.10	0.08	0.09	0.07	0.08	0.09	0.06	0.05	0.08	0.09	0.07	0.07	0.07	0.07	0.06	0.10	0.05	0.06	0.06	0.07
NiO	0.03	0.07	0.05	0.09	0.05	0.06	0.05	0.04	0.02	0.02	0.03	0.08	0.04	0.02	0.07	0.04	0.04	0.05	0.02	0.05	0.05
MgO	16.57	16.62	16.30	16.54	16.53	15.60	16.34	15.49	15.43	15.58	15.33	15.62	15.53	15.81	15.81	16.18	16.47	16.09	16.66	16.79	15.73
CaO	18.92	18.65	18.92	18.90	18.82	21.62	20.93	21.67	21.54	21.42	21.47	21.42	21.63	21.58	21.55	21.22	20.62	21.68	21.18	20.78	21.64
Na ₂ O	1.20	1.27	1.39	1.47	1.35	1.77	1.40	1.79	1.79	1.66	1.83	1.60	1.54	1.50	1.72	1.39	1.40	1.60	1.28	1.39	0.27
Total	99	98	98	99	99	100	100	100	100	100	99	100	99	100	100	100	100	100	100	100	99
Si	1.948	1.952	1.957	1.951	1.957	1.944	1.931	1.942	1.946	1.947	1.947	1.939	1.943	1.929	1.937	1.924	1.925	1.928	1.931	1.919	1.955
Ti	0.007	0.006	0.004	0.004	0.004	0.007	0.004	0.006	0.006	0.006	0.006	0.004	0.005	0.005	0.006	0.003	0.005	0.006	0.006	0.006	0.005
Al	0.164	0.163	0.159	0.161	0.160	0.142	0.150	0.152	0.150	0.146	0.144	0.150	0.147	0.160	0.153	0.157	0.155	0.158	0.148	0.157	0.163
Cr	0.047	0.047	0.049	0.053	0.047	0.048	0.048	0.047	0.050	0.048	0.050	0.049	0.047	0.047	0.050	0.048	0.047	0.045	0.044	0.046	0.048
Fe ³⁺	-	-	-	-	-	-	-	-	-	-	-	-	-	-	-	-	-	-	-	-	-
Fe ²⁺	0.086	0.084	0.082	0.083	0.080	0.061	0.080	0.058	0.063	0.063	0.058	0.069	0.062	0.069	0.058	0.081	0.084	0.060	0.071	0.082	0.060
Mn	0.003	0.003	0.003	0.003	0.002	0.003	0.003	0.002	0.002	0.003	0.003	0.002	0.002	0.002	0.002	0.002	0.003	0.002	0.002	0.002	0.002
Ni	0.001	0.002	0.001	0.003	0.001	0.002	0.001	0.001	0.001	0.001	0.001	0.002	0.001	0.001	0.002	0.001	0.001	0.001	0.001	0.001	0.002
Mg	0.901	0.906	0.889	0.895	0.899	0.845	0.885	0.840	0.834	0.845	0.836	0.848	0.846	0.857	0.852	0.878	0.894	0.868	0.899	0.907	0.850
Ca	0.740	0.731	0.742	0.735	0.736	0.842	0.815	0.845	0.836	0.835	0.842	0.836	0.847	0.841	0.835	0.827	0.805	0.841	0.821	0.807	0.841
Na	0.085	0.090	0.099	0.104	0.096	0.125	0.099	0.126	0.126	0.117	0.130	0.113	0.109	0.106	0.121	0.098	0.099	0.112	0.090	0.098	0.019
Total	3.982	3.982	3.984	3.990	3.983	4.016	4.016	4.017	4.012	4.009	4.015	4.013	4.010	4.016	4.016	4.020	4.018	4.021	4.012	4.023	3.944
Mg#	0.913	0.916	0.916	0.915	0.918	0.933	0.917	0.936	0.929	0.931	0.935	0.925	0.932	0.926	0.936	0.915	0.915	0.936	0.927	0.918	0.934
Wo	0.428	0.424	0.432	0.428	0.429	0.481	0.457	0.484	0.482	0.479	0.484	0.476	0.482	0.475	0.478	0.463	0.451	0.475	0.458	0.449	0.480
En	0.521	0.526	0.518	0.522	0.524	0.483	0.497	0.482	0.480	0.484	0.481	0.483	0.481	0.484	0.488	0.491	0.501	0.490	0.501	0.505	0.485
Fs	0.051	0.050	0.049	0.050	0.048	0.036	0.046	0.034	0.037	0.037	0.035	0.041	0.036	0.040	0.035	0.046	0.049	0.035	0.041	0.046	0.035

Appendix 2.1c cont'd

CPX	Kapsiki 2													
Grain	cpx1	cpx2	cpx3	cpx4	cpx5	cpx6	cpx7	cpx8	cpx9	cpx10	cpx11	cpx12	cpx13	cpx14
SiO ₂	53.49	53.75	53.79	53.43	53.56	53.07	53.68	53.66	53.57	53.62	53.26	53.66	53.10	53.32
TiO ₂	0.12	0.14	0.14	0.14	0.14	0.15	0.15	0.14	0.14	0.15	0.13	0.15	0.14	0.18
Al ₂ O ₃	2.87	3.19	3.05	3.24	3.20	3.07	3.31	3.30	3.25	3.02	3.33	3.23	3.24	3.35
Cr ₂ O ₃	1.30	1.51	1.41	1.48	1.53	1.56	1.54	1.57	1.41	1.45	1.49	1.62	1.54	1.55
Fe ₂ O ₃	-	-	-	-	-	-	-	-	-	-	-	-	-	-
FeO	2.40	2.02	2.50	2.10	1.94	1.97	1.93	1.90	2.69	2.31	2.01	1.99	2.46	2.63
MnO	0.08	0.08	0.07	0.08	0.09	0.08	0.09	0.08	0.09	0.07	0.06	0.07	0.07	0.07
NiO	0.05	0.04	0.04	0.05	0.05	0.06	0.05	0.06	0.07	0.02	0.05	0.02	0.04	0.07
MgO	16.40	16.06	16.46	16.30	15.96	16.21	16.25	16.26	16.55	16.33	15.85	15.82	16.28	16.39
CaO	21.96	22.49	21.89	22.35	22.55	22.57	22.39	22.35	21.33	22.07	22.33	22.49	21.89	21.43
Na ₂ O	1.11	1.20	1.08	1.13	1.17	1.25	1.13	1.14	1.23	1.16	1.14	1.14	1.08	1.13
Total	100	100	100	100	100	100	101	100	100	100	100	100	100	100
Si	1.946	1.941	1.943	1.934	1.940	1.930	1.937	1.937	1.938	1.942	1.939	1.943	1.932	1.933
Ti	0.003	0.004	0.004	0.004	0.004	0.004	0.004	0.004	0.004	0.004	0.004	0.004	0.004	0.005
Al	0.123	0.136	0.130	0.138	0.137	0.132	0.141	0.140	0.139	0.129	0.143	0.138	0.139	0.143
Cr	0.037	0.043	0.040	0.042	0.044	0.045	0.044	0.045	0.040	0.042	0.043	0.046	0.044	0.045
Fe ³⁺	-	-	-	-	-	-	-	-	-	-	-	-	-	-
Fe ²⁺	0.073	0.061	0.076	0.064	0.059	0.060	0.058	0.057	0.081	0.070	0.061	0.060	0.075	0.080
Mn	0.002	0.002	0.002	0.003	0.003	0.003	0.003	0.003	0.003	0.002	0.002	0.002	0.002	0.002
Ni	0.002	0.001	0.001	0.001	0.001	0.002	0.002	0.002	0.002	0.001	0.001	0.001	0.001	0.002
Mg	0.889	0.865	0.886	0.879	0.862	0.879	0.874	0.875	0.892	0.882	0.860	0.854	0.883	0.886
Ca	0.856	0.870	0.847	0.867	0.875	0.880	0.866	0.864	0.827	0.857	0.871	0.873	0.854	0.833
Na	0.078	0.084	0.075	0.079	0.082	0.088	0.079	0.080	0.087	0.081	0.080	0.080	0.076	0.080
Total	4.010	4.008	4.005	4.011	4.007	4.021	4.006	4.007	4.012	4.009	4.005	4.001	4.010	4.008
Mg#	0.92	0.93	0.92	0.93	0.94	0.94	0.94	0.94	0.92	0.93	0.93	0.93	0.92	0.92
Wo	0.470	0.484	0.468	0.478	0.487	0.483	0.481	0.480	0.458	0.473	0.485	0.488	0.471	0.462
En	0.488	0.481	0.489	0.485	0.479	0.483	0.485	0.486	0.495	0.487	0.479	0.477	0.487	0.492
Fs	0.041	0.035	0.043	0.036	0.034	0.034	0.034	0.033	0.047	0.040	0.035	0.035	0.043	0.046

Appendix 2.1c cont'd

CPX	Kapsiki 7															
Grain	cpx1	cpx2	cpx3	cpx4	cpx5	cpx6	cpx7	cpx8	cpx9	cpx10	cpx11	cpx12	cpx13	cpx14	cpx15	cpx18
SiO ₂	53.42	53.39	53.68	53.66	53.37	53.40	53.27	53.67	53.50	53.04	53.38	53.03	53.52	53.17	53.02	53.88
TiO ₂	0.13	0.13	0.15	0.13	0.13	0.13	0.15	0.13	0.14	0.13	0.16	0.27	0.13	0.15	0.14	0.15
Al ₂ O ₃	3.03	3.25	3.34	3.31	3.01	2.95	3.11	3.01	3.12	3.00	3.06	3.35	3.00	2.99	3.17	3.17
Cr ₂ O ₃	1.48	1.53	1.65	1.52	1.53	1.54	1.39	1.24	1.49	1.42	1.55	1.54	1.22	1.54	1.51	1.44
Fe ₂ O ₃	-	-	-	-	-	-	-	-	-	-	-	-	-	-	-	-
FeO	2.55	2.08	1.96	1.97	2.15	2.11	1.92	2.64	1.98	1.96	2.28	2.24	1.88	2.11	1.96	1.96
MnO	0.07	0.07	0.06	0.08	0.08	0.08	0.08	0.08	0.09	0.08	0.08	0.06	0.08	0.09	0.09	0.06
NiO	0.05	0.03	0.02	0.05	0.03	0.06	0.05	0.07	0.05	0.06	0.05	0.03	0.09	0.06	0.03	0.02
MgO	16.76	16.25	16.19	16.58	16.19	16.52	16.26	16.81	15.98	16.17	16.08	16.35	16.21	15.99	15.78	16.36
CaO	21.65	22.29	22.25	21.95	22.12	22.08	22.23	21.06	22.17	21.58	21.90	21.82	22.14	21.94	21.92	22.06
Na ₂ O	1.16	1.10	1.16	1.21	1.13	1.05	1.19	1.15	1.14	1.16	1.08	1.07	1.11	1.16	1.09	1.20
Total	100	100	100	100	100	100	100	100	100	99	100	100	99	99	99	100
Si	1.935	1.935	1.937	1.936	1.942	1.939	1.939	1.947	1.946	1.948	1.944	1.929	1.950	1.945	1.946	1.945
Ti	0.004	0.004	0.004	0.003	0.004	0.004	0.004	0.003	0.004	0.004	0.004	0.007	0.003	0.004	0.004	0.004
Al	0.129	0.139	0.142	0.141	0.129	0.126	0.133	0.129	0.134	0.130	0.131	0.144	0.129	0.129	0.137	0.135
Cr	0.042	0.044	0.047	0.043	0.044	0.044	0.040	0.036	0.043	0.041	0.045	0.044	0.035	0.045	0.044	0.041
Fe ³⁺	-	-	-	-	-	-	-	-	-	-	-	-	-	-	-	-
Fe ²⁺	0.077	0.063	0.059	0.059	0.065	0.064	0.058	0.080	0.060	0.060	0.069	0.068	0.057	0.065	0.060	0.059
Mn	0.002	0.002	0.002	0.003	0.002	0.003	0.003	0.002	0.003	0.003	0.003	0.002	0.003	0.003	0.003	0.002
Ni	0.001	0.001	0.001	0.002	0.001	0.002	0.001	0.002	0.002	0.002	0.001	0.001	0.003	0.002	0.001	0.001
Mg	0.905	0.878	0.871	0.891	0.878	0.894	0.882	0.909	0.866	0.885	0.873	0.886	0.880	0.872	0.863	0.880
Ca	0.840	0.866	0.860	0.848	0.862	0.859	0.867	0.819	0.864	0.849	0.855	0.850	0.864	0.860	0.862	0.853
Na	0.082	0.077	0.081	0.085	0.080	0.074	0.084	0.081	0.081	0.082	0.076	0.076	0.078	0.083	0.078	0.084
Total	4.017	4.008	4.005	4.011	4.008	4.009	4.012	4.008	4.002	4.004	4.002	4.007	4.003	4.006	3.998	4.005
Mg#	0.921	0.933	0.936	0.938	0.931	0.933	0.938	0.919	0.935	0.936	0.926	0.929	0.939	0.931	0.935	0.937
Wo	0.461	0.479	0.480	0.471	0.477	0.472	0.479	0.452	0.482	0.473	0.475	0.471	0.479	0.478	0.482	0.475
En	0.496	0.485	0.486	0.495	0.486	0.491	0.487	0.502	0.483	0.493	0.485	0.491	0.488	0.485	0.483	0.490
Fs	0.044	0.036	0.034	0.034	0.037	0.037	0.034	0.046	0.035	0.035	0.040	0.039	0.033	0.037	0.035	0.034

Appendix 2.1d: Major element composition of spinels from Kapsiki

Spinel	Kapsiki 1															
	Grain	spl1	spl2	spl3	spl4	spl5	spl7	spl8	spl9	spl10	sp11	sp12	sp13	sp14	sp15	sp16
SiO ₂	-	-	0.04	0.03	-	-		0.03	-	-	-	-	-	-	-	-
TiO ₂	0.30	0.26	0.28	0.30	0.13	0.11	0.24	0.21	0.35	0.30	0.30	0.18	0.31	0.17	0.48	
Al ₂ O ₃	25.79	26.67	25.75	29.75	26.03	27.55	27.45	26.72	23.91	26.14	26.04	26.96	25.35	26.86	25.11	
Cr ₂ O ₃	42.43	42.30	42.75	39.01	42.13	41.84	41.79	42.24	44.43	42.64	42.51	42.24	42.52	42.55	43.39	
Fe ₂ O ₃	2.83	2.65	2.92	2.60	3.45	2.29	2.29	2.73	3.18	2.36	2.19	2.00	2.65	1.24	1.28	
FeO	13.20	13.18	13.01	13.18	13.66	13.09	13.29	12.80	13.19	13.66	13.47	13.53	13.19	14.35	14.92	
MnO	0.35	0.30	0.33	0.31	0.37	0.29	0.24	0.35	0.36	0.41	0.43	0.35	0.42	0.38	0.42	
NiO	0.24	0.24	0.22	0.17	0.23	0.23	0.20	0.20	0.22	0.20	0.18	0.22	0.21	0.17	0.20	
MgO	14.71	14.97	14.90	15.36	14.27	15.05	15.05	15.05	14.68	14.53	14.52	14.63	14.48	13.98	13.52	
Na ₂ O	-	-	0.02	0.02	0.06	-	-	0.05	-	-	-	-	-	0.02	-	
Total	100	101	100	101	100	100	101	100	100	100	100	100	99	100	99	
Si	-	-	0.001	0.001	-	-		0.001	-	-	-	-	-	-	-	
Ti	0.007	0.006	0.006	0.007	0.003	0.003	0.005	0.005	0.008	0.007	0.007	0.004	0.007	0.004	0.011	
Al	0.914	0.935	0.909	1.026	0.920	0.963	0.959	0.937	0.851	0.923	0.925	0.949	0.907	0.953	0.903	
Cr	1.009	0.995	1.012	0.903	0.999	0.981	0.979	0.994	1.061	1.010	1.012	0.998	1.020	1.013	1.046	
Fe ³⁺	0.064	0.059	0.066	0.057	0.078	0.051	0.051	0.061	0.072	0.053	0.050	0.045	0.060	0.028	0.029	
Fe ²⁺	0.332	0.328	0.326	0.323	0.343	0.325	0.329	0.319	0.333	0.342	0.339	0.338	0.335	0.361	0.380	
Mn	0.009	0.008	0.008	0.008	0.009	0.007	0.006	0.009	0.009	0.010	0.011	0.009	0.011	0.010	0.011	
Ni	0.006	0.006	0.005	0.004	0.006	0.005	0.005	0.005	0.005	0.005	0.004	0.005	0.005	0.004	0.005	
Mg	0.659	0.664	0.665	0.670	0.638	0.665	0.665	0.667	0.661	0.649	0.652	0.651	0.655	0.627	0.615	
Na	-	-	0.001	0.001	0.004	-	-	0.003	-	-	-	-	-	0.001	-	
Total	3.000	3.000	3.000	3.000	3.000	3.000	3.000	3.000	3.000	3.000	3.000	3.000	2.999	3.000	3.000	
Mg#	0.665	0.669	0.671	0.675	0.650	0.672	0.669	0.677	0.665	0.655	0.658	0.658	0.662	0.635	0.618	
Cr#	0.525	0.515	0.527	0.468	0.521	0.505	0.505	0.515	0.555	0.522	0.523	0.512	0.529	0.515	0.537	

Appendix 2.1d cont'd

Spinel	Kapsiki 2														
Grain	sp1	sp2	sp3	sp4	sp5	sp6	sp7	sp9	sp10	sp11	sp12	sp13	sp14	sp15	
SiO ₂	0.02	0.04	0.02	0.02	-	-	0.06	0.05	0.04	0.06	-	-	-	0.03	
TiO ₂	0.25	0.25	0.21	0.22	0.22	0.21	0.22	0.19	0.13	0.16	0.13	0.14	0.14	0.11	
Al ₂ O ₃	28.76	29.24	31.32	31.23	30.67	30.73	30.76	30.97	32.11	30.63	29.76	29.86	30.10	29.77	
Cr ₂ O ₃	38.85	38.21	36.43	37.27	37.07	37.91	36.86	36.47	36.21	37.62	38.46	38.77	38.02	38.51	
Fe ₂ O ₃	3.09	3.14	3.34	1.79	2.96	1.44	2.64	3.05	2.07	2.49	2.98	2.81	2.54	2.86	
FeO	13.72	13.51	13.17	14.11	13.16	14.30	13.70	13.13	13.85	13.81	13.27	13.43	13.57	13.37	
MnO	0.33	0.36	0.35	0.33	0.37	0.35	0.25	0.35	0.38	0.39	0.40	0.38	0.41	0.35	
NiO	0.25	0.20	0.23	0.19	0.26	0.19	0.24	0.26	0.27	0.23	0.21	0.21	0.23	0.26	
MgO	14.70	14.90	15.40	14.72	15.17	14.42	14.84	15.23	14.87	14.84	14.96	15.07	14.79	14.91	
Na ₂ O	-						0.03	-			0.04	-		0.03	
Total	100	100	100	100	100	100	100	100	100	100	100	101	100	100	
Si	0.001	0.001	0.001	0.001	-	-	0.002	0.001	0.001	0.002	-	-	-	0.001	
Ti	0.006	0.006	0.005	0.005	0.005	0.005	0.005	0.004	0.003	0.004	0.003	0.003	0.003	0.002	
Al	1.007	1.021	1.077	1.083	1.063	1.072	1.070	1.073	1.108	1.061	1.034	1.032	1.048	1.034	
Cr	0.912	0.895	0.840	0.867	0.862	0.887	0.860	0.848	0.838	0.874	0.896	0.899	0.888	0.898	
Fe ³⁺	0.069	0.070	0.073	0.040	0.066	0.032	0.059	0.067	0.046	0.055	0.066	0.062	0.057	0.063	
Fe ²⁺	0.341	0.335	0.321	0.347	0.324	0.354	0.338	0.323	0.339	0.339	0.327	0.329	0.336	0.330	
Mn	0.008	0.009	0.009	0.008	0.009	0.009	0.006	0.009	0.009	0.010	0.010	0.009	0.010	0.009	
Ni	0.006	0.005	0.005	0.005	0.006	0.005	0.006	0.006	0.006	0.006	0.005	0.005	0.006	0.006	
Mg	0.651	0.658	0.669	0.645	0.665	0.636	0.653	0.668	0.649	0.650	0.657	0.659	0.651	0.655	
Na	-	-	-	-	-	-	0.002	-	-	-	0.002	-	-	0.002	
Total	3.000	3.000	3.000	3.000	2.999	2.999	3.000	3.000	3.000	3.000	3.000	2.999	2.999	3.000	
Mg#	0.656	0.663	0.676	0.650	0.673	0.642	0.659	0.674	0.657	0.657	0.668	0.667	0.660	0.665	
Cr#	0.475	0.467	0.438	0.445	0.448	0.453	0.446	0.441	0.431	0.452	0.464	0.466	0.459	0.465	

Appendix 2.1d cont'd

Spinel	Kapsiki 7																
Grain	sp1	sp2	sp3	sp4	sp5	sp6	sp7	sp8	sp9	sp10	sp12	sp13	sp14	sp15	sp16	sp17	sp18
SiO ₂	-	-	-	-	-	-	0.05	-	-	0.03	0.05	0.03	-	-	0.03	0.05	0.03
TiO ₂	0.20	0.19	0.21	0.20	0.22	0.22	0.13	0.14	0.25	0.22	0.18	0.22	0.19	0.23	0.20	0.18	0.21
Al ₂ O ₃	29.61	30.47	30.14	30.57	31.05	30.43	30.63	29.13	30.02	30.44	31.66	31.33	31.02	30.38	31.19	30.60	31.17
Cr ₂ O ₃	37.97	37.03	37.22	36.54	37.71	37.21	36.79	38.27	37.21	36.86	36.11	35.68	36.62	37.00	36.43	36.53	36.44
Fe ₂ O ₃	3.14	2.89	3.31	3.18	1.37	2.85	2.92	3.03	3.06	3.00	3.10	2.94	3.16	2.95	2.94	3.44	2.77
FeO	13.18	13.33	13.13	13.37	13.70	13.20	13.08	13.14	13.56	13.33	13.11	13.26	13.26	13.49	13.25	13.02	14.67
MnO	0.32	0.32	0.32	0.30	0.34	0.33	0.33	0.33	0.34	0.31	0.33	0.34	0.34	0.38	0.38	0.36	0.39
NiO	0.21	0.22	0.25	0.30	0.19	0.21	0.24	0.24	0.23	0.23	0.25	0.22	0.24	0.24	0.26	0.20	0.20
MgO	14.97	15.01	15.11	14.96	14.86	15.08	15.01	14.86	14.82	15.05	15.40	15.06	15.05	14.91	15.13	15.24	14.38
Na ₂ O	0.04	-	-	-	-	0.02	0.04	-	-	-	-	-	0.05	-	-	-	-
Total	100	99	100	99	99	100	99	99	100	99	100	99	100	100	100	100	100
Si	-	-	-	-	-	-	0.002	-	-	0.001	0.001	0.001	-	-	0.001	0.001	0.001
Ti	0.004	0.004	0.005	0.004	0.005	0.005	0.003	0.003	0.006	0.005	0.004	0.005	0.004	0.005	0.004	0.004	0.005
Al	1.034	1.062	1.049	1.065	1.080	1.059	1.068	1.024	1.049	1.060	1.089	1.091	1.074	1.059	1.080	1.063	1.080
Cr	0.889	0.866	0.869	0.854	0.880	0.868	0.861	0.902	0.872	0.861	0.833	0.833	0.851	0.865	0.846	0.851	0.847
Fe ³⁺	0.070	0.064	0.074	0.071	0.031	0.063	0.065	0.068	0.068	0.067	0.068	0.065	0.070	0.066	0.065	0.076	0.061
Fe ²⁺	0.326	0.330	0.324	0.331	0.338	0.326	0.324	0.328	0.336	0.330	0.320	0.328	0.326	0.333	0.325	0.321	0.361
Mn	0.008	0.008	0.008	0.008	0.009	0.008	0.008	0.008	0.009	0.008	0.008	0.009	0.008	0.010	0.009	0.009	0.010
Ni	0.005	0.005	0.006	0.007	0.005	0.005	0.006	0.006	0.006	0.006	0.006	0.005	0.006	0.006	0.006	0.005	0.005
Mg	0.661	0.661	0.665	0.659	0.653	0.663	0.662	0.660	0.655	0.663	0.670	0.663	0.659	0.657	0.662	0.669	0.630
Na	0.002	-	-	-	-	0.001	0.002	-	-	-	-	-	0.003	-	-	-	-
Total	3.000	3.000	2.999	2.999	2.999	2.999	3.000	3.000	3.000	3.000	2.999	2.999	3.000	3.000	2.999	2.999	3.000
Mg#	0.669	0.667	0.672	0.666	0.659	0.671	0.672	0.668	0.661	0.668	0.677	0.669	0.669	0.663	0.671	0.676	0.636
Cr#	0.462	0.449	0.453	0.445	0.449	0.451	0.446	0.468	0.454	0.448	0.433	0.433	0.442	0.450	0.439	0.445	0.440

Appendix 2.2a: Trace element composition of olivines from Kapsiki

Sample	Kapsiki 1									Kapsiki 2										
	ol1	ol2	ol7	ol16	ol25	ol24	ol23	ol28	ol30	ol 5	ol 6	ol7	ol11	ol9	ol25	ol37	ol35	ol33	ol18	ol40
Li	1.65	1.65	1.80	1.72	1.87	1.75	1.67	1.73	1.84	2.42	2.60	2.47	2.48	2.51	2.49	2.55	2.51	2.45	2.39	2.40
B	0.43	0.40	0.42	0.37	0.34	0.34	0.32	0.32	0.28	0.26	0.25	0.25	0.26	0.24	0.25	0.22	0.23	0.22	0.21	0.21
Na	60.3	61.1	62.4	60.6	60.7	62.3	61.4	60.7	61.1	47.8	51.7	48.6	49.1	49.4	49.4	48.4	49.1	47.7	47.9	46.4
Mg	356035	354811	360527	356253	357225	360699	358674	358063	358462	345750	346094	344557	343534	339192	335135	335274	333504	332890	331612	329233
Al	82.0	80.3	77.5	76.2	83.8	89.1	78.9	69.1	92.0	69.4	77.6	68.5	80.3	77.9	63.4	60.8	69.1	67.2	69.3	67.1
P	6.0	8.6	7.4	3.2	5.9	14.6	3.6	5.8	3.3	6.10	5.42	5.82	5.86	6.09	8.10	4.30	8.28	6.45	5.63	6.02
Ca	496	496	535	554	605	556	589	523	600	508	527	514	520	532	511	483	527	504	546	512
Sc	4.11	4.24	4.45	4.22	4.57	4.56	4.59	3.95	4.52	3.83	3.87	3.71	3.91	3.80	3.71	3.69	3.68	3.82	3.85	3.82
Ti	5.85	5.14	5.37	5.89	9.61	9.05	11.38	4.89	13.15	6.85	8.22	6.12	7.46	8.96	5.71	4.84	6.83	5.84	7.89	5.76
V	3.26	3.39	3.53	3.44	3.74	3.99	4.05	2.91	3.82	2.98	3.02	2.92	3.16	3.06	2.88	2.80	2.92	2.97	3.10	2.96
Cr	113	110	125	123	135	131	129	123	148	88.9	123.6	92.1	105	112	96.5	90.3	95.6	87.1	88.8	77.4
Mn	899	894	908	900	901	908	909	902	903	930	938	930	937	928	932	936	932	937	938	933
Fe	21325	21338	21687	21604	21786	22146	22419	22580	22717	25294	25609	25591	25784	25684	26135	26380	26422	26533	26618	26703
Co	138	137	140	138	138	141	143	139	140	142	143	142	143	141	142	143	142	142	142	142
Ni	2673	2689	2726	2685	2724	2729	2690	2753	2778	2798	2835	2797	2820	2798	2841	2820	2835	2829	2821	2864
Zn	48.4	49.7	54.3	53.5	50.2	54.7	62.3	48.2	51.3	51.0	52.8	51.6	53.7	52.5	51.2	54.3	50.2	51.2	51.8	52.6
Y	0.01	0.02	0.02	0.02	0.02	0.02	0.02	0.01	0.02	0.01	0.01	0.01	0.01	0.01	0.01	0.01	0.01	0.01	0.01	0.01
Zr	0.01	0.01	0.01	0.01	0.01	0.01	0.01	0.01	0.01	0.01	0.01	0.01	0.01	0.01	0.01	0.01	0.01	0.01	0.01	0.01

Appendix 2.2a cont'd

Sample	Kapsiki 7									
	o11	o14	o15	o13	o18	o111	o116	o119	o112	o124
Li	2.55	2.41	2.75	2.49	2.58	2.56	2.56	2.56	2.81	2.61
B	0.29	0.27	0.27	0.24	0.27	0.26	0.26	0.26	0.26	0.26
Na	49.8	46.8	52.8	47.5	49.9	49.5	50.5	49.3	51.7	49.9
Mg	351740	352175	353694	353594	355765	351477	347212	349580	348103	345667
Al	72.4	64.8	65.6	65.5	69.2	68.1	77.1	74.4	65.4	71.7
P	11.9	15.0	13.2	10.3	13.5	12.5	14.6	14.9	18.1	11.8
Ca	531	501	529	530	539	523	529	537	514	531
Sc	3.93	3.85	3.92	3.88	3.87	3.90	3.86	3.93	3.67	3.76
Ti	8.15	6.23	6.70	6.36	6.00	7.36	8.12	7.87	6.03	7.43
V	3.06	2.98	2.93	3.04	3.06	2.97	3.09	3.15	2.89	3.00
Cr	112	79.8	122	92.0	99.5	101	115	100	109	103
Mn	925	922	934	932	942	932	930	940	938	930
Fe	23393	23551	23907	24002	24382	24363	24651	25007	25116	25249
Co	140	140	141	141	144	141	141	143	142	142
Ni	2736	2750	2766	2741	2790	2772	2774	2807	2819	2798
Zn	54.3	55.4	55.9	53.8	58.4	52.2	52.7	56.1	55.9	52.8
Y	0.01	0.01	0.01	0.01	0.01	0.01	0.01	0.01	0.01	0.01
Zr	0.01	0.01	0.01	0.01	0.01	0.01	0.01	0.01	0.01	0.01

Appendix 2.2b: Trace element composition of orthopyroxenes from Kapsiki

Sample	Kapsiki 1										Kapsiki 2										
	Grains	opx12	opx10	opx9	opx6	opx4	opx17	opx17_	opx18	opx20	opx26	opx1	opx2	opx5	opx6	opx7	opx9	opx14	opx13	opx18	opx15
Th		0.001	0.083	0.009	0.036	0.005	0.001	0.013	0.018	0.082	0.004	0.015	0.007	0.005	0.011	0.010	0.006	0.015	0.033	0.012	0.030
U		0.002	0.011	0.003	0.007	0.002	0.001	0.004	0.011	0.010	0.002	0.008	0.009	0.006	0.009	0.008	0.008	0.006	0.010	0.007	0.011
Nb		0.008	0.006	0.006	0.005	0.005	0.004	0.005	0.033	0.006	0.005	0.006	0.007	0.006	0.006	0.006	0.005	0.006	0.006	0.006	0.005
La		0.019	0.051	0.021	0.023	0.009	0.002	0.019	0.018	0.032	0.009	0.009	0.017	0.005	0.023	0.014	0.010	0.015	0.013	0.009	0.008
Ce		0.071	0.120	0.052	0.058	0.023	0.004	0.046	0.041	0.065	0.023	0.014	0.018	0.007	0.040	0.017	0.013	0.018	0.014	0.013	0.010
Pb		0.002	0.005	0.001	0.003	0.002	0.001	0.002	0.018	0.004	0.001	0.001	0.001	0.001	0.001	–	–	0.000	0.001	0.001	0.001
Sr		0.87	2.95	1.12	1.28	0.71	0.33	0.47	1.00	3.27	0.48	–	0.11	0.04	0.21	0.09	0.06	0.20	0.20	0.13	0.50
Pr		0.012	0.013	0.006	0.007	0.002	0.000	0.005	0.005	0.006	0.003	0.001	0.001	0.001	0.003	0.002	0.001	0.002	0.001	0.001	0.001
Nd		0.052	0.045	0.020	0.026	0.011	0.001	0.018	0.018	0.026	0.012	0.010	0.003	0.004	0.013	0.006	0.004	0.011	0.007	0.007	0.005
Hf		0.005	0.018	0.012	0.011	0.008	0.005	0.008	0.021	0.020	0.007	0.012	0.007	0.007	0.011	0.008	0.006	0.011	0.012	0.011	0.010
Zr		0.20	0.29	0.21	0.19	0.25	0.26	0.19	0.69	0.31	0.22	0.267	0.177	0.192	0.233	0.220	0.171	0.250	0.253	0.225	0.221
Sm		0.017	0.010	0.006	0.008	0.005	0.002	0.007	0.007	0.008	0.005	0.006	0.002	0.002	0.004	0.004	0.002	0.005	0.004	0.004	0.004
Eu		0.008	0.005	0.003	0.003	0.003	–	0.002	0.003	0.003	0.002	0.003	0.001	0.001	0.002	0.002	0.001	0.002	0.002	0.002	0.002
Gd		0.022	0.014	0.009	0.010	0.009	–	0.009	0.010	0.010	0.010	0.008	0.006	0.006	0.009	0.008	0.004	0.011	0.007	0.010	0.006
Tb		0.004	0.003	0.002	0.002	0.003	0.0003	0.002	0.002	0.003	0.002	0.002	0.001	0.002	0.002	0.002	0.002	0.002	0.002	0.002	0.002
Ti		168	298	243	238	204	145	235	234	320	180	286	251	245	268	275	230	279	282	285	259
Dy		0.027	0.024	0.021	0.019	0.021	0.004	0.018	0.018	0.022	0.018	0.022	0.014	0.018	0.018	0.016	0.016	0.019	0.020	0.019	0.018
Ho		0.007	0.006	0.005	0.004	0.006	0.001	0.005	0.005	0.005	0.006	0.006	0.004	0.006	0.006	0.005	0.005	0.005	0.005	0.006	0.006
Y		0.196	0.161	0.152	0.130	0.164	0.024	0.139	0.139	0.155	0.152	0.158	0.123	0.151	0.147	0.144	0.142	0.165	0.141	0.157	0.151
Er		0.022	0.019	0.020	0.019	0.020	0.003	0.018	0.020	0.021	0.020	0.022	0.018	0.022	0.021	0.019	0.019	0.021	0.021	0.022	0.021
Tm		0.004	0.004	0.003	0.003	0.004	0.001	0.003	0.004	0.004	0.003	0.004	0.004	0.005	0.004	0.004	0.004	0.005	0.005	0.005	0.005
Yb		0.034	0.034	0.035	0.030	0.033	0.009	0.032	0.032	0.037	0.033	0.051	0.044	0.041	0.044	0.044	0.044	0.051	0.048	0.047	0.044
Lu		0.007	0.007	0.006	0.006	0.006	0.002	0.006	0.007	0.007	0.006	0.010	0.009	0.007	0.009	0.010	0.007	0.010	0.009	0.010	0.008
Sc		13.4	14.5	13.7	13.6	14.1	14.1	13.3	13.8	16.0	12.8	16.8	15.7	14.1	16.3	16.0	13.9	16.8	16.4	16.2	15.2
V		46.7	52.9	50.4	51.4	46.7	46.2	51.6	51.5	61.0	46.1	68.5	62.7	62.9	64.9	67.0	56.4	66.8	66.0	66.2	60.6
Cr		2425	3030	2749	2753	2235	2016	2694	2535	3393	2177	2823	2771	2352	2519	2651	2060	2835	2705	2825	2277

Appendix 2.2b cont'd

Sample	Kapsiki 7									
	opx15	opx14	opx17	opx23	opx21	opx4	opx22	opx24	opx12	opx5
Grains	Group I					Group II				
Th	0.018	0.024	0.010	0.022	0.021	0.010	0.007	0.005	0.005	0.007
U	0.009	0.011	0.006	0.009	0.008	0.007	0.007	0.006	0.006	0.006
Nb	0.009	0.011	0.006	0.009	0.008	0.007	0.006	0.006	0.007	0.007
La	0.015	0.058	0.013	0.016	0.020	0.010	0.010	0.007	0.008	0.009
Ce	0.020	0.063	0.020	0.028	0.026	0.014	0.010	0.009	0.009	0.010
Pb	0.001	0.002	0.001	0.001	0.001	0.001	0.000	–	0.001	–
Sr	0.32	0.75	0.17	0.45	0.31	0.19	0.12	0.07	0.07	0.12
Pr	0.002	0.006	0.002	0.004	0.003	0.002	0.001	0.001	0.001	0.001
Nd	0.013	0.027	0.012	0.018	0.014	0.011	0.003	0.004	0.004	0.004
Hf	0.015	0.017	0.012	0.015	0.016	0.012	0.011	0.008	0.009	0.012
Zr	0.303	0.420	0.237	0.314	0.323	0.259	0.24	0.21	0.22	0.25
Sm	0.007	0.011	0.006	0.007	0.008	0.005	0.003	0.003	0.002	0.003
Eu	0.003	0.005	0.002	0.004	0.003	0.003	0.001	0.002	0.001	0.002
Gd	0.012	0.019	0.012	0.013	0.011	0.011	0.006	0.006	0.004	0.006
Tb	0.003	0.004	0.002	0.003	0.002	0.003	0.002	0.002	0.002	0.002
Ti	288	292	263	289	298	291	300	275	288	300
Dy	0.022	0.027	0.021	0.025	0.023	0.020	0.016	0.018	0.017	0.015
Ho	0.006	0.008	0.005	0.006	0.006	0.006	0.005	0.006	0.005	0.005
Y	0.173	0.212	0.167	0.178	0.168	0.164	0.142	0.155	0.144	0.144
Er	0.024	0.027	0.024	0.025	0.023	0.023	0.020	0.023	0.019	0.020
Tm	0.005	0.006	0.004	0.005	0.005	0.005	0.004	0.004	0.004	0.004
Yb	0.046	0.053	0.047	0.050	0.048	0.046	0.039	0.043	0.043	0.040
Lu	0.010	0.010	0.010	0.010	0.010	0.010	0.008	0.008	0.009	0.008
Sc	17.1	18.3	16.8	17.6	17.7	16.6	16.2	15.0	15.4	16.4
V	71.5	73.5	65.1	70.6	72.4	68.0	69.5	64.8	68.4	71.8
Cr	3747	4038	2943	3442	3321	2863	2636	2555	2723	2947

Appendix 2.2c: Trace element composition of clinopyroxenes from Kapsiki

Sample Grains	Kapsiki 1										Kapsiki 2												
	cpx7	cpx10	cpx4	cpx5	cpx6	cpx2	cpx3	cpx8	cpx9		cpx1	cpx2	cpx3	cpx4	cpx5	cpx6	cpx7	cpx8	cpx9	cpx10	cpx11	cpx12	cpx13
	Group A		Group B			Group C																	
Rb	30.3	2.46	–	–	0.11	–	0.07	–	–	–	–	–	–	–	–	–	–	–	0.07	–	–	–	
Th	0.86	0.31	0.14	0.13	0.16	0.34	0.38	0.31	0.26	0.50	0.75	1.04	0.90	0.56	0.35	0.76	0.56	0.58	0.75	0.52	0.38	0.85	
U	0.24	0.09	0.03	0.03	0.04	0.09	0.12	0.08	0.06	0.27	0.35	0.44	0.41	0.30	0.23	0.37	0.30	0.31	0.38	0.29	0.24	0.39	
Ba	4.02	6.15	0.06	0.06	0.18	0.08	0.61	0.09	0.10	0.02	0.03	0.05	0.08	0.04	0.04	0.04	0.03	0.03	0.78	0.04	0.04	0.06	
Nb	5.63	2.19	0.22	0.19	0.21	0.03	0.03	0.03	0.06	0.07	0.06	0.07	0.06	0.05	0.07	0.05	0.05	0.05	0.08	0.05	0.05	0.05	
La	18.3	14.7	10.8	10.7	10.9	6.51	6.40	6.80	7.45	3.18	4.95	8.94	6.69	3.95	1.89	5.21	3.77	3.59	5.08	3.11	2.21	7.04	
Ce	42.2	36.2	24.7	24.2	24.4	12.5	11.0	12.5	14.4	3.99	5.69	9.68	7.23	4.35	2.68	6.00	4.21	4.06	5.26	3.59	2.91	6.65	
Pb	0.65	0.28	0.26	0.33	0.34	0.57	0.71	0.53	0.54	0.09	0.09	0.09	0.10	0.10	0.10	0.09	0.10	0.10	0.11	0.10	0.11	0.09	
Sr	275	367	467	462	456	366	349	379	407	53.8	59.0	71.7	65.1	55.5	52.6	58.3	53.7	55.6	60.6	56.0	51.1	68.4	
Pr	4.55	4.22	2.57	2.49	2.47	1.15	1.01	1.15	1.32	0.37	0.46	0.70	0.53	0.38	0.30	0.47	0.34	0.35	0.42	0.34	0.32	0.47	
Nd	15.1	14.0	7.82	7.41	7.27	3.62	3.91	3.66	4.07	1.42	1.46	1.89	1.56	1.40	1.38	1.53	1.34	1.52	1.44	1.51	1.38	1.49	
Hf	1.39	1.14	0.90	0.93	1.09	0.73	0.96	1.02	1.15	0.39	0.42	0.37	0.42	0.40	0.39	0.41	0.40	0.42	0.43	0.42	0.39	0.41	
Zr	39.9	31.3	16.6	16.2	20.5	16.1	24.8	21.9	22.6	9.70	10.1	9.59	9.69	10.23	9.99	9.82	9.93	9.67	9.56	10.1	10.2	9.59	
Sm	5.21	4.71	2.69	2.62	2.49	1.30	1.50	1.40	1.46	0.48	0.52	0.56	0.51	0.53	0.62	0.51	0.50	0.56	0.54	0.57	0.56	0.49	
Eu	1.69	1.24	0.54	0.54	0.52	0.32	0.40	0.35	0.35	0.19	0.21	0.18	0.20	0.20	0.25	0.20	0.20	0.21	0.19	0.23	0.20	0.18	
Gd	2.53	2.39	1.21	1.22	1.37	0.85	1.62	1.18	1.16	0.72	0.64	0.58	0.66	0.68	0.83	0.68	0.71	0.68	0.63	0.73	0.75	0.61	
Tb	0.36	0.33	0.19	0.16	0.18	0.13	0.23	0.18	0.15	0.11	0.12	0.10	0.10	0.12	0.12	0.12	0.12	0.11	0.10	0.12	0.12	0.11	
Ti	2941	2130	728	691	886	643	1345	1016	1011	782	829	784	793	840	802	789	831	806	789	858	829	797	
Dy	1.96	1.76	1.00	0.92	1.13	0.83	1.27	1.04	1.02	0.70	0.72	0.65	0.70	0.75	0.75	0.72	0.69	0.73	0.69	0.75	0.82	0.63	
Ho	0.30	0.32	0.18	0.17	0.19	0.16	0.23	0.21	0.18	0.13	0.14	0.14	0.14	0.15	0.15	0.14	0.14	0.15	0.14	0.16	0.16	0.14	
Y	8.18	7.57	4.42	4.41	4.65	3.92	5.53	4.78	4.51	3.62	3.60	3.34	3.50	3.81	3.77	3.45	3.69	3.77	3.49	3.98	4.10	3.49	
Er	0.84	0.74	0.47	0.45	0.52	0.47	0.53	0.53	0.54	0.38	0.36	0.38	0.38	0.41	0.39	0.38	0.37	0.35	0.39	0.40	0.41	0.38	
Tm	0.10	0.09	0.06	0.06	0.05	0.06	0.07	0.07	0.07	0.06	0.06	0.04	0.06	0.06	0.05	0.06	0.06	0.06	0.06	0.06	0.06	0.05	
Yb	0.64	0.50	0.37	0.39	0.43	0.42	0.46	0.45	0.40	0.39	0.42	0.33	0.36	0.48	0.46	0.40	0.40	0.43	0.40	0.43	0.49	0.40	
Lu	0.09	0.08	0.05	0.06	0.06	0.05	0.06	0.07	0.06	0.06	0.06	0.05	0.05	0.06	0.06	0.06	0.06	0.06	0.06	0.07	0.06	0.06	
Sc	125	97	142	127	125	142	80	105	98	84.2	98.1	97.6	89.9	90.7	77.2	81.0	91.6	78.9	86.0	84.2	72.0	90.1	
V	335	284	327	297	309	327	249	283	267	247	267	258	253	250	243	248	252	240	248	252	229	250	
Cr	11384	11599	12315	11138	11520	11589	11971	11829	11337	9936	9820	9904	9813	10286	10714	10077	10165	9819	10009	9904	10548	10091	

Appendix 2.2c cont'd

Sample	Kapsiki 7																
Grains	cpx1	cpx2	cpx3	cpx4	cpx5	cpx6	cpx7	cpx8	cpx9	cpx10	cpx11	cpx12	cpx13	cpx14	cpx15	cpx16	cpx17
Rb	–	–	0.01	–	0.03	0.02	0.00	0.02	–	–	0.00	–	0.01	0.03	0.01	–	0.10
Th	0.77	1.03	0.62	0.26	0.45	0.30	0.48	0.73	0.27	0.21	0.67	0.27	0.43	0.40	0.37	1.05	0.45
U	0.34	0.39	0.30	0.17	0.25	0.19	0.24	0.33	0.16	0.15	0.30	0.17	0.23	0.25	0.21	0.43	0.25
Ba	0.04	0.05	0.06	0.04	0.05	0.02	0.03	0.05	0.02	0.03	0.04	0.03	0.03	0.05	0.03	0.05	0.89
Nb	0.07	0.08	0.06	0.10	0.06	0.11	0.05	0.06	0.11	0.06	0.06	0.08	0.04	0.04	0.06	0.07	0.15
La	6.45	10.29	3.88	1.26	2.15	1.54	3.08	5.57	1.59	1.20	4.17	1.46	2.36	1.82	2.18	9.22	2.50
Ce	7.04	11.3	4.45	2.28	2.52	2.37	3.32	5.90	2.40	2.14	4.00	2.31	2.72	2.29	2.78	8.57	2.96
Pb	0.11	0.11	0.12	0.09	0.09	0.08	0.08	0.10	0.09	0.08	0.10	0.09	0.08	0.10	0.08	0.10	0.10
Sr	64.0	77.8	54.5	65.2	49.1	54.0	50.8	60.3	52.0	47.0	54.3	50.4	47.3	45.5	53.4	81.8	50.2
Pr	0.56	0.87	0.38	0.30	0.27	0.29	0.30	0.44	0.31	0.28	0.32	0.28	0.26	0.26	0.29	0.58	0.31
Nd	1.95	2.72	1.68	1.67	1.41	1.62	1.38	1.72	1.56	1.47	1.35	1.46	1.26	1.25	1.49	2.01	1.47
Hf	0.46	0.43	0.45	0.40	0.40	0.42	0.42	0.47	0.44	0.43	0.44	0.42	0.43	0.45	0.39	0.47	0.43
Zr	10.2	9.61	10.3	9.51	9.52	9.76	10.3	10.1	10.1	9.61	10.4	9.85	10.0	10.3	9.58	9.80	10.6
Sm	0.64	0.58	0.58	0.65	0.53	0.59	0.48	0.46	0.60	0.56	0.47	0.61	0.47	0.51	0.53	0.58	0.53
Eu	0.20	0.23	0.20	0.22	0.20	0.21	0.21	0.21	0.23	0.23	0.19	0.24	0.18	0.19	0.20	0.19	0.20
Gd	0.66	0.66	0.72	0.77	0.72	0.78	0.65	0.64	0.72	0.72	0.64	0.78	0.69	0.68	0.69	0.62	0.70
Tb	0.12	0.11	0.12	0.12	0.11	0.12	0.11	0.10	0.12	0.12	0.10	0.12	0.11	0.10	0.11	0.10	0.12
Ti	838	778	810	774	749	769	833	809	807	756	823	786	814	813	792	722	853
Dy	0.63	0.62	0.69	0.68	0.70	0.68	0.66	0.62	0.74	0.72	0.68	0.75	0.73	0.61	0.68	0.68	0.71
Ho	0.13	0.12	0.14	0.13	0.14	0.13	0.14	0.13	0.14	0.13	0.14	0.14	0.14	0.14	0.13	0.13	0.15
Y	3.37	3.18	3.45	3.29	3.42	3.38	3.57	3.29	3.62	3.52	3.45	3.52	3.55	3.55	3.46	3.41	3.75
Er	0.39	0.35	0.36	0.34	0.34	0.37	0.41	0.38	0.41	0.41	0.36	0.41	0.41	0.42	0.39	0.36	0.40
Tm	0.05	0.05	0.06	0.05	0.05	0.05	0.05	0.06	0.05	0.05	0.05	0.05	0.06	0.06	0.06	0.06	0.06
Yb	0.38	0.31	0.40	0.39	0.37	0.34	0.40	0.36	0.40	0.36	0.37	0.37	0.38	0.41	0.36	0.40	0.42
Lu	0.05	0.04	0.06	0.05	0.06	0.05	0.05	0.06	0.05	0.06	0.07	0.06	0.06	0.06	0.06	0.06	0.06
Sc	87.6	94.1	82.3	65.3	67.8	71.9	80.9	97.8	81.4	66.7	80.0	74.6	78.9	77.0	78.2	103	76.0
V	237	245	235	222	213	224	231	250	239	215	225	228	227	229	238	257	227
Cr	9842	9205	9552	12698	9409	9680	9704	9353	9108	9739	9744	9431	9419	9918	9537	10594	10938

Appendix 3.1a: Major element composition of clinopyroxenes from Ngaoundere Likok (N11 and N11a)

CPX Grains	NL1a																							
	Primary clinopyroxene																Secondary clinopyroxene							
	cpx1	cpx1	cpx4	cpx4	cpx6	cpx7	cpx8	cpx9	cpx10	cpx12	cpx15	cpx16	cpx17	cpx18	cpx20	cpx21	cpx22	cpx2	cpx9	cpx11	cpx13	cpx14	cpx19	cpx23
SiO ₂	52.86	52.45	52.60	52.27	52.58	51.90	52.48	52.24	52.10	51.41	52.21	52.25	51.48	52.02	52.04	50.57	51.99	52.63	52.26	51.20	51.35	52.00	51.49	52.47
TiO ₂	0.23	0.22	0.19	0.20	0.22	0.19	0.19	0.20	0.19	0.19	0.18	0.15	0.29	0.18	0.22	0.44	0.20	0.60	0.36	0.30	0.24	0.49	0.24	0.25
Al ₂ O ₃	6.04	6.08	6.08	5.88	6.03	6.16	5.83	5.03	6.18	5.90	6.02	5.72	5.15	5.99	4.23	5.80	5.08	3.20	3.75	3.92	3.84	3.39	3.48	3.48
Cr ₂ O ₃	0.77	0.77	0.77	0.75	0.75	0.81	0.75	0.78	0.80	0.78	0.77	0.71	0.81	0.83	0.72	0.75	0.76	1.03	0.80	0.92	0.96	1.02	0.80	0.70
Fe ₂ O ₃	0.59	0.72	0.27	0.96	0.76	1.93	1.64	1.94	2.05	2.80	1.92	1.50	2.12	2.09	1.60	1.88	0.00	0.78	1.24	2.65	2.29	1.04	2.59	0.00
FeO	2.08	1.98	2.40	1.85	1.95	0.75	1.01	0.86	0.64	0.04	0.80	1.10	0.79	0.62	1.09	0.94	2.59	2.18	1.61	0.21	0.49	1.91	0.41	2.41
MnO	0.09	0.09	0.10	0.09	0.10	0.10	0.09	0.10	0.08	0.09	0.10	0.11	0.08	0.07	0.07	0.05	0.09	0.08	0.09	0.09	0.08	0.08	0.09	0.07
NiO	0.07	0.04	0.03	0.03	0.01	0.01	0.05	0.06	0.01	0.04	0.09	0.04	0.09	0.10	0.09	0.08	0.04	0.10	0.02	0.02	0.06	0.06	0.07	0.07
MgO	15.24	15.00	14.87	14.79	14.95	14.93	15.11	15.60	15.09	14.96	15.03	15.08	15.86	15.12	16.65	15.88	15.55	16.68	16.83	16.40	16.38	16.66	16.64	16.16
CaO	20.91	21.08	20.93	21.04	21.00	21.14	21.11	21.85	21.08	21.22	21.10	21.19	21.59	21.07	22.66	22.80	21.75	22.20	21.86	23.20	22.85	21.66	23.06	22.77
Na ₂ O	1.56	1.52	1.56	1.59	1.60	1.65	1.68	1.26	1.69	1.64	1.68	1.58	1.06	1.64	0.53	0.49	0.80	0.63	0.67	0.47	0.54	0.66	0.43	0.49
K ₂ O	-	-	-	0.01	0.02	0.01	0.01	-	-	0.01	-	0.01	-	0.01	-	-	-	0.02	-	0.01	0.01	0.02	-	0.01
Total	100	100	100	99	100	100	100	100	100	99	100	99	99	100	100	100	99	100	99	99	99	99	99	99
Si	1.901	1.897	1.905	1.901	1.901	1.884	1.897	1.894	1.883	1.876	1.888	1.899	1.878	1.885	1.890	1.844	1.907	1.912	1.905	1.874	1.884	1.908	1.887	1.928
Ti	0.006	0.006	0.005	0.006	0.006	0.005	0.005	0.005	0.005	0.005	0.005	0.004	0.008	0.005	0.006	0.012	0.006	0.016	0.010	0.008	0.007	0.013	0.007	0.007
Al	0.256	0.259	0.260	0.252	0.257	0.264	0.248	0.215	0.263	0.254	0.257	0.245	0.222	0.256	0.181	0.249	0.220	0.137	0.161	0.169	0.166	0.147	0.150	0.151
Cr	0.022	0.022	0.022	0.022	0.021	0.023	0.021	0.022	0.023	0.023	0.022	0.020	0.024	0.024	0.021	0.022	0.022	0.030	0.023	0.027	0.028	0.030	0.023	0.020
Fe ³⁺	0.016	0.020	0.007	0.026	0.021	0.053	0.045	0.053	0.056	0.077	0.052	0.041	0.058	0.057	0.044	0.052	0.000	0.022	0.034	0.073	0.063	0.029	0.071	0.000
Fe ²⁺	0.063	0.060	0.073	0.056	0.059	0.023	0.030	0.026	0.019	0.001	0.024	0.033	0.024	0.019	0.033	0.029	0.079	0.066	0.049	0.006	0.015	0.059	0.013	0.074
Mn	0.003	0.003	0.003	0.003	0.003	0.003	0.003	0.003	0.003	0.003	0.003	0.003	0.003	0.002	0.002	0.002	0.003	0.002	0.003	0.003	0.003	0.003	0.003	0.002
Ni	0.002	0.001	0.001	0.001	0.000	0.000	0.001	0.002	0.000	0.001	0.003	0.001	0.003	0.003	0.003	0.002	0.001	0.003	0.001	0.001	0.002	0.002	0.002	0.002
Mg	0.817	0.809	0.803	0.802	0.806	0.808	0.814	0.843	0.813	0.814	0.810	0.817	0.862	0.816	0.901	0.863	0.850	0.903	0.914	0.895	0.896	0.911	0.909	0.885
Ca	0.806	0.817	0.812	0.820	0.814	0.822	0.817	0.849	0.816	0.830	0.818	0.825	0.844	0.818	0.882	0.891	0.855	0.864	0.854	0.910	0.898	0.852	0.905	0.896
Na	0.109	0.107	0.110	0.112	0.112	0.116	0.118	0.089	0.119	0.116	0.118	0.111	0.075	0.115	0.038	0.035	0.057	0.044	0.047	0.034	0.038	0.047	0.031	0.035
K	-	-	-	0.000	0.001	0.001	0.000	-	-	0.000	-	0.000	-	0.001	-	-	-	0.001	-	0.001	0.001	0.001	-	0.000
Total	4.000	4.000	4.000	4.000	4.000	4.000	4.000	4.000	4.000	4.000	4.000	4.000	4.000	4.000	4.000	4.000	4.000	4.000	4.000	4.000	4.000	4.000	4.000	4.000
Mg#	0.912	0.911	0.909	0.907	0.910	0.915	0.916	0.914	0.915	0.912	0.914	0.916	0.913	0.915	0.921	0.915	0.915	0.911	0.917	0.919	0.920	0.913	0.915	0.923
Cr#	0.078	0.079	0.078	0.079	0.077	0.081	0.079	0.094	0.080	0.082	0.080	0.077	0.096	0.085	0.103	0.080	0.091	0.178	0.125	0.136	0.144	0.168	0.133	0.119
Wo	0.473	0.478	0.478	0.480	0.478	0.481	0.478	0.479	0.478	0.481	0.479	0.480	0.471	0.478	0.474	0.485	0.478	0.465	0.461	0.482	0.479	0.460	0.476	0.483
En	0.479	0.474	0.473	0.470	0.473	0.473	0.476	0.475	0.476	0.472	0.474	0.475	0.481	0.477	0.484	0.470	0.476	0.486	0.493	0.474	0.478	0.492	0.478	0.476
Fs	0.048	0.048	0.049	0.050	0.048	0.046	0.045	0.046	0.046	0.047	0.047	0.045	0.047	0.045	0.042	0.045	0.046	0.049	0.046	0.044	0.043	0.048	0.046	0.041

Appendix 3.1a cont'd

CPX	NL1a																		
	Primary clinopyroxene																Secondary clinopyroxene		
	Grains	cpx 1	cpx 2	cpx 3	cpx 4	cpx 5	cpx 6	cpx 7	cpx 8	cpx 9	cpx 10	cpx 11	cpx 12	cpx 14	cpx 16	cpx 17	cpx 20	cpx2	cpx 19
SiO ₂	53.06	53.09	52.98	53.02	52.91	53.19	52.66	52.89	52.45	53.13	52.89	53.17	52.83	52.97	52.61	52.31		53.14	52.93
TiO ₂	0.18	0.18	0.20	0.22	0.24	0.23	0.22	0.24	0.28	0.22	0.23	0.22	0.23	0.20	0.27	0.34		0.19	0.23
Al ₂ O ₃	5.32	5.62	5.49	5.53	5.68	5.67	5.57	5.82	5.68	5.73	5.77	5.64	5.83	5.46	5.47	5.52		3.84	2.94
Cr ₂ O ₃	0.74	0.80	0.71	0.76	0.81	0.77	0.76	0.79	0.79	0.70	0.79	0.78	0.73	0.81	0.76	0.78		0.81	0.79
Fe ₂ O ₃	0.46	1.12	1.07	1.14	0.57	0.79	1.18	1.06	1.23	0.72	0.98	0.39	0.75	0.82	1.47	1.80		0.39	0.91
FeO	2.14	1.47	1.54	1.48	2.01	1.82	1.43	1.58	1.40	1.92	1.63	2.15	1.85	1.85	1.22	0.90		2.24	1.74
MnO	0.09	0.06	0.09	0.10	0.07	0.10	0.09	0.11	0.10	0.10	0.11	0.08	0.09	0.09	0.08	0.10		0.10	0.06
NiO	0.10	0.06	0.04	0.04	0.06	0.10	0.02	0.04	0.06	0.05	0.01	0.03	0.08	0.05	0.06	0.02		0.03	0.07
MgO	15.52	15.51	15.68	15.67	15.34	15.51	15.48	15.47	15.39	15.55	15.30	15.42	15.34	15.25	15.09	15.06		17.17	16.16
CaO	20.53	20.58	20.63	20.65	20.62	20.47	20.62	20.36	20.54	20.34	20.71	20.49	20.46	20.75	21.09	21.15		21.72	23.60
Na ₂ O	1.58	1.73	1.61	1.63	1.63	1.70	1.63	1.74	1.65	1.69	1.70	1.68	1.68	1.67	1.69	1.69		0.63	0.56
K ₂ O	–	0.01	0.01	0.01	–	0.02	0.02	0.01	0.01	0.02	0.01	–	0.01	0.01	0.01	0.02		0.01	–
Total	100	100	100	100	100	100	100	100	100	100	100	100	100	100	100	100		100	100
Si	1.920	1.910	1.910	1.908	1.911	1.912	1.906	1.905	1.901	1.912	1.906	1.917	1.908	1.914	1.905	1.897		1.919	1.927
Ti	0.005	0.005	0.005	0.006	0.006	0.006	0.006	0.007	0.008	0.006	0.006	0.006	0.006	0.005	0.007	0.009		0.005	0.006
Al	0.227	0.238	0.233	0.235	0.242	0.240	0.238	0.247	0.243	0.243	0.245	0.240	0.248	0.233	0.233	0.236		0.163	0.126
Cr	0.021	0.023	0.020	0.022	0.023	0.022	0.022	0.023	0.023	0.020	0.023	0.022	0.021	0.023	0.022	0.022		0.023	0.023
Fe ³⁺	0.013	0.030	0.029	0.031	0.016	0.021	0.032	0.029	0.034	0.020	0.027	0.011	0.020	0.022	0.040	0.049		0.011	0.025
Fe ²⁺	0.065	0.044	0.047	0.045	0.061	0.055	0.043	0.048	0.042	0.058	0.049	0.065	0.056	0.056	0.037	0.027		0.068	0.053
Mn	0.003	0.002	0.003	0.003	0.002	0.003	0.003	0.003	0.003	0.003	0.004	0.002	0.003	0.003	0.003	0.003		0.003	0.002
Ni	0.003	0.002	0.001	0.001	0.002	0.003	0.001	0.001	0.002	0.001	0.000	0.001	0.002	0.001	0.002	0.000		0.001	0.002
Mg	0.837	0.832	0.842	0.840	0.826	0.831	0.835	0.831	0.831	0.834	0.822	0.828	0.826	0.821	0.814	0.814		0.924	0.877
Ca	0.796	0.793	0.797	0.796	0.798	0.788	0.800	0.786	0.798	0.784	0.800	0.791	0.792	0.803	0.818	0.822		0.840	0.920
Na	0.111	0.121	0.113	0.114	0.114	0.118	0.114	0.122	0.116	0.118	0.119	0.117	0.118	0.117	0.119	0.119		0.044	0.039
K	–	0.000	0.000	0.001	–	0.001	0.001	0.000	0.000	0.001	0.000	–	0.000	0.000	0.001	0.001		0.000	–
Total	4.000	4.000	4.000	4.000	4.000	4.000	4.000	4.000	4.000	4.000	4.000	4.000	4.000	4.000	4.000	4.000		4.000	4.000
Mg#	0.915	0.918	0.918	0.918	0.915	0.916	0.917	0.916	0.916	0.915	0.916	0.916	0.916	0.913	0.914	0.914		0.922	0.918
Cr#	0.085	0.087	0.080	0.085	0.088	0.083	0.084	0.084	0.085	0.076	0.084	0.085	0.078	0.091	0.086	0.087		0.123	0.153
Wo	0.465	0.466	0.464	0.464	0.469	0.464	0.467	0.463	0.467	0.462	0.470	0.466	0.467	0.471	0.478	0.479		0.455	0.490
En	0.489	0.489	0.491	0.490	0.485	0.489	0.487	0.490	0.487	0.491	0.483	0.488	0.487	0.482	0.476	0.475		0.501	0.467
Fs	0.047	0.045	0.046	0.046	0.046	0.047	0.046	0.047	0.046	0.047	0.047	0.046	0.047	0.047	0.046	0.046		0.044	0.043

Appendix 3.1b: Major element composition secondary clinopyroxenes from Enep (En2a)

CPX	Secondary clinopyroxene En2a															
Grains	Cpx1	Cpx2	Cpx3	Cpx4	Cpx5	Cpx6	Cpx7	Cpx8	Cpx9	Cpx10	Cpx11	Cpx12	Cpx13	Cpx14	Cpx15	Cpx16
SiO ₂	48.2	50.8	48.7	48.3	49.7	51.4	49.7	49.3	51.4	49.1	49.3	53.7	49.8	49.6	49.3	47.8
TiO ₂	0.16	0.07	0.14	0.16	0.16	0.07	0.15	0.16	0.07	0.19	0.15	0.02	0.12	0.18	0.18	0.22
Al ₂ O ₃	8.61	4.83	8.07	8.34	7.40	4.94	7.77	7.75	5.17	8.11	7.85	4.53	7.45	7.59	7.88	9.13
Cr ₂ O ₃	3.84	2.82	3.25	3.73	3.49	2.32	2.98	3.24	2.72	3.11	3.41	1.47	3.59	3.51	3.66	3.41
Fe ₂ O ₃	0.56	0.19	0.30	0.87	0.40	0.35	0.74	1.08	0.07	0.81	0.72	1.20	0.93	0.62	0.46	1.55
FeO	1.80	1.79	1.86	1.45	2.14	1.93	1.68	1.40	2.08	1.51	1.57	1.22	1.56	1.83	1.94	0.93
MnO	0.07	0.06	0.07	0.07	0.10	0.07	0.07	0.09	0.07	0.06	0.07	0.10	0.11	0.08	0.10	0.07
NiO	0.07	0.11	0.09	0.07	0.09	0.04	0.09	0.07	0.06	0.06	0.06	0.04	0.03	0.05	0.07	0.05
MgO	12.9	15.1	13.2	13.1	14.5	15.8	14.2	14.3	15.7	14.0	14.2	15.0	14.6	14.7	14.3	13.1
CaO	22.4	22.4	22.8	22.7	20.6	21.7	22.1	21.5	21.7	22.0	21.6	21.5	21.4	20.9	21.2	22.6
Na ₂ O	0.88	0.69	0.78	0.83	1.07	0.77	0.88	0.97	0.76	0.86	0.94	1.83	0.96	0.98	0.95	0.87
K ₂ O	0.00	0.00	0.01	0.01	0.02	0.01	0.01	0.01	0.00	0.01	0.00	0.04	0.01	0.02	0.00	0.01
Total	99	99	99	100	100	99	100	100	100	100	100	101	101	100	100	100
Si	1.776	1.874	1.797	1.778	1.819	1.881	1.808	1.802	1.874	1.795	1.801	1.931	1.807	1.808	1.800	1.757
Ti	0.004	0.002	0.004	0.005	0.004	0.002	0.004	0.004	0.002	0.005	0.004	0.000	0.003	0.005	0.005	0.006
Al	0.374	0.210	0.351	0.362	0.319	0.213	0.333	0.334	0.222	0.350	0.338	0.192	0.319	0.326	0.339	0.395
Cr	0.112	0.082	0.095	0.109	0.101	0.067	0.086	0.094	0.078	0.090	0.099	0.042	0.103	0.101	0.106	0.099
Fe ³⁺	0.016	0.005	0.008	0.024	0.011	0.010	0.020	0.030	0.002	0.022	0.020	0.032	0.025	0.017	0.013	0.043
Fe ²⁺	0.056	0.055	0.057	0.045	0.066	0.059	0.051	0.043	0.063	0.046	0.048	0.037	0.047	0.056	0.059	0.029
Mn	0.002	0.002	0.002	0.002	0.003	0.002	0.002	0.003	0.002	0.002	0.002	0.003	0.003	0.003	0.003	0.002
Ni	0.002	0.003	0.003	0.002	0.003	0.001	0.003	0.002	0.002	0.002	0.002	0.001	0.001	0.001	0.002	0.001
Mg	0.710	0.832	0.726	0.717	0.790	0.858	0.769	0.780	0.854	0.765	0.774	0.803	0.792	0.799	0.779	0.716
Ca	0.885	0.884	0.901	0.897	0.807	0.852	0.861	0.841	0.847	0.862	0.846	0.829	0.831	0.814	0.827	0.890
Na	0.063	0.050	0.056	0.059	0.076	0.055	0.062	0.069	0.054	0.061	0.067	0.128	0.068	0.070	0.067	0.062
K	0.000	0.000	0.000	0.001	0.001	0.000	0.001	0.000	0.000	0.001	0.000	0.002	0.000	0.001	0.000	0.000
Total	4.000	4.000	4.000	4.000	4.000	4.000	4.000	4.000	4.000	4.000	4.000	4.000	4.000	4.000	4.000	4.000
Mg#	0.909	0.932	0.917	0.913	0.912	0.926	0.915	0.915	0.929	0.918	0.920	0.921	0.916	0.917	0.916	0.909
Cr#	0.230	0.281	0.213	0.231	0.240	0.240	0.205	0.219	0.261	0.205	0.226	0.179	0.244	0.237	0.238	0.200
Wo	0.531	0.497	0.532	0.532	0.481	0.478	0.505	0.496	0.479	0.508	0.501	0.486	0.489	0.482	0.492	0.530
En	0.426	0.468	0.428	0.426	0.471	0.482	0.451	0.460	0.483	0.451	0.458	0.471	0.466	0.473	0.463	0.426
Fs	0.044	0.035	0.040	0.042	0.048	0.040	0.043	0.044	0.038	0.042	0.041	0.042	0.045	0.044	0.045	0.044

Appendix 3.1b cont'd

CPX	Secondary clinopyroxene En2a																
	Grains	Cpx33	Cpx34	Cpx35	Cpx36	Cpx37	Cpx38	Cpx39	Cpx40	Cpx41	Cpx42	Cpx43	Cpx44	Cpx45	Cpx46	Cpx47	Cpx48
SiO ₂	48.7	47.7	51.0	48.2	51.6	48.7	51.9	49.5	48.7	51.7	48.3	48.5	49.9	48.2	50.5	48.4	49.8
TiO ₂	0.17	0.21	0.12	0.19	0.11	0.19	0.11	0.19	0.17	0.10	0.27	0.28	0.14	0.20	0.11	0.17	0.17
Al ₂ O ₃	8.59	8.83	5.34	9.02	4.62	8.70	4.57	7.83	8.27	4.81	8.67	8.66	6.94	8.78	6.34	8.58	7.38
Cr ₂ O ₃	3.01	3.78	2.70	3.51	2.19	3.16	2.29	3.25	3.07	2.20	3.47	3.33	3.29	3.62	2.37	3.52	2.81
Fe ₂ O ₃	1.08	1.02	0.00	1.10	0.28	1.06	0.32	0.84	2.14	1.03	1.63	1.46	1.19	1.72	1.43	1.02	1.93
FeO	1.40	1.38	2.18	1.22	1.83	1.31	1.99	1.65	0.31	1.26	0.88	1.09	1.10	0.73	0.96	1.51	0.61
MnO	0.07	0.07	0.06	0.09	0.07	0.09	0.08	0.10	0.07	0.07	0.07	0.07	0.10	0.08	0.09	0.09	0.07
NiO	0.07	0.06	0.10	0.06	0.07	0.01	0.10	0.09	0.03	0.07	0.05	0.08	0.07	0.09	0.08	0.03	0.09
MgO	13.6	13.2	15.2	13.6	15.3	13.9	16.3	14.3	13.9	16.2	13.5	13.7	14.6	13.5	15.5	13.6	15.1
CaO	22.2	21.9	22.1	21.9	22.7	21.7	21.3	21.6	22.7	22.0	22.5	22.1	21.8	22.7	22.0	22.0	21.9
Na ₂ O	0.91	0.92	0.72	0.89	0.73	0.95	0.79	0.94	0.87	0.72	0.87	0.94	0.96	0.84	0.76	0.83	0.86
K ₂ O	0.01	0.00	0.00	0.02	0.01	0.01	0.01	0.02	0.00	0.01	0.01	0.00	0.01	0.01	0.02	0.01	0.01
Total	100	99	100	100	100	100	100	100	100	100	100	100	100	100	100	100	101
Si	1.784	1.765	1.870	1.766	1.888	1.781	1.890	1.802	1.775	1.874	1.764	1.771	1.818	1.760	1.835	1.775	1.802
Ti	0.005	0.006	0.003	0.005	0.003	0.005	0.003	0.005	0.005	0.003	0.008	0.008	0.004	0.006	0.003	0.005	0.005
Al	0.371	0.385	0.231	0.390	0.199	0.375	0.196	0.336	0.355	0.206	0.373	0.373	0.298	0.378	0.271	0.371	0.315
Cr	0.087	0.111	0.078	0.102	0.063	0.091	0.066	0.094	0.089	0.063	0.100	0.096	0.095	0.104	0.068	0.102	0.081
Fe ³⁺	0.030	0.028	0.000	0.030	0.008	0.029	0.009	0.023	0.059	0.028	0.045	0.040	0.033	0.047	0.039	0.028	0.053
Fe ²⁺	0.043	0.043	0.067	0.038	0.056	0.040	0.061	0.050	0.010	0.038	0.027	0.033	0.034	0.022	0.029	0.046	0.019
Mn	0.002	0.002	0.002	0.003	0.002	0.003	0.003	0.003	0.002	0.002	0.002	0.002	0.003	0.003	0.003	0.003	0.002
Ni	0.002	0.002	0.003	0.002	0.002	0.000	0.003	0.003	0.001	0.002	0.002	0.002	0.002	0.003	0.003	0.001	0.003
Mg	0.742	0.725	0.828	0.742	0.835	0.758	0.884	0.777	0.756	0.878	0.736	0.744	0.794	0.732	0.840	0.745	0.812
Ca	0.870	0.868	0.868	0.859	0.891	0.850	0.831	0.840	0.888	0.854	0.881	0.864	0.852	0.887	0.855	0.865	0.849
Na	0.065	0.066	0.051	0.064	0.052	0.067	0.056	0.066	0.061	0.051	0.062	0.067	0.068	0.059	0.054	0.059	0.061
K	0.001	0.000	0.000	0.001	0.001	0.001	0.000	0.001	0.000	0.001	0.000	0.000	0.001	0.001	0.001	0.001	0.000
Total	4.000	4.000	4.000	4.000	4.000	4.000	4.000	4.000	4.000	4.000	4.000	4.000	4.000	4.000	4.000	4.000	4.000
Mg#	0.911	0.911	0.925	0.916	0.929	0.916	0.927	0.914	0.917	0.930	0.911	0.910	0.923	0.913	0.925	0.909	0.919
Cr#	0.190	0.223	0.253	0.207	0.241	0.196	0.252	0.218	0.199	0.235	0.212	0.205	0.241	0.217	0.201	0.216	0.204
Wo	0.516	0.521	0.492	0.514	0.497	0.506	0.465	0.496	0.518	0.474	0.521	0.513	0.497	0.524	0.484	0.513	0.489
En	0.440	0.435	0.469	0.444	0.466	0.451	0.495	0.459	0.441	0.488	0.435	0.442	0.463	0.433	0.476	0.441	0.468
Fs	0.044	0.044	0.039	0.042	0.037	0.043	0.040	0.045	0.041	0.038	0.044	0.045	0.040	0.043	0.040	0.046	0.042

Appendix 3.1c: Major element composition of clinopyroxene spongy rims from Wum (We1a)

CPX	Spongy rims We1a									
Grains	cpx6r2	cpx7r2	cpx8r2	cpx10r2	cpx14r2	cpx31r2	cpx32r2	cpx39r2	cpx43r2	cpx44r2
SiO ₂	50.3	52.7	52.2	51.5	52.1	51.6	51.5	51.9	50.7	51.2
TiO ₂	1.05	0.29	0.32	0.48	0.33	0.18	0.69	0.30	0.67	0.63
Al ₂ O ₃	6.15	5.79	3.91	6.12	5.74	5.16	7.28	5.52	7.09	7.29
Cr ₂ O ₃	0.91	1.09	1.29	1.10	1.05	1.11	0.94	1.16	1.10	1.08
Fe ₂ O ₃	0.57	0.00	1.37	0.54	0.91	0.00	0.17	1.06	1.54	0.84
FeO	2.81	3.46	2.04	2.49	2.42	3.29	3.32	1.93	1.53	2.17
MnO	0.09	0.11	0.10	0.07	0.09	0.10	0.11	0.09	0.08	0.07
NiO	0.04	0.04	0.05	0.08	0.09	0.05	0.05	0.03	0.10	0.06
MgO	14.7	15.7	16.0	15.4	16.0	16.0	14.5	15.8	15.6	15.0
CaO	22.7	21.0	23.0	21.8	21.0	20.4	19.8	22.1	21.2	20.9
Na ₂ O	0.62	1.03	0.54	0.87	1.00	0.80	1.60	0.84	0.97	1.30
K ₂ O	0.01	0.00	0.01	0.00	0.01	0.00	0.00	0.01	0.02	0.00
Total	100	101	101	100	101	99	100	101	101	100
Si	1.840	1.891	1.890	1.864	1.877	1.897	1.866	1.873	1.829	1.847
Ti	0.029	0.008	0.009	0.013	0.009	0.005	0.019	0.008	0.018	0.017
Al	0.265	0.245	0.167	0.261	0.244	0.224	0.311	0.235	0.302	0.310
Cr	0.026	0.031	0.037	0.031	0.030	0.032	0.027	0.033	0.031	0.031
Fe ³⁺	0.016	0.000	0.037	0.015	0.025	0.000	0.005	0.029	0.042	0.023
Fe ²⁺	0.086	0.104	0.062	0.076	0.073	0.101	0.101	0.058	0.046	0.066
Mn	0.003	0.003	0.003	0.002	0.003	0.003	0.003	0.003	0.003	0.002
Ni	0.001	0.001	0.001	0.002	0.003	0.002	0.002	0.001	0.003	0.002
Mg	0.801	0.838	0.862	0.829	0.856	0.878	0.784	0.848	0.838	0.805
Ca	0.889	0.807	0.894	0.845	0.811	0.802	0.771	0.854	0.820	0.807
Na	0.044	0.072	0.038	0.061	0.070	0.057	0.113	0.059	0.068	0.091
K	0.001	0.000	0.000	0.000	0.000	0.000	0.000	0.000	0.001	0.000
Total	4.000	4.000	4.000	4.000	4.000	4.000	4.000	4.000	4.000	4.000
Mg#	0.887	0.890	0.897	0.902	0.898	0.897	0.882	0.907	0.905	0.901
Cr#	0.091	0.112	0.181	0.107	0.109	0.126	0.080	0.124	0.094	0.090
Wo	0.495	0.461	0.481	0.478	0.459	0.450	0.463	0.477	0.469	0.474
En	0.446	0.478	0.464	0.469	0.484	0.492	0.471	0.473	0.479	0.473
Fs	0.058	0.061	0.055	0.052	0.057	0.058	0.065	0.050	0.052	0.053

Appendix 3.1d: Major element composition of clinopyroxene spongy rims from Kuk (K1)

CPX	Spongy rims K1																		
	Grains	cpx2r2	cpx3r2	cpx8r2	cpx9r2	cpx13r2	cpx14r2	cpx15r2	cpx17r2	cpx20r2	cpx21r2	cpx22r2	cpx23r2	cpx24r2	cpx25r2	cpx26r2	cpx28r2	cpx33r2	cpx36r2
SiO ₂	51.6	51.3	51.1	51.2	51.1	51.6	51.5	51.2	51.0	51.0	51.8	50.0	51.0	51.2	50.9	50.8	50.5	51.0	50.5
TiO ₂	0.49	0.44	0.49	0.47	0.53	0.46	0.44	0.46	0.46	0.48	0.47	0.51	0.57	0.47	0.59	0.48	0.45	0.45	0.54
Al ₂ O ₃	6.34	4.64	4.83	4.65	6.02	6.39	4.86	5.15	5.16	6.73	4.45	5.98	5.25	5.11	5.02	5.21	5.20	4.44	4.43
Cr ₂ O ₃	0.72	0.81	0.79	0.76	0.92	0.81	0.77	0.76	0.85	0.74	0.86	1.19	0.93	0.89	0.95	0.89	0.90	0.87	0.91
Fe ₂ O ₃	1.88	1.47	1.75	1.48	1.62	0.80	1.15	1.02	1.21	1.08	1.13	1.03	0.60	0.87	1.02	1.19	2.37	2.07	2.96
FeO	1.55	2.08	2.00	2.01	1.88	2.50	2.04	2.30	2.16	2.30	2.20	2.04	2.53	2.29	2.38	2.08	1.15	1.51	0.58
MnO	0.09	0.10	0.11	0.10	0.11	0.13	0.09	0.11	0.09	0.09	0.12	0.10	0.10	0.11	0.13	0.08	0.09	0.10	0.10
NiO	0.06	0.03	0.08	0.03	0.05	0.08	0.07	0.11	0.05	0.06	0.05	0.05	0.07	0.09	0.08	0.08	0.05	0.05	0.06
MgO	15.2	17.0	17.0	16.8	16.1	15.7	16.5	16.5	16.3	15.0	17.5	16.2	16.6	16.7	17.3	16.5	16.8	16.8	16.9
CaO	20.3	21.0	20.8	21.1	20.3	19.9	21.6	21.2	21.6	19.6	20.6	21.1	20.8	21.1	20.2	21.3	21.4	21.4	21.5
Na ₂ O	1.56	0.52	0.51	0.55	1.01	1.28	0.57	0.54	0.50	1.53	0.51	0.47	0.54	0.50	0.48	0.50	0.47	0.49	0.52
K ₂ O	0.00	0.01	0.01	0.00	0.01	0.00	0.00	0.01	0.00	0.00	0.01	0.00	0.01	0.01	0.00	0.00	0.00	0.00	0.00
Total	99.8	99.3	99.4	99.2	99.6	99.6	99.5	99.4	99.5	98.7	99.7	98.7	99.0	99.4	99.0	99.1	99.3	99.2	99.0
Si	1.870	1.875	1.865	1.875	1.857	1.873	1.877	1.871	1.865	1.870	1.882	1.841	1.869	1.870	1.865	1.862	1.847	1.868	1.854
Ti	0.014	0.012	0.014	0.013	0.014	0.013	0.012	0.013	0.013	0.013	0.013	0.014	0.016	0.013	0.016	0.013	0.012	0.012	0.015
Al	0.271	0.200	0.208	0.201	0.258	0.274	0.209	0.222	0.222	0.291	0.191	0.259	0.227	0.220	0.217	0.225	0.224	0.192	0.192
Cr	0.021	0.024	0.023	0.022	0.026	0.023	0.022	0.022	0.025	0.022	0.025	0.035	0.027	0.026	0.028	0.026	0.026	0.025	0.026
Fe ³⁺	0.051	0.040	0.048	0.041	0.044	0.022	0.032	0.028	0.033	0.030	0.031	0.029	0.017	0.024	0.028	0.033	0.065	0.057	0.082
Fe ²⁺	0.047	0.064	0.061	0.061	0.057	0.076	0.062	0.070	0.066	0.070	0.067	0.063	0.078	0.070	0.073	0.064	0.035	0.046	0.018
Mn	0.003	0.003	0.003	0.003	0.003	0.004	0.003	0.003	0.003	0.003	0.004	0.003	0.003	0.003	0.004	0.003	0.003	0.003	0.003
Ni	0.002	0.001	0.002	0.001	0.002	0.002	0.002	0.003	0.002	0.002	0.001	0.001	0.002	0.003	0.002	0.002	0.001	0.001	0.002
Mg	0.823	0.923	0.927	0.917	0.873	0.850	0.898	0.899	0.890	0.820	0.948	0.891	0.908	0.911	0.942	0.899	0.915	0.919	0.926
Ca	0.790	0.822	0.812	0.828	0.792	0.773	0.843	0.830	0.847	0.771	0.802	0.830	0.815	0.825	0.792	0.838	0.839	0.841	0.847
Na	0.110	0.037	0.036	0.039	0.071	0.090	0.040	0.039	0.035	0.109	0.036	0.034	0.039	0.036	0.034	0.035	0.033	0.035	0.037
K	0.000	0.000	0.000	0.000	0.001	0.000	0.000	0.000	0.000	0.000	0.000	0.000	0.000	0.000	0.000	0.000	0.000	0.000	0.000
Total	4.000	4.000	4.000	4.000	4.000	4.000	4.000	4.000	4.000	4.000	4.000	4.000	4.000	4.000	4.000	4.000	4.000	4.000	4.000
Mg#	0.893	0.899	0.895	0.900	0.896	0.897	0.906	0.901	0.900	0.891	0.906	0.907	0.906	0.906	0.903	0.903	0.901	0.899	0.903
Cr#	0.070	0.105	0.099	0.099	0.093	0.078	0.096	0.090	0.100	0.069	0.115	0.117	0.106	0.105	0.113	0.103	0.104	0.116	0.121
Wo	0.461	0.444	0.439	0.447	0.447	0.448	0.459	0.453	0.461	0.455	0.433	0.457	0.448	0.450	0.431	0.456	0.452	0.451	0.452
En	0.480	0.498	0.501	0.496	0.493	0.493	0.489	0.491	0.484	0.484	0.512	0.491	0.499	0.497	0.512	0.490	0.493	0.492	0.494
Fs	0.059	0.058	0.061	0.057	0.059	0.059	0.052	0.056	0.056	0.061	0.055	0.052	0.053	0.053	0.057	0.054	0.056	0.057	0.055

Appendix 3.2a: Trace element composition of clinopyroxenes from Ngaoundere Likok (N11 and N11a)

CPX Grains	N11								
	cpx1	cpx2	cpx3	cpx5	cpx6	cpx7	cpx8	cpx9	cpx10
Rb	3.53	–	3.58	1.42	3.80	3.94	0.01	–	0.02
Th	0.66	0.97	0.95	1.26	0.76	1.27	0.93	0.91	0.91
U	0.29	0.30	0.29	0.24	0.21	0.38	0.29	0.28	0.28
Ba	8.72	0.07	1.54	6.07	87.86	64.53	0.07	0.09	0.09
Nb	5.38	0.22	1.07	2.14	5.52	6.61	0.22	0.24	0.24
Ta	0.26	0.02	0.06	0.08	0.28	0.29	0.01	0.02	0.02
La	2.64	3.71	3.85	4.11	9.16	9.72	3.70	3.71	3.74
Ce	6.52	7.99	8.55	8.71	19.6	19.0	7.88	7.91	7.98
Pb	0.20	0.31	0.24	0.21	0.25	0.29	0.31	0.27	0.29
Sr	28.6	50.7	45.3	28.9	336	258	53.3	51.6	52.0
Pr	0.94	0.99	1.09	1.09	2.26	1.98	0.98	0.99	1.00
Nd	4.74	4.45	5.02	4.97	9.49	7.61	4.35	4.63	4.55
Hf	2.54	0.65	1.21	1.11	2.15	2.47	0.70	0.78	0.71
Zr	93.1	37.8	81.8	76.1	112	112	42.5	59.1	56.0
Sm	1.68	1.39	1.62	1.54	2.31	1.89	1.38	1.44	1.46
Eu	0.62	0.54	0.60	0.62	1.73	1.86	0.55	0.55	0.54
Gd	2.14	1.83	2.11	1.95	2.58	2.18	1.82	1.81	1.79
Tb	0.36	0.34	0.36	0.35	0.43	0.38	0.33	0.33	0.32
Ti	2276	1483	1458	1374	1991	1423	1628	1248	1293
Dy	2.54	2.36	2.61	2.53	2.92	2.54	2.43	2.20	2.32
Ho	0.53	0.52	0.56	0.54	0.61	0.55	0.51	0.50	0.51
Y	13.8	13.1	14.2	14.0	16.2	14.4	13.4	12.9	12.9
Er	1.58	1.48	1.67	1.61	1.83	1.57	1.52	1.51	1.48
Tm	0.22	0.21	0.23	0.22	0.26	0.23	0.22	0.21	0.21
Yb	1.57	1.45	1.60	1.58	1.81	1.54	1.44	1.39	1.40
Lu	0.21	0.21	0.22	0.22	0.24	0.23	0.21	0.21	0.21
Sc	69.9	69.8	72.3	73.9	69.7	66.1	70.8	69.7	69.0
V	249	240	232	247	242	225	249	237	236
Cr	5111	4953	5294	5444	5002	4618	5108	4788	4943

Appendix 3.2a cont'd

CPX Grains	NL1a																			
	cpx1	cpx1 2	cpx1 3	cpx1 4	cpx 1	cpx 2	cpx3	cpx4	cpx5	cpx6	cpx7	cpx8	cpx9	cpx10	cpx11	cpx12	cpx13	cpx14	cpx15	cpx16
Rb	1.67	7.17	0.01	–	–	–	–	–	–	1.63	0.58	–	0.16	–	–	0.68	0.03	4.85	0.60	0.02
Th	0.62	1.22	0.98	0.98	0.92	0.96	0.88	0.96	0.95	1.03	0.90	0.93	0.93	0.92	0.91	0.89	0.80	1.24	0.31	0.09
U	0.15	0.37	0.31	0.32	0.28	0.31	0.28	0.30	0.30	0.33	0.29	0.29	0.30	0.30	0.29	0.28	0.24	0.20	0.07	0.02
Ba	71.8	67.5	0.08	0.08	0.06	0.08	0.07	0.08	0.07	21.6	0.10	0.07	2.02	0.07	0.07	0.24	10.4	52.3	4.02	0.11
Nb	1.81	4.40	0.29	0.31	0.25	0.26	0.26	0.32	0.27	0.86	0.57	0.30	0.85	0.24	0.30	0.35	0.86	8.65	0.80	0.45
Ta	0.11	0.21	0.03	0.04	0.03	0.03	0.02	0.04	0.03	0.06	0.05	0.04	0.05	0.03	0.04	0.05	0.11	0.69	0.09	0.05
La	7.19	6.14	3.87	3.98	3.85	3.96	3.82	3.90	3.86	3.99	3.75	3.78	3.58	3.82	3.86	3.79	3.96	5.87	3.46	1.47
Ce	15.0	11.7	8.34	8.44	8.24	8.34	8.20	8.22	8.24	8.13	7.90	7.92	7.69	7.83	7.86	7.96	8.09	12.4	8.44	4.62
Pb	0.24	0.32	0.29	0.28	0.27	0.28	0.30	0.28	0.28	0.36	0.29	0.26	0.27	0.29	0.28	0.31	0.28	0.44	0.06	0.02
Sr	333	265	51.1	51.8	51.5	52.2	55.2	52.9	52.6	85.4	52.0	50.9	46.9	52.7	53.1	53.3	63.8	187	69.8	22.0
Pr	1.75	1.30	1.04	1.06	1.05	1.04	1.02	1.03	1.02	0.99	0.94	0.99	0.95	0.94	0.97	0.97	0.98	1.50	1.12	0.74
Nd	6.87	5.52	4.72	4.90	4.72	4.63	4.47	4.78	4.66	4.27	4.22	4.48	4.44	4.26	4.47	4.58	4.66	6.37	5.22	4.08
Hf	1.48	1.73	0.81	0.74	0.98	0.81	0.64	0.82	0.76	1.22	1.37	1.07	0.91	1.20	1.18	2.10	3.26	3.26	1.31	1.14
Zr	95.2	109	64.4	65.5	69.6	64.8	41.6	73.5	66.2	44.9	43.9	77.6	62.8	57.7	87.1	97.0	117	148	88.5	52.0
Sm	1.81	1.56	1.41	1.53	1.47	1.47	1.36	1.51	1.47	1.33	1.28	1.44	1.47	1.36	1.50	1.52	1.43	1.87	1.64	1.62
Eu	1.72	1.06	0.55	0.57	0.56	0.58	0.54	0.58	0.56	0.54	0.51	0.55	0.55	0.54	0.57	0.58	0.57	0.76	0.61	0.62
Gd	2.01	1.95	1.88	1.84	1.85	1.88	1.85	1.99	1.84	1.81	1.78	1.85	1.96	1.93	1.92	1.89	1.85	2.29	2.04	2.27
Tb	0.36	0.33	0.34	0.34	0.33	0.35	0.34	0.36	0.34	0.34	0.34	0.33	0.36	0.34	0.35	0.33	0.34	0.41	0.38	0.40
Ti	1342	1166	1302	1371	1206	1269	1589	1438	1271	1589	1449	1204	1803	1447	1196	1103	991	2477	1711	3105
Dy	2.39	2.22	2.30	2.31	2.31	2.42	2.38	2.40	2.38	2.40	2.38	2.31	2.45	2.48	2.42	2.34	2.26	2.84	2.56	2.83
Ho	0.50	0.47	0.49	0.50	0.51	0.51	0.52	0.52	0.53	0.52	0.53	0.49	0.55	0.54	0.50	0.50	0.50	0.57	0.55	0.61
Y	12.9	12.4	12.8	13.0	13.0	13.4	13.3	13.5	13.3	13.4	13.5	12.9	14.0	13.9	13.4	13.0	12.8	15.5	14.2	15.0
Er	1.42	1.39	1.47	1.51	1.50	1.56	1.53	1.52	1.51	1.54	1.55	1.46	1.54	1.59	1.49	1.52	1.46	1.77	1.60	1.77
Tm	0.20	0.20	0.20	0.21	0.21	0.22	0.21	0.22	0.22	0.22	0.22	0.21	0.21	0.23	0.21	0.21	0.20	0.25	0.23	0.24
Yb	1.40	1.44	1.44	1.48	1.43	1.50	1.46	1.55	1.51	1.54	1.48	1.46	1.49	1.51	1.53	1.53	1.43	1.72	1.60	1.62
Lu	0.22	0.19	0.21	0.21	0.21	0.22	0.20	0.21	0.21	0.20	0.21	0.21	0.22	0.22	0.22	0.21	0.21	0.24	0.23	0.23
Sc	69.0	62.9	67.7	70.9	67.4	69.4	74.1	72.3	71.0	67.0	68.9	67.3	70.3	69.2	68.9	66.2	68.1	68.5	76.6	89.9
V	229	211	268	241	225	234	244	245	237	240	238	222	240	239	228	214	204	233	243	301
Cr	3914	4414	12126	5573	4950	5387	4281	5482	5064	4771	4663	5197	4973	5027	5291	4605	4205	4148	5879	5341

Appendix 3.2b: Trace element composition of secondary clinopyroxenes from Enep (En2a)

CPX	Secondary Clinopyroxene En2a																			
Grains	Cpx1	Cpx2	Cpx4	Cpx5	Cpx6	Cpx7	Cpx8	Cpx9	Cpx10	Cpx11	Cpx12	Cpx13	Cpx14	Cpx15	Cpx16	Cpx17	Cpx18	Cpx19	Cpx20	Cpx21
Rb	0.01	bdl	0.05	0.02	0.06	bdl	0.38	bdl	bdl	0.03	1.28	0.04	bdl	0.03	bdl	0.01	0.02	bdl	0.01	bdl
Th	0.17	0.31	0.25	0.14	0.85	0.26	0.72	0.36	0.28	0.33	0.82	0.41	0.24	0.32	0.29	0.28	0.46	0.23	0.28	0.33
U	0.02	0.03	0.03	0.01	0.12	0.03	0.10	0.04	0.03	0.04	0.16	0.04	0.02	0.03	0.03	0.03	0.05	0.03	0.02	0.03
Ba	0.10	0.08	0.18	0.21	1.04	0.09	2.54	0.08	0.07	0.17	8.95	0.35	0.06	0.21	0.06	0.07	0.28	0.05	0.13	0.15
Nb	1.47	2.61	2.68	1.74	11.7	3.10	13.9	3.67	2.74	4.54	15.9	5.40	3.47	4.43	3.99	3.94	7.07	3.50	3.85	4.97
Ta	0.33	0.72	0.70	0.48	1.88	1.14	2.37	1.23	0.91	1.76	2.65	1.06	1.39	1.74	1.65	1.67	2.65	1.48	1.58	1.87
La	3.04	4.92	4.00	2.81	5.33	4.19	5.46	4.57	3.74	4.65	5.34	4.27	4.12	4.53	4.37	3.74	4.44	3.66	3.64	3.83
Ce	7.87	12.6	10.4	7.26	11.9	10.7	12.7	11.4	9.49	11.9	11.8	10.2	10.3	11.3	10.9	9.36	10.9	9.00	9.17	9.38
Pb	0.06	0.09	0.04	0.03	0.51	0.15	0.81	0.15	0.09	0.05	0.24	0.48	0.03	0.03	0.05	0.03	0.12	0.03	0.28	0.38
Sr	7.62	9.96	9.20	8.53	10.3	9.21	10.6	8.62	9.26	9.80	13.65	9.48	9.83	10.2	9.54	8.71	9.54	9.25	8.85	8.48
Pr	1.02	1.56	1.32	0.99	1.45	1.38	1.62	1.47	1.25	1.52	1.45	1.29	1.30	1.42	1.40	1.21	1.41	1.15	1.20	1.21
Nd	4.20	6.27	5.36	4.08	5.61	5.55	6.54	5.95	5.10	6.23	5.89	5.37	5.48	5.77	5.76	5.07	5.92	4.81	5.17	5.19
Hf	5.60	7.78	8.55	10.6	7.80	10.0	13.0	9.92	9.69	13.8	14.0	11.5	14.6	16.2	15.8	14.0	17.9	13.5	12.8	13.4
Zr	140	202	186	188	205	225	282	228	214	267	274	224	240	269	256	245	290	233	235	267
Sm	0.98	1.41	1.20	0.97	1.22	1.30	1.47	1.37	1.18	1.44	1.32	1.25	1.27	1.32	1.32	1.17	1.36	1.08	1.17	1.18
Eu	0.28	0.42	0.33	0.29	0.33	0.37	0.42	0.41	0.32	0.41	0.39	0.37	0.35	0.39	0.37	0.33	0.39	0.34	0.35	0.35
Gd	0.85	1.19	1.05	0.87	1.06	1.11	1.19	1.18	1.03	1.23	1.07	1.09	1.13	1.10	1.09	1.01	1.17	0.99	1.06	1.07
Tb	0.15	0.21	0.17	0.16	0.18	0.20	0.21	0.22	0.18	0.21	0.19	0.19	0.19	0.20	0.20	0.18	0.20	0.17	0.17	0.18
Ti	889	1354	1113	736	1190	1392	1630	1463	1196	1441	1370	894	1114	1103	1157	1100	1289	1129	1155	1114
Dy	1.06	1.41	1.19	1.01	1.23	1.32	1.47	1.46	1.25	1.48	1.30	1.26	1.27	1.33	1.35	1.22	1.37	1.15	1.22	1.19
Ho	0.25	0.32	0.26	0.22	0.29	0.29	0.33	0.32	0.27	0.31	0.29	0.28	0.28	0.28	0.29	0.25	0.30	0.25	0.26	0.27
Y	6.30	8.60	7.25	5.98	7.75	8.06	8.80	8.78	7.42	8.63	7.93	7.51	7.60	7.60	7.93	7.20	8.07	6.86	6.98	7.31
Er	0.73	1.06	0.82	0.67	0.85	0.97	1.04	1.06	0.86	1.00	0.95	0.86	0.94	0.93	0.90	0.88	0.94	0.83	0.84	0.86
Tm	0.12	0.16	0.13	0.10	0.15	0.15	0.17	0.17	0.14	0.16	0.14	0.14	0.14	0.14	0.14	0.13	0.14	0.12	0.13	0.13
Yb	0.85	1.19	1.05	0.80	1.05	1.08	1.20	1.30	0.98	1.25	1.08	1.00	1.04	1.01	1.12	0.98	1.12	0.97	1.01	0.94
Lu	0.13	0.18	0.15	0.11	0.16	0.16	0.17	0.20	0.15	0.17	0.16	0.15	0.15	0.14	0.16	0.15	0.16	0.14	0.14	0.15
SC	201	206	172	191	165	194	200	198	185	202	195	196	211	189	206	178	198	210	194	186
V	329	477	513	282	616	543	490	688	526	610	506	303	543	366	579	516	539	564	390	388
Cr	16885	20750	20947	19548	16641	22019	23420	23536	17734	21982	22759	20715	22819	20881	20807	23280	22394	21709	24211	21653

Declaration of consent

on the basis of Article 18 of the PromR Phil.-nat. 19

Name/First Name: Siggie Signe, Nformidah-Ndah

Registration Number: 17-133-141

Study program: Earth Sciences

Bachelor Master Dissertation

Title of the thesis: Evolution of the sub-continental lithospheric mantle below a major tectono-volcanic structure: constraints from mantle xenoliths along the Cameroon Volcanic Line

Supervisor: Prof. Jörg Hermann

I declare herewith that this thesis is my own work and that I have not used any sources other than those stated. I have indicated the adoption of quotations as well as thoughts taken from other authors as such in the thesis. I am aware that the Senate pursuant to Article 36 paragraph 1 litera r of the University Act of September 5th, 1996 and Article 69 of the University Statute of June 7th, 2011 is authorized to revoke the doctoral degree awarded on the basis of this thesis. For the purposes of evaluation and verification of compliance with the declaration of originality and the regulations governing plagiarism, I hereby grant the University of Bern the right to process my personal data and to perform the acts of use this requires, in particular, to reproduce the written thesis and to store it permanently in a database, and to use said database, or to make said database available, to enable comparison with theses submitted by others.

Signature

Place/Date: Bern, 6 November, 2021